THE UNIVERSITY
of ADELAIDE

Explicit dynamics finite element modelling of defective rolling element bearings

Sarabjeet Singh

Faculty of Engineering, Computer and Mathematical Sciences

School of Mechanical Engineering

The University of Adelaide

South Australia 5005

Australia

A thesis submitted in fulfilment of the requirements for the degree of

Doctor of Philosophy in Mechanical Engineering

on 16 July 2014. Qualified on 11 November 2014.

Explicit dynamics finite element modelling of defective rolling element bearings

Doctoral thesis

Acoustics, Vibration and Control Group

School of Mechanical Engineering

The University of Adelaide

South Australia 5005 Australia

Printed in Australia.

Abstract

Rolling element bearings are widely used in rotating machinery across various industries and their failure is a dominant factor that contributes to machinery breakdown, consequently causing significant economic losses. Numerous experimental and analytical studies have been conducted in the past to understand the vibration response of non-defective and defective rolling element bearings, which have localised, extended, and distributed defects. Previous models have focused on simulating the defect-related impulses, which are generally observed in practice in measured vibration signals, and they implement envelope analysis to predict the significant defect-related frequency components.

The work presented in this thesis is focused on developing an understanding of the underlying physical mechanism by which defect-related impulses are generated in defective rolling element bearings. A novel explicit dynamics finite element (FE) model of a rolling element bearing having a localised outer raceway defect, line spall, was developed and solved using a commercially available FE software package, LS-DYNA. In addition to simulating the vibration response of the bearing, the dynamic contact interaction between the rolling elements and raceways of the bearing were modelled. An in-depth investigation of the rolling element-to-raceway contact forces was undertaken and variations in the forces, as the rolling elements traverse through the defect, were analysed. The contact force analysis has also led to the development of an understanding of the physics behind the low- and high-frequency characteristic vibration signatures generated by the rolling elements as they enter and exit a defect.

It was found that no impulse-like signals are generated during the gradual de-stressing or unloading of the rolling elements as they enter into a defect, which explains the low-frequency characteristics of the de-stressing event. In contrast, a burst of multiple, short-duration, force impulses is generated as the rolling elements re-stress between the raceways in the vicinity of the end of a defect, which explains the high-frequency impulsive characteristics of the re-stressing event. Based on the results of the FE analysis of the rolling element bearing, a mathematical model was developed to predict the gradual de-stressing of the rolling elements as they enter into a raceway defect.

Experimental testing on a rolling element bearing, commonly used in the railway industry, and having a line spall machined on its outer raceway was undertaken. The numerically modelled vibration response obtained using the FE model of the rolling element bearing was compared with the experimentally measured data, and a favourable agreement between the modelled and measured results was achieved. Numerical rolling element-to-raceway contact forces were compared with corresponding analytical results calculated using a quasi-static load distribution analytical model presented in this thesis.

A parametric study to investigate the effects of varying radial load and rotational speed on the vibration response of the bearing and rolling element-to-raceway contact forces was undertaken. It was found that the magnitude of the defect-related vibration impulses and contact forces generated during the re-stressing of the rolling elements increases with increasing load and speed.

The modelled contact forces were correlated with bearing vibration signals, and it was found that the amplitude of the contact forces and acceleration produced during the re-stressing of the rolling elements is much greater than when the rolling elements strike the defective surface. In other words, although a rolling element can impact the surface of a defect and generate a low amplitude acceleration signal, a much higher acceleration signal is generated when the rolling elements are re-stressed between the raceways as they exit from the defect. These higher acceleration signals, generated

during the re-stressing phase, are the ones that are generally observed in practice, and subsequently used for bearing diagnosis.

The work presented in this thesis has provided definitive physical and quantitative explanations for the impulsive acceleration signals measured when a bearing element passes through a defect.

This page intentionally contains only this sentence.

Statement of Originality

I certify that this work contains no material which has been accepted for the award of any other degree or diploma in my name, in any university or other tertiary institution and, to the best of my knowledge and belief, contains no material previously published or written by another person, except where due reference has been made in the text. In addition, I certify that no part of this work will, in the future, be used in a submission in my name, for any other degree or diploma in any university or other tertiary institution without the prior approval of the University of Adelaide and where applicable, any partner institution responsible for the joint-award of this degree.

I give consent to this copy of my thesis, when deposited in the University Library, being made available for loan and photocopying, subject to the provisions of the Copyright Act 1968.

I also give permission for the digital version of my thesis to be made available on the web, via the University's digital research repository, the Library Search and also through web search engines, unless permission has been granted by the University to restrict access for a period of time.

Sarabjeet Singh

Date: 11 November 2014

This page intentionally contains only this sentence.

Acknowledgements

I would like to acknowledge the efforts of all the people who have contributed towards the work in this thesis. I would like to thank my supervisors Dr Carl Howard and Emeritus Professor Dr Colin Hansen, and external supervisors from Track IQ^{TM}, Dr Uwe Köpke and Dr David Rennison, for their guidance and support. I acknowledge the support of Track IQ^{TM} who provided extensive project facilities and funding. I am especially thankful to Dr David Rennison for providing me with additional funding without which it is unlikely that this thesis would have been possible. I am extremely grateful to Emeritus Professor Dr Colin Hansen and Dr Carl Howard, who also supervised me during my Master's (by research) degree, for proof reading this thesis during their extremely busy times. Thanks to Dr Michael Kidner of Vipac Engineers and Scientists Ltd. for many useful discussions on the subject. Thanks to William Bevan for his help with the test rigs used in the experiments. Thanks also to Billy Constantine for his help with the use of supercomputers for the simulations. I also acknowledge the University of Adelaide for providing an APA scholarship, and Australian Research Council for supporting this project.

I would like to thank my parents S. Jagmehar Singh and S. Pawinder Kaur for their support to get me where I am today. Thanks also to my siblings, Arvinder and Gurwinder, for their support.

Most of all, I would like to thank my wife, Lovleen, and our three-year old daughter, Ujjalman, for their endless support and encouragement during the pursuit of my studies. I do sometimes regret spending very less time with my family, especially with

my daughter, during my studies, and I hope to make up for the elapsed time! Special thanks to Lovleen and my parents for taking care of me when I accidentally squashed my right-hand thumb in the test rig during the experimentation work. Working with one hand for three months was tough!

Finally, thanks to the staff at Track IQ^{TM} and Vipac for sharing many laughs: Greg Huxtable, Jason Hollis, Robert Hudd, Andrew Meyer, Steve Lewis, Alan Wood, Alex Cowley, and Michael Foo.

Contents

List of Figures

List of Tables

This page intentionally contains only this sentence.

Nomenclature

Roman Symbols

a_y	acceleration of a node within the FE model of the rolling element bearing in the global cartesian y-direction
b	half-contact width at the interface of two contacting isotropic elastic solid bodies
$b^{'}$, $b^{''}$	extremeties of contact width $2b$ at the rolling element-to-raceway contact interfaces within a rolling element bearing
b_x, b_y	half-contact width at the rolling element-to-outer raceway contact interfaces within a rolling element bearing in the global cartesian x- and y-directions, respectively
B	bending stiffness of a plate / the outer ring of the FE model of the rolling element bearing
c	local material sound speed
c_b	velocity of bending waves
D_c	outer diameter of the cage within the FE model of the rolling element bearing
D_i	diameter of the inner raceway of a rolling element bearing
D_o	diameter of the outer raceway of a rolling element bearing
D_p	bearing pitch diameter
D_r	diameter of the rolling elements within a rolling element bearing
$E^{'}$	equivalent modulus of elasticity of two contacting isotropic elastic solid bodies
E_1, E_2	modulus of elasticity of isotropic elastic solid bodies '1' and '2'
F	Hertzian contact force at the interface of two isotropic elastic solid bodies
f_{bpi}	inner raceway defect frequency or ball pass frequency inner raceway

f_{bpo}	outer raceway defect frequency or ball pass frequency outer raceway
f_c	cage (rotational) frequency
$F_{dj(\text{grad})}$	gradual variation in the contact forces at the rolling element-to-raceway contact interfaces within a defective rolling element bearing
F_{dj}	contact force at a jth rolling element-to-raceway contact interface within a defective rolling element bearing
F_{dx}	horizontal rolling element-to-raceway contact force for a defective rolling element bearing in the global cartesian x-direction
F_{dy}	vertical rolling element-to-raceway contact force for a defective rolling element bearing in the global cartesian y-direction
f^i_{noise}	rolling element-to-inner raceway rolling contact noise frequency
f^{i-o}_{noise}	beating noise frequency
F_j	contact force at a jth rolling element-to-raceway contact interface within a non-defective rolling element bearing
$F_{\max}$	maximum force at a rolling element-to-raceway contact interface within a rolling element bearing along the load line (y-axis)
f^o_{noise}	rolling element-to-outer raceway rolling contact noise frequency
f_{rc}	ring frequency of a cylindrical shell
f_s	shaft rotational (run speed) frequency
F_x	horizontal rolling element-to-raceway contact force for a non-defective rolling element bearing in the global cartesian x-direction
F_y	vertical rolling element-to-raceway contact force for a non-defective rolling element bearing in the global cartesian y-direction
H_a	height of the adapter within the FE model of the rolling element bearing
h_c	thickness of the cage within the FE model of the rolling element bearing
H_d	depth (height) of the outer raceway defect within a rolling element bearing
h_i	thickness of the inner ring within the FE model of the rolling element bearing
h_o	thickness of the outer ring within the FE model of the rolling element bearing
I	impulsive force

i	imaginary unit ($= \sqrt{-1}$)
j	rolling element
K	contact stiffness at the interface of two isotropic elastic solid bodies
k_{zm}	modal wavenumbers
k_{cs}	contact or spring stiffness at the interface of two contacting segments in an FE model
K_{dj}	stiffness at a jth rolling element-to-raceway contact interface within a defective rolling element bearing
l	length of two contacting isotropic elastic solid bodies
L_{10}	life of a rolling element bearing
L_d	length of a localised raceway defect
L_e	length of an extended defect
l_{fe}	smallest characteristic dimension of an element within an FE model
l_r	length of the rolling elements within a bearing
m	axial mode numbers
m_1, m_2	masses of two segments in contact within an FE model
n	circumferential mode numbers
N_r	number of rolling elements within a bearing
n_s	rotational speed of a rolling element bearing
N_w	window length
$o^{'}$	initial point of contact between two non-conformal isotropic elastic solid bodies
$P_{\max}$	maximum pressure at the interface of two contacting isotropic elastic solid bodies
Q	quality factor of a second-order notch filter
r_c	mean radius of a cylindrical shell
$R_d^{'}$	curvature difference of two contacting isotropic elastic solid bodies
$R^{'}$	curvature sum of two contacting isotropic elastic solid bodies

R_x	equivalent radius of curvature of two contacting isotropic elastic solid bodies in the global cartesian x-direction
R_z	equivalent radius of curvature of two contacting isotropic elastic solid bodies in the global cartesian z-direction
S_d	profile of the outer raceway defect within a rolling element bearing
T	time period of defect-related impulses
t	time vector
u_y	displacement of a node within the FE model of the rolling element bearing in the global cartesian y-direction
V	stressed volume of the bearing material
v_y	velocity of a node within the FE model of the rolling element bearing in the global cartesian y-direction
W	radial (vertical) load in the global cartesian y-direction
w_a	width of the adapter within the FE model of the rolling element bearing
$x(t)$	time-varying signal
$\hat{x}\,(t)$	analytic signal
Z	number of cycles of repeated (stress) loading within a rolling element bearing
z_0	depth at which maximum stress at the rolling element-to-raceway contact interfaces occurs

Greek Symbols

α	contact angle within a rolling element bearing
β_j	a factor for introducing gradual changes at the entry and exit edges of a defect within a rolling element bearing
δ_1, δ_2	deformation of isotropic solid elastic bodies '1' and '2'
δ	total deformation at the contact interface of two isotropic elastic solid bodies
δ_{dj}	total contact deformation at a jth rolling element-to-raceway contact interface within a defective rolling element bearing
δ_i	displacement of the inner ring of a rolling element bearing
δ_j	displacement at a jth rolling element-to-raceway contact interface within a rolling element bearing

$\delta_{\max}$	maximum displacement at the rolling element-to-raceway contact interface within a rolling element bearing along the load line (y-axis)
δ_o	displacement of the outer ring of a rolling element bearing
δ_x, δ_y	deformation at the rolling element-to-outer raceway contact interfaces within a rolling element bearing in the global cartesian x- and y-directions, respectively
ϵ	load distribution factor for a rolling element bearing
γ_j	a factor that zeros the load distribution outside the load zone within a rolling element bearing
κ	Weibull slope for the experimental life of a rolling element bearing
λ_b	bending wavelength
μ	coefficient of friction between mating bearing components in the FE model of the bearing
ω_{mn}	natural frequencies of the outer ring of the FE model of the rolling element bearing
ν_1, ν_2	Poisson's ratio of isotropic elastic solid bodies '1' and '2'
$\Delta\Omega$	band width of a second-order notch filter
ω_c	angular velocity of the cage or rolling elements within a bearing
Ω_o	notch frequency of a second-order notch filter
ω_s	angular velocity of the shaft on which a rolling element bearing is installed
ψ_0	initial angular position of the cage within a rolling element bearing
ψ_c	angular position of the cage within a rolling element bearing
$\Delta\psi_{\text{cw}}$	angular extent of contact width $2b$ at the rolling element-to-raceway contact interfaces within a rolling element bearing
$\Delta\psi_d$	angular extent of the outer raceway defect within a rolling element bearing
ψ_d	centre of the outer raceway defect within a rolling element bearing
ψ_j	angular position of a jth rolling element
$\psi_l^{'}$	half-angular extent of the bearing load zone centred at ψ_{lc}
ψ_{lc}	centre of the bearing load zone

ρ	material density
$\Delta t_{\text{critical}}$	critical time step for the explicit time integration scheme used in LS-DYNA
Δt_{event}	time difference between the consecutive de-stressing or re-stressing events
Δt_{stable}	stable time step used in LS-DYNA
θ_r	angular spacing between the rolling elements within a bearing
Υ	probability of survival of a rolling element bearing
ε_0	maximum orthogonal shear stress in the rolling element-to-raceway contact interfaces
ς	diametral clearance within a rolling element bearing
ζ	damping ratio

Miscellaneous Symbols

$\mathscr{D}$	Dirac delta function
$\mathscr{F}$	Fourier transform
$\mathscr{H}$	Hilbert transform
$\mathscr{K}$	spectral kurtosis
$\mathscr{S}$	short-time Fourier transform

Superscripts

i	inner raceway
$i-o$	inner-to-outer raceway
n	exponent — $n = 3/2$ for point, circular and elliptical contacts, and $n = 10/9$ for line and rectangular contacts
o	outer raceway

Subscripts

1, 2	isotropic elastic solid bodies ‘1’ and ‘2’
b	bending waves
bpi	ball pass inner raceway
bpo	ball pass outer raceway
c	cage for retaining the rolling elements within a bearing

cw	contact width
d	defective rolling element bearing
e	extended defect
fe	finite element
i	inner raceway
j	rolling element
lc	centre of the load zone
max	maximum
o	outer raceway
p	bearing pitch
rc	cylindrical shell
s	shaft
x	global cartesian x-direction
y	global cartesian y-direction
z	global cartesian z-direction

Abbreviations

2-D	two-dimensional
3-D	three-dimensional
AAR	Association of American Railroads
ABMA	American Bearing Manufacturers Association, Inc.
ADINA	Automatic Dynamic Incremental Nonlinear Analysis
ADORE	Advanced Dynamics of Rolling Elements
ANSI	American National Standards Institute, Inc.
BEAST	Bearing Simulation Tool
BEAT	BEAring Toolbox
BPFI	ball pass frequency inner raceway
BPFO	ball pass frequency outer raceway

COBRA	Computer Optimized Ball and Roller Bearing Analysis software
CW	clockwise
CWRU	Case Western Reserve University
DOF	degree-of-freedom
EHL	elasto-hydrodynamic lubrication
EPW	elements-per-wavelength
FE	finite element
FFT	Fast Fourier Transform
IBDAS	Integrated Bearing Dynamic Analysis System
ISO	International Organization for Standardization
PSD	Power Spectral Density
RailBAM®	Railway Bearing Acoustic Monitor
RMS	root mean square
RPM	revolutions per minute
SFM	scale factor on default master penalty stiffness
SFS	scale factor on default slave penalty stiffness
SK	spectral kurtosis
SLSFAC	scale factor for sliding interface penalties
STFT	short-time Fourier transform
TADS®	Trackside Acoustic Detection System
Track IQ™	Trackside Intelligence Pty. Ltd.
TTCI®	Transportation Technology Center, Inc.

Chapter 1

Introduction

1.1 Introduction and significance

Rolling element bearings, also referred to as *anti-friction* bearings [1], are widely used in rotating machinery across various industries that include aerospace, construction, mining, steel, paper, textile, railways, and renewable energy [2, 3]. The damage and failure of rolling element bearings is a dominant factor that contributes to machinery breakdown, consequently causing significant economic losses and even loss of human lives in certain situations; for example, when an aircraft engine fails or a train derails due to a bearing seizure.

The work presented in this thesis is concerned with research to further enhance automated failure diagnosis of rolling element bearings used in the railway industry — the wheel or axle bearings in railway vehicles that include locomotives, freight wagons, and passenger coaches. One of the primary aims of this research is to develop an understanding of the underlying physical mechanism by which defect-related impulses are generated in defective rolling element bearings. This has been accomplished by developing a novel explicit dynamics finite element (FE) model of a rolling element bearing having a localised outer raceway defect, and analysing the *dynamic* contact interaction of the rolling elements and raceways as the rolling elements traverse through the defect.

Such an analysis has not been previously presented in the literature, although *static* analysis that includes investigating static rolling element-to-raceway contact forces and contact stresses within rolling element bearings has been studied in the past; relevant literature will be reviewed in Chapter 2. The dynamic rolling element-to-raceway contact interaction as the rolling elements within a bearing traverse through a localised raceway defect has recently been published [4, 5] by the author of this thesis and in references [6, 7] based on the work described here.

The ever increasing demand for high speed passenger trains and higher load capacity for freight wagons, for example, in mining applications, mandates efficient maintenance practices if potential losses to the rolling stock and railway infrastructure are to be avoided. A number of automated condition-based monitoring systems for assessing the health of rolling stock (wheels, axles, bearings, bogie, couplers, and brake systems) and railway tracks are currently available [8, 9]. Such systems are generally installed adjacent to railway tracks, and are commonly known as *trackside* or *wayside* detection systems. A wayside detection system associated with the condition-based (acoustic) monitoring of wheel or axle rolling element bearings in railway vehicles is known as a *bearing acoustic monitor*. Two commercially available bearing acoustic monitoring systems are Railway Bearing Acoustic Monitor (RailBAM®) [10] by Trackside Intelligence Pty. Ltd. (Track IQ™) [11] and Trackside Acoustic Detection System (TADS®) [12] by Transportation Technology Center, Inc. (TTCI®) [13]. Neither of these systems can distinguish between defects of various sizes. The motivation of this research is to be able to determine the size of a defect using a bearing acoustic monitoring system. However, the first step is to understand the vibration characteristics of defects of various sizes. The explicit dynamics FE model of a rolling element bearing, which is an outcome of this thesis, can be used as a tool to investigate the differences in the vibration characteristics of various defect sizes. The work presented here is concerned with the analysis of rolling element-to-raceway contact interaction and understanding the fundamental mechanism by which defect-related impulses are generated in bearings.

Figure 1.1: A photo of the RailBAM® system [10] showing the wayside cabinets along with a few sensors (courtesy: Track IQ™ [11]).

Figure 1.2: A photo of the TADS® system [12] showing the wayside cabinets (courtesy: TTCI® [13]).

1.1.1 A wayside bearing acoustic monitor

A wayside bearing acoustic monitor operates on the principle of acquiring and analysing the vibro-acoustic signals of axle bearings of a passing train. The signals are acquired using an array of microphones located at a suitable distance, typically about three metres, from the centreline of a railway track [8, 14–16]. The microphone arrays are generally housed in protective cabinets. Photos of the wayside cabinets of RailBAM® [10] and TADS® [12] systems are shown in Figures 1.1 and 1.2, respectively. All the components of the systems, such as sensors, cables, conduits, and protective enclosures, are appropriately located so they do not interfere with the components of a travelling train.

It is well-known that when a defective (spalled) component, either a rolling element, an outer raceway or inner raceway, within an operating bearing interacts with its corresponding mating components, either defective or non-defective, abrupt changes in the contact stresses occur [17]. These changes excite the bearing structure and encompassing structural components connected to the bearing, resulting in the generation of vibrations and consequently acoustic signals, which can be monitored to detect the presence of a defect using appropriate condition-based (vibration and acoustic) diagnostic techniques [17–31].

In the case of a typical railway freight wagon or bogie, the structural components may include an adapter, a side-frame, a wheel, and an axle [32, Chapter 3, pages 67–71] (refer to Figure 1.6; the features and components of a typical railway freight bogie will be discussed in Section 1.1.3). The vibrations induced by a bearing defect propagate through the structural components, and subsequently radiate as sound that may be detected by the microphone arrays of a wayside bearing acoustic monitor [10, 12].

In addition to the vibro-acoustic signals originating from the axle bearings of a railway vehicle, acoustic signals are also generated due to the interaction of the rotating wheels on the supporting rails (commonly referred to as *wheel–rail rolling noise*) [33–50], and other mechanical and structural sources, such as traction motors, brakes, couplers, and bogie components [51]. Suitable signal processing techniques can be used to extract the bearing signals from the extraneous noise, and the diagnostics can be carried out to detect defective bearings [17–31]. The diagnostic data are generally stored in a database [52, 53] that can be queried to compare the condition of a bearing over repeated passes; that is, the database enables the trending of parameters related to the progression of a defect [8, 14–16].

1.1.2 A typical railway axle bearing

The most common bearing configuration used in the railway industry is referred to as a *package bearing unit*, and a representation is shown in Figure 1.3a. It comprises an outer ring (commonly known as a *cup*), a pair of inner rings (commonly known as *cones*), a pair of multiple tapered rolling elements retained in respective cages, and a spacer separating the inner rings. All these components are assembled and held intact by pressing sealing caps (also known as grease seals) on both ends. The components of a package bearing unit in a disassembled condition are shown in Figure 1.3b.

The location of bearings on axle–wheelsets can be either external or internal to a wheel with respect to the field side of a rail — it is the face of the rail that points away from the track; refer to Figure 1.4 for a clear representation of the field and gauge sides. The external and internal bearing locations are more commonly known as *outboard* and *inboard*, respectively. Figure 1.4 shows a schematic of railway axle–wheelsets depicting outboard and inboard bearings, both indicated by circular markers.

The current study will focus exclusively on the fault diagnosis of outboard package bearing units used in railway vehicles.

1.1.3 Outboard bearings for freight and passenger vehicles

Figure 1.5a shows a photo of an outboard package bearing unit mounted onto an axle of a typical three-piece bogie [32, Chapter 3, page 70] of a railway freight wagon; a sectional view of the bearing is shown in Figure 1.5b.

Generically, a three-piece bogie comprises two side-frames and a bolster. A schematic of a three-piece bogie is shown in Figure 1.6. The side-frames rest on the axle bearings of the wheelsets through the adapters that interface with the bearings: the adapters are sandwiched between the side-frames and bearings. The bolster is supported by the side-frames, and contains a centre pivot that couples the bogie to the vehicle body. The schematic of a three-piece bogie in Figure 1.6 highlights the side-frames, bolster,

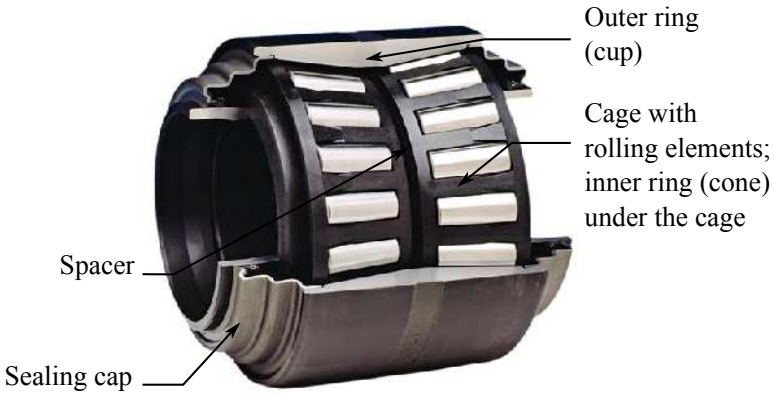

(a) An assembled package bearing unit showing various components.

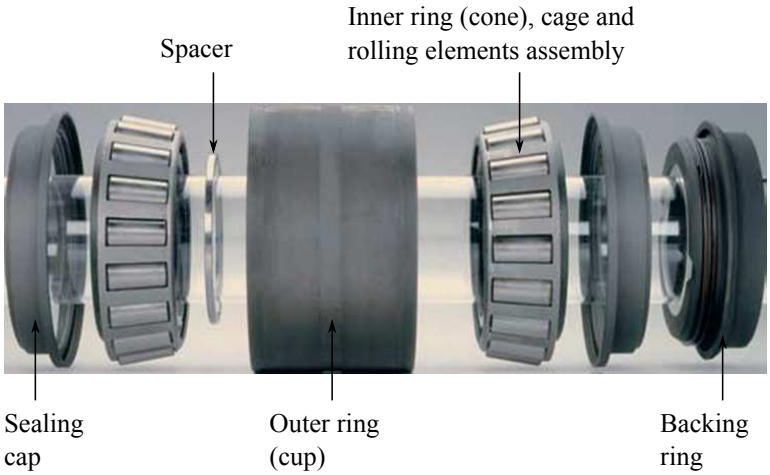

(b) A disassembled package bearing unit.

Figure 1.3: A package bearing unit (courtesy: The Timken Company [54]).

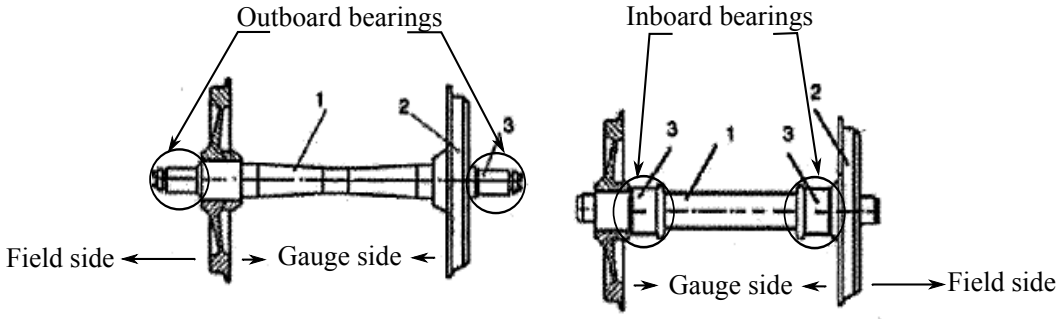

Figure 1.4: Schematics of axle–wheelsets highlighting the location of outboard and inboard bearings using circular markers [32, Chapter 3, page 41].

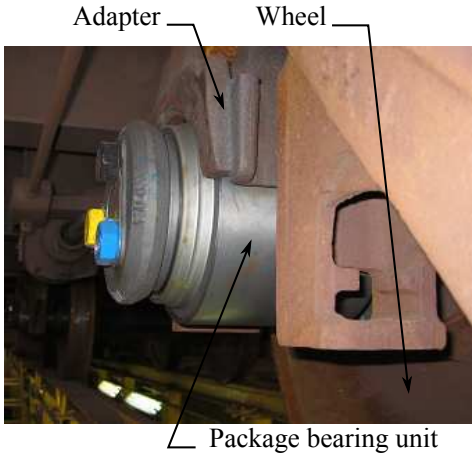

(a) A package bearing unit mounted onto the axle of a railway freight wagon.

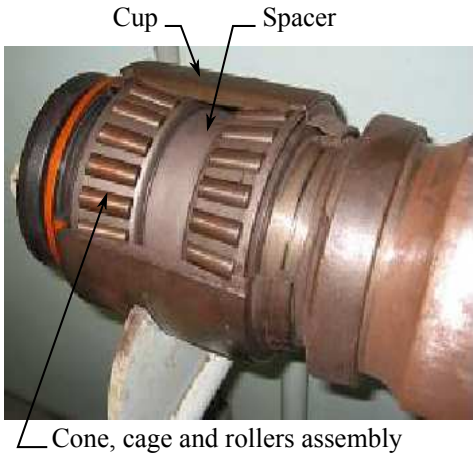

(b) A sectional view of the package bearing unit shown in Figure 1.5a.

Figure 1.5: An outboard configuration of a package bearing unit on a railway freight vehicle (courtesy: Track IQ^{TM} [11]).

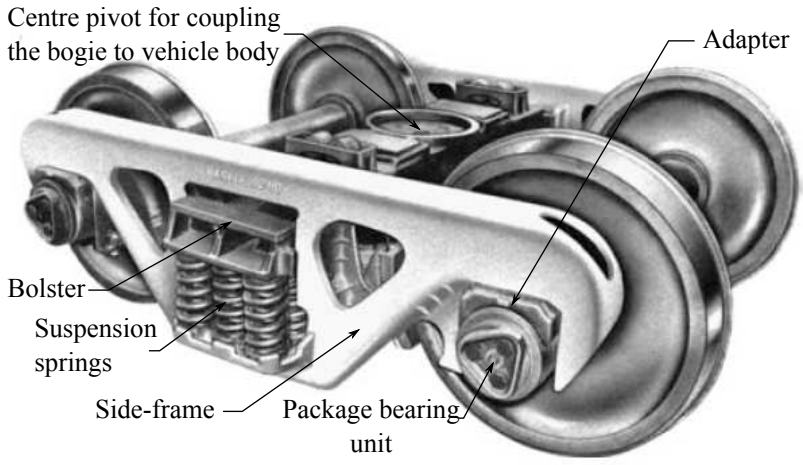

Figure 1.6: A three-piece bogie for railway freight vehicles [32, Chapter 3, page 70].

axle bearings, and adapter. The construction of a three-piece bogie is such that the majority of the outer ring (cup) of a bearing is visible to a wayside (field side) observer; refer to Figure 1.4 for the definition of the field side.

As can be seen in Figures 1.5 and 1.6, the axle bearings are not encapsulated in a housing; however, partial encapsulation may be considered due to the interface of the adapters with the bearings. Due to their outboard location, a direct line of sight is achieved between the bearings and an array of microphones within a bearing acoustic monitor installed next to the railway tracks. Thus, the bearing acoustic monitors can measure the acoustic signatures from the outboard bearings in a typical railway freight wagon (bogie) with no physical obstruction, and can provide a reliable detection and classification of bearing defects [8, 14–16].

In many railway passenger vehicles though, package bearing units can be encapsulated in the structural components associated with the suspension systems of the vehicles. Partial views of two different passenger vehicle bogies highlighting the encapsulation of the bearings are shown in Figures 1.7a and 1.7b. The figures, respectively, show a trailing arm and casing, which incorporate the bearings, are connected to the vehicle body through coil springs. The construction of passenger coaches is more complicated than freight wagons as they incorporate suspension systems that are directly connected to the bearings (for the purpose of minimising the transmission of vibrations to on board passengers) [32, Chapter 3, page 66]. Although the bearings in passenger coaches are outboard, their encapsulation, encompassing structural components and their mechanical connections can result in the dissipation of defect-related vibro-acoustic energy. This can eventually lead to compromising the performance of the bearing acoustic monitors.

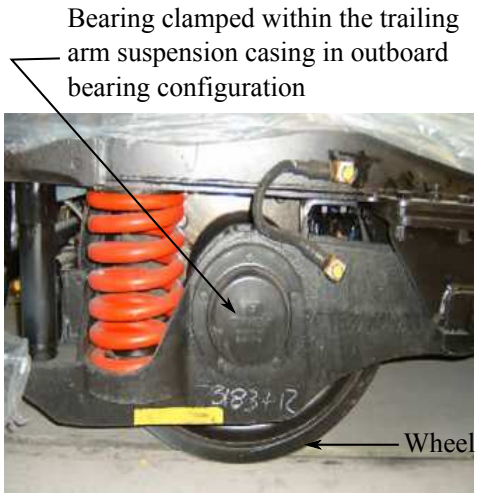

(a) A trailing arm suspension system that incorporates a bearing is connected to a railway passenger vehicle.

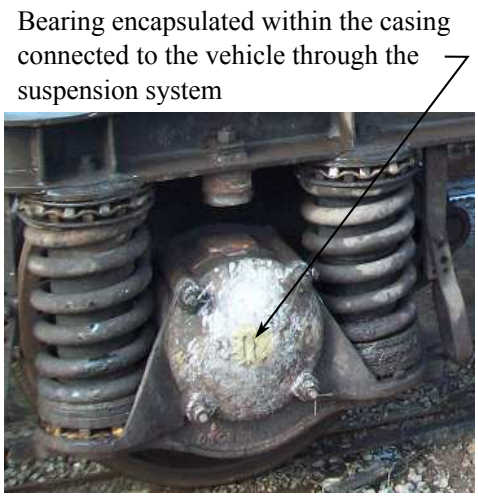

(b) A casing of a suspension system that encapsulates a bearing is connected to a railway passenger vehicle.

Figure 1.7: An outboard configuration of a package bearing unit on a railway passenger vehicle (courtesy: Track IQ^{TM} [11]).

1.2 Motivation

Prototype bearing acoustic monitors were tested in the 1980s [55–58]. The technology underlying the wayside bearing acoustic monitoring systems has improved considerably since then due to advances across the areas of sensors, signal processing methods, and condition-based monitoring techniques applicable to rolling element bearings [17–31]. Bearing acoustic monitors not only seek to identify the defective components within a bearing, but also seek to rank the severity of the defects [8, 14–16].

It is estimated that a total of approximately a hundred wayside bearing acoustic monitoring systems have been installed throughout the world — sixty RailBAM® [10] and thirty-eight TADS® [12] systems. Realising the proven and successful detection and diagnostic capabilities of bearing acoustic monitors, many railways are incorporating their use into their maintenance and scheduling practices; however, in addition to the detection of defective bearings, the current focus is to also provide a reliable prognosis of the bearing defects, which is an evolving subject [23, 29, 31, 59–63]. It would involve the detection and flagging of those defective bearings within a rolling

stock that represent a high operational risk, so as to enable railway operators and/or owners to plan necessary actions in order to prevent potential damages.

Generally, a prognosis involves the use of past and current condition of machinery to predict its future condition with an ultimate aim to using the machinery within a safe buffer period; thereby, avoiding catastrophic failures. The useful life of rolling element bearings can be extended considerably beyond the occurrence of the first spall [31]; therefore, achieving the maximum life of even defective bearings can result in substantial operational and maintenance cost reductions.

The considerable interest in accurate and reliable prognosis of defective rolling element bearings in the railway industry provides motivation for the current study.

1.2.1 Need

Railway operators either develop their own maintenance practices and schedules for inspecting the axle bearings or follow the industry guidelines; for example, those set by the Association of American Railroads (AAR) [64]. Due to the progressively increasing percentage of the wayside bearing acoustic monitors used in the industry, AAR, in year 2009, defined condemnable limits for the removal of defective bearings from service [65]. One of the components of these limits is that a bearing is deemed to represent a high operational risk if the total spalled area (size of a spall) on either of the two bearing raceways, outer or inner, is equal to or greater than 1.5 square inches [65]. This limit has been negotiated as a pragmatic compromise between railroad safety and economic operation in order to prevent the immediate removal of those bearings whose operation does not represent an impending risk, and which can be scheduled for inspection at a later time.

A reliable estimation of the size of a spall from its acoustic signature represents a considerable technical challenge due to a number of factors that can influence the defect-related vibro-acoustic signatures of bearings. These factors may be associated

not only with the wide range of defect types and shapes, such as line and extended area spalls, but also with the varying train operating conditions, which may include load, speed, and rotational direction. In addition, the extraneous noise, such as wheel–rail rolling noise, wheel squealing, and braking [33–51], could further complicate the problem. In addition, vibro-acoustic signatures of bearings can also be affected by the geometrical features of railway vehicles that incorporate the bearings, and the structural arrangement used to connect/couple the bearings to the vehicles. Some of these features, which may affect the performance of the bearing acoustic monitors, include:

- the location of axle bearings with respect to the wheel when viewed from the *field* side of the rail — *outboard or inboard bearings* (refer to Figure 1.4 for clarity): while the former being clearly visible to a wayside observer, the latter being shielded behind the wheels, and
- the type of railway vehicles that incorporate the bearings — *locomotives, freight wagons, or passenger coaches*: depending upon the suspension system in different railway vehicles, the bearings can be either fully, partially, or not encapsulated.

1.2.2 Scope

When investigating the feasibility of achieving a reliable estimate of an average size of a bearing defect from its vibro-acoustic signatures, the first step is to understand how vibrations in defective rolling element bearings are generated. It will be discussed in Chapter 2 (Literature Survey) that despite a significant amount of research on various aspects of rolling element bearings having been undertaken in the past, the mechanism by which defect-related vibrations are generated has received much less attention. Therefore, the work presented in this thesis is focused on understanding the physical mechanisms by which defect-related force impulses, and consequently vibrations, are generated in defective rolling element bearings. An in-depth analysis and interpretation

of the dynamic contact interaction of the rolling elements with raceways, as the rolling elements traverse through a defect within a bearing, are presented in this thesis. The parametric effect of varying load and rotational speed on the vibration characteristics of detective rolling element bearings is also a part of the current research.

As the axle bearings, in the case of a three-piece bogie configuration (Figure 1.6), are not directly connected to the body of the railway vehicle, defect-related vibro-acoustic bearing signatures are less likely to be affected by the geometrical features of a freight bogie compared to a passenger bogie. Therefore, in order to conduct the aforementioned investigations, it would be desirable for the current research to consider, for modelling and experimental work, the structural arrangement of a three-piece bogie. The laboratory testing of package bearing units with a side-frame of a three-piece bogie was not practical; however, an adapter that is directly connected to the bearing for interfacing a radial load was used.

The effect of the geometrical features on bearing signatures, which is not considered in this study, can be investigated in future using and extending the novel explicit dynamics FE model of a package bearing unit that is a result of the research presented in this thesis.

1.3 Aims

The aims of this research are to:

- develop a comprehensive non-linear dynamic finite element model of a rolling element bearing with minimal assumptions and simplifications;
- simulate the vibration response of a defective rolling element bearing having a line spall on its outer raceway;
- analyse the contact forces between non-defective and defective mating bearing components (precisely, rolling element-to-raceway contact forces), which are not

measured in practice;

- gain an understanding of the underlying physical mechanism by which defect-related impulsive forces and vibrations are generated in defective rolling element bearings;
- better understand the vibration characteristics of the de-stressing and re-stressing of the rolling elements as they enter into and exit out of a defect within a bearing, respectively;
- investigate the parametric effect of varying load and rotational speed on the vibration response of the rolling element bearing and rolling element-to-raceway contact forces; and to
- understand the feasibility of the detection of defects from the characteristics of their vibration signatures.

1.4 New knowledge

The novel work presented in thesis has provided the following new knowledge and insights:

- the development of an explicit dynamics finite element model of a defective rolling element bearing: the model can be used to gain an understanding of the complex behaviour of contact interaction between the rolling elements and raceways of a bearing, and the generation of impulsive forces, and subsequent vibration response;
- the development of a quasi-static analytical model of a defective rolling element bearing to predict the rolling element-to-raceway contact forces;
- the development of a mathematical model to predict the gradual decrease in the rolling element-to-raceway contact forces as a rolling element de-stresses upon its

entrance into a bearing defect, and subsequently other rolling elements re-stress between the raceways;

- the development of an understanding of the underlying mechanism by which impulsive forces are generated as the rolling elements and raceways within a bearing interact with each other when either components is defective;
- an in-depth investigation and interpretation of the contact forces between the rolling elements and raceways of a bearing which are not measured in practice;
- the development of an understanding as to why in typically measured bearing vibration signals, multiple defect-related impulses are generated when a bearing element passes through a defect;
- the development of an understanding of the de-stressing and re-stressing of the rolling elements as they traverse through a bearing defect by the analysis of the rolling element-to-raceway contact forces;
- the development of an understanding of the physics behind the gradual de-stressing or unloading of rolling elements as they enter into a defect; and
- the development of an understanding of the low-frequency characteristics of the vibration signatures pertinent to the gradual de-stressing of the rolling elements.

1.5 Structure of the thesis

Chapter 2 presents a review of existing knowledge on the vibration characteristics of rolling element bearings having localised defects. An overview of contact fatigue and spalling within rolling element bearings is presented along with a short discussion on bearing life estimation theories. The knowledge pertinent to the vibration response of rolling element bearings that has been gained through experimental work, as well as a

number of analytical and a few finite element models is discussed. The characteristics of vibration response at the edges of bearing defects are described, and this is followed by a review of the signal processing techniques and algorithms that can be used to estimate the average size of a defect. The literature review is summarised and the gaps in the current knowledge are discussed. Finally, the gaps addressed in this thesis are described.

A quasi-static analytical model for estimating the load distribution within rolling element bearings is presented in Chapter 3. The model was used to calculate the contact forces between the rolling elements and raceways of a rolling element bearing. As the forces at the rolling element-to-raceway contact interfaces are governed by the well-known Hertz theory of elasticity, an overview of Hertz theory essential to develop the analytical model is provided in the beginning of Chapter 3. Static load distribution within a non-defective rolling element bearing, which forms the basis of the quasi-static analytical model, is also described. According to previous models in the literature, incorrect representation of instantaneous step-like decrease and increase in the contact forces at the edges of a defect is provided. In contrast to the instantaneous variations in the rolling element-to-raceway contact forces, a new mathematical model is presented in Chapter 3 to estimate more realistic gradual changes at the edges of a bearing defect as rolling elements traverse through the defect. This model is based on the findings of the explicit FE modelling of a defective rolling element bearing presented in Chapter 4. Results obtained using the new mathematical model are compared with those from the previous models, and the differences are highlighted. The new model was incorporated in the quasi-static analytical model to estimate the load distribution within a defective rolling element bearing. An analysis of the variations in the rolling element-to-raceway contact forces is presented along with some limitations of the quasi-static model.

An explicit dynamics FE model of a defective rolling element bearing is presented in Chapter 4. The model was solved using a commercial FE software package, LS-DYNA. The FE model was used to estimate not only the vibration response of the

defective rolling element bearing, but also the dynamic rolling element-to-raceway contact forces. Along with descriptions of loads and boundary conditions applied to the FE model of the bearing, a detailed discussion on the discretisation of the model into nodes and elements is presented. In order to accurately model the dynamic rolling element-to-raceway contact interaction, it was found that much smaller mesh size than the recommended elements-per-wavelength (EPW) criterion was required to achieve a continuous rolling contact between the rolling elements and bearing raceways, so as to accurately transmit the loads between them. For the FE model of the rolling element bearing presented in this thesis, an optimal element mesh size of 0.5 mm is used, which corresponds to 97 EPW at 40 kHz; this is nearly 5 times greater than the 20 EPW criterion recommended for performing a structural transient dynamic analysis.

Numerical noise, an artefact of the FE model of the bearing, in the simulated results was observed, and was appropriately filtered. A new hypothesis is developed in Chapter 4 to explain the cause of the numerical noise, and the noise frequencies due to the interaction of the rolling elements and raceways were analytically estimated. Favourable agreement between the numerical and analytical noise frequencies was achieved that justifies the proposed hypothesis. The vibration response of the defective rolling element bearing was analysed using standard signal processing techniques associated with the vibration-based monitoring of rolling element bearings. Through time, time–frequency and frequency domain analyses, verification of the modelled vibration time-traces is presented using information, both theoretical and experimental, previously available in the literature. In addition to accurately acquiring the basic bearing kinematics, the FE model of the bearing accurately predicts the low- and high-frequency characteristic vibration signals associated with the de-stressing and re-stressing of rolling elements as they enter into and exit out of the defect, respectively.

For the purpose of verifying the numerically modelled vibration response of the defective bearing obtained using the FE model presented in Chapter 4, experimental work on a defective rolling element bearing was undertaken; this experimental work

is presented in Chapter 5. A commonly used package bearing unit in the railway industry was selected for the experimental work. A line spall on its outer raceway was manufactured using electric spark erosion. The vibration response of the bearing was measured and compared with the corresponding numerically modelled results estimated using the FE model of the rolling element bearing. Several favourable comparisons between the modelled and measured vibration data are presented that indicate the verification of the FE simulation results.

Analyses of numerical rolling element-to-raceway contact forces obtained using the FE model of the rolling element bearing are presented in Chapter 6. Contact force modelling has been implemented in the past; however, the main focus was on presenting the vibration response of bearings, such as acceleration, velocity or displacement, rather than presenting the contact force results. Therefore, the analyses of the rolling element-to-raceway contact forces presented here provide new insights on the dynamic interaction between the rolling elements and raceways of a bearing as the rolling elements traverse through a defect. The numerically modelled rolling element-to-raceway contact forces were verified using the quasi-static analytical solution presented in Chapter 3.

Correlation of the numerical contact forces and bearing vibration response is presented in Chapter 6, and the fundamental mechanism by which defect-related impulses are generated in defective rolling element bearings is explained. The analysis of the numerical rolling element-to-raceway contact forces shows that no impulse-like signatures are generated during the entrance of the rolling elements into a raceway defect, whereas their exit out of the defect produces a burst of multiple, short-duration, force impulses; the entry and exit of rolling elements into and out of a bearing defect are referred to as de-stressing and re-stressing, respectively. This explains the low- and high-frequency characteristics of the de-stressing and re-stressing events, respectively. Novel outcomes from the results of the explicit dynamics FE model of the rolling element bearing are also described in Chapter 6.

A parametric study to investigate the effects of varying radial load and rotational speed on both measured and modelled vibration response of the bearing was undertaken, and this is presented in Chapter 5. Similar effects on the numerically modelled rolling element-to-raceway contact forces were investigated, and this is presented in Chapter 6. It was observed that the magnitude of the defect-related vibration impulses and contact forces generated during the re-stressing of the rolling elements increases with increasing radial load and rotational speed.

Conclusions of the work presented in this thesis are presented in Chapter 7 along with some recommendations for future work.

Chapter 2

Literature Survey

2.1 Introduction

This chapter presents a review of research on the vibration characteristics of rolling element bearings having *localised defects*. Localised defects represent one of the two main classes of bearing defects for which the vibration response of rolling element bearings has been extensively investigated in the past. The other class of bearing defects in the literature is known as *distributed defects*, and similar to the case of localised defects, a number of analytical models related to distributed defects are available for predicting the vibration response of rolling element bearings. While the former class of defects is an ultimate failure mode for a correctly installed bearing, the latter class of defects can result in premature surface fatigue, leading to the development of localised defects, and ultimately to premature bearing failure.

In addition to the two defect classes, there is another type of a bearing defect, which has received much less attention in the past, and consequently, has not been discussed in the literature. This type of defect is called an *extended defect*.

Since the early 1950s, numerous researchers have contributed, experimentally and analytically, with the ultimate objective to understand the vibration response of non-defective (ideal) rolling element bearings [66–89], and defective bearings having lo-

calised [90–120], extended [121] and distributed defects [122–160]. As the work presented in this thesis is concerned with localised [90–120] defects, a detailed review of the models and knowledge related to the characteristics of the vibration response of rolling element bearings having localised defects is presented here.

2.1.1 Structure

This chapter begins with a discussion of contact fatigue in rolling element bearings along with an overview of some typical bearing defects in Section 2.2. A review of the existing knowledge pertinent to the vibration response of rolling element bearings due to localised defects obtained through experimental work [105, 161–165], a number of analytical [90–114], and finite element models [115–120] is presented in Section 2.3. The characteristics of vibration signatures at the entry and exit of rolling elements into and out of a defect [105, 114, 161–165], respectively, are discussed in Section 2.5, and this is followed by the estimation of an average defect size [114, 165] in Section 2.6. The existing knowledge is summarised in Section 2.7 followed by the identification of gaps in the current knowledge in Section 2.8. Finally, the gaps addressed in this thesis are described in Section 2.9.

2.2 Contact fatigue

Contact fatigue is a type of a surface defect or damage [166–168] that is inevitably related to the operational wear of rolling element bearings. It is generally characterised by spalling, pitting, or flaking off the metallic particles from the rolling surfaces of a bearing, namely outer raceway, inner raceway, and rolling elements [23, 169–174]. In the context of bearings, contact fatigue is also referred to as *rolling contact fatigue* because of the rolling and relative sliding movements of the rolling surfaces [172–174].

Loads acting between the rolling elements and raceways within a bearing develop only small areas of contact [3, Chapter 6, page 185]; the geometry of the contact area

and corresponding parameters, such as contact force, stiffness, and deformation, follow the classical Hertz theory of elasticity [175–177]. As a result, the elemental loading may only be moderate; however, the compressive stresses induced on the rolling surfaces of a bearing are extremely high — typically of the order of a few giga-pascals ($\approx$ 2–4 GPa) [3, 174].

It is considered that if a rolling element bearing in service is properly installed, aligned, loaded, lubricated, and kept free from contaminants, then the main mode of its failure is surface fatigue, which would result after an estimated number of rolling cycles (usually of the order of millions) [3, 174, 178, 179]. This (bearing) failure mode is also known as *fatigue spalling* or *pitting*, and is characterised by surface spalls or pits [23, 169–174].

2.2.1 Fatigue spalling

In a properly installed and lubricated rolling element bearing, the onset of micro-scale subsurface fatigue cracks commences below the highly stressed rolling surfaces. These cracks typically occur at micro-structural discontinuities, such as inclusions, inhomogeneity or carbide clusters, as a result of micro-plastic deformation in the region of maximum stresses [180–190]. Due to the continuous and repetitive load (stress) cycles during the operation of a bearing, the micro-scale subsurface fatigue cracks continue to progress towards the surface, eventually causing the material to break loose or flake off, leading to the formation of macro-scale surface spalls or pits [3, 23, 169–174]. Although spalls and pits are indiscriminately used in the literature to refer to the surface defects within rolling element bearings, Littman [169, 170] distinguished between the micro-scale subsurface and macro-scale surface originated fatigue cracks as spalls and pits, respectively [171].

Figure 2.1 shows a number of examples of fatigue spalling on various components of rolling element bearings: a few point spalls on the rollers are shown in Figure 2.1a,

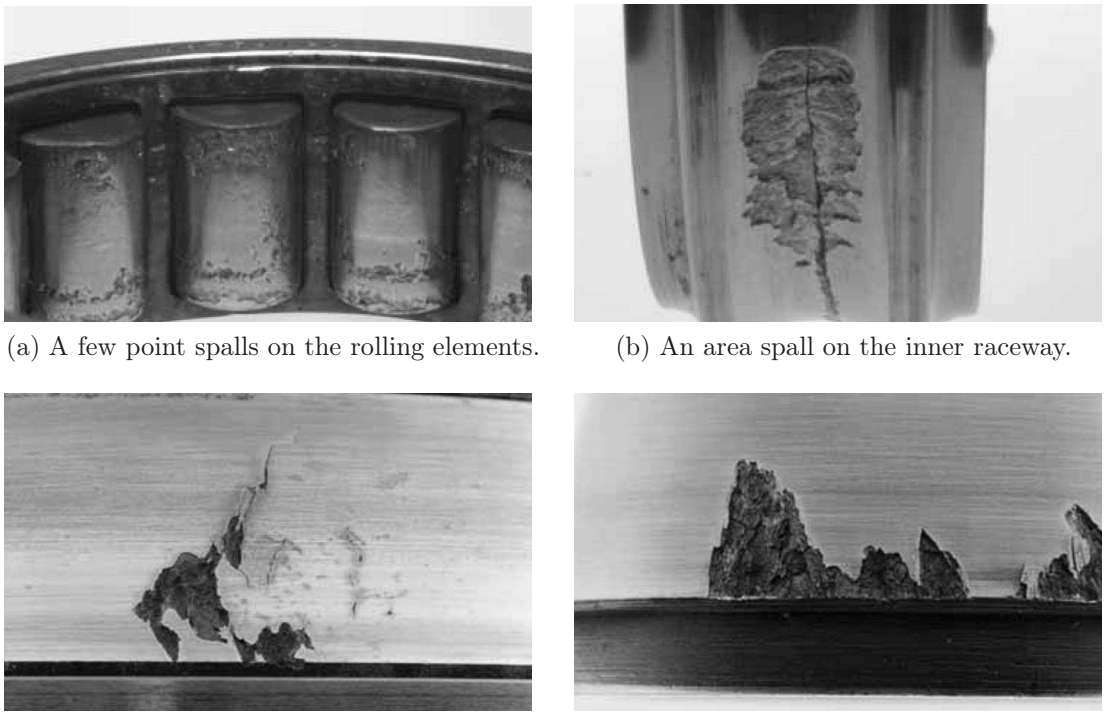

(a) A few point spalls on the rolling elements.

(b) An area spall on the inner raceway.

(c) An area spall on the outer raceway.

(d) An area spall on the outer raceway.

Figure 2.1: Fatigue spalls on various elements of rolling element bearings (courtesy: The Timken Company [54]).

an area spall on the inner raceway is shown in Figure 2.1b, and area spalls of different characteristic shapes and sizes on the outer raceway are shown in Figures 2.1c and 2.1d.

Other failure modes

In addition to the fatigue spalling, there are a number of other modes of bearing failure [191]. These failure modes include wear due to foreign material, smearing, etching–corrosion, brinelling, and burns from electric current discharge [23, 192]. Generally, these damages are caused by a variety of factors that include poor maintenance practices, mishandling, incorrect installation, misalignment, and inadequate lubrication. Often a bearing may commence to fail in one particular mode which then leads on to other failure modes [23]. These damages can cause premature surface fatigue, which eventually reduces the life of rolling element bearings.

(a) Pitting due to hard particle contamination of lubricant.

(b) Bruising due to particle contamination of lubricant.

(c) Corrosion due to etching.

(d) Severe corrosion due to etching.

(e) Race deformation due to excessive heat generation.

(f) Complete bearing lockup due to inadequate lubrication.

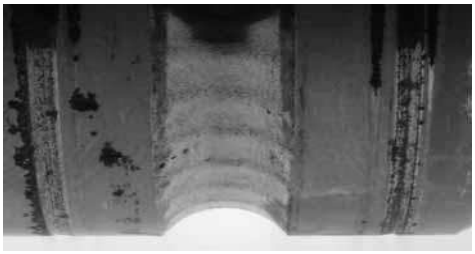

(g) Impact damage due to shock loading.

(h) True brinelling due to shock loading.

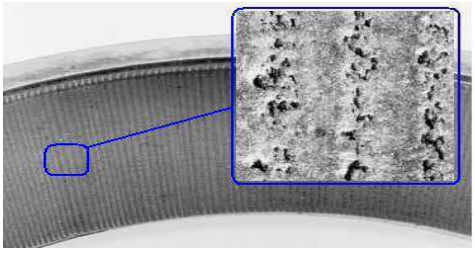

(i) Electric arc fluting .

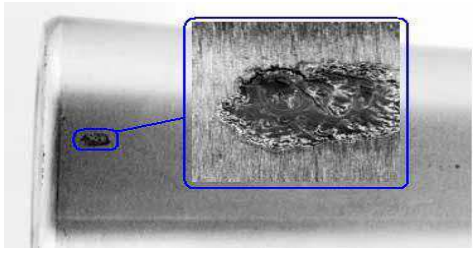

(j) Electric arc pitting.

Figure 2.2: Various types of bearing damage (courtesy: The Timken Company [54]).

A few examples of various defects in rolling element bearings are shown in Figure 2.2, and their overview is provided in Appendix B.

2.2.2 Rolling element bearing life

Understanding the cause for the onset of surface fatigue cracks is of significant interest not only to researchers, but also to bearing manufacturers as it has, historically, been considered to be a limiting factor for the useful life of rolling element bearings [193]. As a result, rolling contact fatigue mechanisms in bearings leading to their life estimation have been investigated by several researchers [194–231]. In the literature, these models are divided into two categories [174] — probabilistic engineering models [194–219] and deterministic research models [220–231]. In general, the engineering models are empirical in nature; they attempt to predict fatigue lives using solutions of the elastic stress field with the scatter in life being incorporated directly using the Weibull probability distribution function [232–234]. In contrast, the research models are mechanistic in nature; they assume an initial crack (either surface or subsurface) of a given length and orientation, and use fracture mechanics [167, 168] to predict the shape of the spall and fatigue life of the contact.

The Lundberg–Palmgren model

In 1924, Palmgren [178] published a paper outlining his approach to bearing life prediction and an empirical formula based upon the concept of an L_{10} life, or the time that 90% of a bearing population would equal or exceed without a fatigue failure. Later on, in 1947, Palmgren along with Lundberg, incorporated his previous work [178] with the work of Weibull [232] to present the pioneering mathematical formulation for calculating the fatigue life of rolling element bearings [194, 195]. Their theory is commonly known as the *Lundberg–Palmgren theory*. It states that for bearing rings subjected to Z cycles of repeated (stress) loading, the probability of survival Υ is given by

$$\ln \frac{1}{\Upsilon} = A \frac{Z^{\kappa} \varepsilon_0^{g} V}{z_0^{q}} \tag{2.1}$$

where, ε_0 is the maximum orthogonal shear stress in the contact, z_0 is the corresponding depth at which this stress occurs, and V is the stressed volume of material. The parameters A, g, and q are material characteristics that are determined experimentally, and the parameter κ is the Weibull slope for the experimental life data plotted on a Weibull probability paper.

Since the development of the Lundberg–Palmgren theory, significant advances have been made in bearing material quality, fracture mechanics, and in the understanding of the role of lubrication through the development of elasto-hydrodynamic theory [173, 235–241], in order to increase the fatigue life of rolling element bearings. The recognition of the limitations of the original Lundberg–Palmgren theory [194, 195] has led to the development of better and improved bearing fatigue life prediction models. The current ISO (International Organization for Standardization) [210], ANSI (American National Standards Institute, Inc., and ABMA (American Bearing Manufacturers Association, Inc.) [242, 243] standards for rolling bearing life are based on a modification of the Lundberg–Palmgren equation [194, 195]; the modifications account for the significant changes in relatively recent material quality, reliability, and operating conditions.

The bearing life models, which are aimed at predicting the fatigue life of rolling element bearings and rolling contact fatigue mechanisms, do not incorporate and investigate the structural vibration response of bearings having fatigue spalls. As the work presented in this thesis is concerned with the understanding of the vibration characteristics of rolling element bearings having localised defects, the bearing life models are not reviewed here; excellent reviews of these models can be found in references [174, 211, 217, 244].

A review of all the models available in the literature for predicting the vibration

response of defective rolling element bearings having localised defects is presented in the following sections.

2.3 Localised defects

Localised defects, one of the two main classes of bearing defects, include cracks, pits, and spalls on various components of a rolling element bearing. The components within a bearing refer to its rolling surfaces — outer raceway, inner raceway, and rolling elements. The localised defects are an ultimate failure mode of a correctly installed and lubricated bearing during its normal operational use. A few examples of surface fatigue spall, localised defects, are shown in Figures 2.1 and 2.2.

In order present a systematic review of the previous analytical and FE models that predict the vibration response of rolling element bearings having localised defects, they are classified into four broad categories. These categories are as follows:

1. *Periodic* impulse-train models [90–93]
2. *Quasi-periodic* impulse-train models [94–99]
3. Non-linear multi-body dynamic models [100–114]
4. Finite element models [115–120]

Although the models that are most relevant to the current study are explicit dynamic FE models [117–120], reviewed in Section 2.3.4.3, it is important to review all the previous models so as to clearly identify the gaps in the current knowledge.

2.3.1 Periodic impulse-train models

A *periodic* impulse-train model refers to a model that simulates the generation of defect-induced impulses at a constant period. Such a model does not include the characteristics of a bearing, such as masses of bearing components and deformation

at the rolling element-to-raceway contact interfaces that is governed by the Hertzian contact theory of elasticity [175–177]. For the case of a stationary outer raceway defect, the impulses are equally spaced, and their characteristics, such as shape, height, and width, are similar to each other. On the contrary, for a rotating inner raceway defect and a rolling element defect, the impulses are generally modulated as per the static load distribution within a rolling element bearing; that is, the amplitude of the defect-induced impulses varies as the inner raceway and rolling element defects rotate in and out of the bearing load zone [3, 245–248].

The first model for simulating the vibration response of a localised single point defect on the inner race of a rolling element (ball) bearing, under a constant radial load, was developed by McFadden *et al.* [90] in 1984. The forces produced by the point defect were modelled as an infinite series of periodic force impulses of equal amplitude using the Dirac delta function [249, Chapter 1, pages 9–10] with a period T as

$$I(t) = \sum_{\xi=-\infty}^{\infty} \mathscr{D}(t - \xi T) \tag{2.2}$$

where, $I(t)$ is the impulse force, $\mathscr{D}$ is the Dirac delta function, t is the time vector, and T is time period of the defect-related impulses. The resonance characteristic in the Fourier domain [250] was sampled at the regular interval of $\frac{1}{T}$. Based on the assumption that the amplitude of the impulse produced by a defect is directly proportional to the load on a rolling element when it strikes the defect, the amplitude of the impulses was multiplied by the actual load on the rolling elements, estimated as per the well-known Stribeck's equation [245].

McFadden *et al.* further extended their defect-induced impulse-train model [90] to incorporate two point defects located on the inner race of a ball bearing [91]. The effects of two point defects were simulated by treating the defects as the sum of a number of localised defects at different phase angles around the inner raceway. Both models [90, 91] incorporated the effects of bearing geometry, shaft rotational speed, bearing

load distribution, transfer function between the bearing and accelerometer, and the exponential decay of vibration. Satisfactory performance of both models was reported on the basis of their predicted vibration (line) spectra agreement with measured vibration responses after performing a standard envelope analysis [251, 252]. While McFadden *et al.* did not predict the amplitude of the defect-related frequency components, fundamental and harmonics, in their first model [90], the predicted amplitudes in their second model [91] were corrected based on their experimental results. They found that the demodulated or envelope vibration spectrum was composed of groups of discrete frequency components, separated by the shaft rotational frequency f_s, while the spacing between the successive groups was the inner raceway defect frequency f_{bpi} (also known as ball pass frequency inner raceway — BPFI; refer to Appendix C for the definition of BPFI and other defect frequencies associated with rolling element bearings). The aforementioned models provided some early insights into the demodulated (envelope) vibration spectrum of a rolling element bearing obtained through accelerometer measurements in practice, and partially helped explain the defect-related frequency components, fundamental, sidebands, and associated harmonics, in an actual vibration spectrum. The models developed by McFadden *et al.* [90, 91] are often referred to as *classical* or *traditional* models in the literature.

Su *et al.* [92] also modelled the vibration frequencies produced by a single point defect and multiple (two) point defects using periodic (equi-spaced) impulse-trains. Extending the models developed by McFadden *et al.* [90, 91], Su *et al.* [92] modelled and studied the vibration response of a rolling element bearing subjected to various types of loading. They proposed periodicities that include fundamental defect frequencies, sidebands and associated harmonics, for the outer raceway, inner raceway, and rolling element defects due to various loading conditions. These loading distributions include shaft unbalance and roller errors, in addition to the only case of stationary loading along the circumference of the inner race as considered by McFadden *et al.* [90, 91].

Su *et al.* [92] reported that for a fixed outer raceway defect, the vibration signature of a bearing has periodicities at $\frac{1}{f_s}$ and $\frac{1}{f_c}$ due to shaft unbalance and roller errors, respectively, where, f_s is the shaft rotational frequency, and f_c is the cage rotational frequency. However, for an inner raceway defect, the vibration response of a bearing has no periodicity due to shaft unbalance, but a periodicity of $\frac{1}{f_s - f_c}$ due to roller errors. The comparison of the predicted defect-related frequencies and sidebands with the experimental results showed good agreement. The effect of the loading distributions due to shaft unbalance and roller errors provided further explanation of the spectral content of the demodulated vibration spectrum of a bearing for cases in addition to the cases considered by McFadden *et al.* [90, 91].

In the late 1990s, an analytical model for predicting the vibration frequencies, fundamental and harmonics, of a rolling element bearing along with the amplitudes of the frequency components, caused by a single point localised defect on the outer raceway, inner raceway, and one of the rolling elements, under radial and axial loads, was proposed by Tandon *et al.* [93]. Similar to the aforementioned models [90–92], Tandon *et al.* [93] also modelled the vibration response using periodic impulse-trains; however, they considered three different types of typical pulse shapes of finite width — rectangular, triangular, and half-sine. The results showed that for an outer raceway defect, a vibration response is generated at the outer raceway defect frequency f_{bpo} (also known as ball pass frequency outer raceway — BPFO; refer to Appendix C for the definition of BPFO) and its multiples. For an inner raceway defect, a response is generated at the inner raceway defect frequency f_{bpi} in the absence of a radial load; however, in its presence, a response is also generated at equi-spaced sidebands at the shaft rotational frequency f_s in addition to the inner raceway defect frequency f_{bpi}. Tandon *et al.* [93] also reported that the vibration amplitude due to the outer raceway defect was higher compared to that of the inner raceway defect, and the amplitudes of the vibration frequencies and their harmonics were affected by the different pulse shapes. Although a fair agreement between the predicted and experimental results

(obtained from reference [253]) was claimed, the comparison was only illustrated for the defect on the inner raceway of a bearing. It was also mentioned in their paper that the amplitudes of the predicted frequency components were normalised (or corrected) for the comparison with the experimental results; however, the normalisation factor was neither discussed nor provided. The problem of amplitude mismatch has also been highlighted by several other authors [103, 104, 109–111] who, later on, developed non-linear multi-body dynamic models; these models will be discussed later in Section 2.3.3.

In the work presented in this thesis, a novel explicit dynamics FE model of a rolling element bearing with an outer raceway defect is developed. It will be shown in Chapter 5 that the acceleration levels predicted by the FE model of the bearing presented here favourably match with the experimentally measured data.

2.3.2 Quasi-periodic impulse-train models

A *quasi-periodic* or an *aperiodic* impulse-train model refers to a model that includes a certain amount of random fluctuations that occur due to the slip associated with the rolling elements within a bearing [95, 96]. Due to the incorporation of randomness in the periodic impulse-train models, the quasi-periodic impulse-train models are also referred to as *stochastic* models.

The periodic impulse-train models [90–93] were based on the consideration of equi-spaced generation of force impulses as the rotating components within a bearing repetitively pass over a defect. However, based on the observations of the experimental results of a ball bearing having an inner raceway defect, Brie [94] suggested that the defect-induced excitation cannot be considered as periodic, but quasi-periodic in nature. As the earlier models [90, 91] could not explain some frequency variations, Brie modelled the response of a bearing using a single-degree-of-freedom (DOF) lumped mass-spring-damper system. A slight variation was introduced to the modelled defect-induced impulse-train, although the cause and amount of the variation were not mentioned.

Ho *et al.* [95] and Randall *et al.* [96] explained that the slippage of the rolling elements causes slight random variation in the spacing between two consecutive defect-related impulses observed in practice. They explained that the random variations occur due to the slip associated with the motion of the rolling elements within a bearing — the contact angle between rolling elements and raceways varies with the position of each rolling element. As a result, each rolling element has a different effective rolling diameter and tries to roll at different speeds. However, the cage limits the deviation of the rolling elements causing some slip and consequently variations between the time intervals associated with the defect-related impulses. These slight random variations lead to smearing in the frequency spectrum of defect-related harmonics at higher frequencies; that is, defect-related frequencies appear as discrete harmonics of negligible amplitude in the low-frequency range, but smeared in the high-frequency range where their amplitude is amplified by correspondence with the structural resonance frequencies of a bearing [30].

In order to address the deficiencies in the prior models [90–93], Ho *et al.* [95] also modelled the localised defect-induced vibration signals as a series of impulse responses of a 1-DOF system. However, they introduced random variations in the time between the impulses so as to gain a close resemblance to the actual vibration signals obtained in practice. The results showed that the incorporation of the fluctuations in the modelled signals provided a realistic update to the traditional models proposed by McFadden *et al.* [90, 91]. The work presented by Ho *et al.* [95] was primarily focused at investigating bearing diagnostic techniques, such as self-adaptive noise cancellation [254] and squared envelope analysis rather than investigating the vibration characteristics.

Adopting the model of Ho *et al.* [95], a few more authors have also incorporated the slippage-related random fluctuations in their proposed defect-induced impulse-train models [96–98]. The force impulses in these models [96–98] were simulated using a 1-DOF system [96] and the Dirac delta function $\mathscr{D}$ [97, 98]. The authors of the models [96–98] used the theory of cyclostationarity [255–259], and characterised the bearing

signals as quasi-cyclostationary; that is, their statistics are quasi-periodic [96] as indicated by Brie [94]. The emphasis of the stochastic models presented in references [95–98] was focused on the diagnostics of defective rolling element bearings using cyclic spectral density analysis [30, 257, 258]. The signal processing techniques successfully detected the defect-related frequencies and associated harmonics.

Unlike the technique followed by previous researchers [90–98] for generating the defect-induced impulse-trains, Behzad *et al.* [99] applied the concept of rough elastic contact between the surfaces of a rolling element bearing. Rough elastic contact mechanics has been exploited by several researchers to analytically model rough surfaces [177, 260–269], and explain the source of high-frequency vibrations in rolling contacts with attention focused on wheel–rail contact [33, 36–42, 45, 51, 270] and rolling bearings [271, 272]. Behzad *et al.* [99] presented a stochastic model for estimating the vibration response of defective rolling element bearings. They considered two measures of roughness to represent non-defective and defective surface areas using the Gaussian probability distribution [273, Chapter 3, pages 59–66]; the localised outer raceway defect had a rougher surface than the non-defective bearing surfaces. Assuming the applicability of the Hertz theory of elasticity [175–177], variations in the contact forces between the rolling elements and raceways contact interfaces were estimated on the basis of the roughness-related profiles of the rolling surfaces. As the defective surface was modelled as rougher compared to the non-defective surfaces, high magnitudes of contact forces, and consequently vibrations, were generated at the interaction of the rolling elements and the summits of the asperities at the localised defective area, compared to rolling elements and non-defective areas. It was shown that the predicted vibration response agreed well the experimental measurements. Behzad *et al.* [99] also reported that the performance of their stochastic model was better than the traditional periodic impulse-train models [90, 91]; however, the performance was not compared with previous stochastic models [95–98].

It is important to note that the randomness or stochasticity in the model proposed

by Behzad *et al.* [99] was due to the roughness profile of the surfaces, and not due to the slippage of the rolling elements [95, 96]. Therefore, their model effectively generates periodic force impulses.

A brief recapitulation of the impulse-train models

The aforementioned *periodic* [90–93] and *quasi-periodic (stochastic)* impulse-train models [94–99] assume that defect-induced vibrations are generated by a single force impulse as the rolling elements interact with the raceways within a bearing, and that the impulse decays exponentially with time. The models do not include the physical characteristics of a bearing, such as the masses of the components (outer ring, inner ring, and rolling elements) and the raceway-to-rolling element contact interaction. The generation of impulse trains can be used to understand the defect-related bearing vibration frequencies, harmonics, and associated sidebands; however, they are not suitable if one has to understand the vibration characteristics of various types of defects, such as line, area, and extended spalls. It was also mentioned that the predicted amplitudes of the frequency components were corrected for comparison with experimental results; however, the correction factor has not been provided. Nevertheless, the impulse-train models provide an excellent understanding of the defect-related (vibration) frequency components (fundamental, harmonics, and sidebands) due to the presence of localised defects on the outer raceway, inner raceway, and one of the rolling elements within a bearing for various loading conditions.

The valuable insights into the vibration spectra of defective rolling element bearings, gained through the impulse-train models [90–99], provided motivation for later researchers to incorporate various components of a bearing and bearing–housing in rotor–bearing systems in their models, which led to the development of non-linear, multi-body dynamic models [100–114]. These models are reviewed in the following section.

2.3.3 Non-linear multi-body dynamic models

The non-linear multi-body dynamic models for rolling element bearings and associated systems are lumped parameter models. In the context of mechanical systems, a *lumped parameter* model (also called a *lumped element* or *lumped component* model), represents a model in which various elements or components of a system are simplified into rigid masses connected by a series of springs (to model linear or non-linear contact interfaces) and dampers (to account for energy losses). The non-linear multi-body dynamic models for predicting the vibration response of a bearing, bearing–pedestal (housing), and rotor–bearing systems, due to the presence of localised bearing defects [100–114] have been developed by several researchers. The localised defects not only include point spalls [100, 103, 106, 108, 109] (as considered for the impulse-train models [90–98]), but also line spalls [101, 102, 104, 105, 110, 112, 114] as a function of width and depth, circular spalls [107, 111], and area spalls (as ellipsoids for ball bearings) [113] as a function of the Hertzian contact deformation [175–177]. The non-linear multi-body dynamic models use lumped parameters to represent the bearing systems as simplified mass-spring-damper systems, and generally consider the outer and inner rings as lumped (rigid) masses and the rolling elements-to-raceways contact interfaces as non-linear springs.

Depending on the components of a system considered, the translational degrees-of-freedom in the multi-body models range from two [109, 111] to thirty-three [112]. The common feature of all models in references [100–114], except the model in reference [113, 114], is that they neglect the bending (flexural) deformation of the outer and inner rings, and rolling elements; however, all models consider the localised non-linear Hertzian contact deformation at the rolling element-to-raceway contact interfaces. In order to simplify the analysis, the majority of the multi-body models available in the literature assume the following:

1. The outer and inner rings are rigidly connected to the housing [100–112] and

shaft [100–114], respectively.

2. The rolling elements are excluded or considered massless [100–103, 105–107, 109–111, 114].

3. The inertial and centrifugal effects of the rolling elements are ignored [100–111, 113, 114].

4. The slippage of the rolling elements [96] is ignored [100–104, 106–112, 114]; thus, eventually resulting in the generation of periodic defect-induced impulses.

5. The elasto-hydrodynamic lubrication (EHL) fluid film [173, 235–241] in rolling contacts is ignored [103, 105–111, 113, 114].

6. The stiffness of a bearing is considered to be linear [101–103, 106, 107, 109–111, 113, 114].

In the work presented here, the explicit dynamics FE model of a rolling element bearing includes all the components within a bearing, namely outer ring, inner ring, rolling elements, and cage. The components are modelled as flexible bodies. The slippage of the rolling elements, and their centrifugal effects are also included in the FE model.

The paragraphs to follow immediately after the next provide a systematic, chronological, review of the non-linear multi-body dynamic models for predicting the vibration response of rolling element bearings having localised defects. The paragraphs are structured in such a way so that each paragraph contains a review of a single model: the paragraphs discuss their features and findings, and conclude with some limitations.

Prior to investigating the vibration response of rolling element bearings (and associated bearing–pedestal and rotor–bearing systems) due to the presence of defects, the research was primarily focused on understanding the characteristics of the vibration response of non-defective bearings [66–89]. The first systematic investigations were conducted by Perret [66–69] and Meldau [70–73] in the early 1950s. They concluded

that rolling element bearings generate cyclic vibrations even in the absence of manufacturing or geometrical imperfections; such vibrations are commonly referred to as *variable compliance vibrations*, which were later described by Sunnersjö [133, 134]. A significant number of experimental and analytical studies on the characteristics of vibrations caused by the geometrical imperfections in rolling element bearings, such as surface roughness, waviness, misaligned raceways, off-sized rolling elements, and out-of-round components, were carried out by Svenska Kullagerfabriken AB (SKF) Industries, Inc. [274] under U.S. Navy Contract Number: NObs-78552 between 1960 and 1963, and seventeen bi-monthly reports were issued. A few special reports can be found in references [122–127], and the summary of the overall work in reference [129]. Later on, several researchers reported on the development of analytical models to predict the vibration response of rolling element bearings due to various distributed defects with attention focused on the waviness of raceways and rolling elements [128, 130–160]. However, from the review of the literature conducted during the course of the current study, it appears that *the first non-linear multi-body dynamic model* for predicting the vibration response of a rolling element bearing (in a bearing–pedestal system), due to a localised (point) defect, was reported in 2002 by Feng *et al.* [100]. Their model was an extension to the model developed by Fukata *et al.* [87] that describes the vibration response of an ideal (non-defective) ball bearing. Fukata *et al.* [87] modelled a rotor–bearing system as a simplified 2-DOF system; while the outer ring was modelled to be stationary, the inner ring was assumed to translationally move in the radial plane (of the model) with two degrees of freedom (global cartesian x- and y-directions).

Building on the 2-DOF model of Fukata *et al.* [87], Feng *et al.* [100] presented a 4-DOF model corresponding to the two translational degrees of freedom, in the radial plane, each for the two lumped masses: the rotor and pedestal masses. No other component was included in the model except the outer ring, which was assumed to be stationary and rigidly connected to the pedestal. As the primary aim of their model was to demonstrate the working capability of the in-house transient analysis software

[275] to simulate the vibration signals due to localised bearing defects, the characteristic dimensions and parameters of the rotor–bearing system model were fictitiously chosen. The 4-DOF model was solved using the fourth-order Runge-Kutta integration scheme [276, Chapter 5], which was incorporated in the developed software [275]. The results of the numerical simulations were not compared with any kind of experimental results, but were simply validated by comparing the values of the defect-related frequency components, f_{bpo} and f_{bpi} for outer and inner raceway defects, respectively (obtained from an envelope analysis [251, 252] of the modelled signals), using the existing knowledge on the basic bearing kinematic defect frequencies [3, Chapter 25, page 994]. Despite being the first multi-body model for predicting the vibration response of a rolling element bearing having a localised defect, the model by Feng *et al.* [100] has not been cited, nor discussed, by many researchers who later on developed their own multi-body models. This is probably because it was not published in a journal, but presented at a conference. However, the 4-DOF model of Feng *et al.* [100] was extended by Sawalhi *et al.* [105, 121] which is described later in this section.

With the objective of acting as an interface element between the rotor and supporting structure, a non-linear multi-body dynamic model of a deep-groove ball bearing was developed by Sopanen *et al.* [101, 102]. Their 6-DOF model considered the outer and inner rings of the bearing as rigidly connected to the housing and shaft, respectively, the non-linear Hertzian contact deformation [175–177] at the rolling elements-to-raceway contact interfaces, and the EHL fluid film in the rolling contacts [173, 235–241]. In addition to modelling the localised defects (line spalls) on the outer and inner raceways, surface waviness (one of the distributed defects) of the raceways was also considered. The model was solved using a commercial multi-body software package, MSC Adams [277]. While Sopanen *et al.* [101, 102] did not conduct any experimental work, they compared their modelling results with those of similar studies available in the literature; for example, for the localised raceway defects, the predicted results were compared with the results in reference [93], and for the waviness, the modelling results

were compared with the results reported in references [138, 139, 144, 148]. Sopanen *et al.* [101, 102] observed that the diametral clearance has a significant effect on the vibration response of the modelled rotor–bearing system, and the amplitude of the defect-related frequency components for similar defects was higher for the outer raceway defect in comparison to the inner raceway defect. The former observation was also reported by Tiwari *et al.* [146, 147], and the latter by Tandon *et al.* [93]. Although they mentioned that the localised line spalls were modelled using two parameters, length and height, Sopanen *et al.* [101, 102] did not provide details on the simulation of the defect-induced impulses. Furthermore, their model ignored the slippage of the rolling elements (balls) [96] and neglected the centrifugal forces acting on them. Although the modelled defect-related frequencies agree well with the earlier results published in the literature [93, 138, 139, 144, 146–148], the model presented by Sopanen *et al.* [101, 102] lacks details on the actual modelling process, and therefore, cannot be clearly followed.

A 3-DOF lumped mass-spring-damper model for predicting the vibration response due to a localised point spall on various elements of a rolling element bearing in a rotor–bearing system was proposed by Choudhury *et al.* [103]. Similar to the assumptions considered in the aforementioned models [100–102], Choudhury *et al.* [103] also considered the outer and inner rings as rigidly connected to the housing and shaft, respectively. The rolling elements were excluded from the model, and on the basis of the findings reported in references [278, 279], the stiffness of the bearing was considered to be linear. The defect-related force impulses were generated as a rectangular-shaped periodic impulse-train without including the slippage of the rolling elements [96]. For the outer raceway defect, it was shown that the amplitude of the vibration (velocity) increased with increasing harmonic order, and for the inner raceway defect, the sidebands (f_s and $f_{\text{bpi}} \pm f_s$) were asymmetrically distributed about the defect frequency. The modelling results (vibration line spectra) for only the inner raceway and rolling element defects were compared with the experimental results. Similar to the findings reported in previous references [93, 101, 102], Choudhury *et al.* [103] also

reported that the amplitude of the frequency components for the outer raceway defect was much higher than that for the inner raceway and rolling element defects. Although a fair agreement between the predicted and experimentally measured defect-related frequency components was shown, their amplitudes did not match well with each other. However, despite their earlier findings reported in reference [93] related to the effect of different pulse shapes (rectangular, triangular, and half-sine) on the amplitudes of defect-related frequencies, Choudhury *et al.* [103] restricted the usage of the pulse shape to rectangular in their proposed multi-body model [103]. The significant mismatch between the amplitude of the frequency components could be due to the (assumed) rectangular shape of the modelled impulses and unknown characteristics of the actual defect-induced impulses. Choudhury *et al.* [103] also mentioned that the predicted results were normalised for the comparison purposes; however, they did not provide the normalisation factor, which was the same limitation found in their previous work [93].

Sassi *et al.* [104] presented a numerical model to predict the vibration response of a deep-groove ball bearing having a localised point spall on the outer and inner raceways, and one of the rolling elements within the bearing. Although the majority of the simplifications considered during the modelling were similar to the aforementioned models [100–103], Sassi *et al.* [104] included the rolling elements (balls) as rigid bodies (lumped point masses), and this was excluded in previous work [100–103]. The defect-related impulses were mathematically modelled as periodic impact forces, and the empirical expression for estimating the impact force was taken from reference [280]. The equations of motion for the coupled 3-DOF system representing the rotor–bearing system were solved using Simulink® [281], and compiled as a toolbox, BEAT (BEAring Toolbox) in the MATLAB® software [282]. Time and frequency domain analyses were conducted on the simulated data, and the predicted results from the model were compared with the experimental results obtained from the bearing data centre at Case Western Reserve University (CWRU) [283]. Similar to the problem encountered by

previous researchers [91, 93, 103], Sassi *et al.* [104] also reported the amplitude mismatch between the predicted and experimental defect-related frequency components; fundamental, sidebands, and harmonics. They mentioned that the amplitude of the predicted frequencies was corrected in order to simply match them with the corresponding experimental results; however, similar to the approach taken by previous researchers [93, 103], the amplitude-correction factor was not discussed.

Extending the work of Fukata *et al.* [87] and Feng *et al.* [100], a detailed analytical model to simulate the vibration response of a defective ball bearing in a gearbox having localised defects (line spalls) was presented by Sawalhi *et al.* [105]. In contrast to the 2- and 4-DOF models presented in references [87] and [100], respectively, the model developed by Sawalhi *et al.* [105] comprised 5-DOF (translations in global cartesian x- and y-directions) — 2-DOF for the inner ring, 2-DOF for the pedestal, and one for measuring the high-frequency response of the pedestal. Unlike the multi-body models reviewed so far [100–104], the lumped mass-spring-damper bearing–pedestal model by Sawalhi *et al.* [105] incorporated the slippage of the rolling elements [96] as a percentage variation (1% to 2%) of the defect-related frequencies in order to gain close resemblance to actual bearing vibration signals measured in practice. Localised line spalls on the outer raceway, inner raceway, and a rolling element of a bearing were modelled by developing mathematical expressions based on the assumed path (trajectory) of the rolling elements as they traverse through the defect. Although the shape of the defects was modelled as rectangular, the definition of the path was based on the hypothesis that the rolling elements gradually enter into and exit out of the defect. However, inertial and centrifugal effects of the rolling elements were ignored. Furthermore, no mathematics behind the gradual entry and exit of the rolling elements into and out of the defect, respectively, was discussed. In the work presented here, a new mathematical model to predict the gradual entrance of the rolling elements into a defect is developed and is described in Chapter 3. In the model by Sawalhi *et al.* [105], a set of relevant ordinary differential equations of motion for the coupled bearing–pedestal system to

simulate its vibration response was solved using Simulink® [281]. A unique feature of the model presented by Sawalhi *et al.* [105] is that the pedestal was modelled using an additional mass-spring system, referred to as a *resonance-changer,* attached to it. With the aim to simulate a typical high-frequency resonant response of a bearing, the values of the mass (1 kg) and the stiffness of the resonance-changer (8.89 N/m) were selected to excite the bearing at 15 kHz (with a damping of 5%). As the resonant mode of the bearing structure was deliberately chosen to be 15 kHz, the magnitude of the simulated vibration response due to the introduction of localised defects was higher around that frequency compared to the response of a non-defective bearing. Due to the mismatch between the modelled and actual resonant modes of the structure, different frequency bands were used to optimally demodulate the simulated and experimentally measured vibration signals using spectral kurtosis [25, 26] and a kurtogram [27]. Nevertheless, good agreement between the simulated and experimental results, analysed using time and frequency domain techniques [23–27], was observed.

Sawalhi *et al.* [105] also observed that both measured and simulated defect-related transient signals were composed of two impulses: the first was related to the entry of the rolling elements into the defect, and the second, to the exit of the rolling elements out of the defect. They named the phenomenon related to the occurrence of the two impulses as the *double-impulse phenomenon.* Although, the results were reported to have the theoretical background that agrees and supports the findings reported in references [161, 162, 164], a detailed investigation of the entry- and exit-related vibration signals was not carried out. However, later on, Sawalhi *et al.* [165] discussed the characteristics of the vibration signals associated with the entry and exit events in a separate publication [165], and subsequently found the double-impulse phenomenon as invalid. These will be described later in Section 2.5.2 of this chapter.

Defect-induced periodic impulse-trains were generated using the Dirac delta function [249, Chapter 1, pages 9–10] in the earlier models in references [90–93] to primarily understand the vibration-related spectral content of rolling element bearings that have

a localised defect. Ashtekar *et al.* [107] presented a new technique to model the localised defects on the raceways of deep-groove and angular contact ball bearings, and studied their effect on the bearing dynamics. They simulated the defect-related impulses by developing a mathematical expression to modify the deflection exponent n in the well-known Hertzian contact force-deflection (also referred to as load-displacement) relationship [175–177], $F = K\delta^n$, where F is the force, K is the contact stiffness, δ is the deflection, and n is the exponent — $3/2$ for point, circular, and elliptical contacts in ball bearings, and $10/9$ for line and rectangular contacts in roller bearings. The expression in reference [107] is a function of the load, ellipticity ratio, and the dimensions of the circular defect (diameter and height). It was used to estimate the modified contact forces at the interaction of the rolling elements and the defect in order to periodically simulate the force impulses. The modelling results were not validated with experimental measurements.

For a coupled shaft–bearing system, a 3-DOF lumped parameter model was proposed by Arslan *et al.* [108]. In contrast to the previous models [100–106], which presented the vibration response of either the bearing or housing, the model by Arslan *et al.* [108] presented displacement of the rolling elements (balls) within the bearing. Although the point mass of rolling elements was included in the model, their inertial and centrifugal effects were ignored as was done in reference [104]. Arslan *et al.* [108] neither reported on the conduct of the experimental work nor carried out the comparison of their modelling results with the results from the literature. The modelling results did not present new findings compared to the understanding provided by earlier researchers [100–106].

With the aim of studying the stability of a rotor–bearing system having a localised point spall on various elements of a ball bearing, Rafsanjani *et al.* [109] presented a 2-DOF numerical model. The model was based on the work of Sunnersjö [134] who also presented a 2-DOF model to demonstrate a method for the estimation of the variable compliance vibration frequencies [129]. The two translational degrees of

freedom were related to the displacement of the inner ring in the radial plane (global cartesian x- and y-directions). In a similar way to previous models [101–105], the outer and inner rings were rigidly connected to the housing and shaft, respectively, the non-linear Hertzian contact deformation [175–177] was considered at the rolling element-to-raceway contact interfaces, the inertial and centrifugal effects of the rolling elements were ignored, and the stiffness of the bearing was considered to be linear [278, 279]. The effect of the localised defects was modelled as periodic impulses ignoring the slippage [96] of the rolling elements. Rafsanjani *et al.* [109] did not conduct any experimental work; however, in a similar way to reference [104], they used the experimental data available at the bearing data centre at CWRU [283] for the comparison of their modelled results. Similar to the problem encountered by previous researchers [91, 93, 103, 104], a substantial amplitude mismatch between the predicted and experimental results for the defect-related frequency components was also reported by Rafsanjani *et al.* [109].

The multi-body models reviewed so far [101–109] only considered the inclusion of a single localised defect within a rolling element bearing. Patel *et al.* [110] included multiple (two) localised defects (line spalls) on both inner and outer raceways in their proposed model for predicting the vibration response of a deep-groove ball bearing. For two raceway defects, two pulses were generated and separated proportionally to the angular separation of the defects. Patel *et al.* [110] presented a 3-DOF shaft-bearing-housing model using lumped masses and springs. The assumptions considered during the development of their model were similar to those mentioned in references [109]. For the no defect case, in addition to the peaks predicted at the cage frequency f_c, shaft rotational frequency f_s and its harmonics, other peaks were present in the modelled results, which were not discussed. It was shown that for two defects on the outer raceway, the vibration amplitudes of the defect-related frequency components were larger than those obtained for a single defect. However, the amplitudes of the predicted vibration spectra (velocity) of the housing did not match with those obtained experimentally. This highlights the amplitude mismatch reported earlier by several

researchers [91, 93, 103, 104, 109].

Based on the earlier models in references [87, 109], Patil *et al.* [111] reported on the development of a 2-DOF lumped parameter model in order to study the effect of the size of localised raceway defects on the vibration response of a deep-groove ball bearing. The shape of the defects was modelled as a half-sine wave, and three defect sizes were considered (diameters as 0.5 mm, 1 mm and 1.5 mm). The modelling results showed that the amplitude of the vibration spectra increased with increasing defect size for both inner and outer raceway defects. The experimental results were only shown for the outer raceway defect. The comparison of the modelled and experimental results shows that neither the outer raceway defect frequency component f_{bpo} and associated harmonics nor their amplitudes match with each other. While the percentage error of approximately 6% was reported between the modelled and measured frequency components, the percentage error between their amplitudes, shown as an acceleration power spectrum (linear), was approximately 60,000%. The mismatch between the modelled and measured frequencies could be due to the ignorance of the slippage [96] of the rolling elements, whereas the amplitude mismatch problem has also been reported by others [91, 93, 103, 104, 109, 110].

A unique approach was presented by Nakhaeinejad *et al.* [112] for modelling the vibration response of a deep-groove ball bearing due to localised line spalls using vector bond graphs [284]. They developed a 33-DOF multi-body dynamic model of a bearing with nine balls and two rings (outer and inner) considering the translations in the radial (global cartesian x- and y-directions) and axial (global cartesian z-direction) planes. Unlike the majority of the multi-body models, the model by Nakhaeinejad *et al.* [112] incorporated the slippage of the rolling elements [96], and their inertial and centrifugal effects. Various widths and heights of the localised defects were modelled on the outer raceway, inner raceway, and one of the rolling elements. The validation of the modelled results was reportedly achieved by comparing them with experimental measurements. Nakhaeinejad *et al.* [112] reported that higher amplitudes are generated for larger

defects.

Based on the previous 2-DOF models reported in references [87, 109, 111], a numerical model was proposed by Tadina *et al.* [113] to simulate the vibration signatures of a ball bearing having localised defects during run-up. In contrast to all the multi-body models reviewed so far [100–112], Tadina *et al.* [113] modelled the outer ring as deformable, using finite elements (two-noded locking-free shear, curved beam elements [285]). Although it was mentioned that the slippage or sliding between the components of the bearing was given by a prescribed function within the model, from the set of equations provided in the text, the slippage-related function could not be found. The localised defects on the raceways were modelled as impressed ellipsoids, which are formed due to the application of a radial load between the raceways and rolling elements of a bearing. On the contrary, the defect on a ball was modelled as a flattened region. The simulated results were subjected to envelope analysis [251, 252]. Tadina *et al.* [113] neither conducted the experimental work to measure the vibration response of defective rolling element bearings nor did they used the results from the literature to compare their modelled results.

Zhao *et al.* [114] used a commercial multi-body dynamics software package, RecurDyn [286], to model a rolling element bearing having localised line spalls. As their objective was to present a technique for estimating the size of a localised defect, they did not provide sufficient details to fully understand the modelling work. Although it was shown that the simulated results agreed well with those of the experimentally measured data taken from the bearing data centre at CWRU [283], the actual modelling process could not be followed due to insufficient details provided in the paper.

2.3.3.1 Rolling element–raceway contact force

For simulating the vibration response of defective rolling element bearings, authors of the aforementioned multi-body dynamic models [100–102, 104–106, 109–113] have included an analytical solution for estimating the rolling element-to-raceway contact

forces as non-linear Hertzian contact springs [175–177]. In these models [100–102, 104–106, 109–113], for the extent or length of a rectangular-shaped bearing defect with sharp, step-like entry and exit edges (refer to Figure 2.3 to see a rectangular-shaped defect), the magnitude of the contact forces instantly decreases to zero and increases to its static load value [3, Chapter 7, pages 234–237] as the rolling elements enter into and exit out of the defect, respectively. This is largely due to assuming that the rolling elements traversing through the defect follow its geometry (or profile); for example, in the model by Sawalhi *et al.* [105], the path of a rolling element was modelled such that its centre follows the geometry of the defect. As a result, this produces very large, erroneous, impulsive forces in a system at the entry and exit points of a defect due to an instantaneous change in the system acceleration in order to maintain its equilibrium. It will be discussed later in Section 2.5 that an impulsive response, mainly characterised by energy in high-frequency range, at the exit point of a defect is realistic; however, similar high-frequency impulsive response at the entry point is unrealistic and not observed in practice [4, 5, 161, 162, 165].

To prevent the occurrence of unrealistically large impulsive forces and to achieve the simulated vibration response comparable to measured data, the sharp step-like variations were modified to occur gradually [101, 102, 105, 112]. This was achieved by modifying the shape of the defect so it resembles an assumed path of a rolling element while traversing the defect. However, apart from the suggestions that a gradual response should be used to reflect a realistic scenario [105], no analysis has been presented nor has the mathematics behind the modification been discussed in the literature. It is also interesting to note that despite the incorporation of the rolling element-to-raceway contact modelling by previous researchers [100–102, 104–106, 109–113], their main focus was on the presentation of the vibration response of rolling element bearings, such as acceleration, velocity or displacement, rather than the presentation of the contact force results. Based on the work presented here, the author of this thesis has recently published [4, 5] an analysis of the dynamic rolling element-to-raceway contact interac-

tion as the rolling elements traverse through a localised defect within a bearing.

In the work presented here, a new mathematical model has been developed to accurately predict the gradual decrease in the contact forces as the rolling elements enter into a raceway defect within a bearing. This will be presented in Chapter 3, and several comparisons between the results estimated using the new model and previous models will be shown.

A brief recapitulation of the non-linear multi-body dynamic models

The non-linear multi-body dynamic lumped parameter models were developed including various components of a rolling element bearing and associated rotor–bearing systems. The outer and inner rings were generally modelled as rigid (lumped) masses and the contacts between the raceways and rolling elements were modelled as non-linear springs. The problem of amplitude-mismatch discussed during the review of the impulse-train models [91, 93] was also highlighted during the discussion of the multi-body models [103, 104, 109–111]. Amplitude-correction factors were applied to the predicted results; however, they were neither discussed nor provided [93, 103, 104]. The well-known envelope analysis technique [30, 251, 252] was implemented on the simulated time-traces of the vibration signals (acceleration and velocity) generated as a result of localised defects on the components of a rolling element bearing in order to demonstrate the significant defect-related frequency components; fundamental, harmonics, and associated sidebands.

2.3.4 Finite element models

This section is concerned with those numerical models that use either commercial FE codes or a combination of analytical and FE codes in order to simulate the response of a rolling element bearing or associated bearing structure due to the localised bearing defects. Commercially available FE codes can be classified on the basis of their

solver time integration schemes. These schemes include *implicit* [287–294] and *explicit* [292, 295–305] time integration methods. Based on the implementation of the time integration methods, FE models available in the literature for studying various aspects of rolling element bearings, can be broadly categorised into *implicit static* and *explicit dynamic* models. An explanation of the difference between implicit and explicit time integration schemes is provided in Appendix D.

Although the explicit dynamic FE models are most relevant to the work presented in this thesis, implicit FE models are also briefly reviewed here.

2.3.4.1 Combination of analytical and implicit FE models

Kiral *et al.* [115, 116] simulated the vibration response of a bearing structure (pedestal — a plummer block), which houses a ball bearing with and without a defect. Although the concept of mathematically generating the periodic defect-induced impulse-train forcing model to simulate the impulsive force as a result of ball–defect interaction was not new, the output of the model was provided as an input to a commercial FE software package, I-DEAS [306]. The outer ring of the bearing and structure were modelled as a rigid assembly using I-DEAS. A localised defect on the outer raceway was modelled by simply amplifying the magnitudes of the radial forces at two adjacent nodes considered to represent the edges of the defect; the depth of the defect was not considered. The mathematical logic behind the values of the amplification factors was not discussed; however, they were chosen to be 6 [115] and 10 [116]. The width of the localised defect was chosen to be the width of two neighbouring nodes as a result of the discretisation of the assembly structure into finite elements. While a single defect was simulated in their former model [115], Kiral *et al.* simulated multiple defects (two, three, and four) on the outer raceway, located at the angular separation of 90°, in their latter model [116]. Standard condition-based monitoring techniques, time (root mean square (RMS) value and kurtosis [23]) and frequency domain (envelope analysis [251, 252]), were applied to the FE modelling results for verification purposes. They reported that

the envelope analysis technique can efficiently detect outer and inner raceway defects, but not the rolling element defects.

2.3.4.2 Implicit static models

In the context of the present study, *implicit static* FE models refer to those models that use a certain type of commercial FE software package or code to analyse, generally, the static stress and/or load distribution within rolling element bearings. A few examples of the FE software packages, which are primarily used for their implicit solving capabilities, are ANSYS [307], Abaqus [308], ADINA [309], ALGOR [310], I-DEAS [306] and NASTRAN [311].

For the case of non-defective rolling element bearings, a number of researchers [312–328] have conducted FE modelling studies using the aforementioned software packages to primarily investigate the following static parameters — stresses at the rolling element-to-raceway contact interfaces, rolling element-to-raceway contact forces, load-deflection relationships, load carrying capacity of rolling elements, stiffness matrix calculation, and fatigue life. As the models in references [312–328] do not include a defect within the bearing models, they are not directly relevant to the current study, and therefore, are not reviewed here. However, from the title of one of the publications [317], it appears that the author had carried out an FE modelling study to predict the vibration response due to a defect located at the outer raceway of a bearing. It is important to clarify that the work presented in reference [317] was related to the transient dynamic analysis conducted using ANSYS [307]. In a transient analysis, loads have to be manually defined as a function of time, and the load-versus-time curve has to be divided into suitable load steps. The force-versus-time curve presented in reference [317] simply hypothesied and simulated the change in the contact force, similar to that of a square wave pattern with vertical step responses at the edges of the defect, representing a step decrease and increase in the contact force. The FE model in reference [317] did not included any other component of a bearing except half of the outer ring

structure. As the change in the dynamic forces between the rolling elements and a defect within a bearing is primarily responsible for generating impulsive vibration signals, the force cannot be simply simulated using a square wave-like function. Therefore, the work presented in reference [317] does not represent an accurate simulation of bearing dynamics.

The explicit dynamic FE models that are most relevant to the work presented in this thesis are reviewed in the following section.

2.3.4.3 Explicit dynamic models

In the context of the present study, *explicit dynamic* models refer to those models that were developed using explicit dynamic FE software packages; for example, LS-DYNA [329], ANSYS Autodyn [330], Abaqus/Explicit [308], and NASTRAN Explicit [311]. These are commercial FE codes that use an explicit time integration scheme [292, 295–305] during the solution phase to solve for time-varying acceleration, velocity, and displacement results.

As for the case of implicit models [312–328], explicit FE models for non-defective rolling element bearings have been developed [331–334]. These models simulate deep-groove ball bearings, and compare the numerically estimated stress distribution results, obtained using LS-DYNA [329], at the rolling element-to-raceway contact interfaces, with the analytical results obtained using the classical Hertz theory of elasticity [175–177].

Only four publications [117–120] have been found during the survey of the literature that are concerned with the modelling of localised defects within rolling element bearings using an explicit FE software package. It should be noted that all four publications have appeared very recently in the literature and after the current study began. A critical review of these finite element models is provided below.

First publication: In 2010, a dynamic FE model of a deep-groove ball bearing was presented by Shao *et al.* [117]: the three-dimensional (3-D) model was solved using

LS-DYNA [329]. The bearing was installed in a bearing structure (pedestal); the model of the bearing pedestal was similar to the one presented by Kiral *et al.* [115, 116] as discussed above. Shao *et al.* [117] modelled the same-sized defect on the outer raceway, inner raceway, and one of the rolling elements; however, the size of the defect was not mentioned. The numerically obtained time-varying acceleration results at two nodes, located on the bearing structure, were shown for four simulations: 1) no-defect, 2) an outer raceway defect, 3) an inner raceway defect, and 4) a rolling element defect. While one of the nodes (referred to as *P1*) was located at the 6 o'clock position in close proximity to the outer ring of the bearing, the other (referred to as *P2*) was located in a mounting hole of the pedestal, at a horizontal distance of approximately 60 mm from *P1*. The results showed that the magnitude of the acceleration was highest for the outer raceway defect followed by the inner raceway defect, and lowest for the rolling element defect. It was also found that, for the outer raceway defect simulation results, the magnitude of the acceleration signal was significantly lower at *P2* in comparison to *P1*. Because the node at *P1* was in close proximity to the outer raceway defect, the low level of the acceleration signal at *P2* showed that the defect-related impulsive energy attenuates as the output location is moved away from the defect location. Standard time domain statistical parameters, such as RMS, peak value, and kurtosis [23] were compared for the four numerical simulations. As the paper was presented at a conference, no further details were provided, such as loads and boundary conditions.

Second publication: In 2012, Guochao *et al.* [118] presented a 3-D FE model of a deep-groove ball bearing having a localised defect on its outer raceway. The model was solved using LS-DYNA [329], and the time-varying acceleration, velocity, and displacement results at three nodes located on the outer ring were shown. The nodal locations were: 1) either at the defect or in close proximity to the defect — neither the nodal location nor the defect was shown in the model, 2) 90° to nodal location '*1*', and 3) 180° to nodal location '*1*'. As the modelling results were not compared with experimental results, Guochao *et al.* [118] validated the modelled results by comparing the

numerical outer raceway defect frequency (BPFO) f_{bpo}, (obtained after implementing the Fast Fourier transform (FFT) [250] on the time domain acceleration results) with that of the analytically estimated kinematic defect frequency [3, Chapter 25, page 994]. Although it was shown that the numerical and analytical f_{bpo} estimates matched reasonably well with each other, the FE model and results have significant ambiguities and/or potential errors. These are discussed below in the following paragraphs along with appropriate reasoning.

On the one hand, it was mentioned that the outer ring was modelled as rigid and all the degrees of freedom, translations in the global cartesian x-, y-, and z-directions, of the nodes located on the outer ring were translationally constrained; that is, fixed. On the other hand, the nodal acceleration, velocity, and displacement results at the aforementioned three nodes located on the outer ring were shown to be varying with time. These two results are contradictory because the response at nodes that are translationally constrained in all the three directions cannot vary with time; that is, the nodal results should be zero throughout the solution.

The magnitude of the numerically estimated time-varying nodal acceleration results for the nodes located at the outer ring were of the order of 10^7 g, which is unrealistically high. One of the reasons for such high acceleration magnitudes is due to modelling the outer ring as a rigid body, which may have resulted in the over-stiffening of the bearing model; in the context of FE models, rigid bodies cannot undergo bending or flexural deformation as is the case for the majority of the multi-body models in references [100–112], except for the models in references [113, 114], reviewed earlier in this chapter. The other reason for such high acceleration magnitudes is that the model did not include structural damping. Furthermore, as described in the preceding paragraph, it is unclear how the time-varying nodal results could be achieved, despite translationally constraining the outer ring.

Guochao *et al.* [118] mentioned that no axial and radial clearances were built into the bearing model. Although not discussed, the pictorial presentation of the stress

distribution at the rolling element-to-raceway contact interfaces, Figure 2 in reference [118], does not seem to provide realistic information. This is because, in the case of zero radial clearance, the extent of the load zone is typically 180° around the circumference of the outer and inner rings; that is, ±90° from the point where the radial load is applied [3, Chapter 7, pages 235, 239]. This implies that the rolling elements located within the 180° radial load zone extent should have the applied radial load distributed as per the well-developed analytical static solution [3, Chapter 7, pages 234–237]. However, from the pictorial presentation, the number of rolling elements shown to be loaded or (mechanically) stressed were three, whereas the correct number should have been at least four as per the static load distribution solution [3, Chapter 7, pages 234–237].

In addition to the aforementioned ambiguities and/or errors, Guochao *et al.* [118] did not provide several details, which are necessary to clearly understand the modelling work. These include the following:

- Modelled defect — neither the shape of the modelled defect nor the precise location of node '*1*' was clearly mentioned; node '*1*' was mentioned to be either located at the defect or in close proximity of the defect.

- Material model and behaviour — except mentioning that the outer ring was modelled as a rigid body, it was not mentioned whether the remaining components within the model of the bearing, such as inner ring, rolling elements and cage, were modelled as rigid or flexible bodies.

- Friction — it was not mentioned whether friction between the rolling elements and the raceways was applied.

Third publication: With the aim of studying the effect of the shape of a localised defect on the vibration signatures, Liu *et al.* [119], in 2013, presented a 3-D FE model of a deep-groove ball bearing. The localised defects were modelled on the outer raceway of the bearing, and three different shapes of the defects were modelled — rectangular,

hexagonal, and circular. The model was solved using LS-DYNA [329], and the effects of various defects were studied using standard time domain statistical parameters, such as RMS, crest factor, and kurtosis [23]. It was mentioned that while the numerically modelled vibration, displacement, response of the inner ring was mainly influenced by the shape of the localised defects, it was also slightly affected by the radial load, axial load, and shaft speed. Although the model presented by Liu *et al.* [119] is better than that of the previous model in reference [118], a few limitations of the model in reference [119] are critiqued in the following paragraphs.

The outer surface of the outer ring was modelled as a rigid surface, and all the six degrees of freedom, translational and rotational, for all the nodes located on the outer surface of the outer ring were constrained. Although not mentioned by Liu *et al.* [119], according to the understanding of the author of this thesis, one of the reasons for modelling the outer surface as rigid was to simulate a rigid support along its circumference, such as a bearing mounted in a housing or pedestal. It is also understood that the purpose of translationally constraining the outer ring was to prevent it from rotation during the simulation, as its (frictional) contact interaction with the rolling elements can cause the outer ring to rotate, which is fundamentally incorrect for the simulated rotating-inner-race-fixed-outer-race configuration. While modelling the outer surface as rigid may cause over-stiffening of the outer ring, constraining the outer ring causes incorrect load distribution on the rolling elements [3, 245–248], which consequently can affect the vibration response, as the (loaded or stressed) rolling elements interact with the defective surface.

Liu *et al.* [119] presented two types of validation for the numerical modelling results:

1. The *first validation* was related to simply comparing the numerical estimate of the BPFO (obtained after the implementation of the FFT on the modelled velocity time-traces) with the analytically estimated kinematic defect frequency [3, Chapter 25, page 994]: this type of validation has not only been followed for

previous FE models [117, 118], but also for the aforementioned multi-body models [100–114]. However, prior to demodulating the numerical velocity time-traces using the envelope analysis technique [251, 252], they were low-pass filtered, with a cut-off frequency of 500 Hz. It is interesting to note that the value of the cut-off frequency was mentioned as 500 Hz in the main text; however, in one of the figures (Figure 2 in reference [119]), it was mentioned as 800 Hz. Nevertheless, it is fundamentally incorrect to low-pass filter the modelling results as it eliminates the characteristics of the defect-related impacts, which are essentially impulses of short-duration; that is, the defect-related impulsive signals contain a significant amount of energy in the high-frequency range.

2. The *second validation* was related to comparing the shape of the numerically obtained acceleration waveform with the experimental results. While the simulated acceleration results were low-pass filtered, with a cut-off frequency of either 500 Hz or 800 Hz, the experimentally measured acceleration results were low-pass filtered, with a cut-off frequency of 2000 Hz. Although the comparison of the shapes of the waveforms for the numerical and experimental results shows some resemblance, their amplitudes were significantly different — the amplitude of the experimentally measured acceleration data (after low-pass filtering) was less than 100 g compared to approximately 4,000 g for the numerically modelled results (after low-pass filtering). One of the reasons for such a high magnitude could be the over-stiffening of the outer ring, as transforming its outer surface to rigid prevents the ring from flexurally deforming. It should be noted that the amplitudes of the numerically modelled acceleration time-traces shown in reference [118] were of the order of 10^7 g. Such high values of the acceleration magnitude are unrealistic. As mentioned earlier, the amplitude mismatch problem has also been reported for several multi-body modelling results [91, 93, 103, 104, 109–111].

In addition to the above-listed concerns, Liu *et al.* [119] did not provide the following

details:

- Nodal location of the numerical results — for various cases of the numerical simulations, the time-varying displacement, in the global cartesian y-direction (the displacement in global x-direction was constrained), at the centre of the inner ring was shown. As there was no mention of a shaft in the FE model and the centre of the bearing model was hollow, the location of the displacement results is unclear.

- Application of the low-pass filter to the numerical results — it is unclear whether the numerically modelled displacement results were low-pass filtered before estimating the time domain statistical parameters; RMS, crest factor, and kurtosis.

- Noise in the simulation results — on the one hand, it was mentioned that the surfaces within the bearing model were smooth and no noise was generated during the numerical simulations. On the other hand, it was mentioned that the reason for applying the low-pass filter was to remove undesired high-frequency noise. These are contradictory statements. It will be demonstrated later in this thesis, Chapter 4, that a numerical solution estimated using LS-DYNA generates a significant amount of numerical noise, which is an inherent feature of its solution phase [335, page 1110]. As part of the current study, an explicit dynamics FE model of a rolling element bearing was generated and solved using LS-DYNA. This model is presented in Chapter 4. In Section 4.5, Chapter 4, the cause of the numerical noise is explained by developing a novel hypothesis and analytically estimating the rolling contact noise frequencies.

- Application of damping — it is not clear whether damping was applied to the FE model.

- Radial and axial clearances — it was not mentioned whether the clearances were built within the model.

Fourth publication: A 3-D FE model of a deep-groove ball bearing with localised defects on the outer and inner rings was presented by Utpat [120] in 2013. He discussed the effects of various sizes of defects on the magnitudes of the numerically modelled acceleration at a node located on the outer surface of the outer ring. The FE model was solved using LS-DYNA, and it was shown that the vibration levels increased with increasing defect size and shaft rotational speed. Although the numerical results were shown to be in close agreement with experimental results, Utpat [120] did not provide important details necessary to verify the presented modelling results. The following paragraphs describe some of the potential issues with the work presented in reference [120].

The inclusion of the cage within the FE model of the bearing was neither mentioned nor shown in the image of the FE model (Figure 2a in reference [120]). The function of a cage in a bearing is to retain the rolling elements, and that is why, it is often referred to as a *retainer*. Without the presence of a cage, the rolling elements will interact with each other causing bearing lockup — in summary, a rolling element bearing cannot work without a cage in a real bearing. Despite the absence of the cage from the bearing model, the numerically modelled acceleration results presented in reference [120] resemble a typical vibration time-trace of a defective bearing, which is puzzling considering the omission of a critical bearing component. It is, however, possible that the centre of the rolling elements could have been connected and rotated, thereby, constraining their centrifugal and inertial effects, but it was not mentioned in the publication.

Utpat [120] described the discretisation of the bearing model (outer ring, inner ring, and rolling elements) into nodes and elements (Figures 2a and 2b in reference [120]). Although the element mesh size was not mentioned, the meshing of the components is coarse, especially, the tetrahedral mesh of the outer ring. To the experience of the author of the thesis, it is impossible to achieve smooth rotation of the rolling elements about their own axes with such a coarse meshing. It will be shown later in this thesis,

Chapter 4, that for an explicit dynamics FE modelling of a rolling element bearing, the meshing at the rolling element-to-raceway contact interfaces within the load zone must be fine enough so that the contact between the rolling elements and raceways of the bearing can be maintained at all times. This is because if the rolling element-to-raceway contact is lost, the transmission of the forces (load) between the components will be incorrect, which can affect the vibration response of the bearing. It is generally recommended to use at least 20 EPW for a transient dynamic structural analysis [336, chapter 5]; however, the element mesh size that was found to be necessary to discretise the FE model of the bearing for the current study corresponds to 97 EPW, which is nearly 5 times the recommended EPW criterion [336, chapter 5]. This will be further discussed in details in Section 4.2.2, Chapter 4.

It was mentioned in reference [120] that the numerical acceleration time-traces were estimated at a node located at the outer surface of the outer ring. On the one hand, for the case of the simulated outer raceway defect, no units of the acceleration levels were shown (Figure 4 in reference [120]); the limits of the instantaneous acceleration levels were approximately $\pm 20 \times 10^4$. On the other hand, for the case of the modelled inner raceway defect, the limits of the instantaneous acceleration levels were approximately $\pm 15 \times 10^4$ (approximately 25% less than the outer raceway modelling acceleration levels), and the units were shown as $\mathrm{m/s^2}$ (Figure 6 in reference [120]). The frequency domain representation of acceleration results for both outer and inner raceway defects were shown on a linear scale, and the amplitudes at the fundamental outer and inner defect frequencies, f_{bpo} and f_{bpi}, respectively, were mentioned as $905\,\mathrm{mm/s^2}$ and $693\,\mathrm{mm/s^2}$, respectively. Given that these amplitudes are approximately 25% different from each other, it is highly likely that the units for the numerically modelled acceleration time-traces related to the outer raceway defect simulation (which are not shown in Figure 4 in reference [120]) could also be $\mathrm{m/s^2}$. Nevertheless, even for the case of the modelled inner raceway defect, the instantaneous levels of the acceleration time-traces, $\pm 15 \times 10^4\,\mathrm{m/s^2}$ (approximately $\pm 15,000\,\mathrm{g}$), are unrealistically high. It is interesting to

note the instantaneous amplitudes of the experimentally measured acceleration data were between $\pm 100\,\mathrm{m/s^2}$ (approximately $\pm 10\,\mathrm{g}$). The excellent match between the numerical and experimental results shown in Figure 11 in reference [120] is surprising. It should also be noted that unrealistically high acceleration levels of $10^7\,\mathrm{g}$ [118] and 4,000 g [119] were also reported in the previous modelling results discussed above.

In addition to the aforementioned concerns, the following details were not provided by Utpat [120], which are necessary to understand the modelling work:

- Material behaviour — it was not mentioned whether the components of the bearing model, outer ring, inner ring and balls, were modelled as rigid or flexible bodies.

- Loads and boundary conditions — the boundary conditions applied to the model were not described. It is especially, important to know how the outer ring was kept stationary, because in the event of rotation of the inner ring and rolling elements, the outer ring would also rotate, if not constrained. However, in the experience of the author of this thesis, the outer ring cannot be translationally constrained in either global cartesian x-, y- or z-directions, as it will cause an incorrect load distribution, and consequently affect its vibration response. It should be noted that Liu *et al.* [119] modelled the outer surface of the outer ring as rigid so it can be fixed in its position. However, this resulted in the overstiffening of the outer ring, which might have resulted in the very high numerical acceleration levels of 4,000 g compared to the experimental acceleration levels of less than 100 g.

- Friction — it was not mentioned whether friction between the rolling elements and the raceways was applied.

- Clearance — it was not mentioned whether any clearance between the rolling elements and raceways was built into the model.

- Defect size — despite the model being 3-D, the defect sizes were mentioned as 0.25 mm, 0.5 mm, 1 mm and 2 mm. It is not clear whether these figures represent length, width, or height.

A brief recapitulation of the explicit dynamic FE models

From the aforementioned review of the explicit dynamic FE models [117–120], it appears that the modelling of rolling element bearings having localised defects did not provide information additional to the useful insights gained through the multi-body models [100–114]. The authors of the explicit FE models [117–120] have compromised performance by modelling either the whole outer ring as rigid or its outer surface as rigid. This has caused over-stiffening of the bearing structures leading to unrealistically high acceleration levels. Therefore, the performance of the FE models can be considered on a par with that of the multi-body models. The problem of significant mismatch between the predicted and measured amplitude levels reported for the multi-body models [91, 93, 103, 104, 109, 110] remains a problem with existing FE models.

2.4 Extended defects

Although the work presented in this thesis is concerned with localised defects, a brief review of the models for predicting the vibration response of bearings with extended defects is provided in this section.

An *extended defect* can be characterised as a defect that is larger than a localised defect (for example, its size can be greater than the spacing between two rolling elements), but smaller than a distributed defect (for example, waviness is generally along full raceways). Once a localised defect (a spall) is created on either raceway of a bearing due to surface fatigue [23, 169–174], the continuous and repetitive passage of the rolling elements over the spall results in the generation of impulsive (contact) forces. This cyclic operation wears the edges, especially the trailing edge, of the spall causing

it to gradually grow or expand in size, and results in the generation of an extended defect [337].

It was mentioned at the beginning of this chapter that extended defects have received much less attention compared to localised [90–120] and distributed defects [122–160]. Only one publication [121] could be found in the literature that discusses the vibration modelling of a rolling element bearing having an extended defect. This is discussed in the following paragraphs.

Extending their previous work on the vibration modelling of a rolling element bearing due to a localised defect [105] (discussed in Section 2.3.3), Sawalhi *et al.* [121] presented a combined non-linear multi-body dynamic model for gears and bearings in which an extended defect on either of the two raceways can be studied in the presence of gear interaction. They characterised the extended defects as faults that extend beyond the spacing between two rolling elements, and have been smoothened by the successive passage of the rolling elements, so that no sharp impulses are generated, and no defect-related frequencies are detected in the envelope (demodulated) spectrum. They referred to the extended defects as *rough surfaces*.

Similar to the considerations in their previous model [105], Sawalhi *et al.* [121] modelled the inner and outer rings as rigid bodies, and the rolling element-to-raceway interfaces as non-linear contact springs. The mass of the rolling elements, and their inertial and centrifugal effects were not considered due to the low run speeds used in the experiments. Slippage of the rolling elements [96] was included in their model to obtain a closer resemblance between the predicted and measured vibration spectra. Damping was included via a grounded damper attached to the inner raceway. An additional mass-spring-damper system, resonant-changer, representing a typical high-frequency bearing resonance (15 kHz) was attached to the outer raceway.

The objective of the work presented by Sawalhi *et al.* [121] was the differential diagnosis of gear and bearing defects [96–98], which was achieved by utilising the difference in the cyclostationary properties of the gear and bearing signals [255, 256, 259].

The simulated results included acceleration signals for inner and outer raceway extended spalls, and their corresponding squared envelope [95] and cyclic spectral densities [30, 257, 258]. The modelled results were compared with the experimental data for a bearing where extended faults were etched on both of its raceways, and good similarity between the two results was achieved. Due to the rough surface characteristics of the extended defect, the ineffectiveness of the envelope spectrum to detect the inner race defect frequency f_{bpi} was also demonstrated. It was found that use of the spectral correlation function enabled detection of the defect frequencies.

2.5 Defect-related vibration characteristics

The main objective of the models, impulse-train [90–99], multi-body [100–114], and FE models [115–120], reviewed so far was to predict the significant vibration frequency components; fundamental, harmonics, and associated sidebands, related to the localised surface defects in rolling element bearings. The emphasis on investigating the change in the characteristics of bearing vibration signals at the edges of a defect, leading and trailing, has been far less compared to the efforts expended on the development of the aforementioned models. On the one hand, as point spalls were considered by the majority of researchers [90–98, 100, 103, 106–111], it is logical to say that the change in the characteristics of vibrations at the two edges of point spalls could not possibly be studied. On the other hand, a few researchers have modelled localised defects as line spalls [99, 101, 102, 104, 105, 112–114, 116, 119] as a function of width and depth; however, the change in the vibration characteristics was only briefly mentioned in references [105, 112, 114] in the context of estimating the average size of bearing defects.

It is the aim of this section to present a review of existing knowledge corresponding to the characteristics of the vibration response at the leading and trailing edges of a bearing defect.

2.5.1 Entry- and exit-related transient features

Epps, in his doctoral thesis [161] and a conference paper co-authored by McCallion [162], provided a detailed insight into the characteristics of the vibration response at the two edges of a bearing defect. They measured the acceleration waveforms (time-traces) of ball bearings with three different sizes of localised defects. The defects were artificially etched on the outer and inner raceways, and their sizes ranged from 0.2 mm to 3.0 mm. On the basis of the experimental observations, they hypothesised that the defect-related (vibration) transient, as a result of the traverse of a rolling element over the defect, was essentially composed of two parts or events — first, the entry of the rolling element into the defect, and second, its exit out of the defect. For the ease of relating the entry and exit of the rolling elements into and out of a bearing defect, the leading and trailing edges of a defect are referred to as the starting and ending positions, respectively, throughout this thesis.

Figure 2.3 shows a schematic of a two-dimensional (2-D) model of a rolling element bearing comprising an outer ring, an inner ring, a few rolling elements, and a geometric rectangular defect located on the outer raceway of the bearing. The *starting* and *ending* positions of the defect are illustrated in the figure. For discussion purposes, one of the figures from Epps's thesis [161] is shown in Figure 2.4. It represents the experimentally measured acceleration of the ball bearing having an outer raceway defect of width 3.0 mm. The two annotations in the figure, '*Point of Entry*', and '*Point of Impact*', correspond to the entry and exit of a rolling element into and out of the defect, respectively. The change in the defect-related transient between the two points, shown in Figure 2.4, is clearly evident.

Epps *et al.* [161, 162] suggested that the entry of the rolling elements into a defect can be considered as a low-frequency event with no evidence of impulsiveness, and in contrast, their exit out of the defect can be considered as a high-frequency impulsive event that can lead to the excitation of a broad range of frequencies, and consequently,

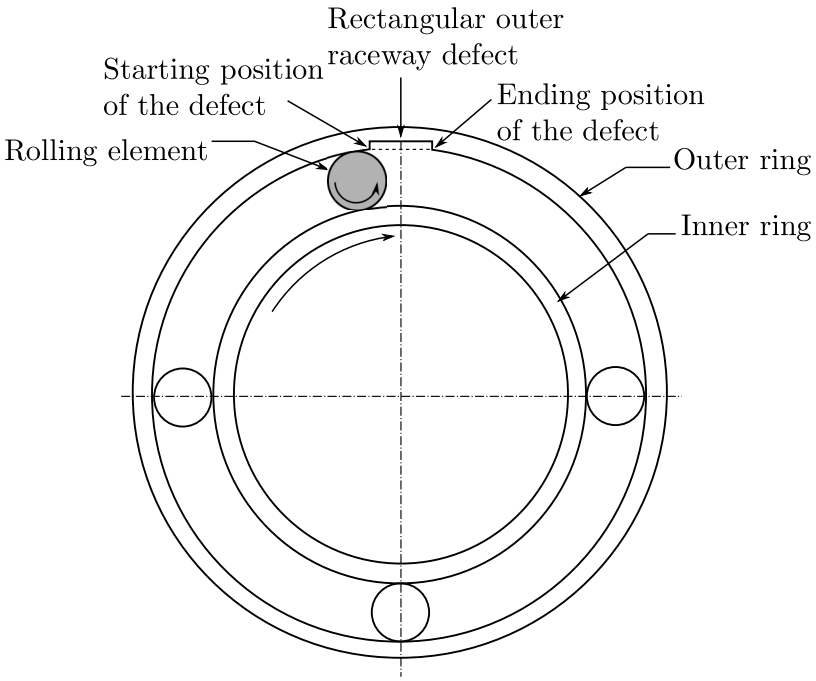

Figure 2.3: A 2-D schematic of a rolling element bearing comprising an outer ring, an inner ring, a few rolling elements, and a geometric rectangular defect on the outer raceway.

resonant bearing modes. Epps *et al.* [161, 162] found that the time difference between the entry and exit points in the measured acceleration signals approximately correlate with the size of the defects. The correlation, therefore, successfully supported the distinction of the entry- and exit-related events, and also transients, as the rolling elements traverse through the defects.

Previous experimental studies [21, 338] have suggested that as the width of a bearing defect increases, the magnitude of the defect-related vibration impulses increases, but the characteristic shape of the impulsive signals is not affected. Similarly, for increasing rotational speed, the magnitude of the impulses increases, but their shape does not change. However, Epps [161] found that not only the magnitude of the impulses, but also their characteristic shapes were influenced by the radial load, rotational speed, and the position of a defect with respect to the bearing load zone [3, 245–248].

For condition-based monitoring of machinery, Dowling [164] highlighted the potential need for the application of non-stationary analysis, such as wavelet transform

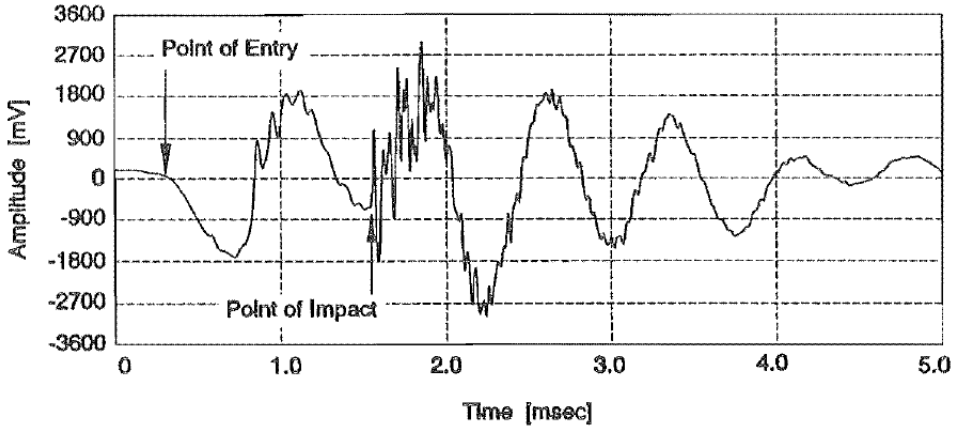

Figure 2.4: Experimentally measured acceleration response of a rolling element (ball) bearing having an outer raceway defect of 3.0 mm, taken from references [161, 162].

[23, 339, 340] and Wigner-Ville distribution [339, 341–343]. He discussed the non-stationary characteristics of machinery-based vibration signatures, generally measured in practice, with attention focused on the stochastic nature of signatures associated with defective bearings. He presented a recorded waveform from a helicopter gearbox bearing, having an outer raceway defect, from an earlier reference [163], and briefly described the nature of the defect-related transient signal. The waveform is shown in Figure 2.5 for discussion purposes.

With regards to the results in Figure 2.5, it was mentioned that a rolling element took approximately 0.3 milli-seconds (ms) to traverse through the outer raceway spall. The time separation of 0.3 ms is shown in the figure: the two ends of the time separation marker correspond to the aforementioned entry- and exit-related events. It was described that the transient vibration commenced as the rolling element entered the defect, and upon its exit from the defect, an impact was generated that interfered with the transient that occurred at the beginning, resulting in a 180° phase shift. Thus, Dowling [164] related the change in the characteristics of the defect-related vibration signatures associated with the entry and exit of the rolling element into and out of the defect, respectively, by a 180° phase reversal. However, no further discussion pertinent to the charactersitics of the transient vibration response was provided.

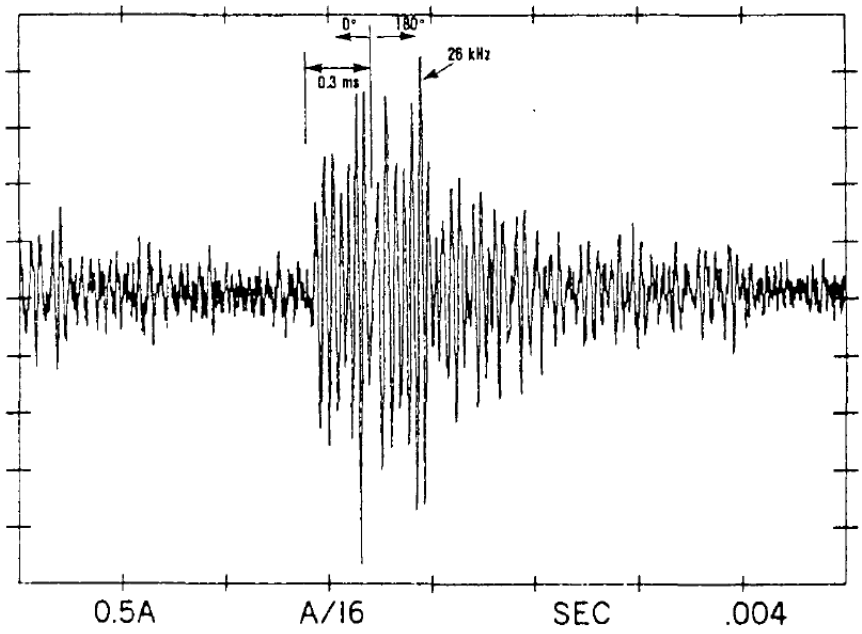

Figure 2.5: Band-pass filtered accelerometer time-trace from a helicopter gearbox bearing having an outer raceway spall, taken from references [163, 164].

Although the results in Figure 2.5 [164] are not as clear as those presented by Epps *et al.* [161, 162] (Figure 2.4), both represent similar findings — no evidence of impulsiveness at the entry of the rolling element into the defect, and impulse-like signatures at its exit out of the defect.

A careful observation of Figure 2.5 shows an additional peak after the exit-related impulse; however, the occurrence of the multiple impulses was not discussed. Sawalhi *et al.* [105] initially considered that the occurrence of the two impulses was associated with the entry and exit of the rolling elements into and out of a bearing defect, respectively; however, later on, they invalidated their claim [165]. This double-impulse phenomenon described in the next section.

2.5.2 Double-impulse phenomenon

Sawalhi *et al.* [105] observed double impulses in the results simulated using their proposed non-linear multi-body dynamic model for predicting the vibration response

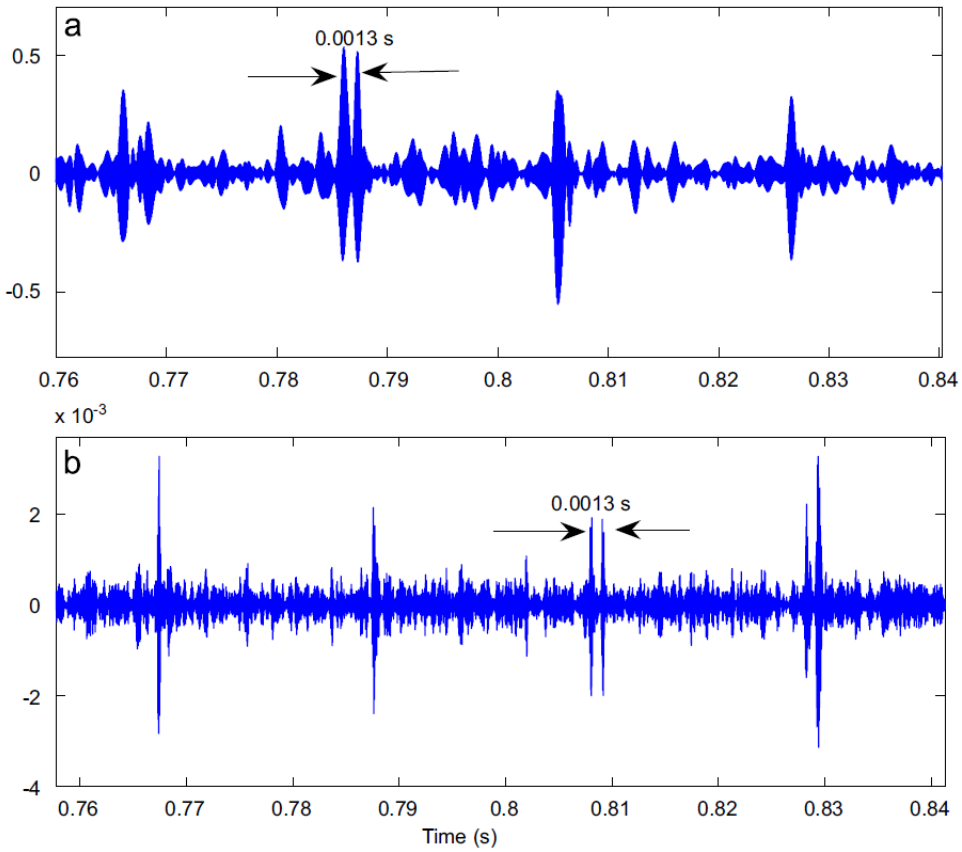

Figure 2.6: Band-pass filtered signals (one complete rotation of the shaft) with a spall in the outer race, taken from reference [105]: (a) measured, (b) simulated.

of a rolling element bearing having a localised raceway defect: the review of their analytical model [105] is provided in Section 2.3.3. Interestingly, they also found the presence of double impulses in the experimentally measured results. For discussion purposes, a figure that compares the measured and simulated results from their work [105], illustrating the presence of double impulses is shown in Figure 2.6.

It was reported that the time separation of 0.0013 seconds between the two impulses, highlighted in the subplots of Figure 2.6, corresponds approximately to time that a rolling element takes to traverse the width of the outer raceway defect. The close match between the simulated and measured results not only helped Sawalhi *et al.* [105] validate their model, but also provided their results with a firm theoretical background, which appeared to be in agreement with the findings reported earlier by Epps

et al. [161, 162] and Dowling [164]. On the basis of the agreement, Sawalhi *et al.* [105] considered the two impulses to be associated with the entry and exit of the rolling elements into and out of the defect, respectively. They coined the phrase, '*double-impulse phenomenon*', to represent the occurrence of two defect-related vibration impulses.

From the results presented in Figure 2.6 [105], it appears that the entry- and exit-related impulses have similar characteristics in terms of their frequency content. In other words, the results in Figure 2.6 implies that both entry- and exit-related events appear to be high-frequency events. This represents a stark contrast to previous results reported by Epps *et al.* [161, 162] and Dowling [164], who suggested that the entry of the rolling elements into a defect is a low-frequency event with no impulse-like characteristics. Although Sawalhi *et al.* [105] did not discuss the characteristics (frequency content) of the double impulses, the results presented in Figure 2.6 [105] imply that the entry of the rolling elements into a defect may not be a low-frequency event. As will be discussed in the next section, it is possible that there is an error associated with the results shown in Figure 2.6.

2.5.2.1 Problems associated with the double-impulse phenomenon

In 2011, Sawalhi *et al.* [165] reported results from a series of laboratory tests conducted on self-aligning double-row rolling element bearings with inner and outer raceway defects. Line spalls of width 0.6 mm and 1.2 mm were artificially manufactured on the raceways, and the tests were conducted at various shaft rotational speeds, ranging from 800 to 2400 revolutions per minute (RPM).

In their earlier findings, as discussed in the preceding section (refer to Figure 2.6), Sawalhi *et al.* [105] mentioned that the time separation of 0.0013 seconds between the two impulses corresponds approximately to the time it takes for a rolling element to traverse the width of the manufactured outer raceway defect of 0.8 mm. However, later on, they mentioned that the time separation actually corresponds to the time it takes for a rolling element to traverse the half the size of the defect [165]. Furthermore, when

they repeated the experiments, pertinent to the results in Figure 2.6, at various shaft rotational speeds, they found that the time separation between the two impulses did not change [165]. Therefore, unlike their earlier findings [105] that implied that the entry of the rolling elements into a defect may not be a low-frequency event, the recent experimental findings by Sawalhi *et al.* [165] correlate with those observed by Epps *et al.* [161, 162] and Dowling [164]; thereby, confirming the entry of the rolling elements into a defect as a low-frequency event.

Invalidating the double-impulse phenomenon, Sawalhi *et al.* [165] suspected that the two impulses could be due to a beating effect related to a small difference in the resonance frequencies of a bearing possibly due to stiffness non-linearity.

From the survey of the literature conducted during the course of the current research, the reason for the occurrence of multiple impulses in typically measured bearing vibration signals is not clearly known. However, the explicit dynamics FE modelling of defective rolling element bearings presented in this thesis will be shown to provide an insightful explanation for the occurrence of the defect-related multiple impulses; this will be discussed in Section 6.4.2, Chapter 6.

2.6 Defect size estimation

This section discusses existing knowledge on the estimation of the average size of a defect in rolling element bearings. Similar to the literature on the vibration characteristics of defective bearings, the extent of knowledge for estimating the average size of a bearing defect is also limited.

It has previously been mentioned that a defect-related transient is composed of two parts. While the entry-related event was considered to be a low-frequency event, the exit of the rolling elements from a defect was found to be a high-frequency impulsive event. Based on the distinct vibration signatures, Epps *et al.* [161, 162] suggested correlating the time difference between the two events as a measure of an average

defect size.

In order to estimate the average size of a bearing defect, Sawalhi *et al.* [165] proposed two algorithms to enhance the vibration signals related to the entry and exit of the rolling elements into and out of a defect, respectively. The first algorithm comprised a joint treatment of the entry- and exit-related transient signals. The signals were first pre-whitened using an autoregressive model [344, 345] in order to balance the low- and high-frequency energies. The pre-whitened signals were then subjected to a complex octave band wavelet analysis (using Morlet wavelets [346, 347]) to allow selection of the best band (or scale) to balance the two events with similar frequency content. The squared envelope [95, 96] was generated next using Hilbert transform methods [348, 349], and finally, a real cepstrum [350–352] was used to estimate the average separation of the entry- and exit-related signatures. The second algorithm treated the entry- and exit-related signatures separately; all the steps mentioned above were separately applied to the vibration responses, so that they could be equally represented in the signal.

A mathematical expression for estimating half the actual width of a bearing defect was presented by Sawalhi *et al.* [165]. It was reported to be limited in its capacity to estimate the smallest size of 0.6 mm. It was proposed that the results would perhaps be more reliable for larger defects.

Zhao *et al.* [114] utilised the combination of empirical mode decomposition [345] and approximate entropy method [353–356] to separate the entry- and exit-related transients. The vibration signals were decomposed into finite components, called as intrinsic mode functions, using the empirical mode decomposition method. The complexity in choosing the appropriate intrinsic mode functions that contain the defect-related entry- and exit-related vibration signatures was demonstrated. Zhao *et al.* [114] compared their signal processing algorithms with those presented by Sawalhi *et al.* [165], and reported to be better in representing the separation of the signals.

2.6.1 Limitations of using time separation between entry- and exit-related vibration signatures as a parameter for defect size estimation

It should be noted that the mathematical expressions, for estimating the average size of a bearing defect, developed by Sawalhi *et al.* [165] and followed by Zhao *et al.* [114], are applicable to those defects whose lengths are smaller than the angular spacing between the rolling elements of a bearing. In other words, the expressions that use time separation between the entry- and exit-related vibration signatures will produce reliable defect size estimates if a rolling element that enters a defect must exit the defect prior to any other rolling element entering and exiting the defect. In the case of extended defects whose lengths extend beyond the spacing between two consecutive rolling elements [121], the consecutive entry- and exit-related events pair will correspond to different rolling elements. In other words, a rolling element may enter a defect, but prior to its exit, other rolling elements will exit out of the defect, resulting in a smaller than actual time separation between the events, and thereby, leading to incorrect estimation of the defect size.

For further clarification of the explanation provided in the preceding paragraph, refer to Figure 2.7. It shows two schematics of a partial defective bearing raceway and a few rolling elements, labelled as '1', '2', and '3'. In Figure 2.7a, the length L_d of the localised defect is smaller than the angular spacing θ_r between two consecutive rolling elements, whereas in Figure 2.7b, the length L_e of the extended defect is greater than the angular spacing θ_r between two consecutive rolling elements. Consider that the rolling elements are travelling from the left to right hand side in both schematics.

In Figure 2.7a, the rolling element, labelled as '2', will enter into the defect and exit out of the defect, prior to the entry and exit of rolling element '3' into and out of the defect, respectively. In other words, for the case of a localised defect whose length is smaller than the angular spacing between two consecutive rolling elements, the entry-

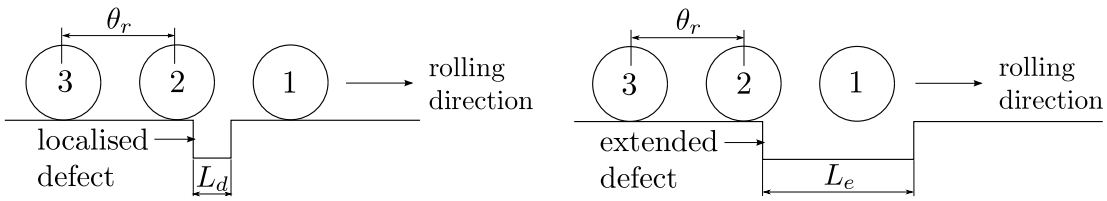

(a) A localised defect whose length L_d is smaller than the angular spacing θ_r between two consecutive rolling elements.

(b) An extended defect whose length L_e is greater than the angular spacing θ_r between two consecutive rolling elements.

Figure 2.7: Schematics of a partial defective raceway of a rolling element bearing and a few rolling elements.

and exit-related vibration signatures are generated due to the entry and exit of a single rolling element into and out of the defect, respectively. In such a scenario, using the time separation between the two distinct vibration signatures, low- and high-frequency, will enable a reliable estimation of the size of a defect.

In Figure 2.7b, rolling element '1' is already in the defective region. Following the entrance of rolling element '2' into the defect, rolling element '1' will exit out of the defect, prior to the exit of rolling element '2'. In other words, a low-frequency vibration signature is generated due to the entry of rolling element '2' into the defect, whereas a high-frequency signal is generated due to the exit of rolling element '1' out of the defect. Therefore, in contrast to a localised defect, for the case of an extended defect whose length typically extends beyond the angular spacing between two consecutive rolling elements, the entry- and exit-related vibration signatures are generated due to the entry and exit of different rolling elements. In such a scenario, it is not practical to use the time separation between the two signals as it will result in an incorrect estimation of a defect size, which would be smaller than the actual defect size.

2.6.2 Entry- and exit-related vibration models

On the basis of the experimental findings, Sawalhi *et al.* [165] suggested that the low-frequency entry of the rolling elements into a defect and the high-frequency exit of the rolling elements out of a defect can be described as a *step response* and an

impulse response, respectively. They developed two analytical models in order to represent the two responses [165]. Sawalhi *et al.* [165] tested the performance of their proposed algorithms [165], discussed above, on the simulated entry- and exit-related responses for estimating the average size of a bearing defect. They mentioned that simulations were beneficial in highlighting the importance of selecting suitable wavelet filter characteristics. While the resonance frequency of 6500 Hz used for the impulse response analytical model was selected on the basis of the experimental results, no explanation was provided on the selection of the 1084 Hz resonance frequency for the step response analytical model, which was one-sixth of the resonance frequency of the impulse response.

Zhao *et al.* [114] also used the step and impulse response analytical models as proposed by Sawalhi *et al.* [165] to test the performance of their proposed methods for estimating the average size of a bearing defect. However, similar to Sawalhi *et al.* [165], Zhao *et al.* [114] also did not provide a clear explanation for choosing the resonance frequencies for the step and impulse response models.

It should be noted that the entry of rolling elements into a defect was modelled as a vertical step response representing a sudden drop of the rolling element-to-raceway contact force [114, 165]. It will be shown in this thesis, Chapters 3 and 6, that it is not a vertical step response, but a gradual decrease. Based on the results from the FE analysis of a rolling element bearing having a localised raceway defect, a novel mathematical model that explains the physics behind the gradual decrease in the rolling element-to-raceway contact force has been formulated in this thesis, and will be discussed in Section 3.5, Chapter 3.

2.7 Summary of literature

The existing models for predicting the vibration response of rolling element bearings with localised defects have provided an excellent understanding of the defect-related

vibration frequency components. Several authors have used analytical, numerical, finite element, and a combination of analytical/numerical and FE methods to predict the vibration response of rolling element bearings and associated rotor–bearing systems. The characteristics of vibrations at the starting and ending positions of a defect have also been established.

This section aims to summarise the review of the literature presented in this Chapter. The gaps in the current knowledge are identified in the next section, and this is followed by the gaps addressed in this thesis.

Impulse-train models The periodic impulse-train models [90–93] to simulate point defects on the rolling surfaces of a bearing, outer and inner raceways, and a rolling element, provide useful insights into understanding the presence of various discrete frequency components in typically measured bearing acceleration signals. The defect-induced force impulses were generated using the Dirac delta function $\mathscr{D}$ and a 1-DOF system response. Three typical pulse shapes, rectangular, triangular and half-sine, of finite widths were considered, and their effects on the vibration (line) spectra, including frequencies and amplitudes, were investigated under radial and axial loads [93]. The equi-spaced force impulses of equal amplitude were modelled for the case of a stationary outer raceway bearing defect, whereas for rotating inner raceway and rolling element defects, the amplitude of the impulses was modulated as per the static load distribution [3, 245–248] within a rolling element bearing. The periodic impulse-train models were extended with the inclusion of the slippage of the rolling elements [95, 96], so as to gain close agreement with typical vibration measurements obtained in practice [94–98].

The impulse-train models successfully predict the significant defect-related frequencies (fundamental, sidebands, and harmonics); however, they could not provide a reasonable prediction of their amplitudes. The problem was specifically highlighted by Tandon *et al.* [93] who showed the comparison of the predicted vibration (line) spectra with experimentally measured results; other authors only provided defect periodicities

[90, 92]. The problem of amplitude mismatch is largely due to the following factors:

- the mismatch between the mathematically modelled defect-related impulses (rectangular, triangular, and half-sine) and unknown characteristics of actual defect-induced impulses,
- the exclusion of basic bearing components, such as the outer ring, inner ring and rolling elements, and structure from the analytical models compared to measuring the vibration response of a bearing, which is generally installed in some kind of housing, such as a pedestal, and
- the consideration of several assumptions and simplifications during the development of the models.

The amplitudes of the frequency components were also normalised or corrected; however, neither the normalisation factor was provided nor the mathematics behind the normalisation factor were discussed [93].

Non-linear multi-body dynamic models Unlike the impulse-train models, the non-linear multi-body dynamic models [100–114] include various components of a rolling element bearing, and predict the vibration response of bearings, bearing–pedestal and rotor–bearing systems, due to the presence of localised bearing defects. The localised defects not only include point spalls [100, 103, 106, 108, 109] (as was inadvertently the case for the impulse-train models [90–93]), but also line spalls [101, 102, 104, 105, 110, 112, 114] (as a function of width and depth), circular spalls [107, 111], and area spalls (ellipsoids) [113] (as a function of Hertzian contact deformation). The multi-body models simplify the bearing systems as lumped mass-spring-damper systems. They neglect the bending deformation of the outer and inner rings [100–112], except in references [113, 114], and model the rolling element-to-raceway contacts as non-linear springs. The majority of the models that consider displacements in the radial

plane were 2-D [100–105, 107, 109–111, 113, 114]; however, some also consider displacements in the axial plane [106, 108, 112]. While the rolling elements were excluded in many models [100–103, 105–107, 109–111, 114], they were included in a few models [104, 108, 112, 113] as point masses; however, their inertial and centrifugal effects were mostly ignored [104, 108]. The slippage of the rolling elements was only considered by a few authors [105, 112, 113] in order to gain close resemblance with a typical vibration response measured in practice, and ignored by the rest. While localised damping at the contact interfaces between the rolling elements and raceways was included in a few models [103, 104, 106], global (structural) damping [100–102, 105, 108–114] was included in majority of the models by grounding a linear viscous damper to either the inner raceway (shaft) [108–111] or outer raceway (pedestal) [100–102, 105, 110]; no damping was include in reference [107]. All the models predicted the time-domain vibration response of the outer ring/housing and inner ring [100–107, 109–114]; however, one model predicted the time-domain displacement of the rolling elements [108].

The main emphasis of the multi-body models was to demonstrate the generation of vibration time-traces, and subsequently perform an envelope analysis [251, 252] on the simulated signals to primarily predict the defect-related frequency components and corresponding sidebands for model validation purposes. The problem of amplitude-mismatch between modelled and measured vibration frequencies observed in the impulse-train models [91, 93] was also reported by the authors of the multi-body models [103, 104, 109–111]. While in some cases, the predicted amplitudes have simply been corrected based on experimental results without providing an explanation [103, 104], some did not compare the modelling results with experimental measurements [100–102, 106–108, 113]; they instead compared the results with previous studies in the literature.

Explicit dynamic FE models Explicit dynamic FE modelling of deep-groove ball bearings, using a commercial FE software package, LS-DYNA [329], has been pre-

sented by four authors [117–120]. One of the advantages of using such a code is that one can minimise the number of assumptions that are generally considered in analytical methods. For example, the outer and inner rings, and rolling elements can be modelled as flexible bodies, the inertial and centrifugal effects of the rolling elements can be modelled, the dynamic contact interaction between the rolling elements and raceways can be studied, and above all, the interaction of defective and non-defective bearing components can be investigated. Existing FE models [117–120], however, did not fully exploit the benefits of the explicit FE methods. The performance of the models was compromised because either the whole outer ring of the bearing [118] or its outer surface [119] was modelled as rigid. The material behaviour, rigid or flexible, of the bearing components was not mentioned in references [117, 120]. Very high instantaneous acceleration levels of magnitudes 10^7 g, 4,000 g, and 15,000 g were reported in references [118], [119], and [120], respectively, which are unrealistic. While no experimental results were shown in references [117, 118], the measured acceleration levels were shown as 100 g and 10 g in references [119] and [120] compared to the simulated levels of 4,000 g and 15,000 g, respectively. Furthermore, the numerically modelled results were low-pass filtered with a cut-off frequency of either 500 Hz or 800 Hz resulting in the elimination of all high-frequency characteristics of the defect-related impulses [119]. As the FE modelling results were not validated against the experimental results due to the significant mismatch between their acceleration levels [119, 120], they were validated on the basis of the comparison of their predicted frequency components with those of the basic kinematic bearing frequencies [3, Chapter 25, page 994].

It can be concluded that the amplitude mismatch between the modelled and measured vibration results is not limited to the impulse-train [90–98] and non-linear multi-body dynamic models, but is also evident in the case of FE models [100–114]. In summary, existing FE models [117–120] do not provide additional information compared to the understanding provided by the impulse-train [90–98] and multi-body models [100–114].

Defect-related vibration characteristics It was found that a defect-related transient vibration signal is composed of two parts; 1) the entry of rolling elements into a defect, and 2) the exit of the rolling elements out of the defect [161, 162]. The characteristics of the vibration signatures at the entry and exit of rolling elements into and out of a localised bearing defect, respectively, were investigated by a few researchers [161, 162, 165]. While the entry-related event was considered to be a low-frequency event with no indication of impulse-like characteristics, the exit-related event was considered to be a high-frequency event responsible for generating an impact and exciting a broad range of frequencies that can cause the ringing of bearing resonant modes [161, 162, 165]. With the aim of estimating the average size of a defect, a few authors have proposed algorithms (signal processing techniques) to enhance the separation of the distinct entry- and exit-related vibration signatures [114, 165].

2.8 Gaps in current knowledge

A number of authors have contributed significantly to a variety of aspects related to rolling element bearings since the late 1800s [193]. These aspects broadly range from understanding the onset of subsurface fatigue cracks and their subsequent growth to surface spalls [169–172, 174], to the development of bearing life prediction models [194–231], to understanding the science of bearing materials for enhancing the material quality [180–190] in order to increase bearing life. The kinematics and dynamics [357–373] of rolling element bearings have been understood, and several commercial codes and software packages are available to solve the dynamics of rolling element bearings — ADORE (Advanced Dynamics of Rolling Elements) [374], COBRA (Computer Optimized Ball and Roller Bearing Analysis) [375], BEAST (Bearing Simulation Tool) [376], and IBDAS (Integrated Bearing Dynamic Analysis System) [377]. The vibration response for non-defective [66–89] and defective rolling element bearings [90–121, 128–160] along with the diagnosis of rolling element bearing faults [17–31] have also been

well documented in the literature. Despite a wealth of literature, the identified gaps in the current knowledge are as follows.

A comprehensive non-linear dynamic model of a rolling element bearing From the review of the literature presented in this chapter, it is evident that numerous models are available for predicting the vibration response of rolling element bearings, having localised, extended and distributed defects, under various loading conditions. However, due to the incorporation of several assumptions, the majority of the models could not reasonably predict the amplitudes of significant frequency components. Unfortunately, the capability of explicit modelling methods also has not been fully utilised. In summary, an analytical model of a rolling element bearing requires simplification of the actual system and this can affect the accuracy of the system dynamics. Therefore, there is a need to develop a comprehensive dynamic model with minimal assumptions and simplifications.

In the work presented in this thesis, an explicit dynamics FE analysis of a defective rolling element bearing has been undertaken using a commercial software package, LS-DYNA [329]. Although LS-DYNA has its own numerical limitations, it has been used to accurately model the kinematics and dynamics of rolling element bearings (as a multi-body system) without requiring any assumptions, except for the material model, material properties, time integration (time-stepping) scheme, magnitude of damping and friction forces. This part of the work is presented in Chapter 4 of this thesis.

The dynamic interaction of rolling elements with raceways, when either of them has a defect On the one hand, the rolling elements were excluded from the majority of the analytical models to predict the vibration response of rolling element bearings, so an investigation of the dynamic interaction of the rolling elements with raceways was not possible. On the other hand, the models that include the rolling element-to-raceway contact modelling focused on presenting the vibration response of

bearings, such as acceleration, velocity or displacement, rather than presenting the contact force results. The FE models reported in the literature did not present the contact force results either.

In the work presented in this thesis, the dynamic contact interaction between the rolling elements and raceways of a bearing as the rolling elements traverse through a localised raceway defect is presented. The investigation of the contact forces in conjunction with the vibration response provides new insights into how vibration is generated in defective rolling element bearings. This part of the work is presented in Chapter 6 of this thesis.

The physical mechanism by which defect-related impulsive forces and vibrations are generated It is understood that repetitive passage of mating components over a defect within a rolling element bearing causes abrupt changes in the contact stresses that structurally excite the bearing, resulting in the generation of defect-related vibration impulses. However, the physical mechanisms by which defect-related impulses are generated have not been investigated. One of the reasons which can be attributed to the mismatch of modelled and measured defect-related vibration amplitudes could be due to varying characteristics of actual vibration impulses and analytically modelled impulses. Analytical models typically use a single force impulse with an exponential decay, whereas multiple impulses are generally observed in practice with a non-uniform decay.

In the work presented in this thesis, the physical mechanism by which defect-related impulsive forces and vibrations in defective bearings are generated is explained. Furthermore, the work presented here also provides an insightful explanation of the occurrence of multiple vibration impulses in practice, which are associated with the traverse of a single rolling element through a bearing defect. This part of the work is presented in Chapter 6 of this thesis.

The gradual de-stressing of rolling elements as they enter into a raceway defect within a rolling element bearing It is understood that the multi-body dynamic models include a quasi-static solution for rolling element-to-raceway contact forces as non-linear Hertzian contact springs. In these models, for the angular extent of a defect having sharp (step-like entry and exit) edges, the contact forces vary instantly across the edges of the defect, causing unrealistic impulsive responses in the system acceleration. Although the instantaneous variations in the contact forces at the edges of the defect were modified to occur gradually, the mathematics behind the modification has not been discussed in the literature.

In the work presented in this thesis, a novel mathematical model has been developed to accurately predict a gradual decrease in the rolling element-to-raceway contact forces as the rolling elements enter into a raceway defect within a bearing. This model is based on the results obtained from the explicit FE modelling of a rolling element bearing having an outer raceway defect. The mathematical model was incorporated in the quasi-static analytical load distribution model to estimate the contact forces between the rolling elements and raceways of a bearing. This part of the work is presented in Chapter 3 of this thesis.

The use of time separation between the entry- and exit-related vibration signatures as a parameter for defect size estimation It has been established in the literature that the vibration response of a defective rolling element bearing comprises two parts; first, low-frequency signatures associated with the entry of the rolling elements into a defect, and second, high-frequency impulsive signatures associated with the exit of the rolling elements out of the defect. Time separation between these distinct vibration signatures have been used in the past to estimate the size of a bearing defect. However, the time separation between the entry- and exit-related signatures can only be used for the case of a localised defect whose length is smaller than the angular spacing between two consecutive rolling elements, but not for the case of an

extended defect whose length typically extends beyond the angular spacing between the rolling elements. There is a need to investigate the vibration response of rolling element bearings with extended defects and seek additional features that may distinguish the vibration response of bearings having extended defects from the vibration response of bearings having localised defects.

This work is beyond the scope of the work presented in this thesis, and is recommended for future works.

2.9 Gaps addressed in this thesis

Following are the gaps in the literature that are addressed in this thesis:

- the development of a comprehensive non-linear explicit dynamics FE model of a defective rolling element bearing with minimal assumptions and simplifications — presented in Chapter 4;
- an in-depth investigation and interpretation of the dynamic contact interaction of the rolling elements with raceways of a defective rolling element bearing, which is not measured in practice — presented in Chapter 6;
- the development of an understanding of the physical mechanism by which defect-related impulses are generated in defective rolling element bearings by correlating the rolling element-to-raceway contact forces and vibration response — presented in Chapter 6;
- the development of an understanding of the de-stressing and re-stressing of the rolling elements as they traverse through a bearing defect by analysing the rolling element-to-raceway contact forces — presented in Chapters 3 and 4; and
- the development of a mathematical model to predict the gradual decrease in the rolling element-to-raceway contact forces as a rolling element de-stresses upon its

entry into a bearing defect, and subsequently other rolling elements re-stress — presented in Chapter 3.

The next chapter describes a quasi-static analytical model for estimating the load distribution within rolling element bearings.

This page intentionally contains only this sentence.

Chapter 3

Quasi-static Load Distribution in Rolling Element Bearings

3.1 Introduction

This chapter presents an analytical model for estimating the quasi-static load distribution in rolling element bearings, both non-defective and defective. The model was developed using the static load distribution model for a non-defective bearing, which has been well-documented in the literature [3, 245–248]. The main objective of the new analytical model proposed here is to accurately model the rolling element-to-raceway contact forces along with predicting and explaining the de-stressing of the rolling elements upon their entrance into a raceway defect.

The static load distribution represents the estimation of load (or force) on the rolling elements (precisely, rolling element-to-raceway contact interfaces) within a bearing. As described earlier in Section 2.3.3.1, Chapter 2, previous authors of multi-body dynamic models [100–102, 104–106, 109–113] have included an analytical solution for estimating the rolling element-to-raceway contact forces to simulate the vibration response of bearings. Based on the assumption that the path of a rolling element traversing a rectangular-shaped defect (having sharp entry and exit edges) follows its profile [105],

the magnitude of the contact forces instantly decreases to zero as the rolling element enters into the defect, it remains zero through the extent of the defect, and then it instantly increases to its static load value [100–102, 104–106, 109–113]. This produces very large, erroneous, impulsive forces in a system at the entry and exit points of a defect due to an instantaneous change in the system acceleration in order to maintain its equilibrium. Although a high-frequency impulsive response at the exit point of a defect is realistic, similar impulsive response at the entry point is unrealistic and not observed in practice [4, 5, 161, 162, 165], as discussed in Section 2.5, Chapter 2. To prevent the occurrence of unrealistically large impulsive forces, the sharp step-like variations were modified to occur gradually [101, 102, 105, 112] by modifying the shape of the defect so it resembles an assumed path of a rolling element traversing the defect. However, apart from the suggestions that a gradual response should be used to reflect a realistic scenario [105] so as to achieve comparable simulated and measured results, no analysis has been presented nor has the mathematics behind the modification been discussed in the literature. Furthermore, as described earlier, despite the incorporation of the rolling element-to-raceway contact modelling by previous researchers [100–102, 104–106, 109–113], their main focus was on the presentation of the vibration response of bearings, such as acceleration, velocity or displacement, rather than the presentation of the contact force results.

As a gradual slope for the decrease in the contact force at the entrance of rolling elements into a bearing defect is necessary to simulate a low-frequency vibration signature [161, 162, 165], it is important to formulate a mathematical model to develop an understanding of the gradual de-stressing or unloading of the rolling elements, so it could be implemented in future multi-body analytical models of defective rolling element bearings.

In addition to the previous work described above, it should be mentioned that quasi-static load distribution models have also been developed recently by Petersen *et al.* [6] and Moazenahmadi *et al.* [7], who are collaborating on this Australian Research

Council funded project, concerned with modelling the vibration response of defective rolling element bearings. The quasi-static load distribution models in references [6, 7] use a different (but equally valid) modelling approach to that described in this chapter. Their approach and its points of difference to the approach described in this chapter are discussed briefly in the next section.

Relevant work reported recently in references [6, 7] based on the research presented in this thesis

The work published in references [6, 7], which progressed in parallel with the research described in this thesis, is concerned with the development of multi-body analytical models to predict the vibration response of rolling element bearings. Their work was inspired by the insights gained from the explicit dynamics FE modelling results, presented in this thesis (Chapters 4 and 6) and published recently [4, 5] by the author of this thesis, that led to a joint publication [6].

One of the significant findings from the FE simulations [4, 5] is the gradual decrease in the rolling element-to-raceway contact forces as the rolling elements enter into a raceway defect. Despite modelling a rectangular-shaped profile of the defect, the gradual decrease, in contrast to instantaneous decrease estimated by previous researchers [100–102, 104–106, 109–113], was surprising. This inspired the development of the proposed mathematical model, presented in this chapter, to predict the gradual decrease in the rolling element-to-raceway contact forces. The FE modelling results [4, 5] also inspired the work in references [6, 7], which reported on the estimation of quasi-static load distribution along with the gradual change in the forces. In contrast to earlier models, which calculate the contact deformation and force at a single point, the model in reference [7] considers a finite number of points on the circumference of the rolling elements to estimate the contact-related parameters. As a result of multiple points sharing the load, the contact force at the edges of a defect can be

shown to vary gradually. This approach is different from (but equally valid to) the proposed mathematical model presented in this chapter, which uses the size of the rolling element-to-raceway contact width to estimate the gradual change in the contact forces. The proposed model, presented in Section 3.5, is based on the outcomes of the explicit dynamics FE modelling of a defective rolling element bearing, which have been published in references [4, 5] and will be presented later in this thesis.

3.1.1 Aims

The aims of the work described in this chapter are to:

- develop a novel mathematical model using the well-known Hertzian contact theory [175–177] for predicting the gradual decrease in the rolling element-to-raceway contact force as a rolling element de-stresses upon its entry into a raceway defect;
- develop a quasi-static analytical model of a defective rolling element bearing for estimating the load distribution on various rolling elements within the bearing;
- analyse the analytically modelled rolling element-to-raceway contact forces obtained using the proposed quasi-static analytical model; and to
- provide a clear distinction between the instantaneous response at the edges of a bearing defect as per earlier models [100–102, 104–106, 109–113] and the gradual response as per the novel mathematical model developed in this chapter.

3.1.2 New knowledge

The novel work presented in this chapter has provided the following new knowledge and insights:

- the development of a mathematical model to explain the physics behind the gradual de-stressing of a rolling element, and subsequent re-stressing of other rolling elements within a defective rolling element bearing; and

- the analysis of the contact forces modelled using the quasi-static analytical load distribution model.

3.1.3 Structure

This chapter commences with an overview of the Hertz contact theory in Section 3.2 along with the key results necessary for the development of the models. The static load distribution for a non-defective rolling element bearing that forms the basis of the proposed quasi-static analytical model is presented in Section 3.3. A description of a defective rolling element bearing is provided in Section 3.4 along with descriptions of a localised defect, its profile, and an instantaneous change in the contact forces at the edges of the defect as per the previous models in the literature. A novel mathematical model to predict the gradual de-stressing of a rolling element is presented in Section 3.5 along with the comparison of new modelling results with those obtained from the previous models. Incorporating the mathematical model for the de-stressing of rolling elements, a quasi-static analytical load distribution model is developed in Section 3.6, followed by the analysis of modelled quasi-static contact forces in Section 3.7. The limitations of the developed quasi-static model are discussed in Section 3.8, followed by the conclusions in Section 3.9.

3.2 Hertz theory of elasticity

As the contact interaction between the rolling elements and raceways of a rolling element bearing is governed by the traditional Hertz theory of elasticity [175–177], a brief overview of the Hertz theory along with the key results, which are used in the development of the proposed analytical models, is provided in this section.

Figure 3.1a shows a 3-D schematic of the geometry of two non-conformal isotropic elastic solid bodies '1' and '2' in contact at point o'. At this initial state of contact, the bodies are not loaded; therefore, a point or line contact develops at point o' depending

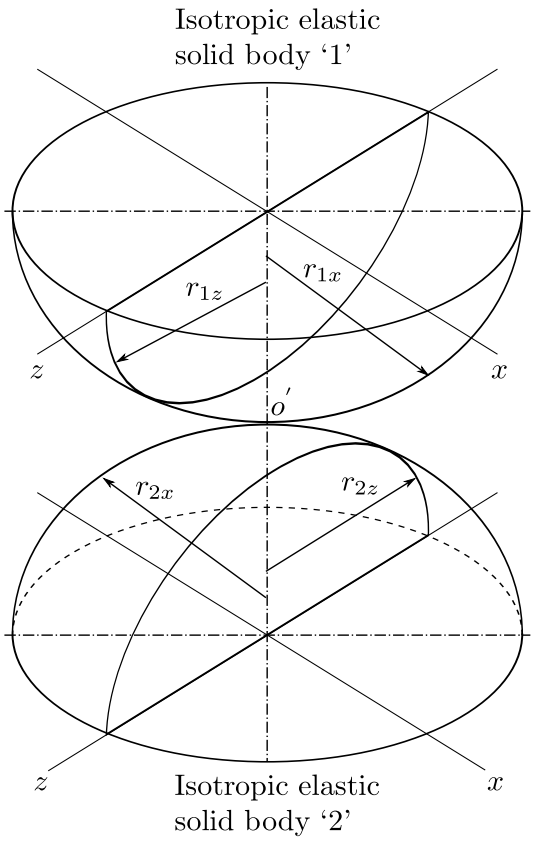

(a) A 3-D representation of the unloaded and undeformed bodies '1' and '2' during the initial state of their contact at point $o^{'}$.

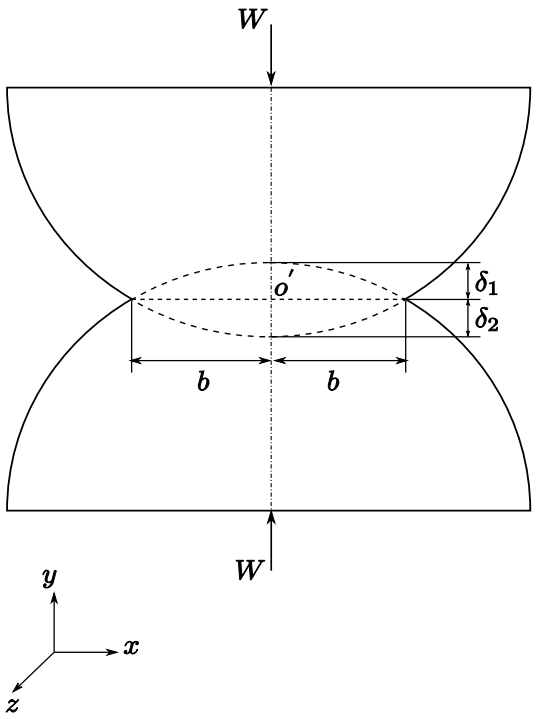

(b) A 2-D representation (sectional view in the x-y plane) of the normally loaded bodies with a radial force W, showing the corresponding deformations δ_1 and δ_2 in the vicinity of their point of initial contact $o^{'}$, resulting in the generation of a finite contact area.

Figure 3.1: Schematics of the geometry of two non-conformal isotropic elastic solid bodies '1' and '2' in contact.

on the geometry or curvature of the bodies; that is, spherical or cylindrical, respectively. A 2-D representation (sectional view in the x-y plane) of the elastically deformed bodies due to the application of a normal (radial) load W is shown in Figure 3.1b. The deformation of the bodies δ_1 and δ_2 occurs in the vicinity of their initial point of contact $o^{'}$ resulting in the generation of a finite contact area, circular, elliptical or rectangular, which is much smaller than the dimensions of the bodies.

The curvature of bodies in contact can be either positive or negative: it is assumed throughout this thesis that convex surfaces shown in Figure 3.1 represent positive cur-

vature, and concave surfaces represent negative curvature. The curvature sum and curvature difference are two important quantities that are used in analysing contact stresses and deformations. The curvature sum $R^{'}$ and difference $R^{'}_{d}$ are given by Equations (3.1) and (3.2), respectively [177, Chapter 4, pages 85–87]

$$\frac{1}{R^{'}} = \frac{1}{R_x} + \frac{1}{R_z} \tag{3.1}$$

$$R^{'}_{d} = R^{'}\left(\frac{1}{R_x} - \frac{1}{R_z}\right) \tag{3.2}$$

where,

$$\frac{1}{R_x} = \frac{1}{r_{1x}} + \frac{1}{r_{2x}} \qquad \text{and} \qquad \frac{1}{R_z} = \frac{1}{r_{1z}} + \frac{1}{r_{2z}} \tag{3.3}$$

In Equation (3.3), R_x and R_z represent equivalent or effective radii of curvature of the bodies '1' and '2' in x- and z-directions, respectively, and r_{1x}, r_{2x}, r_{1z} and r_{2z} represent the individual radii of curvature of the bodies in x- and z-directions. For the case of two spheres (often referred to as solids of revolution), which constitutes a basic Hertzian contact problem, $r_{1x} = r_{1z}$ and $r_{2x} = r_{2z}$, whereas $r_{1z} = r_{2z} = \infty$ for two contacting cylindrical bodies with their axes parallel to each other.

A simplified 2-D geometry of a rolling element bearing is considered in this thesis for modelling purposes, which effectively represents a cylindrical roller bearing. Therefore, the key Hertzian contact-related parameters for a line (or rectangular) contact only are provided here; a comprehensive analysis of the Hertz theory is provided in reference [177, Chapter 4].

For two cylindrical bodies in contact over length l with their axes parallel to each other, the half-contact width b, maximum elastic deformation $\delta_{\max}$, and maximum contact pressure $P_{\max}$ for the rectangular contact area developed due to the application of a normal load W are given by Equations (3.4), (3.5), and (3.6), respectively

$$b = \left(\frac{4WR^{'}}{\pi l E^{'}}\right)^{1/2} \tag{3.4}$$

$$\delta_{\max} = \frac{2W}{\pi l E'} \ln\left(\frac{2\pi l E' R'}{W} - 1\right) \tag{3.5}$$

$$P_{\max} = \left(\frac{W E'}{\pi l R'}\right)^{1/2} \tag{3.6}$$

Here, R' is the curvature sum of the bodies, given by Equation (3.1), and E' is the equivalent modulus of elasticity of the bodies, given by

$$\frac{1}{E'} = \frac{1-\nu_1^2}{E_1} + \frac{1-\nu_2^2}{E_2} \tag{3.7}$$

where, E_1, E_2 and ν_1, ν_2 represent the modulus of elasticity and Poisson's ratio, respectively, of the two bodies in contact.

The maximum force developed at the contact interface of the bodies is directly proportional to their maximum elastic deformation (or displacement) $\delta_{\max}$. The contact force F at the interface, which is generally referred to as the Hertzian contact force, is given by

$$F \propto \delta^n = K\delta^n \tag{3.8}$$

where, K is the contact stiffness and the exponent $n = 3/2$ for point, circular, and elliptical contacts (for example, in ball bearings), and $n = 10/9$ for line and rectangular contacts (for example, in roller bearings).

The aforementioned expressions will be used during the estimation of the static load distribution in a rolling element bearing, which is presented in the next section.

3.3 Static load distribution

The static load distribution within a non-defective rolling element bearing has been well-documented in the literature [3, 245–248]. The static load includes the magnitude of the horizontal (x-direction) and vertical (y-direction) load (force) on the rolling elements of a bearing as a function of the relative displacement of the outer and in-

ner raceways, (diametral or radial) bearing clearance, angular location of the rolling elements, and the curvature of the raceways and rolling elements in addition to their material properties. The solution for the static load distribution within a non-defective rolling element bearing forms a basis for the proposed quasi-static analytical load distribution in a defective bearing. The static load distribution model along with the importance of key parameters, such as load zone extent, load constant, and bearing clearance, is described below. The model has been adapted from Harris *et al.* [3, Chapter 7, pages 234–237].

Figure 3.2 shows three 2-D schematics of a non-defective rolling element bearing comprising an outer ring, an inner ring, and rolling elements in different arrangements; only a few rolling elements are shown in the schematics. The outer and inner rings of the bearing in a concentric position, separated by a uniform radial clearance $\varsigma/2$, are shown in Figure 3.2a. The formation of the initial *point* contact between the outer raceway and a few rolling elements due to the displacement of the outer ring by a distance equivalent to the radial clearance $\varsigma/2$ is illustrated in Figure 3.2b. The displacement of the outer ring was a result of the application of a slight radial (normal) load on it along the y-axis in the downward $(-y)$ direction. The application of a further radial load W will cause elastic deformation of the rolling elements, and consequently, of the outer and inner raceways. As a result, the clearance between a limited number of rolling elements and raceways will be eliminated around an arc of length $2\psi_l'$ as illustrated in Figure 3.2c. The angular extent of $2\psi_l'$ represents the bearing load zone centred at ψ_{lc} along the y-axis where the radial load was applied ($\psi_{lc} = 90°$); the estimation of the load zone will be discussed in the next section. The rolling elements filled using the solid gray colour correspond to loaded (mechanically stressed or compressed) elements in the load zone, whereas the others represent non-loaded elements.

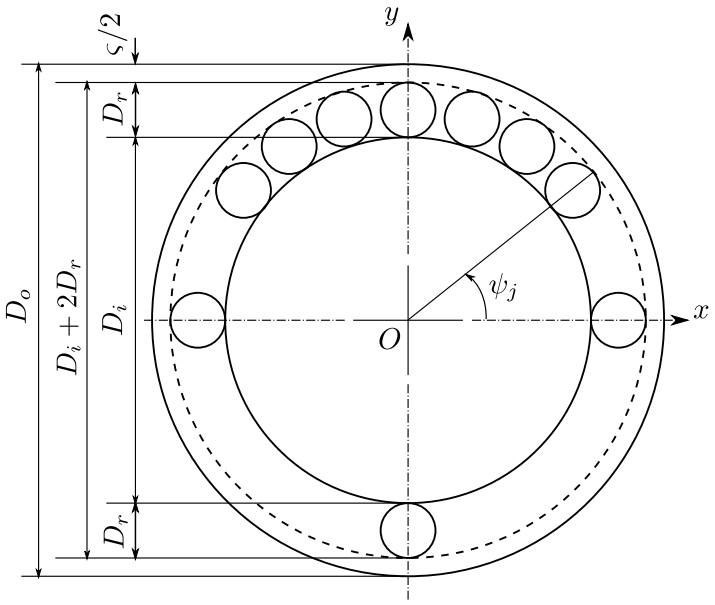

(a) A concentric arrangement of the outer and inner rings, highlighting a uniform radial clearance of $\varsigma/2$ between the outer raceway and rolling elements.

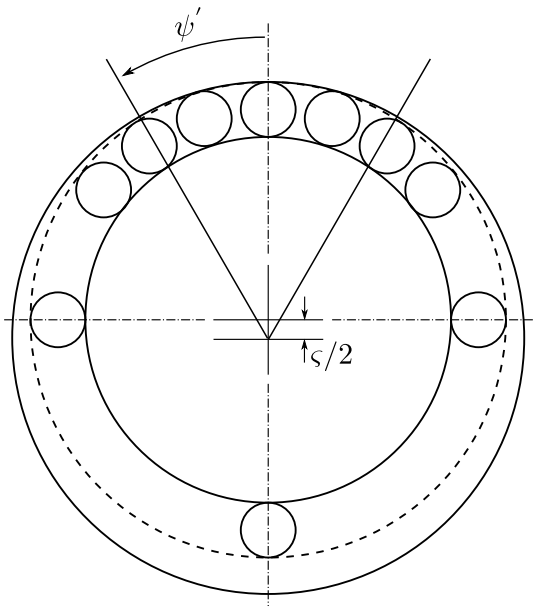

(b) An initial contact between the outer raceway and a certain number of rolling elements due to the displacement of the outer ring by the amount of the radial clearance $\varsigma/2$.

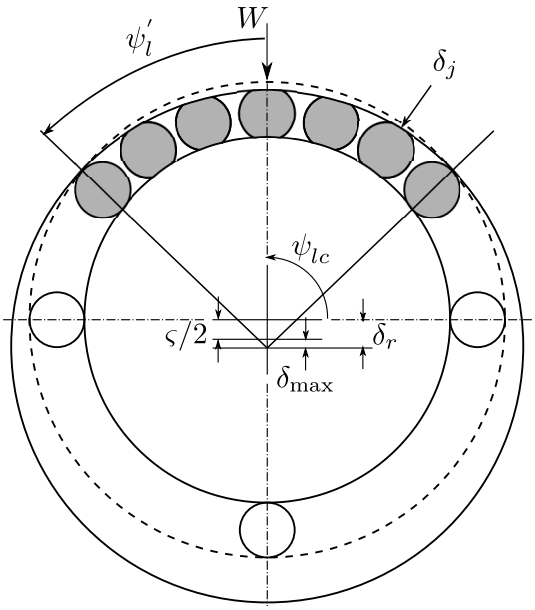

(c) An interference between the raceways and rolling elements due to the application of a radial load W along the y-axis, resulting in the deformation of the rolling elements, and outer and inner raceways.

Figure 3.2: 2-D schematics of a non-defective rolling element bearing, comprising an outer ring, an inner ring, and a few rolling elements, in different arrangements.

3.3.1 Hertzian contact force-displacement model

Referring to Figure 3.2c, the maximum elastic deformation or displacement of the rolling element and raceways along the load line (y-axis) is represented by $\delta_{\max}$. Assuming that the raceways and rolling elements of a radially loaded rolling element bearing are rigid except at the rolling element-to-raceway contact interfaces, the radial elastic deformation at a rolling element angular position ψ_j, with respect to $\delta_{\max}$ at the load line, is given by

$$\delta_j = \left(\delta_{\max} + \frac{\varsigma}{2}\right) \sin \psi_j - \frac{\varsigma}{2} \tag{3.9}$$

where, $\left(\delta_{\max} + \frac{\varsigma}{2}\right)$ represents the total radial displacement of the raceways occurring at $\psi_{lc} = 90°$, which has been denoted by δ_r in Figure 3.2c. It should be noted that $\delta_{\max}$ comprises the deformation of both outer and inner raceways as

$$\delta_{\max} = \delta_o + \delta_i \tag{3.10}$$

where, δ_o and δ_i are the contact deformation of the outer and inner raceways, respectively, which can be estimated using Equation (3.5). Equation (3.9) can be re-written for clarity as

$$\delta_j = \delta_r \sin \psi_j - \frac{\varsigma}{2} \tag{3.11}$$

Introducing a load distribution factor ϵ and rearranging Equation (3.11) in terms of maximum deformation $\delta_{\max}$ gives

$$\delta_j = \delta_{\max} \left(1 - \frac{1}{2\epsilon} \left(1 - \sin \psi_j\right)\right) \tag{3.12}$$

The load distribution factor ϵ primarily depends on the clearance ς of a rolling element bearing in addition to the deformation of the raceways — $\epsilon = 0.5$ for zero clearance, $0 < \epsilon < 0.5$ for positive clearance, and $0.5 < \epsilon < 1$ for negative clearance, more commonly referred to as bearing preload. The load distribution factor ϵ is

estimated as

$$\epsilon = \frac{1}{2}\left(1 - \frac{\varsigma}{2\delta_r}\right) \tag{3.13}$$

The angular extent of the load zone $2\psi_l^{'}$ is also a function of the bearing clearance ς and the load distribution factor ϵ. By substituting $\delta_j = 0$ in Equation (3.12), the half-angular extent $\psi_l^{'}$, with respect to the load line ($\psi_{lc} = 90°$), is given by

$$\psi_l^{'} = \cos^{-1}\left(\frac{\varsigma}{2\delta_r}\right) = \cos^{-1}\left(1 - 2\epsilon\right) \tag{3.14}$$

Figure 3.3 shows various 2-D schematics of a rolling element bearing, highlighting the extent of the load zone for various bearing clearances.

Using the Hertzian contact force-displacement relationship given by Equation (3.8), the force (load) at a rolling element-to-raceway contact interface and its corresponding displacement with respect to the maximum load and deformation, respectively, along the load line can be expressed as

$$\frac{F_j}{F_{\max}} = \left(\frac{\delta_j}{\delta_{\max}}\right)^n \tag{3.15}$$

where, F_j and δ_j are the load and displacement, respectively, at a jth rolling element, $F_{\max}$ and $\delta_{\max}$ are the maximum force and displacement, respectively, at the rolling element along the load line, and n is the exponent (equal to 3/2 for ball bearings and 10/9 for roller bearings). The maximum force $F_{\max}$ on a rolling element under pure radial load for zero clearance ($\varsigma = 0$) within a bearing can be estimated using Stribeck's equation (3.16) [245] as

$$F_{\max} = \begin{cases} \dfrac{4.37W}{N_r \cos\alpha} & \text{for ball bearings} \\ \dfrac{4.37W}{N_r} & \text{for cylindrical roller bearings} \end{cases} \tag{3.16}$$

where, W is the applied radial load, N_r is the number of rolling elements, and α is the

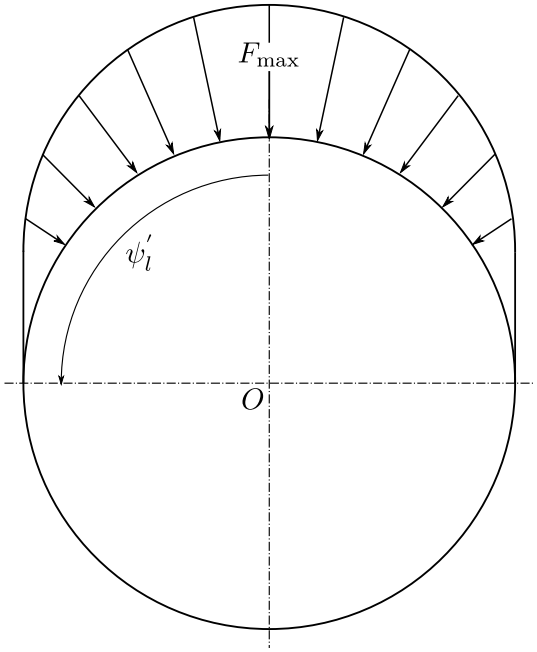

(a) $\epsilon = 0.5$, $\psi_l' = \pm 90°$ for zero clearance.

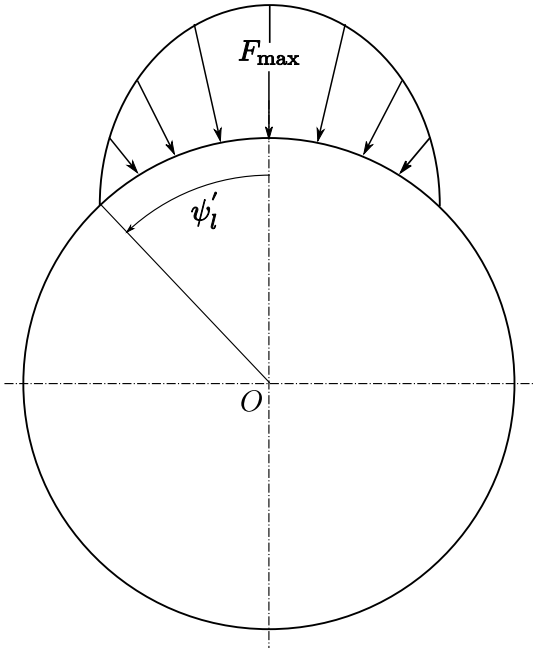

(b) $0 < \epsilon < 0.5$, $0° < \psi_l' < 90°$ for positive clearance.

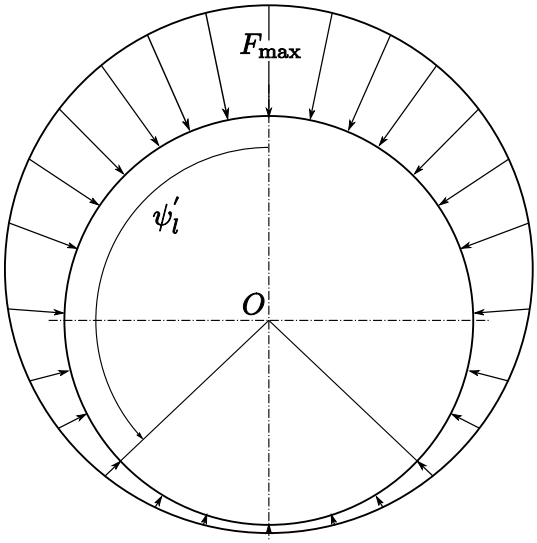

(c) $0.5 < \epsilon < 1$, $90° < \psi_l' < 180°$ for negative clearance or preload.

Figure 3.3: 2-D schematics illustrating the load distribution in a rolling element bearing for different clearances.

contact angle. For bearings with positive or negative clearance, the load constant 4.37 must be increased or decreased, respectively.

Substituting Equation (3.12) into Equation (3.15) gives the total force on a rolling element j within a bearing with respect to the maximum force along the load line. It is given as [3, Chapter 7, page 236]

$$F_j = F_{\max}\left[1 - \frac{1}{2\epsilon}\left(1 - \sin\psi_j\right)\right]^n \tag{3.17}$$

In order to establish the static equilibrium of the system, the applied radial load W must be equal to the sum of the horizontal F_x and vertical F_y load components over the rolling elements within the load zone $2\psi_l^{'}$. Therefore, re-writing Equation (3.17) to resolve both components gives net horizontal and vertical contact forces as

$$\begin{bmatrix} F_x \\ F_y \end{bmatrix} = \sum_{\psi_{lc}}^{\pm\psi_l^{'}} \begin{bmatrix} F_j\cos\psi_j \\ F_j\sin\psi_j \end{bmatrix} = F_{\max}\sum_{\psi_{lc}}^{\pm\psi_l^{'}} \left[1 - \frac{1}{2\epsilon}\left(1 - \sin\psi_j\right)\right]^n \begin{bmatrix} \cos\psi_j \\ \sin\psi_j \end{bmatrix} = \begin{bmatrix} 0 \\ W \end{bmatrix} \tag{3.18}$$

3.3.2 Modelling results

Model parameters The dimensions of the raceways and rolling elements within a rolling element bearing considered for the current simulation are as follows: outer raceway diameter $D_o = 200\,\text{mm}$, inner raceway diameter $D_i = 163.96\,\text{mm}$, rolling element diameter $D_r = 18\,\text{mm}$, effective rolling element length $l_r = 40\,\text{mm}$, and the number of rolling elements $N_r = 24$. The nominal diametral clearance ς in the bearing was defined as $0.04\,\text{mm}$. These dimensions are representative of a typical package bearing unit commonly used in the railway industry, which has been experimentally tested for the current study; the experimental results will be presented in Chapter 5. A finite element model of the rolling element bearing model with the aforementioned dimensions was also build and solved using the explicit dynamics FE software package,

LS-DYNA [329]; the FE modelling results will be presented in Chapters 4 and 6.

A radial load W of 50 kN was applied to the bearing: this is equivalent to approximately the half load carrying capacity of a typical railway package bearing unit. As a package bearing unit is a double-row bearing, for a non-defective rolling element bearing, each row carries half of the load $W/2$. For the analytical and explicit dynamics FE modelling of a rolling element bearing presented in this thesis, only a single-row bearing has been considered due to the 2-D modelling undertaken here. For a rolling element bearing under pure radial load, which is considered for the current study, the load distribution on the rolling elements within both rows of the bearing would be similar. Therefore, the consideration of a single row bearing does not affect an analysis of the rolling element-to-raceway contact forces, which is a principal aim of this thesis.

Figures 3.4a and 3.4b show the magnitude of the static horizontal F_x and vertical F_y contact forces on the rolling elements of the non-defective rolling element bearing. The angular positions of the rolling elements on the x-axis have been shown relative to the centre of the load zone ($\psi_{lc} = 90°$) along the y-axis. In Figures 3.4a and 3.4b, the vertical bars correspond to the magnitude of the contact forces at the rolling element positions, whereas the red-coloured, dashed lines along with the blue-coloured, circular markers at the rolling element positions depict the load profiles.

As per the modelled bearing parameters, seven rolling elements, spaced 15° apart, are under the load zone $2\psi_l^{'}$ that extends to approximately ±53° (refer to Equation (3.14)) from the load zone centre ψ_{lc}. The summation of the x-directional contact force components for the rolling elements within the load zone equals 0, whereas the summation of the y-directional contact force components equals 25 kN (half the applied radial load as a single row of the bearing has been considered here).

The vertical load profile in Figure 3.4b is easy to visualise and correlate with the schematics in Figure 3.3, whereas the horizontal load profile in Figure 3.4a is comparatively difficult to visualise. The equal but inverse horizontal contact forces F_x are due to the negative and positive horizontal displacement δ_x of the rolling elements located

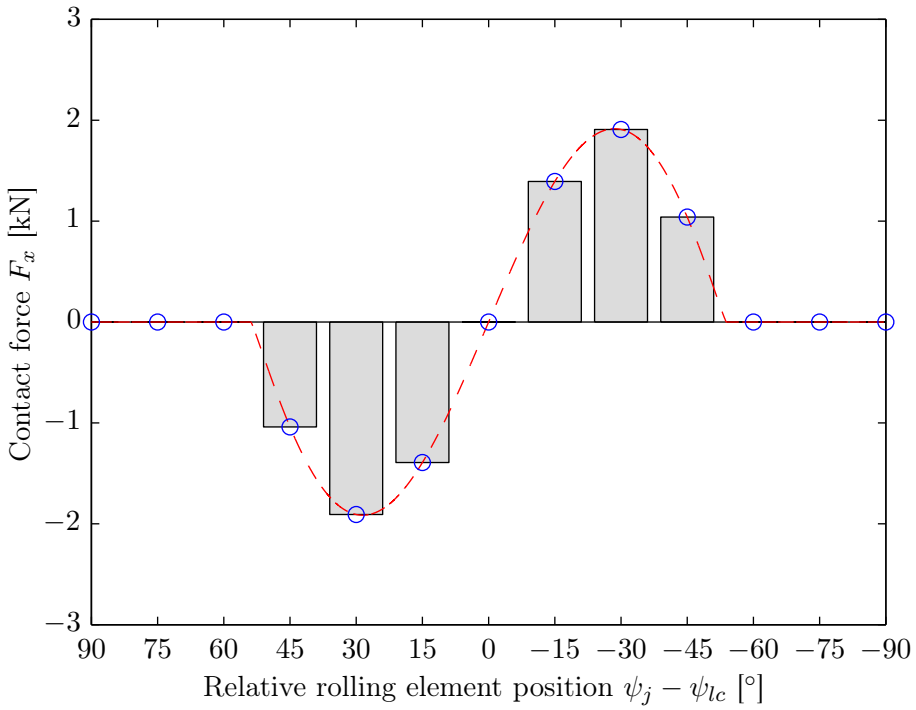

(a) Horizontal contact force (load) distribution.

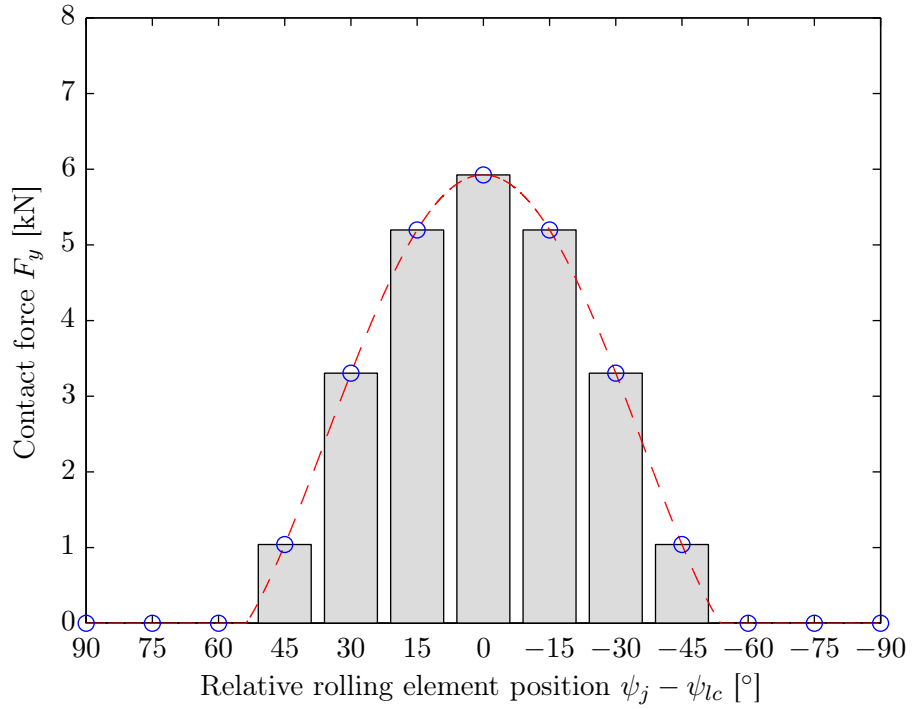

(b) Vertical contact force (load) distribution.

Figure 3.4: Analytically estimated static contact force (load) distribution on the rolling elements of the non-defective rolling element bearing for a radial load W of 50 kN. The height of the vertical bars corresponds to the magnitude of the contact forces, whereas the red-coloured, dashed lines depict the load profiles.

Roller position (°)		Contact width (mm)		Displacement (mm)		Force (kN)	
actual ψ_j	relative $\psi_j - \psi_{lc}$	$2b_x$	$2b_y$	δ_x	δ_y	F_x	F_y
135	45	-0.045	0.045	-0.0012	0.0012	-1.03	1.03
120	30	-0.083	0.144	-0.0022	0.0039	-1.91	3.31
105	15	-0.060	0.226	-0.0016	0.0061	-1.39	5.19
90	0	0	0.257	0	0.0069	0	5.94
75	-15	0.060	0.226	0.0016	0.0061	1.39	5.19
60	-30	0.083	0.144	0.0022	0.0039	1.91	3.31
45	-45	0.045	0.045	0.0012	0.0012	1.03	1.03

Table 3.1: Analytically estimated contact-related parameters at the rolling element-to-outer raceway contact interfaces of the non-defective rolling element bearing for a radial load W of 50 kN.

at the left- and right-hand sides of the load zone, respectively.

Contact width and displacement

In addition to the contact forces, other Hertzian contact-related parameters, displacement δ and contact width $2b$, at the loaded rolling element-to-outer raceway interfaces are shown in Table 3.1. Both horizontal (x-direction) and vertical (y-direction) components of the contact width and displacement are included in the table. These results will be compared with those from the numerical simulations in Chapter 6 estimated using the explicit dynamics FE model of a rolling element bearing.

The next section illustrates the instantaneous erroneous step-like response, change in the rolling element-to-raceway contact forces, at the edges of a bearing defect as implemented by the previous researchers.

3.4 Defective bearing

Prior to developing the proposed mathematical model to predict the gradual change in the rolling element-to-raceway contact forces related to the de-stressing of a rolling element, it is useful to describe a defect within a rolling element bearing. Following

the description of a localised bearing defect and its profile, the contact forces modelled by previous researchers [100–102, 104–106, 109–113] are also presented in this section. These forces will then be compared with the results obtained using the proposed mathematical model in the next section.

A defect profile may range from a simple step-like rectangular-shaped profile to more sophisticated surface roughness models [99, 121, 177, 261–263, 265–271] that are generally characterised by a normal Gaussian distribution [273, Chapter 3, pages 59–66]. In previous analytical multi-body dynamic models [100–114], reviewed in Section 2.3.3, Chapter 2, a simple step-like rectangular (localised) defect profile has been considered in a majority of models [100–102, 104, 106, 109–113], whereas a rough surface profile of a defect was considered by a few researchers [6, 99, 121]. Here, a rough surface profile of a localised defect should not be confused with the overall roughness on the rolling surfaces of a bearing, raceways and rolling elements, which is associated with distributed defects [122–160] (briefly mentioned in Sections 2.1, 2.3.3, and 2.4 of Chapter 2).

Figure 3.5 shows a 2-D schematic of a defective rolling element bearing, which comprises an outer ring, an inner ring, and rolling elements; out of twenty-four rolling elements in a single row of the modelled bearing, only a few rolling elements are shown here. They are numbered in counterclockwise direction, commencing from the rolling element $j = 1$, located immediately at the left-hand side of the bearing defect (refer to Figure 3.5 for clarity); the actual ψ_j and relative $\psi_j - \psi_{lc}$ positions of the rolling element $j = 1$ are 94° and 4°, respectively. The rectangular-shaped localised defect, having step-like entry (starting defect position) and exit (ending defect position) edges, is centrally located at the top of the outer raceway; such a defect is generally referred to as a *line spall*. The centre of the defect ψ_d coincides with the centre of the load zone ψ_{lc} along the y-axis ($\psi_d = \psi_{lc} = 90°$). The length (angular extent) and height (or depth) of the defect are represented by $\Delta\psi_d$ and H_d, respectively. Throughout this thesis, the subscript d symbolises parameters for a defective rolling element bearing; and therefore, should not be confused with a derivative notation.

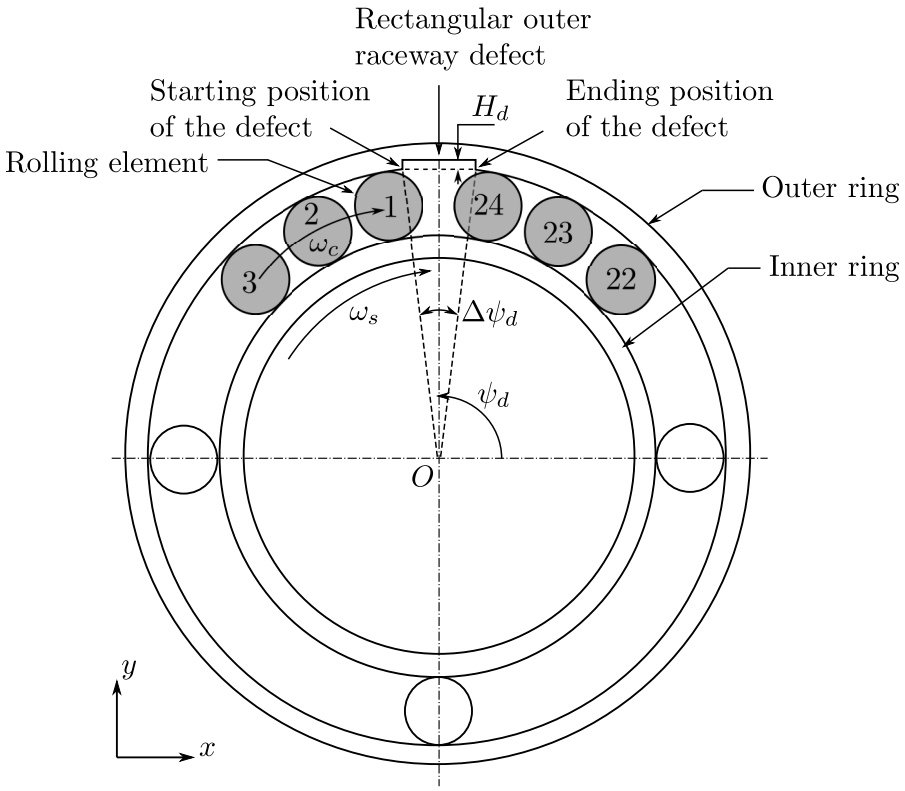

Figure 3.5: A 2-D schematic of a rolling element bearing comprising an outer ring, an inner ring, a few rolling elements, and a localised rectangular-shaped defect centrally located at the top of the outer raceway; the angular extent and height of the defect are denoted by $\Delta\psi_d$ and H_d, respectively. The rolling elements filled using solid gray colour represent loaded elements, whereas the others represent non-loaded elements.

For convenience, the starting and ending positions of the defect in Figure 3.5 are defined as per clockwise rotation of the bearing, so that during the traverse of the rolling elements $j = 1, 2, 3 \ldots$ through the defect, they enter into the defect at its starting position and exit out of the defect at the ending position. In this thesis, clockwise bearing rotation has been considered for modelling (both analytical and numerical) and experimental work. In the literature, the starting and ending positions of a bearing defect are generally referred to as leading and trailing edges, respectively [105, 121, 161, 162, 165]; however, as mentioned earlier in Section 2.5, Chapter 2, the extremities of a defect will be referred to as the starting and ending positions in this study.

3.4.1 Defect profile

For the defect shown in Figure 3.5, a rectangular-shaped step-like defect profile S_d can be generated as

$$S_d\left(\psi_j\left(t\right)\right) = \begin{cases} -H_d & \text{if} \quad \psi_d - \dfrac{\Delta\psi_d}{2} \leqslant \psi_j\left(t\right) \leqslant \psi_d + \dfrac{\Delta\psi_d}{2} \\ 0 & \text{otherwise} \end{cases} \tag{3.19}$$

where, ψ_d represents the angular position of the centre of the defect, $\Delta\psi_d$ the angular extent of the defect, and H_d the height of the defect. For $\Delta\psi_d = 6°$ and $H_d = 0.2\,\text{mm}$, Figure 3.6 shows the rectangular-shaped profile of the outer raceway defect, obtained using Equation (3.19). These dimensions of the defect were selected based on the inspection of numerous defective bearings, available at Track IQ$^{\text{TM}}$ [11], from operational use in the railway industry [378]. For the current bearing model, the angular extent $\Delta\psi_d$ of 6° corresponds to a length L_d of 10 mm. No roughness on the surfaces of the outer raceway, inner raceway, or the rolling elements is considered for the current study.

3.4.2 Instantaneous response at the edges of a defect

In previous analytical multi-body dynamic models [100–102, 104–106, 109–113], the quasi-static solution for the rolling element-to-raceway contact forces was estimated using Hertzian contact theory [175–177]. For the rectangular-shaped profile of a defect in Figure 3.6, such a solution causes instantaneous variations in the contact force estimates — instant decrease and increase in the contact forces at the starting and ending positions of a defect, respectively.

The horizontal and vertical contact forces between a rolling element and the defective outer raceway within a bearing, obtained using the quasi-static solution as per the previous models, are shown in Figures 3.7a and 3.7b, respectively; these force estimates

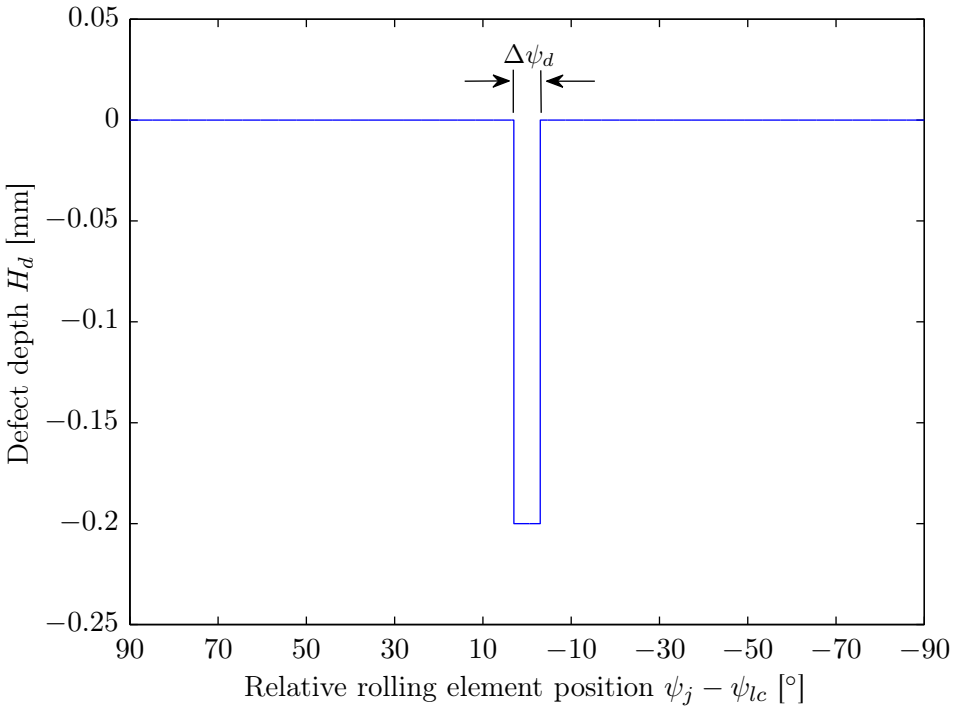

Figure 3.6: A rectangular-shaped step-like profile of the bearing raceway defect shown in Figure 3.5.

are represented using the blue-coloured, solid lines. For comparison, the corresponding contact forces for a non-defective rolling element bearing are also plotted in the figures using the red-coloured, dashed lines. The gray-coloured shaded area in Figures 3.7a and 3.7b highlights the angular extent of the localised outer raceway defect $\Delta\psi_d$.

The instantaneous change in the contact forces from the static load value occurring in a single instance or time step is evident when compared to the corresponding results for a non-defective rolling element bearing. As the defect, located at the top of the outer raceway, is under maximum load due to the application of the radial load W, the magnitude of the vertical contact force F_y is higher than the corresponding horizontal force F_x.

In Figure 3.7b, the entry of a rolling element into the defect results in an instant decrease in the vertical contact force from its static load of approximately 6 kN to zero. In contrast, it also results in an instant increase in the horizontal contact force in Figure 3.7a from its static load of approximately −0.3 kN to zero — a difference

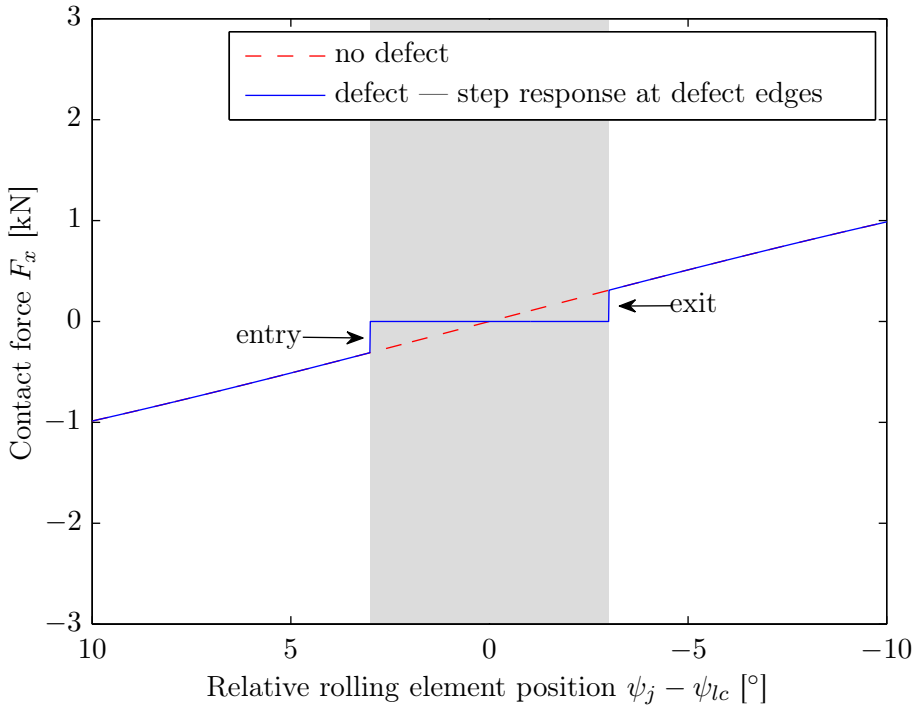

(a) Horizontal contact forces.

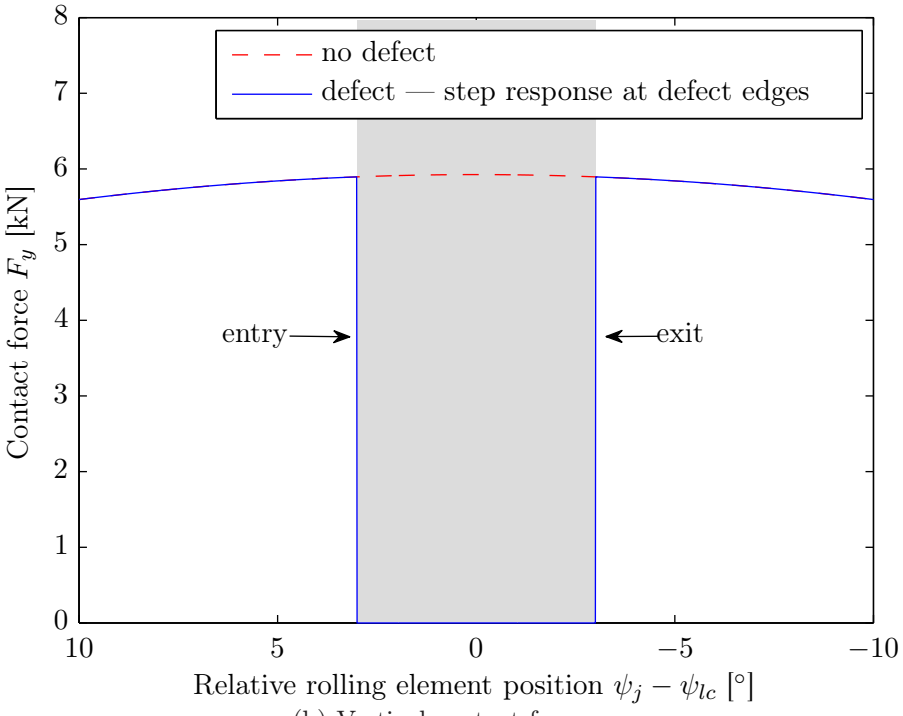

(b) Vertical contact forces.

Figure 3.7: Analytically estimated rolling element-to-outer raceway contact forces for a non-defective and a defective rolling element bearing for a radial load W of 50 kN, depicting the instantaneous step-like decrease and subsequent increase in the contact forces for simulating the entry and exit of a rolling element into and out of the defect, respectively. The gray-coloured shaded area highlights the angular extent $\Delta\psi_d$ of the rectangular-shaped defect.

of 300 N compared to 6 kN for the vertical contact force. Similarly, the exit of the rolling element from the defect is represented by an instant increase of both contact force estimates from zero to their respective static load values. As a result of the sharp changes in the contact forces that follow the profile of the rectangular-shaped defect, a large (high-frequency) impulsive response (time-varying system vibration), is erroneously generated in order to maintain the equilibrium of the system [105].

The instantaneous change in the contact forces occurs due to the consideration of a single point contact at the rolling element-to-raceway contact interface. In other words, instantaneous change can be explained if the rolling element-to-raceway contact interfaces are considered to have developed point contacts. However, this consideration violates the contact behaviour at the interfaces that follows Hertzian contact theory [177, Chapter 4].

3.4.2.1 Unrealistic point contacts at rolling element-to-raceway contact interfaces

Figure 3.8 shows a partial schematic of a rolling element and the raceways of a bearing; it is a zoomed version of the defective rolling element bearing shown in Figure 3.5. The rolling element-to-raceway contact interfaces are depicted as point contacts using solid, black-coloured, circular markers. The position of the rolling element is such that the contact point a coincides with the starting angular position of the defect $\psi_d + \frac{\Delta\psi_d}{2}$. Although it is unrealistic for a loaded rolling element, within the load zone of a bearing, to have developed a point contact with bearing raceways as highlighted in Figure 3.8, the point contacts are only shown to discuss the erroneous instantaneous step-like modelling of the contact forces implemented by previous researchers as discussed above (Figure 3.7). An appropriate representation of a loaded rolling element-to-raceway contact interface is to show an area contact (elliptical for ball bearings and rectangular for roller bearings); this will be discussed in the next section along with a novel mathematical model for simulating a gradual response at the defect edges.

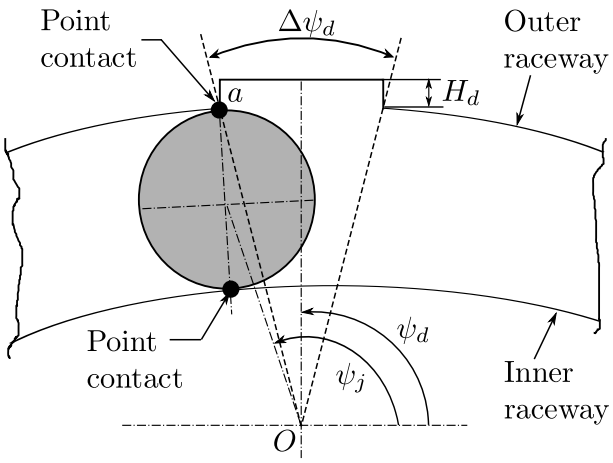

Figure 3.8: A partial and zoomed view of the schematic in Figure 3.5, showing the outer raceway defect and a rolling element in its vicinity; the consideration of point contacts between the rolling element and raceways explains the erroneous instantaneous step-like changes in the rolling element-to-raceway contact forces as implemented by previous researchers.

Considering the clockwise rotation of the bearing in Figure 3.8, a slight change in the angular position of the rolling element from the starting position of the defect would cause the rolling rolling element-to-raceway contact force to instantaneously plummet to zero (see Figure 3.7). This implies erroneously that the loaded rolling element fully unloads or de-stresses in a single instance, triggering an instantaneous system response. In order to prevent the instant changes in the system response, a few researchers [101, 102, 105] have modified the sharpness of the entry-related event from instantaneous to gradual by modifying the shape of the defect; however, they did not incorporate this idea into a mathematical model.

Based on the rolling element-to-raceway contact width, the following section presents a novel mathematical model to predict the slope for the rolling element-to-raceway contact force as a rolling element enters into a raceway defect within a bearing.

3.5 Novel mathematical model for a gradual response at the edges of a defect

A mathematical model for estimating the gradual decrease in the rolling element-to-raceway contact force upon the entrance of a rolling element into a defect within a defective rolling element bearing is developed considering the following assumptions:

- the raceways and the rolling elements of a bearing are rigid except for the rolling element-to-raceway contact interfaces according to the Hertzian contact theory of elasticity [175–177];
- the deformation at the contact interfaces does not exceed the elastic limit of the materials;
- the dynamics of the rolling elements, such as their path (trajectory) and centrifugal forces acting on them, are not considered;
- the raceways and rolling elements are perfectly circular and their surfaces are perfectly smooth; and
- no slippage occurs between the rotating components.

As mentioned earlier, the mathematical model is based on the findings of the explicit dynamics FE modelling of a defective rolling element bearing, which is a result of thesis and will be presented in Chapters 4 and 6.

3.5.1 Realistic line contacts at rolling element-to-raceway contact interfaces

In contrast to unrealistic point contacts at the rolling element-to-raceway contact interfaces in Figure 3.8, realistic line contacts at the interfaces are shown in Figure 3.9 using solid, black-coloured, rectangular markers. It shows a schematic, a partial and

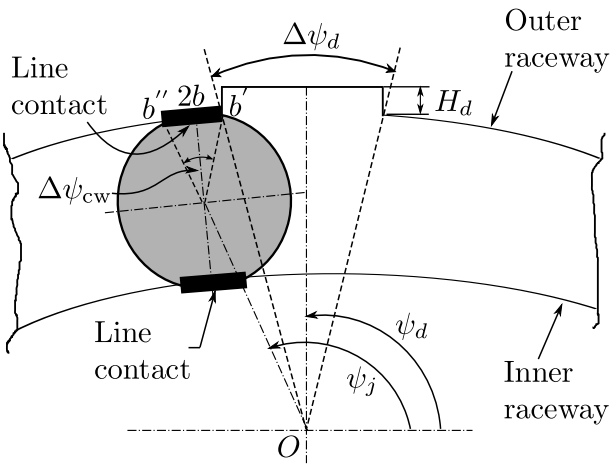

Figure 3.9: A partial and zoomed view of the schematic in Figure 3.5, showing an outer raceway defect and a rolling element in the vicinity of the defect; the realistic line contacts (width $2b$ and angular extent $\Delta\psi_{\text{cw}}$) between the rolling element and raceways will result in the gradual loss of contact as the rolling element rolls over the defect.

zoomed version of the defective rolling element bearing of Figure 3.5, and shows a loaded rolling element at the verge of the starting position of the outer raceway defect $\psi_d + \dfrac{\Delta\psi_d}{2}$. For the cylindrical roller bearing being considered in this thesis for analytical modelling, the length of the line contact at the rolling element-to-raceway contact interface is denoted by $2b$, and its corresponding angular extent is represented by $\Delta\psi_{\text{cw}}$. The extreme ends of the contact width $2b$ are represented by $b^{'}$ and $b^{''}$, where $b^{'}$ coincides with the starting position of the defect.

3.5.2 Gradual de-stressing of the rolling elements

Referring to Figure 3.9, as the angular position of the loaded rolling element increases by a small/ single time instance in clockwise direction, the contact width $2b$ or $\Delta\psi_{\text{cw}}$ between the rolling element and outer raceway decreases. In other words, as the rolling element rolls into the defect, the length of the contact patch reduces resulting in a reduction of the contact area as well as the contact force. The contact width $2b$ will continue to decrease until the extreme end $b^{''}$ rolls over the starting position of the defect. When $b^{''}$ has just traversed past the starting position of the defect, it is at that

instant the rolling element is considered to have completely unloaded or de-stressed. This hypothesis is based on the results from the explicit dynamics FE modelling of a defective rolling element bearing, which is presented in Chapters 4 and 6, and has recently been published in references [4, 5] by the author of this thesis. For validating the hypothesis, the results from the analytical modelling presented in this chapter will be compared with the FE modelling results in Chapter 6.

Depending on the clearance within a rolling element bearing and applied radial load, it has been mentioned earlier that a few rolling elements, located withing the bearing load zone $2\psi_l^{'}$ are loaded. It should be noted that the decrease in the contact force as a result of the rolling element entering the defect will cause the re-distribution of the load among the remaining rolling elements in the load zone. This will be demonstrated and discussed in Section 3.7 during the quasi-static modelling for estimating the load distribution within a defective bearing.

Mathematical contact force model for a gradual change at the edges of a defect

Based on the above discussion, a mathematical model to predict the gradual variation in the contact forces $F_{dj(\text{grad})}$ across the edges of the bearing defect can be given as

$$F_{dj(\text{grad})}\left(\psi_j(t)\right) = \begin{cases} -\dfrac{F_j}{\Delta\psi_{\text{cw}}}\left(\psi_j(t) - \left(\psi_d + \dfrac{\Delta\psi_d}{2}\right)\right) & \text{if } \psi_d - \dfrac{\Delta\psi_d}{2} < \psi_j(t) \\ & < \psi_d - \dfrac{\Delta\psi_d}{2} + \Delta\psi_{\text{cw}} \\ 0 & \text{if } \psi_d - \dfrac{\Delta\psi_d}{2} + \Delta\psi_{\text{cw}} \leqslant \psi_j(t) \\ & \leqslant \psi_d + \dfrac{\Delta\psi_d}{2} - \Delta\psi_{\text{cw}} \\ \dfrac{F_j}{\Delta\psi_{\text{cw}}}\left(\psi_j(t) - \left(\psi_d - \dfrac{\Delta\psi_d}{2}\right)\right) & \text{if } \psi_d + \dfrac{\Delta\psi_d}{2} - \Delta\psi_{\text{cw}} < \psi_j(t) \\ & < \psi_d + \dfrac{\Delta\psi_d}{2} \\ F_j & \text{otherwise} \end{cases} \tag{3.20}$$

The first part of Equation (3.20) which represents the linear decrease in the rolling element-to-raceway contact force corresponds to the de-stressing of the rolling element upon its entry into the defect, whereas the third part that is a symmetrical inverse of the first, representing a linear increase, corresponding to the re-stressing of the rolling element upon its exit from the defect. The second part of the equation corresponds to the traverse of the (unloaded or de-stressed) rolling element through the defect after and before its de-stressing and re-stressing, respectively. Finally, the fourth part represents the static load on the rolling element corresponding to its contact with the non-defective sections of the outer raceway.

As mentioned earlier, the models presented in this chapter do not include the dynamics of the rolling elements. It should, therefore, be noted that the re-stressing of the rolling elements, which is highly dependent on the centrifugal forces acting on them, has not been correctly represented here. It will be shown in Chapter 6 that the re-stressing of rolling elements upon their exit from a raceway defect results in the generation of multiple force impulses, one of the significant outcomes of this study. Neither the instant step-like nor the gradual increase in the rolling element-to-raceway contact force represent the actual re-stressing event. In order to accurately model the

re-stressing of the rolling elements, one has to include their trajectories (path) as a result of centrifugal forces acting on them, as they traverse through the defect. This is shown in the next chapter where a novel explicit dynamics FE modelling of a defective rolling element bearing is presented.

Using Equation (3.20), the horizontal and vertical contact forces between a rolling element and the defective outer raceway of a bearing, as the rolling element traverses through the defect, are shown in Figures 3.10a and 3.10b, respectively; these force estimates are plotted using black-coloured, solid, thick lines. For comparison, the instantaneous changes in the contact forces at the defect edges are also shown using blue-coloured, solid, thin lines, along with the contact forces for a non-defective bearing plotted using red-coloured, dashed lines. The difference between the instantaneous and gradual responses can be seen to vary across the angular extent of the contact width $\Delta\psi_{\text{cw}}$.

As contact forces between mating bearing components are generally not measured in practice, the contact force results from the analytical simulations will be compared with the explicit dynamics FE modelling results in Chapter 6.

Contact width and area

As the contact width (area) and force are interrelated Hertzian contact parameters, their corresponding variations can also be estimated using the contact force estimates in Equation (3.20).

Figure 3.11 compares the instantaneous and gradual variation in the normal rolling element-to-outer raceway contact width and area as a loaded rolling element traverses through the raceway defect. The blue-coloured, solid line represents the instantaneous step-like changes at the defect extremities, whereas the black-coloured, solid, thick line shows the gradual changes across the edges of the defect. The variation in the contact width for a non-defective bearing is represented using the red-coloured, dashed line. The difference between the instantaneous and gradual changes is similar to that of the

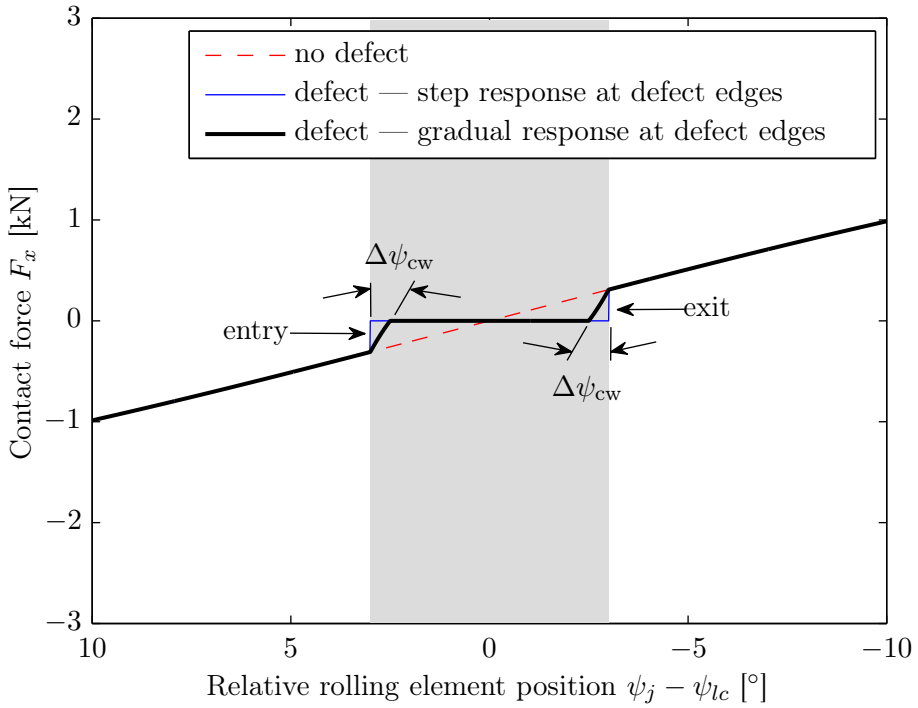

(a) Horizontal contact forces.

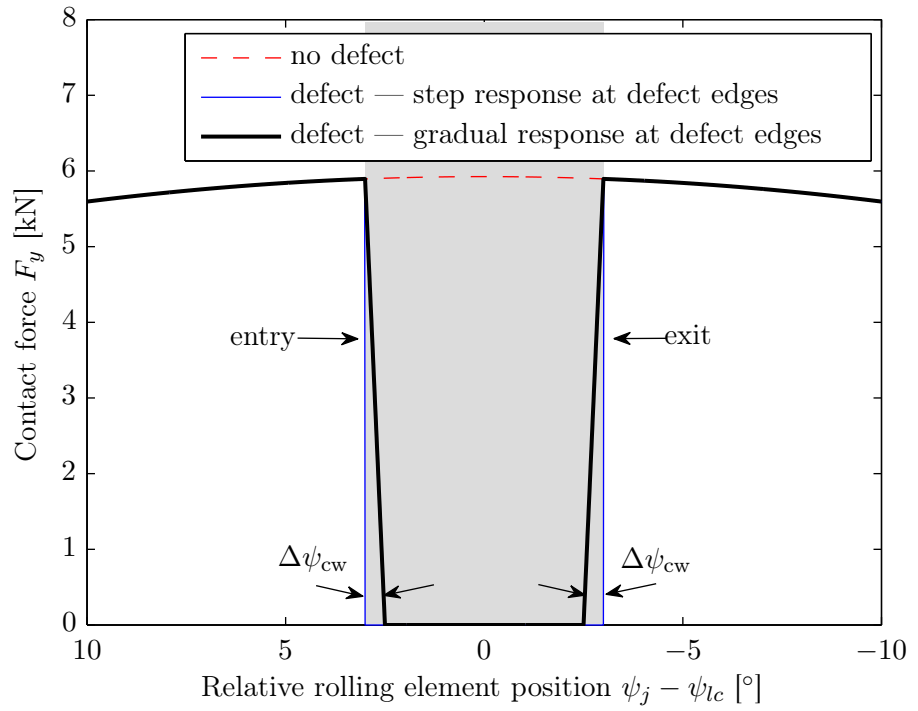

(b) Vertical contact forces.

Figure 3.10: Comparison of the analytically estimated rolling element-to-outer raceway contact forces, highlighting the difference between the erroneous instantaneous step-like and gradual response at the edges of the defect for simulating the entry and exit of a rolling element into and out of the defect, respectively. The gray-coloured shaded area highlights the angular extent $\Delta\psi_d$ of the rectangular-shaped defect.

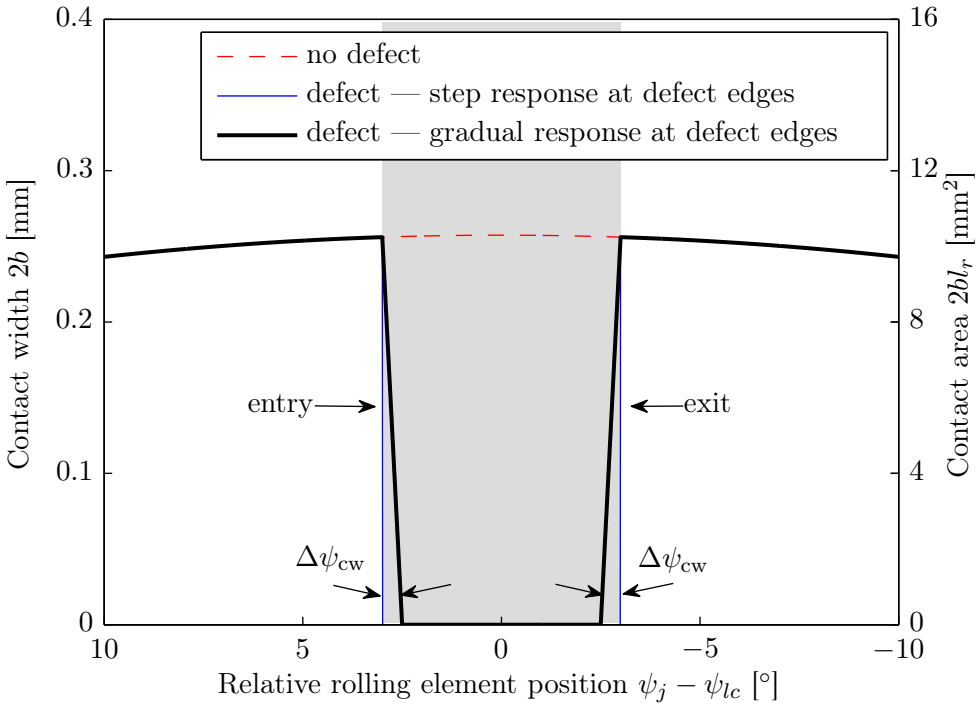

Figure 3.11: Comparison of the analytically estimated rolling element-to-outer raceway contact width and area, highlighting the difference between the erroneous instantaneous step-like and gradual response at the edges of the defect for simulating the entry and exit of a rolling element into and out of the defect, respectively. The gray-coloured shaded area highlights the angular extent $\Delta\psi_d$ of the rectangular-shaped defect.

contact forces shown in Figure 3.10. For the roller length $l_r = 40\,\text{mm}$, the equivalent rectangular contact area is shown on the right-hand side y-axis of Figure 3.11.

3.6 Quasi-static load distribution

An analytical model for estimating the quasi-static load distribution within a rolling element bearing can be developed by incorporating the bearing kinematics in the static load distribution model; that is, modelling the parameters as a function of time or rotational speed of the bearing.

The load-displacement expressions described in Section 3.3.1 were more focused on looking at the radial (y-direction) components so as to facilitate the estimation of the load distribution factor ϵ, angular extent of the load zone $2\psi_l'$, and the load constant.

3.6.1 Bearing kinematics

For a shaft rotating at a speed $\omega_s = 2\pi f_s$, the nominal angular rotation of the cage (or rolling elements) ω_c is given by

$$\omega_c = \frac{\omega_s}{2}\left(1 - \frac{D_r}{D_p}\cos\alpha\right) \tag{3.21}$$

where, D_p is the bearing pitch diameter, D_r the rolling element diameter, and α the contact angle.

The angular position ψ_j of a jth rolling element is given by

$$\psi_j(t) = \psi_c(t) + (j-1)\frac{2\pi}{N_r} \tag{3.22}$$

where, ψ_c is the cage position, and for its initial position ψ_0, it is given by

$$\psi_c(t + \Delta t) = \psi_0(t) + \omega_c \Delta t \tag{3.23}$$

3.6.2 Hertzian contact force-displacement model

It was mentioned in Section 3.3 that the contact deformation δ_j for a jth rolling element is a function of the displacement of the raceways relative to each other, the angular position of the rolling element ψ_j, and the clearance ς. The total contact deformation δ_{dj} for the jth rolling element within a defective rolling element bearing is given by [6, 105] (subscript d symbolising the parameters for a defective bearing — not to be confused with a derivative notation)

$$\delta_{dj}(t) = \delta_x(t)\cos\psi_j(t) + \delta_y(t)\sin\psi_j(t) - \frac{\varsigma}{2} - \beta_j(\psi_j(t))\, S_d(\psi_j(t)) \tag{3.24}$$

where, δ_x and δ_y are the relative displacements of the inner and outer raceways, re-

spectively, and are given by

$$\delta_x(t) = x_i(t) - x_o(t) \qquad \text{and} \qquad \delta_y(t) = y_i(t) - y_o(t) \tag{3.25}$$

In Equation (3.24), $S_d(\psi_j(t))$ represents the rectangular-shaped defect profile given by Equation (3.19), and $\beta_j(\psi_j(t))$ is a factor that introduces the gradual changes at the entry and exit edges of the defect, as discussed in Section 3.5.2. Based on the new mathematical model given by Equation (3.20), $\beta_j(\psi_j(t))$ can be estimated as

$$\beta_j(\psi_j(t)) = \begin{cases} -\dfrac{H_d}{\Delta\psi_{\text{cw}}}\left(\psi_j(t) - \left(\psi_d + \dfrac{\Delta\psi_d}{2}\right)\right) & \text{if } \psi_d - \dfrac{\Delta\psi_d}{2} < \psi_j(t) \\ & < \psi_d - \dfrac{\Delta\psi_d}{2} + \Delta\psi_{\text{cw}} \\ -H_d & \text{if } \psi_d - \dfrac{\Delta\psi_d}{2} + \Delta\psi_{\text{cw}} \leqslant \psi_j(t) \\ & \leqslant \psi_d + \dfrac{\Delta\psi_d}{2} - \Delta\psi_{\text{cw}} \\ \dfrac{H_d}{\Delta\psi_{\text{cw}}}\left(\psi_j(t) - \left(\psi_d - \dfrac{\Delta\psi_d}{2}\right)\right) & \text{if } \psi_d + \dfrac{\Delta\psi_d}{2} - \Delta\psi_{\text{cw}} < \psi_j(t) \\ & < \psi_d + \dfrac{\Delta\psi_d}{2} \\ 0 & \text{otherwise} \end{cases} \tag{3.26}$$

Applying Hertz's contact load-displacement model (Equation (3.8)), the total load F_{dj} on a jth rolling element of a defective rolling element bearing can be estimated as

$$F_{dj}(t) = K_{dj}(t)\,\delta_{dj}^{n}(t)\,\gamma_j(t) \quad \text{for } \gamma_j(t) = \begin{cases} 1 & \text{if } \delta_{dj}(t) > 0 \\ 0 & \text{if } \delta_{dj}(t) \leqslant 0 \end{cases} \tag{3.27}$$

where, K_{dj} is the contact stiffness, δ_{dj} the displacement (given by Equation (3.24)), and n is an exponent ($= 3/2$ for ball bearings and $= 10/9$ for roller bearings). As the rolling element-to-raceway contact deformation can only occur at the contact interfaces

that are under the load zone, γ_j is a factor that zeros the load distribution outside the load zone.

The horizontal and vertical contact forces on the rolling elements of a defective bearing can be estimated using the following equation [6, 105]

$$\begin{aligned}
\begin{bmatrix} F_{dx}(t) \\ F_{dy}(t) \end{bmatrix} &= \sum_{\psi_{lc}}^{\pm\psi_l'} \begin{bmatrix} F_{dxj}(t) \\ F_{dyj}(t) \end{bmatrix} = \sum_{\psi_{lc}}^{\pm\psi_l'} F_{dj}(t) \begin{bmatrix} \cos\psi_j(t) \\ \sin\psi_j(t) \end{bmatrix} \\
&= \sum_{\psi_j=0}^{\pm\psi_l'} K_{dj}(t)\,\delta_{dj}^{n}(t)\,\gamma_j(t) \begin{bmatrix} \cos\psi_j(t) \\ \sin\psi_j(t) \end{bmatrix} \\
&= \sum_{\psi_j=0}^{\pm\psi_l'} K_{dj}(t) \left(\delta_x(t)\cos\psi_j(t) + \delta_y(t)\sin\psi_j(t) - \frac{\varsigma}{2} - \beta_j(\psi_j(t))\,S_d(\psi_j(t))\right)^{n} \gamma_j(t) \\
&\qquad \begin{bmatrix} \cos\psi_j(t) \\ \sin\psi_j(t) \end{bmatrix}
\end{aligned} \tag{3.28}$$

Setting $S_d(\psi_j(t)) = 0$ in Equation (3.28) will yield results for a non-defective rolling element bearing. The analysis of the modelled quasi-static contact forces for a defective bearing is presented in the next section.

3.7 Contact force analysis

For the bearing parameters described in Section 3.3.2 along with the dimensions of the outer raceway defect in Section 3.4.1, Figures 3.12a and 3.12b show three plots of each of the horizontal and vertical rolling element-to-outer raceway contact forces. The forces plotted using the black-coloured, solid, thick lines represent the gradual response at the edges of the defect, whereas the instant response is plotted using the blue-coloured, solid, thin lines. The contact forces for a non-defective bearing are plotted using the red-coloured, dashed lines. The plots in Figures 3.12a and 3.12b are

annotated with four events; their descriptions along with explanations are provided later in Sections 3.7.1 to 3.7.4.

Although the difference between the instantaneous step-like and gradual response for the rolling element-to-raceway contact forces across the edges of the defect has been highlighted in Figure 3.10, it is useful to show the effect of the difference at other rolling element positions (within the bearing load zone). Figures 3.13a and 3.13b show the zoomed plots of the contact forces shown in Figures 3.12a and 3.12b, respectively, highlighting not only the difference between the two responses, but also its effect associated with the increase in the contact forces at a rolling element position adjacent to the defect. This increase in the force (load) on the rolling element, annotated as event #3, will be discussed in Section 3.7.3. Following the pattern of the previous figures, the gray-coloured shaded area in Figures 3.12 and 3.13 corresponds to the angular extent of the outer raceway defect $\Delta\psi_d$.

As mentioned earlier, the re-stressing of the rolling elements presented in this chapter does not provide a realistic representation of the actual re-stressing event. The numerically modelled contact force results that include the dynamics will be presented in Chapter 6. The limitations of the developed quasi-static model will be discussed in Section 3.8.

In order to provide a clear understanding of the changes in the rolling element-to-raceway contact forces within a defective rolling element bearing, the four events indicated in Figures 3.12 and 3.13 are described below.

3.7.1 Event #1: Entry of the rolling elements into the defect — the 'de-stressing' phase

The gradual decrease in the rolling element-to-outer raceway contact forces in Figure 3.12 and 3.13, which has been indicated as event #1, corresponds to the entry of the rolling element into the defect.

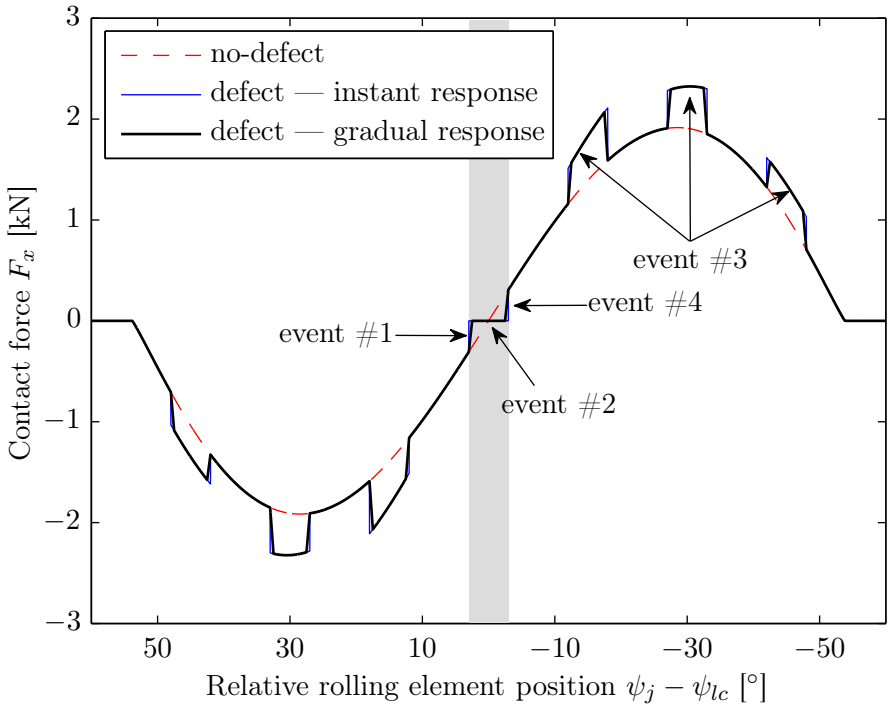

(a) Horizontal contact forces.

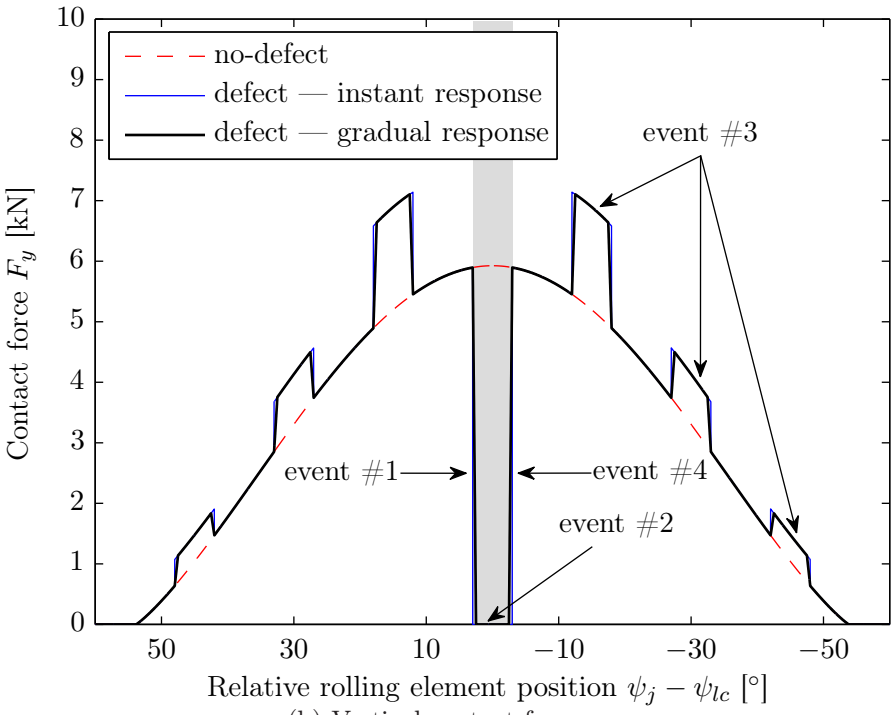

(b) Vertical contact forces.

Figure 3.12: Analytically estimated rolling element-to-outer raceway contact forces for a non-defective and a defective rolling element bearing for a radial load W of 50 kN, obtained using the developed quasi-static analytical model. The difference between the erroneous instantaneous step-like and gradual response at the edges of the defect, which is not clearly visible here, is shown in Figure 3.13.

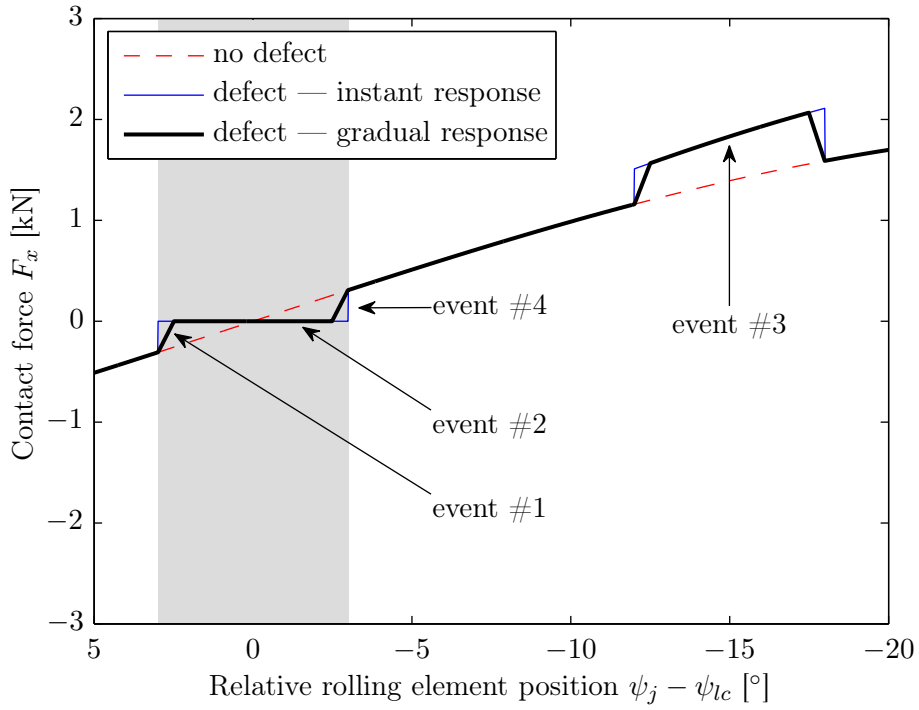

(a) Horizontal contact forces.

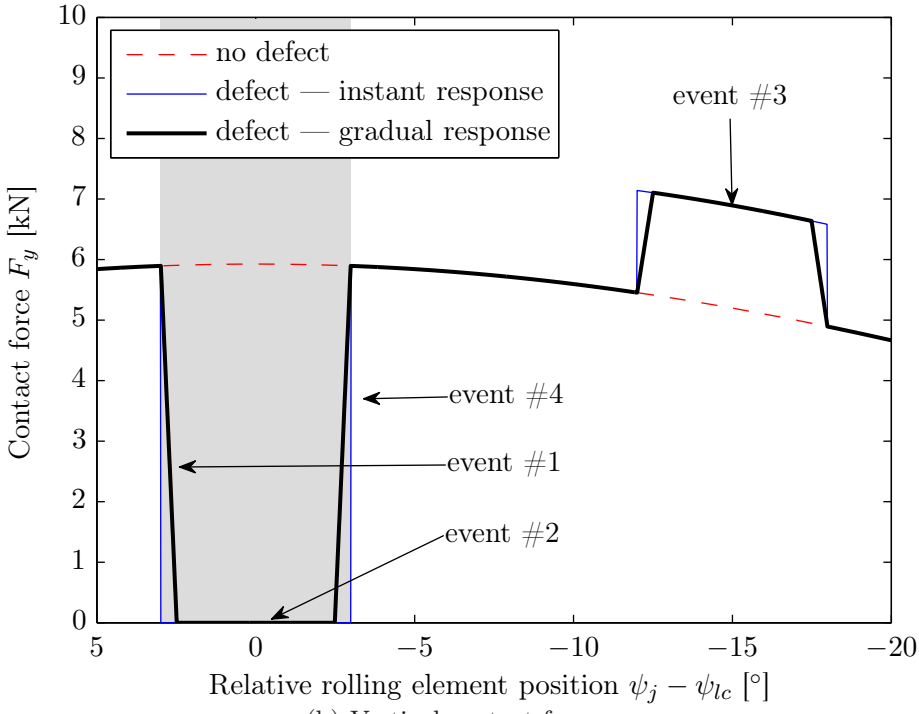

(b) Vertical contact force.

Figure 3.13: The zoomed version of the quasi-static rolling element-to-outer raceway contact forces in Figure 3.12, highlighting the difference between the erroneous instantaneous and gradual responses.

As a stressed (loaded) rolling element starts entering the defect, located on the outer raceway, it gradually starts losing contact with the outer raceway as discussed in Section 3.5.2. Consequently, the contact force between the rolling element and the outer raceway starts decreasing gradually (not instantaneously) to zero. The reduction in the vertical contact force from approximately 6 kN to zero implies that the rolling element has no mechanical stress in contrast to its location between the raceways where it was stressed and loaded due to the application of the radial load W.

3.7.2 Event #2: Traverse of the rolling elements through the defect

The zero-valued contact forces in Figures 3.12 and 3.13, which have been indicated as event #2, correspond to the traverse of the rolling element through the defect.

As no centrifugal effects of the rolling elements are considered for the current simulation, the de-stressed rolling element remains unloaded during its traverse through the defect. In practice though, the rolling elements within a bearing are acted on by centrifugal forces during its operation. An explicit dynamics FE modelling of a defective rolling element bearing that includes the centrifugal effects acting on the rolling elements will be presented in Chapter 6. It will then be shown that during their traverse through a raceway defect, the de-stressed rolling elements at some instance will strike the defective surface.

3.7.3 Event #3: Re-distribution of a load on the rolling elements — the load compensation phase

It has been described in the preceding section that a rolling element loses contact with the defective part of the raceway, as it traverses through the defect. The loss of the load (force) on the rolling element must be compensated in order to have the equilibrium of the system maintained at all times. Therefore, as one rolling element loses contact

(unloads), other rolling elements in the load zone (located at the non-defective sections of the raceways) take the lost load resulting in a re-distribution of the radial load.

Event #3, indicated in Figures 3.12 and 3.13, highlights the load compensation. Similar to the gradual decrease in the rolling element-to-raceway contact force, the increase at other rolling element positions occurs gradually. The sum of the vertical force components at the rolling elements equals 25 kN (half of the applied radial load due to the consideration of a single bearing row here), while the sum of the corresponding horizontal force components equals zero.

3.7.4 Event #4: Exit of the rolling elements from the defect — the 're-stressing' phase

Re-stressing of the rolling elements refers to their exit from a defect within a bearing. In Figures 3.12 and 3.13, the increase in the contact forces from zero to a certain value, which is related to the corresponding static load distribution, indicated as event #4, represents the re-stressing event. Compared to their de-stressing, which is a low-frequency event, the re-stressing of the rolling elements is generally an impulsive (high-frequency) event [161, 162, 165].

Without the consideration of the centrifugal forces acting on the rolling elements, the re-stressing event cannot be accurately modelled using the developed quasi-static model. The dynamic numerical simulation results in Chapter 6 will show a better representation of the re-stressing event.

The four events discussed above will be further discussed in the same chronological order in Chapter 6, and the quasi-static modelling results will be compared with those of the explicit FE modelling simulation results.

Contact forces versus time

The contact forces can also be plotted as function of time t. For a rotational speed n_s of 500 RPM, Figures 3.14a and 3.14b show the horizontal and vertical rolling element-to-outer raceway contact forces, corresponding to the results shown in Figure 3.12. For the rolling element bearing model considered here, the rotation speed $n_s = 500\,\text{RPM}$ corresponds to the train speed of approximately 95 km/hr for a 1 m wheel diameter. Referring to Figure 3.5, the rolling elements j from 1 to 6 correspond to the rolling elements initially positioned to the left-hand side of the defect, whereas the rolling elements from 24 to 22 were positioned to the right-hand side of the defect.

3.8 Limitations of the quasi-static model

A limitation of the quasi-static load distribution model developed in this chapter is the exclusion of the centrifugal forces acting on the rolling elements. As a result, the quasi-static model cannot accurately predict the following:

- Event #2 — potential impacts of the rolling elements with the defective surface. In practice, depending on the size (length) of a defect and rotational speed, rolling elements may or may not strike the surface of the defect. Without incorporating their centrifugal effects, the de-stressed rolling elements traversing through a defect cannot freely follow their trajectory that tends to project them outwards from the centre of the bearing; their trajectory is restricted to what it is when they are within the non-defective section of the outer and inner raceways. Therefore, the quasi-static model cannot predict the current location of the rolling elements once they enter a defect.

- Event #4 — re-stressing of the rolling elements. Due to the exclusion of the centrifugal forces acting on the rolling elements, their re-stressing during their exit from a raceway defect cannot be predicted by the developed quasi-static

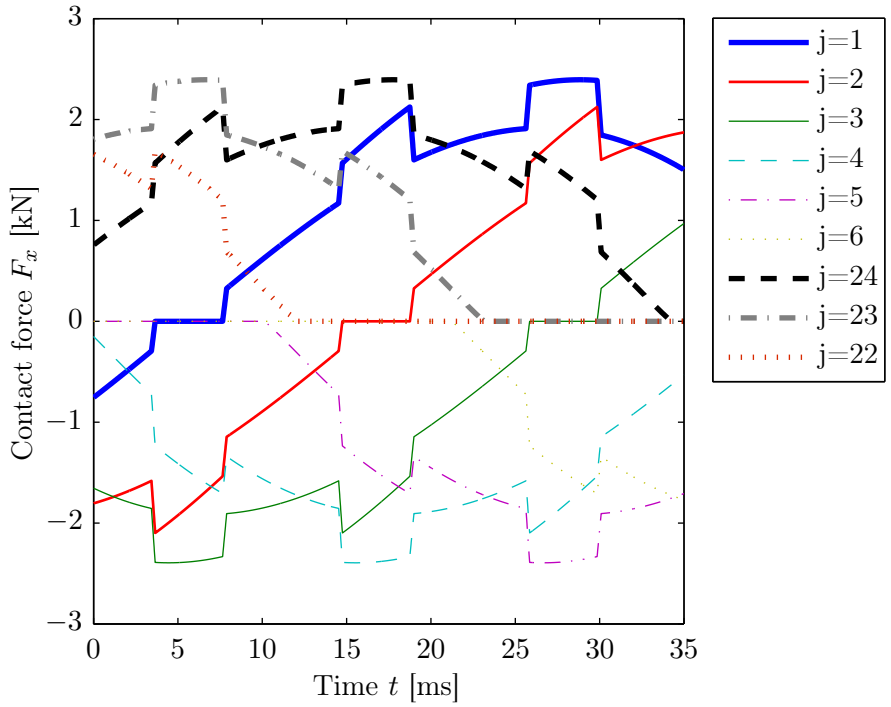

(a) Horizontal contact forces.

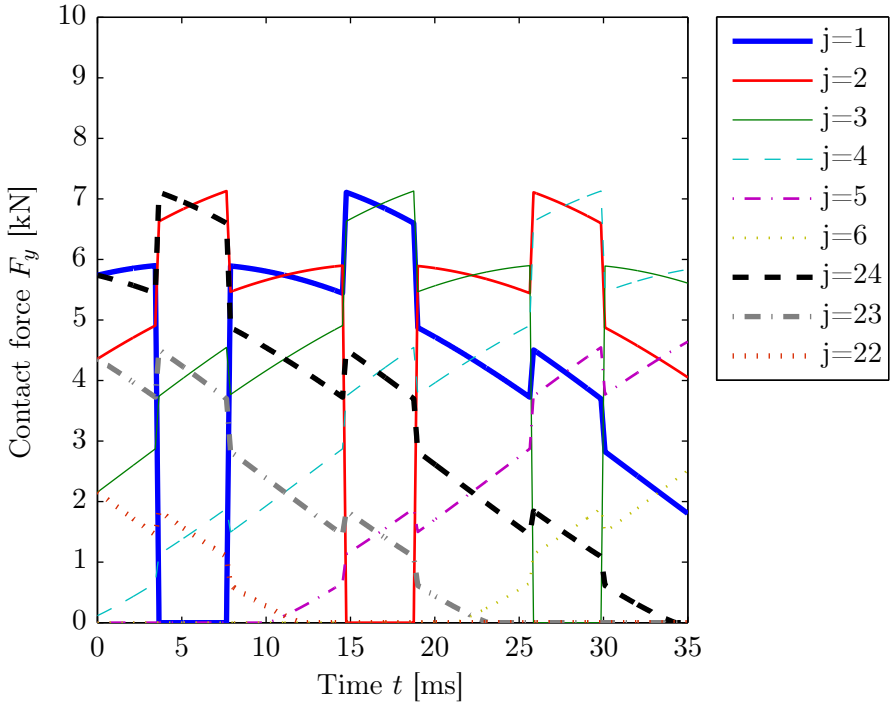

(b) Vertical contact forces.

Figure 3.14: Analytically estimated rolling element-to-outer raceway contact forces as the rolling elements traverse through the outer raceway defect for a radial load W of 50 kN and rotational speed n_s of 500 RPM.

model.

Incorporating the centrifugal forces acting on the rolling elements and analytically modelling the trajectory of the de-stressed rolling elements is a considerable task, and beyond the scope of the analytical model presented in this chapter. Furthermore, the principal aim of the new mathematical model was to predict the de-stressing of the rolling elements, which is independent of the centrifugal and inertial effects. Incorporating these dynamic effects along with the slippage [95] (or randomness) of the rolling elements will provide a more realistic estimate of the contact forces associated with the re-stressing event.

A novel explicit dynamics FE model of a defective rolling element bearing has been developed in this study, and is presented in the next chapter. The FE model, which incorporates the centrifugal forces acting on the rolling elements and calculates their path as they traverse through the defect, does not suffer from the aforementioned limitations. The analytically estimated quasi-static contact force results presented in this chapter will be compared with the numerically modelled dynamic rolling element-to-raceway contact forces in Chapter 6.

3.9 Conclusions

A quasi-static model for estimating the load distribution within a rolling element bearing has been developed by extending a well-known static load distribution model [3, Chapter 7]. The main aim of this chapter was to predict the de-stressing of the rolling elements as they enter into a raceway defect. A novel mathematical model for estimating the gradual decrease in the rolling element-to-raceway contact force corresponding to the de-stressing of a rolling element within a bearing was developed. Considering a linear slope, the mathematical model was based on the finite contact area developed at the interface of the rolling elements and raceways of a bearing according to Hertzian contact theory.

The gradual change in contact width, area, and force was highlighted and compared to the instantaneous step-like response at the edges of a bearing defect implemented by previous researchers. The analysis of the analytically modelled contact forces was presented and limitations of the developed quasi-static model were discussed. Although the developed model is not capable of predicting the re-stressing of the rolling elements due to the exclusion of centrifugal forces acting on the rolling elements, the model can predict the de-stressing of the rolling elements, which will be compared with the FE modelling results in Chapter 6. A gradual change in the contact force is necessary for generating a low-frequency entry event; therefore, the model developed in this chapter can be incorporated in future multi-body dynamic models for predicting the vibration response of a defective rolling element bearing.

As contact forces between mating bearing components are generally not measured in practice during their condition-based monitoring, the analytical modelling results from the quasi-static model will be compared in Chapter 6 with those from a more comprehensive explicit dynamics FE model of a defective rolling element bearing.

The next chapter presents the FE modelling of a defective rolling element bearing solved using a commercial FE software package, LS-DYNA [329].

This page intentionally contains only this sentence.

Chapter 4

Explicit Finite Element Modelling of Rolling Element Bearings

4.1 Introduction

This chapter presents an explicit dynamics finite element model of a defective rolling element bearing solved using a commercial software package, LS-DYNA [329]. It is a multiphysics simulation package capable of simulating complex dynamics problems, and is used by numerous industries, such as automotive, aerospace, construction, military, manufacturing, and bioengineering. LS-DYNA uses the second-order central difference method [299, 302], an explicit time integration scheme, for simulating highly non-linear transient dynamic events of very short-duration. This type of FE code is different from the implicit FE solvers, such as ANSYS [307], in terms of time integration methods. Differences between explicit and implicit time integration schemes are given in Appendix D.

It was mentioned in Chapter 2 (Literature Survey) that numerous researchers have developed multi-body analytical [90–114] and FE models [115–120] for estimating the vibration response of defective rolling element bearings: a review of these models was presented in Sections 2.3.1 to 2.3.4.3. One of the problems reported by several re-

searchers [91, 93, 103, 104, 109–111] was the mismatch between the instantaneous levels of the modelled and measured defect-related vibration signals, although amplitude-correction factors were applied by some researchers [93, 103, 104] but without providing justifications. The use of analytical and theoretical methods often involves several assumptions and simplifications, which for the previous models, were discussed during their review in Sections 2.3.1, 2.3.2, and 2.3.3, Chapter 2. Unlike the analytical models, one can minimise the assumptions in FE methods and achieve comparatively better results; however, one has to still assume values or choices for parameters, such as material model, material properties, time integration (time-stepping) scheme, damping, and friction, in addition to adequately discretising a model into finite elements so as to accurately model its structural response.

During the survey of the literature, only four publications [117–120] were found, published between the years 2010 and 2013, which described the modelling of defective rolling element bearings for predicting their vibration response using an explicit FE software package [329]. As these FE models are directly relevant to the work presented in this thesis, a critical review of the models [117–120] along with significant potential problems associated with the models was provided in Section 2.3.4.3, Chapter 2. It was found that the authors of the FE models [117–120] have compromised performance by modelling either the whole outer ring as rigid or its outer surface as rigid. This causes artificial over-stiffening of the bearing structure that lead to unrealistically high instantaneous acceleration levels of approximately 4,000 g [119] and 15,000 g [120] compared to the corresponding experimental measurements of 100 g and 10 g in references [119] and [120], respectively. In reference [118], the numerically predicted acceleration levels of 10^7 g were not compared with experimental results. The significant mismatch between the predicted and measured amplitude levels reported for the multi-body models [91, 93, 103, 104, 109–111] remains a problem with the existing FE models.

In the explicit dynamics finite element model of a defective rolling element bearing developed in this chapter, the bearing components are modelled as flexible bodies,

which facilitates a more accurate representation of the bearing stiffness, and hence the vibration response of the bearing. Furthermore, much emphasis was given to discretising the model adequately to ensure a smooth and continuous rolling contact between the rolling elements and bearing raceways, so as to accurately transmit the load between them during the numerical simulations. Unlike previous FE models [117–120], which focused on presenting the vibration response of defective rolling element bearings, the work presented in this thesis not only comprises the numerical modelling of the dynamic rolling element-to-raceway contact forces as rolling elements traverse through a defect, but also their analysis and correlation with the bearing vibration signals. Such an analysis has not been previously presented in the literature except published recently by the author of this thesis [4, 5] based on the work presented here. In this chapter, however, only numerically modelled vibration signals are presented; the analysis of the contact forces along with the aforementioned correlation will be presented in Chapter 6, following the experimental verification of the FE model of the bearing in Chapter 5.

It has been established in the literature [4–7, 161, 162, 165] that the entry of the rolling elements into a bearing defect generates a low-frequency (de-stressing) event, whereas their exit (re-stressing) from a defect generates highly impulsive signals. In contrast to previous models [90–111, 113–120], which could not predict the de-stressing of the rolling elements, the explicit FE model of the bearing developed here accurately predicts this event, in addition to the re-stressing of the rolling elements. The instantaneous peak acceleration levels of the defect-related impulses predicted by the explicit FE model of the rolling element bearing here also compare favourably with corresponding measured data; this comparison will be presented in Chapter 5.

4.1.1 Aims

The aims of this chapter are to:

- develop a comprehensive non-linear explicit dynamics finite element model of a defective rolling element bearing with minimal assumptions and simplifications, which is better than existing FE models [117–120] and more detailed than analytical multi-body models [90–114];
- present a new hypothesis for explaining the cause of rolling contact noise observed in the numerical results;
- analytically estimate the numerical rolling contact noise frequencies; thereby, facilitating the justification of the proposed hypothesis;
- reasonably filter the numerically simulated vibration signals — acceleration, velocity, and displacement time-traces; and to
- analyse the numerical vibration signals using standard signal processing techniques associated with the vibration-based condition monitoring of rolling element bearings [25, 26, 30, 251, 252].

4.1.2 New knowledge

The novel work presented in this chapter has provided the following new knowledge and insights:

- the capability of the model to predict vibration signals, which are characterised by energy mainly in low-frequency range, associated with the de-stressing of rolling elements as they enter into a raceway defect;
- the development of a hypothesis to explain the cause of numerical rolling contact noise observed in the modelled results; and

- the analytical estimation of the contact noise frequencies along with the demonstration of the *beating* phenomenon to justify the proposed hypothesis.

This chapter is limited to describing the development of the explicit dynamics FE model of a defective rolling element bearing and presenting its vibration response. The new knowledge related to the dynamic contact interaction of the rolling elements and raceways is described in Chapter 6, which presents a detailed analysis of the rolling element-to-raceway contact forces along with their correlation with the vibration response of the bearing as the rolling elements traverse through a defect.

4.1.3 Structure

The development of the FE model of a rolling element bearing with an outer raceway defect is described in Section 4.2 along with an elaborate discussion on the meshing requirement (recommended and required EPW criterion) in Section 4.2.2. In order to demonstrate the dynamic structural response of the model, modal analysis was conducted on the outer ring of the bearing, and the numerically predicted resonance frequencies are compared with the analytical results in Section 4.3. The numerically modelled acceleration results are presented in Section 4.4 and the accurate acquisition of the bearing kinematics is discussed. A new hypothesis is developed in Section 4.5 to explain the cause of numerical rolling contact noise observed in the modelled results along with the estimation of the noise frequencies and demonstration of the *beating* phenomenon to justify the proposed hypothesis. Standard signal processing techniques associated with the vibration-based monitoring of rolling element bearings were implemented on the numerically predicted vibration results, and the corresponding analyses are presented in Section 4.6. The capability of the developed FE model to predict the low-frequency de-stressing of the rolling elements upon their entrance into the defect is demonstrated within Section 4.6. Following the summary of the numerically modelled FE results, the conclusions of the chapter are presented in Section 4.7.

4.2 Numerical FE model of a defective rolling element bearing

This section describes various steps that are necessary to perform an explicit finite element analysis of a defective rolling element bearing using LS-DYNA.

4.2.1 Description of the model

A 2-D FE model of a rolling element bearing was built using ANSYS DesignModeler [379]. The model comprises the following components: an outer ring, an inner ring, a cage retaining a total of twenty-four rolling elements, and an adapter that distributes a (radial) load to the outer ring, which is also transmitted to the inner ring through the rolling elements. The dimensions of the modelled components are shown in Table 4.1, and are similar to those considered during the quasi-static load distribution analytical model presented in Section 3.3.2, Chapter 3. There was a nominal diametral clearance $\varsigma = 0.04\,\text{mm}$ between the rolling elements and outer raceway of the bearing. The clearance between the rolling elements and their corresponding cage slots was 0.35 mm. These dimensions are representative of a typical package bearing unit used in the railway industry that has been experimentally tested during the course of this research; this experimental work will be presented in the next chapter for the comparison of the modelled and measured results.

The bearing was modelled with a localised rectangular defect that was located centrally at the top on the outer raceway. The dimensions of the defect were: circumferential length $L_d = 10\,\text{mm}$ and height (or depth) $H_d = 0.2\,\text{mm}$. These dimensions were selected based on the inspection of numerous defective bearings, obtained from operational use in the railway industry [378]. As mentioned earlier, such a defect is often referred to as a *line spall*. Figure 4.1a shows a localised line spall of circumferential length of approximately 15 mm on the outer raceway of an axle bearing generated

Component name	Description and dimensions (mm)			
Outer ring	outer race diameter	$D_o = 200$	thickness	$h_o = 10$
Inner ring	inner race diameter	$D_i = 163.96$	thickness	$h_i = 10$
Cage	outer diameter	$D_c = 196$	thickness	$h_c = 4$
Rolling element	diameter	$D_r = 18$	total number	$N_r = 24$
Adapter	width	$w_a = 160$	height (central)	$H_a = 40$

Table 4.1: Dimensions of the components within the finite element model of the rolling element bearing.

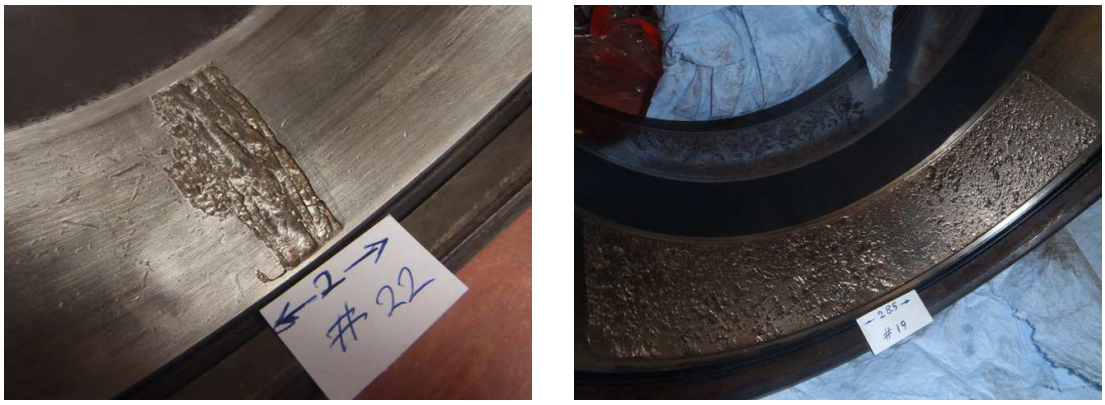

(a) A line spall. (b) An extended spall.

Figure 4.1: Photos of actual defects on the outer raceway of axle rolling element bearings generated during operational use in the railway industry [378] (courtesy: Track IQ^{TM} [11]).

during operational use in the railway industry. In contrast, a much larger operational defect, an *extended spall* of length 230 mm, on the outer raceway of an axle bearing is shown in Figure 4.1b, although such a defect is not considered in this study but is shown only to highlight the severity of defects in railway bearings.

For the current bearing model, the circumferential length of 10 mm corresponds to an angular extent of approximately 6°. Similar defect dimensions were considered during the quasi-static analytical modelling presented in Chapter 3, so that the numerically predicted contact forces could be compared with the analytical results. Analyses of the contact forces will be presented in Chapter 6.

Element type and material model 2-D shell elements were used to model the bearing as a solid structure. A 2-D element is defined by four nodes having 2-DOF at

each node: translations in the nodal x- and y-directions. The shell elements were modelled as plane strain elements [329, Chapter 3, pages 3.25–3.30]. The components of the bearing were modelled using the material properties of steel of density $\rho = 7850\,\mathrm{kg/m^3}$, modulus of elasticity $E = 200\,\mathrm{GPa}$, and Poisson's ratio $\nu = 0.3$. The isotropic elastic material model was chosen for the current analysis. Refer to Appendix E, which describes the isotropic elastic material model used in LS-DYNA [329].

4.2.2 Discretisation of the model

The discretisation of a model into nodes and elements is an important step in a finite element analysis as the accuracy of the results depends on the quality of the mesh, and size and aspect ratio of the elements. Elements with poor aspect ratio can lead to severe (elemental) distortion or *hourglassing* [329, Chapter 3, 7, pages 3.4–3.16, 7.6–7.9]. Prior to discussing the discretisation of the bearing model, a few conditions that are pivotal to accurately simulating the real-time operation of a bearing are emphasised below.

4.2.2.1 Compliance of conditions

During the operation of a bearing, the rolling elements need to maintain a continuous rolling contact with the outer and inner raceways of the bearing in order to transmit the load between the raceways. For meshing the rolling elements and raceways, the optimal element size was determined based on the compliance of the FE simulation results with the following two conditions:

1. the surfaces of the bearing raceways and rolling elements, which are under the influence of load zone, should be in contact at all times during the simulation, and

2. the rolling elements should predominantly roll and not slide during the simulation.

It should, however, be noted that in practice, there is a small amount of sliding or slipping associated with the rolling elements [96]. Fulfilment of the first condition is necessary to achieve the correct load distribution on the rolling elements as per the analytical static solution [3, pages 234–237] (presented in the previous chapter). Accomplishment of the second condition is necessary to accurately acquire the rotational speed of the rolling elements (cage) ω_c, which would eventually result in the correct prediction of the bearing kinematics; that is, the outer raceway defect frequency f_{bpo} for the current simulation.

In a typical operation of a bearing in practice, the rolling elements rotate about the axis of the bearing and their own axes simultaneously. In order to simulate the real-scenario of a bearing operation, no boundary conditions were applied to the rolling elements, and they were rotated due to their contact interaction with the rotating inner and stationary outer rings. Therefore, satisfactory achievement of the second condition is significantly important for the reasons mentioned in the preceding paragraph. It should, however, be noted that the two conditions are interrelated, as the loss of rolling element-to-raceway contact will affect the rotational speed of the rolling elements, resulting in their sliding, and thereby, causing incorrect prediction of the bearing kinematics.

The general EPW criterion is discussed next; however, many more than the recommended EPW were required to accurately model the kinematics of a rolling element bearing in order to achieve compliance with the aforementioned conditions.

4.2.2.2 Elements-per-wavelength criterion

The determination of an optimal element size not only depends on the size of a model, but also on the type of an analysis. Having a certain number of EPW is recommended as a general guideline for various types of analyses [307]; for example, in the case of an acoustics analysis, at least 12 EPW are sufficient to accurately model the propagation of sound waves [380], whereas at least 20 EPW are recommended for a transient dynamic

structural analysis [336, Chapter 5] for (structural) wave propagation studies.

The transmission of bending waves, which are a combination of compressional (longitudinal) and shear (transverse) waves, is important in solids. Having the tendency to flex a solid structure, bending waves, often referred to as *flexural waves*, propagate parallel to the surface of the structure, resulting in its normal displacement [381, Chapter 8, pages 354–359]. Generally, an EPW value can be estimated on the basis of the bending wave speed of a structure to be modelled. In the work presented in this thesis, vibration signals of a defective rolling element bearing were modelled and measured at the outer surface of the outer ring of the bearing. Therefore, it is useful to ensure sufficient elements in the outer ring of the bearing so as to model its flexibility or modal vibration response.

Above the ring frequency of a cylindrical shell, its curvature effects largely disappear and the shell vibrates like an equivalent flat plate [382]. The ring frequency of a cylindrical shell is given by [382, Chapter 1, page 32]

$$f_{rc} = \frac{1}{2\pi r_c}\sqrt{\frac{E}{\rho\,(1-\nu^2)}} \tag{4.1}$$

where, r_c is the mean radius of a cylindrical shell, E is the modulus of elasticity, ρ is the density, and ν is the Poisson's ratio. For the dimensions of the outer ring of the bearing model considered here, its ring frequency f_{rc} is approximately 8025 Hz. For bearing fault diagnosis that is commonly implemented using envelope analysis [251, 252], vibration signals are generally demodulated in high-frequency range [30, 31, 59]. Although the vibration signals can be demodulated in the natural frequency range of a bearing that could include its low-frequency resonant modes, the reason for implementing the demodulation in high-frequency range is the defect-related impulses are amplified by high-frequency structural resonant modes of a rolling element bearing [17]. It is shown in Figure 4.4, which presents results of a modal analysis of the outer ring of the bearing to be discussed in Section 4.3, that there are numerous natural

frequencies (modes) of the outer ring above its ring frequency f_{rc}. As defect-related impulses can excite all the natural frequencies, it is reasonable to demodulate the signals at any frequency. However, as will be shown in Section 4.6.3 through the use of spectral kurtosis [25] and kurtograms [26], the frequency band with the highest content of impulsive energy is 18–23 kHz. Therefore, in this case, it is justifiable to consider that the outer ring of the bearing behaves like a flat plate at high frequencies of interest.

The following discussion describes an estimation of an element size for building the finite element model of the rolling element bearing. This is based on the vibration characteristics of the outer ring of the bearing, which would seem as a reasonable criterion, so as to capture the dynamics of the system. However, it will be shown that the mesh size is actually governed by the need to accurately simulate the rolling element-to-raceway contact forces and bearing kinematics as mentioned in Section 4.2.2.1.

Above its ring frequency f_{rc}, considering the outer ring of the rolling element bearing model as a flat plate, the velocity c_b of bending waves is given by [382, Chapter 1, pages 26–38]

$$c_b = \sqrt{\omega} \left[\frac{E h_o^2}{12(1-\nu^2)\rho} \right]^{\frac{1}{4}} \tag{4.2}$$

where, h_o is the thickness of the outer ring and ω is the angular frequency, which corresponds to the highest frequency of interest at which results are sought. Considering that the results are sought at 40 kHz, the bending wave speed at 40 kHz for a 10 mm thick plate (modelled thickness of the outer ring) equates to approximately 1960 m/s, and the corresponding bending wavelength λ_b, equals 0.049 m. A mesh element size of 2 mm would result in approximately 24 EPW which easily meets the recommended EPW criterion of 20 for a transient dynamic structural analysis [336, Chapter 5].

Mesh element sizes of 2 mm, 1 mm, 0.75 mm, 0.5 mm and 0.3 mm were tested. For the FE models of the bearing meshed using the element sizes of 2 mm, 1 mm, and 0.75 mm, it was found that a continuous contact between the rolling elements and raceways could not be maintained during the simulation. The loss of the contact

caused incorrect load distribution on the rolling elements. In contrast, for the FE models meshed using the element sizes of 0.5 mm and 0.3 mm, the two aforementioned conditions were fulfilled, which consequently resulted in the accurate acquisition of the bearing kinematics. The simulation results, rolling element-to-raceway contact forces and instantaneous acceleration levels, for the FE models meshed using 0.5 mm and 0.3 mm element sizes, were very similar to each other. Therefore, the mesh element size of 0.5 mm was chosen to reduce the CPU run times without significantly compromising the accuracy of the numerical solution.

All the components within the rolling element bearing model were meshed using quadrilateral elements, except for the rolling elements, which due to their geometry, could not be meshed with the quadrilateral elements. Consequently, they were meshed with a mixture of quadrilateral and triangular elements. It is interesting to note that the chosen element mesh size of 0.5 mm corresponds to 97 EPW (at 40 kHz), which is nearly 5 times the recommended EPW value for a transient dynamic structural analysis [336, Chapter 5]. The use of a much smaller than the minimum required mesh element size so as to ensure continuous rolling contact eliminates the need to assume that the outer ring of the bearing behaves like a flat plate. In other words, the importance of accurately modelling the rolling element-to-raceway contact interaction and bearing kinematics ironically devalues the ring/plate vibration dynamics for estimating an appropriate mesh element size. However, one should not ignore the aforementioned discussion that is related to the vibration dynamics of the outer ring because it provides a reasonable guide to model discretisation if one has to conduct an implicit FE analysis that could include modal or harmonic analysis [307].

Figure 4.2 shows the meshed FE model of the rolling element bearing annotated with the names of the components. The geometrical rectangular defect located centrally at the top of the outer raceway, which cannot be seen in Figure 4.2a, is shown in Figure 4.2b for clarity. The centre of the rolling element located immediately to the left-hand side of the defect is offset by 4° from the y-axis; the rolling elements within

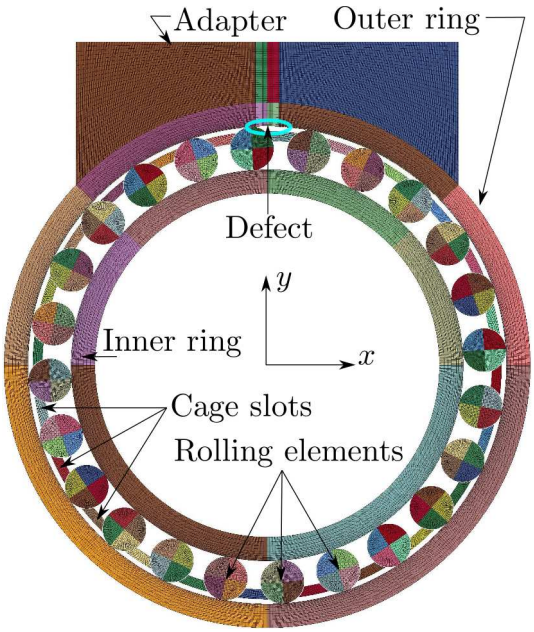

(a) The meshed FE model of the bearing along with the adapter.

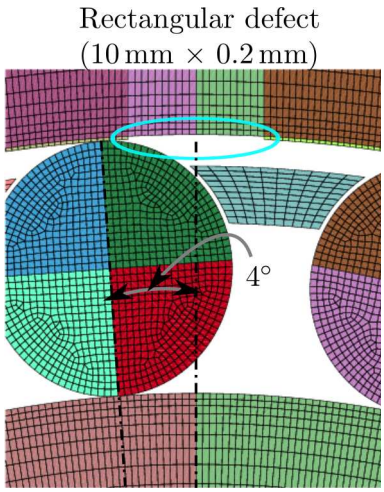

(b) A partially zoomed version of Figure 4.2a, showing the 1-element deep rectangular defect on the outer raceway, highlighted using the ellipse; the centre of the rolling element to the left-hand side of the defect is offset by 4° from the y-axis.

Figure 4.2: Images of the 2-D finite element model of the defective rolling element bearing.

the model are spaced 15° apart.

In order to confirm that the chosen element mesh size is adequate for modelling the structural flexibility of the bearing model, modal analysis was performed on the outer ring of the bearing. The reason for selecting only the outer ring and not the whole bearing is the complexity associated with modelling the contact between a few rolling element-to-raceway interfaces that are under a load, while most of the rolling elements remain unloaded. For a radial load W of 50 kN on the bearing, it was estimated in Section 3.3.2, Chapter 3, that only seven rolling elements are loaded; refer to Figure 3.4, Chapter 3. Another reason for only considering the outer ring is that the resonance frequencies obtained from the finite element modal analysis can be compared to the analytical solution [383, Chapter 12]. Although the EPW for the current bearing model exceeds the recommended criterion by nearly 5 times, the modal analysis of the outer ring will ensure that the structural response has been appropriately acquired. The modal analysis will be presented in Section 4.3.

4.2.3 Contact interactions

A frictional contact with a low coefficient of friction $\mu = 0.005$ was defined for the following contact interfaces within the model: rolling elements–outer ring, rolling elements–inner ring, and rolling elements–cage. The chosen frictional coefficient is comparable to that generally recommended for rolling element bearings in practice [3, Chapter 12].

One of the crucial aspects associated with simulating the operation of a rolling element bearing using LS-DYNA is understanding the functional capabilities of the impact–contact algorithm [329, Chapter 26] integrated in LS-DYNA. It is vital to accurately model the non-linear Hertzian contact forces [175–177] between the rolling elements and bearing raceways. More importantly, the traverse of a rolling element through a bearing defect often involves its impact with the defective surface and race-

ways. During the analyses of the numerically modelled rolling element-to-raceway contact forces, it will be shown in Chapter 6 that the re-stressing of rolling elements generates multiple force impulses that cause the bearing structure to vibrate. Therefore, in order to understand the usage of various parameters associated with the in-built contact algorithm, a simple test case involving the impact of a sphere with a plate was numerically solved using LS-DYNA. A detailed report on the validation of the test case is presented in Appendix F. It investigates the effects of altering element mesh sizes, contact stiffness, and contact penalty factor on the numerical results. In summary, it was found that in the vicinity of the sphere–plate contact interface, a fine mesh was required to accurately model the impact force and contact duration. The stiffness penalty factor was also altered from its default value in order to achieve the contact displacement comparable to that of the analytical solution.

4.2.3.1 Contact–impact algorithm

For modelling the contact interaction between the mating components of a rolling element bearing, the segment-based contact algorithm [329, Chapter 26], built within LS-DYNA, was implemented. It detects the penetration of one segment into another and applies a force, proportional to the penetrating depth, to the segment nodes, as opposed to the penetrating nodes only, for the standard node-to-surface penalty-based contact technology often used in numerous implicit FE solvers including ANSYS [307], Abaqus [308], and NASTRAN [311]. As an example, when two 4-noded segments come into contact, a penalty force is applied to the eight nodes to resist the segment penetration in the case of the surface-to-surface segment-based contact, rather than to the penetrating nodes only for the node-to-surface penalty-based contact.

The contact stiffness between contacting bodies, also referred to as *spring stiffness*, is calculated as [329, Chapter 26, page 26.10]

$$k_{cs}(t) = \frac{1}{2}(\texttt{SLSFAC}) \times (\texttt{SFS or SFM}) \left(\frac{m_1 m_2}{m_1 + m_2}\right) \left(\frac{1}{\Delta t_{\text{critical}}}\right) \tag{4.3}$$

where, SLSFAC is the default penalty scale factor, SFS or SFM are the default slave and master penalty stiffness factors, respectively, m_1 and m_2 are segment masses of the bodies in contact, and $\Delta t_{\text{critical}}$ is critical time step that advances the numerical solution. This time step will be discussed in more details in Section 4.2.5.1. The default value of SLSFAC defined in the contact–impact algorithm built within LS-DYNA is 0.1, and for SFS and SFM, it is 1. The effective penalty factor is the product of SLSFAC and SFS or SFM. The effects of altering the penalty factors are described in Appendix F. It was found that too much increase in the penalty factor causes artificial over-stiffness that reduces displacement (or deformation) of the sphere and plate at their contact interface. Consequently, it leads to ill-conditioning of the global stiffness matrix, and thereby, causes an unstable solution.

4.2.4 Boundary conditions and loads

The following boundary conditions were applied to the FE model of the rolling element bearing in order to simulate the real-time operation of a bearing in a typical railway application. These boundary conditions also effectively simulate the experimental setup conditions applicable to a bearing during its testing; the experimental work will be described in the next chapter.

- A radial load W of 50 kN on the top edge of the adapter in the downward (negative) global cartesian y-direction was applied so as to radially load the bearing; this load represents half of the load carrying capacity of the bearing.

- The inner ring was constantly rotated with a uniform rotational speed n_s of 500 RPM in a clockwise direction; this speed corresponds to a train speed of approximately 95 km/hr for a 1 m wheel diameter.

- In a typical three-piece railway bogie (refer to Figure 1.6, Chapter 1), the adapter is located on the top of a bearing, and is sandwiched between the bearing and one of the two side-frames; the essential constructional features of a three-piece bogie [32, Chapter 3, page 70] were also discussed in Section 1.1.3, Chapter 1, along with the corresponding schematic in Figure 1.6. During the travel of a train (operation of a bearing), the adapter remains at its position due to the weight of the railway vehicle, which is transferred on to the (four) bearings within a bogie through the side-frame-to-adapter structural coupling. The coupling between the adapter and the outer ring of a bearing is such that there is a conformal contact between them, as a result of which the outer ring of a bearing also remains in its position, and does not rotate. Implementing the coupling between the adapter and outer ring in the FE model of the bearing was challenging because no direct constraints could be applied to the outer ring as this would result in over-constraining its translations and vibration response, consequently causing an incorrect load distribution on the rolling elements. In order to overcome this problem, a frictional contact with a high coefficient of friction $\mu_{a-o} = 0.1$ between the outer ring and adapter was implemented. The top edge of the adapter was translationally constrained in the global x-direction, and as a result of the frictional contact, the outer ring was prevented from rotating during the simulation. This way of constraining the outer ring effectively simulates a real-scenario of a bearing in a typical railway application, as no constraints were directly applied to it.

  It has been mentioned earlier in Section 2.3.4.3, Chapter 2, and briefly in Section 4.1, that in previous explicit FE models [118–120], either the whole outer ring [118] or its outer surface [119] was modelled as rigid so as to constrain its rotation. This causes artificial over-stiffening of the bearing structure that lead to unrealistically high instantaneous acceleration levels of approximately 4,000 g [119] and 15,000 g [120] compared to the corresponding experimental measure-

ments of 100 g and 10 g in references [119] and [120], respectively; in reference [118], the numerically predicted acceleration levels of 10^7 g were not compared with experimental results. It will be shown in Chapter 5 that the numerically modelled acceleration levels, obtained using the explicit dynamics FE model of the rolling element bearing developed in this chapter, compare favourably with experimentally measured data.

- As mentioned earlier, a frictional contact with a low coefficient of friction $\mu = 0.005$ was defined for the following contact interfaces: rolling elements–outer ring, rolling elements–inner ring, and rolling elements–cage. In addition to modelling the surface-to-surface contact at the aforementioned interfaces, the segment-based contact formulation [329] was implemented during the numerical simulation as described in Section 4.2.3.1.

- A global (mass-weighted) damping of 2% was used in the FE model of the bearing. Higher values of damping, 3% to 5%, were also tested, but these higher values affected the rotational speed ω_c of the rolling elements causing slippage; thereby, resulting in the incorrect bearing kinematics. Therefore, the results corresponding to the high values of damping are not shown here. In the current FE modelling work, the effect of damping on the bearing kinematics should not be confused with that on the vibration characteristics of the system. It is well-known that the presence of damping in a mechanical system reduces its structural resonant response in terms of both amplitude and natural frequencies [381, Chapter 10, pages 517–522]. For example, in a mass–spring–damper system having the mass driven by an external force, the damping will not only reduce the amplitude of the displacement of the mass but it will also slightly reduce the natural frequency of the system by a factor of $\sqrt{1-\zeta^2}$, where ζ is the damping ratio [381, Chapter 10, pages 517–522]; this reduced frequency is referred to as a damped natural frequency.

In contrast, when friction and damping are included in a system that involves movement between two bodies, the relative movement between the bodies will decrease if they are not continuously driven. For example, consider an imaginary FE model of a ball rolling over flat surface. Refer to Figure 4.3 which shows schematics of a ball on a flat surface — a frictionless ball–surface contact is shown in Figure 4.3a, whereas a frictional ball–surface contact is shown in Figure 4.3b. In order for the ball to roll on the flat surface, there has to be frictional contact between the curved surface of the ball and the flat surface. If there is no friction (Figure 4.3a), then the ball would simply slide along the flat surface and would not roll. If friction is included in the model (Figure 4.3b), one would expect that if the ball is not continuously forced, it would eventually stop rolling.

In the finite element model of the bearing considered here, it was mentioned in Section 4.2.2.1 that no boundary conditions were applied to the rolling elements, but frictional contact between the rolling elements and raceways was included. Furthermore, the inclusion of damping, applied globally to all the nodes withing the FE model, resists the motion of the nodes by a force F^{damp} proportional to their velocity $\dot{u}_{\text{nod}}$ as given by $F^{\text{damp}} = C_D m_{\text{nod}} \dot{u}_{\text{nod}}$ [329, Chapter 31], where C_D is the damping constant and m_{nod} is the nodal mass. The acceleration $\ddot{\mathbf{u}}_t$ at time t is then estimated as [329, Chapter 31, page 31.4]

$$\ddot{\mathbf{u}}_t = \mathbf{M}^{-1} \left(\mathbf{F}_t^{\text{ext}} - \mathbf{F}_t^{\text{int}} - \mathbf{F}_t^{\text{damp}} \right) \tag{4.4}$$

where, $\mathbf{M}$ is the mass matrix, $\mathbf{F}_t^{\text{ext}}$ is the applied external force vector, $\mathbf{F}_t^{\text{int}}$ the internal force vector, and $\mathbf{F}_t^{\text{damp}}$ is the damping force vector. Hence, it follows that the inclusion of friction and damping would lead to a reduction in the rotational speed of the rolling elements.

- The standard Earth's gravity was also applied to the model.

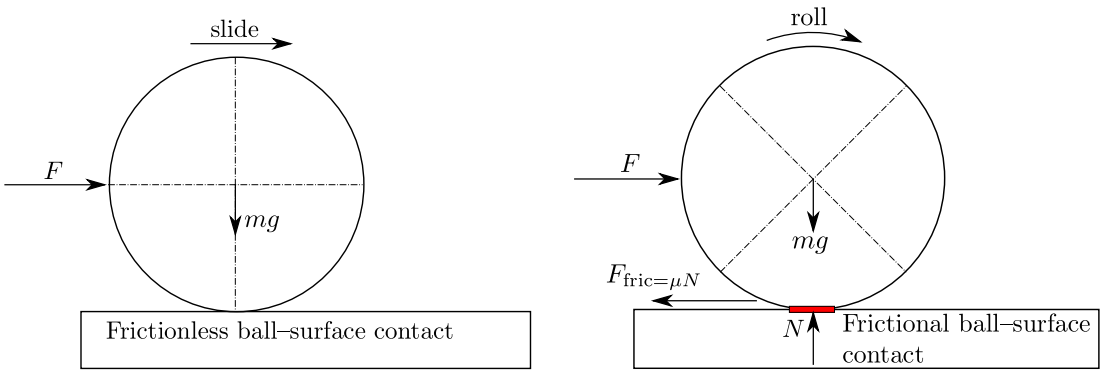

(a) Frictionless ball–surface contact causes the ball to slide.

(b) Frictional ball–surface contact causes the ball to roll.

Figure 4.3: Schematics of a ball on a flat surface.

4.2.5 Analysis and control settings

The termination time of the numerical simulations was set to 30 milli-seconds (ms). The results, in the form of binary text files, were written at an interval of 0.01 ms, which corresponds to a sampling rate of 100 kHz. Despite requesting the results at specific time intervals, LS-DYNA often writes the output file at varying intervals, which are irregularly spaced but close to the requested intervals. This is due to the varying time steps that advance the explicit dynamics numerical simulation, and is discussed below. Therefore, as part of post-processing the numerical results, the software MATLAB® was used to interpolate the results based on the minimum output time interval.

4.2.5.1 Time step

The irregular time intervals of the output results are caused by the adaptive time step method used by the numerical solver. To ensure the stability and accuracy of the solution, the size of the time step used in the explicit time integration scheme is limited by the Courant-Friedrichs-Lewy (CFL) criterion [384]. This implies that the time step is limited in such a way that a stress wave, which propagates through the entire model, cannot travel further than the smallest characteristic dimension of an element in a single step.

In the finite element software package used here, a critical time step is given as [329, Chapter 22, page 22.3]

$$\Delta t_{\text{critical}} = \left(\frac{l_{\text{fe}}}{c}\right)_{\text{min}} \tag{4.5}$$

where, l_{fe} is the characteristic dimension of an element, and c is the local material sound speed in an element.

In an LS-DYNA solution, a stable time step Δt_{stable} is always less than the critical time-step by a default factor `tsf` of 0.9 to ensure stability of the solution at all times. The stable time step is

$$\Delta t_{\text{stable}} = (\texttt{tsf}) \times \left(\frac{l_{\text{fe}}}{c}\right)_{\text{min}} = 0.9 \times \Delta t_{\text{critical}} \tag{4.6}$$

The stable time step is adaptive and automatically calculated for each solution cycle based on the smallest characteristic dimension of an element within a model. The variation of the time step during the progression of the solution has the tendency to generate noise in the numerical results; the reasons for varying time steps along with some potential causes of numerical noise in a typical LS-DYNA solution will be discussed in Section 4.5.1.

For the numerical simulations of a rolling element bearing presented in this thesis, numerical noise was also generated due to the contact interaction of the *polygonised* rolling elements and raceways. This will be discussed in more details in Section 4.5 along with the analytical estimation of the numerical noise frequencies.

One aspect of the accuracy of an FE analysis is associated with the distortion of the elements within an FE model; other aspects generally include achieving a favourable agreement between the numerical and analytical solutions. The accuracy of the FE analysis undertaken here has been verified by checking the distortion of the elements as well as by comparing the numerical results with corresponding analytical and experimental results. In the FE software package used here, erroneous or severe distortion

of the elements leading to poor element aspect ratio is referred to as *hourglassing* or zero-energy modes [329, Chapters 3, 7, pages 3.4–3.16, 7.6–7.9]. It is generally recommended that the hourglass energy of an element should be less than 10% of its internal energy. For the current explicit simulation of the rolling element bearing, the hourglass energy was found to be less than 0.2% of the internal energy, indicating negligible distortions of the elements. One of the reasons for having such a low hourglass energy is the uniform discretisation of the bearing model into finite elements using mostly the quadrilateral elements, and a sufficiently high mesh density that can accommodate the applied loads. The comparison of the FE simulations results with those of the analytical and experimental results will be presented in Chapters 5 and 6.

4.3 Modal analysis

Prior to performing the explicit analysis of the rolling element bearing, a modal analysis of the outer ring of the bearing was undertaken. As mentioned earlier, the purpose of numerically modelling the structural modal response of the outer ring is to verify the adequacy of the mesh size used to discretise the bearing model into finite elements. The reason for only selecting the outer ring and not the whole bearing has been discussed earlier in Section 4.2.2.2.

The implicit solving capability of the FE software package, LS-DYNA, was used to solve for the natural frequencies and mode shapes of the outer ring of the rolling element bearing model. The outer ring was modelled as a 10 mm thick cylindrical shell. 2-D shell elements were used to discretise the model with a mesh element size of 0.5 mm; the element type and size are same for modal and explicit dynamic analyses, so as to ensure consistency across both analyses.

From the description of the boundary conditions, mentioned in Section 4.2.4, applied to the FE model of the rolling element bearing shown in Figure 4.2, the outer ring can neither be considered as fully fixed nor it can be considered as free. As mentioned

earlier in Section 4.2.4, a frictional contact with a high coefficient of friction $\mu_{a-o} = 0.1$ between the outer ring and adapter was implemented, and due to constraining the top edge of the adapter in the global catersian x-direction, the outer ring was prevented from rotating during the simulation. An approximate consideration would be to treat the edges of the outer ring as simply-supported. Nevertheless, two different boundary conditions were tested for the model verification — free and simply-supported ends.

Figures 4.4a and 4.4b show the numerically obtained modal (natural) frequencies of the outer ring for the aforementioned boundary conditions along with the corresponding analytical estimations. The analytical solution was taken from reference [385]; a simple formula used to estimate the resonance frequencies of the outer ring is given as (see references [383, 386, 387] for a comprehensive analysis of various theories on the circular cylindrical shells)

$$\omega_{mn}^2 = \frac{B}{\rho h}\left[k_{zm}^2 + \left(\frac{n}{R_o}\right)^2\right] + \frac{k\left(1-\nu^2\right)}{\rho h R_o^2}\left[\frac{k_{zm}^2}{k_{zm}^2 + \left(\frac{n}{R_o}\right)^2}\right]^2 \tag{4.7}$$

where, the parameter B (bending stiffness) is given as $B = \dfrac{Eh_o^3}{12(1-\nu^2)}$, $k = \dfrac{Eh_o}{1-\nu^2}$, E is the modulus of elasticity, ρ is the density of the material, ν is the Poisson's ratio, h_o is the thickness of the outer ring, R_o is the radius of the outer ring, L is the length of the outer ring, and m, n are the axial and circumferential mode numbers, respectively. For different boundary conditions, the modal wavenumber k_{zm} takes different forms as

$$k_{zm} = \begin{cases} \dfrac{m\pi}{L} & \text{for simply-supported ends} \\ \dfrac{\left(m-\frac{1}{2}\right)\pi}{L} & \text{for free ends} \end{cases} \tag{4.8}$$

For no boundary conditions at the edges of the outer ring simulating free ends, the numerical and analytical estimates of the first natural frequency of the outer ring are 528 Hz and 514 Hz, respectively. In contrast, for simply supported ends, the numerical

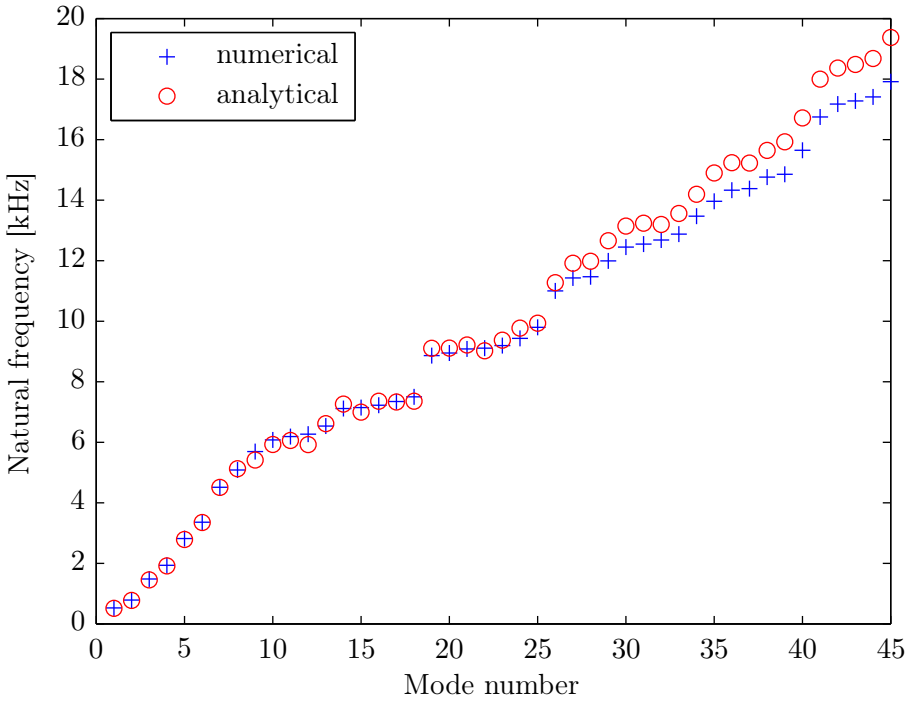

(a) No boundary condition at the edges of the outer ring.

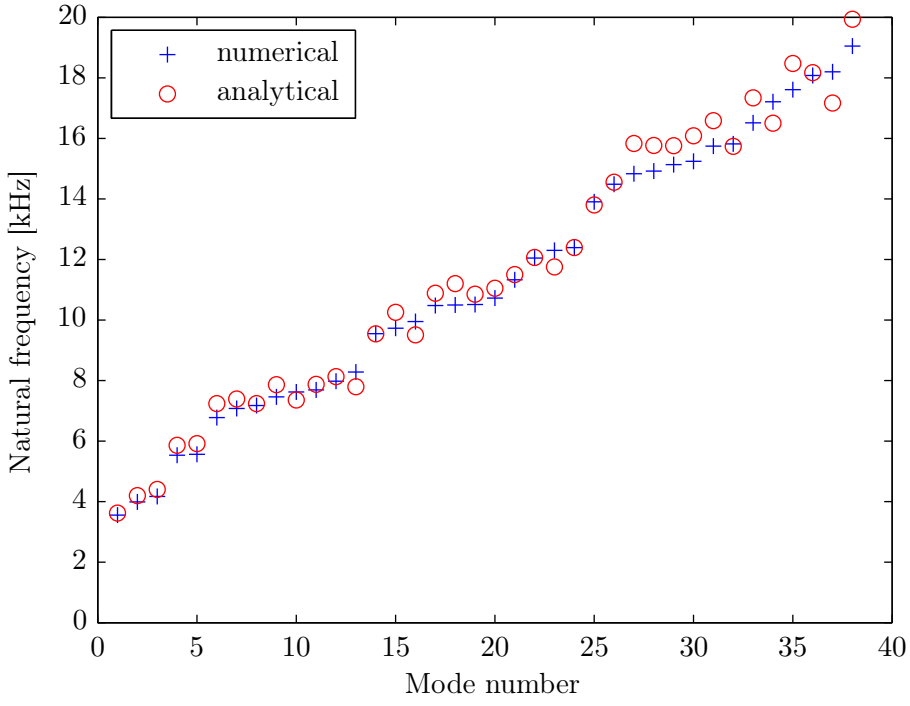

(b) Edges of the outer ring were simply supported.

Figure 4.4: Comparison of the numerically and analytically estimated natural frequencies of the outer ring of the FE model of the rolling element bearing for two different boundary conditions.

and analytical estimates of the first natural frequency of the outer ring are 3554 Hz and 3621 Hz, respectively. As can be seen from the Figures 4.4a and 4.4b, a reasonable agreement between the analytical and numerical results was achieved. In both cases, the maximum error in the numerical estimates of the natural frequencies is within 8% of the corresponding analytical results. The favourable agreement of the results from the modal analysis obtained using LS-DYNA and the analytical predictions indicates that the discretisation of the model is adequate.

Experimental work to measure the natural frequencies of the outer ring was not undertaken during the course of the current study. This is because: 1) the numerically predicted natural frequencies obtained using LS-DYNA agree favourably with the well-developed analytical models [383, 386, 387], and 2) the modal analysis of the outer ring was only undertaken to verify the adequacy of the mesh element size used to discretise the model of the bearing into finite elements. The principal aim of this thesis is to present an analysis of the dynamic rolling element-to-raceway contact forces as the rolling elements traverse through a localised raceway defect, and correlation of these forces with the vibration response of the bearing. As the numerically predicted vibration response will be validated using experimental results in the next chapter, the experimental verification of the analytical and numerical natural frequencies of the outer ring was deemed unnecessary, and would not have contributed towards the main aims of this thesis.

In the remainder of this chapter, the results from the explicit dynamics FE modelling of the defective rolling element bearing are presented.

4.4 Numerical acceleration time-trace

A common technique used in vibration-based condition monitoring of rolling element bearings is the measurement of acceleration levels, and subsequent implementation of the envelope analysis technique [30, 251, 252] to detect the defect-related bearing frequencies. Similarly, in this section, the nodal acceleration results obtained from the numerical modelling are presented. In addition to the acceleration, nodal velocity and displacement results were also obtained; these results along with standard signal processing analyses will be presented in Section 4.6, following the discussion of the numerical noise in Section 4.5.

The current simulations were conducted using a high-performance super computer, Tizard [388], using eight parallel processors — 4 AMD Operton$^{\text{TM}}$ 6238, 12-core, 2.6 GHz CPUs; it took approximately 250 CPU hours to solve the FE model of the rolling element bearing.

4.4.1 Time domain analyses

Figure 4.5 shows the (unfiltered) time-trace of the numerically obtained acceleration a_y (in the global cartesian y-direction) for a node located on the outer surface of the outer ring. The three consecutive defect-related impulses, evident in the plot, are separated by approximately 0.011 seconds, which corresponds to the outer raceway defect frequency, commonly referred to as a ball pass frequency outer raceway (BPFO), f_{bpo}, of 90.91 Hz. The analytical estimation of the nominal BPFO, f_{bpo}, is given by [3, Chapter 25, page 994]

$$f_{\text{bpo}} = \frac{f_s \times N_r}{2}\left(1 - \frac{D_r}{D_p}\cos\alpha\right) \tag{4.9}$$

where, f_s is the bearing run speed (that is, the rotational speed of shaft or inner ring), N_r is the number of rolling elements, D_r is the rolling element diameter, D_p is the bearing pitch diameter, and α is the contact angle. For the bearing modelled here, the

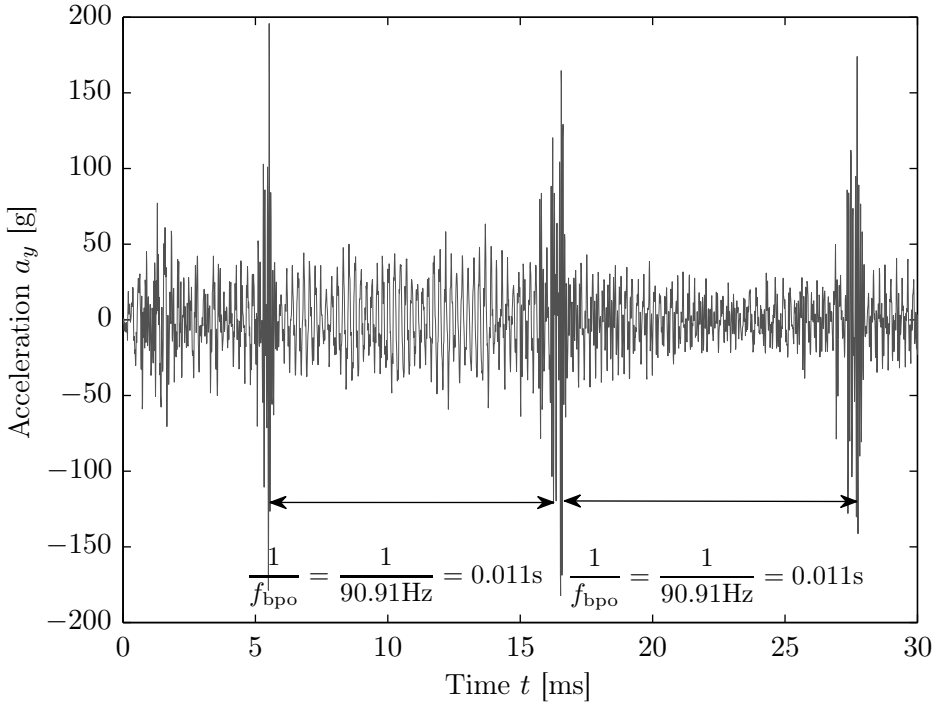

Figure 4.5: Numerically modelled, unfiltered, acceleration a_y time-trace for a node located on the outer surface of the outer ring of the FE model of the rolling element bearing for a radial load W of 50 kN and a rotational speed n_s of 500 RPM.

analytical estimate of the BPFO, calculated using Equation (4.9), is 90.07 Hz, which is 0.9% different from the results of the numerical simulation. The slight difference between the numerical and analytical estimates is because the analytical formula, shown in Equation (4.9), does not account for the slippage of the rolling elements [95, 96], which was accounted in the explicit FE analysis of the bearing undertaken here.

In contrast to previous FE models of rolling element bearings, where unrealistically high instantaneous acceleration levels of 10^7 g [118], 4,000 g [119], and 15,000 g [120] were shown, the model developed here produces realistic acceleration levels of approximately 180 g; the numerical results will be compared with the experimental measurements in the next chapter, and it will be shown that the numerical acceleration levels in Figure 4.5 compare favourably with the corresponding measured data. One of the reasons for this improvement compared to the previous models is the bearing components were modelled as flexible parts so as to correctly represent their stiffness. Other reasons, which could not be compared with previous models due to lack of de-

tails provided in the literature, include optimal discretisation of the model to ensure continuous rolling element-to-raceway contact, correct implementation of the surface-to-surface contact at the interfaces, and the use of a value for the coefficient of friction that is comparable to the recommended practical value in rolling element bearings [3, Chapter 12].

Close agreement between the numerical and analytical values of the outer raceway defect frequency shows that the finite element model has satisfactorily simulated the basic bearing kinematics. However, the acceleration time-trace has a substantial amount of numerical noise, which is explained in the following section.

4.5 Numerical contact noise — an artefact of the model

It can be observed in Figure 4.5 that while the instantaneous peak impulsive acceleration levels for the three visible defect-related impacts range from 0 to approximately $\pm 180\,\mathrm{g}$, the non-impulsive acceleration levels between the impacts are of the order of $\pm 50\,\mathrm{g}$. In order to seek the frequencies associated with the numerical noise, power spectrum of the numerical acceleration signal, shown in Figure 4.5, was calculated using Welch's method [389] with 50% overlap. Although the signal was sampled at 100 kHz, the simulation was run for 30 ms, resulting in only 3010 samples after the interpolation based on the minimum output time interval; it has been mentioned earlier in Section 4.2.5 that the FE simulation results are often output at irregular time intervals due to the adaptive time-stepping. Therefore, the acceleration signal was zero-padded with 2^{15} FFT points in order to interpolate the power spectral estimate for a frequency resolution of 3 Hz. The narrow band power spectral density of the numerically modelled acceleration a_y signal is shown in Figure 4.6. A fundamental tone at 4671 Hz, as indicated in the figure, corresponds to the numerical noise. There is also an indication of the 5^{th} harmonic at approximately 23 kHz in the figure that is associated with the fundamental tone.

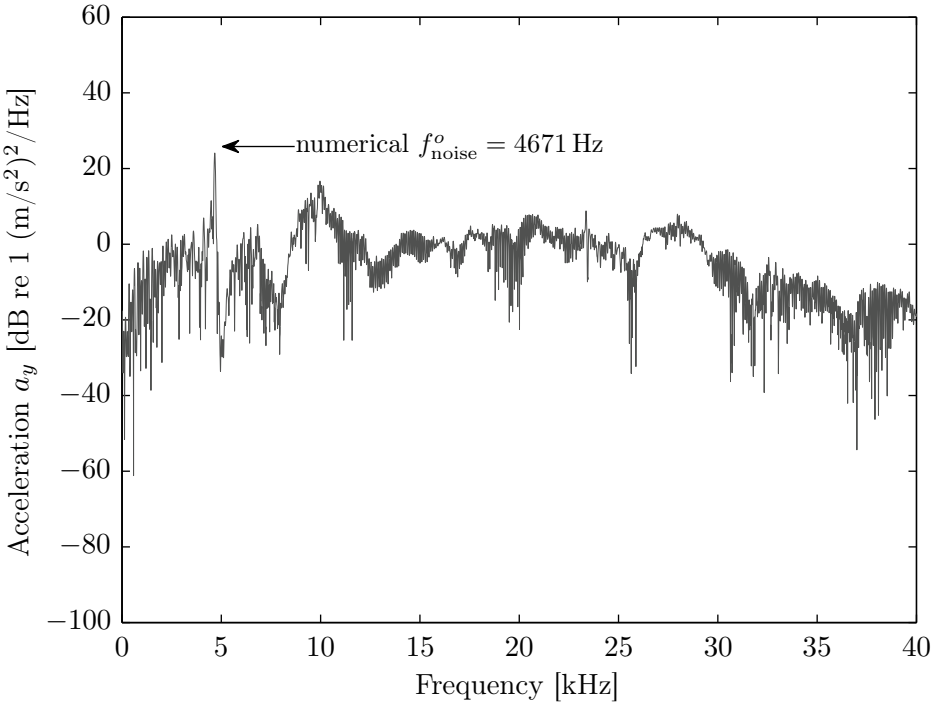

Figure 4.6: Power spectral density of the nodal acceleration a_y time-trace shown in Figure 4.5, highlighting one of the dominant numerical noise frequencies, $f^o_{\text{noise}} = 4671\,\text{Hz}$ observed in the FE simulation results.

In addition to the dominant numerical noise at 4671 Hz, another frequency component that was intermittently observed in the numerical acceleration a_y time-trace was 4545 Hz; however, it is not apparent in the power spectrum shown in Figure 4.6. In order to show the presence of the numerical noise at 4545 Hz within the acceleration a_y time-trace, it was zoomed between the defect-related impulses, which are separated by 0.011 s as indicated in Figure 4.5. These partial time-traces are shown in Figures 4.7a and 4.7b. For clarity, the scale of the y-axis in both figures ranges from ± 100 g, which is half of that in Figure 4.5. The time separation between the consecutive peaks as indicated by three pairs of the circular- and square-shaped data cursors corresponds to 4545 Hz. Despite the presence of the numerical noise at the frequency component of 4545 Hz, it is not apparent in the power spectrum shown in Figure 4.6 in contrast to the dominant noise component of 4671 Hz. A few potential reasons for not having a tonal component at 4545 Hz will be discussed later in Section 4.5.3, which describes the analytical estimation of this frequency component.

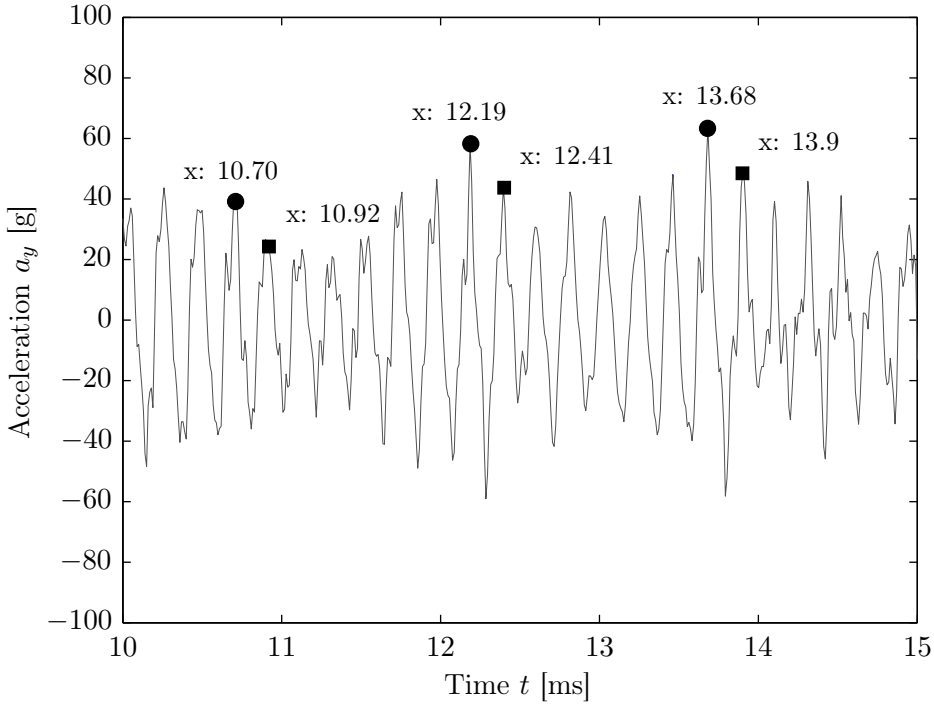

(a) Time-trace zoomed between the first and second defect-related impulses.

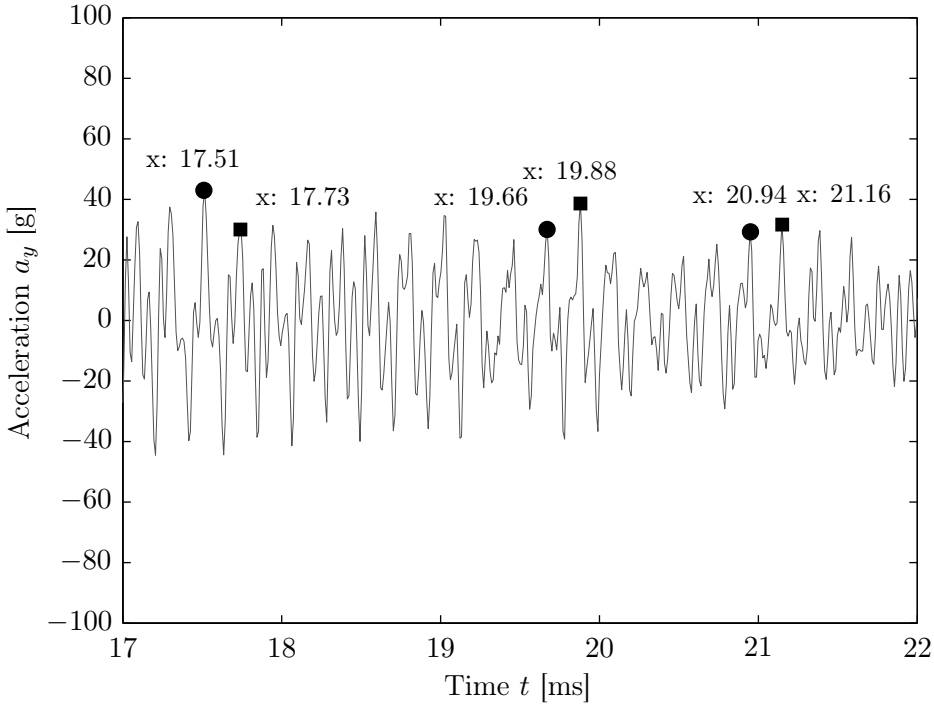

(b) Time-trace zoomed between the second and third defect-related impulses.

Figure 4.7: Partial time-traces of the numerically modelled, unfiltered, acceleration a_y signal shown in Figure 4.5 zoomed between the defect-related impulses. The time separation between the consecutive circular- and square-shaped data cursor pairs corresponds to the numerical noise frequency component of 4545 Hz.

Although the fundamental BPFO and its harmonics are not clearly visible in the power spectrum shown in Figure 4.6, it will be shown in Section 4.6.3 that after conducting an envelope analysis they are presented in Figure 4.29. The natural frequencies of the bearing are also not visible in Figure 4.6. This is potentially because the structure could be more easily excited at some frequencies than others.

A development and justification of a novel hypothesis for explaining the cause of the numerical noise frequencies are described in Section 4.5.2, following a short discussion on the numerical noise.

4.5.1 A short note on general numerical noise

Results from FE simulations calculated using LS-DYNA can contain a significant amount of numerical noise [335, page 1110]. Although not clearly mentioned in the software user and theory manuals [329, 335], it is understood that the majority of noise, often referred to as *spurious oscillations* in the context of explicit FE methods, is generated due to adaptive time-stepping [390]. LS-DYNA uses the second-order central difference method [293, 329], which is a widely used time integration scheme in several explicit FE solvers including Abaqus/Explicit [308] and NASTRAN Explicit [311].

In contrast to implicit methods [287–294], which are *unconditionally stable*, the explicit methods [292, 295–305] are *conditionally stable*; that is, for a single solution cycle only [299, 302, 305]. The stability of an explicit solution depends on the time step as described in Section 4.2.5.1. In the case of LS-DYNA, the stable time step Δt_{stable}, 90% of the critical $\Delta t_{\text{critical}}$, is automatically estimated based on the minimum characteristic dimension of an element within an FE model (see Equations (4.5) and (4.6)). If a linear FE mesh is generated so that the time step is constant for each cycle, results obtained by the central difference scheme [292, 295–305] would be close to exact solutions [305]. However, in practice, it is not feasible to generate a mesh, so as to achieve a constant time step, not only because of the size of a model but

also because of the types of various analyses. As an example, one would require finely meshed areas in the vicinity of contacting bodies compared to non-contacting regions in order to accurately simulate a Hertzian contact problem [177, Chapter 4]. Furthermore, depending on various types of analyses, such as impact, vehicle crash, blast, and metal forming, the elements within a model can undergo severe deformation (elastic or plastic) or distortion or erode during a simulation. The variation in the size of elements during an explicit LS-DYNA solution causes a variation in the size of the time steps so as to ensure the stability of the solution. In other words, as an element size varies, so does the time step. It is the irregularly (time) spaced progression of the solution to determine the state variables, acceleration, velocity, and displacement, that generates spurious oscillations or numerical noise in the results. These spurious oscillations should not be confused with the defect-related impulses, which are separated by 0.011 s, as shown in Figure 4.5.

For the current numerical simulation, Figure 4.8 shows the variation in the step size. It is evident that the step size varies for almost each solution cycle. The maximum variation from approximately 28.87 ns (nano-seconds) to 28.74 ns can be observed at about 5 ms, 16 ms, and 28 ms. These timings can be correlated with those of the timings related to the occurrences of the defect-related impulses, observed in Figure 4.5. It will be discussed during the analysis of the numerically predicted rolling element-to-raceway contact forces in Chapter 6 that the rolling elements strike the outer and inner raceways near the end of the defect. As a result, the size of the elements, involved in the impacts reduces due to the elastic deformation of the elements for a duration equivalent to the duration of an impact, consequently leading to the reduction in the time step at the aforementioned timings in order to maintain the stability of the solution.

In addition to the comparatively higher variations in the step size at 5 ms, 16 ms, and 28 ms, smaller variations in the step size are evident for almost each solution cycle in Figure 4.8. This is because as the rolling elements roll during the simulation, the level of compression or load on them varies with their position; refer to the analytically

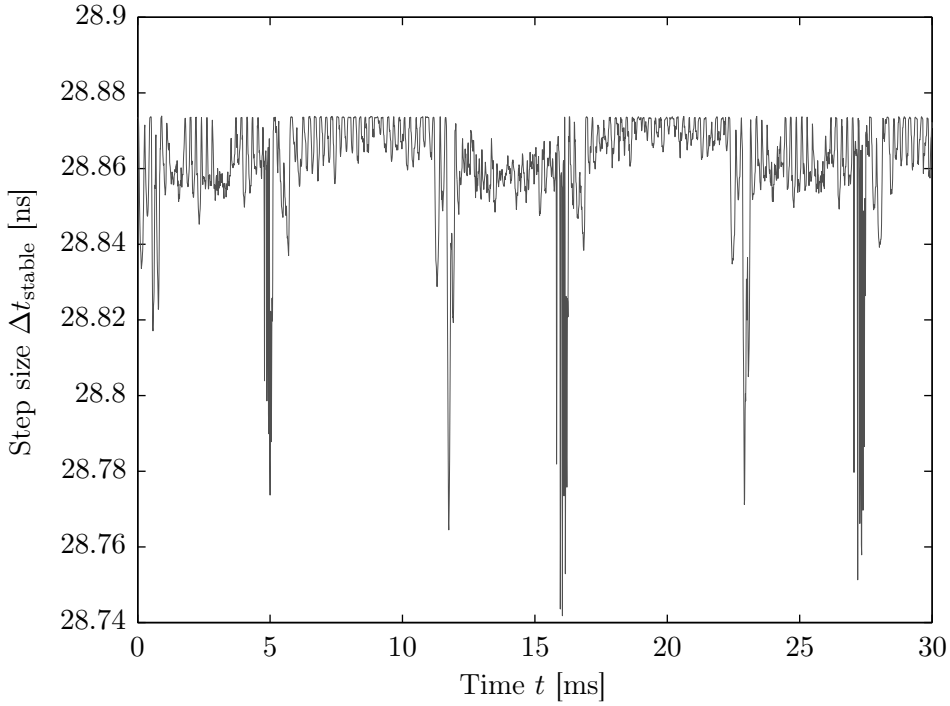

Figure 4.8: Variation in the time step Δt_{stable} as the numerical solution advances.

estimated load profiles in Figure 3.4, Chapter 3. As a result, the size of finite elements located at the edge of the rolling elements and the raceways varies, leading to the variation in the time steps.

As mentioned earlier in Section 4.2.5.1, the accuracy of the finite element analysis was verified by checking the hourglass energy of the elements, which is recommended to be less than 10% of the elemental internal energy [329, Chapters 3, 7, pages 3.4–3.16, 7.6–7.9]. Although the hourglass energy was found to be less than 0.2% of the internal energy, which indicates negligible elemental distortions, the elemental deformations were enough to cause the slight variations in the time step.

In the explicit FE model of a rolling element bearing developed here, the numerical noise is also generated due to the interaction (contact) of the rolling elements and raceways in addition to the inherent numerical noise described in the preceding paragraphs. In order to explain the cause of numerical rolling contact noise along with the estimation of the noise frequencies, a detailed hypothesis is presented below.

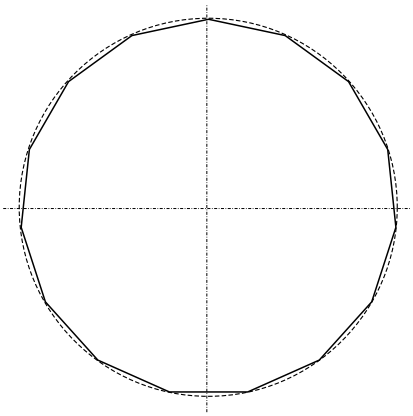

Figure 4.9: A 2-D schematic of a polygonised rolling element having 15 edges or points (not to scale).

4.5.2 Hypothesis for explaining the cause of numerical contact noise

The hypothesis presented in this section is a novel and original contribution of this thesis.

Because the circular rolling elements were discretised into a number of finite elements, the edges of the rolling elements were transformed from circular to multi-point polygons. Figure 4.9 shows a schematic of a polygonised rolling element. It does not represent the actual size of a rolling element, which is included in the FE model of the rolling element bearing. In the schematic, only a few points, 15, were used to create the polygon for clarity; however, in the FE model, the rolling elements were discretised using the element size of 0.5 mm, which generates a polygon with 113 edges $\left(= \dfrac{\pi D_r}{0.5}\right)$, where $D_r = 18\,\text{mm}$.

As they roll during the simulation, the *polygonised* rolling elements create small impacts as their points contact the outer and inner raceways. In this case, the frequencies of these impacts would be a function of the element size l_{fe} used to mesh the rolling elements and the rotational velocity of the rolling elements $\omega_c = 2\pi f_c$.

In order to estimate the numerical rolling noise frequency components, a basic

equation of motion can be used as follows

$$f_{\text{noise}} = \frac{1}{T_{\text{noise}}} = \frac{2\pi f_c \times D_{\text{race}}}{2l_{\text{fe}}} \tag{4.10}$$

where, l_{fe} is the distance between two nodes on the (polygonised) edge of the rolling elements within the FE model of the bearing (mesh element size, 0.5 mm), ω_c is the angular velocity with which the rolling elements roll during the simulation (refer to Equation (3.21), Section 3.6.1, Chapter 3), and D_{race} can either be the diameter of the outer raceway ($D_o = 200$ mm) or inner raceway ($D_i = 163.96$ mm) which contact the rolling elements. Solving Equation (4.10) for the values of D_{race} as 200 mm and 163.96 mm, the rolling contact noise frequencies equal 4712 Hz and 3864 Hz, respectively. From now onwards, these frequencies will be referred to as the '*rolling element-to-outer raceway*' f^o_{noise}, and '*rolling element-to-inner raceway*' f^i_{noise} rolling contact noise frequencies, respectively.

The analytically estimated rolling element-to-outer raceway rolling contact noise frequency f^o_{noise}, 4712 Hz, differs from one of the noisy frequency components, 4671 Hz, observed in the numerical acceleration signal (Figure 4.6) by 0.8% only. This indicates that the presence of the numerical noise at 4671 Hz is highly likely due to the interaction of the rolling elements with the outer raceway. The slight difference between the analytical and numerical noise frequency estimates is a result of the rolling elements not following a pure rolling movement during the simulation, indicating a small amount of slip. It was mentioned earlier that no boundary conditions were applied to the rolling elements, and they were driven by their interaction with the rotating inner and stationary outer raceways.

Another reason for the difference between the analytical and numerical estimations of the rolling element-to-outer raceway rolling contact noise frequency f^o_{noise} is associated with the interaction between the rolling elements and corresponding cage slots. It was found that at certain instances, the rolling elements were driven (pushed) by

the cage slots that consequently results in slipping of rolling elements. The interaction between the rolling elements and cage will be briefly discussed in Chapter 6. However, it is not within the scope of this thesis to investigate the rolling elements-to-cage interaction.

The FE model of the rolling element bearing was also solved for two additional rotational speeds n_s of 300 RPM and 800 RPM. These results will be presented in the next chapter during their comparison with the experimental results for validation purposes and investigation of the parametric effect of varying radial load W and rotational speed n_s on the vibration response of the bearing. For the rotational speeds of 300 RPM and 800 RPM, the numerical rolling element-to-outer raceway rolling contact noise frequencies f^o_{noise} due to the polygonised rolling elements were found to be 2811 Hz and 7487 Hz, respectively. These numerical noise frequencies f^o_{noise} compare favourably with the corresponding analytical noise frequencies f^o_{noise} of 2830 Hz and 7548 Hz, respectively, estimated using Equation (4.10). Similar to the aforementioned difference of 0.8% between the numerical and analytical rolling element-to-outer raceway rolling contact noise frequencies f^o_{noise} for the rotational speed n_s of 500 RPM, the numerical and analytical noise frequencies f^o_{noise} due to the polygonised effect also differ by 0.8% for the cases when the bearing was rotated at 300 RPM and 800 RPM. This favourable comparison, therefore, indicates the validation of the proposed hypothesis for determining the cause of the numerical noise that it is generated due to the interaction of the polygonised rolling elements with the outer raceway of the bearing.

4.5.3 Beating phenomenon

There is a difference of approximately 17% between the other intermittent numerical noise frequency, 4545 Hz, and the analytically estimated rolling element-to-inner raceway rolling contact noise frequency f^i_{noise}, 3864 Hz. As the difference is significant, the analytical and numerical noise frequencies cannot be related. Therefore, the concept

of beating [381, Chapter 1, page 45] was applied to explain the occasional presence of the 4545 Hz noise frequency component found in the numerical acceleration results.

As mentioned earlier, the *polygonised* edges of the rolling elements create small impacts with outer and inner raceways as they roll during the simulation. The interaction of the rolling elements with the raceways would result in the generation of two sinusoidal waves with a slight difference between their carrier frequencies. The amplitude of the sinusoidal waves would also slightly differ from each other. For the purpose of validating the aforementioned hypothesis, and demonstrating the beating effect, the sum of two interfering sinusoidal waves is as follows

$$A(t) = A_1 \cos(2\pi f^o_{\text{noise}} t) + A_2 \cos(2\pi f^i_{\text{noise}} t + \phi) \tag{4.11}$$

where, the amplitudes, $A_1 = A_2 = 1$, t is the time vector, ϕ is the phase, and f^o_{noise} and f^i_{noise} are the analytically estimated noise frequencies using Equation (4.10).

Figure 4.10a shows the resultant sinusoidal wave, and the same wave along with its envelope, zoomed from 10 ms to 15 ms for clarity, is shown in Figure 4.10b. The time separation of the two consecutive peaks, whose data cursors are shown in Figure 4.10b, corresponds to 4545 Hz. This frequency exactly matches the other noise frequency component occasionally observed in the numerically modelled acceleration results. From now onwards, this frequency will be referred to as the *beating noise frequency*, and represented as f^{i-o}_{noise}.

The beating effect can also be clearly observed in Figure 4.5 between the first two defect-related impulses from approximately 5 ms to 16 ms, but not as clearly between the second and third impulse from approximately 17 ms to 28 ms. One potential reason for not having a clear beating effect is the slippage of the rolling elements which eventually results in no tonal component at the beating noise frequency f^{i-o}_{noise}, in contrast to the strong fundamental tone at the rolling element-to-outer raceway noise frequency f^o_{noise}, as shown in the power spectrum of the acceleration signal in Figure 4.6. Another

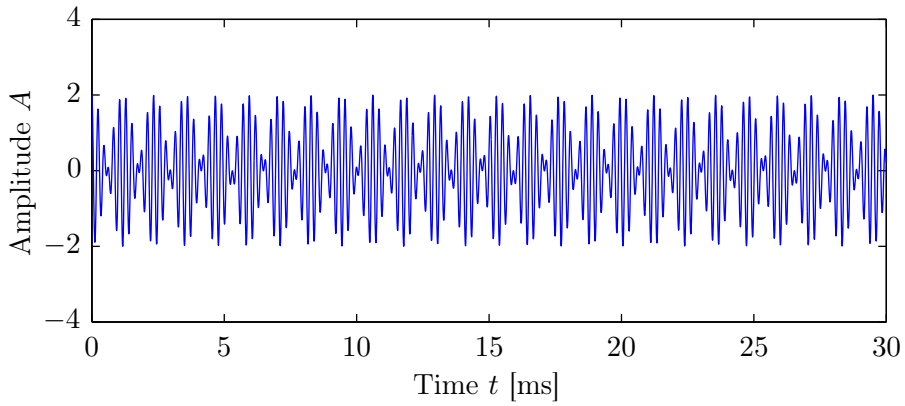

(a) The resultant sinusoidal wave.

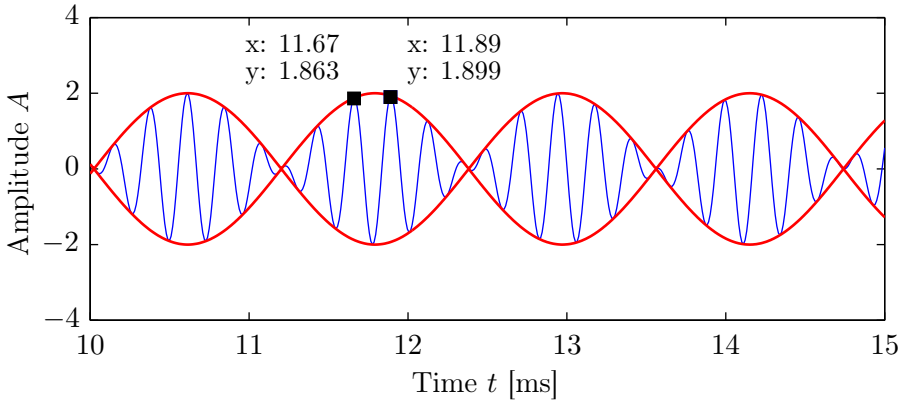

(b) The sinusoidal wave in Figure 4.10a along with its envelope zoomed for clarity.

Figure 4.10: Demonstration of the beating effect due to the interference of two sinusoidal waves at the two analytically estimated rolling contact noise frequencies $f^{o}_{\text{noise}} = 4712\,\text{Hz}$ and $f^{i}_{\text{noise}} = 3864\,\text{Hz}$.

reason for there being no tonal component at 4545 Hz could be because the acceleration signal was extracted at a node located on the outer ring of the bearing. In other words, the nodal results on the outer ring are significantly influenced by the interaction of the rolling elements and outer raceway, but comparatively less by the rolling elements-to-inner raceway contact interaction.

For the rotational speeds n_s of 300 RPM and 800 RPM, the numerically obtained beating noise frequencies f^{i-o}_{noise} were 2632 Hz and 7143 Hz, respectively. Following the methodology as described above, the beating noise frequencies f^{i-o}_{noise} were analytically estimated, which equal 2632 Hz and 7143 Hz for the rotational speeds n_s of 300 RPM and 800 RPM, respectively. The exact match between the numerical and analytical

results, therefore, indicates the validation of the proposed hypothesis.

4.5.4 Filtering the rolling contact noise frequencies

Based on the power spectral density of the numerical acceleration signal in Figure 4.6, a notch filter was designed to eliminate the tonal noise at 4671 Hz. The transfer function, in the z-transform, of a second-order notch filter can be estimated as [391, Chapter 5, page 339]

$$H(z) = \frac{1 - 2\cos\Omega_o z^{-1} + z^{-2}}{1 - 2r\cos\Omega_o z^{-1} + r^2 z^{-2}} \tag{4.12}$$

where, Ω_o is the notch frequency at which the content has to be eliminated from a signal and r is the pole radius, which is related to the band width $\Delta\Omega$ as [391, Chapter 5, page 337]

$$r \approx 1 - \frac{\Delta\Omega}{2} \tag{4.13}$$

The quality factor Q of the filter is given as [381, Chapter 7, page 298]

$$Q = \frac{\Omega_o}{\Delta\Omega} \tag{4.14}$$

For $\Omega_o = 4671\,\text{Hz}$, a second-order infinite impulse response notch filter was implemented with a quality factor Q of 15, resulting in the band width $\Delta\Omega$ of 311 Hz. Figure 4.11 shows the frequency response, both magnitude and phase, of the filter, whereas its equivalent pole-zero plot is shown in Figure 4.12.

The notch filtered numerical acceleration signal is shown in Figure 4.13. For comparison, the unfiltered acceleration results from Figure 4.5 are also plotted along with the notch filtered results using a gray-coloured, dashed line. The performance of the filter is evident in Figure 4.13; the instantaneous levels of the non-impulsive acceleration signals, which prior to the application of the notch filter ranged between approximately $\pm 50\,\text{g}$, were reduced to approximately $\pm 20\,\text{g}$ after filtering the dominant rolling element-to-outer raceway rolling contact noise frequency f^o_{noise}. However, there is still

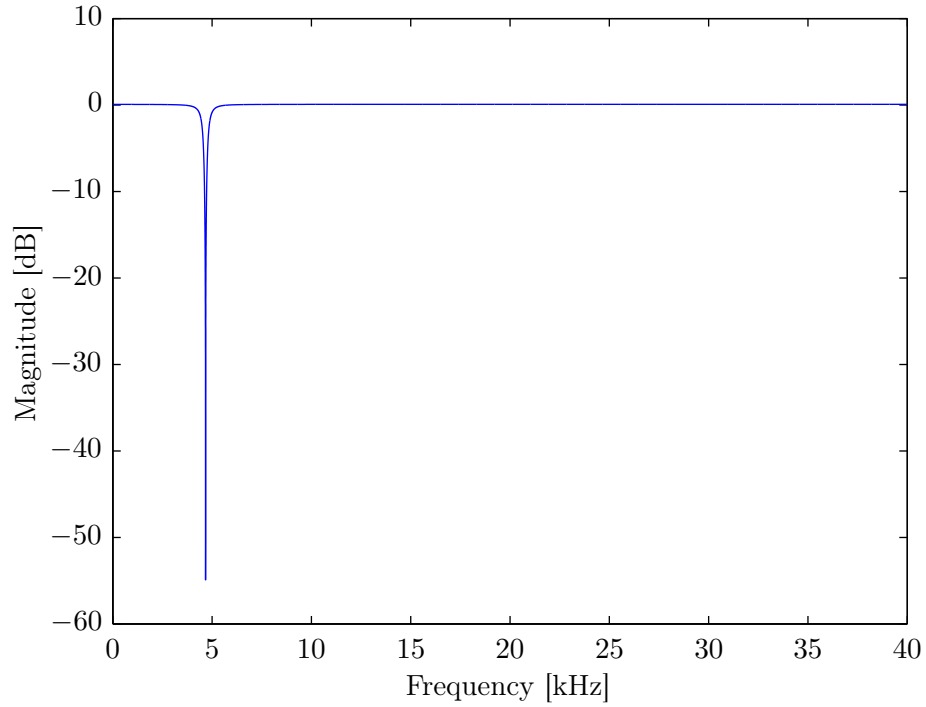

(a) Magnitude response of the filter.

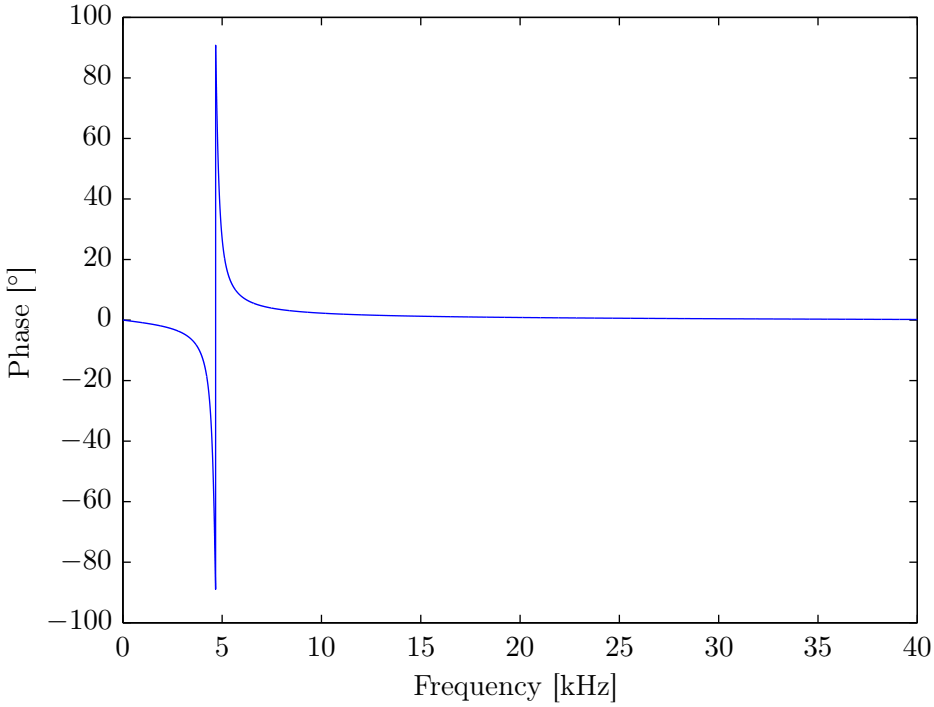

(b) Phase response of the filter.

Figure 4.11: Frequency response of the second-order notch filter designed to eliminate the rolling element-to-outer raceway rolling contact noise at $f^o_{\text{noise}} = 4671\,\text{Hz}$ from the numerical simulation results.

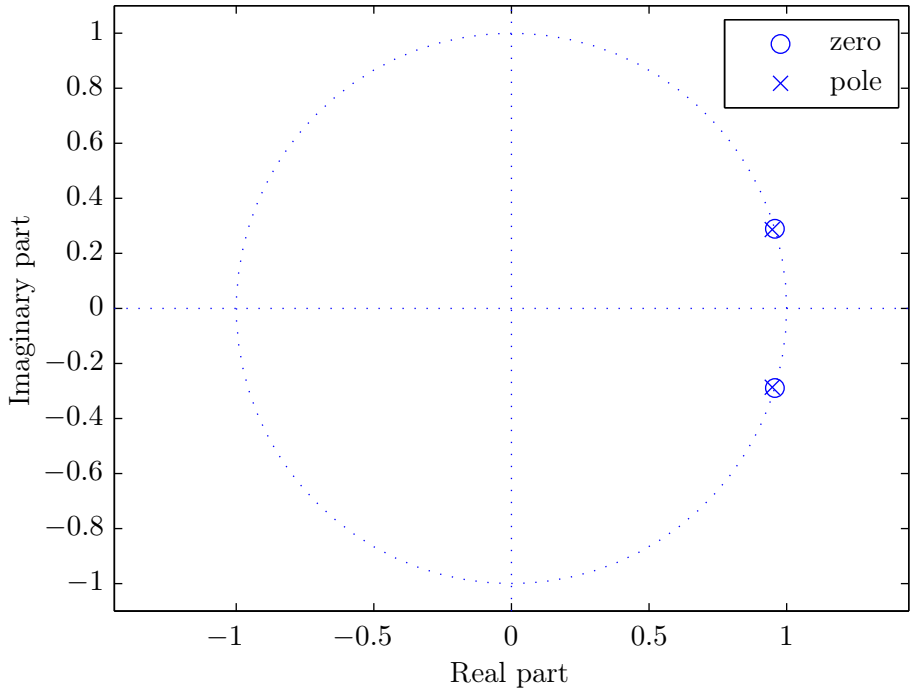

Figure 4.12: Pole-zero plot of the second-order notch filter shown in Figure 4.11.

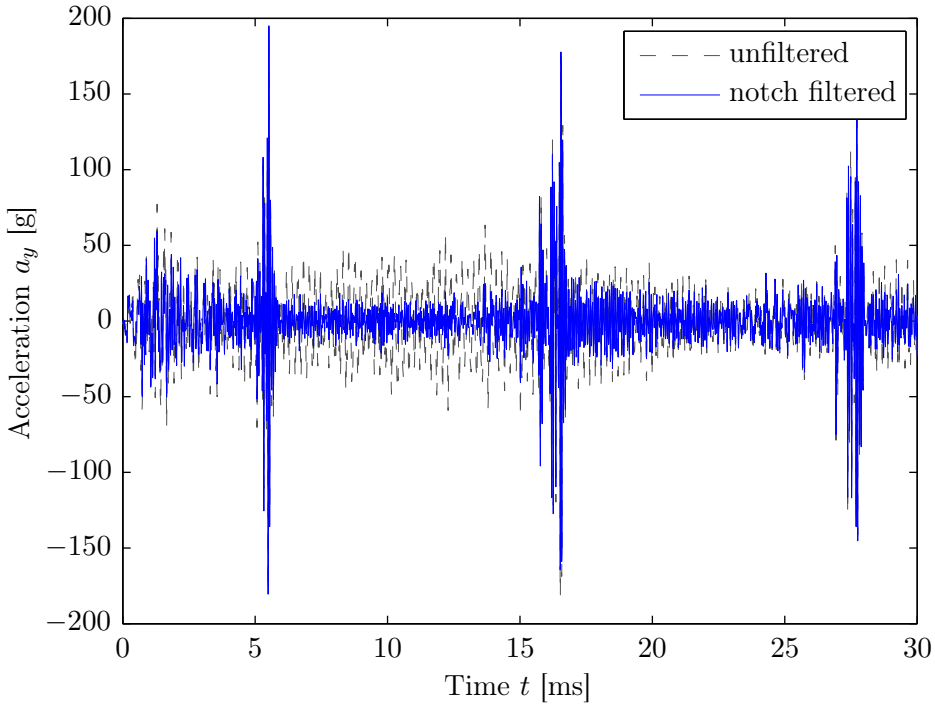

Figure 4.13: Effect of filtering out the rolling element-to-outer raceway rolling contact noise at $f^o_{\text{noise}} = 4671\,\text{Hz}$ on the numerically modelled acceleration a_y time-trace shown in Figure 4.5 for a radial load W of 50 kN and rotational speed n_s of 500 RPM.

some residual noise. As mentioned earlier, it is likely that the remaining noise is due to the sliding (slippage) of the rolling elements as a result of their interaction with the cage slots in addition to the inherent adaptive time-stepping variations as discussed in Section 4.5.1 (also refer to Figure 4.8). These noise frequencies are stochastic, and therefore, could not be estimated and filtered without affecting the signals related to the vibration response.

The power spectrum of the unfiltered (Figure 4.6) and notch filtered acceleration a_y time-traces are compared in Figure 4.14. In order to clearly see the difference between the two power spectra, the results in Figure 4.14a are zoomed from 4–6 kHz, and the corresponding plots are shown in Figure 4.14b. It can be seen that the tone at the numerical rolling element-to-outer raceway rolling contact noise frequency f^o_{noise} has been attenuated by approximately 25 dB without affecting the majority of the response. However, the power spectrum at the frequencies within the filter bandwidth is affected slightly. In contrast to the primarily attenuated sharp fundamental noise tone at $f^o_{\text{noise}} = 4671\,\text{Hz}$, slight attenuation (by 4 dB) of the comparatively weak tone at the beating noise frequency $f^{i-o}_{\text{noise}} = 4545\,\text{Hz}$ can also be seen as indicated in Figure 4.14b.

On the one hand, as bearing vibration signals are generally demodulated in high-frequency range [30], of the order of 15 kHz, the aforementioned rolling contact noise frequencies will not influence the bearing diagnosis; it will be shown later in this chapter that the demodulated power spectra of numerical vibration signals estimated using envelope analysis [30, 251, 252] are not affected by the numerical noise. On the other hand, one might question the need to filter the rolling contact noise frequencies. It will be shown later in this chapter that the elimination of the tonal noise, as discussed above, will help in enhancing the vibration signals associated with the de-stressing of the rolling elements when they enter into a raceway defect.

In summary, it can be concluded that the introduction of noise in the simulation results is an artefact of the numerical modelling. A favourable agreement between the numerical and analytical rolling contact noise frequencies justifies the proposed

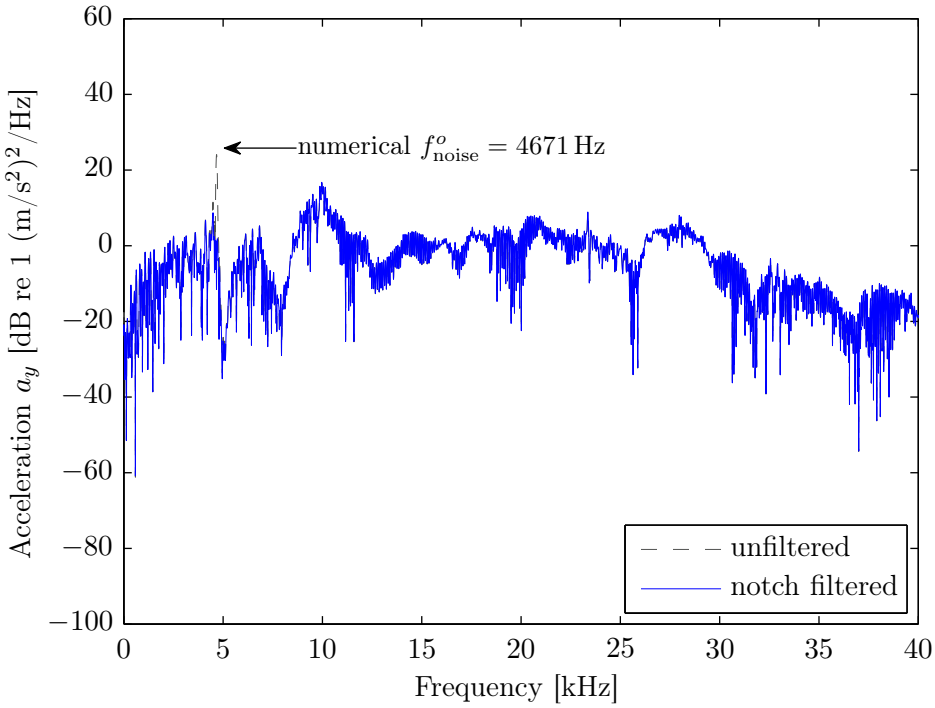

(a) Power spectral densities of the unfiltered and notch filtered acceleration a_y time-traces, highlighting the tonal noise at $f^o_{\text{noise}} = 4671\,\text{Hz}$ for the unfiltered time-trace.

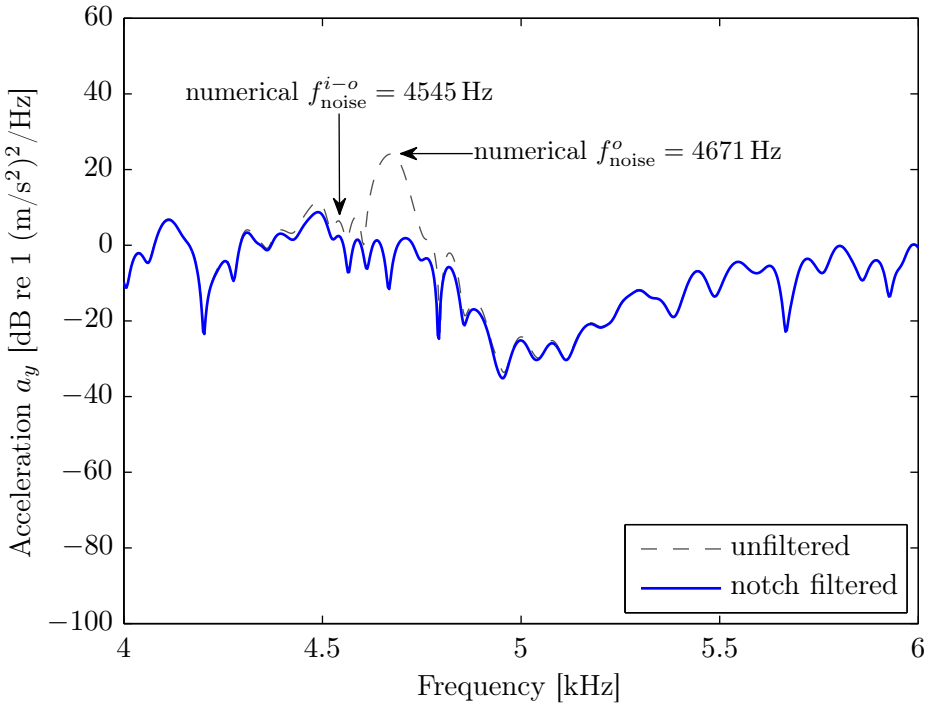

(b) Comparison of the power spectral densities shown in Figure 4.14a on a zoomed frequency scale of 4–6 kHz, highlighting the attenuation of the tonal noise by 25 dB after filtering.

Figure 4.14: Power spectrum of the numerically modelled, unfiltered and notch filtered, acceleration a_y time-traces shown in Figure 4.13 for a radial load W of 50 kN and rotational speed n_s of 500 RPM.

hypothesis for explaining the cause of numerical contact noise observed in the modelled acceleration results.

Further analyses of the numerically modelled vibration signals are presented in the next section in order to evaluate additional defect-related vibration characteristics and demonstrate a *novel* capability of the developed FE model to predict the de-stressing of the rolling elements as they enter into the defect, which has not been predicted by previous models [90–111, 113–120].

4.6 Analyses of the modelled vibration response of the defective rolling element bearing

This section presents analyses of the bearing vibration response obtained from the FE modelling of the defective rolling element bearing. The analyses were conducted using standard signal processing techniques commonly used for the vibration-based monitoring of rolling element bearings. The analyses are divided into time domain, time–frequency domain, and frequency domain.

4.6.1 Time domain analysis

The numerically modelled velocity v_y and displacement u_y time-traces at the same node where the acceleration a_y signal was obtained, are shown in Figures 4.15 and 4.16, respectively. Both figures compare the unfiltered and notch filtered nodal velocity and displacement time-traces. Similar to the numerical acceleration results in Figure 4.13, the effect of filtering out the numerical rolling contact noise frequency f^o_{noise} is clearly evident in Figures 4.15 and 4.16. The defect-related impulses are separated by 0.011 s, which corresponds to the outer raceway defect frequency f_{bpo} of 90.91 Hz, and they are clearly evident in the velocity v_y time-trace in a similar way to the acceleration a_y signal shown in Figures 4.5 and 4.13. In contrast, for the displacement u_y signal in

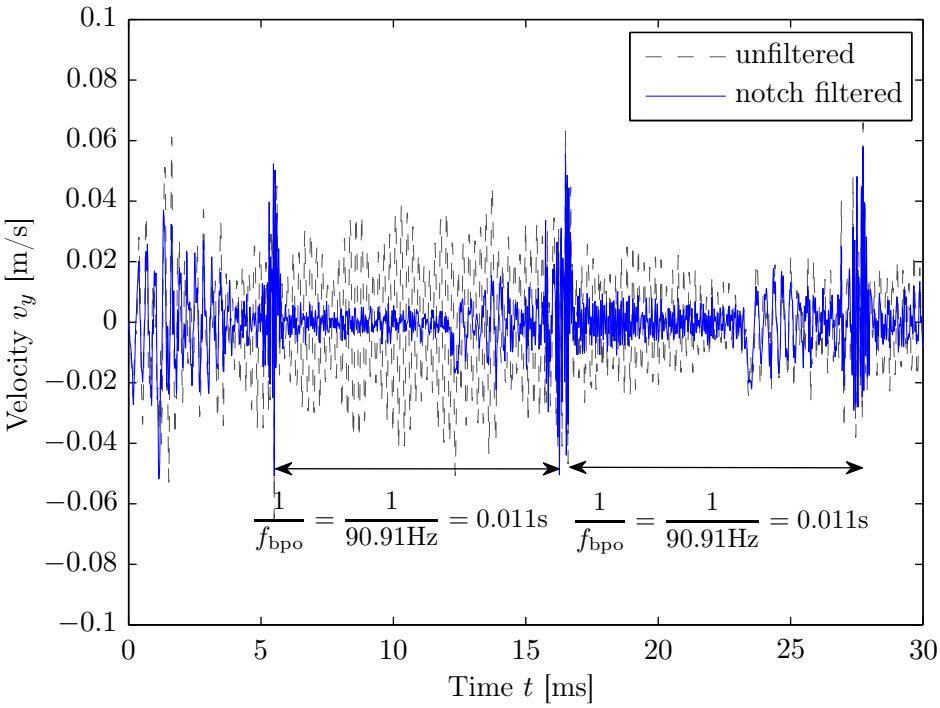

Figure 4.15: Numerically modelled, unfiltered and notch filtered, velocity v_y time-traces for a node located on the outer surface of the outer ring of the FE model of the bearing for a radial load W of 50 kN and rotational speed n_s of 500 RPM.

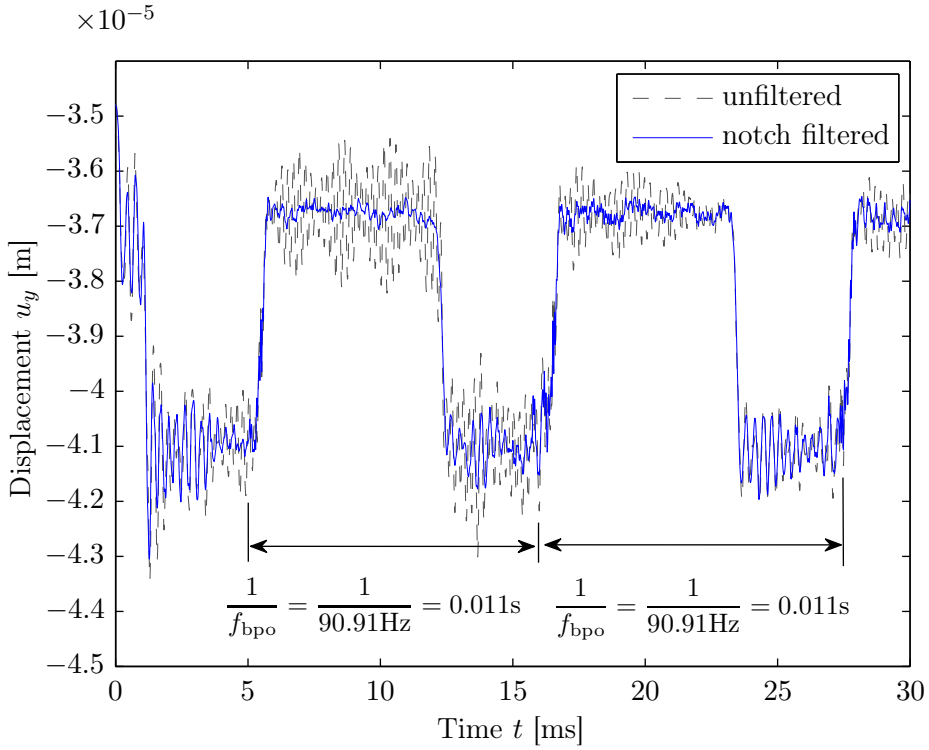

Figure 4.16: Numerically modelled, unfiltered and notch filtered, displacement u_y time-traces for a node located on the outer surface of the outer ring of the FE model of the bearing for a radial load W of 50 kN and rotational speed n_s of 500 RPM.

Figure 4.16, the impulses are not as clear as for the cases of acceleration a_y and velocity v_y signals; however, the change (fall and rise) in the displacement signal indicates the traverse of the rolling elements through the defect, which is discussed in the following paragraphs.

It has been established in the literature [4–7, 161, 162, 165] that the entry of a rolling element into a defect is a low-frequency de-stressing event, whereas its exit from a defect is a high-frequency re-stressing impulsive event that excites a broad range of the structural resonant modes of a bearing [17, 30]. It is crucial for the numerically modelled vibration response obtained from the developed explicit FE model of the bearing to show such characteristics for model validation, in addition to correctly acquiring the bearing kinematics, which has already been demonstrated in Figures 4.5, 4.15, and 4.16. Although the de-stressing event has been experimentally measured by a few researchers [5, 161, 162, 165], previous models [90–111, 113–120] could not predict the vibration signals associated with this event.

The observation of the numerical acceleration a_y time-trace of the defective bearing in Figure 4.13 does not reveal a distinction between the low- and high-frequency entry- and exit-related events, respectively. In fact, the entry of the rolling elements into the outer raceway defect is not visible compared to their exit indicated by the defect-related impulses whose separation corresponds to $f_{\text{bpo}} = 90.91\,\text{Hz}$. In contrast, careful observation of the notch filtered numerical velocity v_y in Figure 4.15 provides some indication of change in the signal characteristics before the defect-related impulsive signals.

Without the unfiltered results, the notch filtered nodal velocity time-trace is reproduced in Figure 4.17 for clarity, along with some markers and associated annotations. The elliptical and rectangular markers indicate the de-stressing (entry) and re-stressing (exit) of the rolling elements as they traverse through the outer raceway defect. Despite being noisy, the distinction between the vibration signatures associated with the de-stressing and re-stressing events is evident in the modelled velocity results. Simi-

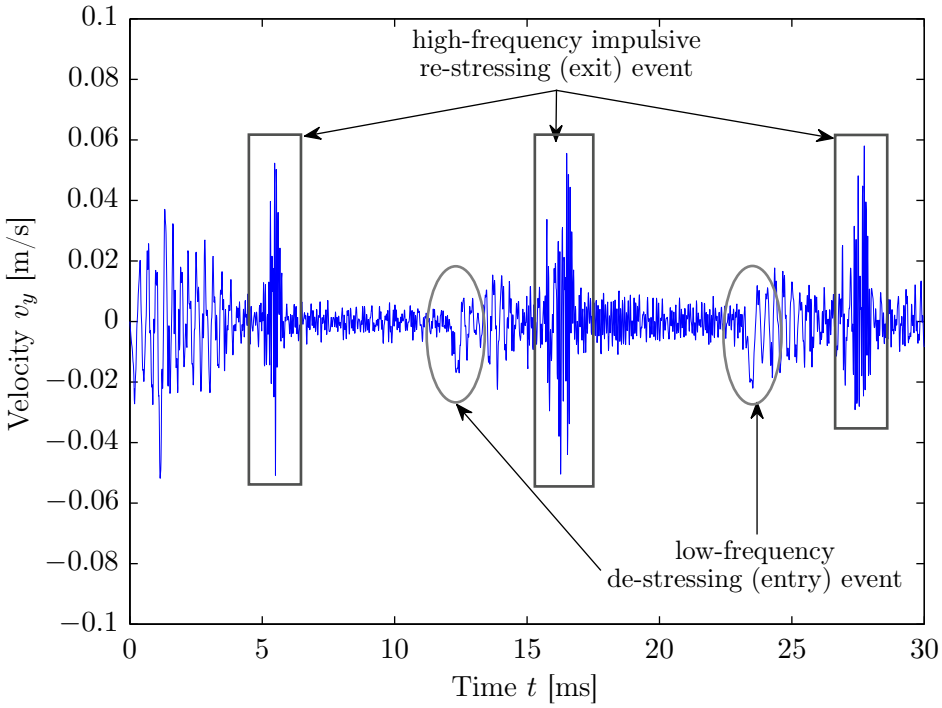

Figure 4.17: Numerically modelled, notch filtered, velocity v_y time-trace shown in Figure 4.15, highlighting the low-frequency de-stressing (entry) and high-frequency re-stressing (exit) events using the elliptical and rectangular markers, respectively.

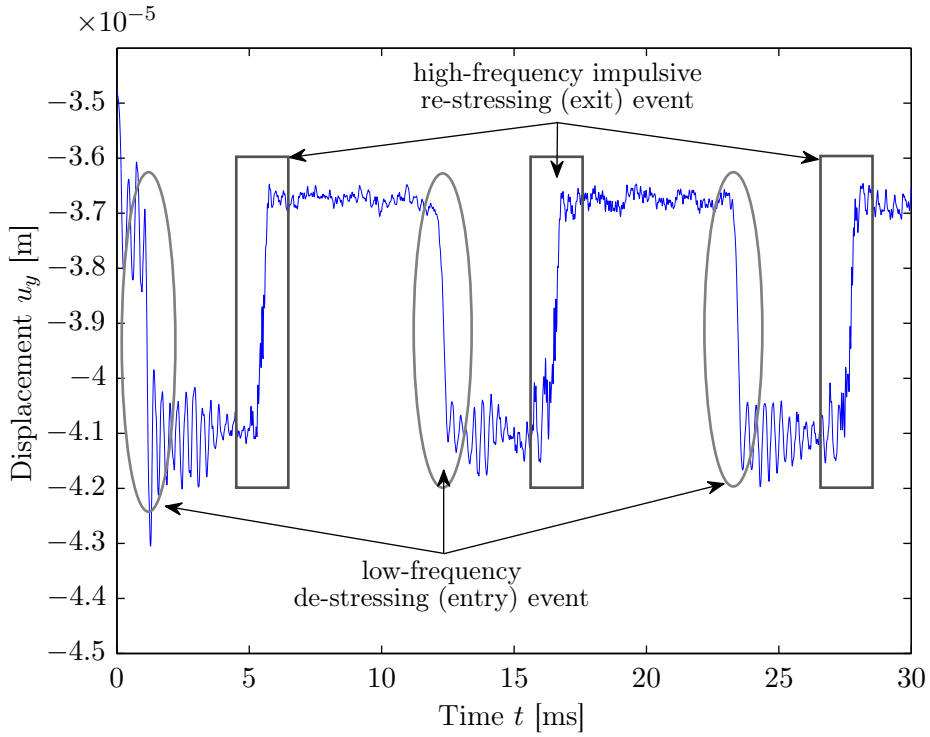

Figure 4.18: Numerically modelled, notch filtered, displacement u_y time-trace shown in Figure 4.16, highlighting the low-frequency de-stressing (entry) and high-frequency re-stressing (exit) events using the elliptical and rectangular markers, respectively.

lar experimental findings related to the events were observed during the experimental work carried out for the current research; the experimental work will be presented in the next chapter for model verification purposes.

Based on the understanding gained from Figure 4.17, the de-stressing and re-stressing events can also be distinguished from the nodal displacement u_y results in Figure 4.16. For clarity, the notch filtered displacement time-trace is reproduced in Figure 4.18 along with the indications of the entry and exit of the rolling elements into and out of the defect, using the elliptical and rectangular markers, respectively.

The de-stressing of the rolling elements upon their entrance into the defect is clearly evident in the notch filtered velocity v_y and displacement u_y time-traces in Figures 4.17 and 4.18, respectively, as indicated by the elliptical markers; however, no such signatures are visible in the notch filtered acceleration a_y results in Figure 4.13. It is highly likely that the low-frequency signals related to the de-stressing event are masked by the (stochastic) numerical noise due to the adaptive time-stepping, as explained in Section 4.5.1. Time–frequency analysis, which is commonly used to investigate the energy or power distribution in a typical vibration signal, can be used to check the frequency content of the two events for the modelled vibration signals. It will also help in identifying if the numerical acceleration signal contains the low-frequency de-stressing signals. The time–frequency analysis is presented in the next section.

4.6.2 Time–frequency analysis

One of the common forms for preliminary investigation of the energy content of a time-varying signal is to plot its sonogram. It is also referred to as the short-time Fourier transform (STFT). STFT is also known by the names of waterfall plot, isoplot, contour plot, and spectrogram. It is evaluated by applying a windowing function to a time-trace and evaluating the conventional Fourier transform of the resulting finite length time signal. For a time-varying signal $x(t)$, moved over a time window $w(t)$, the STFT

is given by [31, Chapter 3, page 130]

$$\mathrm{STFT}\,(\tau, f) = \mathscr{S}\,(\tau, f) = X\,(t, f) = \int_{-\infty}^{\infty} x\,(t)\, w\,(t-\tau) \exp\,(-i2\pi f t) \tag{4.15}$$

The amplitude squared $\mid X\,(t, f)\mid^2$ that is generally displayed on a time–frequency diagram is often called as a spectrogram. A limitation associated with an STFT analysis is the inherent relation between time and frequency resolution where a finer frequency resolution is achieved at the expense of a coarse time resolution and vice-versa.

Figures 4.19, 4.20, and 4.21 show the spectrogram plots of the numerically modelled nodal acceleration a_y, velocity v_y, and displacement u_y results, respectively, discussed in the preceding sections. The numerical noise was removed by de-trending the vibration time-traces along the time (x-) axis. In other words, the mean of the power spectral density for each frequency was removed. Being consistent with the usage of the markers in the previous figures, the signatures related to the de-stressing and re-stressing of the rolling elements upon their entry into and exit out of the defect are indicated using elliptical and rectangular markers, respectively. The distinction between the two events is clearly evident in all spectrogram plots. The energy of the de-stressing event is concentrated below 3 kHz, whereas the impulses generated during the re-stressing of the rolling elements appear to be characterised mainly by energy in the high-frequency band of 10–25 kHz. In addition, there is also a slight indication of the low-frequency content at the timings corresponding to the re-stressing events. This is due to the generation of the defect-related impulses, which excite both high- and low-frequency resonance modes of the bearing.

Compared to the notch filtered time-trace of the numerical acceleration a_y in Figure 4.13, where the de-stressing of the rolling elements could not be seen, the time–frequency analysis of the acceleration signal in Figure 4.19 facilitated the appearance of the de-stressing event, as indicated using the elliptical markers.

As the de-stressing signals are mainly characterised by signals in low-frequency re-

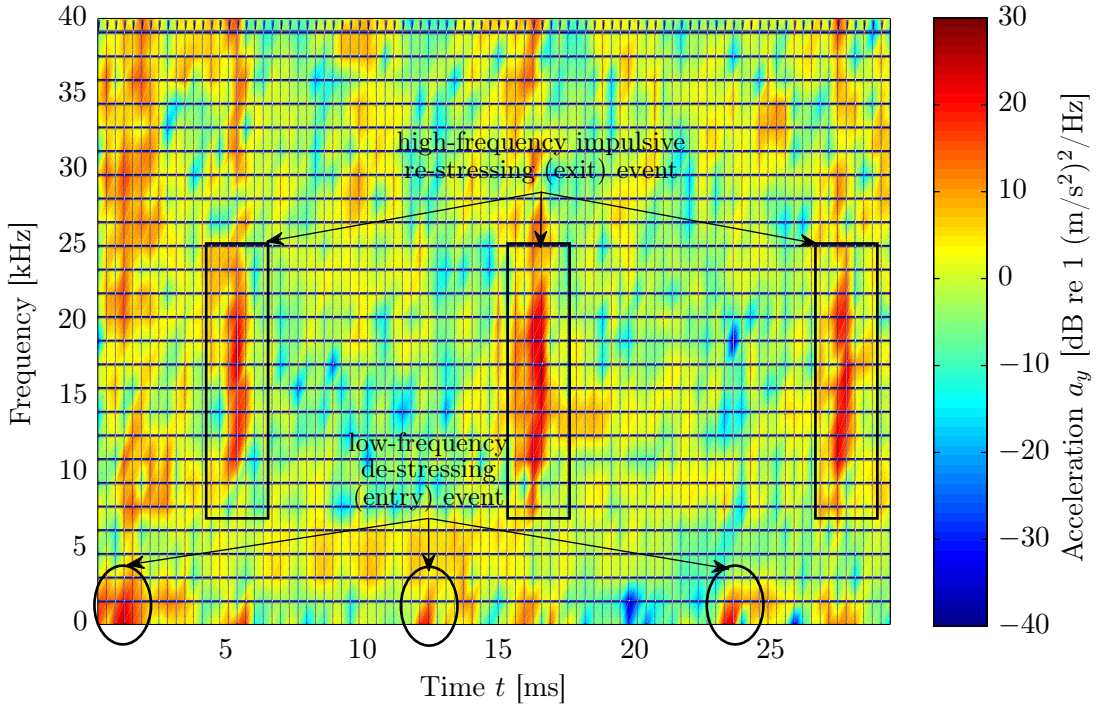

Figure 4.19: A spectrogram of the numerically modelled, unfiltered, acceleration a_y time-trace shown in Figure 4.5, highlighting the low-frequency de-stressing and high-frequency re-stressing events using the elliptical and rectangular markers, respectively.

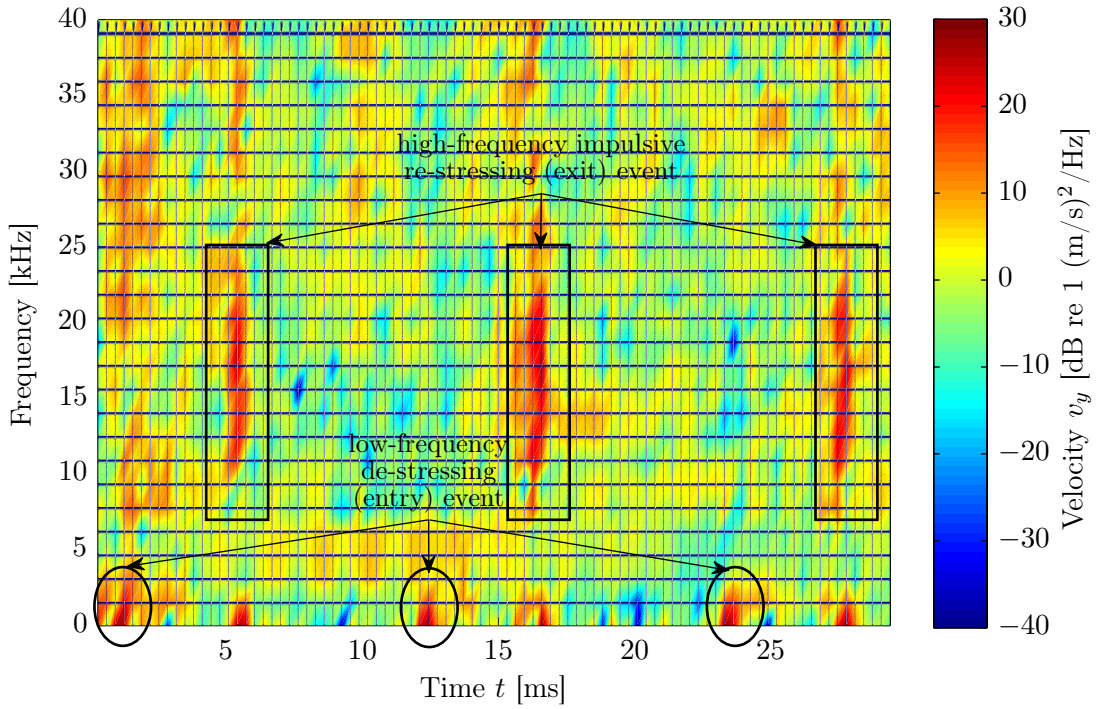

Figure 4.20: A spectrogram of the numerically modelled, unfiltered, velocity v_y time-trace shown in Figure 4.15, highlighting the low-frequency de-stressing and high-frequency re-stressing events using the elliptical and rectangular markers, respectively.

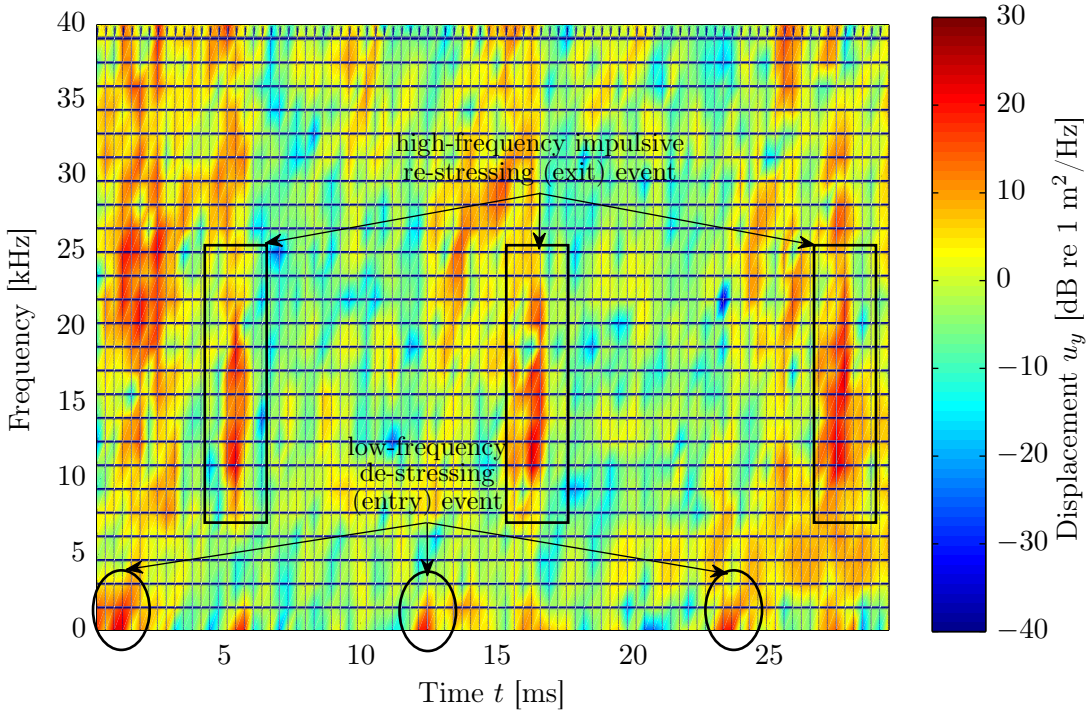

Figure 4.21: A spectrogram of the numerically modelled, unfiltered, displacement u_y time-trace shown in Figure 4.16, highlighting the low-frequency de-stressing and high-frequency re-stressing events using the elliptical and rectangular markers, respectively.

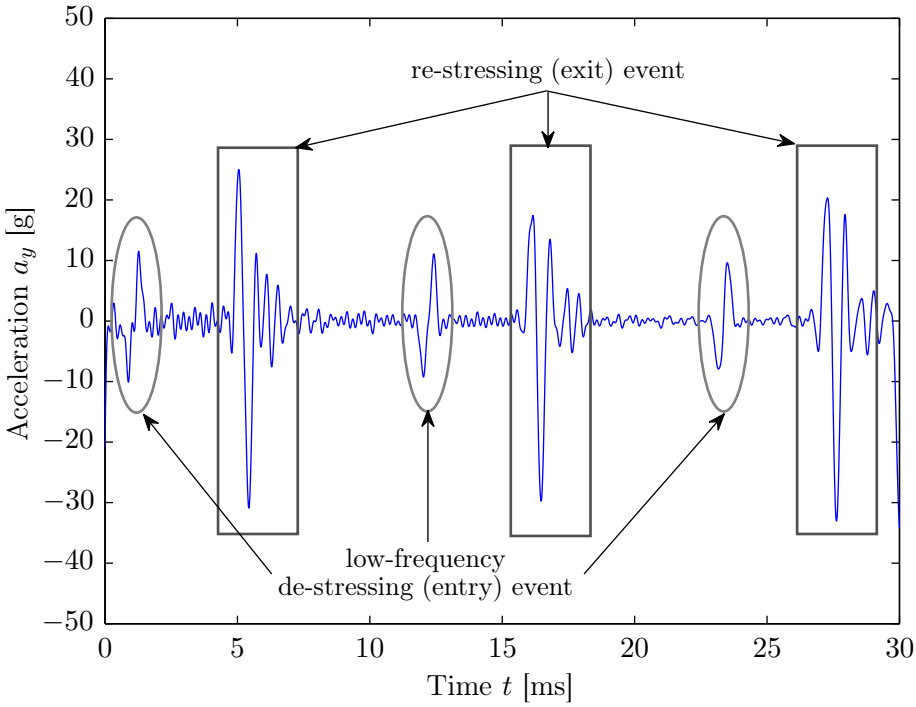

Figure 4.22: Numerically modelled, unfiltered, acceleration a_y time-trace shown in Figure 4.13 has been low-pass filtered, highlighting the low-frequency de-stressing (entry) and re-stressing (exit) events using the elliptical and rectangular markers, respectively.

gions, it was found useful to low-pass filter the numerical acceleration a_y time-trace using a third-order Butterworth filter [392] with a cut-off frequency of 2.5 kHz. The corresponding results are plotted in Figure 4.22. On the one hand, the occurrences of the de-stressing event, which could not be previously seen in the acceleration a_y time-trace in Figure 4.13, can be clearly distinguished with the elimination of the high-frequency content. On the other hand, the application of the low-pass filter resulted in the loss of high-frequency defect-related impulsive characteristics, but the impulsive signatures related to the re-stressing of the rolling elements are still visible. This is because the re-stressing event excites a broad range of frequencies that include both low- and high-frequency resonance modes of a bearing as mentioned earlier. Therefore, the impulses related to the re-stressing event that remained after the low-pass filter effectively have low-frequency characteristics. The instantaneous level of the re-stressing impulses in Figure 4.22 is significantly reduced from approximately 180 g to 20 g as a result of the low-pass filtering. It should be noted that the low-pass filter has only been implemented to enhance the de-stressing of the rolling elements, and that the low-pass filtered signals will not be used for data analysis.

The capability of the explicit FE model presented here to predict the de-stressing of the rolling frequency is *novel* and unique, compared to previous multi-body analytical [90–111, 113–116] and FE models [117–120], which could not predict this event.

Frequency domain analysis is presented in the next section.

4.6.3 Frequency domain analysis

Frequency domain analysis, commonly referred to as *spectral analysis*, enables the transformation of a time-trace into its equivalent frequency domain representation by taking the Discrete Fourier Transform (DFT) of the time-trace. In digital signal processing, spectral analysis is typically performed using the Fast Fourier Transform (FFT)

algorithm. The Fourier transform $\mathscr{F}$ of a time-varying signal $x(t)$ is defined as

$$\mathscr{F}\left\{x\left(t\right)\right\} = X\left(f\right) = \int_{-\infty}^{\infty} x\left(t\right) \exp\left(-i2\pi ft\right) dt \tag{4.16}$$

One of the main purposes of performing spectral analysis on bearing vibration data is to identify major frequency components, such as defect-related fundamental and harmonics, which can indicate the presence of a defect. The envelope analysis technique [30, 251, 252], which is widely used for bearing diagnosis, has been implemented in this study.

It is well-known that the generation of defect-related impulses within a bearing results in the excitation of bearing resonance modes [17, 22, 30, 253]. As a result, the impulses are often amplified by resonances of the bearing structure [30]. Implementation of the envelope analysis involves band pass filtering a bearing vibration signal in a high-frequency range around the bearing structural resonances. It is then amplitude demodulated to form the envelope signal, whose spectrum contains the desired diagnostic information in terms of both repetition frequency (ball pass frequency or ball spin frequency) as well as modulation by the appropriate frequency at which the fault is passing through the load zone [30].

A prerequisite associated with the envelope analysis technique is that the most suitable frequency band for demodulation is chosen. While an estimate may be determined from the time–frequency analysis, spectral kurtosis [25] and kurtograms [26] are commonly used to find the frequency band with the highest content of impulsive energy.

4.6.3.1 Spectral kurtosis

Spectral kurtosis (SK) was introduced by Dwyer [393] as a statistical tool for detecting non-Gaussian components and their locations in the frequency domain. It was used to supplement the power spectral density estimate in situations pertinent

to defect-related transients in noisy signals [394, 395]. SK was originally defined as the normalised fourth-order moment of the real part of the short-time Fourier transform (STFT). Later, Ottonello and Pangan [396, 397] proposed a modified definition of SK as the fourth-order moment of the magnitude of the STFT, which led to considerably simplified properties. Lately, Capdevielle *et al.* [398] provided an enhanced definition of the SK as the fourth-order cumulant of the Fourier transform; the definition worked well for stationary signals, but not for non-stationary signals. SK, for stationary signals, was further investigated by Vrabie *et al.* [399, 400]. More recently, Antoni [25] laid the theoretical foundation for the comprehensive formalisation of SK for non-stationary signals followed by its application to the vibration-based condition monitoring of rotating machines [26].

Spectral kurtosis extends the concept of (global) kurtosis to that of a function of frequency, which indicates the impulsiveness of the signal in a frequency band. It provides a means of determining which frequency bands contain a signal of maximum impulsivity. Spectral kurtosis $\mathscr{K}$ of a time-varying signal $x(t)$ may be computed from the STFT; that is, local Fourier transform, at time t by moving a window along the signal. Mathematically, it is defined as [30]

$$\mathscr{K}\left\{x\left(t\right)\right\} = \mathrm{SK}\left(f\right) = \frac{\left\langle \left|X\left(t,f\right)\right|^4 \right\rangle}{\left\langle \left|X\left(t,f\right)\right|^2 \right\rangle^2} - 2 \tag{4.17}$$

where, the squared magnitude, $\left|X\left(t,f\right)\right|^2$ — the spectrogram — returns the power spectrum at time t and its average over time, $\left\langle \left|X\left(t,f\right)\right|^2 \right\rangle$ — the power spectral density.

For various window lengths N_w (power of 2), Figures 4.23, 4.24, and 4.25 show the spectral kurtosis of the notch filtered numerical acceleration a_y, velocity v_y, and displacement u_y time-traces shown in Figures 4.13, 4.17, and 4.18, respectively. A common characteristic of the shown spectral kurtoses plots is that the defect-related impulsivity within the vibration signals is approximately between 12 kHz and 22 kHz. These findings are similar to those shown in the spectrogram plots in Figures 4.19, 4.20,

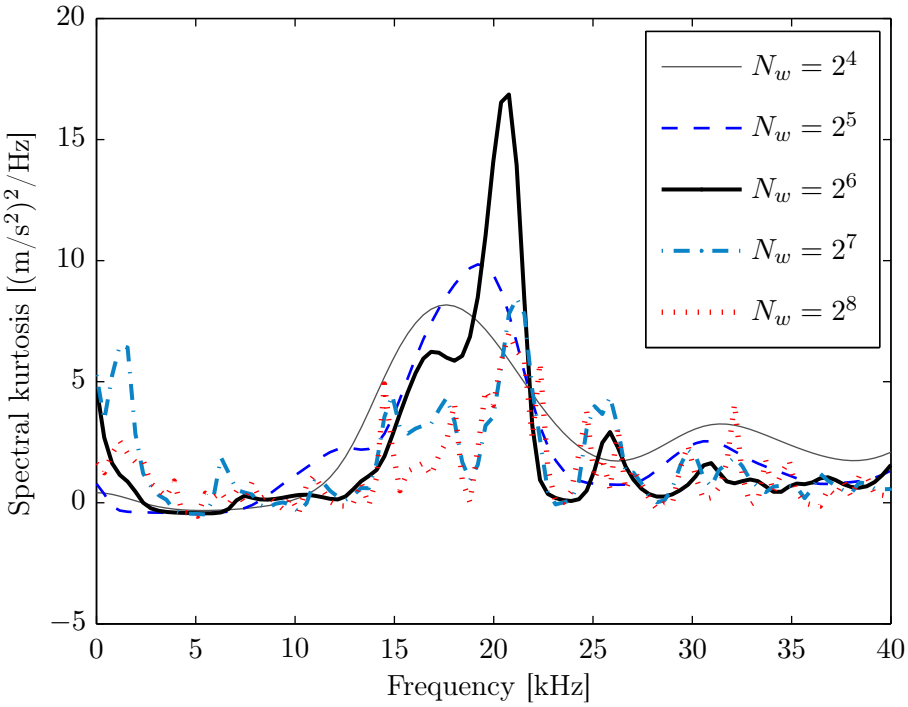

Figure 4.23: A spectral kurtosis plot of the numerically modelled, notch filtered, acceleration a_y time-trace shown in Figure 4.13 corresponding to a radial load W of 50 kN and rotational speed n_s of 500 RPM for various window lengths N_w.

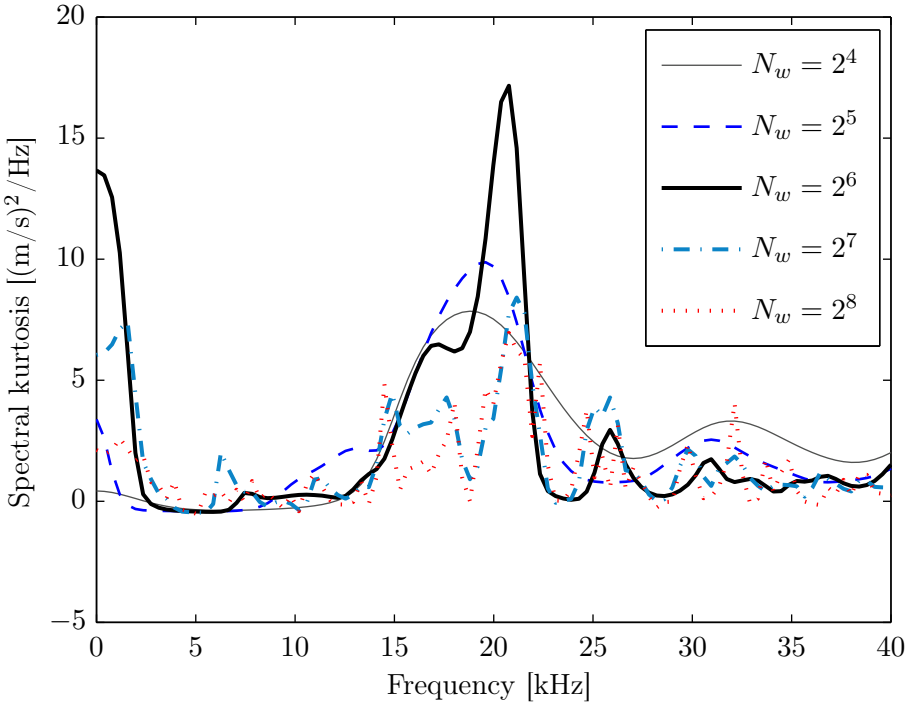

Figure 4.24: A spectral kurtosis plot of the numerically modelled, notch filtered, velocity v_y time-trace shown in Figure 4.17 corresponding to a radial load W of 50 kN and rotational speed n_s of 500 RPM for various window lengths N_w.

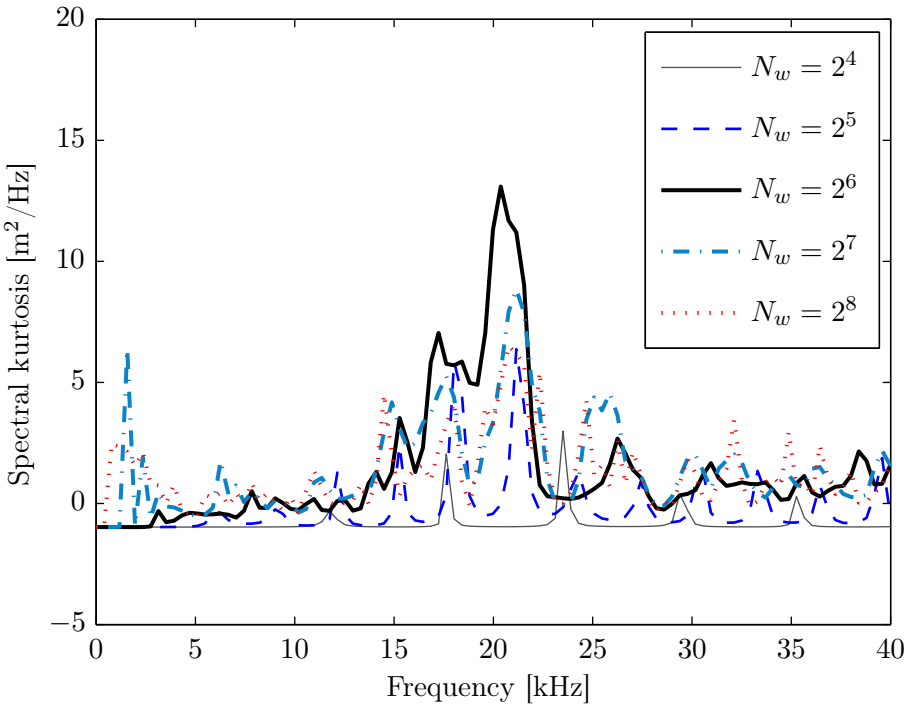

Figure 4.25: A spectral kurtosis plot of the numerically modelled, notch filtered, displacement u_y time-trace shown in Figure 4.18 corresponding to a radial load W of 50 kN and rotational speed n_s of 500 RPM for various window lengths N_w.

and 4.21, where the energy of the defect-related (re-stressing) impulses can be seen to have concentrated between 10 kHz and 25 kHz. These results provide an indication of the frequency bands for the envelope analysis; however, as the SK varies for various window lengths, the frequency bands need to be judiciously chosen. A kurtogram helps to determine the optimal frequency band and is described next.

4.6.3.2 Kurtogram

Kurtogram, a term coined by Antoni and Randall [26], refers to the representation of SK as a function of both frequency and window length. A kurtogram is basically a cascade of spectral kurtoses obtained for different values of the STFT window length N_w, but for a much finer grid.

Figures 4.26, 4.27, and 4.28 show the full kurtogram plots of the numerically modelled acceleration, velocity, and displacement results, shown in Figures 4.13, 4.17, and 4.18, respectively. The results consistently show that the defect-related impulsivity is

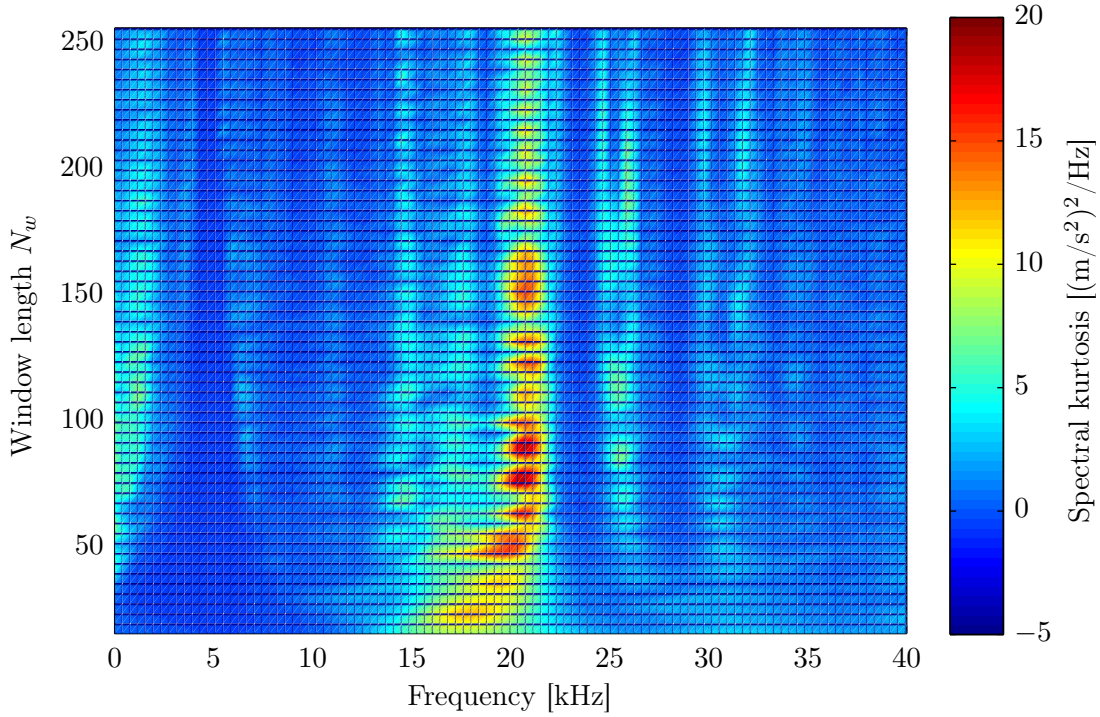

Figure 4.26: A kurtogram of the numerically modelled, notch filtered, acceleration a_y time-trace shown in Figure 4.13 for a radial load W of 50 kN and rotational speed n_s of 500 RPM.

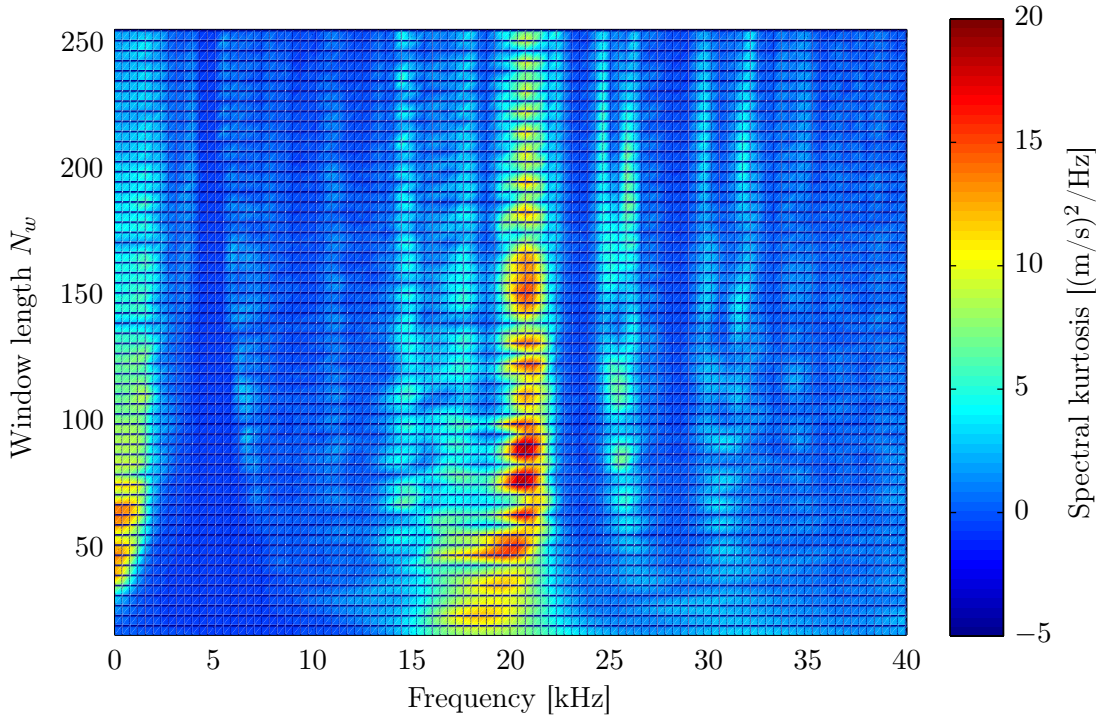

Figure 4.27: A kurtogram of the numerically modelled, notch filtered, velocity v_y time-trace shown in Figure 4.17 for a radial load W of 50 kN and rotational speed n_s of 500 RPM.

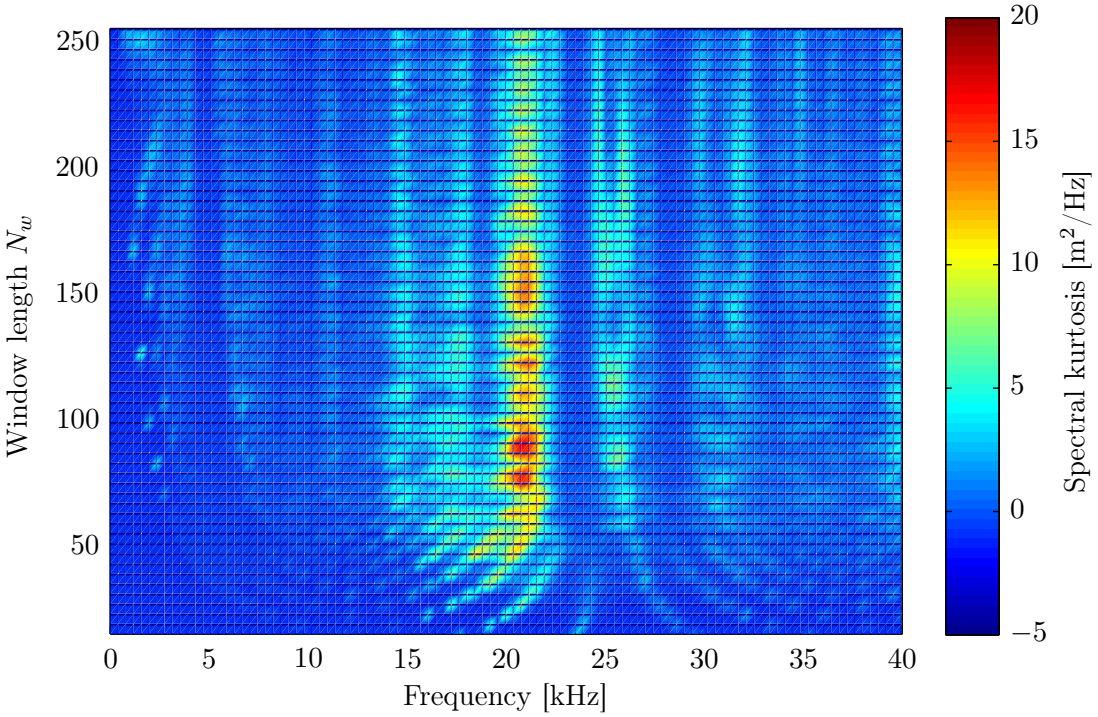

Figure 4.28: A kurtogram of the numerically modelled, notch filtered, displacement u_y time-trace shown in Figure 4.18 for a radial load W of 50 kN and rotational speed n_s of 500 RPM.

concentrated around 20 kHz. Although the information in spectral kurtosis and kurtogram plots is similar, one can achieve precise information from the latter due to the mapping of the former over a wide range of STFT window lengths.

4.6.3.3 Envelope analysis

In this thesis, envelope analysis [30, 251, 252] has been carried out using the Hilbert transform [348, 349]. For a real-valued time signal $x(t)$, the Hilbert transform $\mathscr{H}$ is the imaginary component of its complex analytic signal $\hat{x}(t)$. These variables are related as

$$\mathscr{H}\{x(t)\} = \tilde{x}(t) \tag{4.18}$$

$$\hat{x}(t) = x(t) + i\tilde{x}(t) \tag{4.19}$$

Unlike the Fourier transform $\mathscr{F}$, which moves the independent variable of a signal from the time to the frequency domain or vice-versa, the Hilbert transform $\mathscr{H}$ leaves

the signal in the same domain; however, it causes a phase shift of 90° in the frequency domain or a quarter of a wavelength in the time domain. An excellent tutorial on the applications of the Hilbert transform to mechanical vibrations is provided in reference [349].

From the kurtogram plots in Figures 4.26, 4.27, and 4.28, the impulsive frequency band of 18–23 kHz was chosen for demodulating the numerical bearing vibration signals, and subsequently the envelope analysis technique was implemented. The power spectrum of the envelope signals was estimated using Welch's method [389] with 50% overlap. As the simulated signals have only 3010 data points, they were zero-padded with 2^{16} FFT points in order to smoothly interpolate the results for a frequency resolution of 1.5 Hz.

Figures 4.29, 4.30, and 4.31 show the envelope power spectrum of the numerical acceleration a_y, velocity v_y, and displacement u_y time-traces. The tonal peaks at the fundamental and harmonics, as indicated in the figures, correspond to the outer raceway defect frequency f_{bpo}. The envelope power spectra of the vibration time-traces follow the standard pattern of having the highest amplitude of the fundamental and decreasing amplitudes for subsequently harmonics. These envelope power spectra shown in the figures clearly indicate the presence of a defect within a rolling element bearing.

4.6.3.4 Power spectrum

The power spectral density of the notch filtered velocity v_y and displacement u_y time-traces was estimated to be similar to that of the numerical acceleration signal, as described in Section 4.5. The corresponding power spectra are shown in Figures 4.32 and 4.33 along with the unfiltered velocity and displacement results, respectively. The fundamental tone at the numerical rolling element-to-outer raceway rolling contact noise frequency $f^o_{\text{noise}} = 4671$ Hz in the unfiltered power spectra, as indicated in Figures 4.32 and 4.33, is similar to that observed in the power spectrum of the acceleration signal

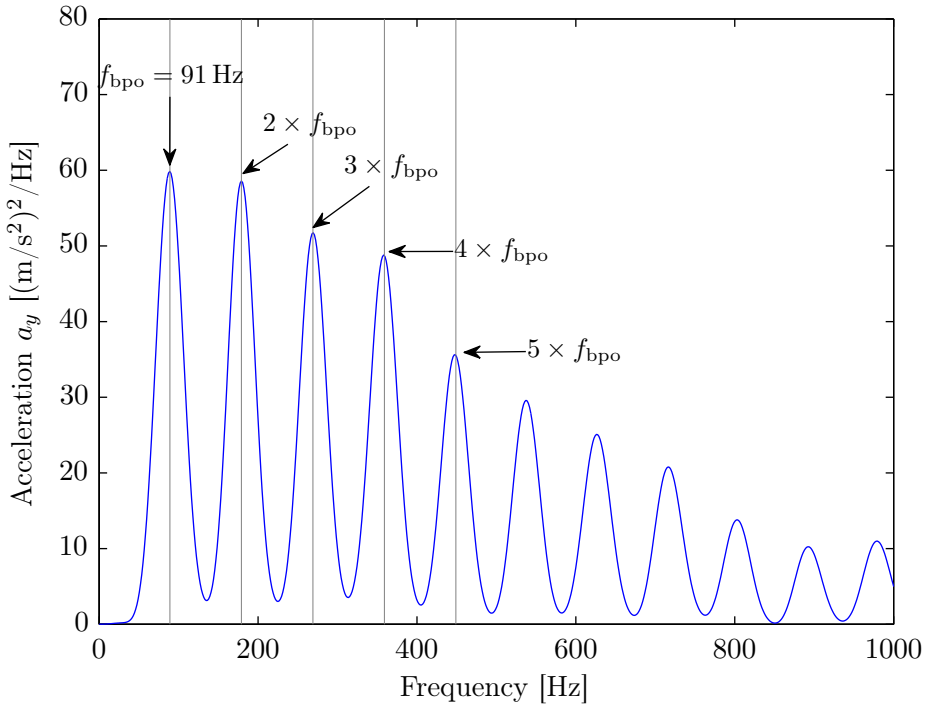

Figure 4.29: Envelope (demodulated) power spectrum of the numerically modelled, band-pass filtered, acceleration a_y time-trace shown in Figure 4.13 for $W = 50\,\text{kN}$ and $n_s = 500\,\text{RPM}$; the vertical lines indicate the fundamental f_{bpo} and its harmonics.

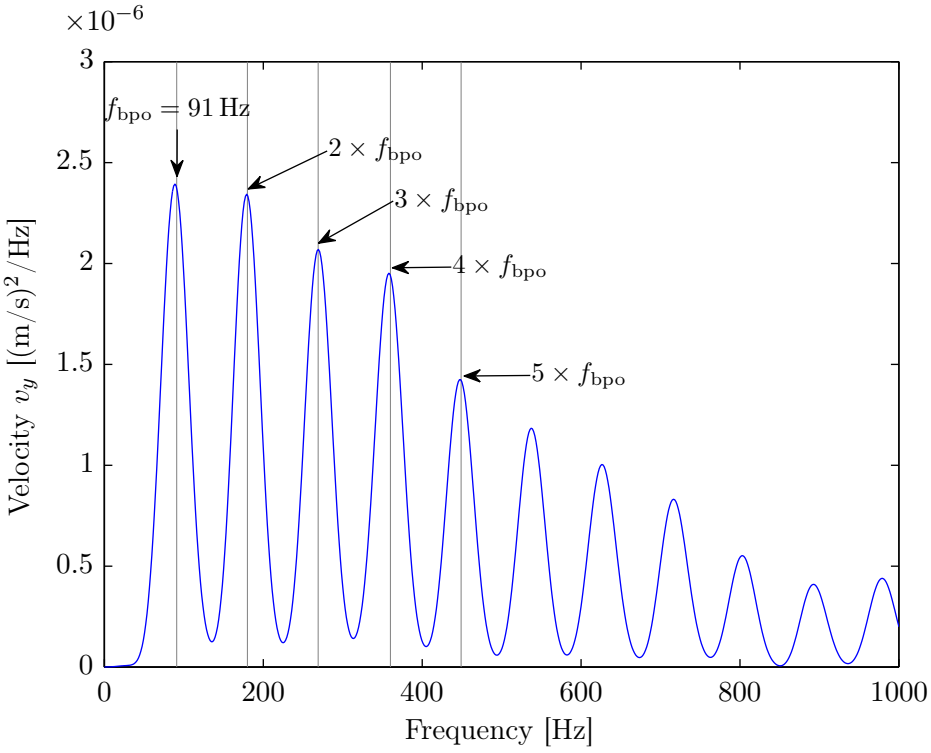

Figure 4.30: Envelope (demodulated) power spectrum of the numerically modelled, band-pass filtered, velocity v_y time-trace shown in Figure 4.17 for $W = 50\,\text{kN}$ and $n_s = 500\,\text{RPM}$; the vertical lines indicate the fundamental f_{bpo} and its harmonics.

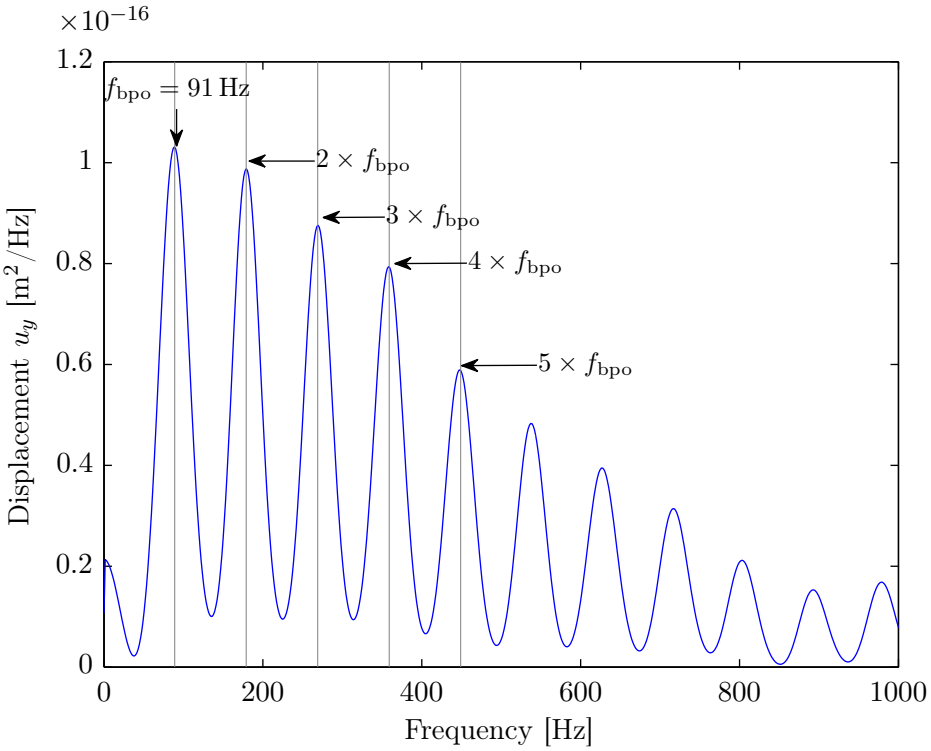

Figure 4.31: Envelope (demodulated) power spectrum of the numerically modelled, band-pass filtered, displacement u_y time-trace shown in Figure 4.18 for $W = 50\,\text{kN}$ and $n_s = 500\,\text{RPM}$; the vertical lines indicate the fundamental f_{bpo} and its harmonics.

plotted in Figure 4.14. The attenuation of the tonal noise by approximately 25 dB, as a result of the notch filter, can be clearly seen in Figures 4.32b and 4.33b, which show comparisons of the unfiltered and notch filtered power spectra at a zoomed frequency scale of 4–6 kHz.

In contrast to the narrow band spectrum, it is often more useful to conduct an octave or one-third octave band spectral analysis in order to seek detailed information about the frequency characteristics of a time-varying signal [381, Chapter 1, pages 41–43]. Figures 4.34, 4.35, and 4.36 show the one-third octave band spectrum of the numerical acceleration a_y, velocity v_y, and displacement u_y time-traces, respectively. For comparison, both unfiltered and notch filtered results are plotted. As can be seen from the comparison that the spectra of the unfiltered and notch filtered signals are similar to each other except at 4 kHz and 5 kHz. As a result of the tonal noise at the rolling element-to-outer raceway numerical rolling contact frequency $f^o_{\text{noise}} = 4671\,\text{Hz}$,

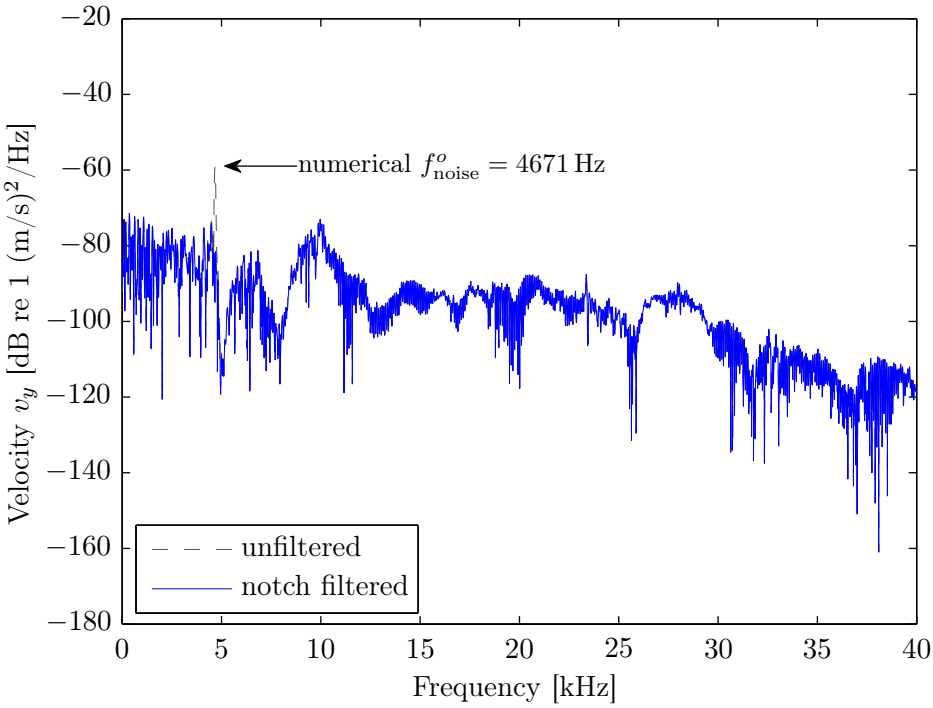

(a) Power spectral densities of the unfiltered and notch filtered velocity v_y time-traces, highlighting the tonal noise at $f^o_{\text{noise}} = 4671$ Hz for the unfiltered time-trace.

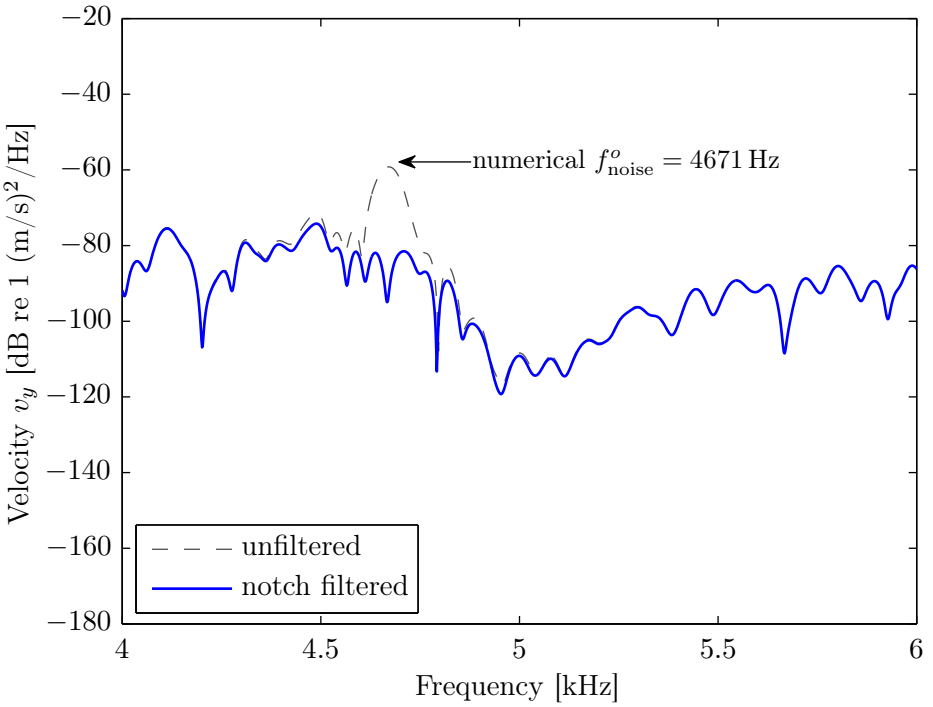

(b) Comparison of the power spectral densities shown in Figure 4.32a on a zoomed frequency scale of 4–6 kHz, highlighting the attenuation of the tonal noise by 25 dB after filtering.

Figure 4.32: Power spectrum of the numerically modelled, unfiltered and notch filtered, velocity v_y time-traces shown in Figure 4.15 for a radial load W of 50 kN and rotational speed n_s of 500 RPM.

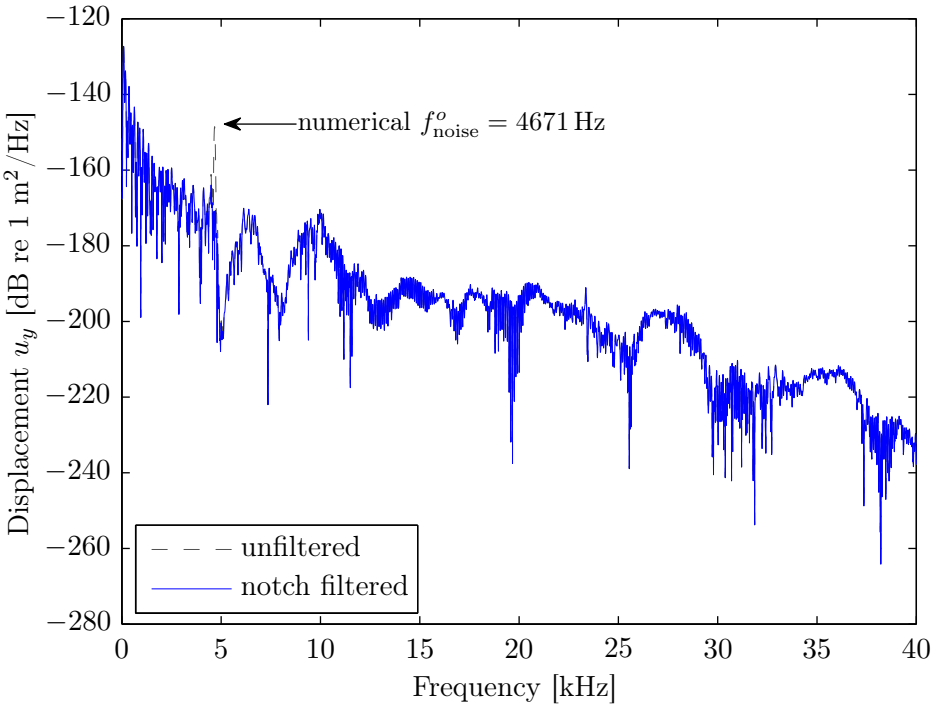

(a) Power spectral densities of the unfiltered and notch filtered displacement u_y time-traces, highlighting the tonal noise at $f^o_{\text{noise}} = 4671$ Hz for the unfiltered time-trace.

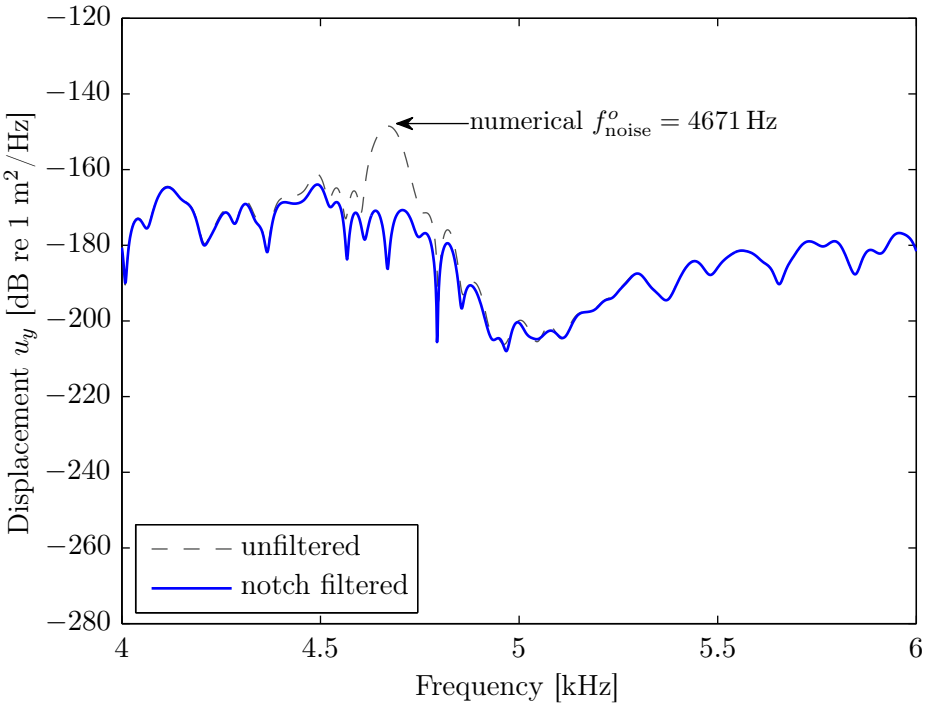

(b) Comparison of the power spectral densities shown in Figure 4.33a on a zoomed frequency scale of 4–6 kHz, highlighting the attenuation of the tonal noise by 25 dB after filtering.

Figure 4.33: Power spectrum of the numerically modelled, unfiltered and notch filtered, displacement u_y time-traces shown in Figure 4.16 for a radial load W of 50 kN and rotational speed n_s of 500 RPM.

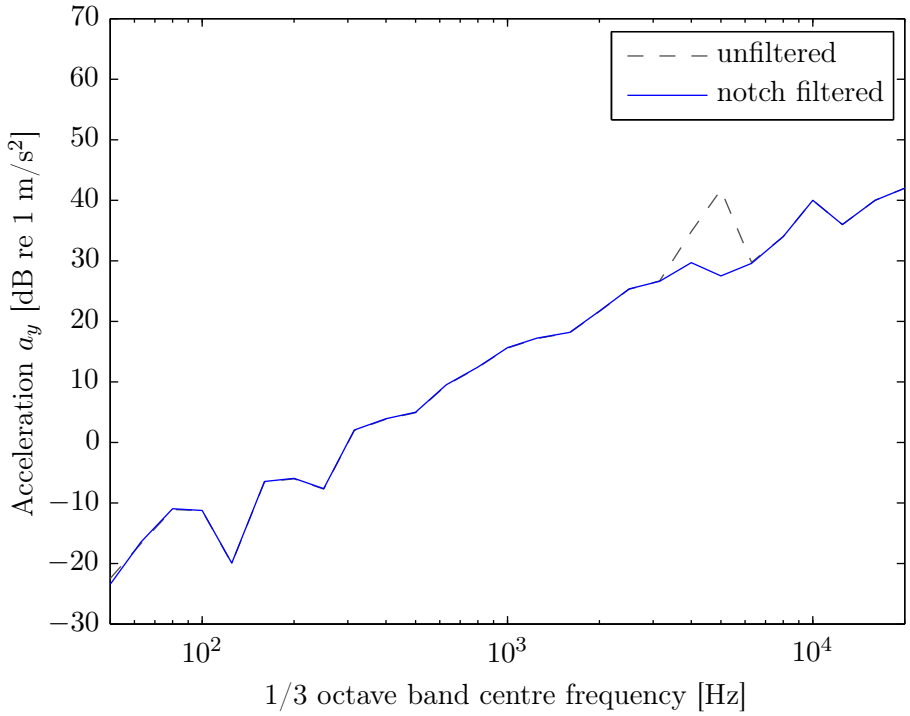

Figure 4.34: One-third octave band spectrum of the numerically modelled, unfiltered and notch filtered, acceleration a_y time-traces shown in Figure 4.13 for a radial load W of 50 kN and rotational speed n_s of 500 RPM.

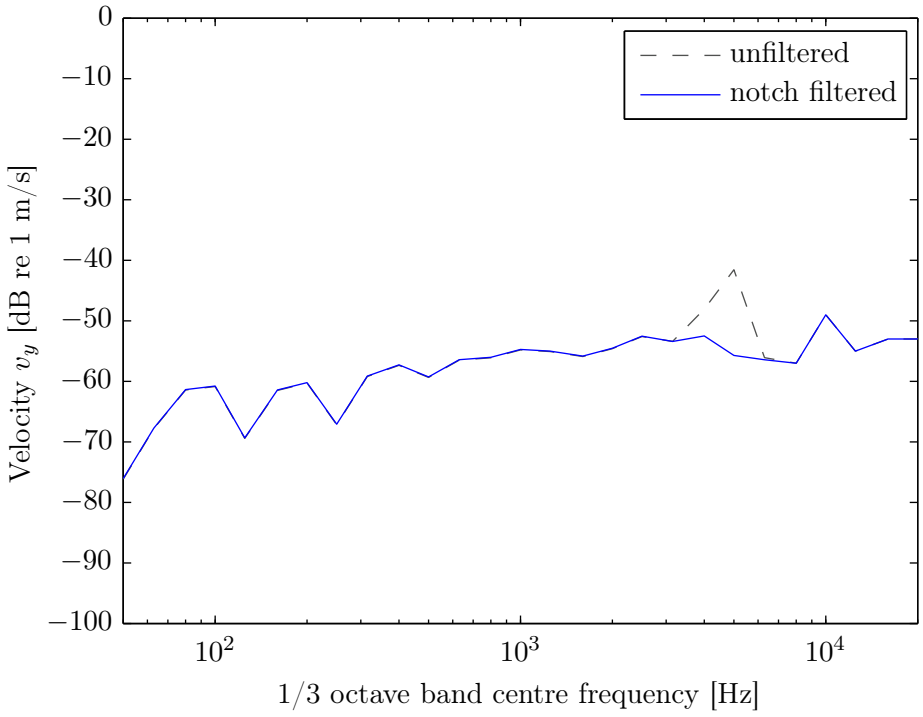

Figure 4.35: One-third octave band spectrum of the numerically modelled, unfiltered and notch filtered, velocity v_y time-traces shown in Figure 4.15 for a radial load W of 50 kN and rotational speed n_s of 500 RPM.

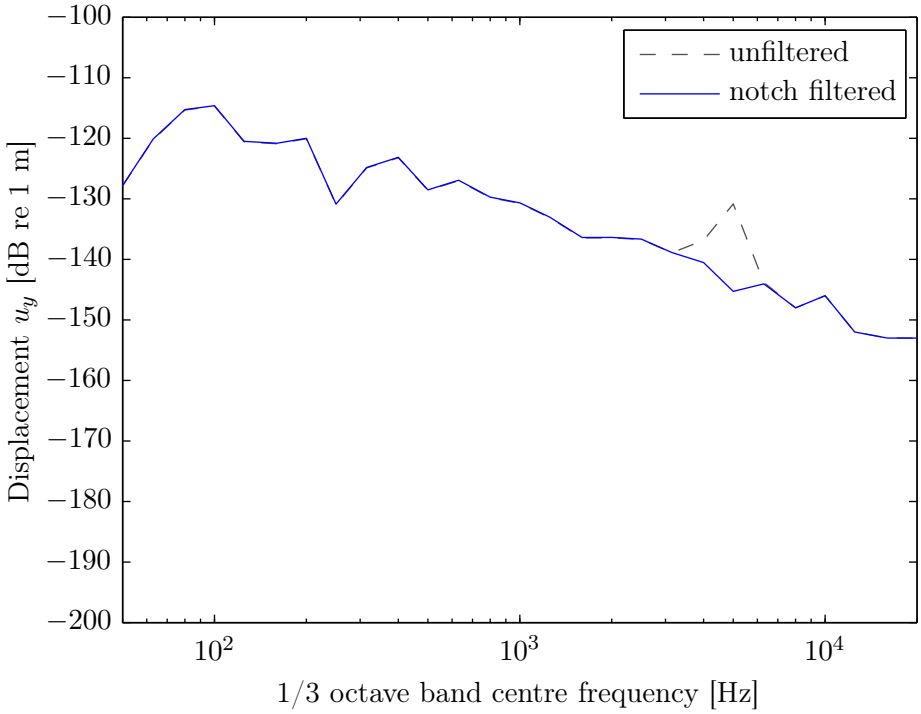

Figure 4.36: One-third octave band spectrum of the numerically modelled, unfiltered and notch filtered, displacement u_y time-traces shown in Figure 4.16 for a radial load W of 50 kN and rotational speed n_s of 500 RPM.

the spectrum of the unfiltered signals peaks at 5 kHz. The other peak at 10 kHz is highly likely due to one of the structural resonances around 10 kHz. As shown in Figure 4.4, there are a few structural vibration modes at around 10 kHz. These results will be compared with the experimental results in the next chapter.

4.6.4 Summary of the numerical results

In the preceding sections, standard signal processing techniques, applicable to the vibration-based monitoring of rolling element bearings, were used to analyse the numerically modelled vibration signals obtained using the novel explicit dynamics FE model of the defective bearing. The main emphasis of the analyses was to discuss the verification of the modelled results based on the relevant analytical and experimental knowledge from the literature, such as bearing kinematics f_{bpo}, and low- and high-frequency characteristics of the de-stressing and re-stressing events, respectively.

A favourable match between the analytical and numerical f_{bpo}, indicating accurate acquisition of the bearing kinematics, has been shown in Figures 4.5, 4.15, and 4.16. The envelope power spectrum plots shown in Figures 4.29, 4.30, and 4.31 also show the fundamental and subsequent harmonics at f_{bpo}. The low- and high-frequency characteristics of the signatures associated with the de-stressing and re-stressing of the rolling elements have been demonstrated not only in the notch filtered vibration time-traces in Figures 4.17, 4.18, and 4.22, but also in the spectrogram plots in Figures 4.19, 4.20, and 4.21.

Further verification of the developed FE model of the rolling element bearing will be discussed in the next chapter, which presents the results of experimental testing of a rolling element bearing having a machined line spall on its outer raceway.

4.7 Conclusions

A novel explicit dynamics finite element model of a defective rolling element bearing has been developed and solved using a commercial FE software package, LS-DYNA. All the steps required to perform the modelling were described, including the boundary conditions and loads. It was shown that a much finer mesh element size was required to accurately model the interaction of the rolling elements and bearing raceways so as to ensure a continuous rolling contact between them. The elements-per-wavelength necessary to properly discretise the bearing model exceeded the recommended EPW criterion by nearly 5 times.

The FE model of the rolling element bearing presented in this chapter is more comprehensive than recently published similar FE models [117–120] and existing analytical multi-body dynamic models [90–114]. The performance of previous FE models was compromised due to treating either the whole outer ring or its outer surface as rigid. This caused artificial over-stiffening of the bearing structure leading to unrealistically high acceleration levels of 10^7 g [118], 4,000 g [119] and 15,000 g [120]. In contrast

to the previous FE models, the explicit FE model of the rolling element bearing developed here models all the bearing components as flexible bodies, which facilitates a more accurate representation of the bearing stiffness. As a result, the FE model presented here predicts realistic acceleration levels, $\pm 180\,\mathrm{g}$, in contrast to unrealistically high acceleration levels by previous FE models [117–120] as mentioned above. It will be shown in the next chapter, which presents the experimental verification of the numerically modelled results, that the predicted instantaneous acceleration levels compare favourably with measured data. Several favourable comparisons between the modelled and measured data will also be presented in the next chapter.

In contrast to the multi-body models, which used rigid bearing raceways [100–112], excluded rolling elements [100–103, 105–107, 109–111, 114], and ignored their inertial and centrifugal effects [100–111, 113, 114], the explicit FE model developed here modelled all the bearing components as flexible bodies, included the rolling elements and considered their centrifugal effects. Although simplified to consider the translations in the plane of the bearing, the FE model of the bearing presented here does not require assumptions, except for the finite element type, material model, friction, and damping.

The significance of including the rolling elements and modelling their centrifugal effects will be highlighted in Chapter 6, which presents an in-depth analysis of the numerically predicted rolling element-to-raceway contact forces as the rolling elements traverse through a raceway defect. As such an analysis has not been previously presented in the literature, the contact force analysis will provide new knowledge and insights on the dynamic interaction of the rolling elements and raceways, leading to the development of an understanding about the physical mechanism that generates defect-related impulses as the rolling elements traverse through a bearing defect. As no boundary conditions or constraints were applied to the rolling elements in the FE model of the rolling element bearing here, they were acted on by centrifugal forces during the bearing rotation. It is due to these centrifugal forces that result in estimating their varying position (trajectory) during their traverse through the outer

raceway defect, as opposed to assuming their path to follow the defect profile. While the centrifugal forces tend to project the rolling elements outward from the centre of the bearing, their outward trajectory is restricted between the outer and inner raceways when the rolling elements are stressed between the raceways. During the analysis of the rolling element-to-raceway contact forces, to be presented in Chapter 6, it will be shown that the rolling elements completely de-stress during their traverse through the defect, they tend to freely follow their outward trajectory, and eventually strike the defective surface a multiple times.

In addition to discussing the reasons for the numerical noise observed in the modelled bearing vibration response, a new hypothesis was developed to explain the cause of spurious oscillations due to the rolling contact interaction of the polygonised rolling elements and raceways. The rolling contact noise frequencies, rolling element-to-outer raceway f^{o}_{noise} and rolling element-to-inner raceway f^{i}_{noise}, and beating f^{i-o}_{noise}, were analytically estimated, and were found to be within 1% of those observed in the numerically modelled vibration time-traces.

A unique and novel capability of the explicit FE model presented here is to predict the vibrations signals associated with the de-stressing of the rolling elements upon their entrance into a bearing defect. Although the low-frequency characteristics of the de-stressing event have been measured by a few researchers [161, 162, 165], previous multi-body analytical models [90–111, 113–120] could not predict this event. Existing FE models [118–120] also did not report on the signals related to the de-stressing event: similar to the multi-body models, the emphasis of the previous FE models was to predict the defect-related (re-stressing) impulses and validate the modelling results through envelope analysis. In contrast to the previous FE models, the FE model of the rolling element bearing presented here also predicts the rolling element-to-raceway contact forces and other Hertzian contact-related parameters. These results will be presented in Chapter 6.

The frequency characteristics of the de-stressing and re-stressing events, obtained

from the developed FE model, were discussed and demonstrated using the spectrogram plots of the numerically modelled vibration time-traces. It was shown that the de-stressing signals are dominated by energy below 3 kHz, whereas the defect-related impulses generated during the re-stressing of the rolling elements are characterised mainly by energy in the frequency band of 10–25 kHz.

Standard signal processing techniques, associated with the vibration-based condition monitoring of rolling element bearings, were implemented on the numerical vibration signals including the most commonly used envelope analysis technique.

The next chapter presents results from the experimental testing of a package railway bearing unit having a machined line spall on its outer raceway. The numerical results will be compared with experimental measurements for model validation purposes.

This page intentionally contains only this sentence.

Chapter 5

Experimental Verification

5.1 Introduction

This chapter presents the findings of the experimental work undertaken on a package bearing unit having a manufactured line spall on its outer raceway. The bearing chosen for its vibration testing is an axle bearing, commonly used in the railway industry, especially in freight wagons, but not uncommon in passenger coaches too. The reason for manufacturing the line spall is that it is representative of a typical defect found in many railway axle bearings. The size of the manufactured defect was chosen based on the inspection of numerous railway bearings [378], available at Track IQ^{TM} [11], one of the sponsors of this research.

In contrast to bearing defects resulting from operational use that have rough profiles, the manufactured outer raceway defect has a clean rectangular profile. Such a defect profile cannot be generated during the operation of a bearing; however, for the current study, it was specifically chosen to satisfactorily accomplish the following two conditions, with minimal influence of the roughness-related characteristics of the defect:

- to validate the explicit dynamics FE model of the defective rolling element bearing presented in Chapter 4; and
- to clearly distinguish the vibration signatures associated with the de-stressing

and re-stressing of the rolling elements, as they enter into and exit out of the defect, respectively.

Once the FE model of the bearing is validated, the numerically estimated rolling element-to-raceway contact forces will be analysed, which will help facilitate the development of an understanding of the physical mechanism by which defect-related impulses are generated in defective rolling element bearings. An analysis of the contact forces along with their correlation with bearing vibrations, will be discussed in the next chapter.

In this chapter, the results pertinent to the vibration testing of the defective bearing are presented. The experimental work was conducted for various radial loads W applied to the bearing and for various rotational speeds n_s. The experimental data were analysed using standard signal processing techniques [17–31], and compared with the numerically modelled data obtained using the novel explicit dynamics FE model of the rolling element bearing presented in the previous chapter.

5.1.1 Aims

The aims of the work presented in this chapter are to:

- test the rolling element bearing having a manufactured line spall on its outer raceway subjected to various radial loads and rotational speeds;
- measure the vibration levels of the defective rolling element bearing;
- analyse the measured data using standard signal processing techniques associated with vibration-based monitoring of rolling element bearings;
- compare the experimental results with the numerical results obtained using the explicit FE model of the rolling element bearing; and to
- investigate the parametric effect of varying radial load and rotation speed on the vibration response of the defective rolling element bearing.

5.1.2 Structure

This chapter begins with a description of the experimental setup, which includes a description of the defective test bearing and the bearing test rig in Section 5.2. The analysis of the experimentally measured acceleration data, using the signal processing techniques described in the previous chapter, is presented in Section 5.3. Time, time–frequency, and frequency domain analyses of the measured data are presented in Sections 5.3.1 to 5.3.3 along with the corresponding analyses of the numerically modelled acceleration for the validation of the FE model of the rolling element bearing. The comparison of the results is summarised in Section 5.3.5. A mathematical formula is presented in Section 5.3.4 to estimate the size (length) of the defect in the (experimental) bearing using the time separation between the distinct acceleration signatures associated with the de-stressing and re-stressing of the rolling elements. In Section 5.4, the parametric effect of varying radial load and rotational speed on the vibration response of the bearing is discussed. Finally, conclusions are presented in Section 5.5.

5.2 Experimental setup

A description of the test bearing and the bearing test rig used to measure the vibration levels of the test bearing is provided in the following sections.

5.2.1 Test bearing with a manufactured line spall

A commonly used package bearing unit in the railway industry was considered for its vibration testing. The bearing has a number of rolling elements $N_r = 24$, nominal pitch diameter $D_p = 180.2\,\text{mm}$, mean roller diameter $D_r = 17.9\,\text{mm}$, and contact angle $\alpha = 9.1°$. A line spall of length $L_d = 10\,\text{mm}$ and depth $H_d = 0.2\,\text{mm}$, was manufactured on the outer raceway of the bearing using electric spark erosion. A

Figure 5.1: A photo of the line spall of circumferential length $L_d = 10\,\text{mm}$ and depth $H_d = 0.2\,\text{mm}$ machined on the outer raceway of the bearing using electric spark erosion.

photo of the machined line spall on the outer raceway of the test bearing is shown in Figure 5.1.

The dimensions of the bearing including the outer raceway line spall, which were used to build the analytical and FE models of the rolling element bearing presented in Chapters 3 and 4, respectively, were representative of the test bearing described above.

5.2.2 Bearing test rig

The bearing test rig shown in Figure 5.2 was available at the premises of Track IQ$^{\text{TM}}$ [11] and was used to conduct testing of the defective bearing. The test rig comprises a 15 kW three-phase induction motor, a steel structure to support the wheelset axle, a hydraulic piston–cylinder arrangement for applying the radial load, and a variable frequency drive unit (not shown in the figure) for controlling the speed of the motor. The defective bearing, referred to as the *test bearing* in Figure 5.2, and a non-defective bearing on the drive-end were press-fitted onto the axle using a roller bearing puller/installer [401]. The motor was coupled to the axle using V-belts and pulleys. The piston–cylinder arrangement applies radial loads of up to 100 kN to the wheel seat area on the axle through two metallic rollers. The test and drive-end bearings were seated on standard adapters (refer to Figure 1.6, Chapter 1, to see the adapters) which were supported on

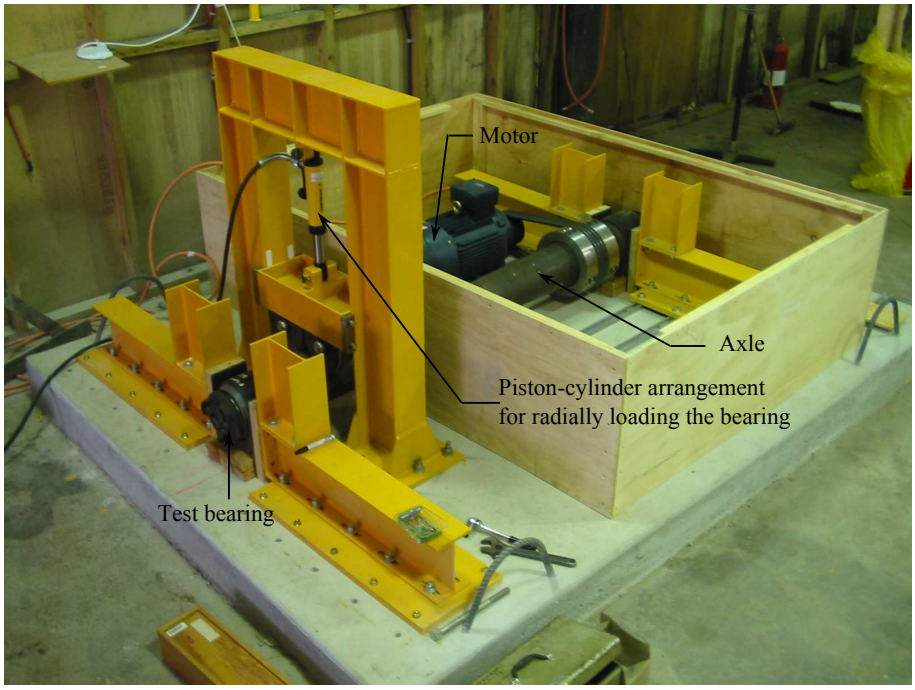

Figure 5.2: A photo of the bearing test rig used to conduct the testing of the defective rolling element bearing.

wooden blocks. The movement of the axle and bearings in the horizontal direction was constrained by sandwiching rubber-lined wooden blocks between the steel structure and the bearings. The test rig setup simulates the operation of the bearings in a typical railway application.

An accelerometer was stud mounted on a base that was attached to the test bearing using super glue (cyanoacrylate). It was mounted on the top of the bearing, diametrically opposite to the location of the outer raceway defect. A tachometer was mounted near the axle in order to measure its rotational speed. The experimental vibration data were acquired using a data acquisition system that comprises a National Instruments (NI) CompactDAQ along with a 3-channel NI 9232 I/O module for the accelerometer and an NI 9234 I/O module for the tachometer signal. The signals were sampled at the rate of 102.4 kHz. The reason for such a high sampling rate is that it was not clear at the beginning of the study what vibration characteristics were to be investigated. Therefore, the highest sampling rate that the equipment permitted was used. Although

a lower sampling rate has not been used during the experimentation work, the high sampling rate has ensured acquiring the impulsive characteristics associated with the re-stressing of the rolling elements with a maximum resolution.

5.3 Analyses of the measured vibration response of the test rolling element bearing

The aim of conducting the experimental work was to validate the numerical results obtained using the explicit dynamics FE model of the defective rolling element bearing presented in Chapter 4. As the FE modelling results were presented for the bearing subjected to a radial (vertical) load W of 50 kN and rotational speed n_s of 500 RPM, the experimentally measured vibration signatures of the defective test bearing corresponding to the aforementioned radial load and rotational speed are presented first along with the necessary comparison with the corresponding numerical FE modelling results. Keeping the rotational speed n_s of 500 RPM unchanged, the comparison between the measured and modelled results corresponding to radial loads W of 25 kN and 80 kN is presented next, and this is followed by the comparison of the results at two additional rotational speeds of 300 RPM and 800 RPM. While a radial load W of 25 kN corresponds to the load of an empty railway wagon on one of the axle bearings, a radial load of 80 kN corresponds to the bearing load of an almost fully loaded wagon. For a 1 m wheel diameter, a rotational speed n_s of 300 RPM corresponds to a train speed of approximately 55 km/hr, whereas a rotational speed of 800 RPM corresponds to the train speed of approximately 120 km/hr.

Table 5.1 presents a test matrix describing various loads and speeds for the experimental work and corresponding FE simulations: for each radial load W applied to the test bearing, it was rotated at three speeds n_s in a clockwise (CW) direction, and the vibration measurements were acquired. The FE simulations were also conducted at

Radial load W (kN)	Rotational speed n_s (RPM)	Direction
25, 50, 80	300, 500, 800	CW

Table 5.1: A matrix for the experimental testing of the rolling element bearing subjected to various radial loads W and rotational speeds n_s.

the loads and speeds described in the table, and the simulated results are compared with those of the measured results.

Similar to the analysis of the numerically modelled vibration results presented in Section 4.6.3, Chapter 4, the analysis of the experimentally measured data presented here is also divided into time, time–frequency, and frequency domain analyses. The analyses, which include implementation of standard signal processing techniques relevant to vibration-based monitoring of rolling elements bearings, are presented in the same chronological order as was followed for analysing the numerically modelled vibration time-traces. Refer to Sections 4.4 and 4.6 for the description of the signal processing techniques.

5.3.1 Time domain analysis

Results for a radial load W of 50 kN and rotational speed n_s of 500 RPM

Figure 5.3 shows the measured acceleration a_y time-trace of the defective test bearing under a radial load W of 50 kN and a rotational speed n_s of 500 RPM. Although the bearing acceleration was measured for approximately 10 seconds, the length of the acceleration time-trace shown here is only 30 ms, so it can be compared with the FE simulation results. The reason for solving the explicit FE model of the bearing for only 30 ms is that it takes extensive CPU (run time) hours to solve the model; for the case of the FE modelling results presented in Chapter 4, it was mentioned that the model took approximately 250 CPU hours to solve using parallel computing [388].

Being consistent with the usage of the markers throughout this thesis, the distinct vibration signatures associated with the de-stressing and re-stressing of the rolling el-

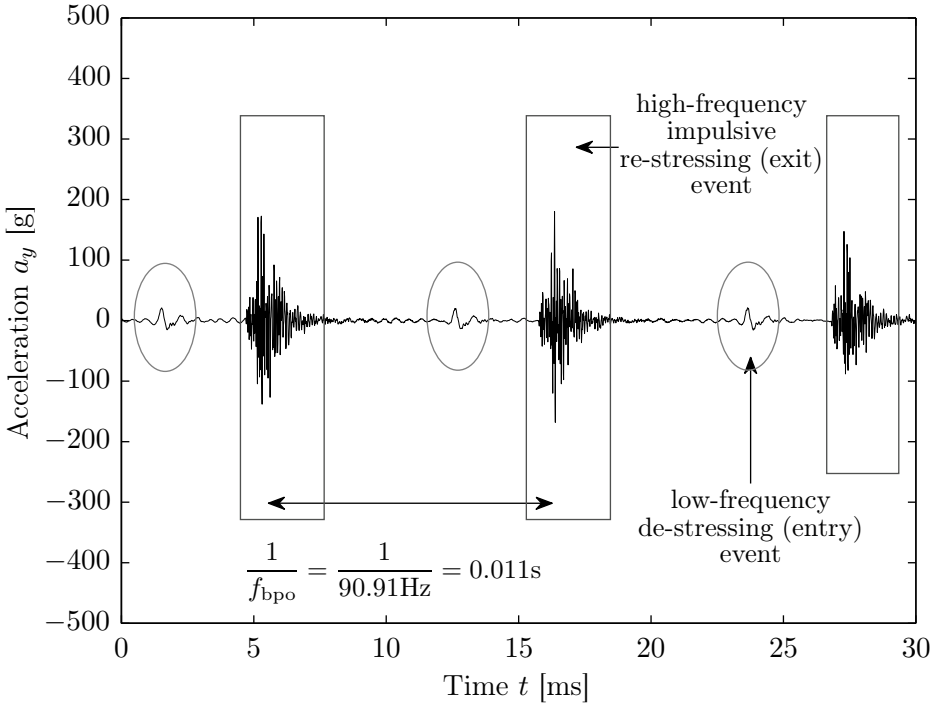

Figure 5.3: Experimentally measured acceleration a_y of the defective test bearing for $W = 50\,\text{kN}$ and $n_s = 500\,\text{RPM}$, highlighting the de-stressing and re-stressing events using the elliptical and rectangular markers, respectively.

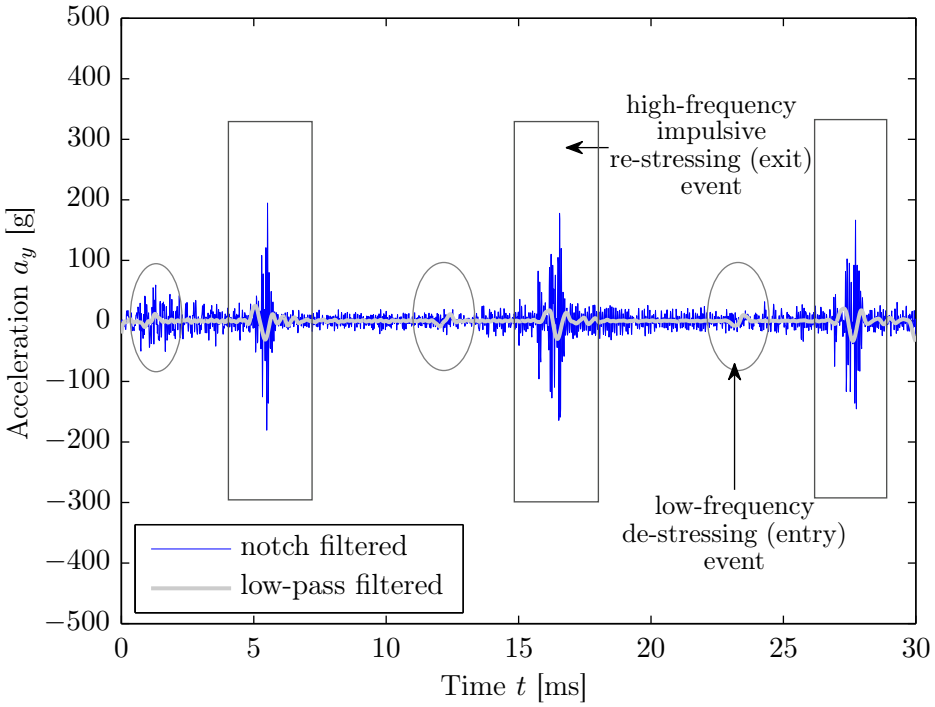

Figure 5.4: Numerically modelled acceleration a_y time-trace that has been notch and low-pass filtered as shown in Figures 4.13 and 4.22, respectively; the de-stressing and re-stressing events are highlighted using the elliptical and rectangular markers, respectively.

ements, as they enter into and exit out of the line spall, respectively, in Figure 5.3, are highlighted using elliptical and rectangular markers, respectively. While the peak instantaneous acceleration level of the de-stressing event is about $\pm 20\,\mathrm{g}$, it is approximately $\pm 180\,\mathrm{g}$ for the defect-related impulses due to the re-stressing of the rolling elements. The time separation between the consecutive events, either de-stressing or re-stressing, as indicated in Figure 5.3, corresponds to the outer raceway defect frequency (BPFO) f_{bpo} of 90.91 Hz. It agrees favourably with the numerically estimated f_{bpo} of 90.91 Hz using the numerical acceleration results in Figure 4.13, Chapter 4, which is different by 0.9% from the theoretical estimate of 90.07 Hz obtained using Equation (4.9). The slight difference between the experimental and theoretical estimations is because the analytical formula, shown in Equation (4.9), does not account for the slippage of the rolling elements [95, 96], which was accounted in the explicit FE analysis of the rolling element bearing undertaken here.

For comparison, a plot of the experimentally measured and numerically modelled acceleration a_y time-traces together on a single graph will cause cluttered results due to the presence of residual numerical noise in the latter results. Instead, the modelled acceleration results from the previous chapter are reproduced here in Figure 5.4. The reasons for the numerical noise in the FE simulation results were described in Section 4.5 of the previous chapter. It was also mentioned that despite filtering the numerical noise at the rolling element-to-outer raceway rolling contact noise frequency $f^{o}_{\mathrm{noise}} = 4671\,\mathrm{Hz}$, some (random) noise still remains in the notch filtered numerical acceleration time-trace. This noise is due to the adaptive time-stepping $\Delta t_{\mathrm{stable}}$ (refer to Sections 4.2.5.1 and 4.5.1) and slippage of the rotating components.

In Figure 5.4, the notch filtered and low-pass filtered numerical acceleration a_y time-traces are represented using the thin, blue-coloured, and thick, gray-coloured, lines, respectively. It was mentioned earlier in Section 4.6.2, Chapter 4, that the numerical acceleration results were low-pass filtered in order to enhance the low-frequency characteristic signatures associated with the de-stressing of the rolling elements, which

were buried in the numerical noise. The enhancement of the low-frequency de-stressing event, which corresponds to the entry of the rolling elements into the defect, was achieved at the expense of compromising the high-frequency impulsive characteristics of the re-stressing of the rolling elements. It should be noted that the low-pass filtered acceleration time-trace was not used in the data analysis presented in Section 4.6, Chapter 4.

From Figures 5.3 and 5.4, it is evident that the time instances related to the occurrences of the de-stressing and re-stressing events for experimentally measured and numerically modelled results are similar. The measured and modelled instantaneous acceleration levels associated with the re-stressing of the rolling elements are also comparable — approximately 180 g. Furthermore, the acceleration levels related to de-stressing event are approximately 20 g and 15 g for the measured and modelled data, respectively, which compare favourably with one another.

Results for radial loads W of 25 kN and 80 kN, and a rotational speed n_s of 500 RPM

Findings similar to those in Figures 5.3 and 5.4 were also observed for additional measurements and corresponding FE simulation results. Figure 5.5 shows a favourable comparison between the experimentally measured and numerically modelled acceleration a_y time-traces of the rolling element bearing corresponding to radial loads W of 25 kN and 80 kN at a rotational speed n_s of 500 RPM. The measured acceleration signals are shown in Figures 5.5a and 5.5c, whereas the corresponding modelled acceleration time-traces, both notch filtered and low-pass filtered, are shown in Figures 5.5b and 5.5d, along with the markers highlighting the entry and exit of the rolling elements into and out of the defect, respectively.

The purpose of presenting these figures is to show a comparison between the experimentally measured and numerically modelled results. Parametric effects of varying radial load W and rotational speed n_s on the vibration response of the rolling element

bearing will be discussed in Section 5.4. However, as can be seen from Figure 5.5, the instantaneous acceleration levels of the defect-related impulses increase with the increasing load for both measured and modelled acceleration results.

Results for radial loads W of 25 kN, 50 kN and 80 kN, and rotational speeds n_s of 300 RPM and 800 RPM

Figures 5.6, 5.7, and 5.8 show a comparison of the measured acceleration a_y time-traces of the test bearing with those of the numerically modelled acceleration results obtained using the FE model of the bearing for radial loads W of 25 kN, 50 kN, and 80 kN, respectively. Each figure comprises four subplots: subplots (a, c) show the measured acceleration signals corresponding to the rotational speeds n_s of 300 RPM and 800 RPM, respectively, and subplots (b, d) show the corresponding modelled acceleration time-traces. It is evident from the figures that the modelled instantaneous acceleration signals compare reasonably well with those of the measured data.

From the results in Figures 5.6, 5.7, and 5.8, it is clear that the acceleration levels increase with the increasing radial loads. For the modelled results, along with the levels of the defect-related impulses, the instantaneous acceleration levels between the impulses also generally increase. Although not annotated, the low- and high-frequency events associated with the entry and exit of the rolling elements into and out of the defect, respectively, can be seen in Figures 5.6, 5.7, and 5.8. As described earlier, the effects of varying load W and speed n_s on the acceleration signals will be discussed in Section 5.4.

Previous FE models versus the novel explicit dynamics FE model of the bearing presented in Chapter 4 of this thesis

Revisiting previous explicit FE models of rolling element bearings [118–120], reviewed in Section 2.3.4.3, Chapter 2 — for the model presented in reference [118], the predicted acceleration level of 10^7 g was not compared with measured results, whereas for the

models in references [119, 120], the predicted acceleration levels were 4,000 g [119] and 15,000 g [120] compared to the experimentally measured levels of 100 g and 10 g, respectively. The potential errors in the previous FE models were discussed during their critical review.

In contrast to the FE models discussed previously in the literature, the acceleration levels predicted by the explicit dynamics FE model of the bearing developed here compare favourably with the corresponding measured results. Although the acceleration signals from the FE simulations contain numerical noise, the results from the simulations and the measured instantaneous acceleration levels of the vibration signatures associated with the de-stressing and re-stressing of the rolling elements show good agreement.

Time–frequency analysis of the experimentally measured acceleration time-traces is presented next.

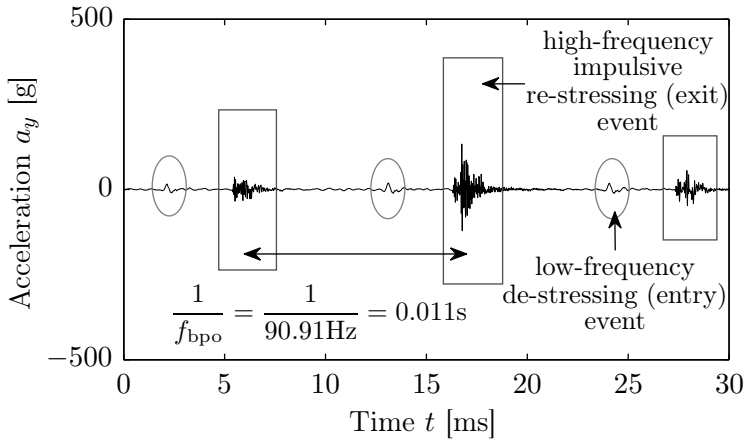

(a) Measured acceleration a_y time-trace for $W = 25\,\text{kN}$ and $n_s = 500\,\text{RPM}$.

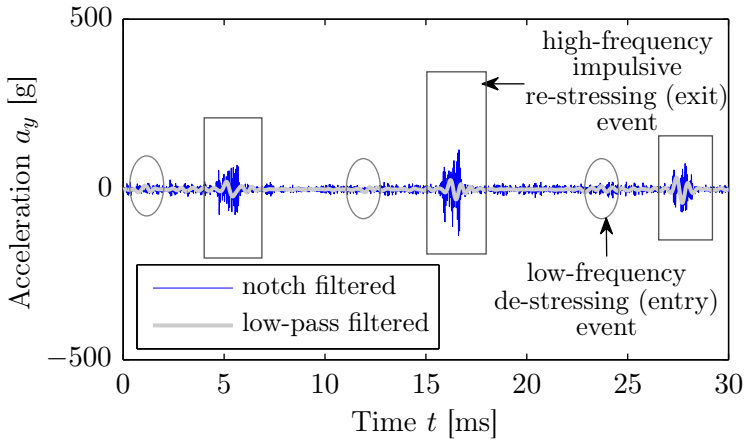

(b) Modelled acceleration a_y time-trace for $W = 25\,\text{kN}$ and $n_s = 500\,\text{RPM}$.

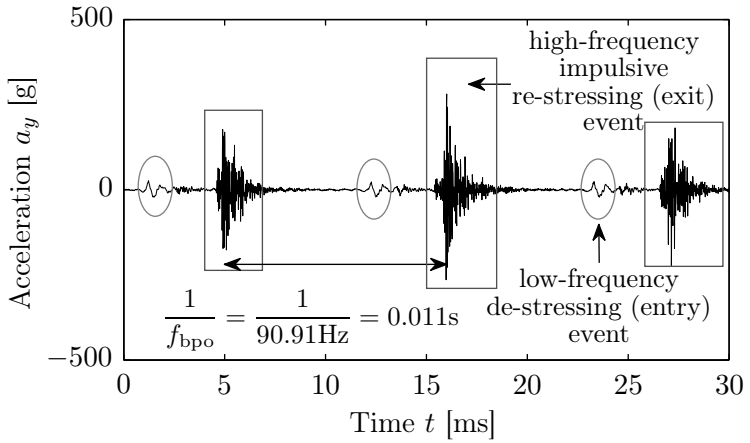

(c) Measured acceleration a_y time-trace for $W = 80\,\text{kN}$ and $n_s = 500\,\text{RPM}$.

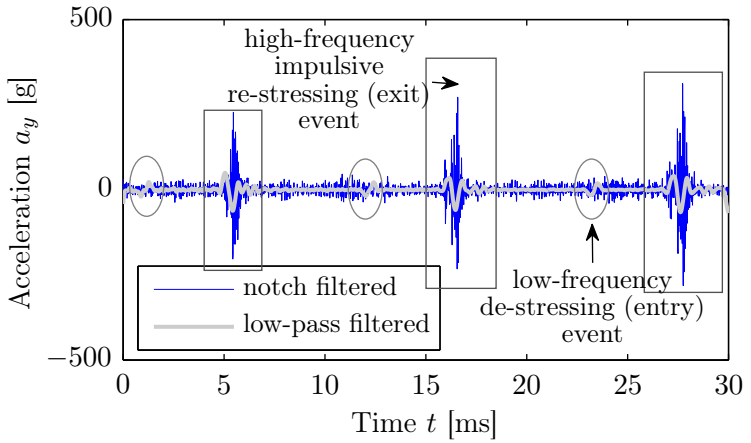

(d) Modelled acceleration a_y time-trace for $W = 80\,\text{kN}$ and $n_s = 500\,\text{RPM}$.

Figure 5.5: Comparison of the experimentally measured and numerically modelled acceleration a_y times-traces of the rolling element bearing for a rotational speed n_s of 500 RPM, and radial loads W of 25 kN and 80 kN.

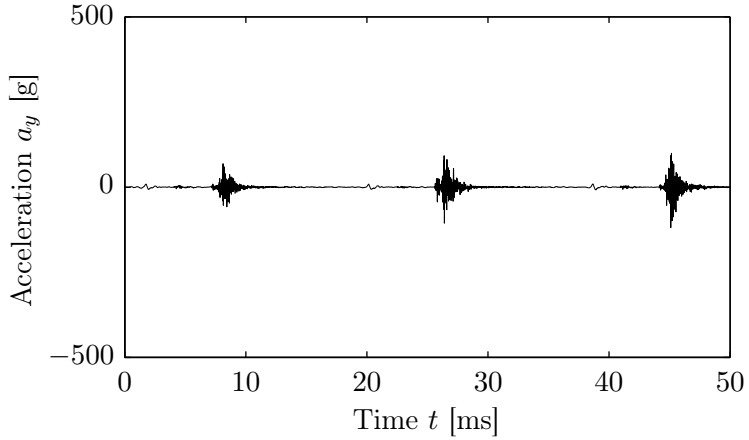

(a) Measured acceleration a_y time-trace for $W = 25\,\text{kN}$ and $n_s = 300\,\text{RPM}$.

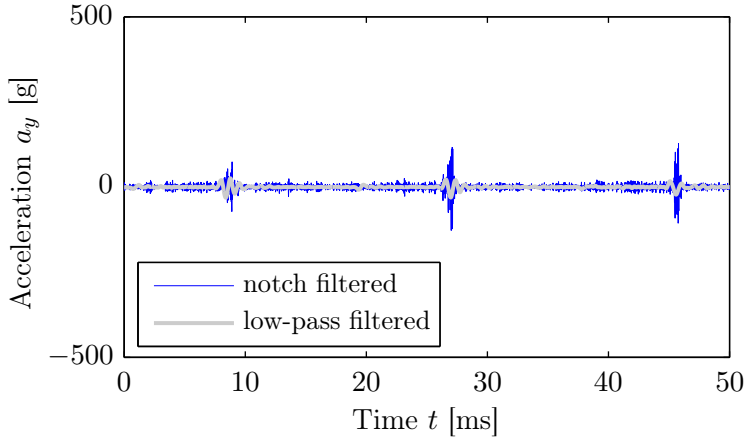

(b) Modelled acceleration a_y time-trace for $W = 25\,\text{kN}$ and $n_s = 300\,\text{RPM}$.

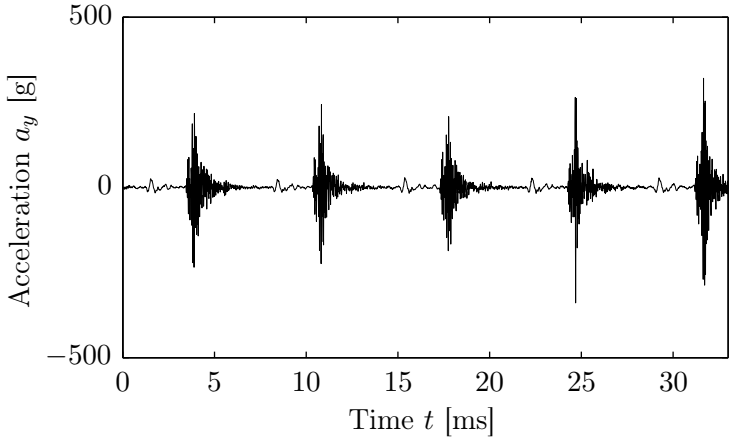

(c) Measured acceleration a_y time-trace for $W = 25\,\text{kN}$ and $n_s = 800\,\text{RPM}$.

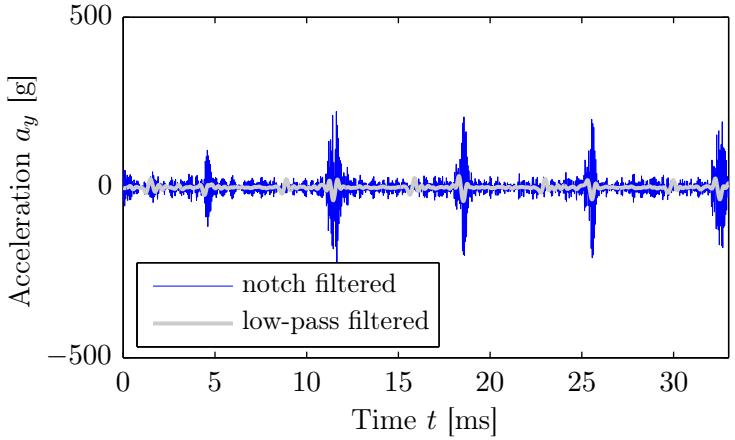

(d) Modelled acceleration a_y time-trace for $W = 25\,\text{kN}$ and $n_s = 800\,\text{RPM}$.

Figure 5.6: Comparison of the experimentally measured and numerically modelled acceleration a_y times-traces of the rolling element bearing for a radial load W of 25 kN, and rotational speeds n_s of 300 RPM and 800 RPM.

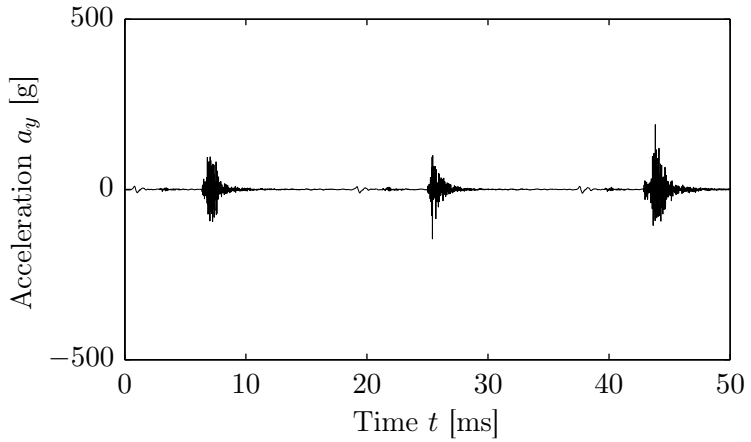

(a) Measured acceleration a_y time-trace for $W = 50\,\text{kN}$ and $n_s = 300\,\text{RPM}$.

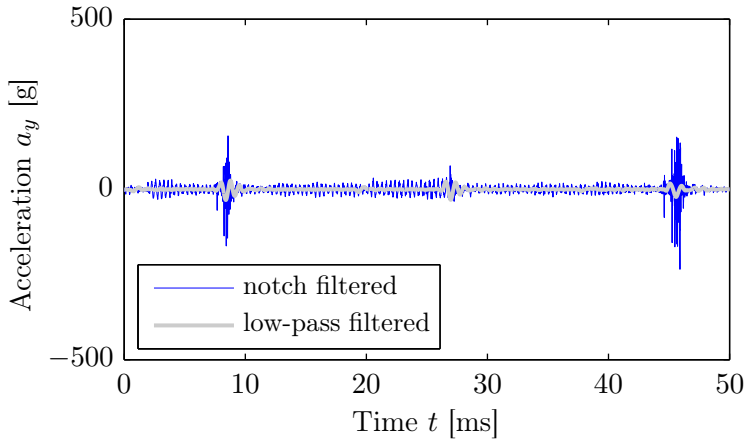

(b) Modelled acceleration a_y time-trace for $W = 50\,\text{kN}$ and $n_s = 300\,\text{RPM}$.

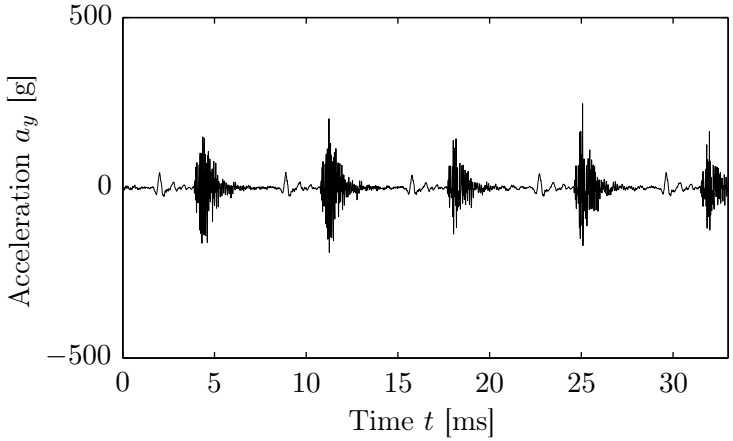

(c) Measured acceleration a_y time-trace for $W = 50\,\text{kN}$ and $n_s = 800\,\text{RPM}$.

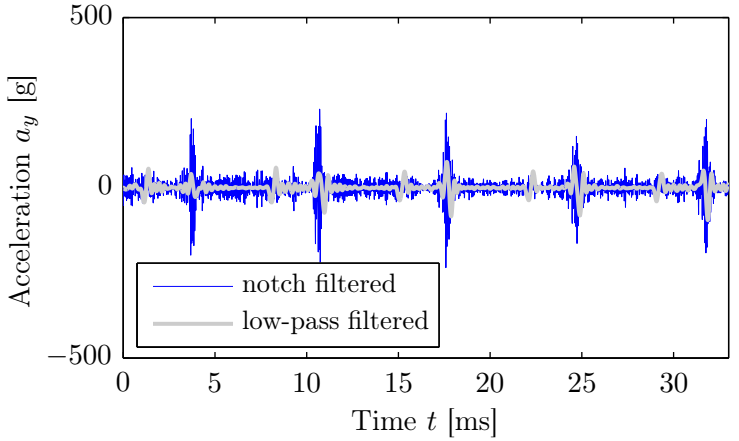

(d) Modelled acceleration a_y time-trace for $W = 50\,\text{kN}$ and $n_s = 800\,\text{RPM}$.

Figure 5.7: Comparison of the experimentally measured and numerically modelled acceleration a_y times-traces of the rolling element bearing for a radial load W of 50 kN, and rotational speeds n_s of 300 RPM and 800 RPM.

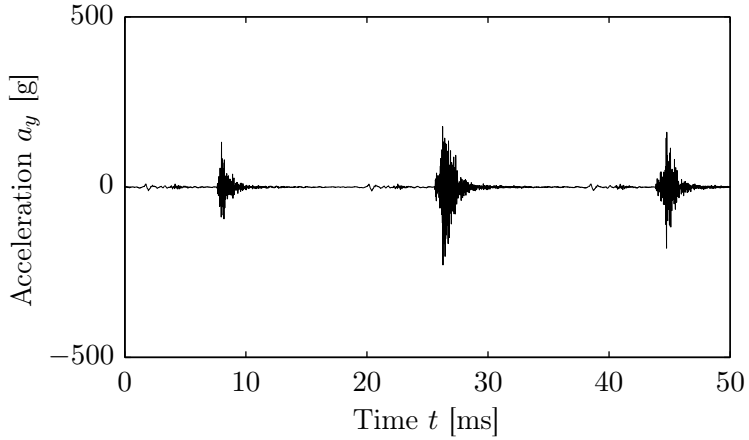

(a) Measured acceleration a_y time-trace for $W = 80\,\text{kN}$ and $n_s = 300\,\text{RPM}$.

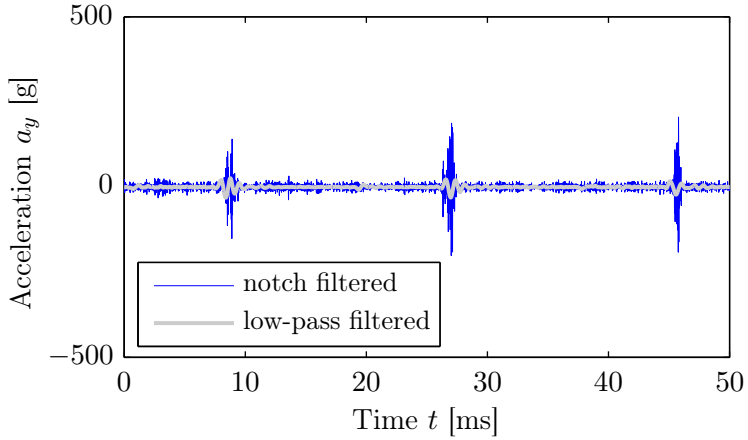

(b) Modelled acceleration a_y time-trace for $W = 80\,\text{kN}$ and $n_s = 300\,\text{RPM}$.

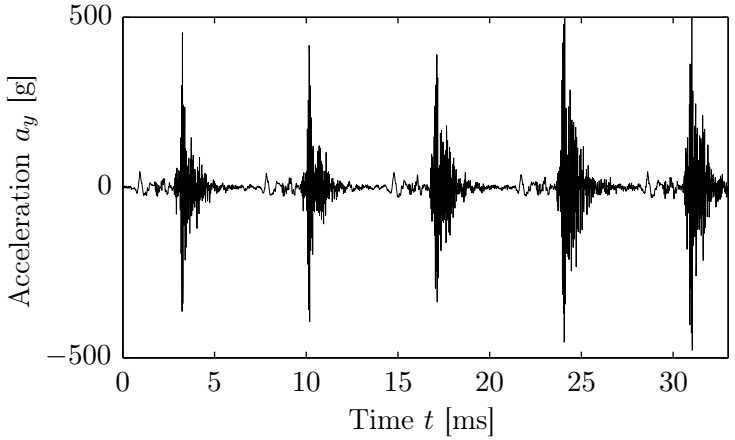

(c) Measured acceleration a_y time-trace for $W = 80\,\text{kN}$ and $n_s = 800\,\text{RPM}$.

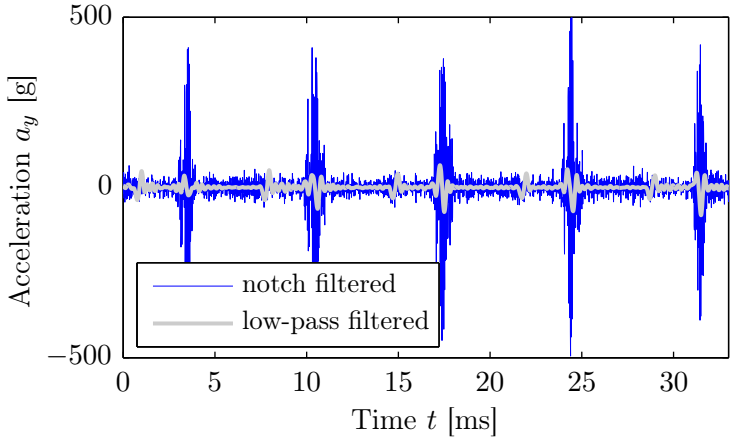

(d) Modelled acceleration a_y time-trace for $W = 80\,\text{kN}$ and $n_s = 800\,\text{RPM}$.

Figure 5.8: Comparison of the experimentally measured and numerically modelled acceleration a_y times-traces of the rolling element bearing for a radial load W of 80 kN, and rotational speeds n_s of 300 RPM and 800 RPM.

5.3.2 Time–frequency analysis

Results for a radial load W of 50 kN and rotational speed n_s of 500 RPM

Figure 5.9 shows a spectrogram of the measured acceleration a_y time-trace, shown in Figure 5.3, corresponding to a radial load W of 50 kN and rotational speed n_s of 500 RPM. The distinction between the de-stressing and re-stressing of the rolling elements, which are indicated using the elliptical and rectangular markers, respectively, is clearly evident in the spectrogram plot. Similar to the findings observed in the spectrogram of the numerical acceleration signal in Figure 4.19, Chapter 4, it can be seen from Figure 5.9 that the energy (or power) of the signals related to the de-stressing event is concentrated below 3 kHz, whereas the impulses generated during the re-stressing of the rolling elements appear to be characterised mainly by energy in the high-frequency band of 10–30 kHz. These findings show excellent agreement with those observed in the spectrogram plot of the numerical acceleration signal in Figure 4.19, where the energy of the signals pertinent to de-stressing and re-stressing events was found to be mainly concentrated below 3 kHz and 10–25 kHz, respectively.

It should be noted that the colour scale of the power spectrum levels shown using colour bars in the spectrogram plots of the measured and modelled acceleration time-traces in Figures 5.9 and 4.19, respectively, are different; -80 dB to 20 dB re $1\,(\mathrm{m/s^2})^2/\mathrm{Hz}$ for measured and -40 dB to 30 dB re $1\,(\mathrm{m/s^2})^2/\mathrm{Hz}$ for modelled results. This is due to the numerical noise in the modelled results which makes the distinct characteristics of the signatures associated with the de-stressing and re-stressing events less clear if the colour scale of the modelled results was made similar to the measured data. Therefore, the colour scale of the spectrogram plots for the modelled vibration results was chosen so as to reasonably highlight the two aforementioned events.

In Figure 5.9, there is also a slight indication of the low-frequency content at the timings corresponding to the re-stressing events. As mentioned earlier, this is due to the generation of the defect-related impulses, which excite both high- and low-frequency

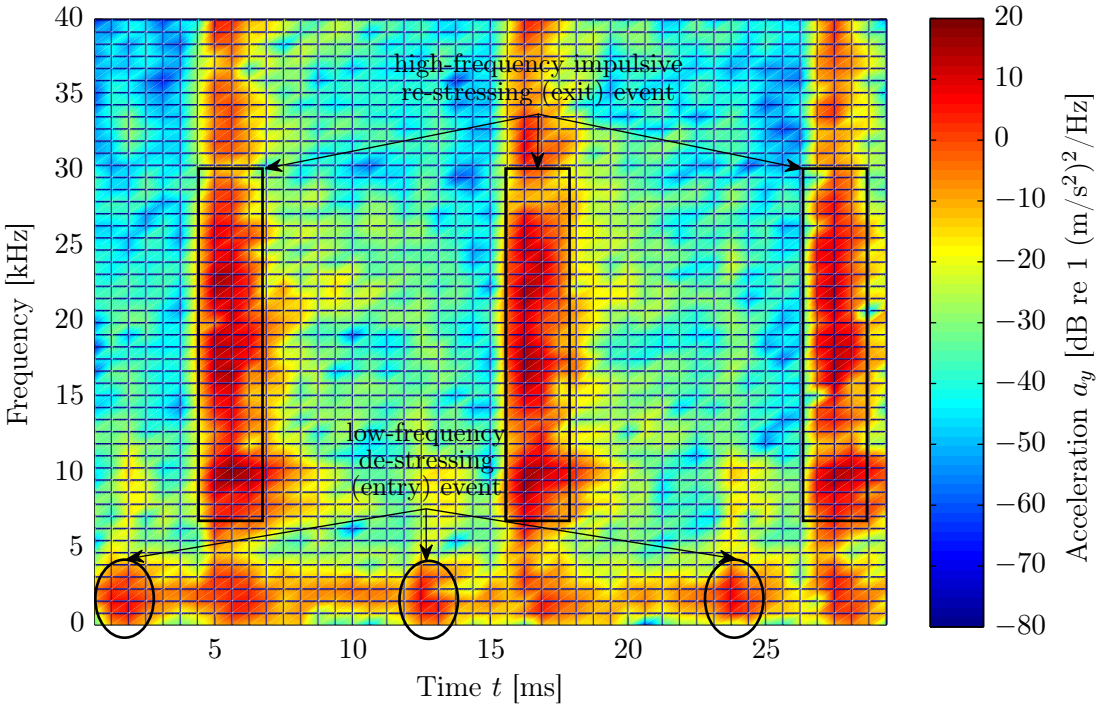

Figure 5.9: A spectrogram of the experimentally measured acceleration a_y time-trace shown in Figure 5.3 for a radial load W of 50 kN and rotational speed n_s of 500 RPM, highlighting the de-stressing and re-stressing events using the elliptical and rectangular markers, respectively.

resonance modes of the bearing.

Results for radial loads W of 25 kN, 50 kN and 80 kN, and rotational speeds n_s of 300 RPM and 800 RPM

For various radial loads W and rotational speeds n_s, findings similar to those in Figure 5.9 can also be observed in Figures 5.10, 5.11, 5.12 and 5.13, which compare the spectrogram plots of the experimentally measured and numerically modelled acceleration a_y time-traces shown in Figures 5.5, 5.6, 5.7 and 5.8, respectively.

The low-frequency de-stressing and high-frequency re-stressing of the rolling elements, respectively, are clearly evident in the spectrogram plots of the measured acceleration data shown in subplots (a, c) of Figures 5.10, 5.11, 5.12 and 5.13. However, the events are comparatively less clear in the spectrogram plots of the modelled acceleration time-traces shown in subplots (b, d) of Figures 5.10, 5.11, 5.12 and 5.13. This

is due to the broadband nature of the numerical noise in the modelled results. For the same reason, as described above, the colour scale of the spectrogram plots for modelled vibration time-traces is different to that of the measured data.

From subplots (b, d) of Figures 5.10, 5.11, 5.12 and 5.13, the energy of the numerical noise is evident between the time instances related to the re-stressing of the rolling elements, although its level is comparatively lower than that of the defect-related impulses. In contrast, the measured acceleration data does not suffer from the noise problem; thereby, providing a clear distinction between the de-stressing and re-stressing events. Nevertheless, the comparison of the spectrogram plots of the measured and modelled data shows a reasonable agreement in terms of the low- and high-frequency de-stressing and re-stressing events, respectively.

Frequency domain analysis is presented in the next section, and it will be shown that the measured and modelled power spectrum results compare favourably with one another.

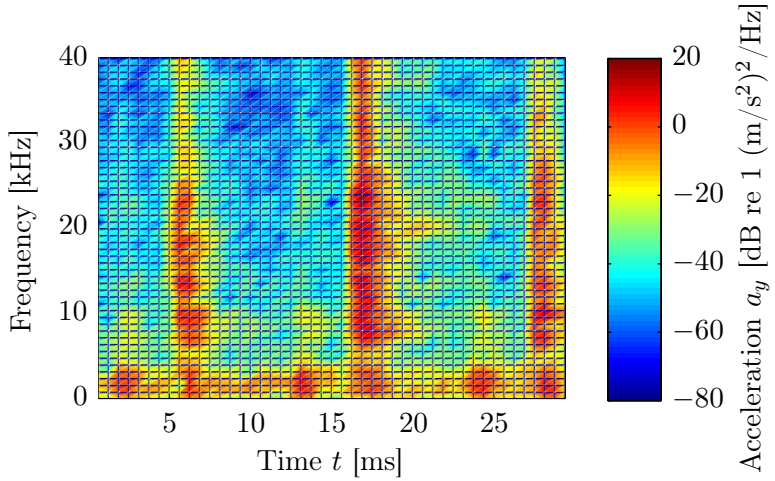

(a) A spectrogram of the measured acceleration a_y time-trace shown in Figure 5.5a for $W = 25\,\text{kN}$ and $n_s = 500\,\text{RPM}$.

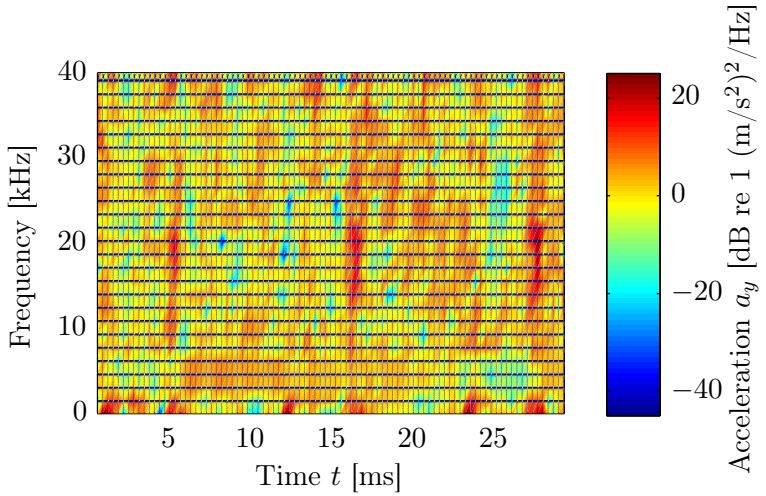

(b) A spectrogram of the modelled acceleration a_y time-trace shown in Figure 5.5b for $W = 25\,\text{kN}$ and $n_s = 500\,\text{RPM}$.

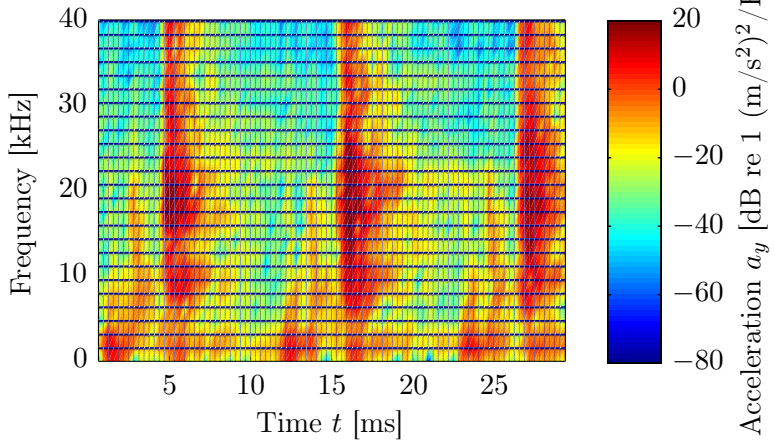

(c) A spectrogram of the measured acceleration a_y time-trace shown in Figure 5.5c for $W = 80\,\text{kN}$ and $n_s = 500\,\text{RPM}$.

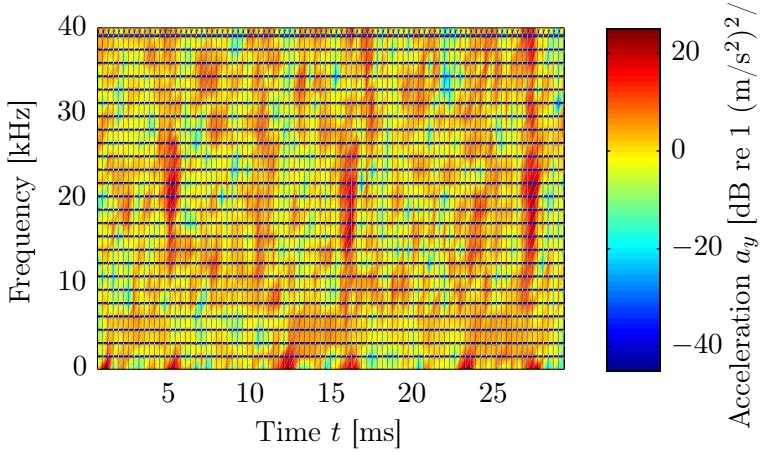

(d) A spectrogram of the modelled acceleration a_y time-trace shown in Figure 5.5d for $W = 80\,\text{kN}$ and $n_s = 500\,\text{RPM}$.

Figure 5.10: Comparison of the spectrograms of the experimentally measured and numerically modelled acceleration a_y time-traces of the rolling element bearing for a rotational speed n_s of 500 RPM, and radial loads W of 25 kN and 80 kN.

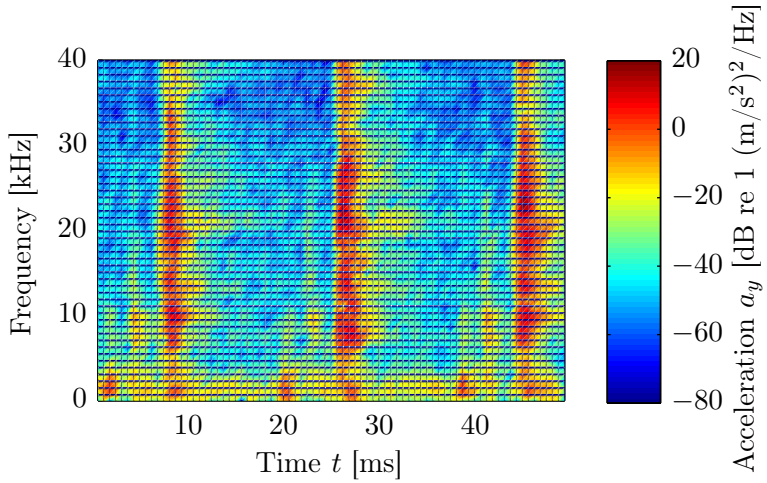

(a) A spectrogram of the measured acceleration a_y time-trace shown in Figure 5.6a for $W = 25\,\mathrm{kN}$ and $n_s = 300\,\mathrm{RPM}$.

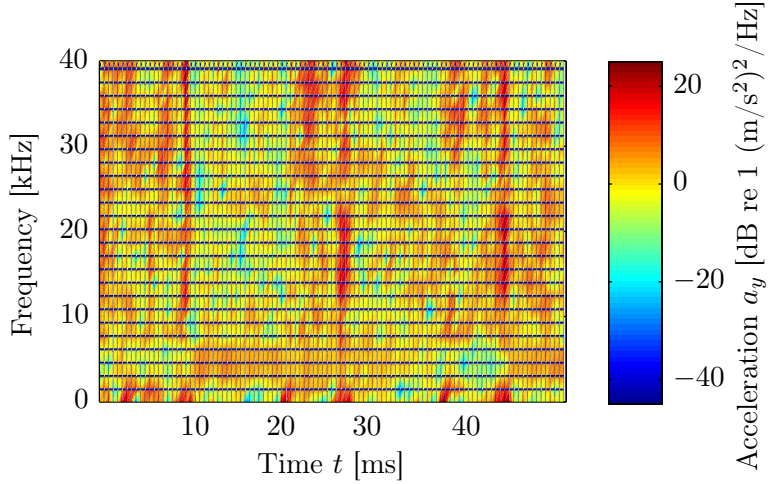

(b) A spectrogram of the modelled acceleration a_y time-trace shown in Figure 5.6b for $W = 25\,\mathrm{kN}$ and $n_s = 300\,\mathrm{RPM}$.

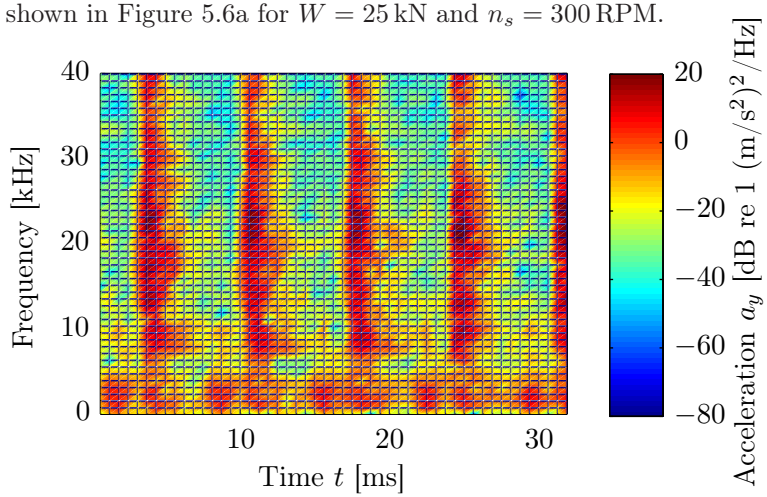

(c) A spectrogram of the measured acceleration a_y time-trace shown in Figure 5.6c for $W = 25\,\mathrm{kN}$ and $n_s = 800\,\mathrm{RPM}$.

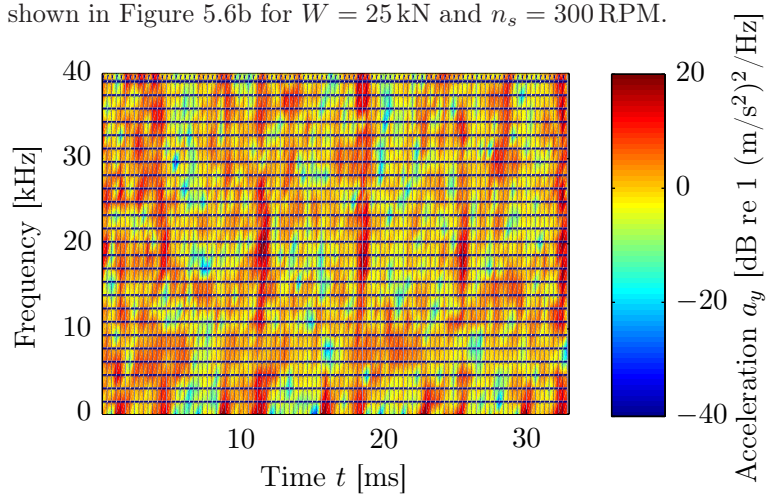

(d) A spectrogram of the modelled acceleration a_y time-trace shown in Figure 5.6d for $W = 25\,\mathrm{kN}$ and $n_s = 800\,\mathrm{RPM}$.

Figure 5.11: Comparison of the spectrograms of the experimentally measured and numerically modelled acceleration a_y time-traces of the rolling element bearing for a radial load W of 25 kN, and rotational speeds n_s of 300 RPM and 800 RPM.

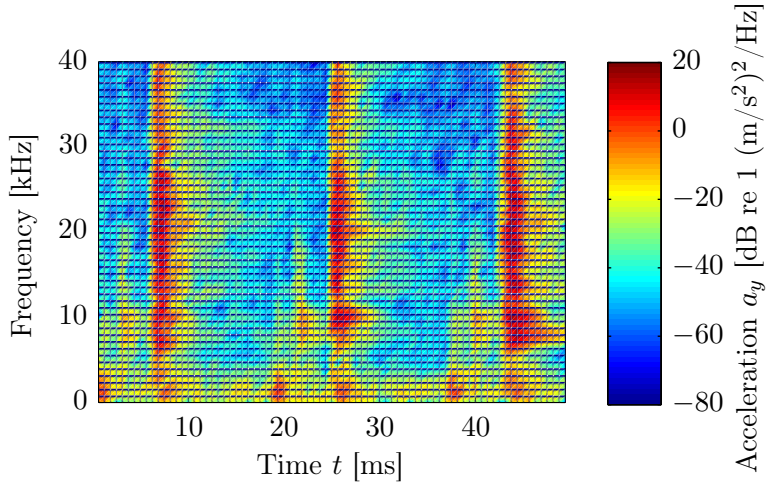

(a) A spectrogram of the measured acceleration a_y time-trace shown in Figure 5.7a for $W = 50\,\text{kN}$ and $n_s = 300\,\text{RPM}$.

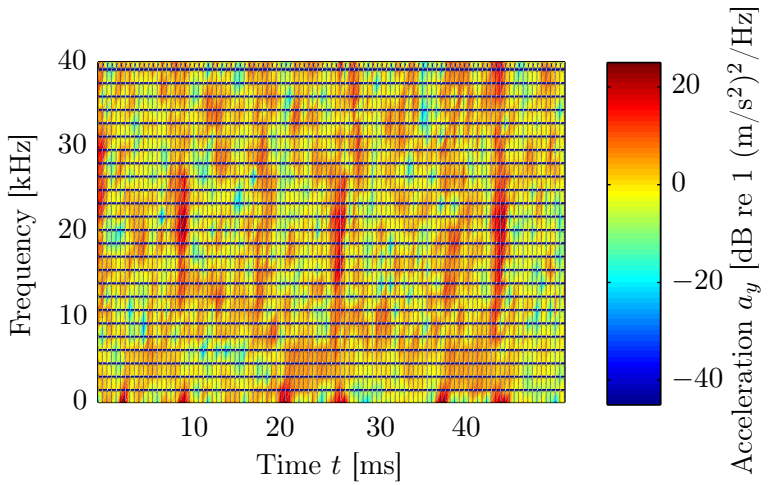

(b) A spectrogram of the modelled acceleration a_y time-trace shown in Figure 5.7b for $W = 50\,\text{kN}$ and $n_s = 300\,\text{RPM}$.

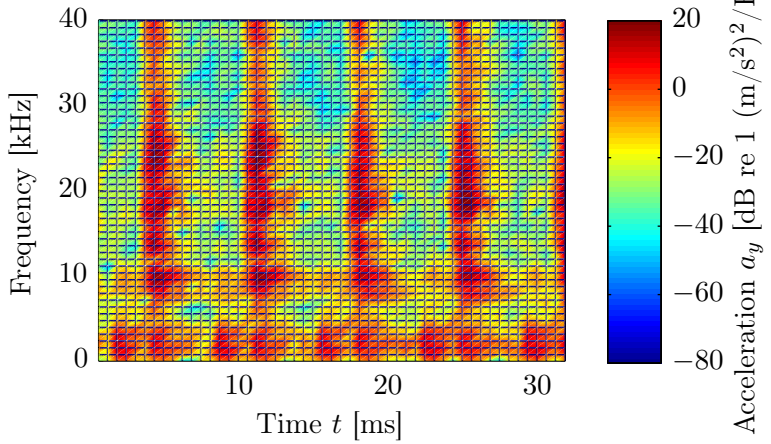

(c) A spectrogram of the measured acceleration a_y time-trace shown in Figure 5.7c for $W = 50\,\text{kN}$ and $n_s = 800\,\text{RPM}$.

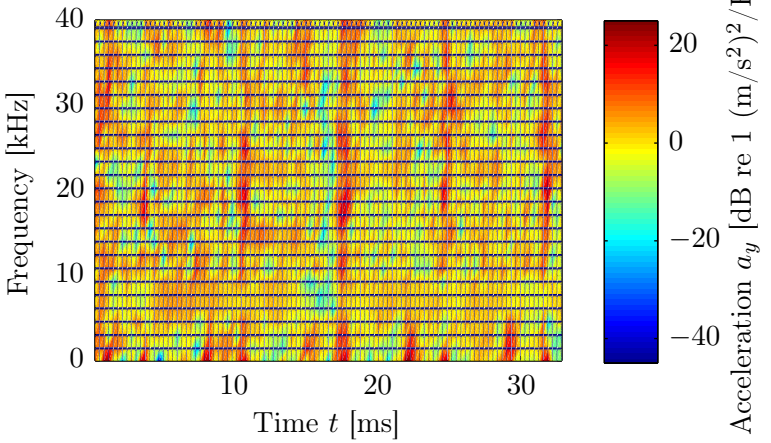

(d) A spectrogram of the modelled acceleration a_y time-trace shown in Figure 5.7d for $W = 50\,\text{kN}$ and $n_s = 800\,\text{RPM}$.

Figure 5.12: Comparison of the spectrograms of the experimentally measured and numerically modelled acceleration a_y time-traces of the rolling element bearing for a radial load W of 50 kN, and rotational speeds n_s of 300 RPM and 800 RPM.

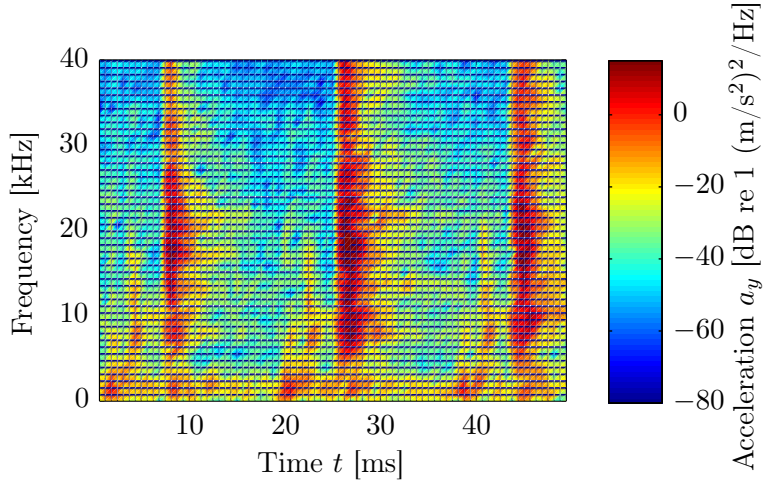

(a) A spectrogram of the measured acceleration a_y time-trace shown in Figure 5.8a for $W = 80\,\mathrm{kN}$ and $n_s = 300\,\mathrm{RPM}$.

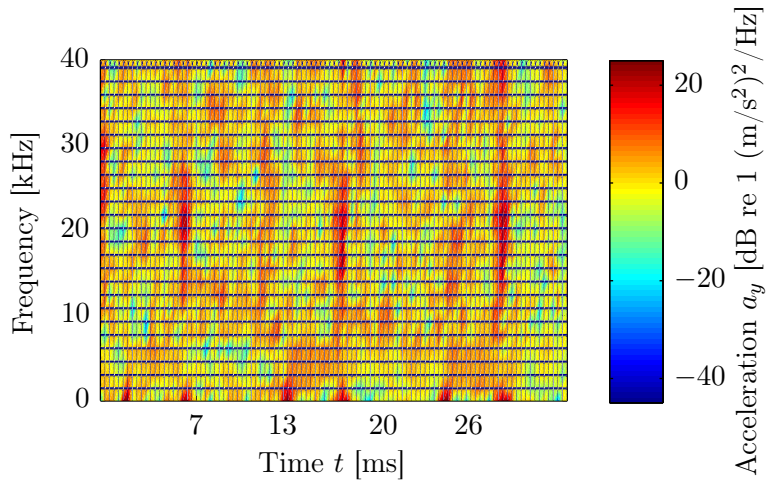

(b) A spectrogram of the modelled acceleration a_y time-trace shown in Figure 5.8b for $W = 80\,\mathrm{kN}$ and $n_s = 300\,\mathrm{RPM}$.

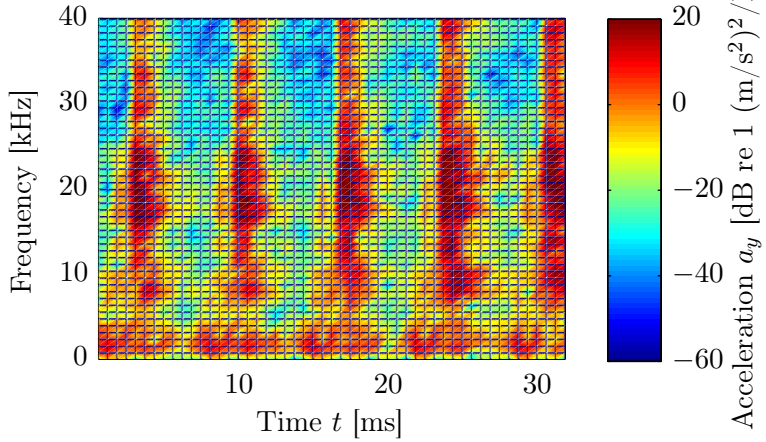

(c) A spectrogram of the measured acceleration a_y time-trace shown in Figure 5.8c for $W = 80\,\mathrm{kN}$ and $n_s = 800\,\mathrm{RPM}$.

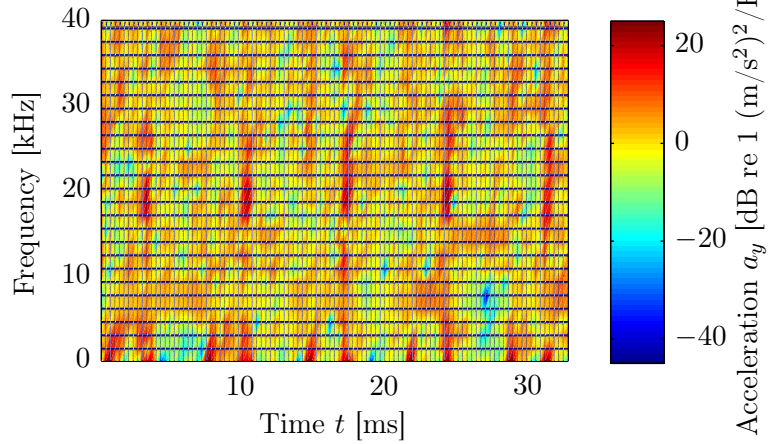

(d) A spectrogram of the modelled acceleration a_y time-trace shown in Figure 5.8d for $W = 80\,\mathrm{kN}$ and $n_s = 800\,\mathrm{RPM}$.

Figure 5.13: Comparison of the spectrograms of the experimentally measured and numerically modelled acceleration a_y time-traces of the rolling element bearing for a radial load W of 80 kN, and rotational speeds n_s of 300 RPM and 800 RPM.

5.3.3 Frequency domain analysis

In this section, frequency domain analysis of the measured acceleration data is presented. The sequence of the signal processing techniques established in Section 4.6.3, Chapter 4, for presenting a frequency domain analysis of the numerically modelled vibration signals, is also followed here. Initially, the spectral kurtosis [25] and kurtogram [26] are generated in order to seek the impulsive bands to be used for demodulating the acceleration signal, followed by envelope analysis [30, 251, 252], and finally, narrow band and one-third octave band spectra are shown. As the aim of conducting the frequency domain analysis is to primarily compare the results of envelope analysis of the measured and modelled acceleration signals, the spectral kurtosis and kurtogram plots, which are tools used prior to implementing the envelope analysis technique, are only shown for a single measurement case corresponding to a radial load W of 50 kN and rotational speed n_s of 500 RPM. The results of envelope analysis and one-third octave band spectra are shown for all the nine measurement cases described in Table 5.1.

5.3.3.1 Spectral kurtosis

For various window lengths N_w (power of 2), Figure 5.14 shows the spectral kurtoses [25] of the measured acceleration a_y time-trace shown in Figure 5.3 corresponding to a radial load W of 50 kN and rotational speed n_s of 500 RPM. The results show that the impulsive characteristics of the measured acceleration signal is between 10 kHz and 25 kHz. This favourably matches the findings of the spectral kurtoses of the numerical acceleration a_y signal in Figure 4.23, Chapter 4, where the defect-related impulsivity was generally found to be between 12 kHz and 23 kHz.

5.3.3.2 Kurtogram

To find the most impulsive frequency band, a kurtogram [26] of the measured acceleration a_y signal in Figure 5.3 was generated, and the corresponding plot is shown in

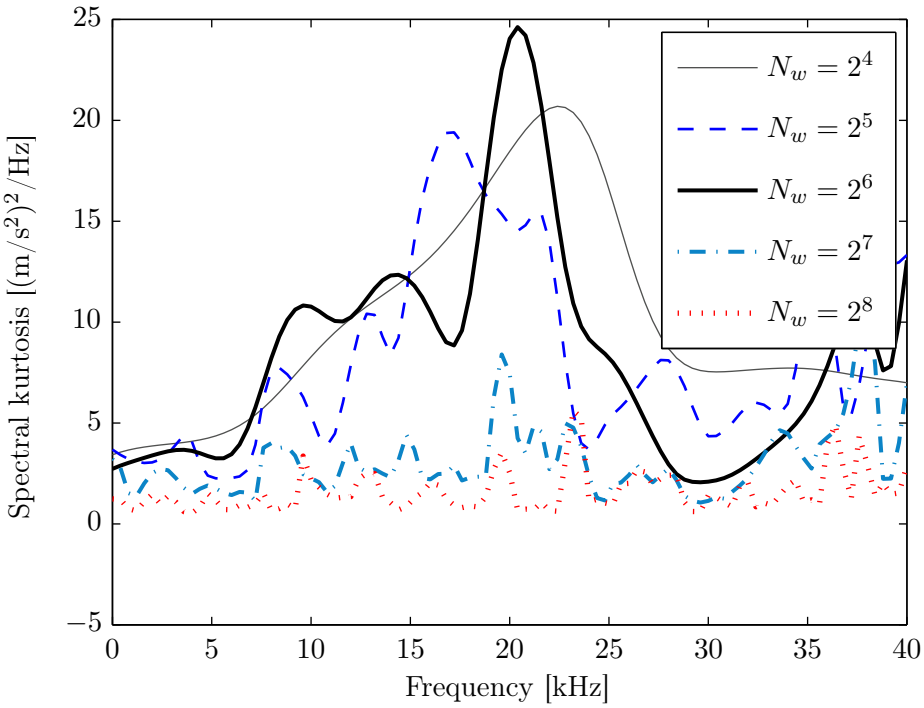

Figure 5.14: A spectral kurtosis plot of the experimentally measured acceleration a_y time-trace shown in Figure 5.3 corresponding to a radial load W of 50 kN and rotational speed n_s of 500 RPM for various window lengths N_w.

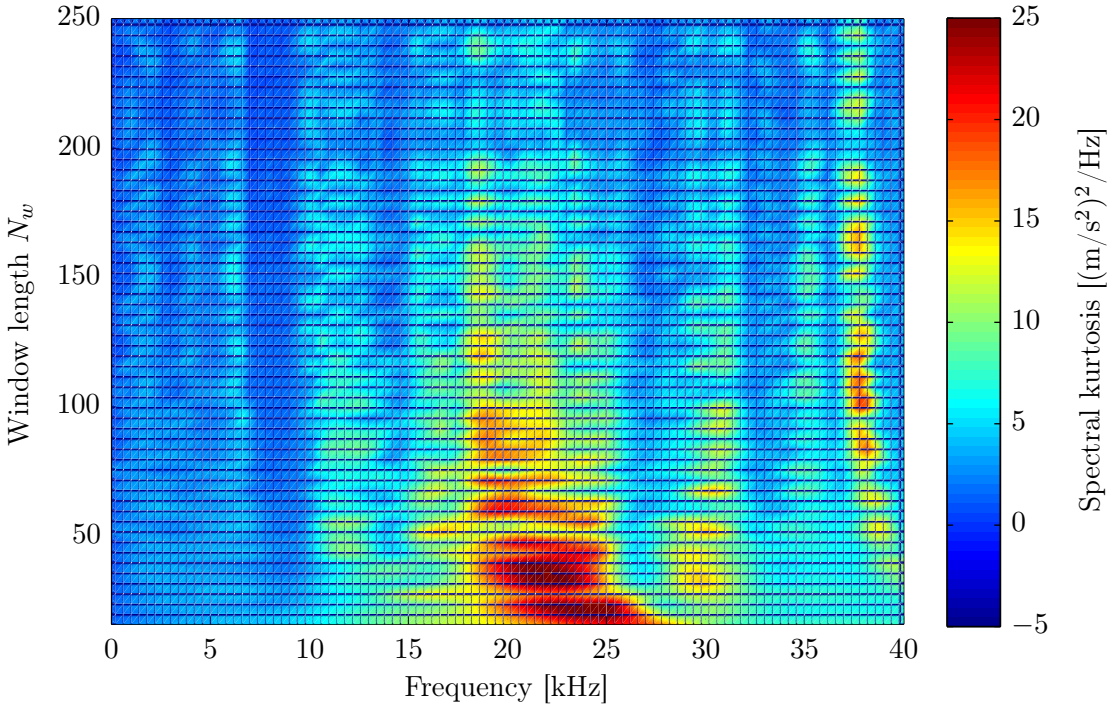

Figure 5.15: A kurtogram of the experimentally measured acceleration a_y time-trace shown in Figure 5.3 for a radial load W of 50 kN and rotational speed n_s of 500 RPM.

Figure 5.15. It is clear from the figure that the energy of the defect-related impulses is concentrated between 20 kHz and 25 kHz. This is slightly different to the frequency range found in the numerical results, where the maximum impulsivity, obtained from the kurtogram plot in Figure 4.26, Chapter 4, was concentrated at about 21 kHz. Despite the slight difference, it is convenient to use one frequency band (18–23 kHz) for demodulating the measured and modelled acceleration signals, so as to compare the results of the most commonly used technique for bearing diagnosis, envelope analysis [30, 251, 252]. It is discussed in the next section.

5.3.3.3 Envelope analysis

For demodulating the measured acceleration a_y signals, the frequency band of 18–23 kHz was chosen; this frequency band is similar to the one used for demodulating the numerically modelled acceleration a_y time-traces. Envelope analysis [30, 251, 252] was implemented using the Hilbert transform $\mathscr{H}$ [30, 348], and the band-pass filtered envelopes of the measured acceleration signals corresponding to a rotational speed n_s of 500 RPM and radial loads W of 25 kN, 50 kN and 80 kN are shown in Figure 5.16, along with the original acceleration time-traces. The original acceleration time-traces are represented using the thin lines, and their band-pass filtered envelopes are represented using the thick, gray-coloured, lines.

Power spectra of the measured envelope signals were calculated using Welch's method [389], as implemented for the numerically modelled vibration signals discussed in Section 4.5, Chapter 4. Figure 5.17 shows the envelope power spectra of the measured, band-pass filtered, acceleration signals shown in Figure 5.16, corresponding to a rotational speed n_s of 500 RPM and radial loads W of 25 kN, 50 kN and 80 kN, along with the corresponding envelope power spectra of the modelled acceleration signals for comparison. The experimentally measured results are represented using thick lines in contrast to relatively thin lines, which represent the numerically modelled results. It can be seen from the comparison of the measured and modelled envelope power spec-

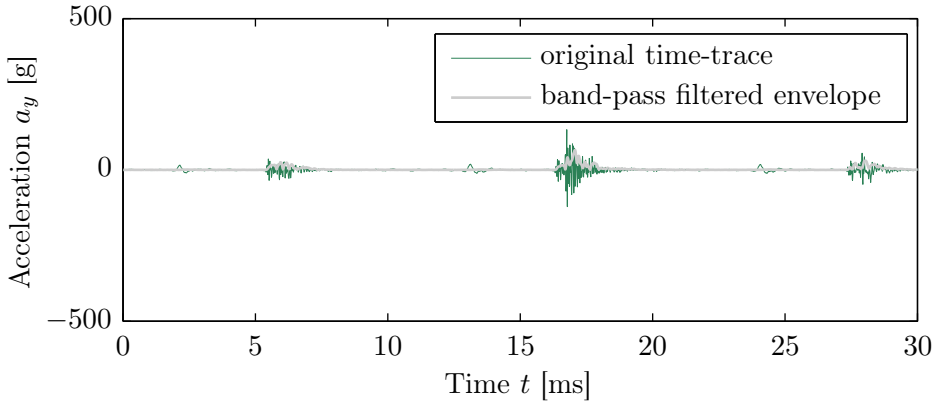

(a) Band-pass filtered envelope of the measured acceleration a_y time-trace shown in Figure 5.5a for $W = 25\,\text{kN}$ and $n_s = 500\,\text{RPM}$.

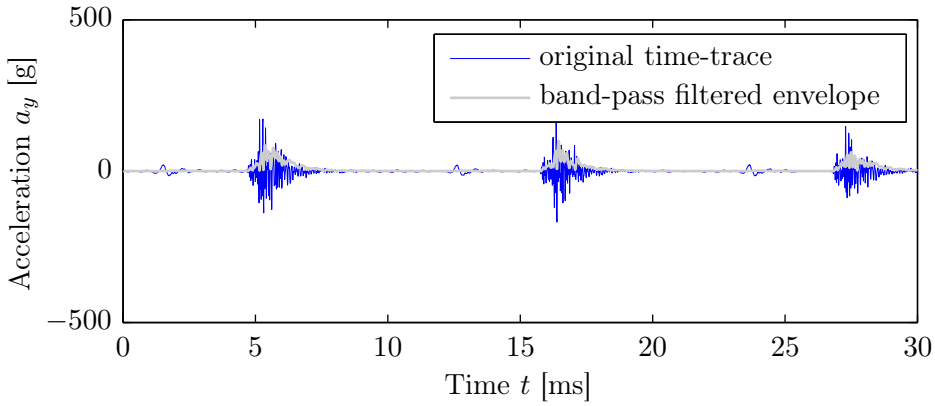

(b) Band-pass filtered envelope of the measured acceleration a_y time-trace shown in Figure 5.3 for $W = 50\,\text{kN}$ and $n_s = 500\,\text{RPM}$.

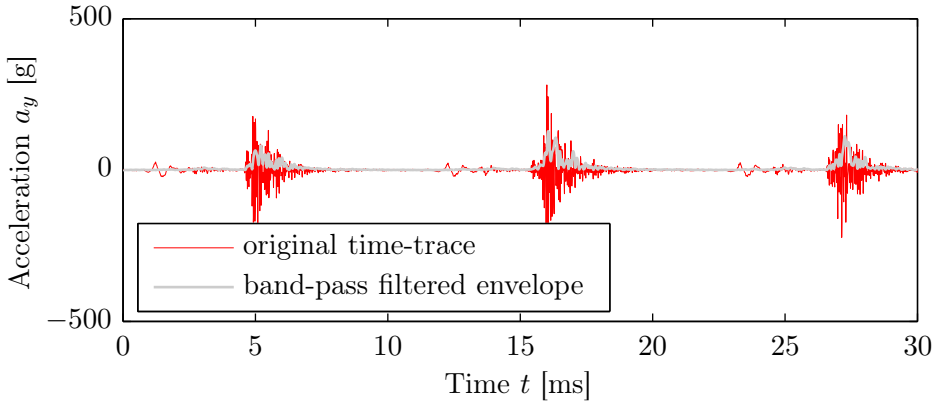

(c) Band-pass filtered envelope of the measured acceleration a_y time-trace shown in Figure 5.5c for $W = 80\,\text{kN}$ and $n_s = 500\,\text{RPM}$.

Figure 5.16: Envelopes of the experimentally measured acceleration a_y time-traces, for a rotational speed n_s of 500 RPM, and radial loads W of 25 kN, 50 kN and 80 kN, estimated using the Hilbert transform $\mathscr{H}$ of the band-pass filtered acceleration signals from 18–23 kHz.

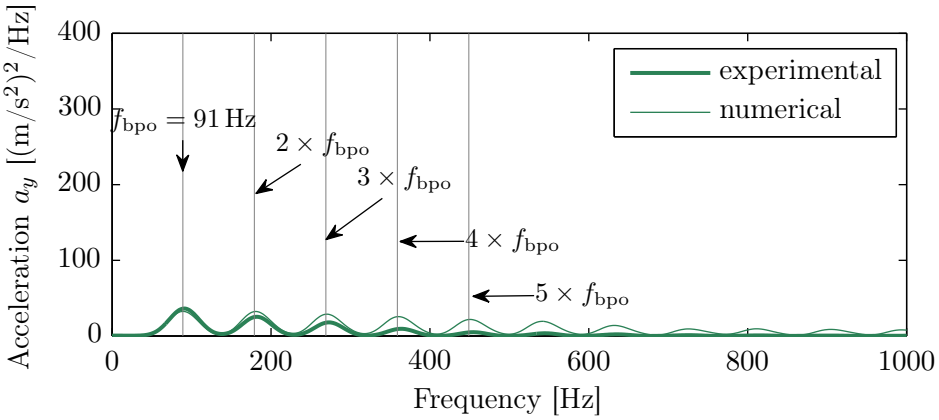

(a) Measured and modelled envelope power spectra for $W = 25\,\mathrm{kN}$ and $n_s = 500\,\mathrm{RPM}$.

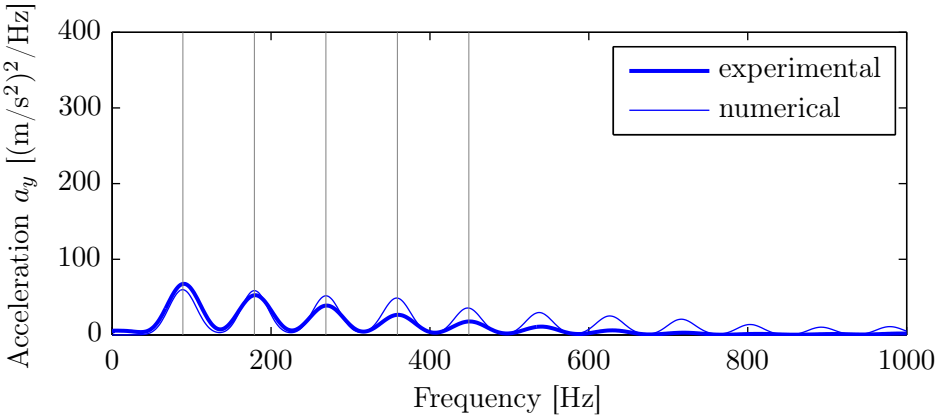

(b) Measured and modelled envelope power spectra for $W = 50\,\mathrm{kN}$ and $n_s = 500\,\mathrm{RPM}$.

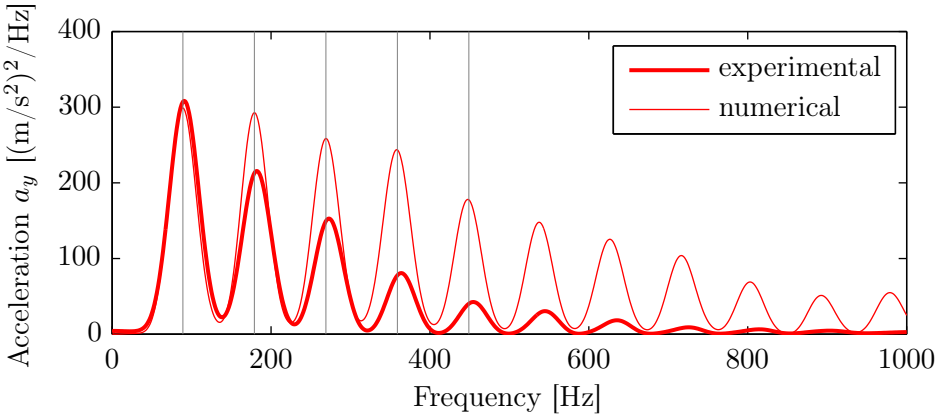

(c) Measured and modelled envelope power spectra for $W = 80\,\mathrm{kN}$ and $n_s = 500\,\mathrm{RPM}$.

Figure 5.17: Comparison of the envelope (demodulated) power spectra of the experimentally measured and numerically modelled acceleration a_y time-traces of the rolling element bearing for a rotational speed n_s of 500 RPM, and radial loads W of 25 kN, 50 kN and 80 kN; the vertical lines in the subplots correspond to the fundamental f_{bpo} and its harmonics.

tra that the fundamental and harmonics of the outer raceway defect frequency f_{bpo}, as indicated in Figure 5.17 using vertical lines and markers, are in excellent agreement. However, the peak amplitudes at the fundamental f_{bpo} and harmonics, especially, from $3 \times f_{\text{bpo}}$ onwards, corresponding to the measured and modelled spectra do not agree favourably. One of the reasons for this difference is the numerical noise in the modelled acceleration data, which could not be completely filtered out, as has been previously discussed in Chapter 4. During the power spectral estimation of the modelled data, along with the defect-related tonal components, the numerical noise signals were inherently included in respective frequency bins. As a result, the peak amplitudes at the defect-related frequency components are higher, and therefore, do not agree favourably with the corresponding measured data. Another reason is the insufficient damping in the FE model of the rolling element bearing; for the FE modelling results presented in this thesis, damping of 2% was used. As mentioned earlier in Section 4.2.4, Chapter 4, higher values of damping, 3% to 5%, were also tested, but these higher values affected the rotational speed of the rolling elements causing slippage; thereby, resulting in the incorrect bearing kinematics. Therefore, the results corresponding to the high values of damping are not shown here.

Similar to the results in Figure 5.17, which correspond to a rotational speed n_s of 500 RPM, the envelope power spectra of the measured, band-pass filtered, acceleration a_y signals for rotational speeds n_s of 300 RPM and 800 RPM are shown in Figures 5.18 and 5.19, respectively. For comparison, the corresponding spectra of the modelled acceleration signals are also plotted in the figures. It is evident from the comparison in Figures 5.18 and 5.19 that the fundamental and harmonics of the outer raceway defect frequency f_{bpo}, as indicated using vertical lines, are in favourable agreement. However, as mentioned in the preceding paragraph, there is a disagreement between the peak amplitudes at the harmonics from $3 \times f_{\text{bpo}}$ onwards of the measured and modelled spectra due to the numerical noise and insufficient damping in the FE modelled results.

The comparison between the analyses of the experimentally measured and numer-

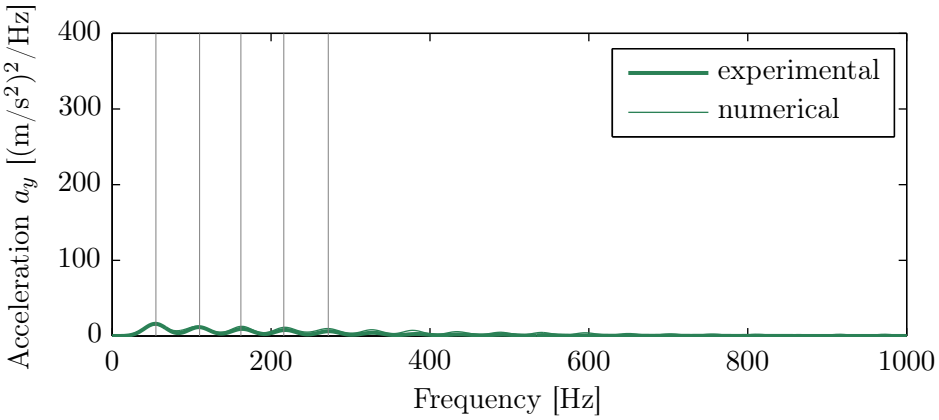

(a) Measured and modelled envelope power spectra for $W = 25\,\text{kN}$ and $n_s = 300\,\text{RPM}$.

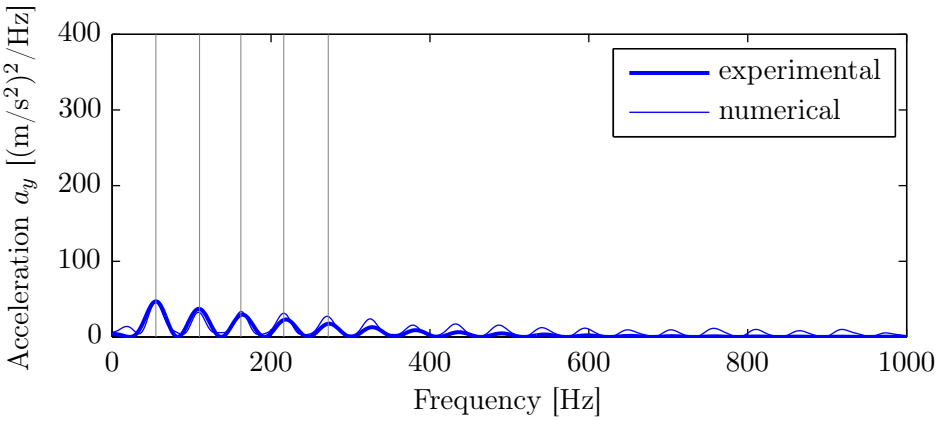

(b) Measured and modelled envelope power spectra for $W = 50\,\text{kN}$ and $n_s = 300\,\text{RPM}$.

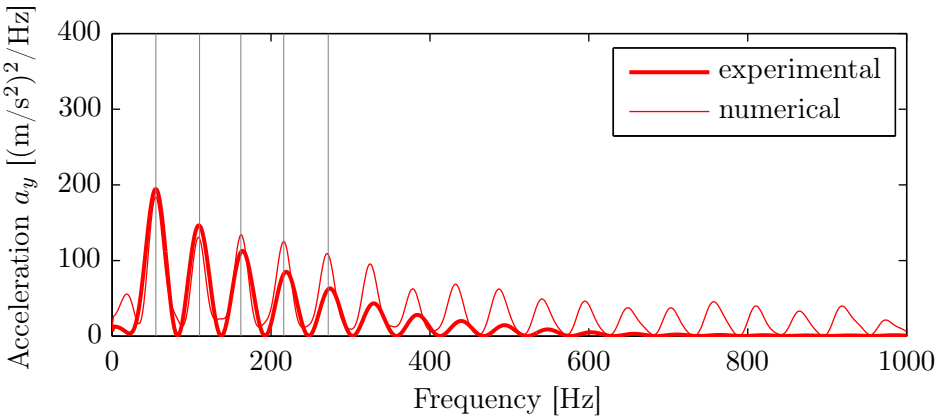

(c) Measured and modelled envelope power spectra for $W = 80\,\text{kN}$ and $n_s = 300\,\text{RPM}$.

Figure 5.18: Comparison of the envelope (demodulated) power spectra of the experimentally measured and numerically modelled acceleration a_y time-traces of the rolling element bearing for a rotational speed n_s of 300 RPM, and radial loads W of 25 kN, 50 kN and 80 kN; the vertical lines in the subplots correspond to the fundamental f_{bpo} and its harmonics.

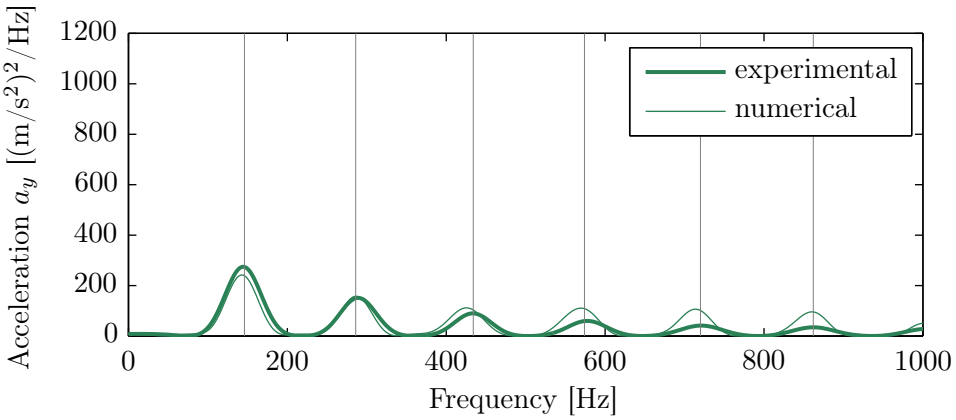

(a) Measured and modelled envelope power spectra for $W = 25\,\text{kN}$ and $n_s = 800\,\text{RPM}$.

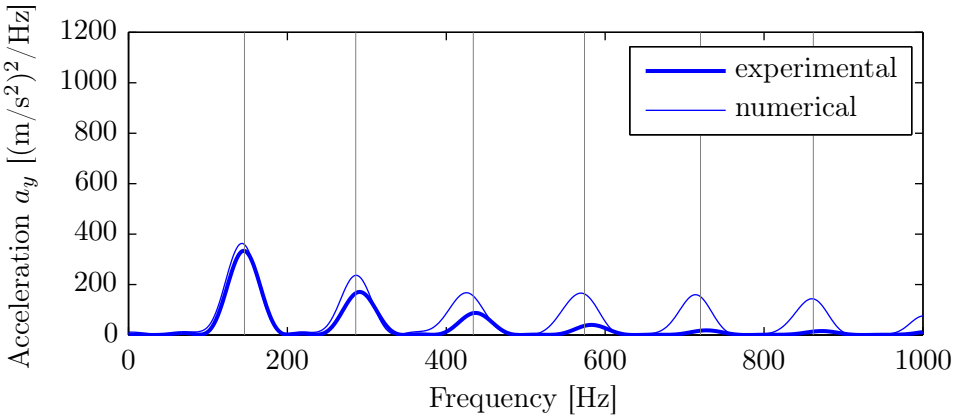

(b) Measured and modelled envelope power spectra for $W = 50\,\text{kN}$ and $n_s = 800\,\text{RPM}$.

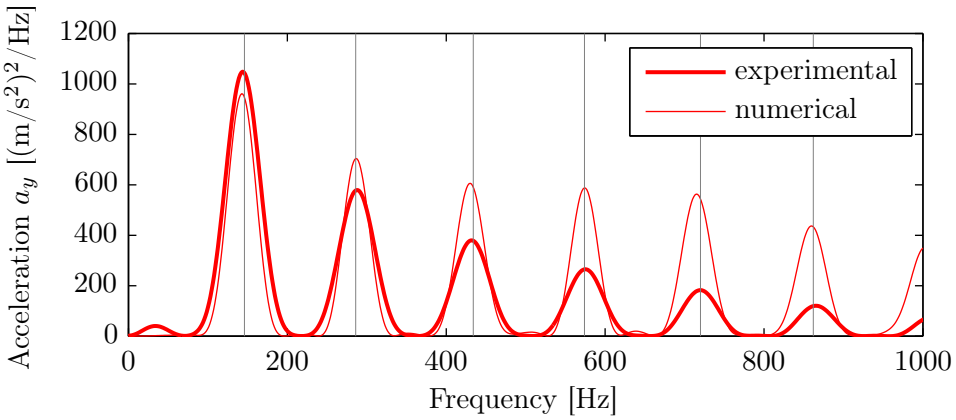

(c) Measured and modelled envelope power spectra for $W = 80\,\text{kN}$ and $n_s = 800\,\text{RPM}$.

Figure 5.19: Comparison of the envelope (demodulated) power spectra of the experimentally measured and numerically modelled acceleration a_y time-traces of the rolling element bearing for a rotational speed n_s of 800 RPM, and radial loads W of 25 kN, 50 kN and 80 kN; the vertical lines in the subplots correspond to the fundamental f_{bpo} and its harmonics.

ically modelled acceleration a_y time-traces shown so far indicates that the modelled results match favourably with the experimental data. The results of the envelope analysis, which is by far the most commonly used technique for bearing diagnosis, indicate a promising agreement between the measured data and simulation results. The parametric effect of varying radial load W and rotational speed n_s on the envelope power spectra of both measured and modelled acceleration results will be described in Section 5.4.

5.3.3.4 Frequency spectrum

Narrow and one-third octave band spectra of the measured and modelled acceleration signals were estimated and are compared below.

Narrow band power spectrum

Using Welch's method [389], as discussed in Section 4.5, Chapter 4, the power spectral density of the measured acceleration a_y time-trace, shown in Figure 5.3, was estimated, and is plotted in Figure 5.20. For comparison, the corresponding spectrum of the modelled acceleration time-trace, obtained using the FE model of the bearing, is also included in Figure 5.20.

Although it is difficult to compare the narrow-band power spectra, generally, the results in Figure 5.20 show a favourable agreement up to 25 kHz. There is a clear disagreement between the measured and modelled spectra from 25 kHz to 31 kHz. In this case, it is convenient to compare the one-third octave bands spectra, as discussed below.

One-third octave band spectrum

For a rotational speed n_s of 500 RPM, Figures 5.21a, 5.21b and 5.21c show a comparison of the one-third octave band spectra of the measured and modelled (notch filtered) acceleration a_y signals corresponding to radial loads W of 25 kN, 50 kN and 80 kN,

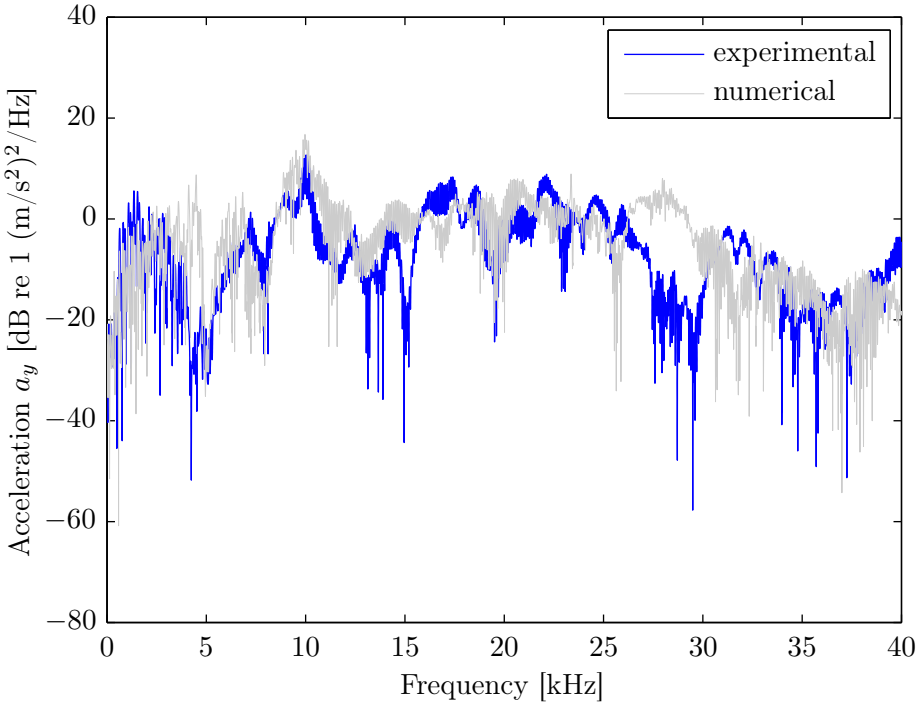

Figure 5.20: Comparison of the power spectral densities of the experimentally measured and numerically modelled, notch filtered, acceleration a_y time-traces of the rolling element bearing shown in Figures 5.3 and 5.4, respectively, for a radial load W of 50 kN and rotational speed n_s of 500 RPM.

respectively. While the spectra pertinent to the measured data are represented using thick lines, the spectra related to the numerically modelled acceleration are represented using relatively thin lines.

From Figure 5.21, it is evident that the spectra generally compare favourably well up to 2.5 kHz and from 7 kHz to 20 kHz, but comparatively less favourably between 2.5 kHz and 7 kHz. The maximum difference of 17 dB in Figures 5.21a and 5.21b is at 5 kHz. The difference between the spectra from 2.5 kHz to 7 kHz is due to the presence of the random numerical noise in the modelled results, as discussed in Section 4.5, Chapter 4. It was mentioned earlier that the noise was eliminated using a notch filter only at the rolling element-to-outer raceway rolling contact noise frequency $f^o_{\text{noise}} = 4671$ Hz; however, the numerical noise generated due to the adaptive time-stepping and sliding is stochastic, and because of its broadband nature, it could not be filtered out. In comparing the one-third octave band spectra of the numerical unfiltered and notch

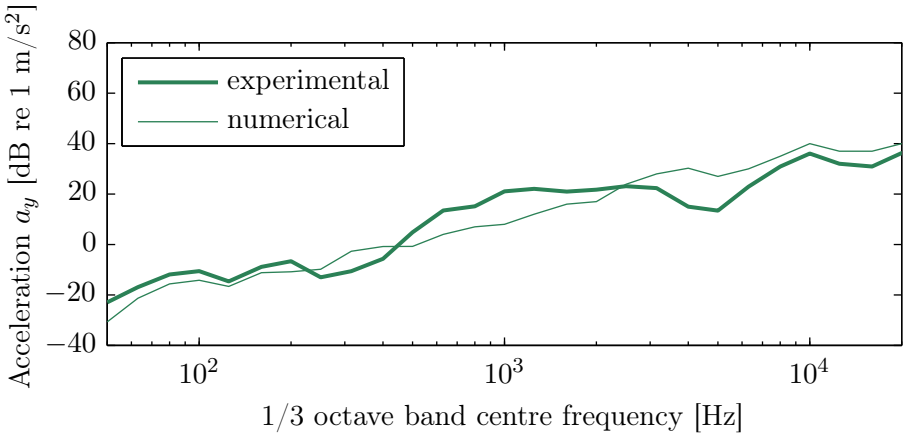

(a) Measured and modelled acceleration spectra for $W = 25\,\text{kN}$ and $n_s = 500\,\text{RPM}$.

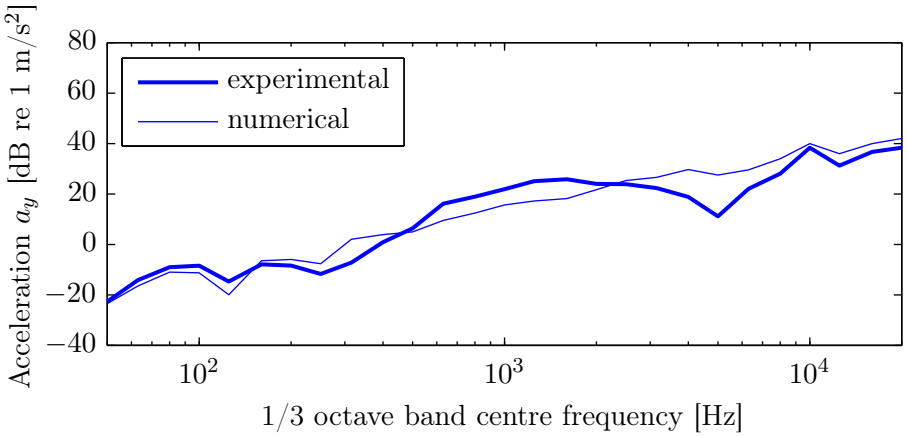

(b) Measured and modelled acceleration spectra for $W = 50\,\text{kN}$ and $n_s = 500\,\text{RPM}$.

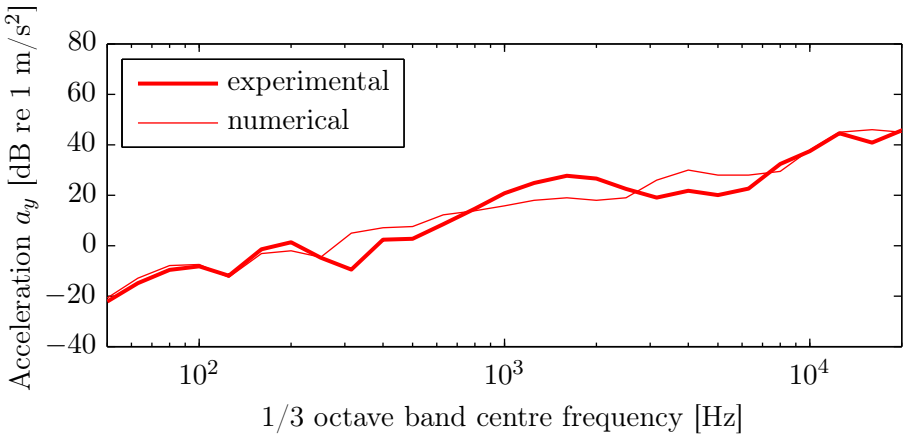

(c) Measured and modelled acceleration spectra for $W = 80\,\text{kN}$ and $n_s = 500\,\text{RPM}$.

Figure 5.21: Comparison of the one-third octave band spectra of the experimentally measured and numerically modelled, notch filtered, acceleration a_y time-traces of the rolling element bearing for a rotational speed n_s of 500 RPM, and radial loads W of 25 kN, 50 kN and 80 kN.

filtered acceleration time-traces, shown in Figure 4.34, Chapter 4, a peak at 5 kHz for the unfiltered acceleration can be observed. Its value of 42 dB was suppressed to 27 dB as a result of the notch filter.

Similar to the plots in Figure 5.21, a comparison between the one-third octave band spectra of the experimentally measured and numerically modelled (notch filtered) acceleration a_y signals corresponding to rotational speeds n_s of 300 RPM and 800 RPM are shown in Figures 5.22 and 5.23, respectively. The spectra in Figure 5.22 compare favourably up to 2 kHz and from 4 kHz to 20 kHz, but comparatively less favourably between 2 kHz and 4 kHz, whereas in Figure 5.23, the spectra agree well up to 3 kHz and from 7 kHz to 20 kHz, but comparatively less favourably between 3 kHz and 7 kHz. The difference between the measured and modelled spectra for the frequency bands of 2–4 kHz and 3–7 kHz as described in the preceding paragraph is due to the numerical noise generated at the rolling element-to-outer raceway rolling contact noise frequencies f^o_{noise} of 2811 Hz and 7487 Hz, respectively. These noise frequencies respectively correspond to the rotational speeds n_s of 300 RPM and 800 RPM that compare favourably with the corresponding analytical results of 2830 Hz and 7548 Hz, respectively, estimated using Equation (4.10). Nevertheless, the one-third octave band spectra of the measured and corresponding modelled acceleration results in Figures 5.21, 5.22, and 5.23 for various loads and speeds generally agree reasonably well with one another.

As bearing vibration signals are generally demodulated in high-frequency range, around 15 kHz [30], where the defect-related impulses are amplified by the structural resonance of a bearing, the discrepancy observed in Figures 5.21, 5.22, and 5.23 does not effect the bearing fault diagnosis. It has been demonstrated using envelope analysis in Figures 5.17, 5.18, and 5.19 that the envelope power spectra of the measured and simulated acceleration results compare favourably with one another.

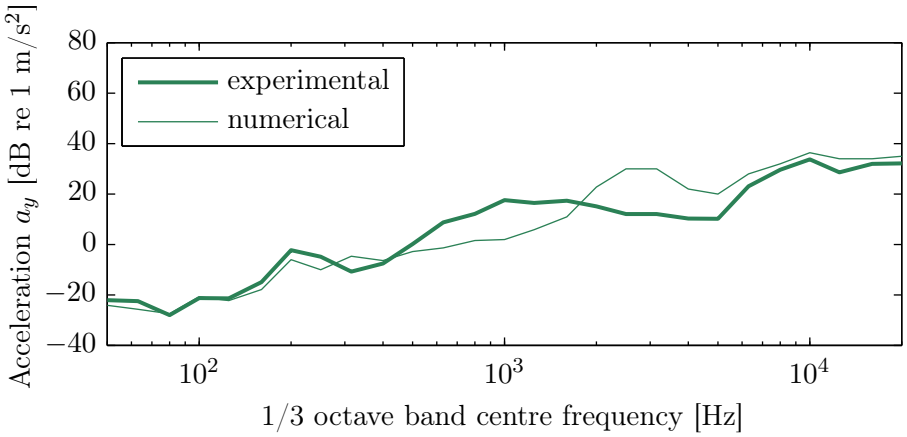

(a) Measured and modelled acceleration spectra for $W = 25\,\text{kN}$ and $n_s = 300\,\text{RPM}$.

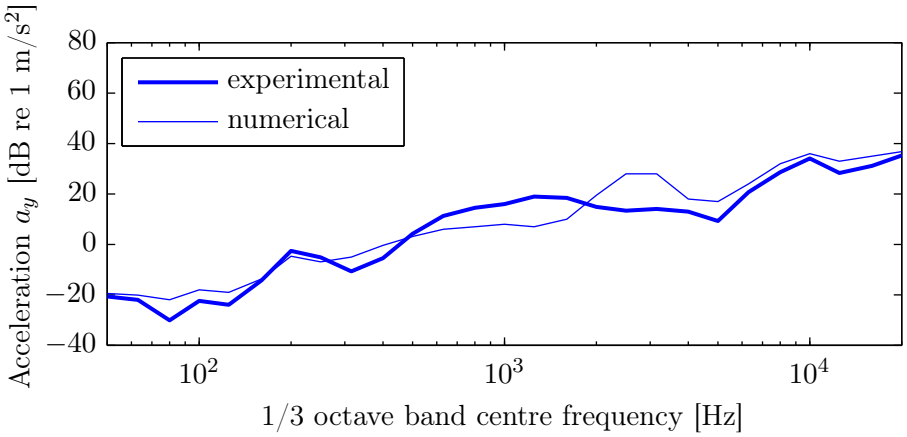

(b) Measured and modelled acceleration spectra for $W = 50\,\text{kN}$ and $n_s = 300\,\text{RPM}$.

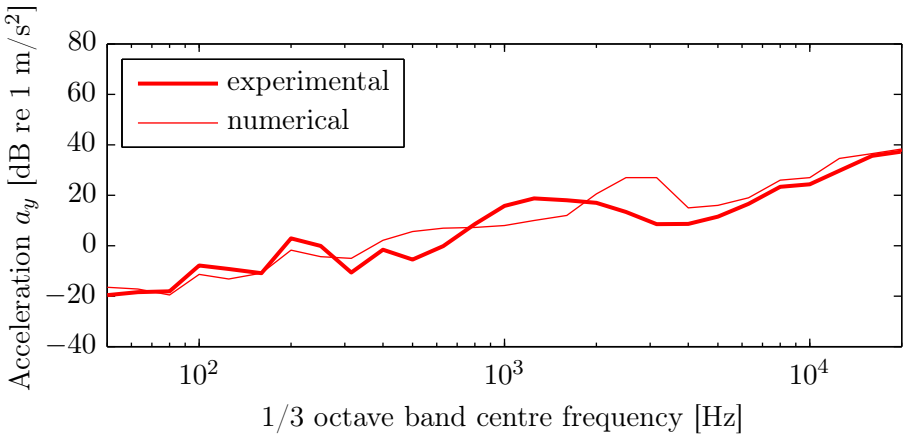

(c) Measured and modelled acceleration spectra for $W = 80\,\text{kN}$ and $n_s = 300\,\text{RPM}$.

Figure 5.22: Comparison of the one-third octave band spectra of the experimentally measured and numerically modelled, notch filtered, acceleration a_y time-traces of the rolling element bearing for a rotational speed n_s of 300 RPM, and radial loads W of 25 kN, 50 kN and 80 kN.

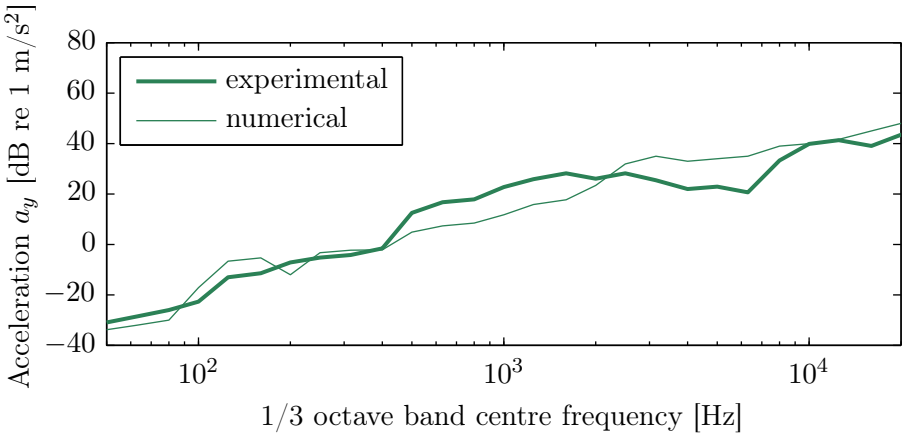

(a) Measured and modelled acceleration spectra for $W = 25\,\text{kN}$ and $n_s = 800\,\text{RPM}$.

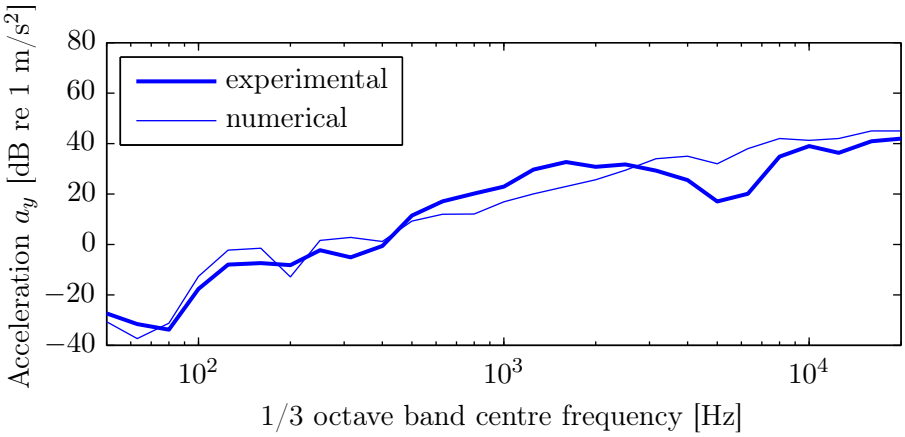

(b) Measured and modelled acceleration spectra for $W = 50\,\text{kN}$ and $n_s = 800\,\text{RPM}$.

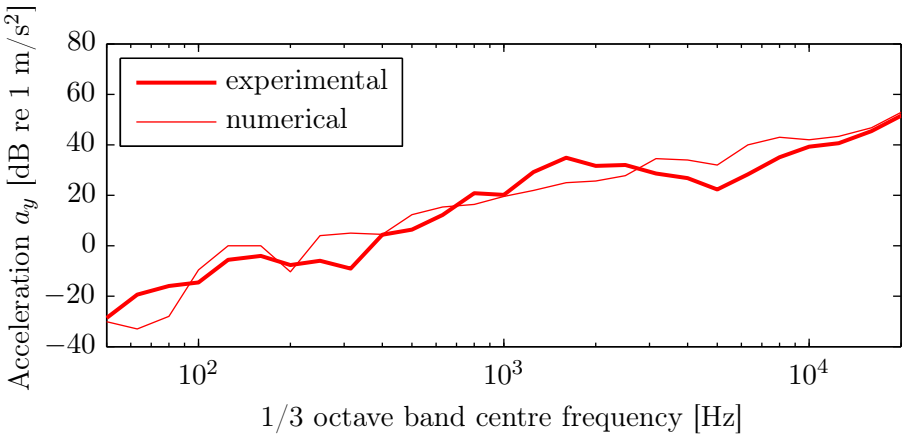

(c) Measured and modelled acceleration spectra for $W = 80\,\text{kN}$ and $n_s = 800\,\text{RPM}$.

Figure 5.23: Comparison of the one-third octave band spectra of the experimentally measured and numerically modelled, notch filtered, acceleration a_y time-traces of the rolling element bearing for a rotational speed n_s of 800 RPM, and radial loads W of 25 kN, 50 kN and 80 kN.

5.3.4 Spall size estimation

The time separation between the distinct de-stressing and re-stressing events for the simple case of a line spall can be used to determine the average size (length L_d) of the defect as

$$L_d = \frac{2\pi f_c D_o \Delta t_{\text{event}}}{2} \tag{5.1}$$

where, L_d is the length of the defect, $2\pi f_c = \omega_c$ is the angular velocity of the rolling elements (refer to Equation 3.21, Chapter 3), D_o is the outer race diameter, and Δt_{event} is the time difference between the consecutive de-stressing or re-stressing events. For the case of the measured data shown in Figure 5.3 corresponding to a radial load W of 50 kN and rotational speed n_s of 500 RPM, the time separation between the events $\Delta t_{\text{event}} = 4$ ms, which corresponds to the estimated length $L_d = 9.5$ mm, compares favourably to the actual length of 10 mm.

In the case of noisy field environments, the signal-to-noise ratio of measured data can be quite low. It is possible that the low-frequency signals associated with the de-stressing of the rolling elements could be buried in noise. As implemented here, the noisy signal could be low-pass filtered to enhance the occurrences of the de-stressing event. Alternatively, relatively sophisticated techniques and algorithms may be employed on practical data for estimating the approximate size of a bearing defect [114, 165].

As discussed in Section 2.6.1, the time separation between the distinct de-stressing and re-stressing vibration signatures to estimate the average size of a defect can only be used for the case of localised bearing defects whose length is smaller than the spacing between two consecutive rolling elements. However, for extended defects, whose length typically extends beyond the spacing between two consecutive rolling elements, the time separation between the signatures will result in an incorrect estimation of a defect size, which would be smaller than the actual defect size.

5.3.5 Summary of the comparison between the measured and modelled results

Standard signal processing techniques relevant to the vibration-based monitoring of defective rolling element bearings were implemented, and various comparisons between the experimentally measured and numerically modelled acceleration a_y time-traces were presented.

The time domain analysis of the measured and modelled data shows that the time instances corresponding to the occurrences of the de-stressing and re-stressing events compare very favourably with one another. The period of the consecutive events that corresponds to the BPFO compares very favourably between the measured and modelled acceleration time-traces, and, in addition, it differs by less than 1% from the nominal theoretical estimate determined analytically using Equation 4.9. Furthermore, the instantaneous acceleration levels of the modelled de-stressing and re-stressing events compare favourably with the corresponding measured data.

The low-frequency and high-frequency energy distribution of the modelled vibration signals related to the de-stressing and re-stressing of the rolling elements, respectively, were also observed to be in excellent agreement with the corresponding measurements. Among other frequency domain analysis techniques, the results of the envelope analysis also shows a favourable agreement between the experimentally measured acceleration data and those simulated using the FE model of the bearing.

In summary, it can be concluded that the novel explicit dynamics finite element model of the rolling element bearing developed here has accurately modelled the complex dynamics of the system.

The next section presents an investigation of the parametric effects of varying radial load and rotational speed on the vibration response of the defective rolling element bearing.

5.4 Parametric effect of load and speed on the vibration response of the rolling element bearing

Envelope power spectra of the acceleration signals shown earlier in Figures 5.17, 5.18, and 5.19 are useful for investigating the parametric effect of varying radial load W and rotational speed n_s on the vibration response of the defective rolling element bearing. The spectra from these figures were taken and plotted in such a way as to show how the power spectrum varies with increasing radial load at different rotational speeds. These results are plotted in Figure 5.24, which comprises six subplots — the measured results are plotted in subplots (a, c, e), and the corresponding modelled results are plotted in subplots (b, d, f). The results corresponding to radial loads W of 25 kN, 50 kN, and 80 kN are represented using green-, blue-, and red-coloured, solid lines having different thicknesses, respectively. For clarity, the scale of the y-axis in Figures 5.24a–5.24d ranges from 0–400 $(\mathrm{m/s^2})^2/\mathrm{Hz}$, which is one-third of that in Figures 5.24e and 5.24f (0–1200 $(\mathrm{m/s^2})^2/\mathrm{Hz}$). The vertical lines in all the subplots represent the outer raceway defect frequency f_{bpo}; fundamental and harmonics.

It can be seen from the results in Figure 5.24 that the power spectra of the acceleration signals, both measured and modelled, increase with increasing radial load W at each rotational speed n_s. However, to clearly present the effect of load and speed on the vibration response of the bearing, the magnitudes of the acceleration power spectra at the fundamental defect frequencies ($1 \times f_{\mathrm{bpo}}$) were taken for each load–speed (W–n_s) test combination, and the corresponding results are plotted in Figure 5.25 as a function of the rotational speed n_s of the bearing. The values corresponding to the experimentally measured data are represented using respective markers, whereas the numerically modelled results are represented using lines. As can be seen from Figure 5.25, both measured and modelled results compare favourably with one another.

From Figure 5.25, it can be observed that the levels of the envelope (acceleration

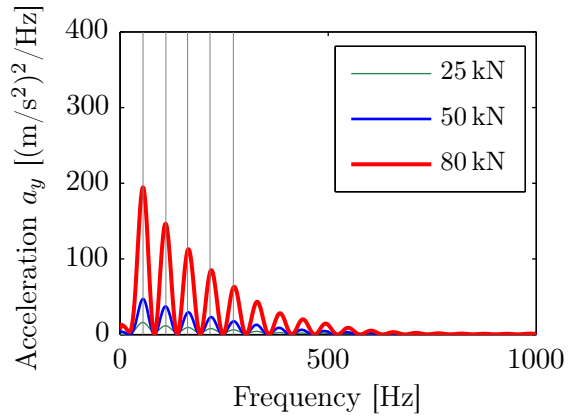

(a) Measured envelope power spectra for n_s = 300 RPM, and W = 25 kN, 50 kN and 80 kN.

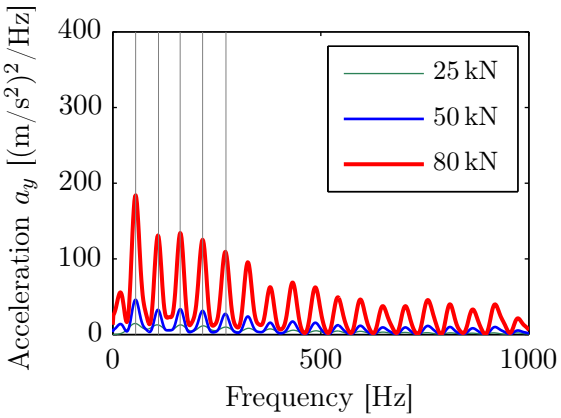

(b) Modelled envelope power spectra for n_s = 300 RPM, and W = 25 kN, 50 kN and 80 kN.

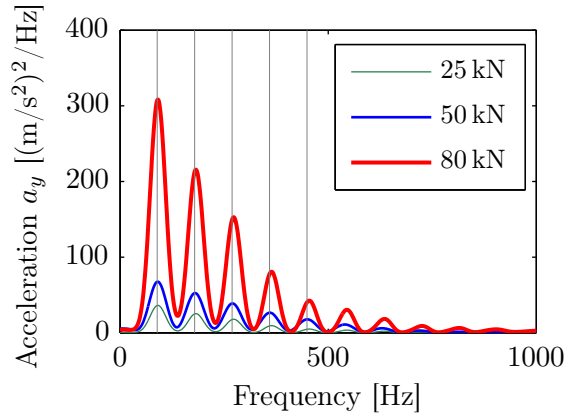

(c) Measured envelope power spectra for n_s = 500 RPM, and W = 25 kN, 50 kN and 80 kN.

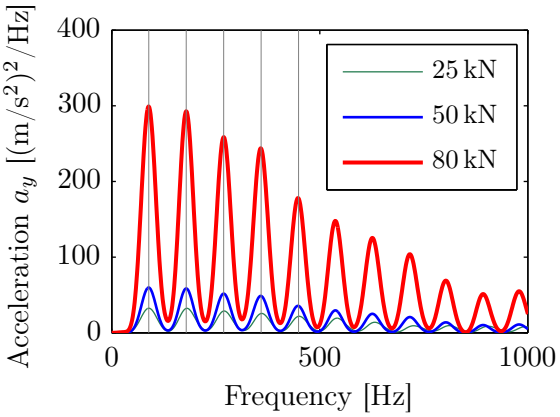

(d) Modelled envelope power spectra for n_s = 500 RPM, and W = 25 kN, 50 kN and 80 kN.

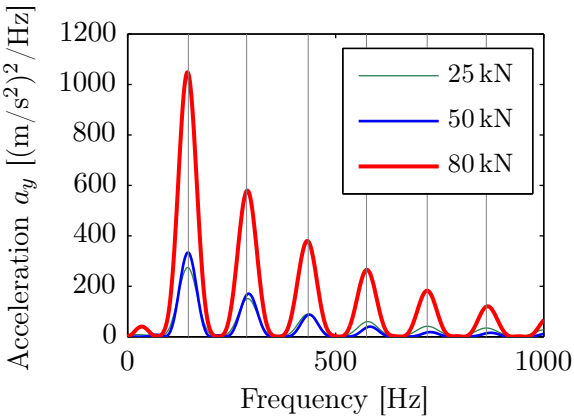

(e) Measured envelope power spectra for n_s = 800 RPM, and W = 25 kN, 50 kN and 80 kN.

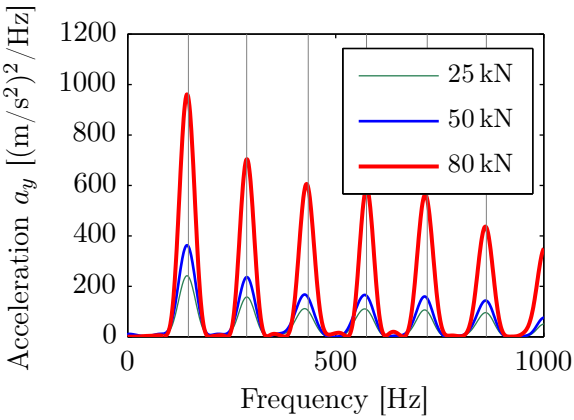

(f) Modelled envelope power spectra for n_s = 800 RPM, and W = 25 kN, 50 kN and 80 kN.

Figure 5.24: Comparison of the envelope (demodulated) power spectra of the experimentally measured and numerically modelled acceleration a_y time-traces of the rolling element bearing for radial loads W of 25 kN, 50 kN and 80 kN, and rotational speeds n_s of 300 RPM, 500 RPM and 800 RPM. For clarity, the scale of y-axis in subplots (a–d) ranges from 0–400 (m/s^2)^2/Hz compared to 0–1200 (m/s^2)^2/Hz in subplots (e, f). The vertical lines in the subplots correspond to the fundamental f_{bpo} and its harmonics.

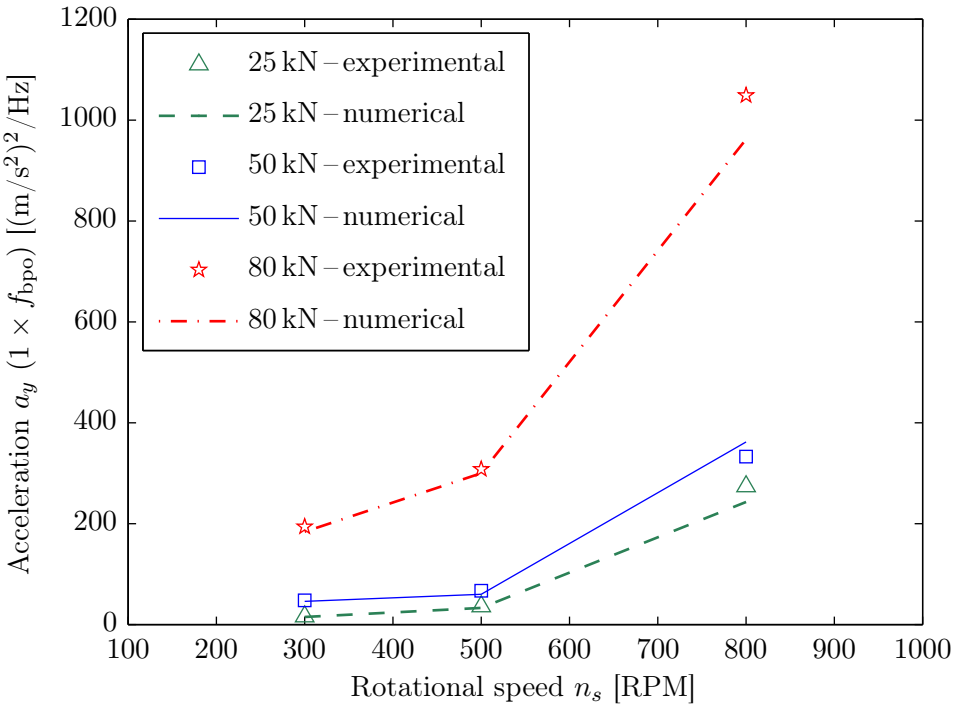

Figure 5.25: Comparison of the envelope (demodulated) power spectrum levels at the fundamental outer raceway defect frequency f_{bpo} for the experimentally measured and numerically modelled acceleration a_y time-traces shown in Figure 5.24 for varying radial load W and rotational speed n_s.

Load W (kN)	Speed n_s (RPM)			Percentage increase from (%)	
	300	500	800	300–500 RPM	500–800 RPM
25	16	36	274	125	661
50	48	67	333	40	397
80	194	308	1049	60	241

(a) Percentage increase in the spectrum levels from 300–500 RPM and 500–800 RPM.

Speed n_s (RPM)	Load W (kN)			Percentage increase from (%)	
	25	50	80	25–50 kN	50–80 kN
300	16	48	194	200	304
500	36	67	308	86	360
800	274	333	1049	22	215

(b) Percentage increase in the spectrum levels from 25–50 kN and 50–80 kN.

Table 5.2: Percentage increase in the envelope power spectrum levels of the measured acceleration a_y signals at the fundamental outer raceway defect frequency f_{bpo} shown in Figure 5.25.

a_y) power spectra generally increase with an increasing radial load W and rotational speed n_s. For the case of the measurements and FE simulations corresponding to radial loads W of 25 kN and 50 kN, the increases in the levels of the envelope power spectra from 300 RPM to 800 RPM are similar for each of the two loads. In contrast, for a radial load of 80 kN, the increase in the spectrum levels from 300 RPM to 800 RPM is higher compared to the increase for radial loads of 25 kN and 50 kN. For example, at 300 RPM, the measured levels increase by 200% from a radial load W of 25 kN to 50 kN; however, they increase by 300% when the load increases from 50 kN to 80 kN. Furthermore, the results also show that the levels increase significantly from 500 RPM to 800 RPM compared to those from 300 RPM to 500 RPM. For example, for an increase in the rotational speed n_s from 300 RPM to 500 RPM, the measured levels increase by 125% for a radial load of 25 kN, by 40% for 50 kN, and by 60% for 80 kN; however, from a rotational speed n_s of 500 RPM to 800 RPM the measured levels increase by 661% for a radial load of 25 kN, by 397% for 50 kN, and by 240% for 80 kN. The aforementioned percentage variations, which are approximate, along with other variations are given in Table 5.2.

From the results presented in this section, it can be summarised that:

- as the rotational speed of the bearing increases, the acceleration levels increase, and
- as the radial load on the bearing increases, the acceleration levels increase.

As will be shown in the next chapter that the defect-related impulses in the acceleration signals are generated due to the re-stressing of the rolling elements, it is useful to discuss the reasons for the increase in the acceleration levels (due to increase in the load and speed) in conjunction with the rolling element-to-raceway contact forces. An analysis of these contact forces and their correlation with the acceleration results are presented in the next chapter. The effects of increasing load and speed on the numerically modelled

contact forces will be discussed in details along with the reasons for the increase in the vibration levels.

In summary, from several comparisons between the experimentally measured and numerically modelled acceleration results presented in this chapter, it can be concluded that the simulated results obtained from the FE model of the rolling element bearing agree favourably with the measured data for various radial loads and rotational speeds.

5.5 Conclusions

The measured vibration data of the rolling element bearing having a machined line spall on its outer raceway were presented. The data were analysed using standard signal processing techniques, and the analysed results were compared with the corresponding numerically modelled data. Time domain analysis was presented in order to investigate the occurrences of the de-stressing and re-stressing of the rolling elements as they entered into and exited out of the defect, respectively. Time–frequency analysis was presented to determine the energy or power of the measured vibration signatures associated with the de-stressing and re-stressing events. Frequency domain analysis was presented to show the fundamental outer raceway defect frequency and its harmonics through the implementation of envelope analysis. Several favourable comparisons between the measured and modelled vibration results were presented, which demonstrated the validity of the novel explicit dynamics FE model of the rolling element bearing developed during the course of this study.

The parametric effect of varying radial load and rotational speed on the vibration response of the bearing was also discussed. It was observed that the magnitude of the envelope power spectra at the fundamental defect frequencies increases with increasing radial load and rotational speed of the bearing. The reasons for the increase in the acceleration levels with increasing load and speed will be described in the next chapter.

The next chapter presents an analysis of the numerically modelled rolling element-

to-raceway contact forces and their correlation with the bearing vibration signals. As contact forces between mating components are generally not measured in practice, the analysis and interpretation of the rolling element-to-raceway contact forces will provide new insights into the fundamental mechanisms that cause the generation of the defect-related impulses that are observed in acceleration signals in practice.

This page intentionally contains only this sentence.

Chapter 6

Analyses of Rolling Element–Raceway Contact Forces and Correlation with Bearing Vibrations

6.1 Introduction

This chapter presents an analysis of the numerical rolling element-to-raceway contact forces obtained from the explicit dynamics FE model of the defective rolling element bearing presented in Chapter 4.

The static rolling element-to-raceway contact forces have previously been modelled in various multi-body dynamic models [100–102, 104–106, 109–114], reviewed in Section 2.3.3, Chapter 2. However, the scope of the previous models has been limited to predicting the vibration response of defective rolling element bearings, such as acceleration, velocity or displacement, and subsequently implementing the well-known envelope analysis technique [30, 251, 252] for bearing fault diagnosis. Previous explicit dynamic FE models [117–120], reviewed in Section 2.3.4.3, Chapter 2, also did not presented the contact forces. Furthermore, during the condition-based monitoring of rolling element bearings, contact forces between mating components are generally not

measured in practice. In short, only static and quasi-static estimation of the contact forces at rolling element-to-raceway interfaces [3, 245–248, 312–328] within a bearing has been previously reported in the literature. However, the quantification of the dynamic contact forces, for the case of a rolling element traversing through a defect, has received much less attention, except published recently [4, 5] by the authors of this thesis and in references [6, 7] based on the work presented in this thesis. Therefore, an in-depth analysis and interpretation of the numerically modelled rolling element-to-raceway contact forces presented here provide new insights into how defect-related impulsive bearing vibration signatures are generated within a defective rolling element bearing.

During the traverse of a single rolling element through a bearing defect, multiple impulses are generally observed in measured bearing vibration signals; however, the reason for their occurrence has not been clearly understood [105, 165]. These multiple impulses should not be confused with the consecutive impulses that are generated due to the traverse of multiple rolling elements through the defect, whose periods correspond to the defect frequencies — either BPFO, BPFI or BSF; refer to Appendix C for the definition of these frequencies. The analysis of the contact forces presented in this chapter shows that during the re-stressing of the rolling elements, a burst of multiple, short-duration, force impulses, rather than a single force impulse [90–96, 103, 114, 165] as has been previously modelled, occurs. These impulses excite resonant modes of a bearing, and this mechanism explains the occurrence of multiple impulses found in measured vibration signatures.

The low-frequency characteristics of the de-stressing of rolling elements, upon their entrance into a defect, have been discussed by a few researchers [4–7, 161–165] using the experimentally measured acceleration time-traces; however, the reason behind the de-stressing has not previously been clearly understood. As discussed in Chapter 3, some researchers [100, 104, 106, 109–114] have considered a single point contact at the rolling element-to-raceway interfaces that causes the contact forces to decrease

to zero in an instantaneous (sharp) step-like response at the starting position of a rectangular-shaped profile of a bearing defect. In contrast, others [101, 102, 105] have modified the shape of the defects so as to model a gradual decrease in the contact forces; however, they did not provide a corresponding explanation. A novel mathematical model to accurately predict the gradual de-stressing of rolling elements was presented in Section 3.5, Chapter 3. The rolling element-to-raceway contact forces calculated using this model will be compared with the numerical FE modelling results, and it will be demonstrated that no impulse-like signatures are generated during the de-stressing of the rolling elements, which explains its low-frequency characteristics.

6.1.1 Aims

The aims of the work described in this chapter are to:

- present a comparison of the numerical rolling element-to-raceway contact forces, modelled using the explicit FE model of the rolling element bearing presented in Chapter 4, with the static and quasi-static analytical solution presented in Chapter 3;
- present an in-depth analysis of the numerically modelled rolling element-to-raceway contact forces;
- provide an interpretation of variations in the contact forces as rolling elements traverse through an outer raceway bearing defect;
- correlate the numerical rolling element-to-raceway contact forces with the modelled bearing vibration signals;
- develop an understanding of the physical mechanism that causes the generation of defect-related impulsive forces, and consequently the vibration signatures, which are generally observed in measured acceleration signals of defective bearings; and to

- explain the occurrence of multiple impulses in experimentally measured, typical, defect-related vibration signals as a rolling element traverses through a bearing defect.

6.1.2 New knowledge

The work presented in this chapter has provided the following new knowledge and insights:

- the presentation and interpretation of the numerically modelled rolling element-to-raceway contact forces;
- the contrast between the low-frequency de-stressing and high-frequency re-stressing of the rolling elements as they enter into and exit out of a defect within a bearing, respectively, through the analysis of the numerical rolling element-to-raceway contact forces;
- that much higher forces and vibrations are generated during the re-stressing of the rolling elements between the raceways compared to when they strike the defective surface;
- the physical mechanism that causes a burst of multiple, short-duration, force impulses during the re-stressing of the rolling elements in the vicinity of the end of a defect;
- that the defect-related vibration impulses generated during the re-stressing of the rolling elements are the ones which are generally observed in practice; and
- why in typically measured bearing acceleration signals, multiple impulses are generated during the traverse of a (single) rolling element through a defect.

6.1.3 Structure

This chapter begins with comparison of the numerically modelled rolling element-to-raceway contact forces along with other contact-related parameters, which follow Hertzian contact theory [177, Chapter 4, pages 84–106], with the corresponding analytical solution in Section 6.2. An elaborate analysis of the rolling element-to-raceway contact forces is presented in Section 6.3. Variations in the contact forces as the rolling elements traverse through the raceway defect were broadly divided into four events, and are discussed in Sections 6.3.1 to 6.3.4. With an aim to develop an understanding of the physical mechanism that causes the generation of defect-related impulses, which are generally observed in practice, the numerical contact forces are correlated with the modelled bearing vibration signals in Section 6.4. The novel outcomes of the analysis of the contact forces in conjunction with the vibration signals obtained from the explicit FE model of the rolling element bearing are listed in Section 6.5. Parametric effects of varying load and speed on the rolling element-to-raceway contact forces are described in Section 6.6. Finally, the conclusions of this chapter are presented in Section 6.7.

6.2 Validation of numerical Hertzian contact-related parameters

The comparison of the numerically predicted acceleration levels obtained from the explicit dynamics FE model of the rolling element bearing has been presented in the previous chapter using experimental data. In this section, comparison of the numerical rolling element-to-raceway contact forces and other contact-related parameters that follow Hertzian contact theory [177, Chapter 4] is presented.

As mentioned earlier, contact forces between mating bearing components are generally not measured in practice during the condition-based monitoring of rolling element bearings, and have not been measured for the current research either. Therefore, the

numerical rolling element-to-raceway contact forces will be compared with the corresponding analytical solution. It is crucial to present this comparison of the contact forces because the development of the understanding of the physical mechanism that causes the generation of bearing defect-related vibration impulses is based on the interpretation of the contact forces and their subsequent correlation with the vibration signals.

6.2.1 Static contact forces

Although the numerically modelled contact forces are dynamic, their corresponding static values can be obtained at time $t = 0$, prior to the commencement of the explicit dynamic analysis. The magnitude of the rolling element-to-raceway contact forces at $t = 0$ corresponds to the mechanically stressed or loaded levels. It is the first phase of the solution, generically referred to as the *implicit (static) phase*, where the applied loads are appropriately converged to a solution, prior to the commencement of the *explicit (dynamic) phase*. In LS-DYNA simulations, the implicit phase is more commonly known as *dynamic relaxation* [329, Chapter 31]. For the FE analysis of the defective rolling element bearing presented in Chapter 4, the applied radial load has to be effectively distributed onto the rolling elements and raceways, or more precisely the rolling element-to-raceway contact interfaces, so as to achieve the required load distribution prior to the rotation of the bearing.

Figures 6.1a and 6.1b show the comparison between the numerical rolling element-to-outer raceway contact forces, both horizontal F_x and vertical F_y, respectively, at time $t = 0$, and the analytical contact forces, shown in Figure 3.4, Chapter 3. While the numerically modelled forces, represented by the blue-coloured, circular markers, were obtained only at the rolling element-to-outer raceway contact interfaces, the analytical solution, represented by the red-coloured, dashed lines, was estimated for finely spaced rolling element positions ψ_j at the resolution of 0.1° in order to smoothly interpolate

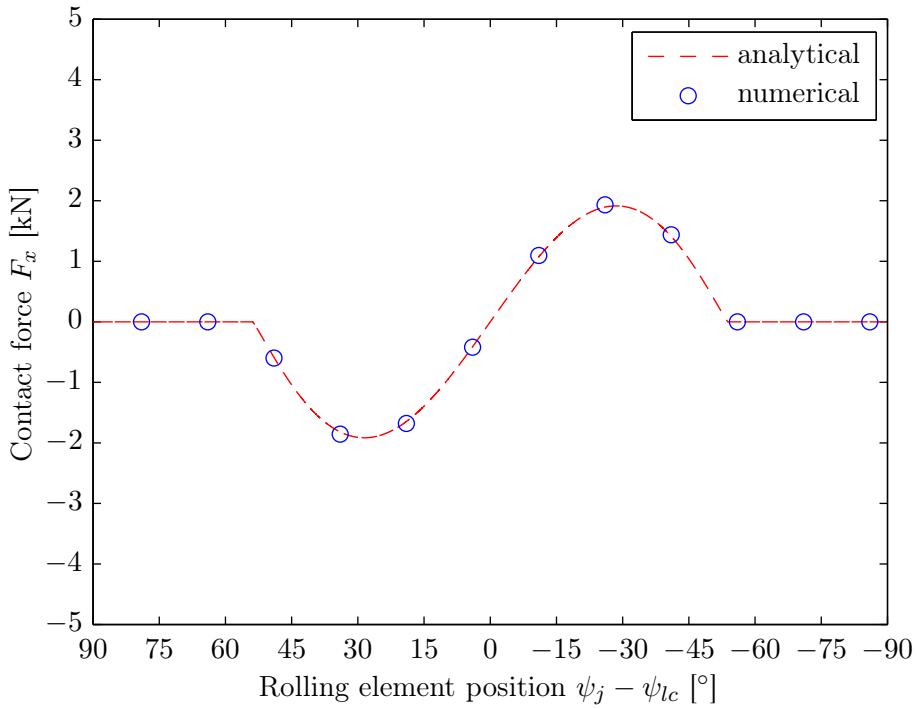

(a) Horizontal contact force (load) F_x distribution.

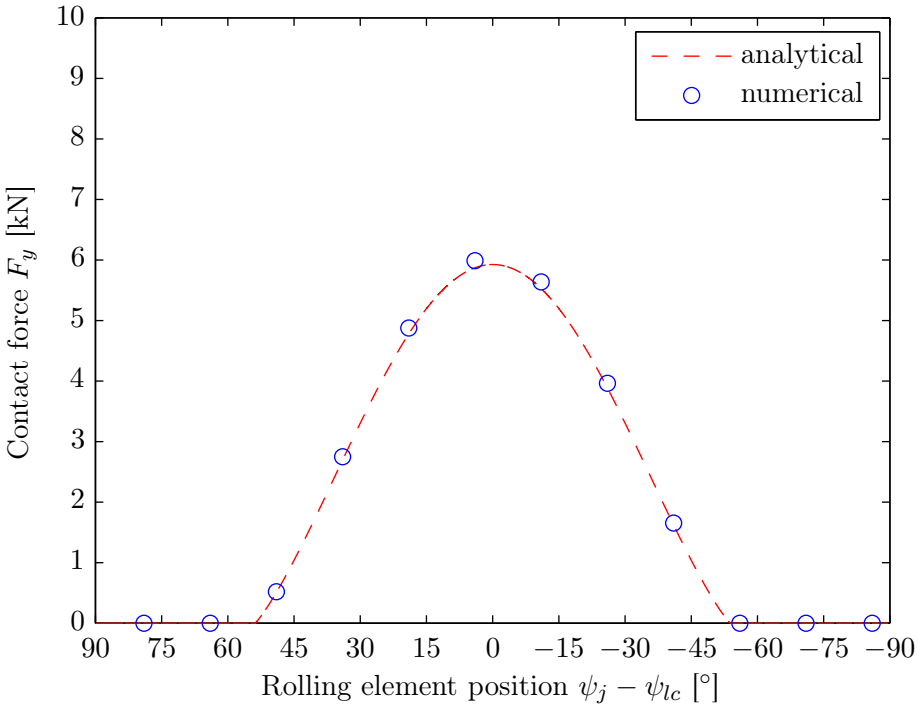

(b) Vertical contact force (load) F_y distribution.

Figure 6.1: Comparison of the analytically and numerically modelled contact forces at the rolling element-to-outer raceway contact interfaces for a radial load W of 50 kN; the numerical values correspond to mechanically stressed levels at time $t = 0$, prior to the commencement of the dynamic analysis.

the horizontal and vertical load profiles. These load profiles have been discussed earlier in Section 3.3.2, Chapter 3, in relation to Figure 3.4.

The positions of the rolling elements ψ_j in Figures 6.1a and 6.1b are plotted relative to the centre of the bearing load zone ψ_{lc}, which is also the centre of the bearing defect ψ_d; ($\psi_{lc} = \psi_d = 90°$) — refer to the schematics of a rolling element bearing in Figure 3.2 for the right-handed coordinate system considered in this thesis. For the finite element model of the bearing (refer to Figure 4.2, Chapter 4), the rolling element $j = 1$, located immediately to the left-hand side of the defect, was offset by 4° from the y-axis, the centre of the bearing zone ψ_{lc}: the actual position ψ_j of the rolling element $j = 1$ is 94°, and its relative position $\psi_j - \psi_{lc}$ is 4°.

The numerical estimates of the contact forces at the rolling element-to-raceway contact interfaces, which are within the bearing load zone $2\psi_l^{'}$ (see Equation 3.14, Chapter 3), are approximately 2% higher than the corresponding analytical results. A favourable agreement between the numerical and analytical contact forces in Figure 6.1 indicates that the applied radial load has been accurately distributed within the FE model of the bearing; thereby, representing the validation of the numerically modelled static contact forces.

6.2.2 Contact deformation

Other numerical contact-related parameters, such as displacement (or deformation) and contact width, which follow Hertzian contact theory [177, Chapter 4, pages 84–106], can also be compared with the corresponding analytical estimates for further verification of the FE simulation results.

Figure 6.2 shows a comparison of the numerical and analytical estimates of the horizontal δ_x and vertical δ_y contact displacements of the rolling elements and outer raceway at various contact interfaces. Similar to the discrepancy of 2% between the analytical and numerical contact forces, mentioned in the preceding paragraph, the

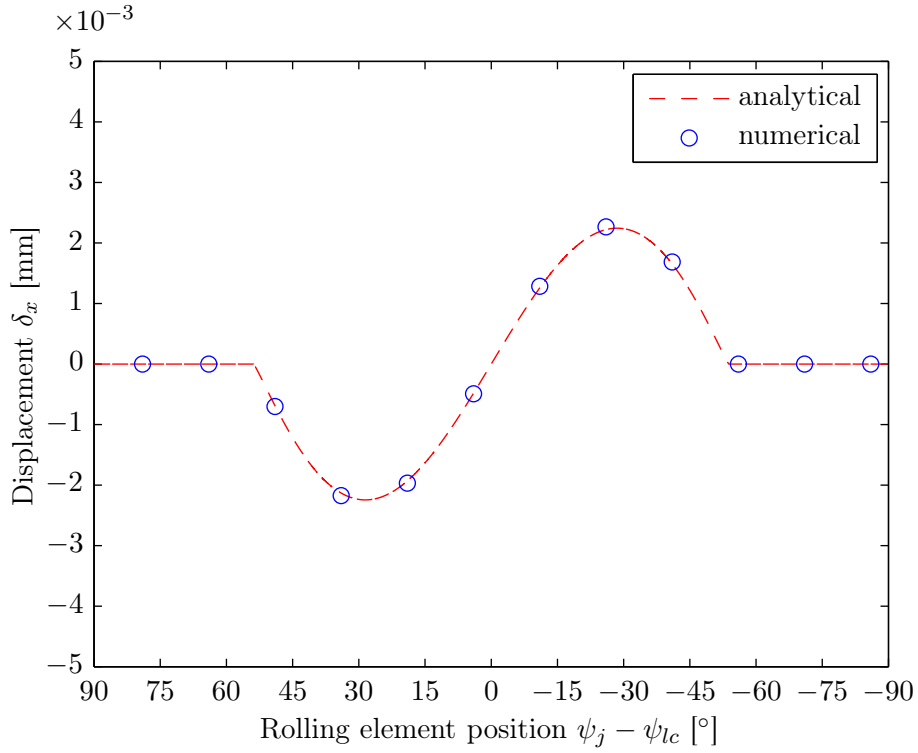

(a) Horizontal contact displacement δ_x.

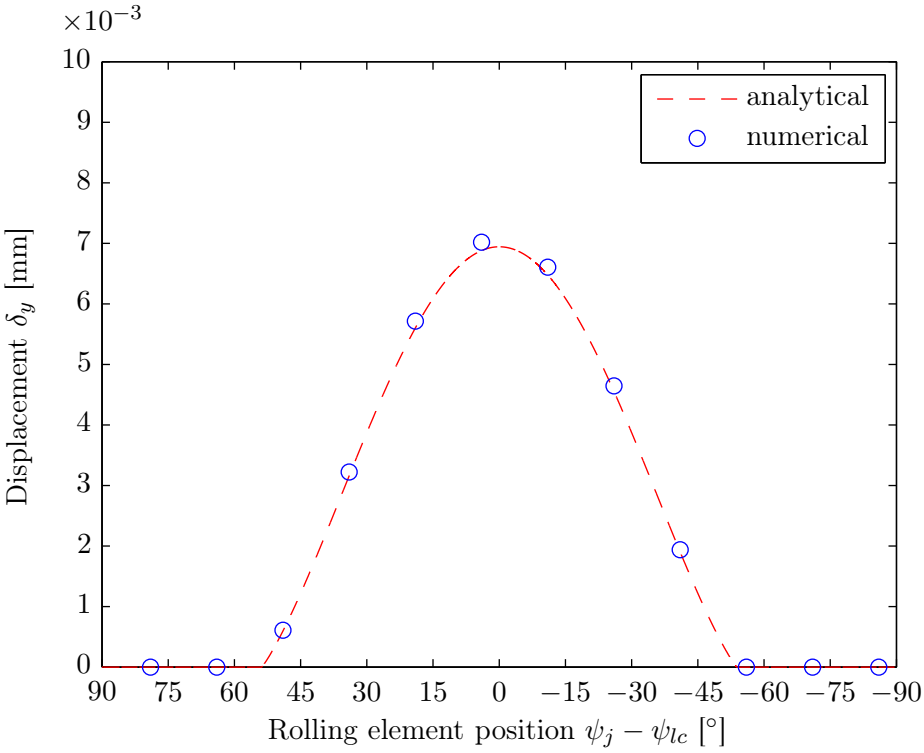

(b) Vertical contact displacement δ_y.

Figure 6.2: Comparison of the analytically and numerically modelled displacement at the rolling element-to-outer raceway contact interfaces for a radial load W of 50 kN; the numerical values correspond to mechanically stressed levels at time $t = 0$, prior to the commencement of the dynamic analysis.

numerically modelled displacement is also, at times, 2% higher than the corresponding analytical solution. Nevertheless, the comparison in Figures 6.2a and 6.2b shows a favourable match between the numerical FE modelling and analytical results.

Contact width

For a 2-D LS-DYNA simulation, the contact width at the interface of contacting bodies is not available from the finite element calculations; instead, it can be estimated on the basis of the contact force, which is resolved during the solution, using Hertzian contact theory [177, Chapter 4, pages 84–106]. For the FE model of the rolling element bearing presented here, the contact width at the rolling element-to-outer raceway contact interfaces was estimated using the numerical contact forces, shown in Figure 6.1, and Equation 3.4, Chapter 3. The results are plotted in Figure 6.3 along with the corresponding analytical solution for comparison. A favourable match between the numerical and analytical contact widths at the rolling element-to-outer raceway interfaces is evident.

From Figures 6.1, 6.2, and 6.3, it is clear that the contact interaction at the rolling element-to-raceway interfaces has been well predicted by the explicit FE model of the rolling element bearing. It should be highlighted here that the contact width at the interfaces is less than 0.5 mm, which is the same as the element mesh size used to discretise the FE model. This means that only one node was present at the rolling element-to-raceway contact interfaces during the numerical simulation. Although this would generate inaccurate results for the standard node-to-surface penalty-based contact formulations [307] used in many other FE software packages [307, 308, 311], the surface-to-surface segment-based contact formulation [329] employed in the FE software package used here does not suffer from this problem. Refer to Sections 4.2.3 and 4.2.4 of Chapter 4 for a discussion on the difference between the node-to-surface penalty-based and segment-based contact formulations. The favourable agreement of

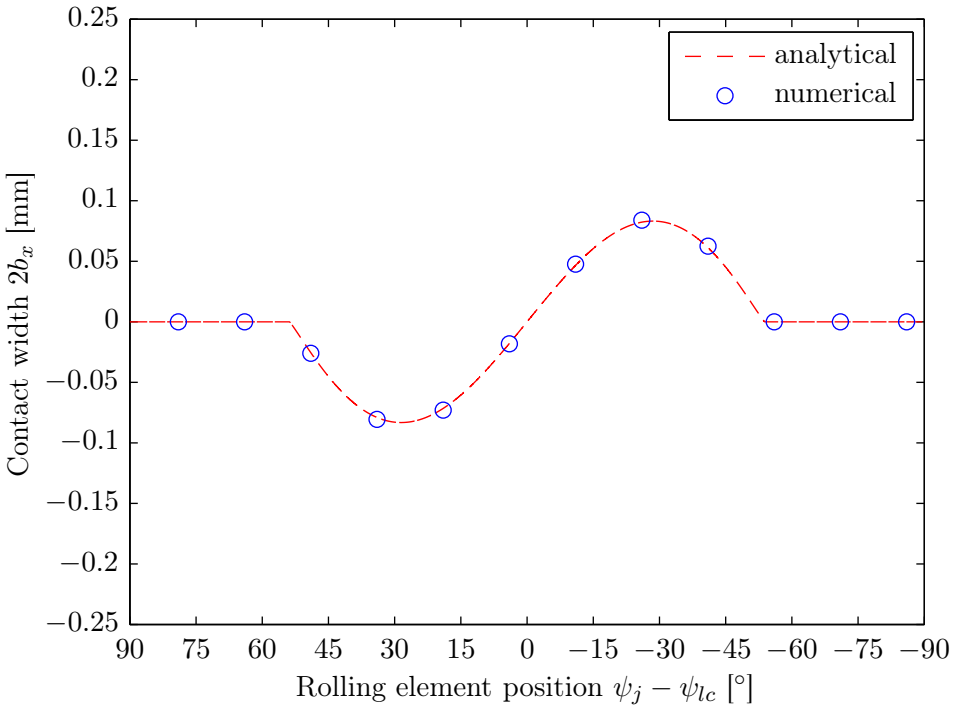

(a) Horizontal contact width $2b_x$.

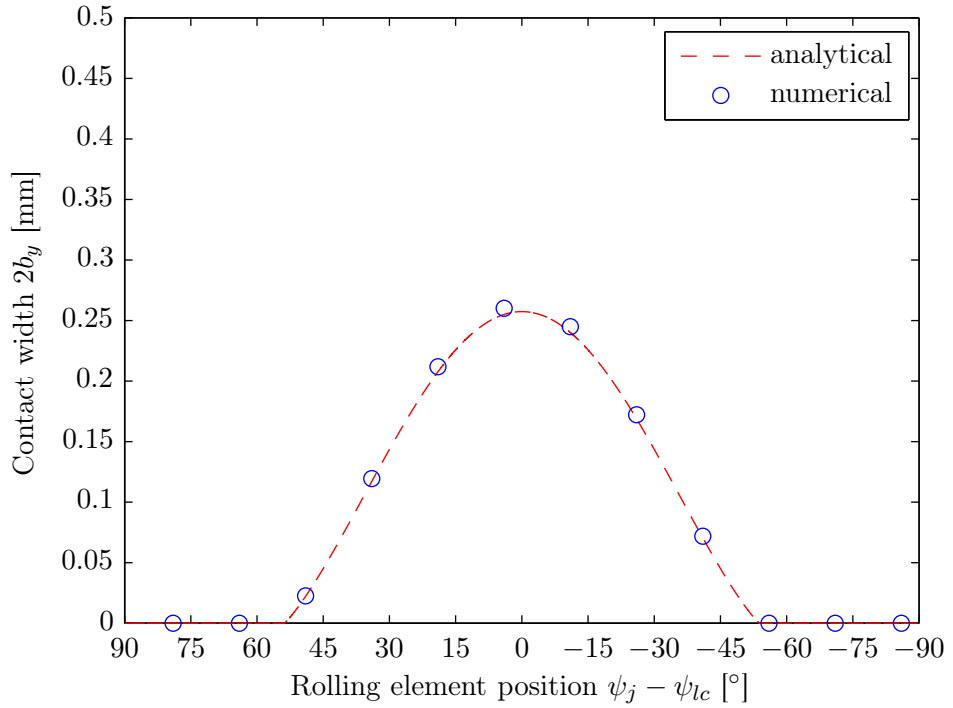

(b) Vertical contact width $2b_y$.

Figure 6.3: Comparison of the analytically and numerically modelled contact width at the rolling element-to-outer raceway contact interfaces for a radial load W of 50 kN; the numerical values correspond to mechanically stressed levels at time $t = 0$, prior to the commencement of the dynamic analysis.

the numerically estimated contact force, deformation, and width with the corresponding analytical results, shown in Figures 6.1, 6.2, and 6.3, respectively, indicates the validation of the explicit FE model of the rolling element bearing.

The dynamic contact forces obtained from the explicit FE model of the bearing are presented next.

6.2.3 Dynamic contact forces

For the FE model of the defective rolling element bearing, Figures 6.4 and 6.5 show the numerically modelled, notch filtered, horizontal F_x and vertical F_y contact forces, respectively, between the outer raceway and the three rolling elements, denoted as $j = 1, 2, 3$, which traversed through the outer raceway defect during the numerical simulation. These results correspond to a radial load W of 50 kN and rotational speed n_s of 500 RPM.

Similar to the numerically modelled vibration results, presented in Chapter 4, the contact forces also contained the numerical noise at the rolling element-to-outer raceway rolling contact noise frequency $f^o_{noise} = 4671$ Hz, which was filtered out using a second-order notch filter; refer to Figure 4.11 for the frequency response of the filter. However, as discussed in Chapter 4, some random noise at other frequencies is still present in the results. Several causes of the noise in the numerical simulation results were discussed in Section 4.5, Chapter 4.

For comparison, the analytically modelled quasi-static contact forces on the corresponding rolling elements have also been plotted in Figures 6.4 and 6.5, using the red-coloured, dashed lines, along with the numerically modelled dynamic contact forces, represented by the blue-coloured, solid lines. The quasi-static analytical model for estimating the contact forces for a defective rolling element bearing, which includes the proposed mathematical model (presented in Section 3.5) to predict the gradual de-stressing of the rolling elements, was presented in Section 3.6, Chapter 3.

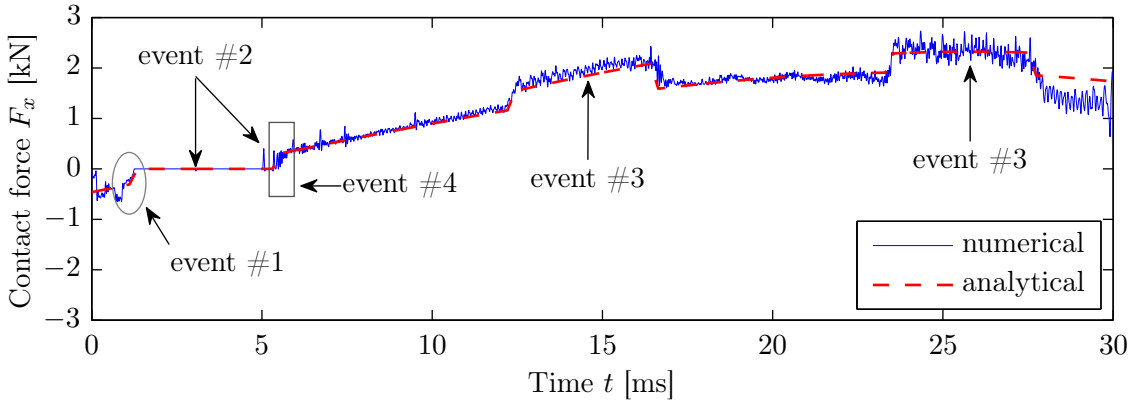

(a) Horizontal contact force between the first rolling element $j = 1$ and outer raceway.

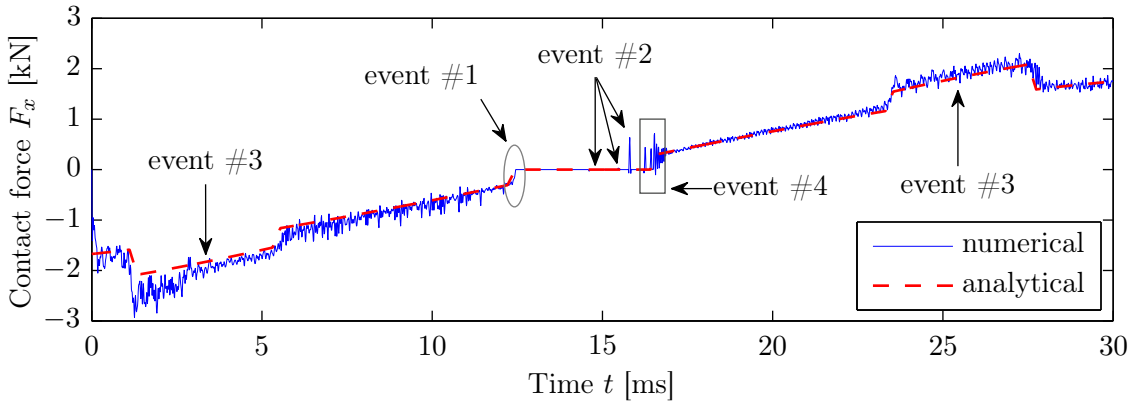

(b) Horizontal contact force between the second rolling element $j = 2$ and outer raceway.

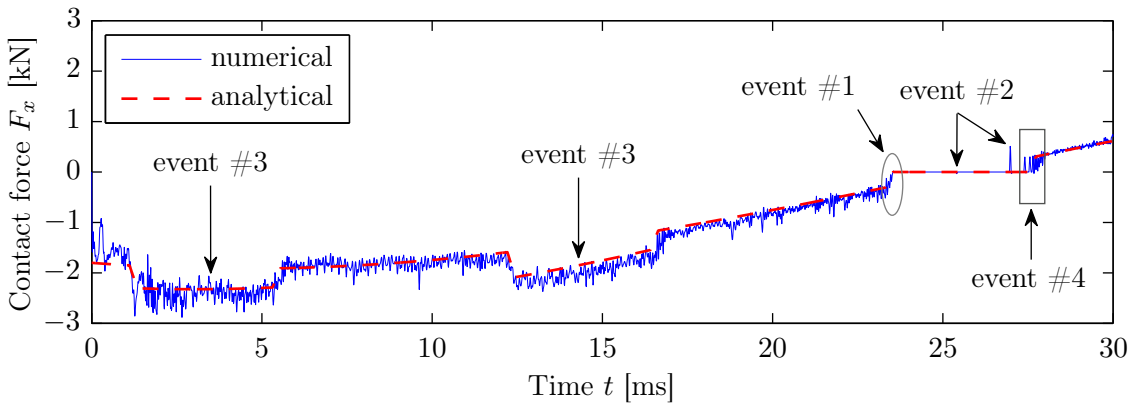

(c) Horizontal contact force between the third rolling element $j = 3$ and outer raceway.

Figure 6.4: Comparison of the numerically (notch filtered) and analytically modelled horizontal rolling element-to-outer raceway contact forces F_x as three rolling elements $j = 1, 2, 3$ traverse through the outer raceway defect for a radial load W of 50 kN and rotational speed n_s of 500 RPM.

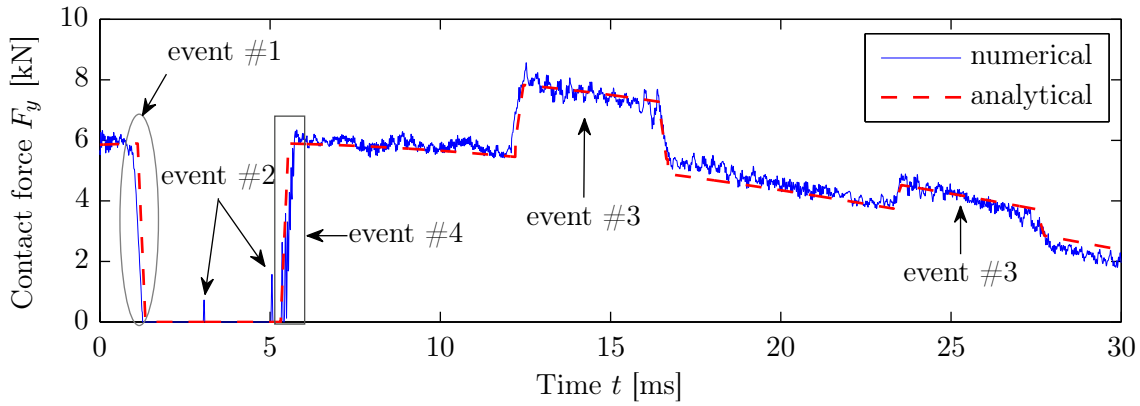

(a) Vertical contact force between the first rolling element $j = 1$ and outer raceway.

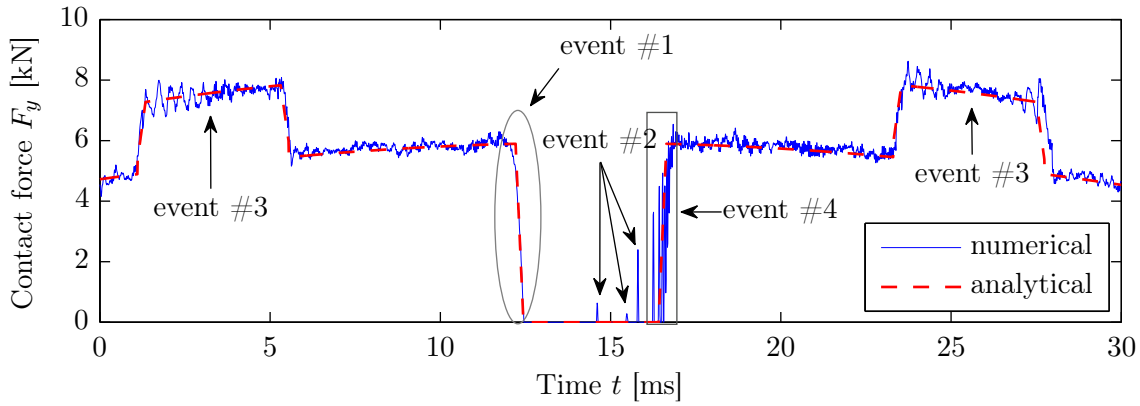

(b) Vertical contact force between the second rolling element $j = 2$ and outer raceway.

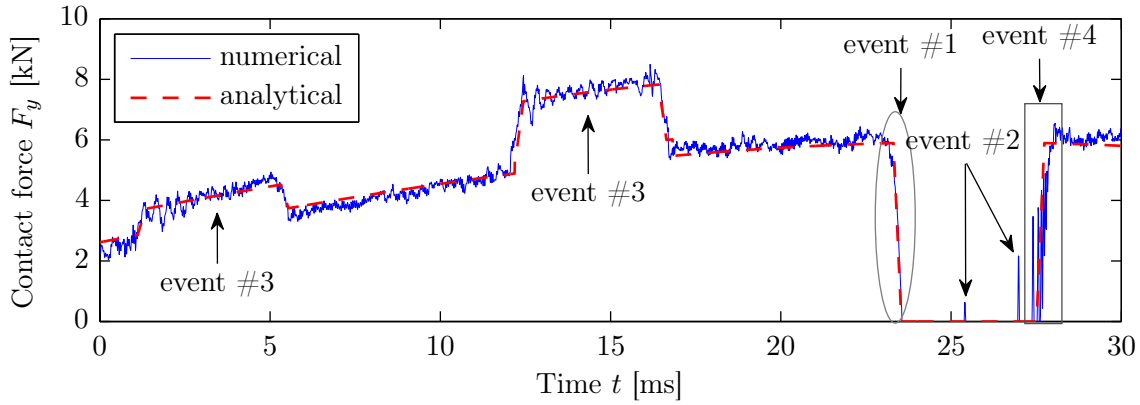

(c) Vertical contact force between the third rolling element $j = 3$ and outer raceway.

Figure 6.5: Comparison of the numerically (notch filtered) and analytically modelled vertical rolling element-to-outer raceway contact forces F_y as three rolling elements $j = 1, 2, 3$ traverse through the outer raceway defect for a radial load W of 50 kN and rotational speed n_s of 500 RPM.

The comparison of the dynamic numerical and quasi-static analytical rolling element-to-outer raceway contact forces, plotted in Figures 6.4 and 6.5, shows that both results agree favourably with one another. The numerical and corresponding analytical estimates of the horizontal F_x and vertical F_y contact forces closely follow each other. The numerical contact forces are within 3% of the corresponding analytical estimates. One of the reasons for the slight mismatch is that during the explicit numerical simulation, the outer ring, inner ring, and the rolling elements were modelled as flexible bodies in contrast to assuming them as rigid bodies during the analytical modelling. The ability of the flexible (finite) elements within the FE model of the bearing to vibrate during the numerical solution, and the interaction of the polygonised edges of the rolling elements and raceways could result in the excitation of non-physical modes. Other reasons may include the generation of numerical noise due to the adaptive time-stepping discussed in Section 4.5, Chapter 4, and the contact interaction of the rolling elements and raceways. Nevertheless, the numerically modelled horizontal and vertical contact forces closely follow the analytical solution. Four events are also indicated in Figures 6.4 and 6.5; these events will be described in the next section.

In summary, the acquisition of the basic bearing kinematics (outer raceway defect frequency f_{bpo}), presented in the numerically modelled vibration time-traces in Figures 4.5, 4.15 and 4.16, and the correct load distribution on the rolling elements, presented in Figure 6.1, indicate the validation of the presented results.

A detailed analysis of the dynamic contact forces is presented in the next section, with the aim of providing an understanding of the variations in the rolling element-to-raceway contact forces. As mentioned earlier, such an analysis has not been previously reported in the literature, except published recently in references [4, 5] by the author of this thesis, and in references [6, 7] based on the research described here.

6.3 Contact force analysis

The variations in the numerically modelled rolling element-to-outer raceway contact forces were broadly divided into four events, which are appropriately labelled as event #1 to event #4 in Figures 6.4 and 6.5. These events are similar to those discussed in Section 3.7, Chapter 3, which concerned the analysis of the analytical quasi-static contact forces shown in Figure 3.12. Event #1 corresponds to the de-stressing of the rolling elements, event #2 to the impact of the rolling elements with the defective surface, event #3 to re-distribution of load, and event #4 corresponds to the re-stressing of the rolling elements.

For the purpose of relating the variations in the numerical contact forces as the rolling elements traverse through the raceway defect, refer to Figure 6.6. This figure shows a schematic of a rolling element bearing model comprising an outer ring, an inner ring, a few rolling elements, and a rectangular defect. The rolling elements marked as '1', '2', and '3' are the ones that traversed through the defect in a clockwise direction during the numerical simulation undertaken here. The *starting* and *ending* positions of the defect are also shown in the schematic. Throughout the discussion to follow in this thesis, the '*top surface of the defect*' is referred to as the '*defective surface of the outer raceway*' as indicated in the schematic.

As the radial load W was applied at the top of the bearing so that the defect is under maximum load, the rolling elements which traverse through the defect will have larger vertical contact forces F_y than the corresponding horizontal forces F_x. It is, therefore, convenient to analyse the variations in the vertical rolling element-to-outer raceway contact forces F_y presented in Figure 6.5, although similar variations can also be seen in the horizontal force components F_x in Figure 6.4, but comparatively less clear.

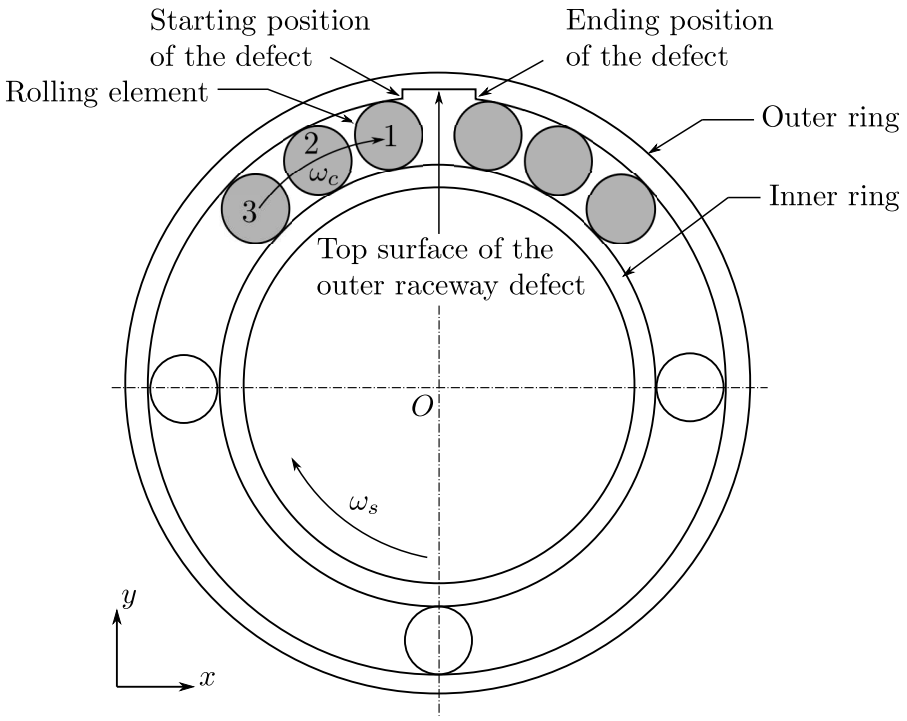

Figure 6.6: A 2-D schematic of a rolling element bearing comprising an outer ring, an inner ring, a few rolling elements, and a localised rectangular-shaped defect centrally located at the top of the outer raceway. The rolling elements filled using solid gray colour represent loaded elements, whereas the others represent non-loaded elements.

6.3.1 Event #1: Entry of the rolling elements into the defect — the 'de-stressing' phase

A radial load on a bearing is distributed among the rolling elements within the bearing load zone, which are stressed between the outer and inner raceways.

The results of the numerically modelled vertical contact forces F_y between the rolling elements and outer raceway in Figure 6.5 show that as a stressed rolling element begins to enter the outer raceway defect, it gradually (not instantaneously) starts losing contact with the outer raceway. From the figure, the time instances at which rolling elements $j = 1$, 2, and 3 begin to enter the defect correspond to approximately 1 ms, 12 ms and 23 ms, respectively. Subsequently, the contact forces between the outer raceway and the rolling elements $j = 1$, 2, and 3 decrease until they reach zero at approximately 1.4 ms, 12.4 ms, and 23.5 ms, respectively. The reduction of the

numerical vertical contact forces F_y from approximately 6 kN to 0 kN in approximately 0.4 ms implies that the stress on the rolling elements is also reduced to zero.

The gradual decrease in the contact force between the outer raceway and the three rolling elements $j = 1, 2, 3$, which traversed through the outer raceway defect during the simulation, is highlighted using the solid, elliptical markers in all the subplots of Figures 6.4 and 6.5. Event #1, which corresponds to the entry of the rolling elements into the defect, is referred to as the *de-stressing* of the rolling elements. The occurrences of the consecutive de-stressing events are separated by approximately 0.011 seconds, which corresponds $f_{\text{bpo}} = 90.91$ Hz compared to the analytically estimated nominal $f_{\text{bpo}} = 90.07$ Hz, a difference of 0.9%.

Based on the aforementioned gradual unloading of the rolling elements, a novel mathematical model for predicting the gradual de-stressing of the rolling elements has been presented earlier in Section 3.5, Chapter 3. The differences between the instant decrease in the contact forces by previous researchers [100–102, 104–106, 109–114] and gradual decrease were shown in Figures 3.10, 3.12, and 3.13 in Chapter 3.

It is evident from the rolling element-to-outer raceway contact forces F_y plotted in Figure 6.5, that the numerically modelled and analytically estimated gradual de-stressing of the rolling elements have favourable agreement.

The gradual decrease in the contact forces highlights that the de-stressing of the rolling elements shows no indication of an impact, and therefore, cannot excite a broad range of frequencies which generally causes the ringing of a bearing [17, 30]. It is the gradual unloading of the rolling elements that indicates the signals associated with the de-stressing event have low-frequency characteristics.

In summary, the gradual de-stressing of the rolling elements leads to the generation of the low-frequency event. The occurrence of the de-stressing event was highlighted in both numerically modelled and experimentally measured vibration signals shown in Chapters 4 and 5, respectively.

6.3.2 Event #2: Traverse of the rolling elements through the defect — impact of the rolling elements with the defective surface

The zero values of the contact forces between the rolling elements and the defective part of the outer raceway indicate that the rolling elements unload as they traverse through the defect. The numerically modelled horizontal F_x and vertical F_y contact forces in Figures 6.4 and 6.5, respectively, show that during the traverse of the rolling elements through the defect, the contact force remains zero for most of the time except for a few instances. These instances, which are indicated as event #2 in the subplots of Figures 6.4 and 6.5, correspond to the impact of the rolling elements with the *top surface of the defect* — the defective surface of the outer raceway (refer to Figure 6.6 to see the top surface of the defect).

During the operation of a bearing, the rolling elements possess centrifugal forces. While the centrifugal forces tend to project the rolling elements outward from the centre of the bearing, their outward trajectory is restricted between the outer and inner raceways when the rolling elements are stressed between the raceways. However, when the rolling elements are de-stressed due to the loss of contact with the outer raceway while they traverse through the defect, they tend to freely follow their outward trajectory. At some point, they strike the top surface of the defect and are indicated in Figures 6.4 and 6.5 as event #2. It should be noted that the magnitude of these impacts for the horizontal contact forces F_x is much lower than the corresponding vertical components F_y; therefore, these impacts are not clearly visible in Figure 6.4, but are visible in Figure 6.5. The reason for the higher magnitude of the vertical contact forces is the application of the radial load W along the y-axis.

One of the limitations of the quasi-static analytical model, mentioned in Section 3.8, Chapter 3, was the inability to predict the aforementioned impacts of the rolling elements with the defective surface during their traverse through the defect. This is

because the model is static and does not include the dynamics (centrifugal effects) of the rolling elements. Incorporating their centrifugal effects and analytically modelling the trajectory of the de-stressed rolling elements is a considerable task, and beyond the scope of the work presented in Chapter 3. Furthermore, the aim of the analytical modelling was to verify the FE simulated contact forces using the quasi-static model.

It can be seen from Figures 6.5a and 6.5c that the first $j = 1$ and third $j = 3$ rolling elements strike the top surface of the defect twice, while in Figure 6.5b, the second rolling element $j = 2$ strikes the defect surface three times. It is also interesting to note that not only do the amplitudes of these impacts differ from each other, but also their timings. The reason for the varying period is the interaction of the rolling elements with the adjacent cage slots. The irregular period of the impact timings implies that at some instances the rolling elements are driven by the cage (slots), and at other instances, the rolling elements drive the cage. The rolling element–cage interaction is also another cause for the slippage of the rolling elements observed in practice, in addition to the explanation provided in reference [96]. It is one of the reasons for the slight difference (0.8%) between the analytical and numerical estimations of the rolling elements-to-outer raceway rolling contact noise frequency f^{o}_{noise}, as discussed in Section 4.5.2, Chapter 4.

6.3.3 Event #3: Re-distribution of a load on the rolling elements — the load compensation phase

It was discussed in the preceding section that the rolling elements lose contact with the defective part of the outer raceway as they traverse through the defect. The loss of the load (force) on a rolling element must be compensated in order to have the equilibrium of the system maintained at all times. Therefore, as one rolling element loses contact (unloads), other rolling elements in the load zone, located at the non-defective sections of the raceways, take the lost load resulting in the re-distribution of the radial load.

Event #3, indicated in Figures 6.4 and 6.5, highlights the load compensation.

In the event of a rolling element traversing through a defect, an increase in the magnitude of load on other rolling elements results in higher contact stresses compared to a non-defective bearing. The higher contact stresses will eventually result in the onset of localised surface fatigue cracks in the raceways at spacings approximately equivalent to roller spacings [337].

6.3.4 Event #4: Exit of the rolling elements from the defect — the 're-stressing' phase

When the rolling elements reach the end (position) of the defect (refer to Figure 6.6 to see the ending position of the defect), they again come into contact with the non-defective surface of the outer raceway. At this point, the contact force (load) on the rolling elements increases from zero to a value that is related to the static load distribution.

The resumption of the contact between the rolling elements and outer raceway causes the *re-stressing* of the rolling elements. Event #4, which corresponds to the re-stressing of the rolling elements between the outer and inner raceways, is highlighted using the solid, rectangular markers in the horizontal F_x and vertical F_y contact force plots in Figures 6.4 and 6.5, respectively. The characteristics of the contact forces pertinent to the re-stressing of the rolling elements are discussed in the following paragraphs.

Prior to regaining full contact with the raceways following the de-stressing of the rolling elements during their traverse through the outer raceway defect (event #2), the free outward trajectory of de-stressed rolling elements is again restricted between inner and outer raceways. The rolling elements are gradually wedged between both raceways, and during this period, they continuously rattle between the raceways until they are fully loaded (stressed) once again. The rattling of the rolling elements causes the

generation of a few short-duration (contact) force impulses that excite the resonance modes of the bearing.

The subplots of Figures 6.4 and 6.5 were zoomed in the vicinity of the re-stressing of the rolling elements, and are shown in Figure 6.7 in order to highlight the occurrence of multiple force impulses. Figures 6.7a, 6.7c, and 6.7e show the horizontal rolling element-to-outer raceway contact forces F_x, whereas Figures 6.7b, 6.7d, and 6.7f show the corresponding vertical contact forces F_y. While the scale of the y-axis for the horizontal contact force plots ranges from 0 kN to 1 kN, it ranges from 0 kN to 10 kN for the vertical contact forces. Despite being different by an order of magnitude, the timings at which the horizontal and vertical multiple force impulses occur are similar.

In contrast to the de-stressing of the rolling elements upon their entrance into the defect where no force impulses were generated (event #2), the contact forces in Figure 6.7 show that the exit of the rolling elements from the defect causes multiple force impulses. Previous analytical models [90–96, 103, 114, 165] were based on the assumption that the defect-related impulsive vibration response of a bearing is generated by a single force impulse that exponentially decays over time. However, the explicit dynamics FE modelling results presented here show that a burst of multiple, short-duration, force impulses occurs as the rolling elements re-stress between the raceways on their exit from the defect. This is a *novel and an important outcome* of the modelling. This will be discussed in more details in Section 6.4.2. Although the re-stressing of the rolling elements has previously been reported using experimental studies [161–165], its cause has not been discussed.

It is also interesting to note that the results of the numerically modelled vertical rolling element-to-outer raceway contact forces F_y in Figure 6.5 show that the amplitude of the impacts produced during the re-stressing phase, approximately 5 kN, is higher than the less than 2 kN (event #2) produced when the rolling elements strike the top surface of the defect. This is *another important outcome* of the modelling, as it indicates that higher forces and stresses are generated during the exit of the rolling

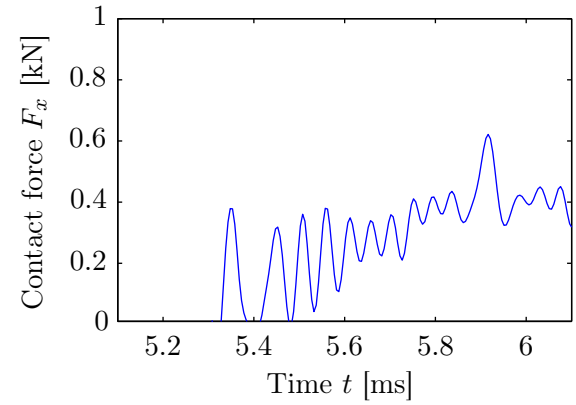

(a) Horizontal contact force between the first rolling element $j = 1$ and outer raceway.

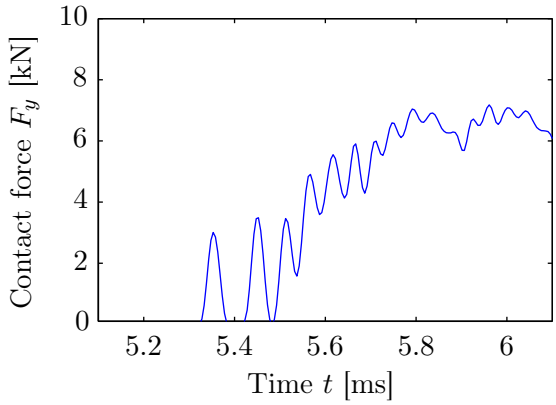

(b) Vertical contact force between the first rolling element $j = 1$ and outer raceway.

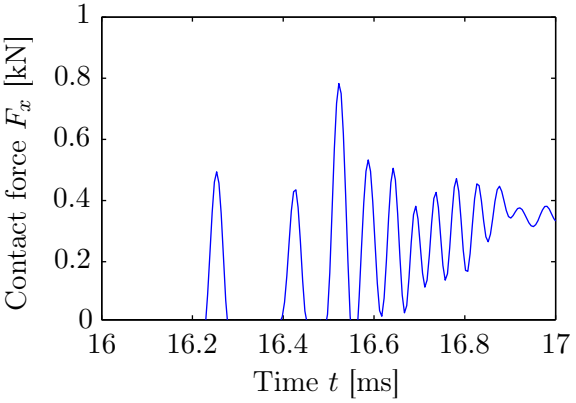

(c) Horizontal contact force between the second rolling element $j = 2$ and outer raceway.

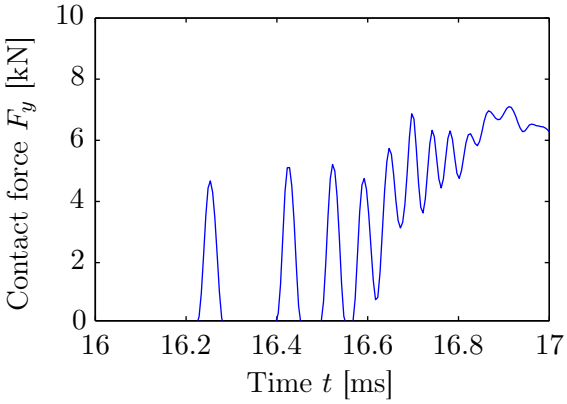

(d) Vertical contact force between the second rolling element $j = 2$ and outer raceway.

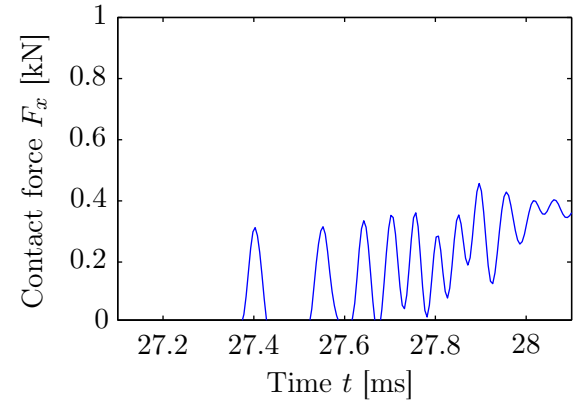

(e) Horizontal contact force between the third rolling element $j = 3$ and outer raceway.

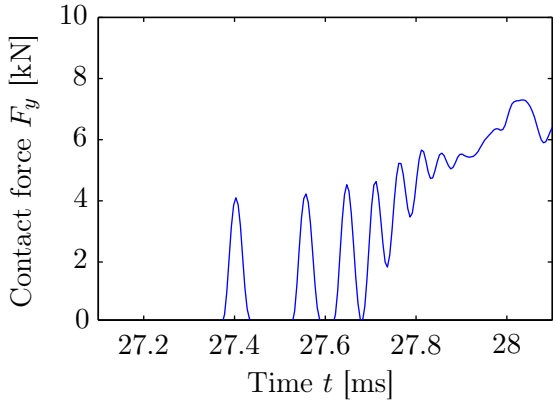

(f) Vertical contact force between the third rolling element $j = 3$ and outer raceway.

Figure 6.7: Numerically modelled, notch filtered, horizontal F_x and vertical F_y rolling element-to-outer raceway contact forces shown in Figures 6.4 and 6.5, respectively, are zoomed in the vicinity of rolling elements $j = 1, 2, 3$ being re-stressed between the raceways. For clarity, the y-axis in (a, c, e) scales from 0–1 kN, and in (b, d, f) from 0–10 kN.

elements from the defect compared to when they strike the defect surface, and hence, could lead to the gradual expansion or lengthening of the defect. These findings show excellent agreement with the experimental study conducted by Hoeprich [337]. He investigated the damage progression in rolling element bearings, and found that the size of a spall progresses in the rolling direction.

The correlation of the numerically modelled dynamic contact forces, plotted in Figures 6.4 and 6.5, with the acceleration signal will be presented in the next section.

6.4 Correlating contact forces with bearing vibrations

As rolling element-to-raceway contact forces are not measured in practice, it is useful to correlate the aforementioned numerical contact forces with the acceleration results, commonly measured in practice. The correlation will also facilitate the development of an understanding of:

- the cause of the generation of bearing defect-related impulsive signals that are generally observed in measured acceleration time-traces, and subsequently used for bearing diagnosis, and
- the physical mechanism that leads to the generation of the defect-related multiple impulsive forces.

6.4.1 Cause of impulsive signals in acceleration results

Figure 6.8 comprises four subplots: subplot (a) shows the numerically modelled, notch filtered, nodal acceleration a_y time-trace shown in Figure 4.13, Chapter 4; and subplots (b) to (d) show the numerically modelled, notch filtered, vertical rolling element-to-outer raceway contact forces F_y shown in Figure 6.5. Of the four events discussed in Section 6.3, the time instances corresponding to the occurrences of events #2 and #4 were primarily correlated between the acceleration and contact forces. The reason

for correlating these events is that the contact–impact kind of interaction was only observed to be associated with events #2 and #4. The time instances corresponding to the occurrence of event #1, which is associated with the low-frequency de-stressing of the rolling elements, will be correlated later between the numerical low-pass filtered acceleration and contact forces.

Events #2 and #4 correspond to the de-stressed rolling elements striking the defective surface of the outer raceway and the re-stressing of the rolling elements, respectively. In Figure 6.8, these events are highlighted using the dashed, elliptical and solid, rectangular markers, respectively. From the correlation of the time instances, implemented using appropriate markers and indicators, it shows that:

1. the dominant impulsive signals in the acceleration time-trace, which are indicated using the rectangular markers, correspond to the re-stressing of the rolling elements — event #4, and

2. the comparatively low amplitude acceleration signals, prior to the re-stressing phase, which are indicated using the dashed, elliptical markers, correspond to the impact of the de-stressed rolling elements with the defective surface as they traverse through the defect — event #2.

For clarification, the acceleration time-trace was zoomed in the vicinity of the second and third defect-related impulses, and the partial time-traces are shown in Figure 6.9b and Figure 6.9c, respectively; Figure 6.9a is the same as Figure 6.8a. It is clear from the correlation of the two events in Figures 6.8 and 6.9 that the dominant impulsive signals correspond to the re-stressing of the rolling elements. The zoomed acceleration time-traces also highlight the occurrence of multiple impulses as a result of the traverse of a single rolling element through the defect rather than a single impulse as has been previously modelled by several researchers [90–96, 103, 114, 165]. Such impulses are generally observed in measured bearing vibration signals; however, the reason for their

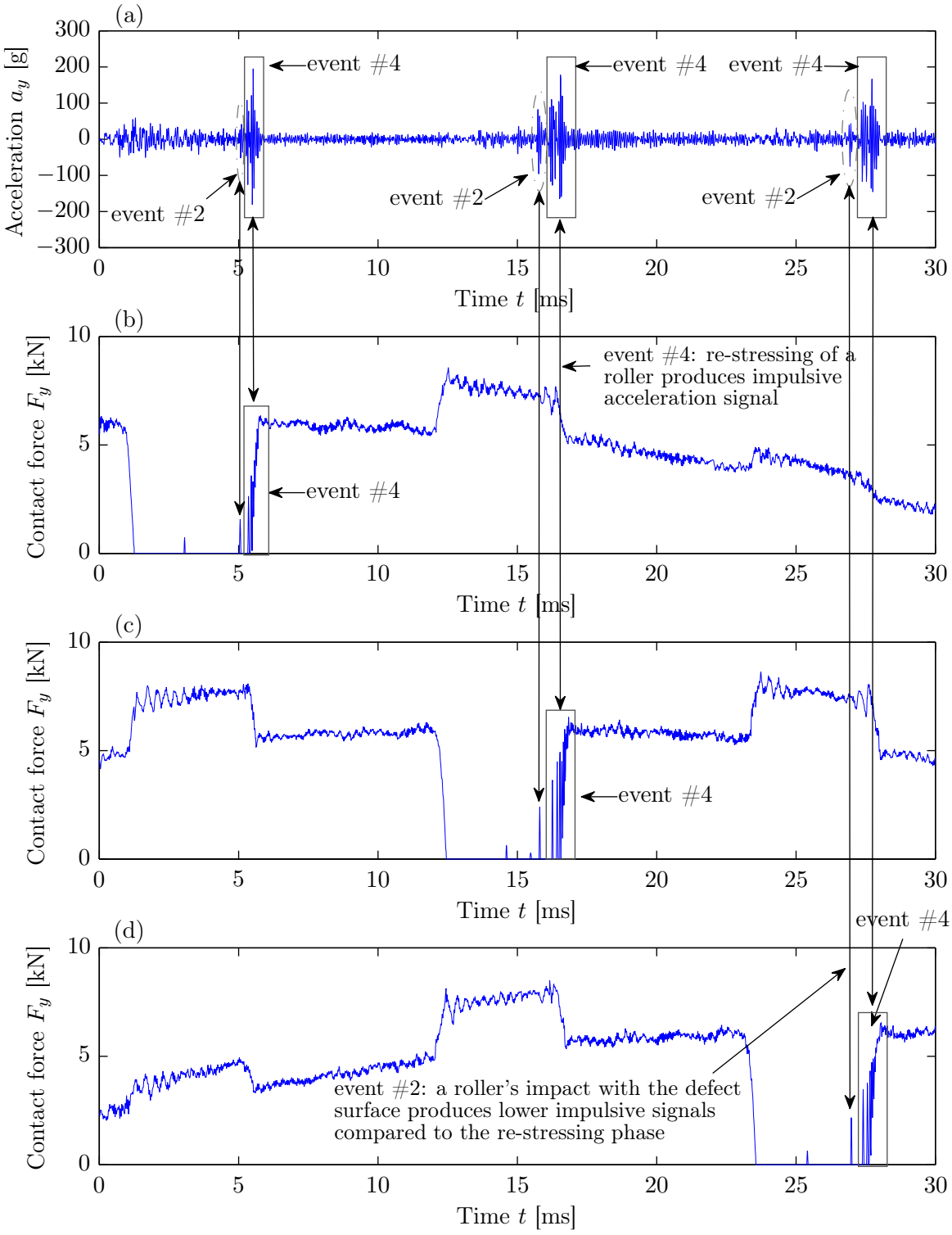

Figure 6.8: Correlation between the numerically modelled, notch filtered, acceleration a_y time-trace shown in Figure 4.13, Chapter 4, and vertical contact forces F_y between the outer raceway and three rolling elements $j = 1, 2, 3$ that traversed through the defect shown in Figure 6.5 for a radial load W of 50 kN and rotational speed n_s of 500 RPM; (a) nodal acceleration, (b) contact force: outer raceway-to-rolling element $j = 1$, (c) contact force: outer raceway-to-rolling element $j = 2$, and (d) contact force: outer raceway-to-rolling element $j = 3$.

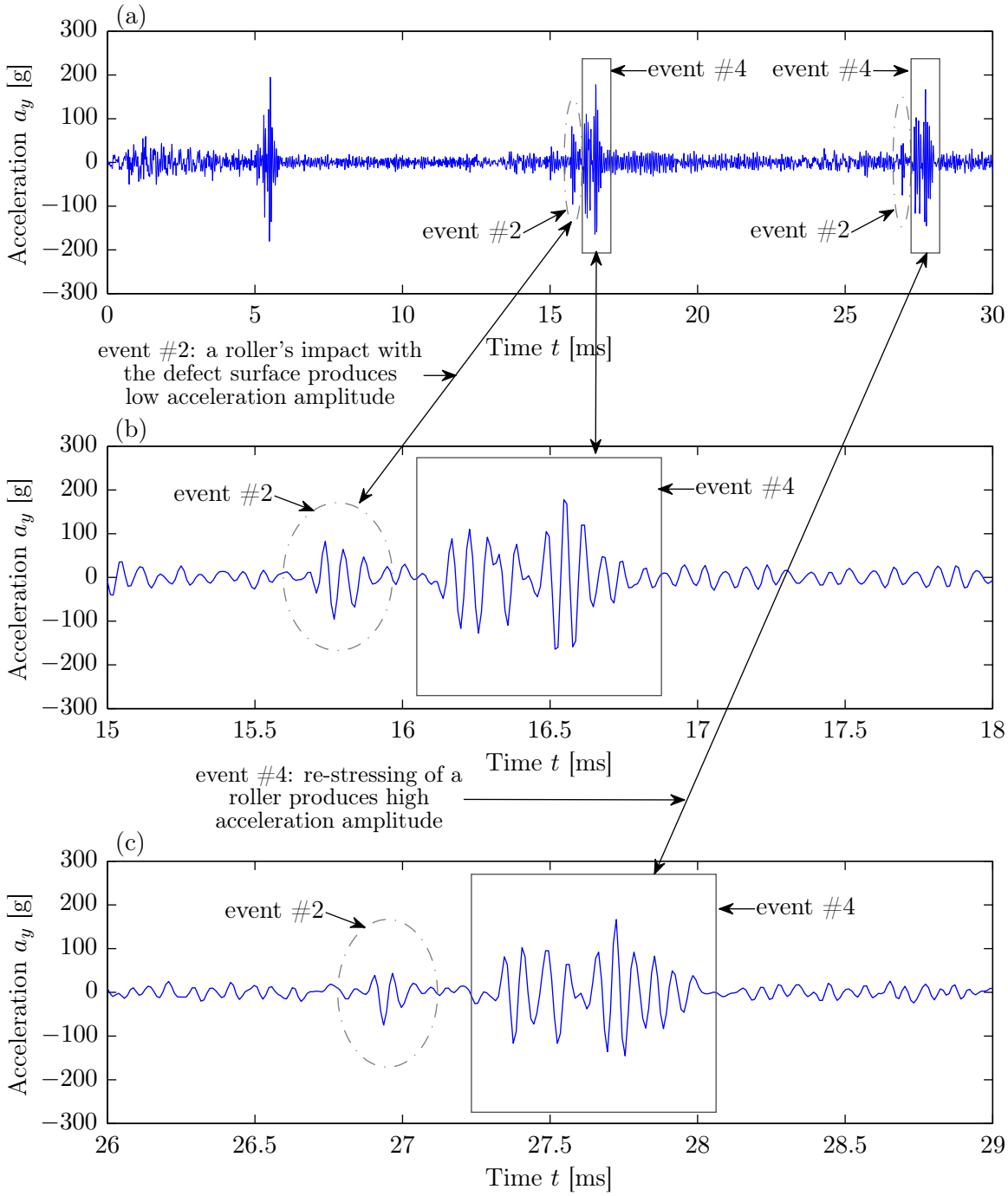

Figure 6.9: Numerically modelled, notch filtered, acceleration a_y time-trace shown in Figure 6.8a; (a) complete time-trace showing the three defect-impulses that occurred during the numerical simulation, (b) partial time-trace zoomed in the vicinity of the second impulse generated due to the re-stressing of rolling element $j = 2$, and (c) partial time-trace zoomed in the vicinity of the third impulse generated due to the re-stressing of rolling element $j = 3$.

occurrence has not been clearly understood [105, 165]. This will be discussed in the next section.

During the analysis of the contact forces in Section 6.3.4, it was also observed that the amplitude of the contact forces resulting from the impacts of the de-stressed rolling elements with the defective surface of the outer raceway; that is event #2, is lower than those related to the re-stressing of the rolling elements between the raceways; that is event #4. This is also reflected in the acceleration results. From Figures 6.8 and 6.9, the instantaneous level of the acceleration signal during the re-stressing of the rolling elements is approximately twice the level of the acceleration during the period where the de-stressed rolling elements strike the defective surface of the raceway.

An *important outcome* of the results from the explicit dynamics FE analysis of the rolling element bearing is that it is the re-stressing of the rolling elements, and not their impact with the defective surface, that causes the generation of the defect-related impulsive signals. In other words, although a rolling element can strike the surface of a defect and generate a low amplitude acceleration signal, a much higher acceleration signal is generated when the rolling elements are re-stressed between the raceways. These higher acceleration signals, generated during the re-stressing phase, are the ones that are generally observed in practice, and subsequently used for bearing diagnosis using the well-known envelope analysis technique [30, 251, 252].

As low-frequency signals related to the de-stressing of the rolling elements could not be observed in the numerical acceleration a_y time-trace until it was low-pass filtered, Figure 6.10 presents the correlation of the low-pass filtered acceleration a_y (shown in Figure 4.22, Chapter 4) with the vertical rolling element-to-raceway contact forces F_y for the sole purpose of correlating the time-instances of the de-stressing event. The occurrences of the de-stressing of the rolling elements, annotated as event #1 and indicated using the solid, elliptical markers in Figure 6.10, was achieved at the expense of eliminating the impulsiveness of the re-stressing event. However, as mentioned earlier in Section 4.6.2, Chapter 4, the low-pass filtering was only implemented to verify the

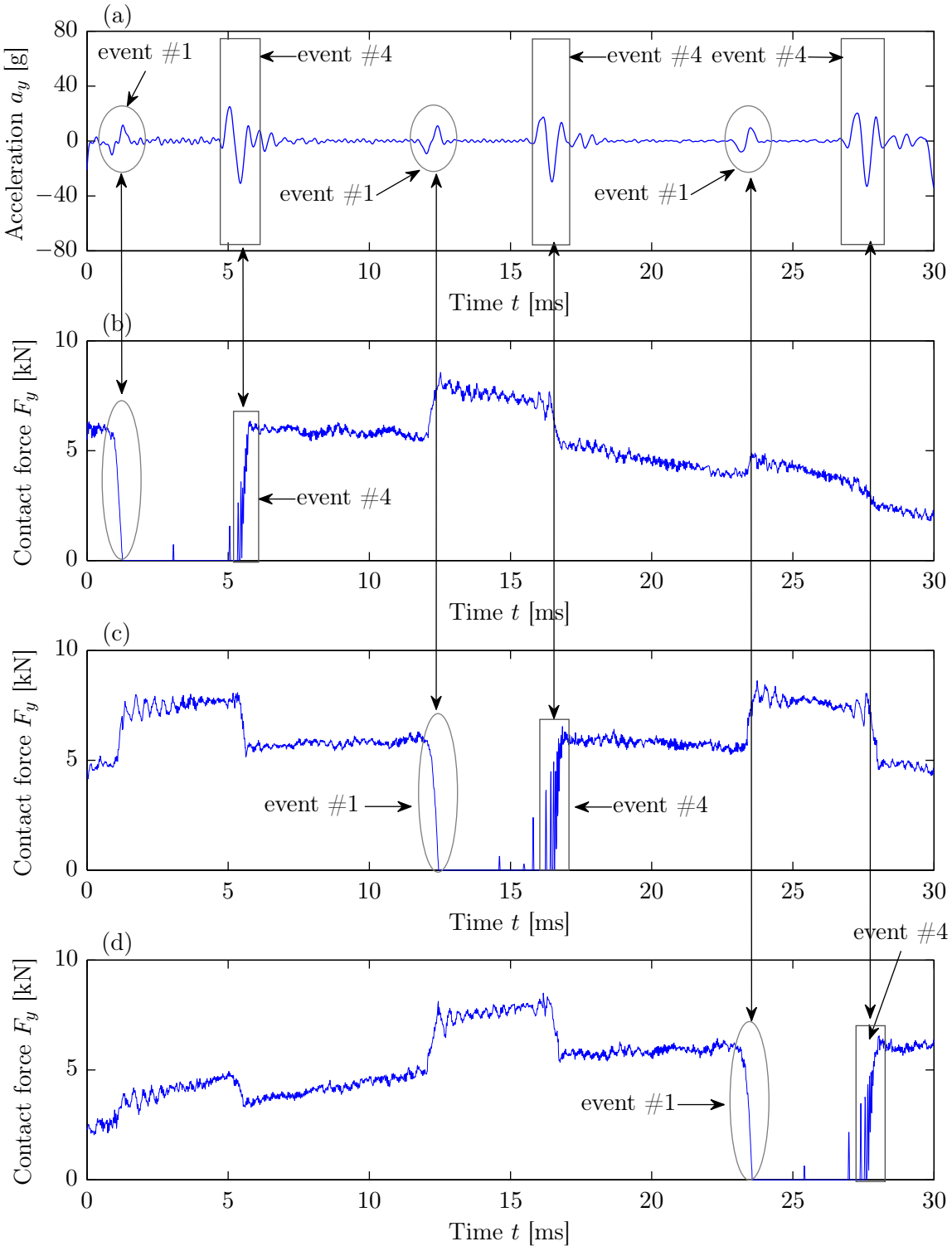

Figure 6.10: Correlation between the numerically modelled, low-pass filtered, acceleration a_y time-trace shown in Figure 4.22, Chapter 4, and vertical contact forces F_y between the outer raceway and three rolling elements $j = 1$, 2, 3 that traversed through the defect shown in Figure 6.5 for a radial load W of 50 kN and rotational speed n_s of 500 RPM; (a) nodal acceleration, (b) contact force: outer raceway-to-rolling element $j = 1$, (c) contact force: outer raceway-to-rolling element $j = 2$, and (d) contact force: outer raceway-to-rolling element $j = 3$.

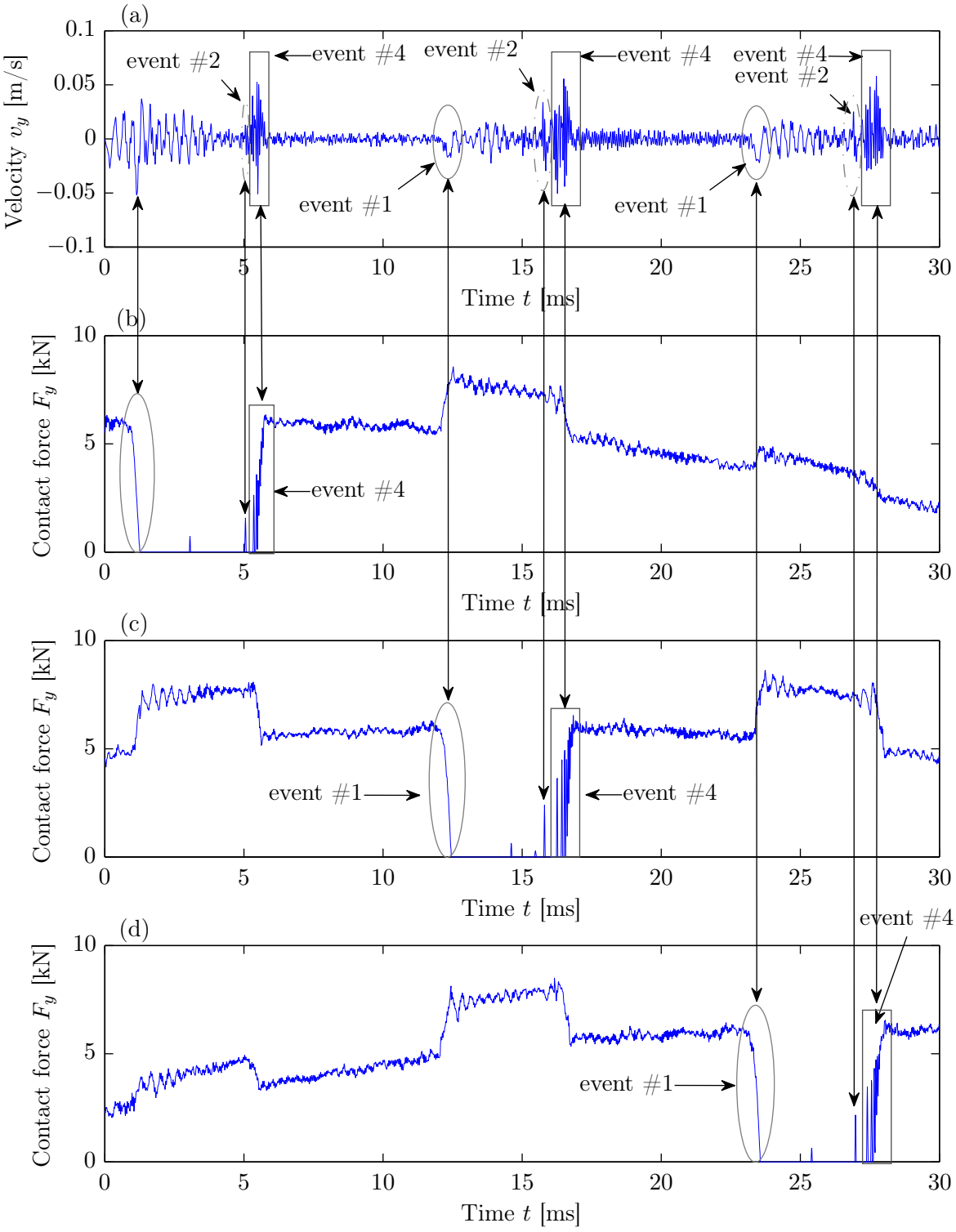

Figure 6.11: Correlation between the numerically modelled, notch filtered, velocity v_y time-trace shown in Figure 4.17, Chapter 4, and vertical contact forces F_y between the outer raceway and three rolling elements $j = 1, 2, 3$ that traversed through the defect shown in Figure 6.5 for a radial load W of 50 kN and rotational speed n_s of 500 RPM; (a) nodal velocity, (b) contact force: outer raceway-to-rolling element $j = 1$, (c) contact force: outer raceway-to-rolling element $j = 2$, and (d) contact force: outer raceway-to-rolling element $j = 3$.

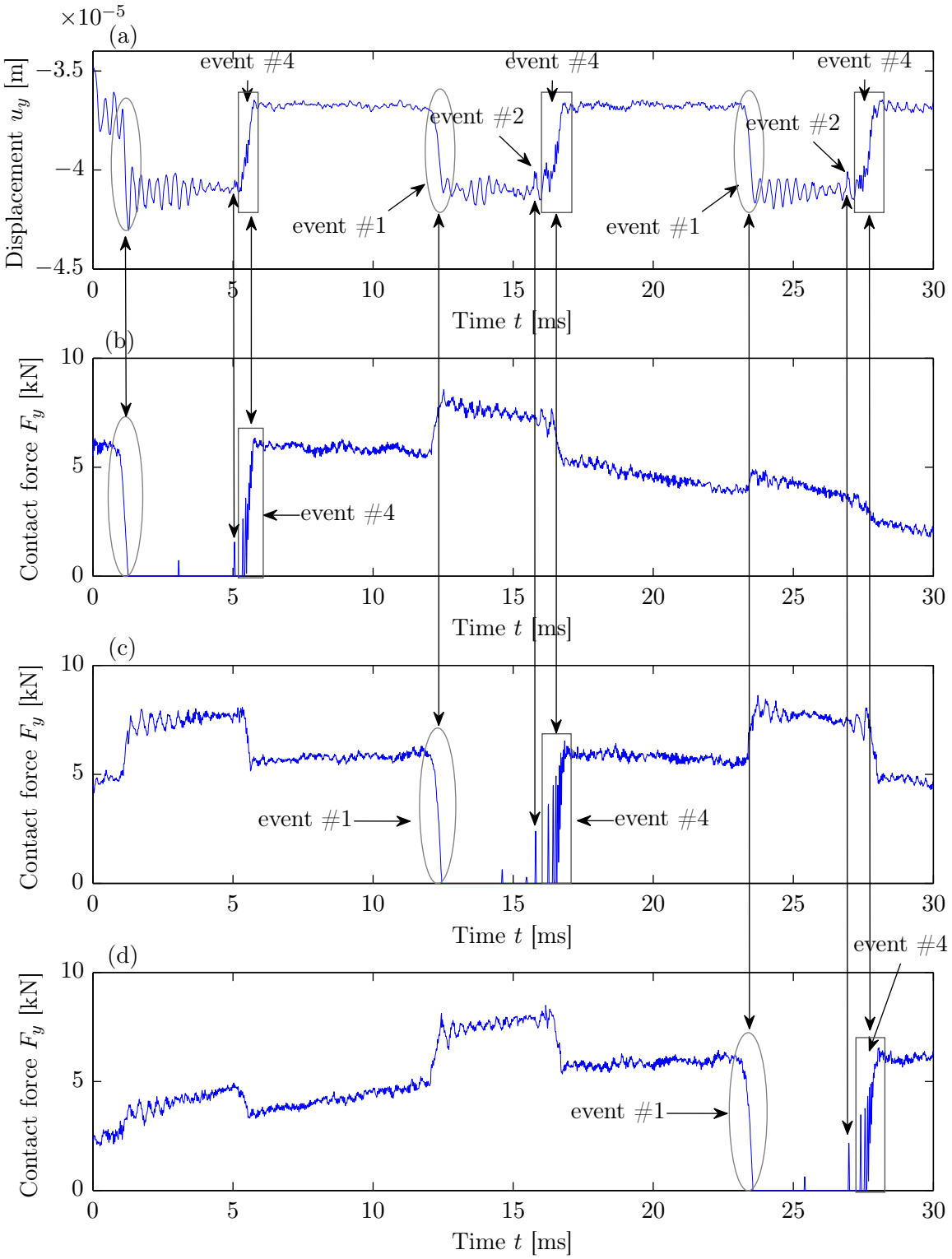

Figure 6.12: Correlation between the numerically modelled, notch filtered, displacement u_y time-trace shown in Figure 4.18, Chapter 4, and vertical contact forces F_y between the outer raceway and three rolling elements $j = 1, 2, 3$ that traversed through the defect shown in Figure 6.5 for a radial load W of 50 kN and rotational speed n_s of 500 RPM; (a) nodal displacement, (b) contact force: outer raceway-to-rolling element $j = 1$, (c) contact force: outer raceway-to-rolling element $j = 2$, and (d) contact force: outer raceway-to-rolling element $j = 3$.

acceleration signatures associated with the de-stressing event.

The numerically modelled, notch filtered, velocity v_y and displacement u_y time-traces shown in Figures 4.17 and 4.18, Chapter 4, respectively, were also correlated with the contact forces in a way similar to that of the acceleration a_y signal. The time instances pertinent to events #1, #2, and #4 were correlated between the vibration time-traces and the contact forces, and the corresponding plots are shown in Figures 6.11 and 6.12. The markers and indicators shown in the figures highlight that the findings are similar to those observed for the correlation of the acceleration with the contact forces as presented in Figures 6.8 and 6.10.

Correlation of the numerically modelled rolling element-to-raceway contact forces and bearing acceleration for radial loads W of 25 kN and 80 kN, and a rotational speed n_s of 500 RPM

The figures shown above were concerned with the results from the FE analysis of the rolling element bearing for a radial load W of 50 kN and a rotational speed n_s of 500 RPM. In order to verify the consistency of the findings observed in Figures 6.8 to 6.10, the correlation of the contact forces and acceleration results was also conducted for two additional radial loads W of 25 kN and 80 kN at a rotational speed n_s of 500 RPM. It has been mentioned earlier in Chapter 5 that a load of $W = 25$ kN on the bearing simulates a radial load of an empty railway wagon, whereas a load of $W = 80$ kN simulates a load of an almost fully loaded wagon.

Figures 6.13 and 6.14 show the correlation of the numerically modelled, notch filtered, acceleration a_y at a rotational speed n_s of 500 RPM with the corresponding rolling element-to-outer raceway, notch filtered, vertical contact forces F_y for radial loads W of 25 kN and 80 kN, respectively. It is evident from the results in the figures that the variations in the contact forces and their correlation with the bearing acceleration, highlighted using relevant indicators and markers, related to events #2 and #4, are similar to those observed in Figure 6.8, which represents the simulation results for

a radial load of 50 kN and rotational speed of 500 RPM.

Similar to Figure 6.9, which shows the numerical acceleration for $n_s = 500$ RPM and $W = 50$ kN, the acceleration a_y time-traces in Figures 6.13 and 6.14 for $W = 25$ kN and $W = 80$ kN, respectively, were zoomed in the vicinity of the defect-related impulses, and the corresponding plots are shown in Figures 6.15 and 6.16 in order to clearly highlight the variations related events #2 and #4.

For correlating the time instances of the de-stressing event (#1), the numerically modelled acceleration a_y time-traces for radial loads W of 25 kN and 80 kN, shown in Figures 6.13 and 6.14, respectively, were low-pass filtered to enhance the low-frequency signatures associated with the entrance of the rolling elements into the defect. Similar to the plots shown in Figure 6.10 for a rotational speed of n_s 500 RPM and radial load W 50 kN, the correlation of the low-pass filtered acceleration with rolling element-to-outer contact forces for the FE simulations for radial loads of 25 kN and 80 kN are shown in Figure 6.17 and 6.18, respectively.

From the correlation of the numerical acceleration with contact forces obtained from the FE simulations undertaken for three different radial loads of 25 kN, 50 kN, and 80 kN at a constant rotational speed of 500 RPM, the findings related to events #2 and #4, as enumerated earlier in this section, were observed to be consistent.

The numerically modelled acceleration a_y time-traces shown in Figures 6.8, 6.13, and 6.14 for radial loads W of 25 kN, 50 kN, and 80 kN, respectively, are plotted on a similar scale, ±300 g, whereas the contact forces F_y are plotted on dissimilar scales — 0–5 kN, 0–10 kN, and 0–15 kN. The reason for plotting the contact forces on different scales is to clearly highlight the distinction between the variation in the force impulses related to events #2 and #4, that is, the impact of the rolling elements with the defective raceway surface and the re-stressing of the rolling elements, respectively. However, for comparison, the rolling element-to-raceway contact forces corresponding to the aforementioned loads and various rotational speeds are plotted together on a single figure, and will be shown in the Figures 6.22 and 6.23 during the discussion of

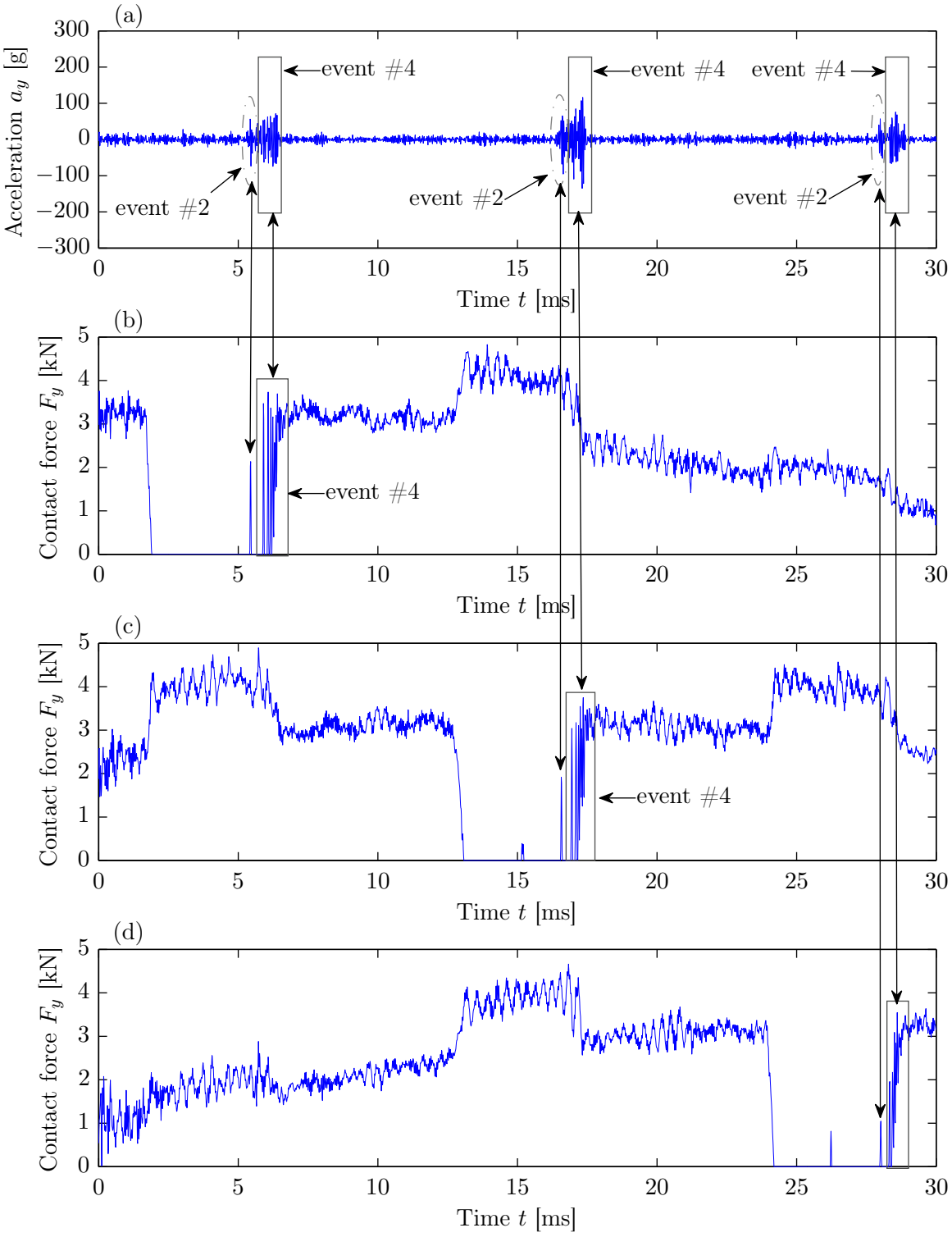

Figure 6.13: Correlation between the numerically modelled, notch filtered, acceleration a_y time-trace shown in Figure 5.5b, Chapter 5, and vertical contact forces F_y between the outer raceway and three rolling elements $j = 1, 2, 3$ that traversed through the defect for a radial load W of 25 kN and rotational speed n_s of 500 RPM (a) nodal acceleration, (b) contact force: outer raceway-to-rolling element $j = 1$, (c) contact force: outer raceway-to-rolling element $j = 2$, and (d) contact force: outer raceway-to-rolling element $j = 3$.

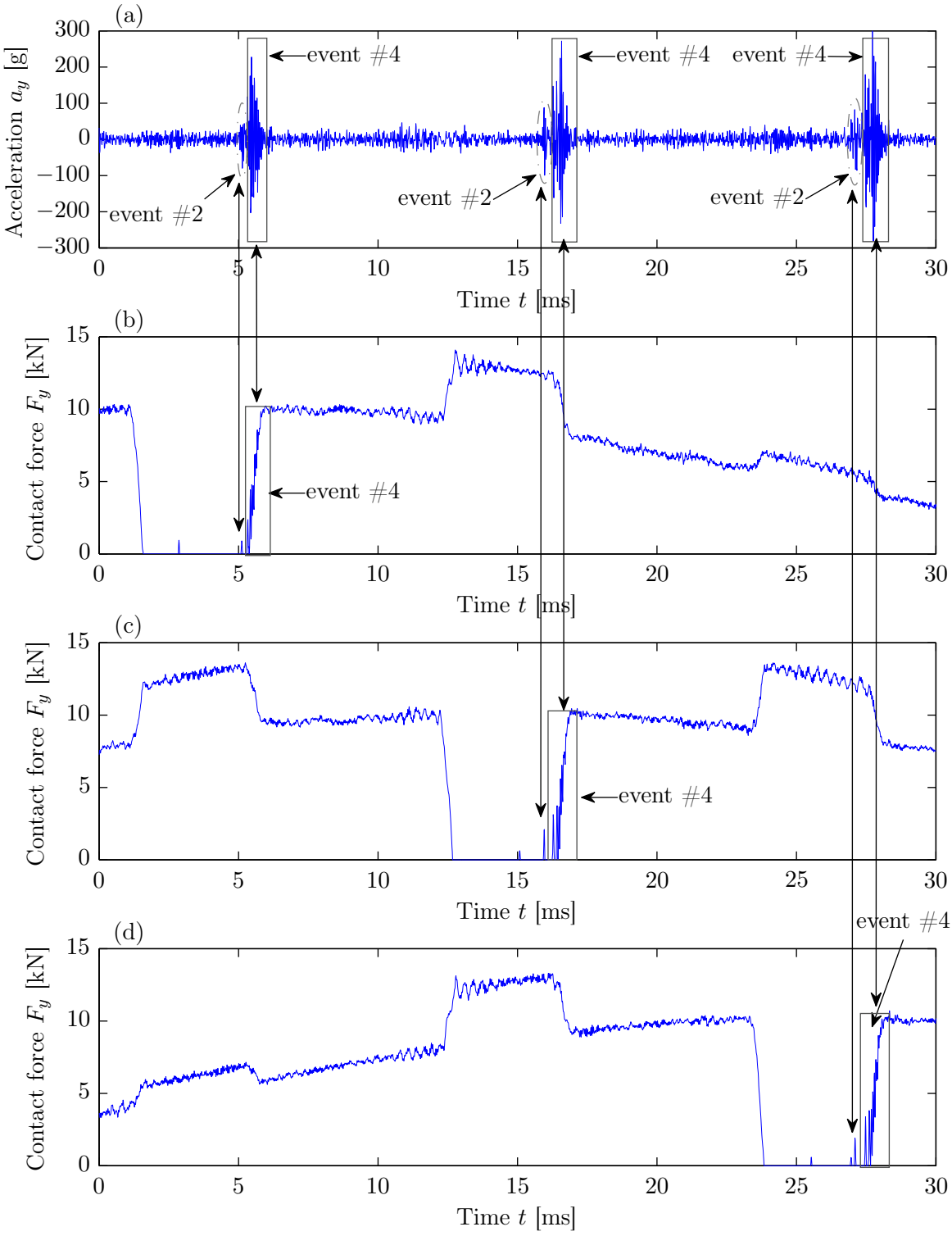

Figure 6.14: Correlation between the numerically modelled, notch filtered, acceleration a_y time-trace shown in Figure 5.5d, Chapter 5, and vertical contact forces F_y between the outer raceway and three rolling elements $j = 1, 2, 3$ that traversed through the defect for a radial load W of 80 kN and rotational speed n_s of 500 RPM; (a) nodal acceleration, (b) contact force: outer raceway-to-rolling element $j = 1$, (c) contact force: outer raceway-to-rolling element $j = 2$, and (d) contact force: outer raceway-to-rolling element $j = 3$.

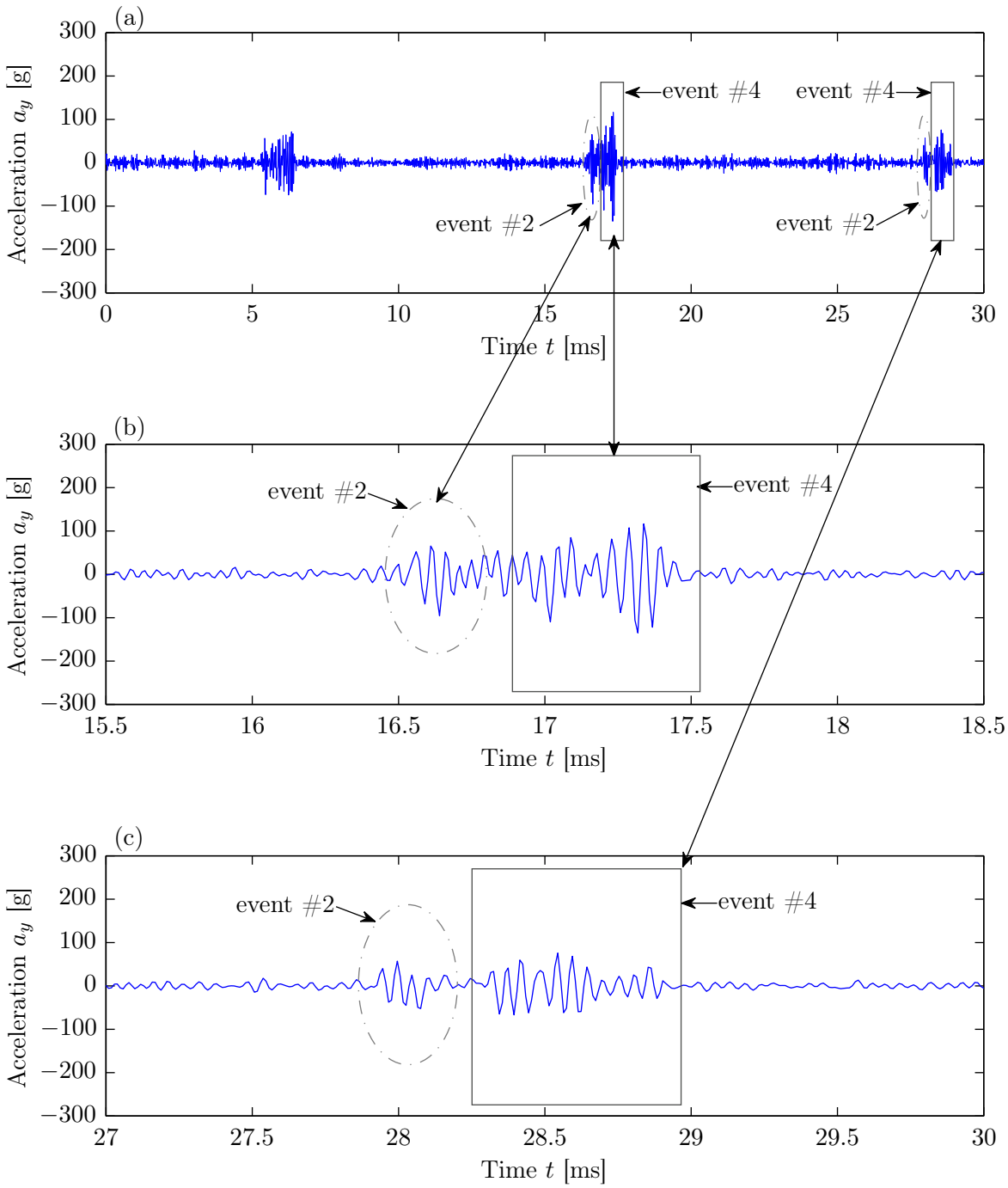

Figure 6.15: Numerically modelled, notch filtered, acceleration a_y time-trace shown in Figure 6.13a; (a) complete time-trace showing the three defect-impulses that occurred during the numerical simulation, (b) partial time-trace zoomed in the vicinity of the second impulse generated due to the re-stressing of rolling element $j = 2$, and (c) partial time-trace zoomed in the vicinity of the third impulse generated due to the re-stressing of rolling element $j = 3$.

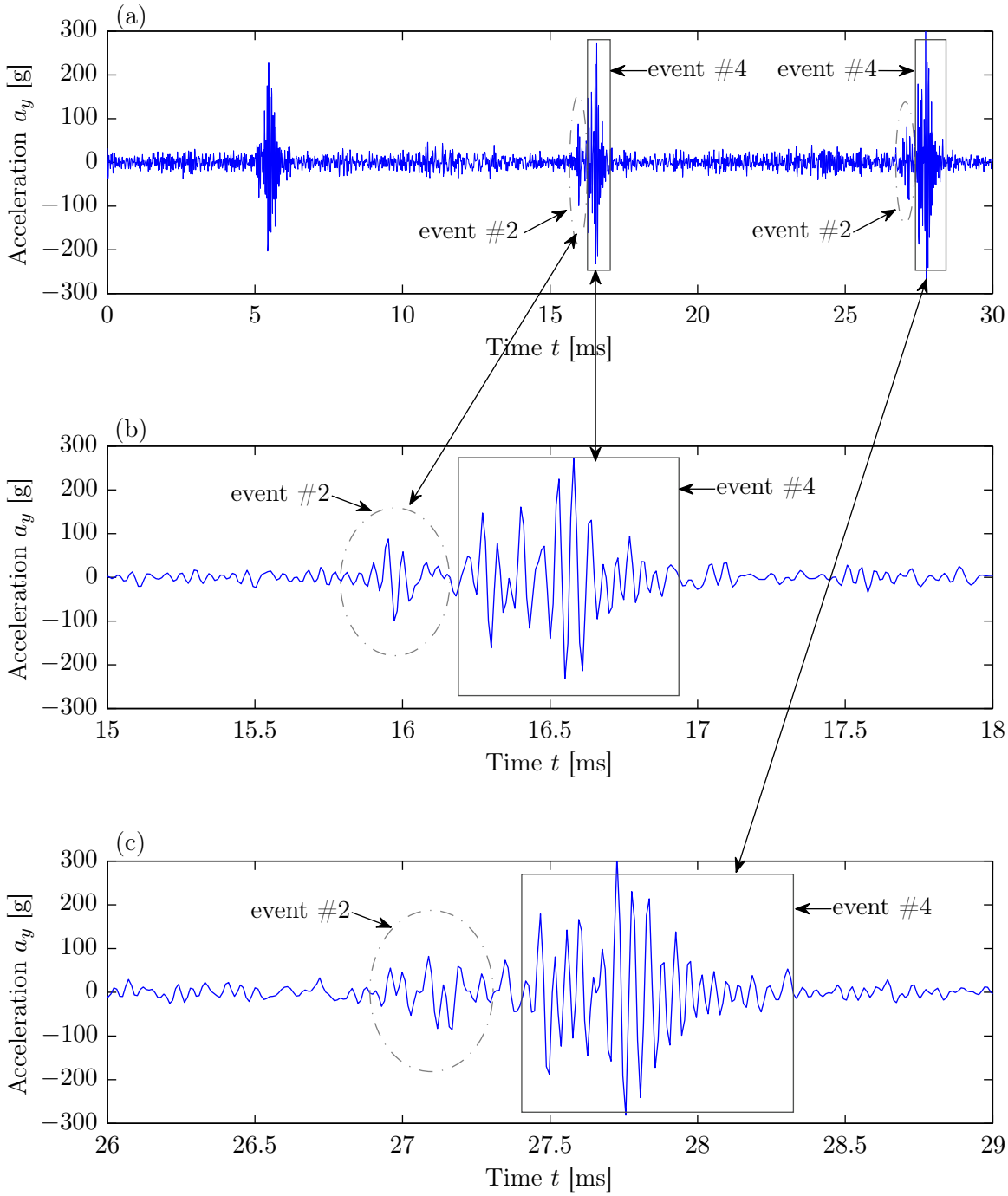

Figure 6.16: Numerically modelled, notch filtered, acceleration a_y time-trace shown in Figure 6.14a; (a) complete time-trace showing the three defect-impulses that occurred during the numerical simulation, (b) partial time-trace zoomed in the vicinity of the second impulse generated due to the re-stressing of rolling element $j = 2$, and (c) partial time-trace zoomed in the vicinity of the third impulse generated due to the re-stressing of rolling element $j = 3$.

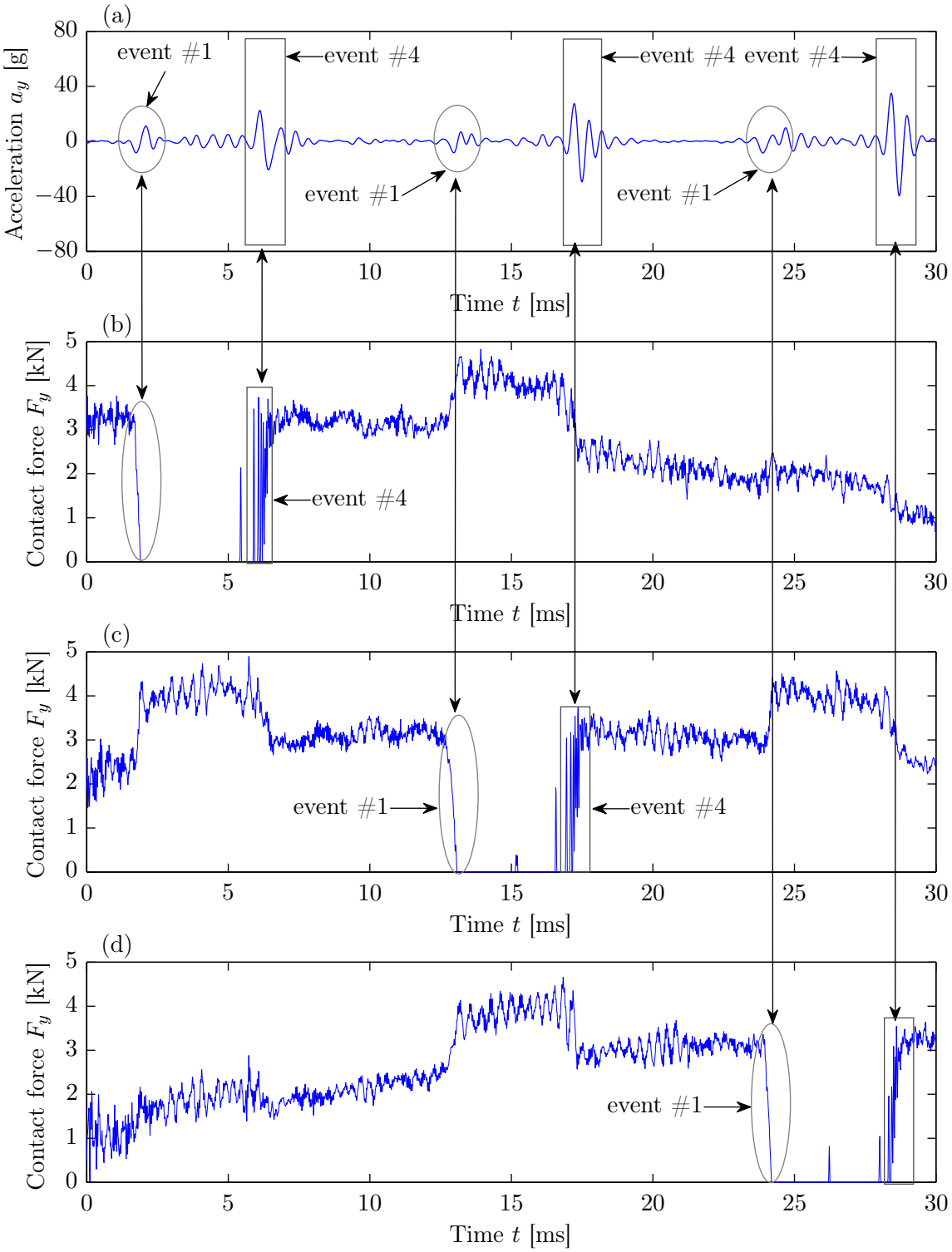

Figure 6.17: Correlation between the numerically modelled, low-pass filtered, acceleration a_y time-trace shown in Figure 5.5b, Chapter 5, and vertical contact forces F_y between the outer raceway and three rolling elements $j = 1$, 2, 3 that traversed through the defect shown in Figure 6.13 for a radial load W of 25 kN and rotational speed n_s of 500 RPM; (a) nodal acceleration, (b) contact force: outer raceway-to-rolling element $j = 1$, (c) contact force: outer raceway-to-rolling element $j = 2$, and (d) contact force: outer raceway-to-rolling element $j = 3$.

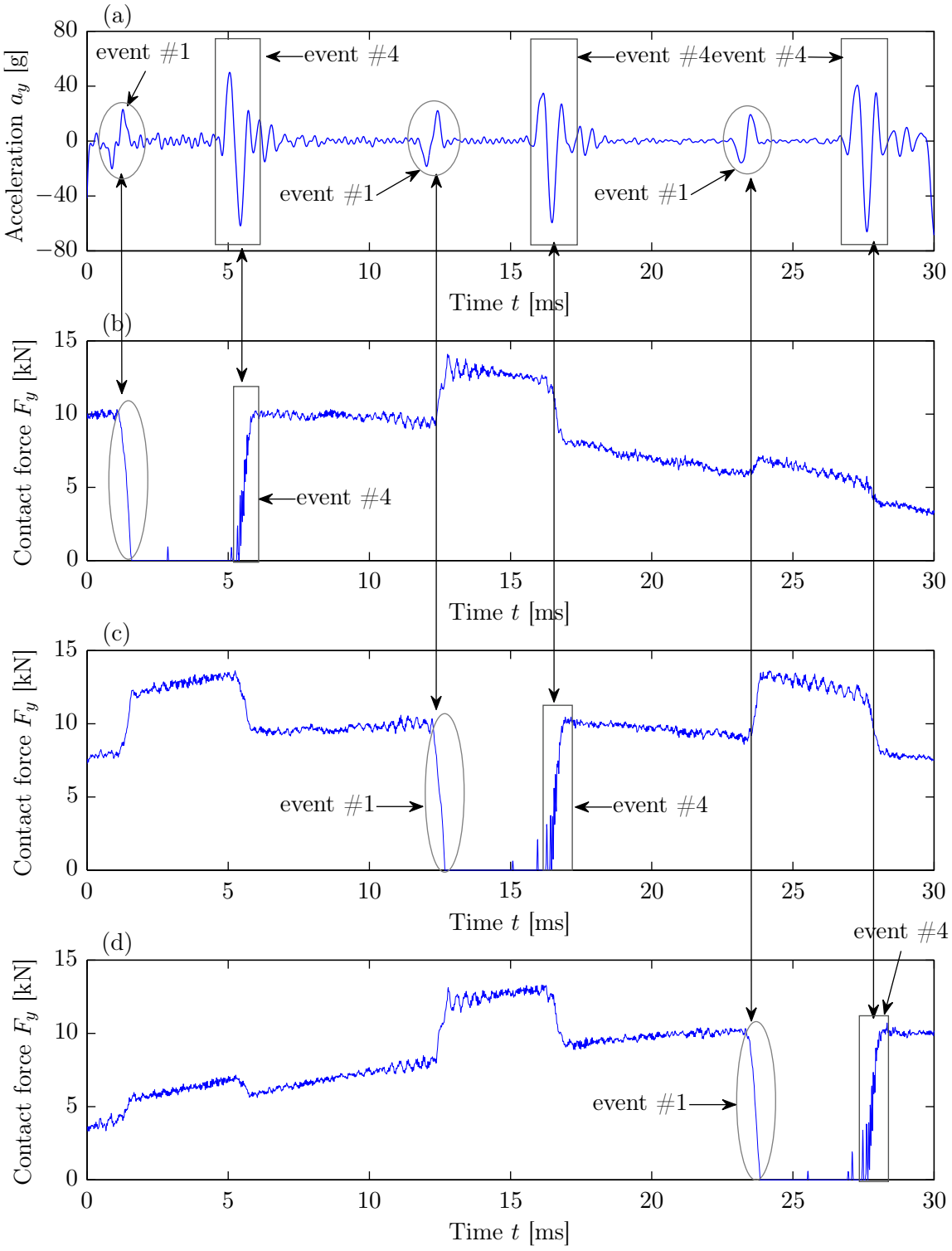

Figure 6.18: Correlation between the numerically modelled, low-pass filtered, acceleration a_y time-trace shown in Figure 5.5d, Chapter 5, and vertical contact forces F_y between the outer raceway and three rolling elements $j = 1$, 2, 3 that traversed through the defect shown in Figure 6.14 for a radial load W of 80 kN and rotational speed n_s of 500 RPM; (a) nodal acceleration, (b) contact force: outer raceway-to-rolling element $j = 1$, (c) contact force: outer raceway-to-rolling element $j = 2$, and (d) contact force: outer raceway-to-rolling element j=3.

the parametric effects on the contact forces in Section 6.6.

The physical mechanism by which the defect-related impulses are generated during the re-stressing of the rolling elements is explained in the next section.

6.4.2 Physical mechanism that generates defect-related impulsive forces

It has been established in the preceding section that the defect-related impulsive signals are generated during the re-stressing of the rolling elements; however, in order to develop an understanding of the physical mechanism that leads to the generation of the impulsive signals, it is useful to compare the contact forces on the rolling elements generated by each of the two bearing raceways.

Figures 6.19a, 6.19c, and 6.19e show the numerically modelled vertical rolling element-to-outer raceway and rolling element-to-inner raceway contact forces as the three rolling elements $j = 1, 2, 3$ traverse through the outer raceway defect for a radial load W of 50 kN and rotational speed n_s of 500 RPM. The rolling element-to-outer raceway contact forces are represented by the blue-coloured, solid lines, whereas the rolling element-to-inner raceway contact forces are represented by the gray-coloured, dashed lines. Both sets of the contact forces closely follow each other; however, in opposite directions. Although not annotated, the four events highlighted in Figure 6.5 for the rolling element-to-outer raceway contact forces, can also be seen in Figures 6.19a, 6.19c, and 6.19e for the rolling element-to-inner raceway contact forces.

The contact forces on the rolling elements due to their compression between both raceways in Figures 6.19a, 6.19c, and 6.19e show that the mating de-stressing and re-stressing of the rolling elements upon their entry into and exit out of the defect, respectively, occur at the same time instances.

As discussed in Section 6.3.4, it is the re-stressing event that causes the defect-related impulsive acceleration signals. Therefore, the rolling element-to-raceway con-

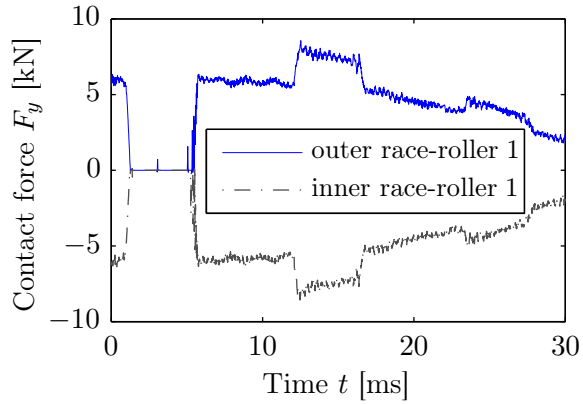

(a) Vertical contact forces on the first rolling element $j = 1$ due to the compression between the outer and inner raceways.

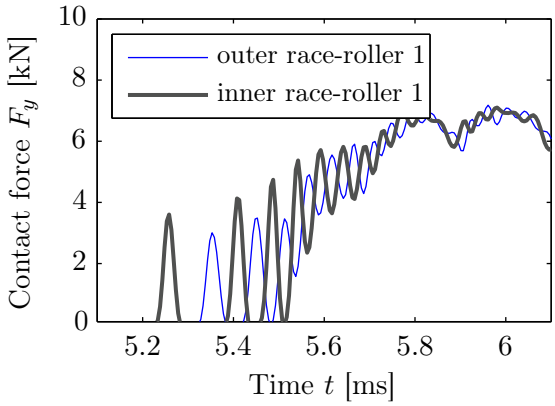

(b) Vertical contact forces in Figure 6.19a zoomed in the vicinity of rolling element $j = 1$ being re-stressed.

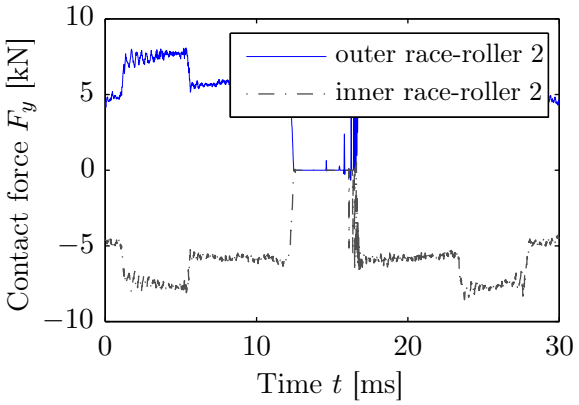

(c) Vertical contact forces on the second rolling element $j = 2$ due to the compression between the outer and inner raceways.

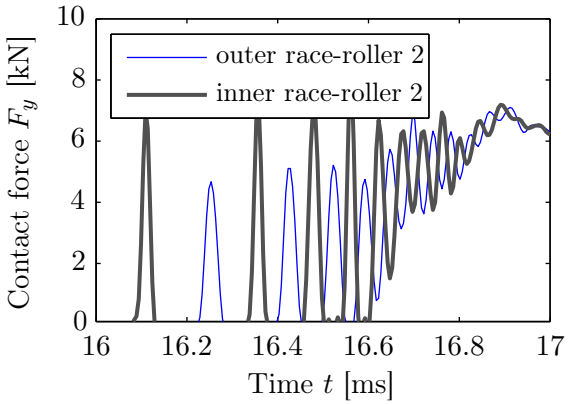

(d) Vertical contact forces in Figure 6.19c zoomed in the vicinity of rolling element $j = 2$ being re-stressed.

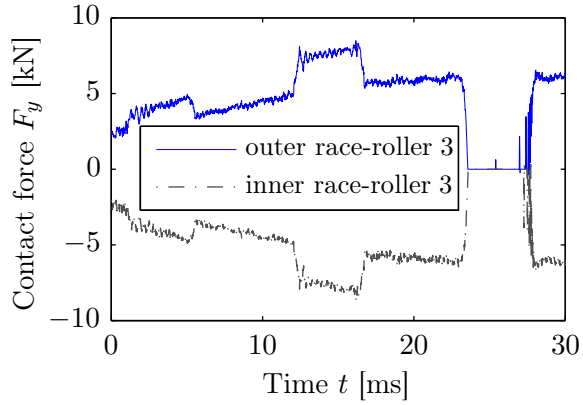

(e) Vertical contact forces on the third rolling element $j = 3$ due to the compression between the outer and inner raceways.

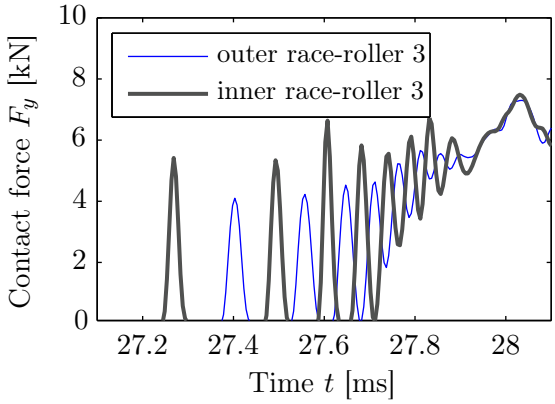

(f) Vertical contact forces in Figure 6.19e zoomed in the vicinity of rolling element $j = 3$ being re-stressed.

Figure 6.19: Numerically modelled, notch filtered, vertical contact forces F_y between two contact interfaces for a radial load W of 50 kN and rotational speed n_s of 500 RPM: 1) rolling element-to-outer raceway interface, and 2) rolling element-to-inner raceway interface; the rolling element-to-inner raceway contact forces represented by the dashed lines in (a, c, e) were inversed and changed to the solid, thick lines in (b, d, f) for clarity.

tact forces plotted in Figures 6.19a, 6.19c, and 6.19e were zoomed in the vicinity of the re-stressing phase, and the corresponding plots are shown in Figures 6.19b, 6.19d, and 6.19f, respectively. For the clear distinction of the time instances pertinent to the interaction of the rolling elements with both raceways, the rolling element-to-inner raceway contact forces in the zoomed plots are inversed; these contact forces in Figures 6.19b, 6.19d, and 6.19f are represented by the gray-coloured, thick, solid lines, a modification from the dashed lines in Figures 6.19a, 6.19c, and 6.19e.

It is evident from the zoomed contact force plots in Figures 6.19b, 6.19d, and 6.19f, as the rolling elements re-stress between the raceways, they alternate between striking the outer and inner raceways. The amplitude of the forces is also higher at the beginning of the re-stressing phase, and it reduces gradually as the rolling elements fully re-stress between the raceways. In contrast to the rolling element-to-outer raceway contact forces, the amplitude of the rolling element-to-inner raceway contact forces is higher during the re-stressing of the rolling elements. This is due to the difference in the geometrical curvature of the outer and inner raceways, which results in different equivalent radii of curvature for the raceways estimated in conjunction with the radius of the rolling element as per the Hertzian contact theory; refer to Equations (3.1)–(3.3), Chapter 3. Compared to the rolling element-to-outer raceway contact interface, the equivalent radii of curvature for the rolling element-to-inner raceway interface is slightly less. As a result, the size of the contact patch at the rolling element-to-inner raceway interface is slightly smaller than at the rolling element-to-outer raceway. This difference eventually causes higher contact stresses (Equation (3.6)), and hence, forces on the inner raceway compared to the outer raceway by 3%.

In practice, it is often observed in measured acceleration signals that the traverse of a single rolling element through a bearing defect produces multiple impulses. The experimentally measured acceleration time-traces shown in Figures 5.3, 5.5–5.8, Chapter 5, clearly shows the occurrence of the multiple impulses in a single rolling element pass-by event. As mentioned earlier, previous analytical models [90–96, 103, 114, 165]

were based on the assumption that the defect-related impulsive vibration response of a bearing is generated by a single force impulse that exponentially decays over time. A tentative explanation about the occurrence of the multiple impulses is provided by Sawalhi *et al.* [165] who suggest that they could be due to the beating effect related to small differences in the resonance frequencies of a bearing. However, from the explicit FE modelling of the defective rolling element bearing presented here, it is now clear that it is not a beating effect, but a burst of multiple, short-duration, force impulses during the re-stressing that consequently causes multiple impulses in the corresponding acceleration signals. This is *another important outcome* of the FE analysis of the rolling element bearing as it provides a firm confirmation as to why, in typically measured vibration signals, multiple impulses are observed during a single rolling element pass-by event through a defect.

Numerically modelled rolling element-to-raceway contact forces for radial loads W of 25 kN and 80 kN, and a rotational speed n_s of 500 RPM

Similar to Figure 6.19, the numerically modelled, notch filtered, vertical rolling element-to-outer raceway and rolling element-to-inner raceway contact forces for radial loads W of 25 kN and 80 kN are shown in Figures 6.20 and 6.21, respectively. While the complete time-traces of the contact forces for the length of the simulation, 30 ms, are plotted in subplots (a, c, e), the forces zoomed in the vicinity of the re-stressing of the rolling elements are plotted in subplots (b, d, f) of both figures. The results in Figures 6.19, 6.20 and 6.21 reveal similar findings as discussed above. As mentioned earlier in Section 6.4.1, the rolling element-to-raceway contact forces were plotted on different scales for clarity.

In summary, it can be concluded that defect-related force impulses in defective rolling element bearings are produced during the re-stressing phase, which occurs in the vicinity of the end of the defect, where the rolling elements alternatively impact the outer and inner raceways.

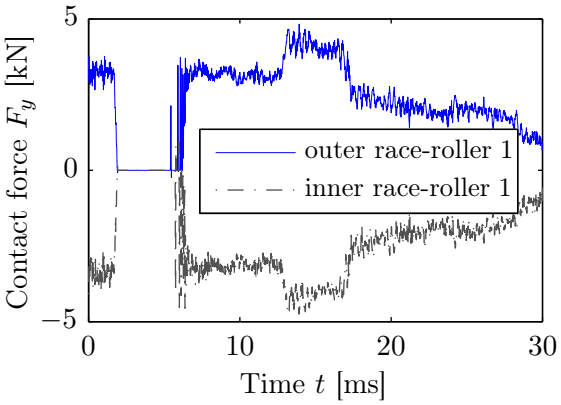

(a) Vertical contact forces on the first rolling element $j = 1$ due to the compression between the outer and inner raceways.

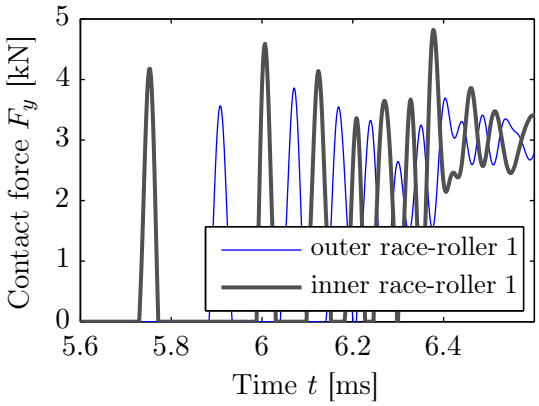

(b) Vertical contact forces in Figure 6.20a zoomed in the vicinity of rolling element $j = 1$ being re-stressed.

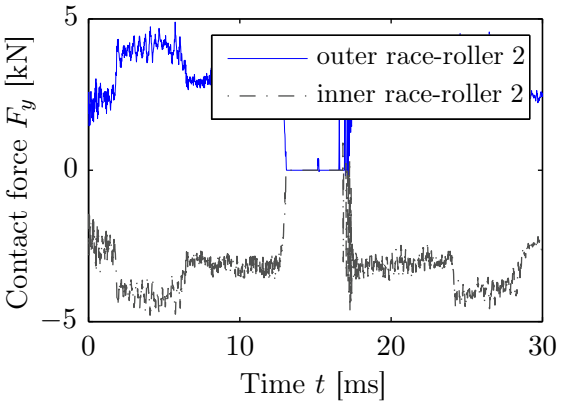

(c) Vertical contact forces on the second rolling element $j = 2$ due to the compression between the outer and inner raceways.

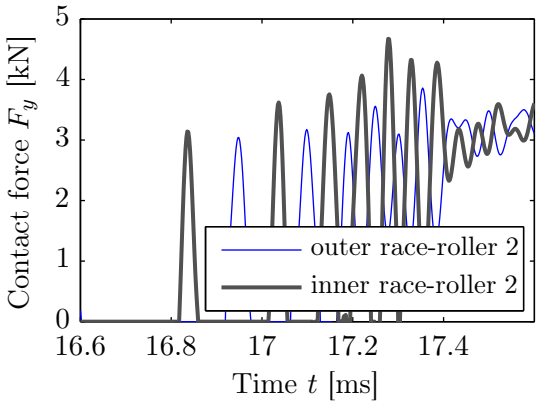

(d) Vertical contact forces in Figure 6.20c zoomed in the vicinity of rolling element $j = 2$ being re-stressed.

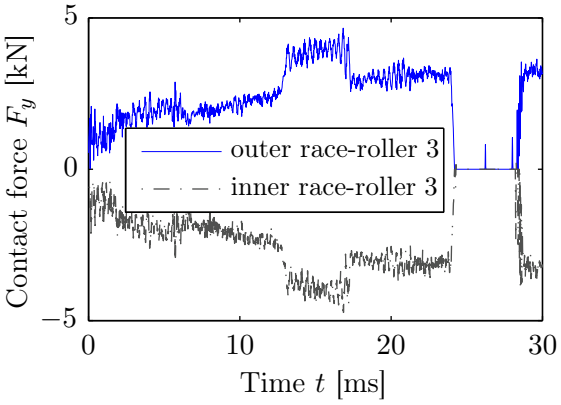

(e) Vertical contact forces on the third rolling element $j = 3$ due to the compression between the outer and inner raceways.

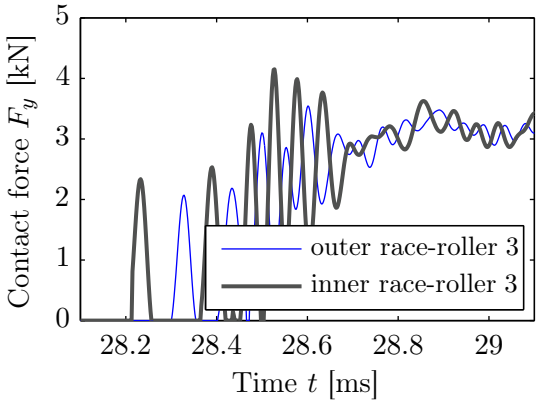

(f) Vertical contact forces in Figure 6.20e zoomed in the vicinity of rolling element $j = 3$ being re-stressed.

Figure 6.20: Numerically modelled, notch filtered, vertical contact forces F_y between two contact interfaces for a radial load W of 25 kN and rotational speed n_s of 500 RPM: 1) rolling element-to-outer raceway interface, and 2) rolling element-to-inner raceway interface; the rolling element-to-inner raceway contact forces represented by the dashed lines in (a, c, e) were inversed and changed to the solid, thick lines in (b, d, f).

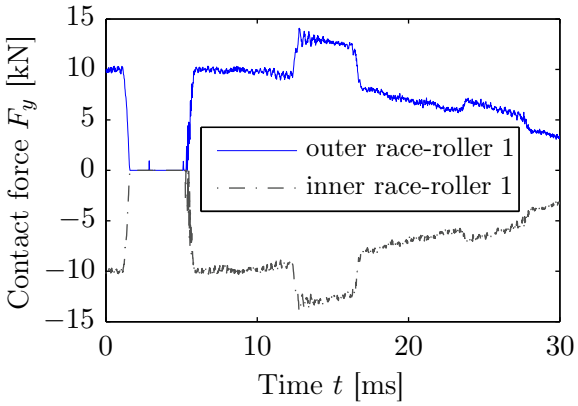

(a) Vertical contact forces on the first rolling element $j = 1$ due to the compression between the outer and inner raceways.

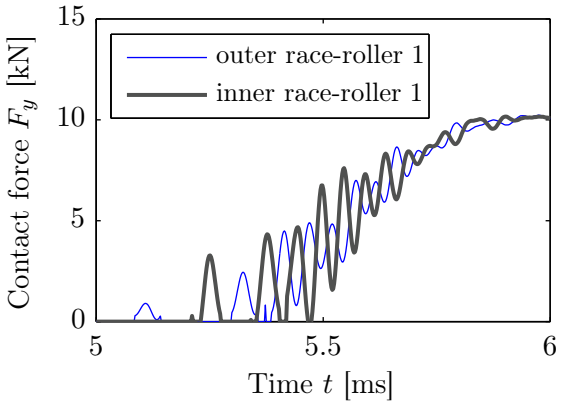

(b) Vertical contact forces in Figure 6.21a zoomed in the vicinity of rolling element $j = 1$ being re-stressed.

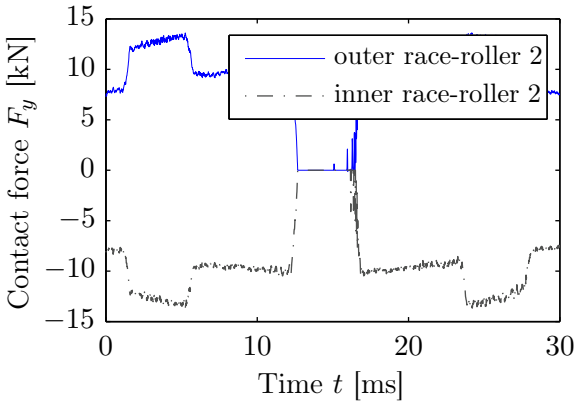

(c) Vertical contact forces on the second rolling element $j = 2$ due to the compression between the outer and inner raceways.

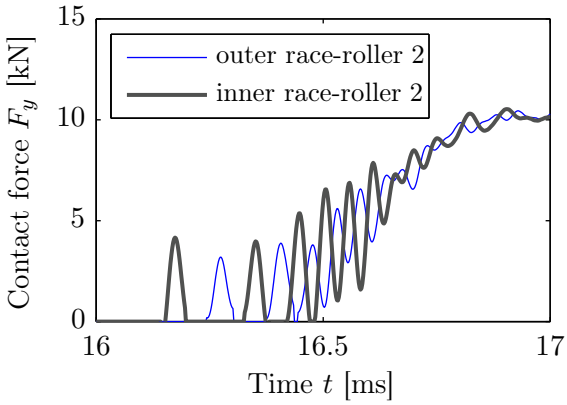

(d) Vertical contact forces in Figure 6.21c zoomed in the vicinity of rolling element $j = 2$ being re-stressed.

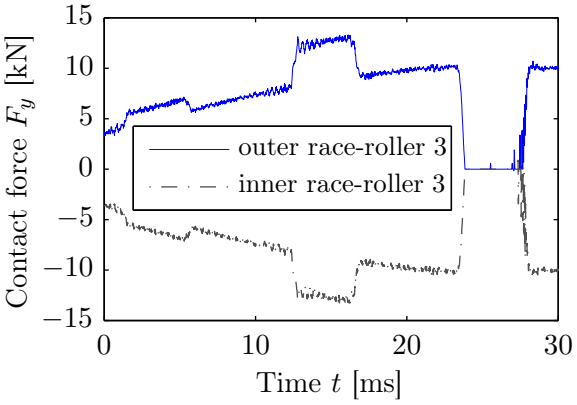

(e) Vertical contact forces on the third rolling element $j = 3$ due to the compression between the outer and inner raceways.

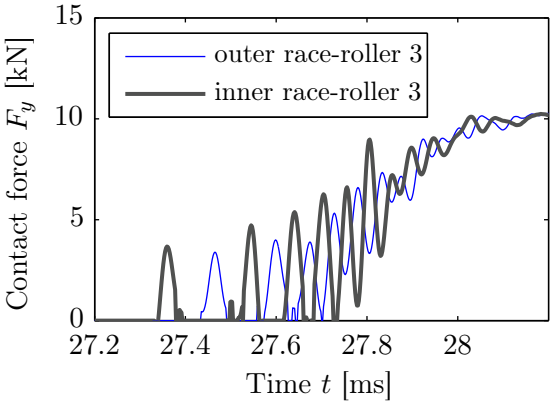

(f) Vertical contact forces in Figure 6.21e zoomed in the vicinity of rolling element $j = 3$ being re-stressed.

Figure 6.21: Numerically modelled, notch filtered, vertical contact forces F_y between two contact interfaces for a radial load W of 80 kN and rotational speed n_s of 500 RPM: 1) rolling element-to-outer raceway interface, and 2) rolling element-to-inner raceway interface; the rolling element-to-inner raceway contact forces represented by the dashed lines in (a, c, e) were inversed and changed to the solid, thick lines in (b, d, f).

6.5 Novel outcomes from the results of the explicit dynamics FE analysis of the rolling element bearing

The following are the novel and significant outcomes of the analysis and correlation of the numerical rolling element-to-raceway contact forces with bearing vibration signals:

- a burst of multiple, short-duration, force impulses is generated during the re-stressing of a rolling element, which leads to the generation of multiple vibration impulses for a single pass-by of a rolling element through a defect,
- the amplitude of the contact forces and acceleration produced during the re-stressing of the rolling elements is much greater than when the rolling elements strike the defective surface,
- a burst of force impulses during the re-stressing leads to the generation of defect-related impulses that are generally observed in measured acceleration signals, and subsequently used for bearing diagnosis, and
- the generation of multiple force impulses during the re-stressing of a rolling element provides pragmatic insights that explain the occurrence of multiple impulses in measured vibration signals as opposed to the tentative explanation of the beating effect in reference [165].

The next section describes the parametric effects of varying load and speed on the rolling element-to-raceway contact forces.

6.6 Parametric effect of load and speed on the rolling element-to-raceway contact forces

Similar to investigating the effect of varying radial load W and rotational speed n_s on the envelope power spectra of the measured and modelled acceleration a_y signals presented in the previous chapter, the effects of various loads and speeds on the rolling element-to-raceway contact forces F_y are described in this section.

In order to facilitate an understanding of the aforementioned effects, the numerically modelled rolling element-to-raceway contact forces are categorised into static and dynamic components for the discussion that follows. While the static component is considered to be the contact forces between the rolling elements and non-defective sections of the raceways, the dynamic component is related to the multiple (contact) force impulses that are generated during the re-stressing of the rolling elements as they traverse through the defect. The static contact force on the rolling elements, which is equivalent to the load distribution within a bearing, can also be analytically estimated using the quasi-static load distribution model described in Chapter 3. The reason for considering the static component to be the contact forces between the rolling elements and non-defective sections of the raceways is discussed in Section 6.6.1.

For the discussion to be presented here, the static contact forces correspond to those excluding the forces related to events #1, #2, and #4, whereas the dynamic contact forces correspond to those related to event #4. As described in Sections 6.3.1, 6.3.2, and 6.3.4 pertinent to explaining the contact force results in Figure 6.5, events #1, #2, and #4 correspond to the de-stressing of the rolling elements, striking of the rolling elements with the defective surface, and the re-stressing of the rolling elements, respectively. As events #1 and #2 are associated with the interaction of the rolling elements with the defect, they are not considered a part of the static load distribution for the discussion that follows.

Rolling element-to-outer raceway contact forces

Figure 6.22, which comprises six subplots, shows the numerically modelled, notch filtered, vertical rolling element-to-outer raceway contact forces F_y corresponding to radial loads W of 25 kN, 50 kN, and 80 kN, and rotational speeds n_s of 300 RPM, 500 RPM, and 800 RPM. Complete time-traces of the contact forces pertinent to the traverse of a single rolling element through the outer raceway defect for each of the nine load–speed (W–n_s) combinations are presented in Figures 6.22a, 6.22c, and 6.22e, whereas their partial time-traces zoomed in the vicinity of the rolling elements being re-stressed between the outer and inner raceways are respectively shown in Figures 6.22b, 6.22d, and 6.22f. In all the subplots of Figure 6.22, the contact forces corresponding to radial loads W of 25 kN, 50 kN, and 80 kN are represented using green-, blue-, and red-coloured lines, respectively.

Rolling element-to-inner raceway contact forces

Corresponding to the rolling element-to-outer raceway contact forces in Figure 6.22, the numerically modelled rolling element-to-inner raceway vertical contact forces F_y are shown in Figure 6.23. Complete time-traces of the contact forces pertinent to the traverse of a single rolling element through the defect are presented in Figures 6.23a, 6.23c, and 6.23e, whereas their partial time-traces zoomed in the vicinity of the re-stressing event are respectively shown in Figures 6.23b, 6.23d, and 6.23f.

6.6.1 Effect on static contact forces

As can be seen from the results in Figures 6.22a, 6.22c, 6.22e, 6.23a, 6.23c, and 6.23e, the magnitude of the static contact forces, corresponding to those between the rolling elements and non-defective section of the raceways, increases with increasing radial load W from 25 kN, to 50 kN, to 80 kN. As mentioned earlier, these contact forces can also be analytically estimated using the quasi-static load distribution model described

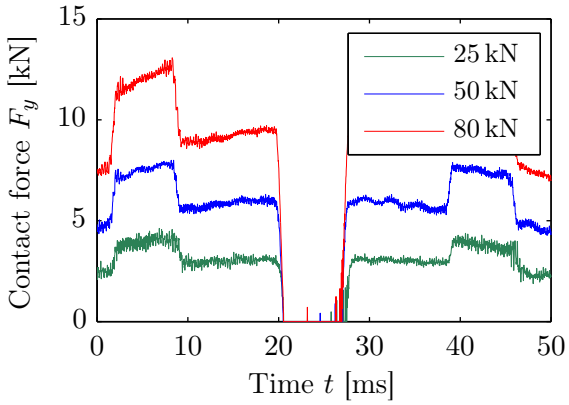

(a) Vertical rolling element-to-outer raceway contact forces for $n_s = 300$ RPM, and $W = 25$ kN, 50 kN and 80 kN.

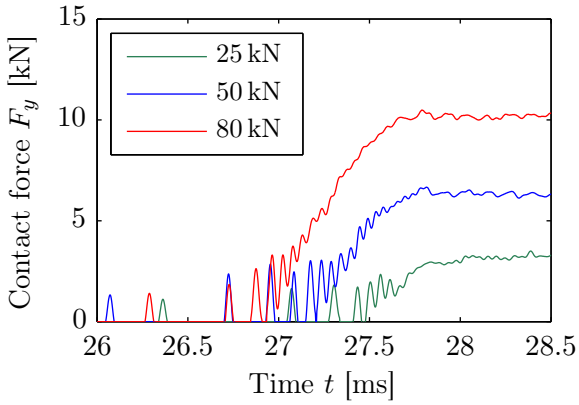

(b) Vertical rolling element-to-outer raceway contact forces in Figure 6.22a zoomed in the vicinity of the rolling elements being re-stressed.

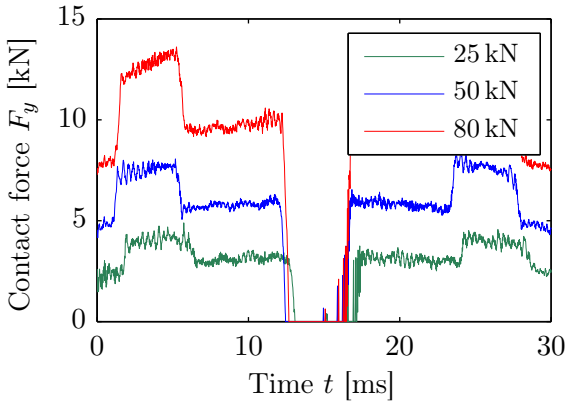

(c) Vertical rolling element-to-outer raceway contact forces for $n_s = 500$ RPM, and $W = 25$ kN, 50 kN and 80 kN.

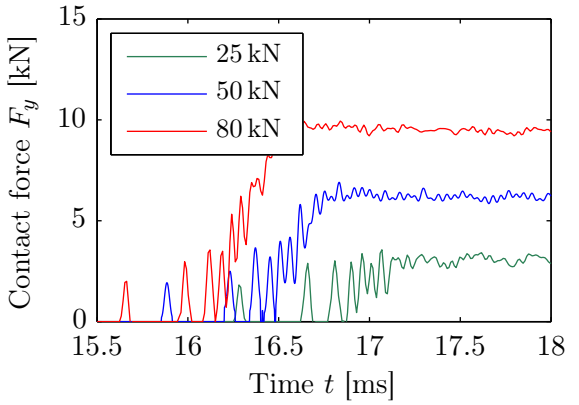

(d) Vertical rolling element-to-outer raceway contact forces in Figure 6.22c zoomed in the vicinity of the rolling elements being re-stressed.

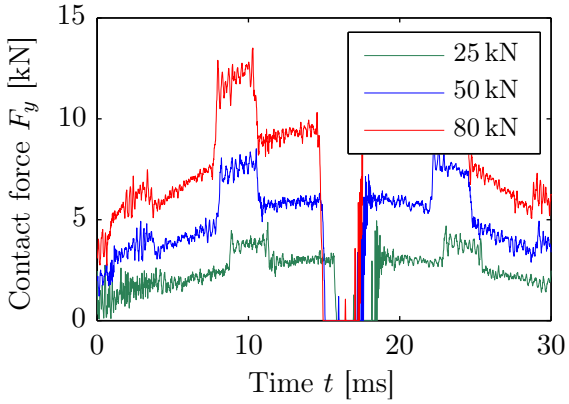

(e) Vertical rolling element-to-outer raceway contact forces for $n_s = 800$ RPM, and $W = 25$ kN, 50 kN and 80 kN.

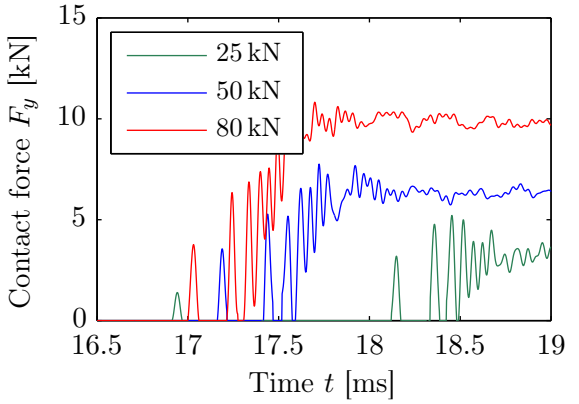

(f) Vertical rolling element-to-outer raceway contact forces in Figure 6.22e zoomed in the vicinity of the rolling elements being re-stressed.

Figure 6.22: Numerically modelled, notch filtered, vertical contact forces F_y between the rolling elements and outer raceway for various radial loads and rotational speeds; (a, c, e) complete time-traces, (b, d, f) partial time-traces zoomed in the vicinity of the rolling elements being re-stressed between the raceways; geen-, blue-, and red-coloured lines correspond to radial loads W of 25 kN, 50 kN, and 80 kN, respectively.

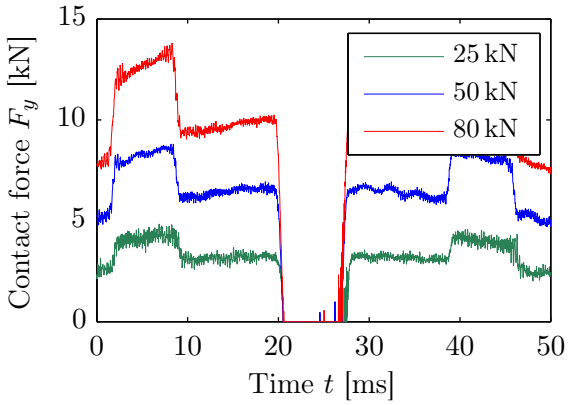

(a) Vertical rolling element-to-inner raceway contact forces for $n_s = 300\,\text{RPM}$, and $W = 25\,\text{kN}$, 50 kN and 80 kN.

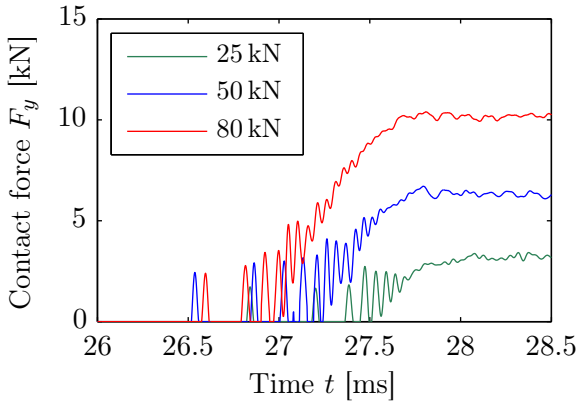

(b) Vertical rolling element-to-inner raceway contact forces in Figure 6.23a zoomed in the vicinity of the rolling elements being re-stressed.

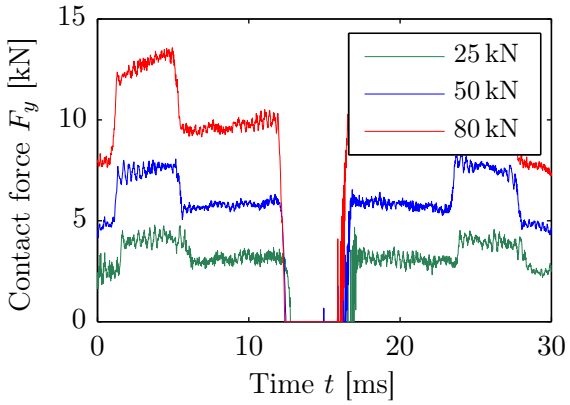

(c) Vertical rolling element-to-inner raceway contact forces for $n_s = 500\,\text{RPM}$, and $W = 25\,\text{kN}$, 50 kN and 80 kN.

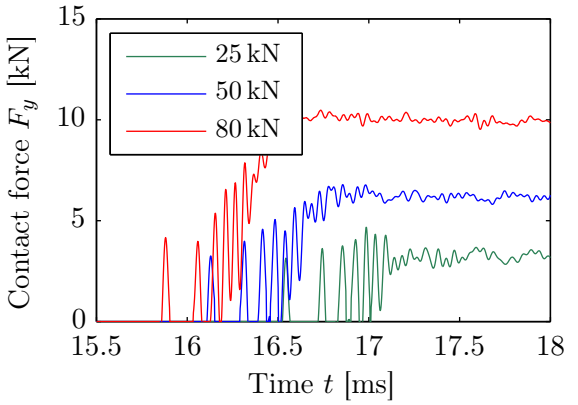

(d) Vertical rolling element-to-inner raceway contact forces in Figure 6.23c zoomed in the vicinity of the rolling elements being re-stressed.

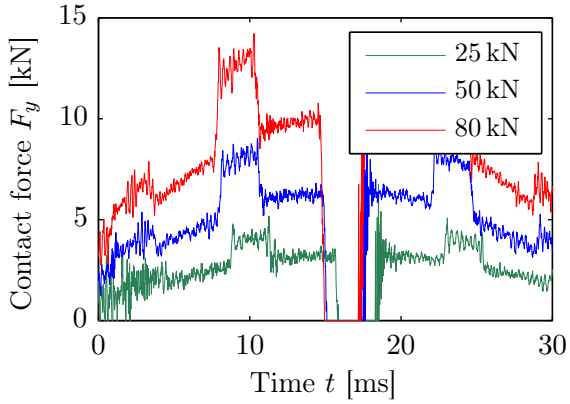

(e) Vertical rolling element-to-inner raceway contact forces for $n_s = 800\,\text{RPM}$, and $W = 25\,\text{kN}$, 50 kN and 80 kN.

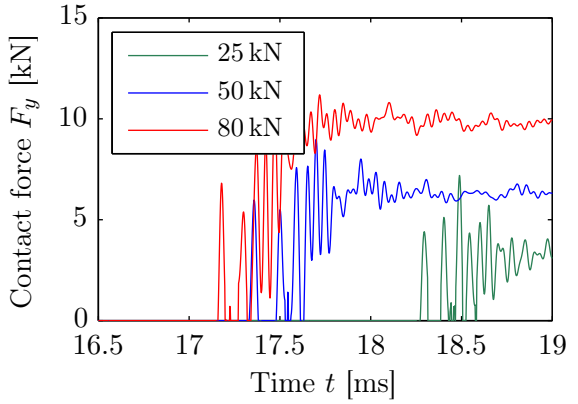

(f) Vertical rolling element-to-inner raceway contact forces in Figure 6.23e zoomed in the vicinity of the rolling elements being re-stressed.

Figure 6.23: Numerically modelled, notch filtered, vertical contact forces F_y between the rolling elements and inner raceway for various radial loads and rotational speeds; (a, c, e) full time-traces, (b, d, f) partial time-traces zoomed in the vicinity of the rolling elements being re-stressed between the raceways; geen-, blue-, and red-coloured lines correspond to radial loads W of 25 kN, 50 kN, and 80 kN, respectively.

in Chapter 3.

From the aforementioned figures, it can be seen that the contact forces are maximised during the re-distribution of a load on the rolling elements at the non-defective sections of the raceways as one of the rolling elements traverses through the defect within a bearing; refer to Section 6.3.3 for the description of the load re-distribution phase. The magnitude of the static contact forces considered for the discussion here corresponds to that immediately prior or subsequent to the de-stressing or re-stressing events, respectively, which represents the interaction of the rolling elements with the non-defective sections of the raceways. This is because in the case of a non-defective rolling element bearing, re-distribution of a load does not occur, and the vertical contact force is a maximum at the centre of the load zone of the bearing. Except for the variation in the rolling element-to-raceway contact forces during the re-distribution of a load, the forces at the non-defective section of the raceways are similar for defective and non-defective bearings; refer to Figure 3.12, Chapter 3, for a comparison between the contact forces for defective and non-defective bearings. Therefore, consideration of the magnitude of the static contact forces immediately prior or subsequent to the de-stressing or re-stressing events, respectively, is deemed practically appropriate because the parametric effect of varying load and speed on the defect-related dynamic force components can be referenced to the static load levels for a non-defective rolling element bearing.

For the FE model of the defective rolling element bearing presented here, the outer raceway line spall was centrally located within the bearing load zone. Therefore, the rolling element-to-raceway vertical contact forces immediately prior and subsequent to the de-stressing and re-stressing of the rolling elements, respectively, are similar to one another. From Figure 6.22a (or Figures 6.22c or 6.22e), the magnitude of these rolling element-to-outer raceway contact forces F_y are approximately 3 kN, 6 kN, and 10 kN for radial loads W of 25 kN, 50 kN, and 80 kN, respectively. In contrast, the levels of the rolling element-to-inner raceway contact forces in Figure 6.23a (or Figures 6.23c

or 6.23e) are slightly higher than the corresponding rolling element-to-outer raceway contact forces by approximately 3%. This is due to the difference in the geometrical curvature of the outer and inner raceways that causes slightly higher rolling element-to-inner raceway contact forces compared to the corresponding rolling element-to-outer raceway contact forces, as mentioned in Section 6.4.2. The magnitude of the rolling element-to-inner raceway contact forces prior to de-stressing and subsequent to re-stressing events are similar and equal to 3.1 kN, 6.2 kN, and 10.3 kN for radial loads W of 25 kN, 50 kN, and 80 kN, respectively.

The static contact forces (load distribution) are independent of the rotational speed n_s of the bearing; however, the defect-related dynamic contact forces, associated with the re-stressing of the rolling elements, vary significantly with the rotational speed as discussed in the next section.

6.6.2 Effect on dynamic contact forces

Dynamic rolling element-to-outer raceway vertical contact forces F_y related to the re-stressing of the rolling elements have been shown in Figures 6.22b, 6.22d, and 6.22f for the rotational speeds n_s of 300 RPM, 500 RPM, and 800 RPM, respectively, at various radial loads W. Similarly, the dynamic rolling element-to-inner raceway vertical contact forces F_y related to the re-stressing events have been shown in Figures 6.23b, 6.23d, and 6.23f. As can be seen from these figures, multiple force impulses of varying magnitudes are generated during the re-stressing of the rolling elements. In a similar way to selecting a single value for the static forces for various loads, it would be useful to choose a single value for the dynamic contact forces for various load–speed (W–n_s) combinations. However, from the multiple impulses, it was difficult to pick a particular impulse for representing a maximum level of the dynamic contact forces. Therefore, in order to ensure consistency across various FE simulations and facilitate choosing a maximum of the dynamic contact forces, they were band-pass filtered from 18 kHz to

23 kHz, which is similar to the frequency band used to demodulate the acceleration a_y signals. The envelopes of the band-pass filtered rolling element-to-raceway contact forces were then estimated using the Hilbert transform $\mathscr{H}$ [348] as discussed in the previous chapters.

For clarity, the defect-related dynamic rolling element-to-outer raceway contact forces shown in Figures 6.22b, 6.22d, and 6.22f are reproduced in Figures 6.24a, 6.24b, and 6.24c, respectively, along with their band-pass filtered envelopes. While the contact forces are plotted using thin lines, the envelopes are plotted using relatively thick lines. For radial loads W of 25 kN, 50 kN, and 80 kN, the contact forces and their corresponding envelopes are represented using green-, blue-, and red-coloured lines, respectively.

Similarly, the defect-related dynamic rolling element-to-inner raceway contact forces that have been shown in Figures 6.23b, 6.23d, and 6.23f are reproduced in Figures 6.25a, 6.25b, and 6.25c, respectively, along with their band-pass filtered envelopes.

From Figures 6.24 and 6.25, a maximum of the envelopes of the band-pass filtered rolling element-to-raceway contact forces are plotted in Figure 6.26 as a function of the rotational speed n_s of the bearing for each radial load W. These results for the rolling element-to-outer raceway contact forces are plotted in Figure 6.26a, and for the rolling element-to-inner raceway forces are plotted in Figure 6.26b. Along with the maximum of the defect-related force impulses, which are represented using dash, solid, and dash-dotted lines for radial loads of 25 kN, 50 kN, and 80 kN respectively, three horizontal (dotted) lines having dotted markers are also plotted. These lines represent the static contact force levels immediately subsequent to the re-stressing of the rolling elements as mentioned in the preceding section. In Figure 6.26a, the static forces are plotted at 3 kN, 6 kN, and 10 kN corresponding to radial loads of 25 kN, 50 kN, and 80 kN, respectively, whereas in Figure 6.26b, the static forces are plotted at 3.1 kN, 6.2 kN, and 10.3 kN. As mentioned earlier, the static contact forces are independent of the rotational speed of the bearing.

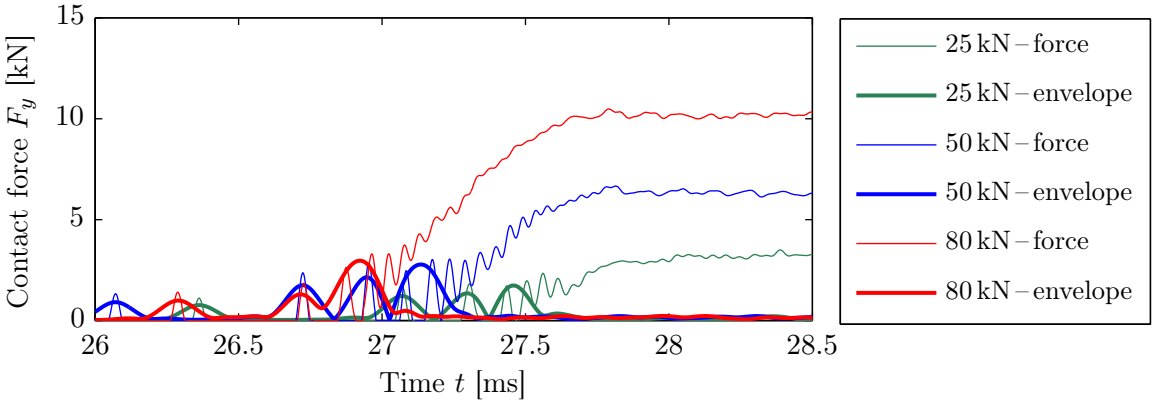

(a) Vertical rolling element-to-outer raceway contact forces shown in Figure 6.22b along with their respective band-pass filtered envelopes.

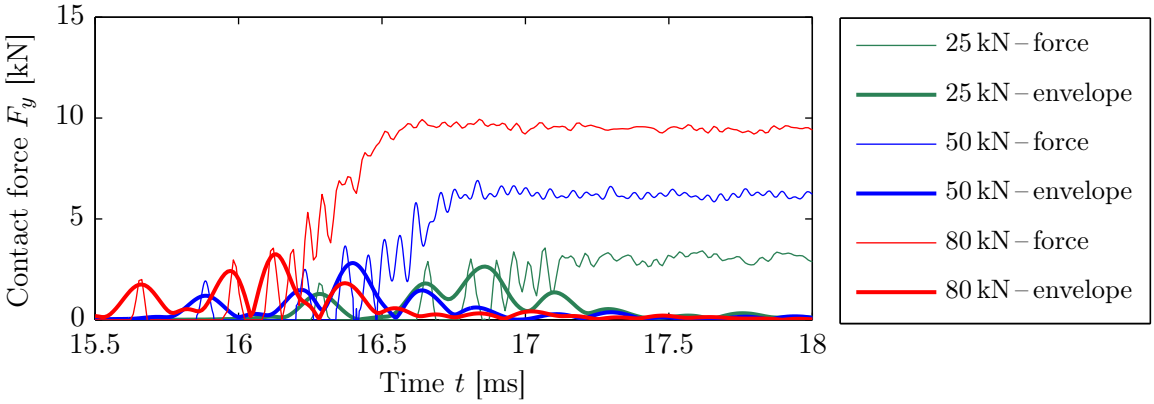

(b) Vertical rolling element-to-outer raceway contact forces shown in Figure 6.22d along with their respective band-pass filtered envelopes.

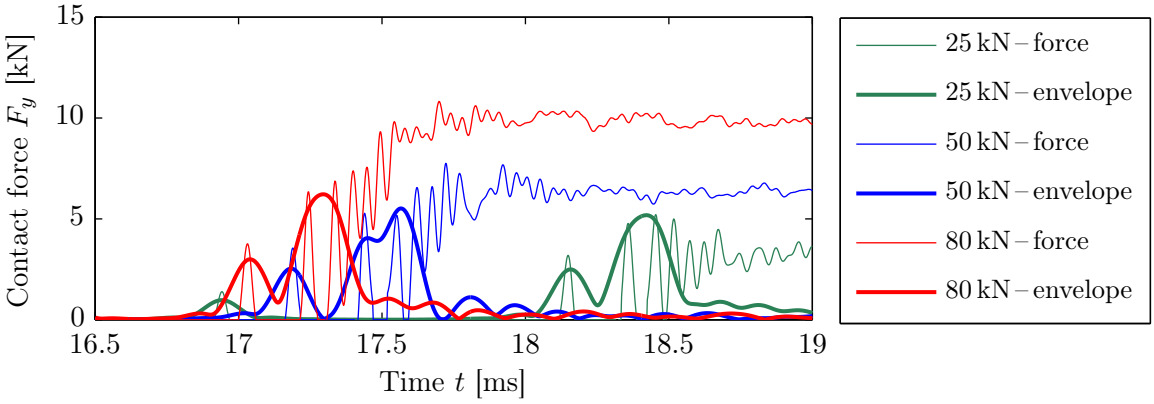

(c) Vertical rolling element-to-outer raceway contact forces shown in Figure 6.22f along with their respective band-pass filtered envelopes.

Figure 6.24: Numerically modelled, notch filtered, vertical contact forces F_y between the rolling elements and outer raceway for various radial loads and rotational speeds; geen-, blue-, and red-coloured lines correspond to radial loads W of 25 kN, 50 kN, and 80 kN, respectively; thin lines correspond to the defect-related dynamic contact forces generated during the re-stressing of the rolling elements, and thick lines correspond to the band-pass filtered envelopes of the contact forces.

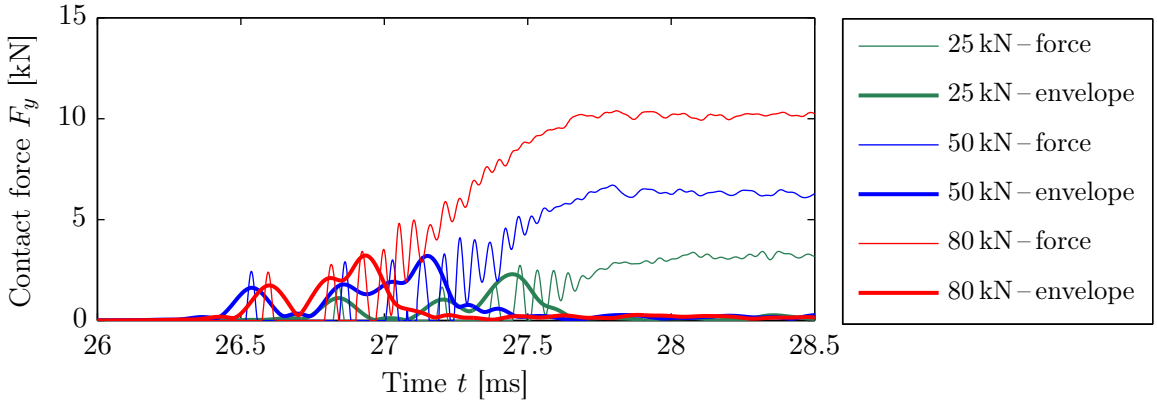

(a) Vertical rolling element-to-outer raceway contact forces shown in Figure 6.23b along with their respective band-pass filtered envelopes.

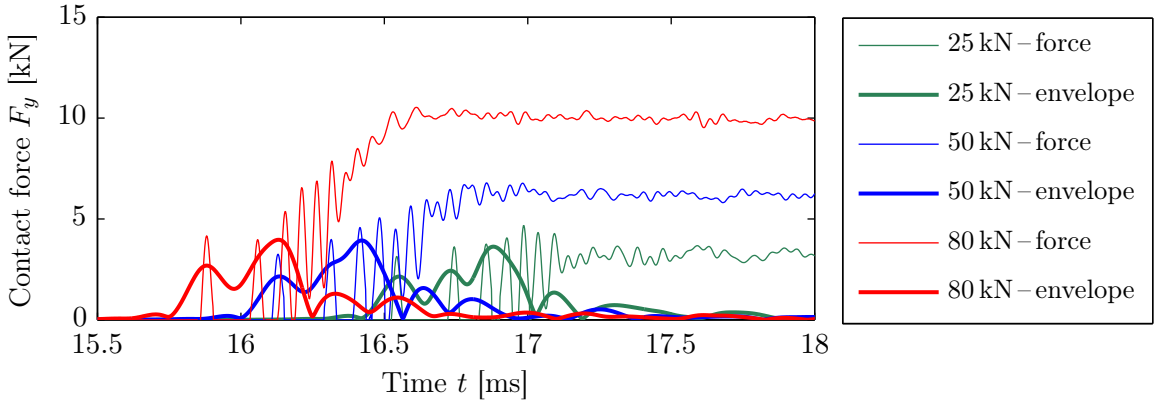

(b) Vertical rolling element-to-outer raceway contact forces shown in Figure 6.23d along with their respective band-pass filtered envelopes.

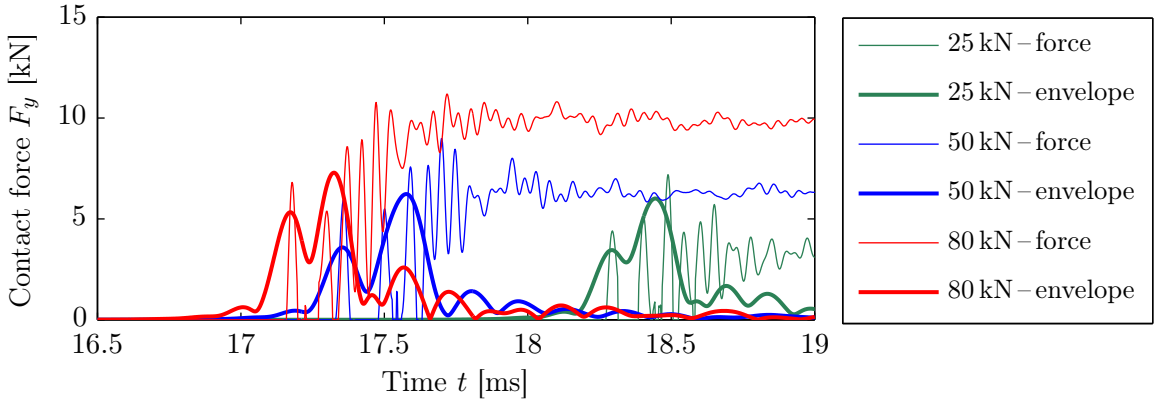

(c) Vertical rolling element-to-inner raceway contact forces shown in Figure 6.23f along with their respective band-pass filtered envelopes.

Figure 6.25: Numerically modelled, notch filtered, vertical contact forces F_y between the rolling elements and inner raceway for various radial loads and rotational speeds; geen-, blue-, and red-coloured lines correspond to radial loads W of 25 kN, 50 kN, and 80 kN, respectively; thin lines correspond to the defect-related dynamic contact forces generated during the re-stressing of the rolling elements, and thick lines correspond to the band-pass filtered envelopes of the contact forces.

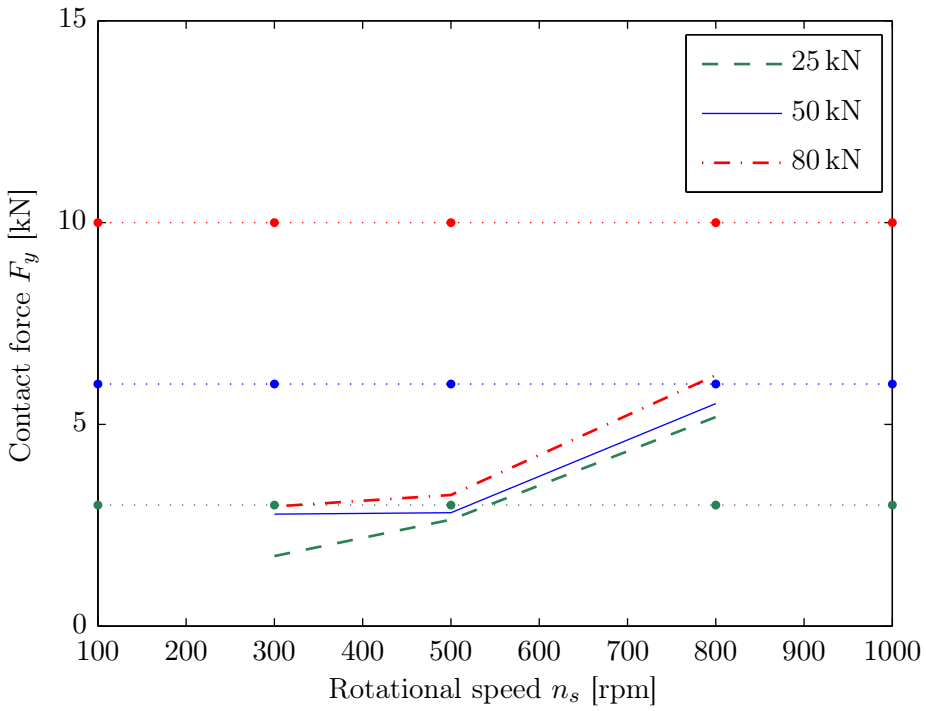

(a) Rolling element-to-outer raceway contact forces.

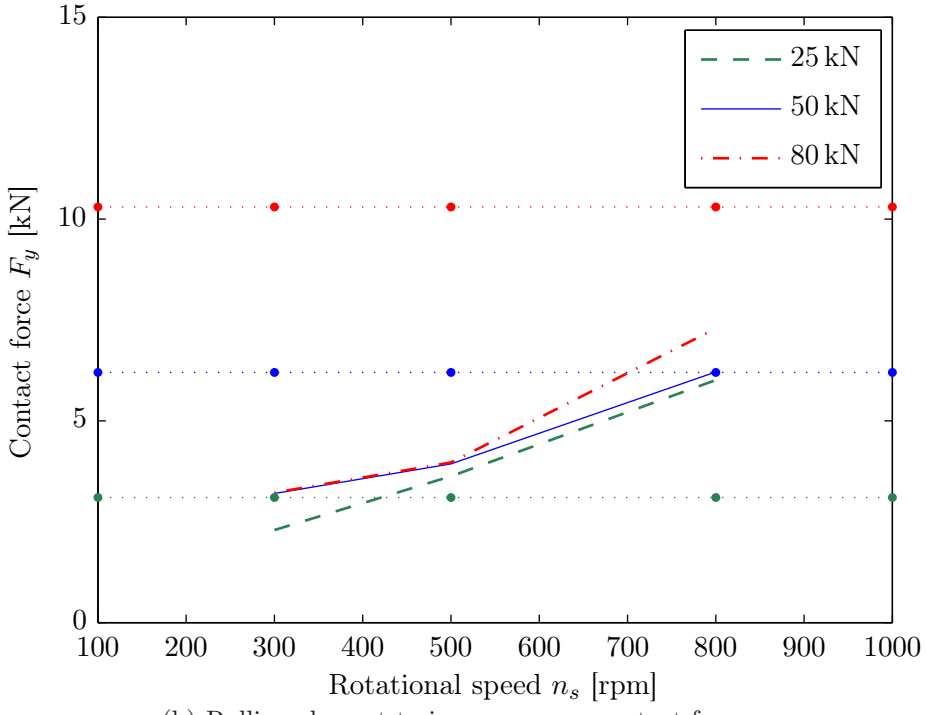

(b) Rolling element-to-inner raceway contact forces.

Figure 6.26: Maximum of the envelopes of the band-pass filtered rolling element-to-raceway contact forces F_y shown in Figures 6.24 and 6.25 for various radial loads and rotational speeds; the horizontal lines along with dotted markers represent the static rolling element-to-raceway contact force levels immediately prior or subsequent to the de-stressing or re-stressing events, respectively, for radial loads W of 25 kN, 50 kN, and 80 kN.

Load W (kN)	Maximum of the envelope of the band-pass filtered dynamic rolling element-to-outer raceway contact force F_y			Percentage increase in the maximum of the envelope from	
	Speed n_s (RPM)				
	300	500	800	300–500 RPM	500–800 RPM
25	1.74	2.64	5.18	51.7	96.2
50	2.78	2.81	5.52	1.08	96.4
80	2.97	3.25	6.22	9.43	91.4

(a) Percentage increase in the dynamic rolling element-to-outer raceway forces from 300–500 RPM and 500–800 RPM.

Speed n_s (RPM)	Maximum of the envelope of the band-pass filtered rolling element-to-outer raceway dynamic contact force F_y			Percentage increase in the maximum of the envelope from	
	Load W (kN)				
	25	50	80	25–50 kN	50–80 kN
300	1.74	2.78	2.97	59.8	6.83
500	2.64	2.81	3.25	6.44	15.6
800	5.18	5.52	6.22	6.56	12.7

(b) Percentage increase in the dynamic rolling element-to-outer raceway forces from 25–50 kN and 50–80 kN.

Table 6.1: Percentage increase in the maximum of the envelopes of the band-pass filtered rolling element-to-outer raceway dynamic, defect-related, contact forces F_y shown in Figure 6.26a for various radial loads and rotational speeds.

As can be seen from Figures 6.26a and 6.26b, the magnitude of the dynamic contact force impulses generally increases with increasing rotational speed n_s of the bearing and also with the increasing radial load W. The percentage increase in the maximum of the envelopes of the band-pass filtered rolling element-to-outer raceway dynamic contact forces is shown in Table 6.1; the increase in terms of the rotational speed at each load is shown in Table 6.1a, whereas the increase in terms of load at each rotational speed is presented in Table 6.1b. Similarly, the percentage increase in the maximum of the envelopes of the band-pass filtered rolling element-to-inner raceway dynamic contact forces is shown in Table 6.2.

The percentage increase in the dynamic contact forces shown in Tables 6.1 and 6.2

Load W (kN)	Maximum of the envelope of the band-pass filtered rolling element-to-inner raceway dynamic contact force F_y			Percentage increase in the maximum of the envelope from	
	Speed n_s (RPM)				
	300	500	800	300–500 RPM	500–800 RPM
25	2.29	3.63	6.01	58.5	65.6
50	3.21	3.93	5.52	22.4	58.0
80	3.22	3.97	7.29	23.3	83.6

(a) Percentage increase in the dynamic rolling element-to-inner raceway forces from 300–500 RPM and 500–800 RPM.

Speed n_s (RPM)	Maximum of the envelope of the band-pass filtered rolling element-to-inner raceway dynamic contact forces F_y			Percentage increase in the maximum of the envelope from	
	Load W (kN)				
	25	50	80	25–50 kN	50–80 kN
300	2.29	3.21	3.22	40.2	0.31
500	3.63	3.93	3.97	8.26	1.02
800	6.01	6.21	7.29	3.33	17.4

(b) Percentage increase in the dynamic rolling element-to-inner raceway forces from 25–50 kN and 50–80 kN.

Table 6.2: Percentage increase in the maximum of the envelopes of the band-pass filtered rolling element-to-inner raceway dynamic, defect-related, contact forces F_y shown in Figure 6.26b for various radial loads and rotational speeds.

indicates that the higher the rotational speed of the rolling elements traversing through the defect, the greater are the centrifugal forces acting on them. As a result, the rolling elements traversing at higher speeds will strike the end of the defect with higher forces that consequently lead to higher magnitudes of the impulsive forces generated during the re-stressing of the rolling elements. Similarly, the higher the load on the rolling elements in conjunction with the increasing rotational speed, the greater are the magnitude of the contact stresses, and hence the contact forces.

During the discussion of the correlation of the rolling element-to-raceway contact forces with the acceleration results in Section 6.4, it was concluded that the impulsive acceleration signatures, generally observed in practice, are generated due to the

re-stressing of the rolling elements between the outer and inner raceways. As the magnitude of the dynamic contact forces associated with the re-stressing of the rolling elements increases with increasing radial load W and rotational speed n_s, the impulsive acceleration levels also increase. The parametric effects of increasing load and speed on both experimentally measured and numerically modelled acceleration levels were described in Section 5.4, Chapter 5.

6.6.2.1 Comparison of the defect-related dynamic contact forces with the static load distribution

This section presents a comparison of the defect-related dynamic contact forces with the static force levels.

Rolling element-to-outer raceway contact forces

The effects of increasing the rotational speed n_s of the bearing for a particular radial load W, on the dynamic rolling element-to-outer raceway contact forces F_y, presented in Figures 6.24a, 6.24b, and 6.24c, are discussed below with reference to the aforementioned static force components.

- Figure 6.24a — for the FE model of the rolling element bearing rotated at 300 RPM and subjected to a radial load of 25 kN, it can be observed in Figure 6.24a that the maximum of the envelope of the band-pass filtered dynamic contact force, 1.74 kN (at 27.5 ms), is less than that of the static force component immediately subsequent to the re-stressing event, 3 kN (at 28 ms) — a difference of approximately 72%. For the FE simulation corresponding to a radial load of 50 kN, from Figure 6.24a, the difference between the maximum of the envelope, 2.78 kN (at 27.1 ms), and static force component, 6 kN (at 28 ms), is approximately 115%, which is almost 1.6 times the previous one. Similarly, for a load of 80 kN, from Figure 6.24a, the difference between the maximum of the envelope,

2.97 kN (at 26.9 ms), and static force, 10 kN (at 28 ms), is approximately 236%.

- Figure 6.24b — similar to aforementioned discussion, from the results in Figure 6.24b corresponding to a rotational speed n_s of 500 RPM, the differences between the maximum of the band-pass filtered envelopes and static force components are approximately 13%, 113%, and 207% for radial loads W of 25 kN, 50 kN, and 80 kN, respectively.

- Figure 6.24c — from the results in Figure 6.24c corresponding to the rotational speed n_s of 800 RPM, the differences between the maximum of the envelopes and static force components are approximately -42%, 8%, and 60% for radial loads W of 25 kN, 50 kN, and 80 kN, respectively. It should be highlighted here that the maximum of the band-pass filtered envelope of the dynamic contact force corresponding to the FE simulation at a rotational speed of 800 RPM and load of 25 kN (5.18 kN at 18.4 ms) is higher than that of the static force component (3 kN); thereby, resulting in a percentage increase in contrast to percentage decrease for all the other FE simulations.

The above described results along with the percentage variations between the static and maximum of the defect-related dynamic rolling element-to-outer raceway contact forces are summarised in Table 6.3. For each radial load W, it can be observed from the results in Table 6.3 that as the rotational speed n_s of the bearing increases, the percentage difference between the maximum of the envelope of the dynamic and static contact force components decreases. In other words, the magnitude of the force impulses generated during the re-stressing of the rolling elements generally increases with increasing rotational speeds. The reason for the increase in the magnitude of the dynamic contact forces has been explained in the preceding section.

As mentioned earlier with reference to the results in Figure 6.24c, for the FE model of the bearing rotated at 800 RPM and subjected to a radial load of 25 kN, the magnitude of the defect-related dynamic contact forces generated during the re-stressing

Load W (kN)	Static contact force F_y (kN)	Maximum of the envelopes of the band-pass filtered rolling element-to-outer raceway dynamic contact force F_y (kN)			Percentage difference between static and dynamic force components at various speeds (%)		
		Rotational speed n_s (RPM)					
		300	500	800	300	500	800
25	3	1.74	2.64	5.18	72.4	13.6	-42.1
50	6	2.78	2.81	5.52	115.8	113.5	8.70
80	10	2.97	3.25	6.22	236.7	207.7	60.8

Table 6.3: Percentage difference between the vertical static force components and the maximum of the envelopes of the band-pass filtered rolling element-to-outer raceway dynamic, defect-related, contact forces shown in Figure 6.26a for various radial loads and rotational speeds.

Load W (kN)	Static contact force F_y (kN)	Maximum of the envelopes of the band-pass filtered rolling element-to-inner raceway dynamic contact force F_y (kN)			Percentage difference between static and dynamic force components at various speeds (%)		
		Rotational speed n_s (RPM)					
		300	500	800	300	500	800
25	3.1	2.29	3.63	6.01	35.37	-14.60	-48.42
50	6.2	3.21	3.93	6.21	93.15	57.76	-0.161
80	10.3	3.22	3.97	7.29	219.9	159.4	41.29

Table 6.4: Percentage difference between the vertical static force components and the maximum of the envelopes of the band-pass filtered rolling element-to-inner raceway dynamic, defect-related, contact forces shown in Figure 6.26b for various radial loads and rotational speeds.

event is higher than the corresponding static contact force subsequent to the re-stressing of the rolling elements. However, for the rotational speeds of 500 RPM and 300 RPM, the magnitude of the dynamic contact forces is still lower than the corresponding static contact forces. It indicates that if the rotational speed of a loaded rolling element bearing is increased, the levels of the defect-related force impulses will eventually exceed the static contact force levels. It is difficult to comment on the implications on the operation of a bearing if the levels of the defect-related dynamic force impulses exceed the static force levels, as briefly described below.

One the one hand, higher load on the rolling elements, which increases the static load distribution within a bearing, can cause higher contact stresses at the rolling element-to-raceway interfaces. This will lead to an increase in the probability of initiating surface contact fatigue on the bearing components. On the other hand, the increase in the magnitude of the impulsive contact forces generated during the re-stressing of the rolling elements can cause an expansion of a defect, thereby extending the length of the defect in the rolling direction [337]. This poses an interesting research question as to which is more severe for an operating rolling element bearing, load or speed?

For non-defective rolling element bearings, application of higher than recommended loads can significantly reduce the fatigue life of the bearing components. However, for defective rolling element bearings, to answer the question one has to undertake a full parametric study, which could involve the application of an axial load, a combination of axial and radial loads, varying amounts of clearance, and various types (size and profiles) of defect. Such investigations are not a part of the current study, but can be realised in future using the explicit FE model of the bearing developed in this thesis.

Rolling element-to-inner raceway contact forces

Findings, similar to those discussed above pertinent to the dynamic rolling element-to-outer raceway contact forces in Figure 6.24, can also be observed in Figure 6.25a, 6.25b, and 6.25c. These figures show rolling element-to-inner raceway contact forces zoomed in the vicinity of the re-stressing of the rolling elements along with their band pass-filtered envelopes. The percentage variations between the maximum of the envelopes of the rolling element-to-inner raceway contact forces and corresponding static force components for varying radial load W and rotational speed n_s are provided in Table 6.4.

It can be observed from the results in Table 6.4 that for the FE simulation results corresponding to rotational speeds n_s of 500 RPM and 800 RPM, and a radial load W of 25 kN, the levels of the defect-related dynamic force impulses are higher than the static force component. This is also the case for the simulation corresponding to a rotational speed of 800 RPM and a radial load of 50 kN. These findings are similar to those discussed above for the numerically modelled rolling element-to-outer raceway contact forces corresponding to the rotational speed of 800 RPM and load of 25 kN. As mentioned earlier, the magnitude of the rolling element-to-inner raceway contact forces are slightly higher than the corresponding rolling element-to-outer raceway contact forces due to the difference in the geometrical curvature of the outer and inner raceways, which results in different equivalent radii of curvature of the raceways estimated in conjunction with the radius of the rolling element as per the Hertzian contact theory.

In summary, from the results of the parametric study presented here, it can be concluded as the rotational speed of a rolling element bearing increases, the magnitude of the defect-related force impulses generated during the re-stressing of the rolling elements increases.

6.7 Conclusions

An in-depth analysis of the numerical rolling element-to-raceway contact forces, obtained from the explicit dynamics finite element model of a defective rolling element bearing, was presented along with their correlation with the bearing vibration signals.

The numerically modelled contact forces were validated against the static and quasi-static analytical solution presented in Chapter 3. In addition to the contact forces at the rolling element-to-raceway interfaces, the numerically modelled contact width and displacement were also compared and found to be in a favourable agreement with the corresponding analytical solution.

The variations in the contact forces as the rolling elements traverse through the outer raceway defect were broadly divided into four events, namely event #1 to event #4. While the low-frequency de-stressing of the rolling elements upon their entry into the defect was labelled as event #1, the highly impulsive re-stressing of the rolling elements corresponding to their exit from the defect was labelled as event #4. The impact of the de-stressed rolling elements with the defective surface was labelled as event #2, and event #3 was related to compensating for the lost load in the case of a rolling element being unloaded in the defective region.

It was found that the re-stressing of the rolling elements that occurs near the end of a raceway defect generates a burst of multiple, short-duration, force impulses. The modelling results also highlight that much higher contact forces and accelerations are generated on the exit of the rolling elements from the defect compared to when they strike the defective surface.

As contact forces between mating bearing components are generally not measured in practice during the condition-based monitoring of rolling element bearings, the dynamic modelling of the rolling element-to-raceway contact forces presented here adds significant knowledge to the understanding of the characteristic vibration response of defective rolling element bearings.

The parametric effects of varying radial load and rotational speed on the rolling element-to-raceway contact forces, both static and dynamic components, were described. While the static forces corresponding to the load distribution are independent of the rotational speed, the defect-related dynamic forces related to the re-stressing of the rolling elements vary significantly with both load and speed. It was observed that the magnitude of the dynamic contact forces increases with:

- increasing radial load on the bearing; and
- increasing rotational speed of the bearing.

The conclusions of the work presented in this thesis are presented in the next chapter along with recommendations for future work.

This page intentionally contains only this sentence.

Chapter 7

Summary and Conclusions

7.1 Summary

The primary aim of the work presented in this thesis was to develop an understanding of the underlying physical mechanism by which defect-related impulses are generated in defective rolling element bearings. It was accomplished by modelling and analysing the dynamic contact interaction of the rolling elements and bearing raceways, as the rolling elements traverse through a localised raceway defect.

A comprehensive non-linear explicit dynamics finite element model of a rolling element bearing having a localised line spall on its outer raceway was developed. The model was solved numerically using a commercial FE software package, LS-DYNA. In addition to predicting the rolling element-to-raceway contact forces, the vibration response of the bearing was also modelled. The numerical modelling results were verified using both analytical modelling results and experimental data measured during the course of this research.

During the condition-based monitoring of rolling element bearings, a common practice is to measure the acceleration signals and analyse them using standard signal processing techniques associated with the vibration-based monitoring of bearings. Contact forces between mating bearing components are not measured in practice. As it was

important to verify the numerically modelled rolling element-to-raceway contact forces, a quasi-static analytical model for a defective rolling element bearing was developed to estimate the load (force) distribution within the bearing. The numerical contact forces were compared with the corresponding analytical results, and a favourable agreement between the numerical and analytical contact forces was achieved. The quasi-static model was based on the static load distribution model for a non-defective rolling element bearing available in the literature.

Based on the findings of the numerically modelled rolling element-to-raceway contact forces, a hypothesis was developed to explain the gradual decrease in the contact forces as a rolling element enters into a defect. A new mathematical model was developed to estimate this gradual decrease in the rolling element-to-raceway contact forces, and the model was incorporated in the quasi-static analytical model. The inertial and centrifugal effects of the rolling elements, which determine the trajectory (path) of the de-stressed rolling elements as they traverse through the defect, were not included in the quasi-static model. Therefore, the quasi-static analytical model could not predict the multiple force impulses, which are generated as the rolling elements re-stress between the raceways near the end of a defect; however, the model accurately predicted the de-stressing of the rolling elements indicating the verification of the developed hypothesis.

The numerically predicted vibration response of the defective rolling element bearing was analysed. Standard, vibration-based, signal processing techniques were implemented on the numerical vibration time-traces, and the results of the time, time–frequency, and frequency domain analyses were presented. Time domain analysis was used to determine the basic bearing kinematics; that is, the time separation of the defect-related impulses representing the outer raceway defect frequency f_{bpo}. Time–frequency analysis was used to investigate the low- and high-frequency characteristic vibration signatures, which are generated at the entry and exit of the rolling elements into and out of the defect, respectively. The most impulsive frequency band was

determined using spectral kurtosis and a kurtogram, and the numerically modelled vibration time-traces were band-pass filtered, prior to implementing the well-known envelope analysis technique in order to predict the significant frequency components; fundamental f_{bpo} and corresponding harmonics.

A significant amount of numerical noise was observed in the numerically modelled vibration time-traces. The instantaneous noise levels were high enough to mask the low-frequency characteristic vibration signatures associated with the de-stressing of the rolling elements. A novel hypothesis was developed to explain the cause of the rolling contact noise, and the noise frequencies due to the interaction of the polygonised rolling elements with both bearing raceways were analytically estimated. A favourable match between the numerical and analytical rolling contact noise frequencies was observed, which justifies the proposed hypothesis.

The numerical acceleration results predicted using the explicit dynamics FE model of the bearing were validated using the corresponding measured data. A package bearing unit having a line spall machined on its outer raceway was experimentally tested and its vibration levels were measured. Several favourable comparisons between the modelled and measured data were presented, which indicates the validation of the numerically modelled results.

With the aim of understanding the dynamic contact interaction of the rolling elements and raceways of a bearing, an in-depth analysis of the rolling element-to-raceway contact forces was undertaken. The variations in the contact forces as the rolling elements traverse through the outer raceway defect were broadly divided into four events: event #1 — the de-stressing of the rolling elements, event #2 — the impact of the rolling elements with the defective surface, event #3 — the load compensation, and event #4 — the re-stressing of the rolling elements.

The physics behind the low- and high-frequency characteristic vibration signatures generated at the entry and exit of the rolling elements into and out of the defect, respectively, was explained. It was found that no impulse-like signatures were generated

during the de-stressing of the rolling elements as they enter into a raceway defect; thus, explaining the low-frequency characteristics of the vibration signatures for this event. In contrast, a burst of multiple, short-duration, force impulses is generated as the rolling elements re-stress between the raceways in the vicinity of the end of a defect, which explains the high-frequency characteristics of the re-stressing event.

As the rolling elements re-stress between the raceways, they alternate between striking the outer and inner raceways, leading to the generation of multiple, short-duration, force impulses in the vicinity of the end of a defect. The numerically modelled rolling element-to-raceway contact forces were correlated with the vibration time-traces, and the cause of the defect-related impulsive vibration signals generally observed in measured acceleration time-traces was explained.

It was found that although a rolling element can impact the surface of a defect and generate a low amplitude acceleration signal, a much higher acceleration signal is generated when the rolling elements are re-stressed between the raceways. These higher acceleration signals, generated during the re-stressing phase, are the ones that are generally observed in practice, and subsequently used for bearing diagnosis using envelope analysis.

A parametric study to investigate the effects of varying radial loads W and rotational speeds n_s on the vibration response of the bearing and contact forces was undertaken. The magnitude of the band-pass filtered envelope (demodulated) power spectra at the fundamental defect frequency ($1 \times f_{\text{bpo}}$) was chosen as representative of the vibration response, whereas a maximum of the band-pass filtered envelope of the rolling element-to-raceway contact forces was used to represent the magnitude of the multiple, short-duration, force impulses. It was found that the magnitude of the defect-related vibration impulses and contact forces generated during the re-stressing of the rolling elements increases with increasing load and speed.

7.2 Conclusions

The conclusions of the work presented in this thesis are as follows:

- a burst of multiple, short-duration, force impulses is generated during the re-stressing of a rolling element near the end of a defect, which leads to the generation of multiple vibration impulses for a single pass-by of a rolling element through a defect;
- the amplitude of the contact forces and acceleration produced during the re-stressing of the rolling elements is much greater than when the rolling elements strike the defective surface;
- a burst of multiple force impulses during the re-stressing event leads to the generation of defect-related impulses that are generally observed in measured acceleration signals, and subsequently used for bearing diagnosis;
- the generation of multiple force impulses during the re-stressing of a rolling element provides pragmatic insights that explain the occurrence of multiple impulses in measured vibration signals; and
- the amplitude of defect-related dynamic contact forces and impulsive acceleration signals, generated during the re-stressing of the rolling elements, increases with increasing radial load and rotational speed.

7.3 Recommendations for future work

Some recommendations for future work are listed below.

- A parametric study that includes a combination of various radial loads and rotational speeds on the vibration response and rolling element-to-raceway contact forces of the defective rolling element bearing having a rectangular line spall on its

outer raceway has been presented in this thesis. Similar studies can be conducted for various defect sizes ranging from line, to area, to extended spalls in order to understand the characteristic vibration signatures for various defect sizes. The profiles of the defects can also be varied ranging from smooth to more realistic rough surfaces.

- Results from the FE modelling of the rolling element bearing presented here can be incorporated into a statistical energy analysis software, such as VA One [402], in order to predict the acoustic pressure levels corresponding to the defect-related vibration response of the bearing. Transfer functions between the input defect-related vibration and/or contact force levels and output sound pressure levels can be investigated to understand the characteristics of the acoustics-related signatures of the vibration impulses. This can be useful for further enhancing the performance of the bearing acoustic monitors in the railway industry.

- The FE model of a rolling element bearing presented in this thesis is 2-D; therefore, only radial loads could be applied to the bearing model. In order to understand the effect of an axial load and a combination of axial and radial loads on the bearing vibration response, a 3-D model can be developed.

- Despite filtering the numerical noise, residual noise was present in the vibration response and rolling element-to-raceway contact force results. This noise is inherent to the numerical solution and is due to the implementation of the central difference method, which is an explicit time integration scheme, in LS-DYNA. A new explicit time integration scheme has recently been developed [305] and integrated in a commercially available FE software package, ADINA [309]. From the comparison of results, shown in reference [305], obtained using the central difference method and the new time integration method, it is understood that the new time integration scheme produces less numerical noise. The dynamics of

a rolling element bearing can be solved using ADINA to explore the possibility of achieving cleaner results.

This page intentionally contains only this sentence.

Appendix A

Publications Arising from this Thesis

Journal publications

- S. Singh, U. Köpke, C. Howard, and D. Petersen. Analyses of contact forces and vibration response for a defective rolling element bearing using an explicit dynamics finite element model. *Journal of Sound and Vibration*, 333(21):5356–5377, 2014. doi:10.1016/j.jsv.2014.05.011

- D. Petersen, C. Howard, N. Sawalhi, A. Ahmadi, S. Singh. Analysis of bearing stiffness variations, contact forces and vibrations in radially loaded double row rolling element bearings with raceway defects. *Mechanical Systems and Signal Processing*, 50–51:139–160, 2015. doi:10.1016/j.ymssp.2014.04.014

Conference publications

- S. Singh, U. Köpke, C. Howard, D. Petersen, and D. Rennison. Impact generating mechanisms in damaged rolling element bearings. In *Proceedings of Acoustics*, Paper number 106, Victor Harbor, SA, Australia, November 2013. Australian Acoustical Society.

- S. Singh, C. Howard, C. Hansen, and U. Köpke. Numerical noise generation in modelled bearing vibration signals. In *Proceedings of the 43rd International*

Congress on Noise Control Engineering, Melbourne, Victoria, Australia, November 16–19, 2014.

Appendix B

Various Types of Bearing Damage

Bearing damage can occur as a result of a number of different operating conditions. Those listed in this section are the most commonly found in rolling element bearings, and often caused by the following [54]:

- insufficient maintenance practices;
- mishandling;
- improper installation and adjustment practices;
- inadequate lubrication

An overview of various types of damage commonly found in rolling element bearings is provided here.

B.1 Wear — foreign material

One of the most common sources of trouble in rolling element bearings is wear and damage caused by foreign particles. Foreign particle contamination can cause abrasive wear, bruising, grooving, circumferential lining or debris contamination.

B.1.1 Abrasive wear

Fine foreign material in the bearing can cause excessive abrasive wear. Sand, fine metal from grinding or machining, and fine metal or carbides from gears will wear or lap the rolling elements and races. In roller bearings, the roller ends and cone (inner ring) rib will wear to a greater degree than the races. This wear will result in increased axial endplay or internal clearance, which can reduce fatigue life and result in misalignment in the bearing. Abrasive wear also can affect other parts of the machine in which the bearings are used. The foreign particles may get in through badly worn or defective seals. Improper initial cleaning of housings and parts, ineffective filtration or improper filter maintenance can allow abrasive particles to accumulate.

B.1.2 Pitting and bruising

Hard particles rolling through the bearing may cause pitting and bruising of the rolling elements and races. Metal chips or large particles of dirt remaining in improperly cleaned housings can initiate early fatigue damage.

B.1.3 Grooving

Grooving is caused by extremely heavy wear from chips or metal particles. These contaminants become wedged in the soft cage material and cause cut grooves in the rolling elements. This condition results in improper rolling contact geometry and can reduce service life.

B.1.4 Debris contamination

Common causes of external debris contamination include dirt, sand and environmental particles. Common causes of internal debris contamination include wear from gears, splines, seals, clutches, brakes, joints, housings not properly cleaned, and damaged or

spalled components. These hard particles travel within the lubrication, through the bearing and eventually bruise (dent) the surfaces. Raised metal around the dents that act as surface-stress risers cause premature spalling and reduced bearing life.

B.2 Etching — corrosion

Etching or corrosion is one of the most serious problems encountered in rolling element bearings. The high degree of surface finish on races and rolling elements makes them susceptible to corrosion damage from moisture and water if not adequately protected.

Etching is most often caused by condensate collecting in the bearing housing due to temperature changes. The moisture or water oftentimes gets in through damaged, worn or inadequate seals. Improper washing and drying of bearings when they are removed for inspection also can cause considerable damage.

B.3 Inadequate lubrication

Inadequate lubrication can create a wide range of damage conditions. Damage happens when the lubricant intended for a bearing is not sufficient to separate the rolling and sliding contact surfaces during service. The damage caused by inadequate lubrication varies greatly in both appearance and performance. Depending on the level of damage, it may range from very light heat discoloration to total bearing lockup with extreme metal flow.

B.4 Brinell and impact damage

Improper mounting practices and/or extremely high operational impact or static loads may cause brinelling. Brinell due to improper mounting is caused where a force is applied against the unmounted race. When mounting a bearing on a shaft with a tight

fit, pushing the outer race will exert an excessive thrust load and bring the rolling elements into sharp contact with the race, causing brinell.

Extremely heavy impact loads, which may be short in duration, can result in brinell of the bearing races and sometime even fracture the races and rolling elements.

B.5 False brinelling

False brinelling is, as the name implies, not true brinelling or denting. False brinelling is actually fretting wear. It is caused by slight axial movement of the rolling elements while the bearing is stationary. A groove is worn into the race by the sliding of the rolling element back and forth across the race. Vibration causes the sliding movement. There are times when this cannot be prevented, such as when automobiles or other types of equipment are shipped by rail or truck for relatively long distances. It also can occur during shipment by ocean freight. The vibration present may cause enough movement to produce some of this false brinelling. It can be greatly reduced or eliminated by reducing the potential for relative movement and decreasing the static weight present during shipment or storage.

False brinelling can be distinguished from true brinelling by examining the depression or wear area. False brinelling will actually wear away the surface texture, whereas the original surface texture will remain in the depression of a true brinell.

B.6 Burns from electric current

Arcing, which produces high temperatures at localised points, results when an electric current that passes through a bearing is broken at the contact surfaces between the races and rolling elements. Each time the current is broken while passing between the ball or roller and race, a pit is produced on both parts. Eventually fluting develops. As it becomes deeper, noise and vibration result. A high-amperage current, such as

a partial short circuit, will cause a rough, granular appearance. Heavy jolts of high-amperage charges will cause more severe damage, resulting in the welding of metal from the race to the ball or roller. These protrusions of metal on the roller will, in turn, cause a crater effect in the race, resulting in bearing noise and vibration.

Causes of arcing include static electricity from charged belts or processes that use calendar rolls, faulty wiring, improper grounding, welding, inadequate or defective insulation, loose rotor windings on an electric motor and short circuits.

This page intentionally contains only this sentence.

Appendix C

Bearing Defect Frequencies

For the case of a stationary outer ring and rotating inner ring, following are the characteristic defect frequencies of a rolling element bearing rotating at a frequency f_s [3, Chapter 25, page 994]:

$$f_c = \frac{f_s}{2}\left(1 - \frac{D_r}{D_p}\cos\alpha\right) \tag{C.1}$$

$$f_{\text{bpo}} = \frac{f_s \times N_r}{2}\left(1 - \frac{D_r}{D_p}\cos\alpha\right) \tag{C.2}$$

$$f_{\text{bpi}} = \frac{f_s \times N_r}{2}\left(1 + \frac{D_r}{D_p}\cos\alpha\right) \tag{C.3}$$

$$f_{\text{bs}} = \frac{f_s \times D_p}{2 \times D_r}\left[1 - \left(\frac{D_r}{D_p}\cos\alpha\right)^2\right] \tag{C.4}$$

f_{c} cage frequency, commonly referred to as fundamental train frequency — it is the rotational speed of the cage in a rolling element bearing,

f_{bpo} ball pass frequency outer raceway (BPFO), commonly referred to as outer raceway defect frequency — it is the rate at which the rolling elements pass a point on the outer raceway within a rolling element bearing,

f_{bpi} ball pass frequency inner raceway (BPFI), commonly referred to as inner raceway defect frequency — it is the rate at which the rolling elements pass a point on the inner raceway within a rolling element bearing,

f_{bs} ball spin frequency (BSF), commonly referred to as ball or roller defect frequency — it is the rate of rotation of a rolling element about its own axis,

D_p bearing pitch diameter,

D_r rolling element diameter,

N_r number of rolling elements, and

α contact angle.

These frequencies are kinematic frequencies that are based on the geometry of a rolling element bearing. These frequencies do no take into account the slippage of the rotating components [30]. As a result, actual characteristic defect frequencies slightly differ from those predicted using the aforementioned equations.

Appendix D

Implicit and Explicit Time Integration Schemes

Finite element analysis that involves simulating short-duration large deformation dynamics and quasi-static problems with large deformations and multiple non-linearities or complex contact–impact problems requires the use of either implicit [287–294] or explicit [292, 295–305] solution techniques. Examples of these types of simulations are crashworthiness analysis, drop testing, deep drawing, rolling, extruding, pipe whip, bird strike and many more [307, 329].

Both implicit and explicit solution techniques involve a numerical time integration scheme to solve for the unknown displacement solution, which is the basis for calculating resulting strains and stresses. Implicit integration schemes, such as Newmark time integration method [288], assume a constant average acceleration over each time step, between t_n and t_{n+1}. The value t_n is the time at the beginning of each time step and the value t_{n+1} is the time at the end of each time step. The governing equation is evaluated and the resulting accelerations and velocities at t_{n+1} are calculated, followed by the estimation of unknown displacements at t_{n+1}. Explicit integration schemes, central difference method [299, 302], assume a linear change in displacement over each time step. The governing equation is evaluated and the resulting accelerations and

velocities at t_n are calculated, followed by the estimation of unknown displacements at t_{n+1}.

The implicit solution method requires matrix inversion of the structural stiffness matrix, whereas the explicit solution does not. In contrast to implicit methods [287–294], which are *unconditionally stable*, the explicit methods [292, 295–305] are stable only if the time step size Δt is smaller than the critical time step size $\Delta t_{\text{critical}}$ for the structure being simulated. In other words, explicit solutions are *conditionally stable*. Newmark and central difference time integration methods, which are commonly used implicit and explicit solution techniques, respectively, for approximating the dynamics of a system are described below.

D.1 Description of structural and other second-order systems

For most structural dynamics problems of a mechanical system, the spatial discretisation for the principle of virtual work using the finite element method gives the finite element semi-discrete equation of motion as follows [403, Chapter 17]

$$\mathbf{M}\ddot{\mathbf{u}}(t) + \mathbf{C}\dot{\mathbf{u}}(t) + \mathbf{F}^i(t) = \mathbf{F}^a(t) \tag{D.1}$$

where,

$\mathbf{M}$ structural mass matrix,

$\mathbf{C}$ structural damping matrix,

$\ddot{\mathbf{u}}(t)$ nodal acceleration vector,

$\dot{\mathbf{u}}(t)$ nodal velocity vector,

$\mathbf{u}(t)$ nodal displacement vector,

$\mathbf{F}^i$ internal load vector, and

$\mathbf{F}^a$ applied load vector.

D.1.1 Newmark time integration scheme for nonlinear systems

The Newmark method assumes that at time t_{n+1} the semi-discrete equation of motion given in Equation (D.1) can be rewritten as [403, Chapter 17]

$$\mathbf{M}\ddot{\mathbf{u}}_{n+1} + \mathbf{C}\dot{\mathbf{u}}_{n+1} + \mathbf{F}^i_{n+1}\mathbf{u}_{n+1} = \mathbf{F}^a_{n+1} \tag{D.2}$$

where,

$\ddot{\mathbf{u}}_{n+1}$ is the nodal acceleration vector at time t_{n+1},

$\dot{\mathbf{u}}_{n+1}$ is the nodal velocity vector at time t_{n+1},

$\mathbf{u}_{n+1}$ is the nodal velocity vector at time t_{n+1}, and

$\mathbf{F}^a_{n+1}$ is the applied load vector at time t_{n+1}.

Note that $\mathbf{F}^i_{n+1}\mathbf{u}_{n+1}$ is dependent on the current displacement $\mathbf{u}_{n+1}$ at time t_{n+1}. In addition to Equation (D.2), the Newmark family of time integration algorithms requires the displacement and velocity to be updated as follows [403, Chapter 17]

$$\dot{\mathbf{u}}_{n+1} = \dot{\mathbf{u}}_n + [(1-\Lambda)\ddot{\mathbf{u}}_n + \Lambda\ddot{\mathbf{u}}]\Delta t \tag{D.3}$$

$$\mathbf{u}_{n+1} = \mathbf{u}_n + \dot{\mathbf{u}}_n\Delta t + [(\frac{1}{2} - \Gamma)\ddot{\mathbf{u}}_n + \Gamma\ddot{\mathbf{u}}_{n+1}]\Delta t^2 \tag{D.4}$$

where,

Λ, Γ are the Newmark's integration parameters,

$\ddot{\mathbf{u}}_n$ is the nodal acceleration vector at time t_n,

$\dot{\mathbf{u}}_n$ is the nodal velocity vector at time t_n, and

$\mathbf{u}_n$ is the nodal velocity vector at time t_n.

By introducing the residual vector $\mathbf{R}_{n+1}\mathbf{u}_{n+1}$, Equation (D.2) can be written as [403, Chapter 17]

$$\mathbf{R}_{n+1}\mathbf{u}_{n+1} = \mathbf{F}^a_{n+1} - \mathbf{F}^i_{n+1}\mathbf{u}_{n+1} - \mathbf{M}\ddot{\mathbf{u}}_{n+1} + \mathbf{C}\dot{\mathbf{u}}_{n+1} \tag{D.5}$$

It is important to note that the time integration operator given in either Equation (D.2) or Equation (D.5) represents a nonlinear system of simultaneous algebraic equations. Therefore, a linearised form of the time integration operator can be obtained by the Newton-Raphson method as follows [403, Chapter 17]

$$\mathbf{R}_{n+1}\mathbf{u}^k_{n+1} + \frac{\partial \mathbf{R}_{n+1}\mathbf{u}^k_{n+1}}{\partial \mathbf{u}^i_{n+1}}\Delta\mathbf{u}^k_{n+1} = [0] \tag{D.6}$$

where, $\mathbf{u}^k_{n+1}$ the estimate of $\mathbf{u}_{n+1}$ at the kth iteration, and $\Delta\mathbf{u}^k_{n+1}$ the displacement increment of $\mathbf{u}_{n+1}$ at the kth iteration.

$$\mathbf{R}_{n+1}\mathbf{u}^k_{n+1} = \mathbf{F}^a_{n+1} - \mathbf{F}^i_{n+1}\mathbf{u}^k_{n+1} - \mathbf{M}\ddot{\mathbf{u}}_{n+1} + \mathbf{C}\dot{\mathbf{u}}_{n+1} \tag{D.7}$$

Equation (D.6) gives [403, Chapter 17]

$$[(a_0\mathbf{M} + a_1\mathbf{C}) + \mathbf{K}^{\mathrm{T}}_{n+1}\mathbf{u}^k_{n+1}]\Delta\mathbf{u}^k_{n+1} = \mathbf{R}_{n+1}\mathbf{u}^k_{n+1} \tag{D.8}$$

where, $a_0 = \dfrac{1}{\Gamma\Delta t^2}$, $a_1 = \dfrac{\Lambda}{\Gamma\Delta}$, and $\mathbf{K}^{\mathrm{T}}_{n+1}\mathbf{u}^k_{n+1}$ is tangent stiffness matrix at time t_{n+1}. For nonlinear problems:

- The solution is obtained using a series of linear approximations (Newton-Raphson method), so each time step may have many equilibrium iterations.
- The solution requires inversion of the nonlinear dynamic equivalent stiffness matrix.

- Small, iterative time steps may be required to achieve convergence.
- Convergence tools are provided, but convergence is not guaranteed for highly nonlinear problems.

D.1.2 Central difference time integration scheme for nonlinear systems

For the explicit method, the central difference time integration method is used. The the semi-discrete equation of motion at time n are given as [329, Chapter 24]

$$\mathbf{M}\ddot{\mathbf{u}}_n = \mathbf{F}_n^{\text{ext}} - \mathbf{F}_n^{\text{int}} + F_n^{\text{hg}} \tag{D.9}$$

where, $\mathbf{F}_n^{\text{ext}}$ is the applied external and body force vector, $\mathbf{F}_n^{\text{int}}$ is the internal force vector, and F_n^{hg} is the hourglass resistance force. To advance to time t_{n+1}, acceleration evaluated at time n are given by as

$$\ddot{\mathbf{u}}_n = \mathbf{M}^{-1}(\mathbf{F}_n^{\text{ext}} - \mathbf{F}_n^{\text{int}} + F_n^{\text{hg}}) \tag{D.10}$$

The velocities and displacements are then evaluated as

$$\dot{\mathbf{u}}_{n+1/2} = \dot{\mathbf{u}}_{n-1/2} + \ddot{\mathbf{u}}_n \Delta t \tag{D.11}$$

$$\mathbf{u}_{n+1} = \mathbf{u}_n + \dot{\mathbf{u}}_{n+1/2} \Delta t_{n+1/2} \tag{D.12}$$

where,

$$\Delta t_{n+1/2} = \frac{\Delta t_n + \Delta t_{n+1}}{2} \tag{D.13}$$

The geometry is updated by adding the displacement increments to the initial geometry $\mathbf{X}_0$

$$\mathbf{X}_{n+1} = \mathbf{X}_0 + \mathbf{u}_{n+1} \tag{D.14}$$

For nonlinear problems:

- A lumped mass matrix is required for simple inversion.
- The equations become uncoupled and can be solved for directly (explicitly).
- No inversion of the stiffness matrix is required.
- All non-linearities (including contact) are included in the internal force vector.
- The major computational expense is in calculating the internal forces.
- No convergence checks are needed since the equations are uncoupled.
- Very small time steps are required to maintain the stability limit.

Appendix E

Material Model for the Explicit FE Model of the Rolling Element Bearing

For the explicit dynamics finite element simulations undertaken for the current study, isotropic elastic material model was used. The model is defined by density, modulus of elasticity, and Poisson's ratio. In this model, the co-rotational rate of the deviatoric Cauchy stress tensor is computed as [329, Chapter 19, page 19.14]

$$s_{ij}^{\nabla^{n+1/2}} = 2G\dot{\varepsilon}_{ij}^{n+1/2} \tag{E.1}$$

and pressure as

$$p^{n+1} = -K \ln V^{n+1} \tag{E.2}$$

where, G is the elastic shear modulus, K is the bulk modulus, V is the relative volume; that is, the ratio of the current volume to the initial volume, and $\dot{\varepsilon}_{ij}$ is the strain rate tensor.

This page intentionally contains only this sentence.

Appendix F

Contact–Impact Analysis of a Sphere with Plate using LS-DYNA

List of Symbols

$E_1,\ E_2$	modulus of elasticity of a sphere and plate (half-space)
$E^{'}$	equivalent modulus of elasticity
F_c	time-varying contact–impact force
F_m	maximum force at the sphere–plate (half-space) contact interface
h_f	fall height
$h^{'}$	initial fall height
k_{cs}	contact or spring stiffness
m	mass of a sphere
r	radius of a sphere
v_i	impact velocity

δ_m	maximum displacement at the sphere–plate (half-space) contact interface
$\Delta t_{\text{critical}}$	critical time step
ν_1, ν_2	Poisson's ratio of a sphere and plate (half-space)
ρ	material density
τ	contact–impact time duration

F.1 Introduction

In order to understand the functional capabilities and features of the contact–impact algorithm used in LS-DYNA [329, Chapter 26], a problem of a sphere impacting a plate was modelled using LS-DYNA. In this appendix, a detailed step-by-step analysis of the problem along with necessary theoretical background is presented. The importance of meshing and adjusting the stiffness penalty factor is highlighted for achieving accurate results. Several comparison between the numerically modelled and analytically estimated results has highlighted the need to alter the default analysis and control settings pertinent to the contact–impact algorithm built within LS-DYNA. Altering the default settings has helped achieved a close agreement between numerical and theoretical results.

F.2 Analytical solution

The solution to the problem of a sphere impacting a plate is governed by the Hertz theory of elasticity [175, 176]. An overview of the Hertz theory has already been presented in Section 3.2, Chapter 3; therefore, only key formulae relevant to modelling an elastic impact of a sphere with plate are mentioned here. A comprehensive account on the contact of two bodies can be found in reference [177, Chapters 4].

Considering an elastic sphere of mass m and radius r that impacts normally on a plate, which is modelled as an elastic half-space, with velocity v_i, the maximum displacement δ_m during the impact is given as [177, Chapter 11, page 353]

$$\delta_m = \left(\frac{15 m v_i^2}{16 r^{1/2} E'} \right)^{2/5} \tag{F.1}$$

where, $E^{'}$ represents the equivalent modulus of elasticity of the sphere and half-space, which can be estimated as

$$\frac{1}{E'} = \frac{1-\nu_1^2}{E_1} + \frac{1-\nu_2^2}{E_2} \tag{F.2}$$

where, E_1 and ν_1 are the modulus of elasticity and Poisson's ratio of the sphere respectively, and similarly E_2, ν_2 represent same definitions for the half-space.

The contact duration τ related to the impact of the sphere with half-space is given by

$$\tau = 2.94 \frac{\delta_m}{v_i} \tag{F.3}$$

The force–time relationship of the contact–impact between two bodies was investigated by Hunter [404]. It can be approximated as a function of half-sine wave, and is given by [405, 406]

$$F_c(t) = \frac{1.14 v_i^2}{k_1 \delta_m} \sin \frac{1.068 v_i t}{\delta_m}, \qquad 0 \leq t \leq \frac{\pi \delta_m}{1.068 v_i} \tag{F.4}$$

where, $k_1 = \dfrac{3}{4\pi\rho r}$. The maximum force developed during a contact of two elastic bodies was also reported by Hertz, which can be estimated as [177]

$$F_m = \frac{2}{3} \frac{E_1}{(1-\nu_1^2)} r^{1/2} \delta_m^{3/2} \tag{F.5}$$

In order to compare Equations (F.4) and (F.5), the maximum force magnitudes

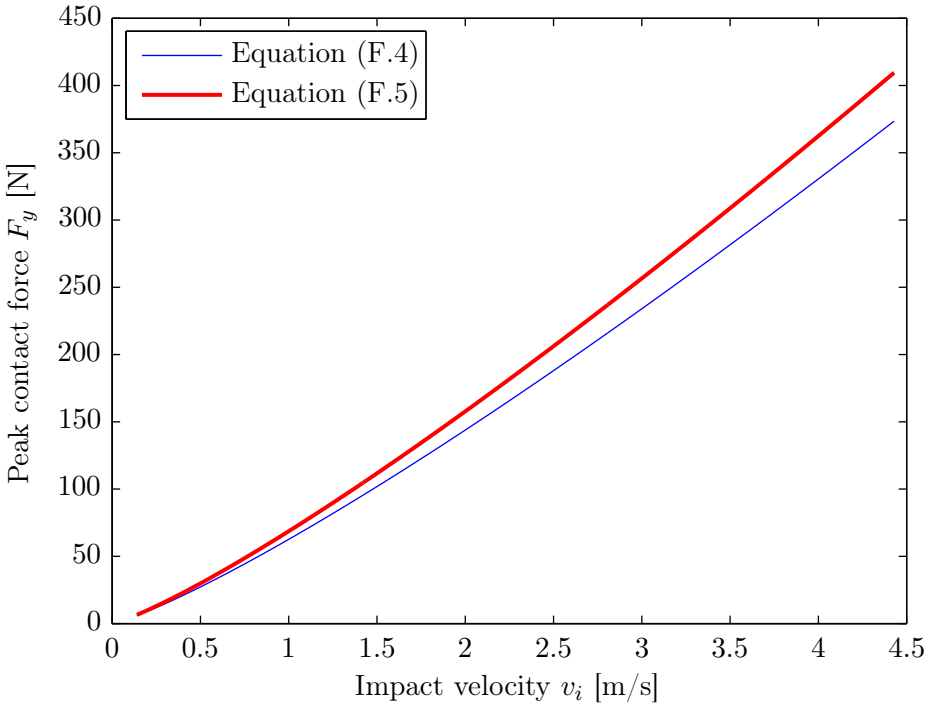

Figure F.1: A plot showing differences between peak contact force magnitudes obtained using Equations (F.4) and (F.5).

using these equations were estimated, and the comparison of the results is shown in Figure F.1. As can be seen from the figure that the estimates of the equations diverge with increasing impact velocity v_i or fall height h_f; the results obtained using Equation (F.5) are higher compared to those obtained using Equation (F.4).

It is not the intention of this study to investigate the highlighted differences, but to validate numerical modelling results, so as to understand the analysis methods of the LS-DYNA software, especially the contact–impact algorithm. Therefore, the numerical modelling results will be compared with those of the analytical estimates from the aforementioned equations:

- Equation (F.1) for comparing maximum displacement δ_m,
- Equation (F.3) for comparing contact–impact duration τ,
- Equation (F.4) for comparing force-time curve F_c, and
- Equations (F.4) and (F.5) for comparing peak contact–impact force F_m.

F.3 Numerical modelling

This section describes the numerical modelling and validation of the contact–impact analysis of a sphere and plate conducted using the FE software package, LS-DYNA [329]. The steps related to conducting the FE contact–impact analysis of the sphere and plate are described below. These steps include: (1) building the model; (2) meshing the model; (3) defining contact interactions; (4) applying boundary conditions and loads; and (5) solving the model.

F.3.1 Building the model

A three-dimensional (3-D) geometrical model of a sphere of radius $r = 2\,\text{mm}$ and a plate of dimensions (length×depth×height) $5 \times 5 \times 1\,\text{mm}$ was built. The sphere and plate were separated by a distance of 1 mm along the y-axis of the global coordinate system.

Of the ten element types available in the element library within the FE software package, LS-DYNA, eight-noded solid brick elements [329, Chapter 3] were used for defining and meshing the sphere and plate. Each node of the element has the following degrees-of-freedom: translations, velocities and accelerations in the nodal x-, y- and z-directions.

For the current analysis involving the simulation of an elastic impact of a sphere with plate, the isotropic material model was chosen. For defining an elastic material, its density ρ, Young's modulus E, and Poisson's ratio υ, must be defined. The material steel was used to model the sphere and plate with values of $\rho = 7850\,\text{kg/m}^3$, $E = 200\,\text{GPa}$, and $\nu = 0.3$.

F.3.2 Meshing the model

The discretisation of a model into nodes and elements is an extremely important step in an FE analysis as the accuracy of the results depends on the quality of the mesh and

elements. Depending upon the nature and type of contacts between multiple bodies, the location of regions of high stress concentration can vary constantly. Therefore, it is generally recommended to mesh a model using uniform element sizes for explicit analyses; however, for the current contact analysis of a sphere impacting a plate, the region of high stress concentration is known a priori. Therefore, the regions of the sphere and plate to be in contact can be meshed with fine elements, and the rest of the regions of the model can be meshed with comparatively coarse elements.

Figure F.2 shows a meshed, quarter, model of the sphere-plate geometry. The sphere and plate were meshed using tetrahedral and hexahedral elements, respectively [329]. As mentioned earlier in Chapter 4, the smallest element size in a model controls the time step that is used to advance the explicit solution. Refer to Section 4.2.5.1, Chapter 4, for the definitions of the critical $\Delta t_{\text{critical}}$ and stable Δt_{stable} time steps, which are limited by the Courant-Friedrichs-Lewy (CFL) criterion [384].

Finely meshed models with small sized elements would provide reliable estimates, but result in large CPU run times. In contrast, coarsely meshed models can be solved in less time comparable to models with fine mesh, but can result in inaccurate estimations. Therefore, in order to investigate the effects of various mesh sizes, the sphere-plate impact analyses were conducted for three different element mesh sizes — 0.2 mm, 0.1 mm, and 0.05 mm.

F.3.3 Contact interactions

Interactions between multiple bodies within a model refer to defining the type of contact between the bodies and the parameters related to the contact algorithm. A detailed explanation of the aforementioned topics is provided in LS-DYNA theory manual [329, Chapter 26]. For the current analyses, a frictionless contact between the sphere and the plate was defined.

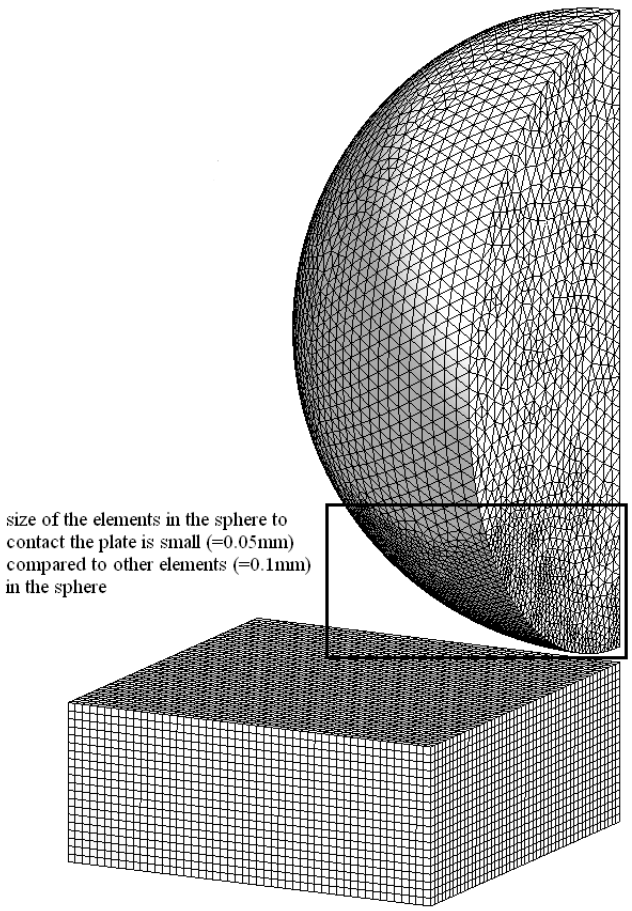

Figure F.2: A 3-D quarter model of a sphere and plate displaying the meshing.

F.3.3.1 Contact–impact algorithm

The surface-to-surface segment-based contact algorithm [329, Chapter 26] was chosen to model the contact between the sphere and plate. The segment-based contact algorithm is a general-purpose penalty-based algorithm. This algorithm invokes contact between the surfaces of the bodies in contact, and provides more accurate contact analysis compared to the node-surface penalty-based algorithm [329].

AS mentioned earlier in Section 4.2.3.1, Chapter 4, the contact stiffness between contacting bodies, also referred to as *spring stiffness*, is calculated as [329, Chapter 26, page 26.10]

$$k_{cs}(t) = \frac{1}{2}(\texttt{SLSFAC}) \times (\texttt{SFS or SFM}) \left(\frac{m_1 m_2}{m_1 + m_2}\right) \left(\frac{1}{\Delta t_{\text{critical}}}\right) \tag{F.6}$$

where, SLSFAC is the default penalty scale factor, SFS or SFM are the default slave and master penalty stiffness factors, respectively, m_1 and m_2 are segment masses of the bodies in contact, and $\Delta t_{\text{critical}}$ is critical time step that advances the numerical solution (discussed in Section 4.2.5.1, Chapter 4). The default value of SLSFAC defined in the contact–impact algorithm built within LS-DYNA is 0.1, and for SFS and SFM, it is 1. The effective penalty factor is the product of SLSFAC and SFS or SFM.

In a typical contact analysis, it is required to achieve an acceptable amount of penetration of one body into the other; the amount of penetration depends on the nature of contact analysis and material properties. As the default stiffness penalty factors defined in the LS-DYNA code have to cater for a wide range of contact-related real world problems, it can result in unnecessarily high penetration, consequently leading to inaccurate results. Therefore, in order to achieve an acceptable amount of penetration, the default penalty factors may need adjustment. Although increasing the stiffness penalty factors results in decreasing the amount of penetration, such increase can cause the ill-conditioning of the global stiffness matrix [329]; and can consequently lead to unstable solution. Therefore, judicious scaling of these factors may be required.

Understanding the effects of altering the stiffness penalty factors on the accuracy of contact–impact analyses is one of the crucial steps involved in such analyses. For the contact–impact analysis of the sphere and plate, the penalty factor, SLSFAC, was increased gradually to the limit beyond which the solution becomes unstable; this limit is problem dependent as will be discussed in this appendix later.

F.3.4 Boundary conditions and loads

For the current analyses, the sphere was dropped from several heights h_f: 1 mm, 5 mm, 25 mm, 50 mm, and 100 mm. Instead of starting the simulation from 5 mm, 25 mm,

50 mm and 100 mm, the simulations were started at the height of 1 mm, and the initial free fall of the sphere was modelled by applying initial velocity to all the nodes of the sphere using the formula $\sqrt{2gh'}$, where h' is the initial free fall height. This was implemented to reduce the CPU run times.

To model the plate as half-space, an impedance boundary condition was applied to all its exterior faces (and edges) except the top surface which will make contact with the falling sphere. The application of the impedance boundary condition prevents stress waves being generated at model boundaries from re-entering the model. The bottom surface of the plate was constrained, translationally and rotationally, in x-, y- and z-global directions. The standard earth gravity was applied to the model in the global y-direction.

F.3.5 Analysis and control settings

Appropriate termination time was defined for various FE simulations to capture the first impact so as to enable the output of contact–impact force F_c, contact–impact duration τ and maximum displacement δ_m. The results, in the form of binary text files, were output at the interval of 0.0001 ms. All the results were post-processed using a commercially available software, MATLAB®.

F.4 Numerical FE results

In order to investigate the influence of mesh sizes on the numerical modelling results, FE simulations were conducted for three different mesh element sizes — 0.2 mm, 0.1 mm and 0.05 mm. For all these element sizes, the analyses were also conducted with default and scaled stiffness penalty factors. These results are systematically presented in the following sections.

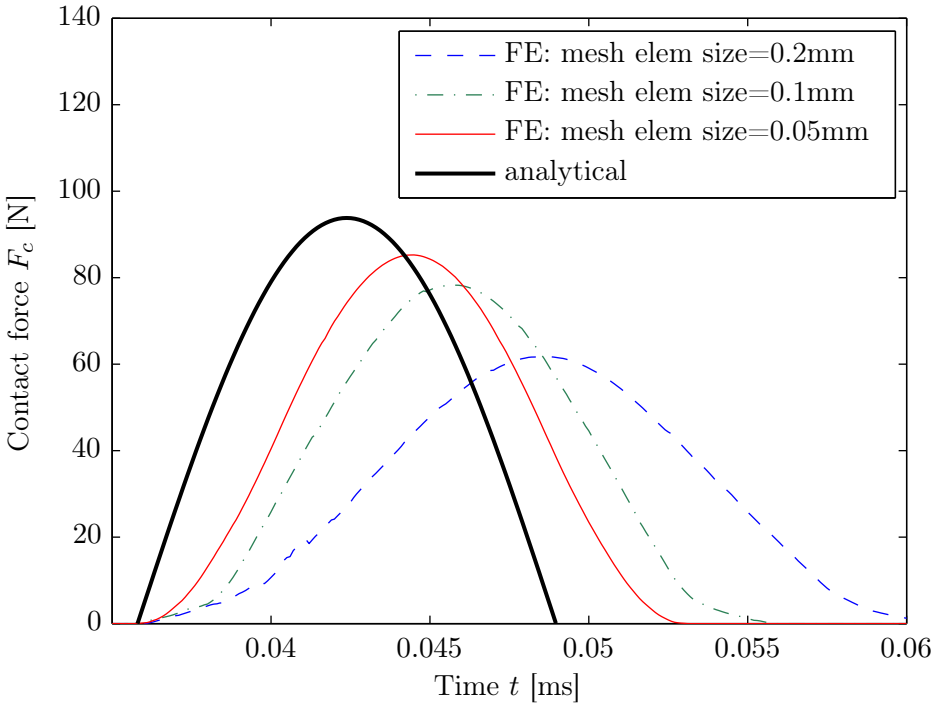

Figure F.3: Numerical and analytical contact forces generated during the free fall normal impact of the sphere, from the height h_f of 100 mm, with the plate, modelled as a half-space; the numerical results are shown for three different mesh element sizes of 0.2 mm, 0.1 mm, and 0.05 mm.

F.4.1 Influence of different mesh sizes

For the free fall height h_f of 100 mm, Figure F.3 shows various plots of the numerically modelled contact forces pertinent to the impact of the sphere with plate (modelled as half-space) for the three mesh sizes of 0.2 mm, 0.1 mm and 0.05 mm. The analytical solution of the contact force versus time, calculated using Equation (F.4), is also plotted in the figure along with the numerical modelling results for comparison.

It is clear from the results shown in Figure F.3 that the accuracy of the FE analyses strongly depends on the size of the elements used for meshing the model. The contact–impact durations τ for these simulations vary from 0.0248 ms, to 0.0199 ms, to 0.0173 ms for the mesh element sizes of 0.2 mm, 0.1 mm and 0.05 mm, respectively. Compared to the analytically estimated contact–impact duration, the numerically modelled contact durations differ by (the percentage error of) 85.4%, 49.5% and 30.3% for the mesh element sizes of 0.2 mm, 0.1 mm and 0.05 mm, respectively.

Mesh element size (mm)	Maximum displacement δ_m(mm)		Error (%)
	numerical	analytical	
0.2	0.0129	0.0063	104.72
0.1	0.0100		58.73
0.05	0.0085		35.72

Table F.1: Numerical and analytical results for the maximum displacement δ_m during the contact–impact of the sphere and plate.

As the analytical force–time relationship (Equation (F.4)) was approximated as a function of half-sine wave, it can be seen from Figure F.3 that at the start and end of the contact, the theoretical force-time curve follows a parabolic path. In contrast, the numerically modelled force-time curves plateau during the start and end of the contact, before gradually increase to follow a linear path; however, different to that of the analytical solution.

Table F.1 shows the amount of maximum displacement δ_m of the sphere during its contact with the plate for the three FE simulations with the aforementioned mesh element sizes. The analytical solution for the maximum displacement, calculated using Equation (F.1), is also shown in the table along with the respective percentage errors between the numerical and analytical results. The errors between numerical and analytical results vary significantly from 104.72% to 58.73% to 35.72% for the mesh element sizes of 0.2 mm, 0.1 mm, and 0.05 mm, respectively.

For the above mentioned numerical analyses, the penalty factors were not altered from their default values of 0.1 for `SLSFAC,` and 1 for `SFS` and `SFM`. Although the difference between numerical and theoretical results, highlighted in Figure F.3 and Table F.1, reduces with refining the mesh, numerically modelled higher contact durations τ and maximum displacements δ_m indicate the need to alter the default stiffness penalty factors within the FE software package, LS-DYNA. This is described next.

F.4.2 Altering the stiffness penalty factor

For all the three numerical simulations described above, the default penalty stiffness factors were altered, and force-time curve F_c, contact–impact τ duration and maximum displacement δ_m were obtained. These results are shown below.

F.4.2.1 Mesh element size of 0.2 mm

For the sphere-plate model discretised using the element size of 0.2 mm, various FE simulations were conducted with different stiffness penalty factors. The penalty factors were increased from its default value of 0.1 to the limit where the solution became unstable. The criterion for unstability in the solution was chosen to be the introduction of unnecessary noise (spikes) in the results due to increased stiffness of the elements in contact.

Contact force versus time

Figure F.4 shows the numerically modelled contact forces pertinent to the impact of the sphere and plate, obtained using LS-DYNA, for various penalty factors. The analytical estimated contact force F_c as a function of time is also plotted, represented by a solid, thick, line, along with the FE simulation results, so as to facilitate the comparison.

The effect of increasing the stiffness penalty factor is evident in Figure F.4; the numerically modelled contact force (and consequently contact duration) vary significantly before reaching a state where solution stabilises, and ultimately resulting in an unstable solution. The magnitude of the peak contact force increases from approximately 62 N for the penalty factor of 0.1 to 94 N for the penalty factor of 1. For the penalty factors ranging from 10 to 35, the numerical contact force–time curves are similar to each other with their respective peak force magnitudes at around 105 N.

The analytical peak contact force estimates obtained using Equations (F.4) and (F.5) are 93 N and 103 N (differences between the maximum force magnitudes from

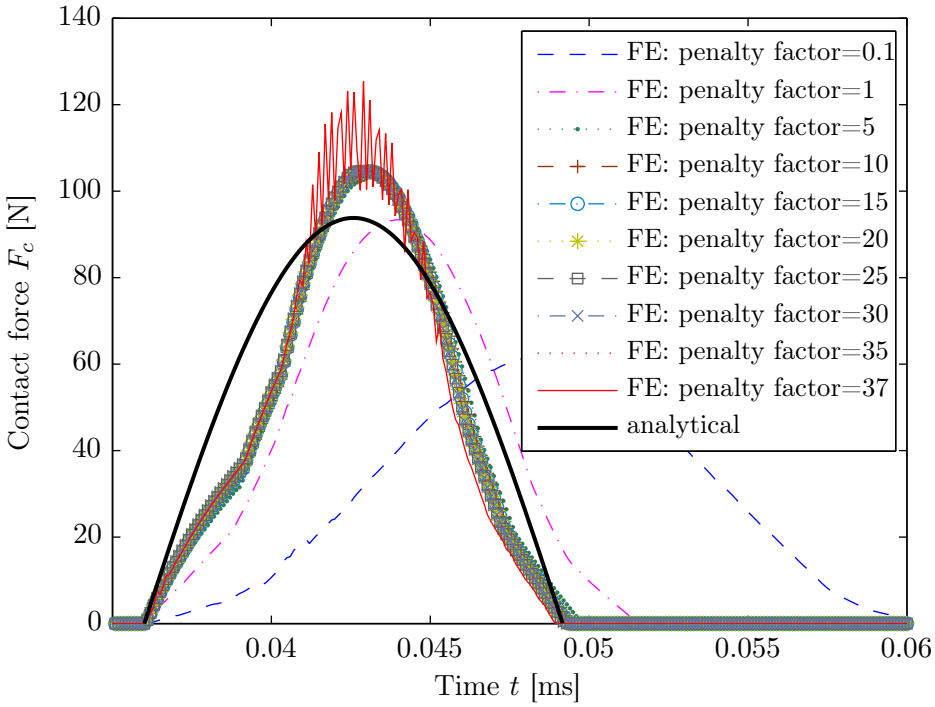

Figure F.4: Numerical and analytical contact forces F_c generated during the free fall impact of the sphere, from the height $h_f = 100\,\text{mm}$, with the plate for various penalty factors; the sphere-plate model was meshed using 0.2 mm-sized elements.

these equations were shown in Figure F.1). The comparison of the analytical solution with that of the numerically modelled peak contact force of 105 N shows percentage errors of 9.41% and 2.08%, respectively. It was mentioned in the literature [404], the analytical force-time relationship given by Equation (F.4) is an approximation; therefore, the above described comparison between the numerical and analytical peak contact forces indicates that Equation (F.5) provides a better estimate for calculating the peak contact force. However, Equation (F.4) is also required for plotting the force-time curve and comparing it with respective numerical results.

As mentioned earlier, too much increase in the stiffness of a structure can cause the ill-conditioning of the global stiffness matrix, which can result in unstable solution and loss of accuracy. The unstability in Figure F.4 can be seen when the LS-DYNA analysis was conducted with the stiffness penalty factor of 37.

Contact–impact duration versus penalty factor

The contact–impact durations τ pertinent to the results of the FE simulations shown in Figure F.4 were plotted over the corresponding penalty factors, and the respective plot is shown in Figure F.5. The 'unstable' numerical solution is indicated using a circular marker filled with a solid, red, colour; the size of this marker is biggest compared to all the other markers in the figure. The 'stable–converged' refers to those FE simulations for which the numerical contact durations τ are within 2% of the analytical estimate; these numerical results are indicated using unfilled circular markers. The 'stable–unconverged' refers to those simulations for which the difference between the numerical and analytical contact durations is $\geq$ 4%; these numerical results are indicated using circular markers filled with a solid, blue, colour; the size of these markers is smallest compared to all the other markers in the figure. The usage of the words 'converged' and 'unconverged' in this appendix is purely related to comparing the numerical and analytical results.

The corresponding analytical solution is also plotted in Figure F.5 as a dash-dotted horizontal line. The contact duration τ of 0.0248 ms obtained using the default penalty factor continues to reduce with the increasing penalty factors; using the penalty factor of 35, contact duration of 0.0131 ms was obtained. The error between the analytical and numerical solution for the contact duration converges from 88.39% (for default penalty factor) to 0.49% (for penalty factor of 35). It can be seen from Figure F.5 that the numerical contact durations corresponding to the penalty factors from 10 to 35 agree well with the theory.

Maximum displacement versus penalty factor

Numerical solution for the maximum displacement δ_m of the sphere pertinent to the FE simulation results in Figure F.4 are shown in Figure F.6 for varying stiffness penalty factors, along with the respective analytical solution as a dash-dotted horizontal line.

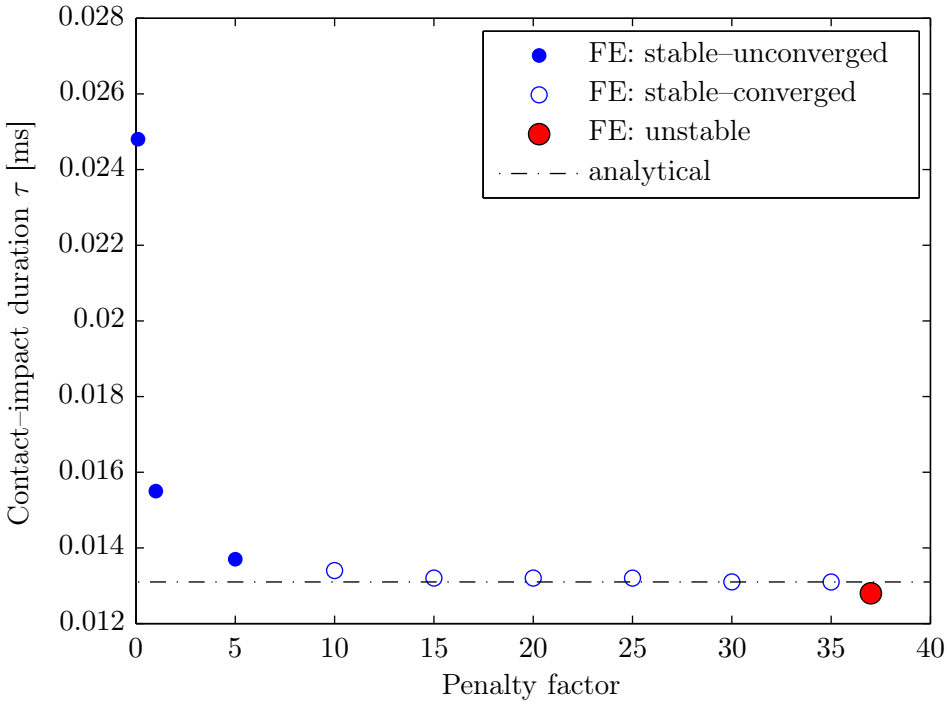

Figure F.5: Numerical and analytical contact–impact durations τ for the free fall impact of the sphere, from the height $h_f = 100\,\text{mm}$, with the plate for various penalty factors; the sphere-plate model was meshed using 0.2 mm-sized elements.

Although the numerical results corresponding to the penalty factors ranging from 10 to 35 plateau at around 0.0071 mm, they differ by approximately 15% in comparison with that of the analytical solution. For the penalty factor of 37, the 'unstable' FE simulation has been indicated using a circular marker filled with solid, red, colour, which is bigger in size compared to the rest of the circular markers filled with blue colour.

Despite achieving favourable agreement between the analytical and numerical results for the contact–impact duration τ (Figure F.5), the disagreement of the numerically estimated maximum displacement δ_m (shown in Figure F.6) with that of the analytical estimate indicates the lack of accuracy in LS-DYNA analyses. This inaccuracy is also highlighted by the lack of smoothness in the numerical contact force-time plots shown in Figure F.4.

As the influence of mesh element size on FE simulation results has already been highlighted in Figure F.3, the aforementioned inaccuracy can be caused by inade-

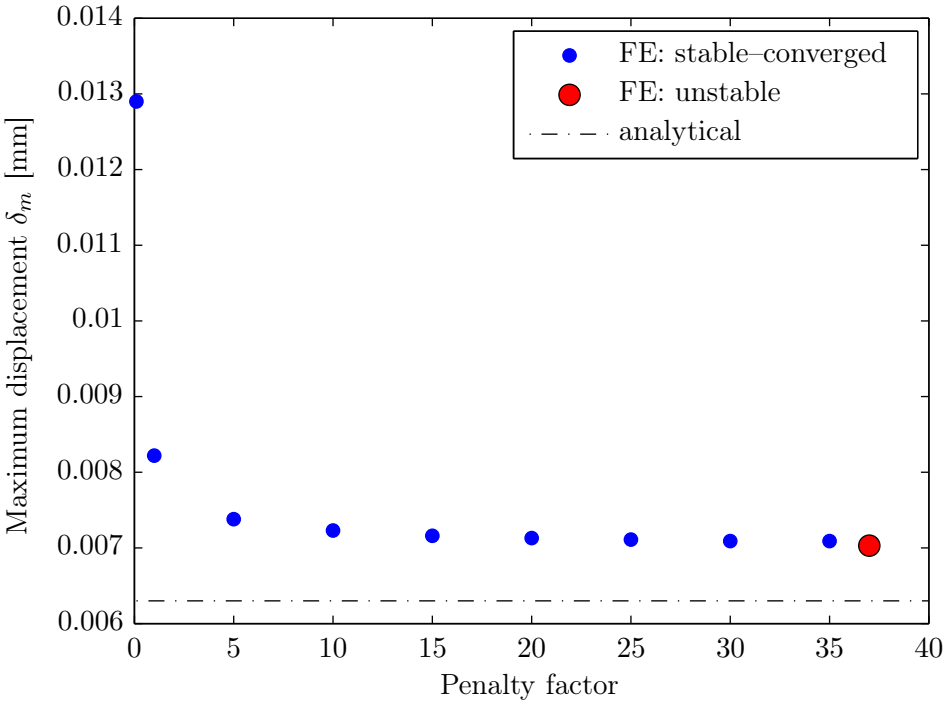

Figure F.6: Numerical and analytical maximum displacements δ_m for the free fall impact of the sphere, from the height $h_f = 100\,\text{mm}$, with the plate for various penalty factors; the sphere-plate model was meshed using 0.2 mm-sized elements.

quate meshing. Therefore, the aforementioned FE simulations were conducted with fine meshing, and are presented below.

F.4.2.2 Mesh element size of 0.1 mm

The sphere-plate geometrical model was discretised using the mesh element size of 0.1 mm, which is half the size of of the element size used for the previous analyses.

Contact force versus time

Figure F.7 shows the numerically modelled contact forces, obtained using LS-DYNA, for various penalty factors. The analytically estimated contact force as a function of time is also plotted in the figure, represented by a solid, thick, line, along with the numerical results for comparison. The penalty factors were increased from the default value in the way similar to that of the aforementioned simulations, and the effect of increasing the penalty factor was also observed to be similar to the previous simulations.

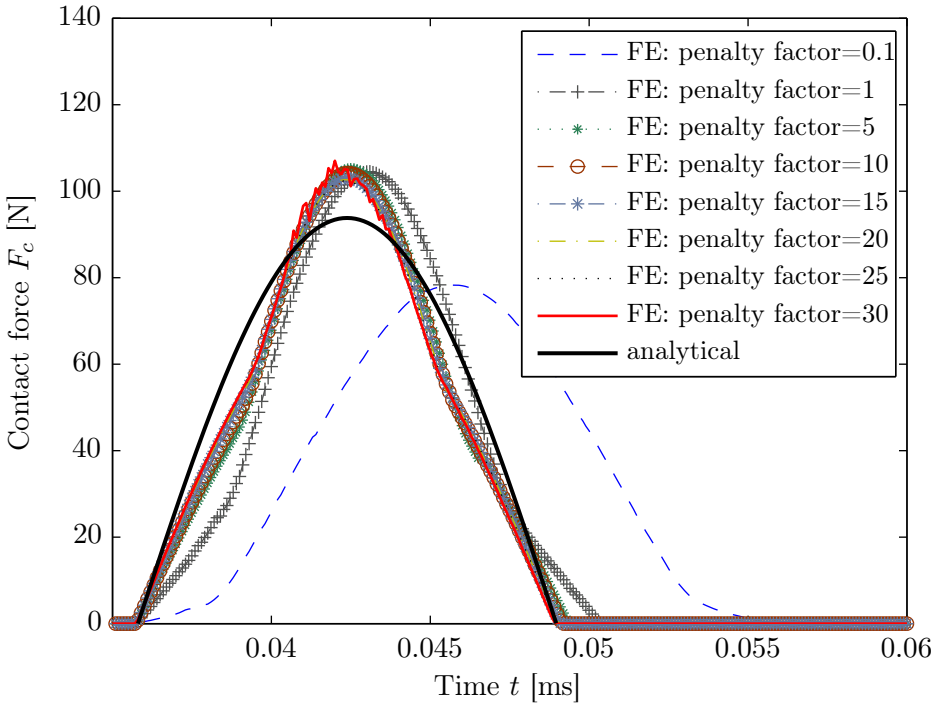

Figure F.7: Numerical and analytical contact forces F_c generated during the free fall impact of the sphere, from the height $h_f = 100\,\text{mm}$, with the plate for various penalty factors; the sphere-plate model was meshed using 0.1 mm-sized elements.

Figure F.7 shows that the numerical results for the peak contact force increase from approximately 78 N for the penalty factor of 0.1 to approximately 105 N for the penalty factors ranging from 1 to 25. The contact force-time curves corresponding to the penalty factors of 10 to 25 are similar. The FE simulation corresponding to the penalty factor of 30 resulted in instability as evident from the noise in the curve; the relevant curve is indicated using a thin, solid, red, line in Figure F.7.

Compared to the results shown in Figure F.4 where the penalty factor of 37 caused instability in the analysis, the penalty factor of 30 caused similar instability when the element size of 0.1 mm was used to discretise the sphere-plate model. This is because the contact stiffness used during an contact–impact analysis depends on the masses of the elements in contact and time step, which is also dependent on the size of the elements within an FE model.

The comparison of Figures F.4 and F.7 clearly shows the influence of mesh refinement as the contact-force plots shown in the latter figure are smoother than the plots

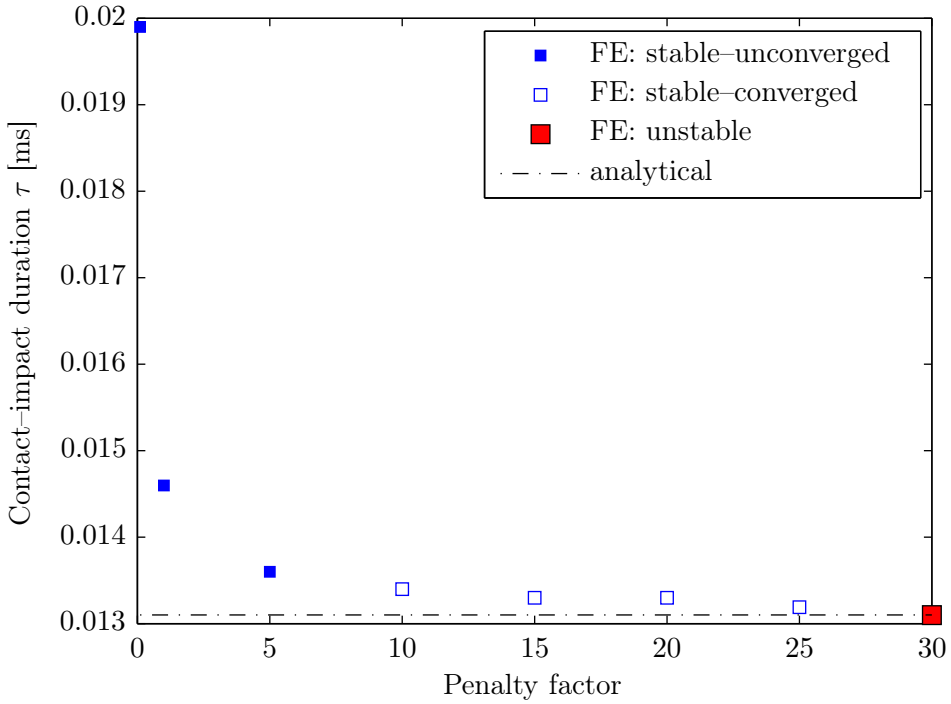

Figure F.8: Numerical and analytical contact–impact durations τ for the free fall impact of the sphere, from the height $h_f = 100\,\text{mm}$, with the plate for various penalty factors; the sphere-plate model was meshed using 0.1 mm-sized elements.

in the former figure.

Contact–impact duration versus penalty factor

Similar to numerical results plotted in Figure F.5 for the mesh element size of 0.2 mm, the numerical impact-contact durations τ for the mesh element size of 0.1 mm are shown in Figure F.8. Except for the shape of the markers used in Figure F.5, similar definition (variation in the size and fill pattern) was followed to distinguish between 'stable–unconverged', 'stable–converged', and 'unstable' FE simulations. The analytical solution of the contact duration is also plotted in Figure F.8, represented as a dash-dotted horizontal line. It is evident from the figure that the numerical impact-contact durations for the penalty factors from 10 to 25, referred to as 'stable–converged' analyses, agree well with the analytical solution; numerical and analytical results are within 1.8%.

The variation in the sizes of the square-shaped markers was used to distinguish

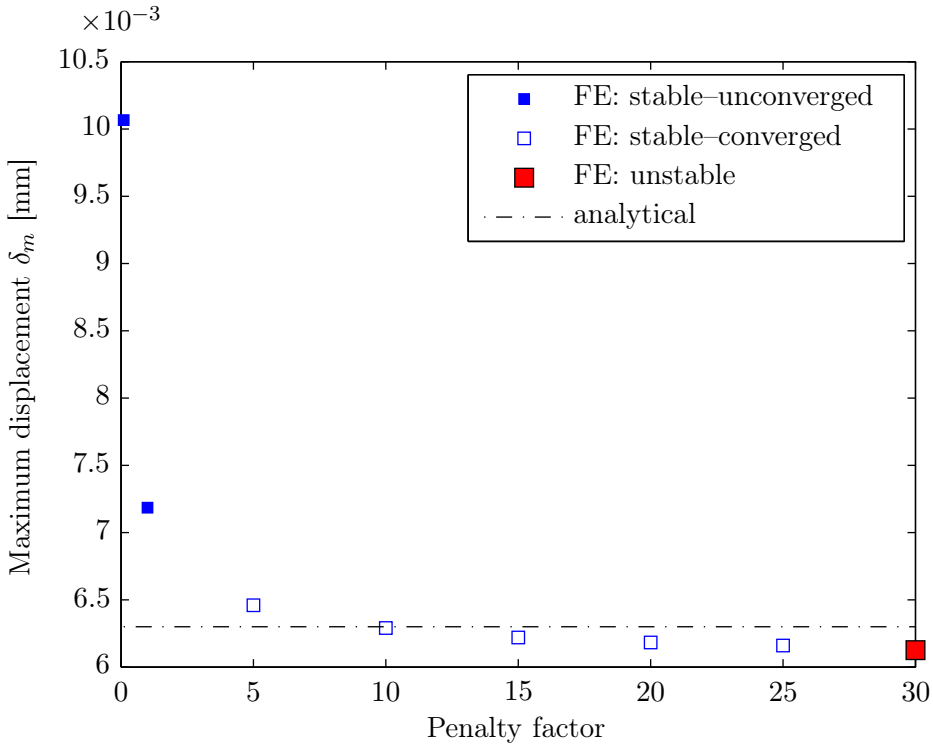

Figure F.9: Numerical and analytical maximum displacements δ_m for the free fall impact of the sphere, from the height $h_f = 100\,\text{mm}$, with the plate for various penalty factors; the sphere-plate model was meshed using 0.1 mm-sized elements.

between 'stable–unconverged', 'stable–converged', and 'unstable' FE simulations.

Maximum displacement versus penalty factor

The maximum displacement of the sphere during its impact with the plate, pertinent to the results in figure F.7 for various penalty factors, is shown in Figure F.9. The respective analytical estimate is also plotted in the figure as a dash-dotted horizontal line. It can be seen from the figure that the numerical results corresponding to the penalty factors from 5 to 25 agree well with the analytical solution; numerical and analytical results are within 2.5%.

The comparison of Figures F.6 and F.9 shows significant improvement in the accuracy of the FE modelling results as the difference between the analytical and numerical results reduced from 15% to 2.5%; these error percentages correspond to the discretisation of the sphere-plate model using 0.2 mm and 0.1 mm sized elements, respectively.

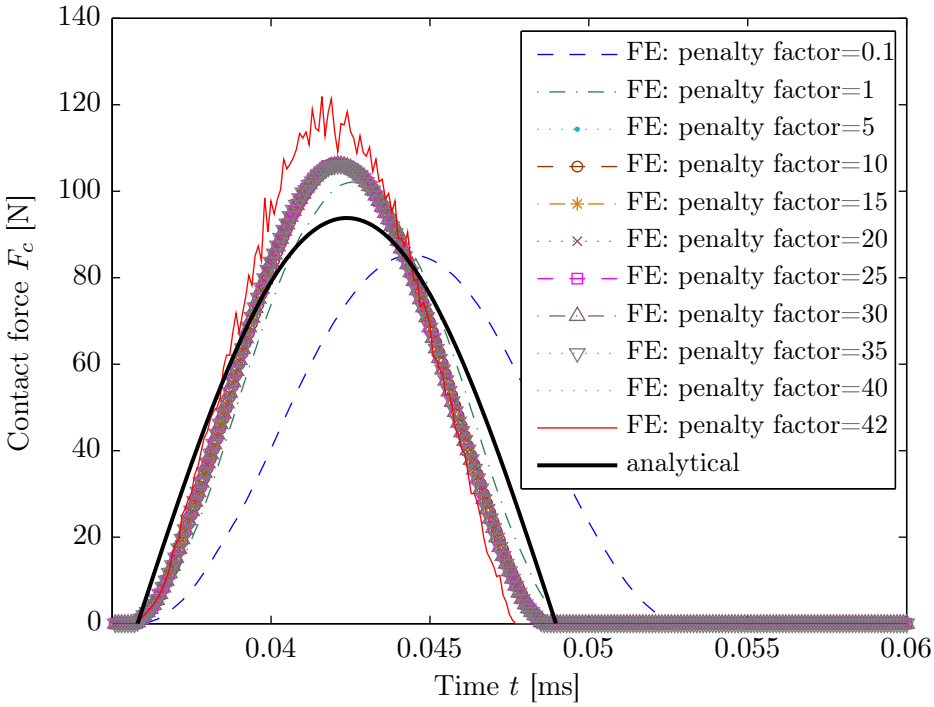

Figure F.10: Numerical and analytical contact forces F_c generated during the free fall impact of the sphere, from the height $h_f = 100\,\text{mm}$, with the plate for various penalty factors; the sphere-plate model was meshed using 0.05 mm-sized elements.

F.4.2.3 Mesh element size of 0.05 mm

The size of the elements used to discretise the sphere-plate model was further refined to 0.05 mm, and the FE simulations similar to those mentioned above were conducted.

Contact force versus time

Figure F.10 shows the results of numerically modelled contact forces for various penalty factors along with the analytical solution for comparison purposes. The increase of the penalty factors from the default value was carried out in the way similar to that of the above-described FE simulations, and the effect of increasing the penalty factor was also observed to be similar to the previous simulations.

The numerically modelled peak contact force increased from approximately 85 N for the penalty factor of 0.1 to approximately 106 N for the penalty factors ranging from 5 to 40. The numerical contact force-time curves which correspond to the aforementioned

range of the penalty factors are also similar to each other. These force-time curves are relatively smooth in comparison to the plots of the contact forces shown in Figures F.4 and F.7.

The LS-DYNA results corresponding to the penalty factor of 42 shows 'unstable' solution indicated by thin solid, red, line.

Contact–impact duration versus penalty factor

The contact–impact durations τ pertinent to the FE simulations in Figure F.10 are plotted for the corresponding penalty factors, and the respective plot is shown in Figure F.11. The 'stable–unconverged', 'stable–converged', and 'unstable' FE simulations are distinguished using variation in the size and fill pattern of the diamond-shaped markers. The contact–impact durations pertinent to the 'stable–converged' simualtions are similar to the analytical solution, which is shown as a dash-dotted horizontal line. As evident from Figure F.11, the numerically modelled contact durations plateau at around 0.0128 ms, which differs by 2.3% from the analytical estimate of 0.0131 ms.

Maximum displacement versus penalty factor

For the FE simulations corresponding to the mesh element size of 0.05 mm, the maximum displacement δ_m versus penalty factor plot is shown in Figure F.12. The numerical results pertinent to the 'stable–converged' simulations agree well with the analytical solution; numerical and analytical results are within 3%.

Although the percentage errors between the numerical and analytical results shown in Figures F.11 and F.12 (corresponding to the mesh element size 0.05 mm) is slightly higher than those of the errors shown in Figures F.8 and F.9 (corresponding to the mesh element size 0.1 mm), the latest FE simulations for 0.05 mm sized elements are also considered as reliable and accurate. This is because of the relative smoothness of the contact force-time plots; the smoothness is clearly evident in Figure F.10 compared to Figures F.4 and F.7.

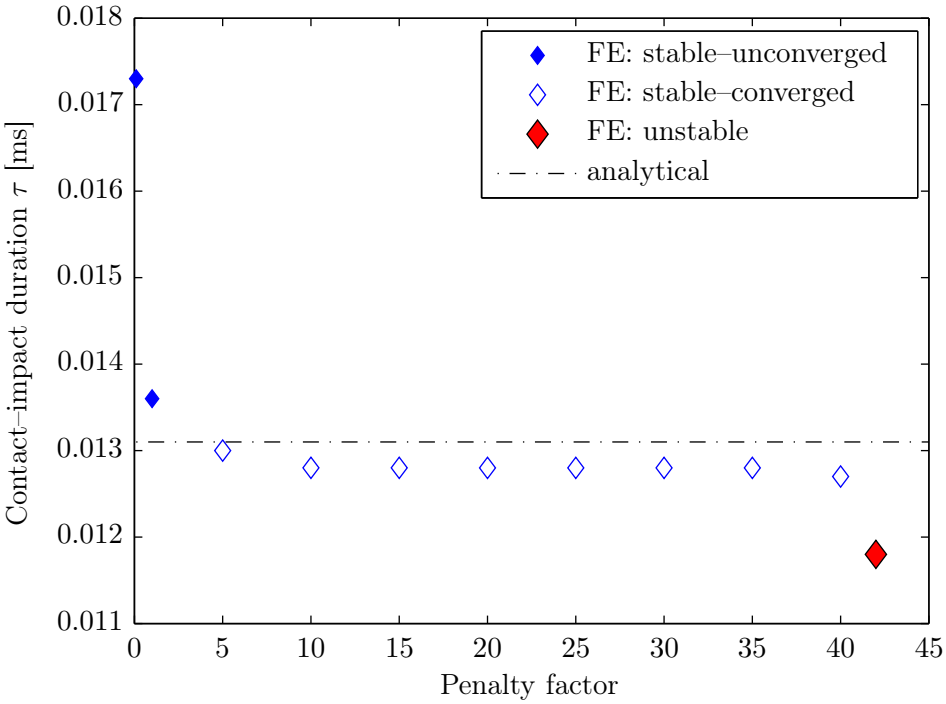

Figure F.11: Numerical and analytical contact–impact durations τ for the free fall impact of the sphere, from the height $h_f = 100\,\text{mm}$, with the plate for various penalty factors; the sphere-plate model was meshed using 0.05 mm-sized elements.

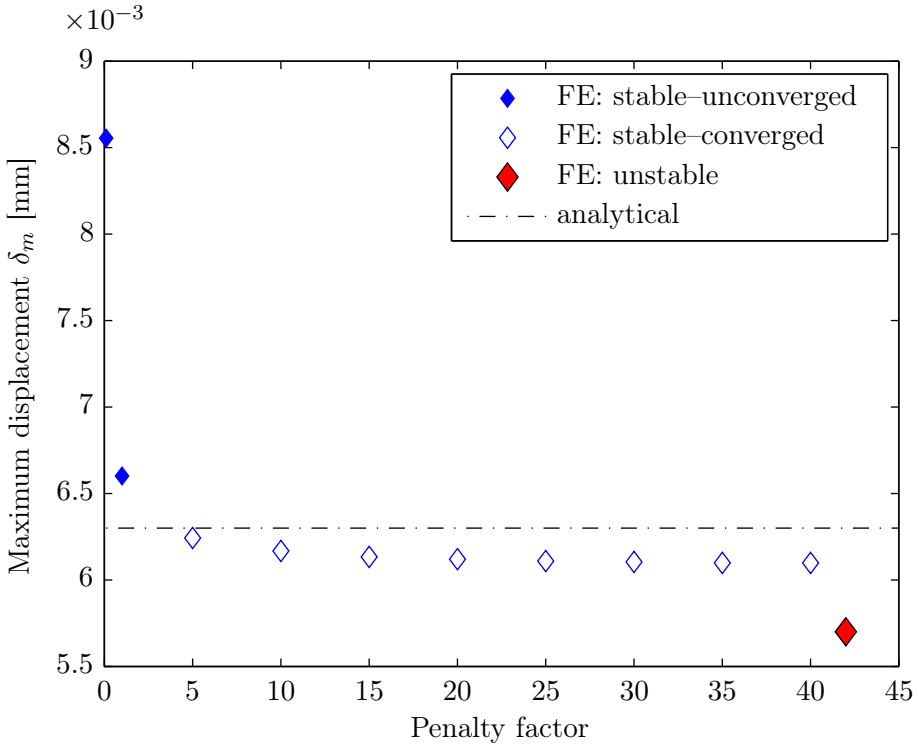

Figure F.12: Numerical and analytical maximum displacements δ_m for the free fall impact of the sphere, from the height $h_f = 100\,\text{mm}$, with the plate for various penalty factors; the sphere-plate model was meshed using 0.05 mm-sized elements.

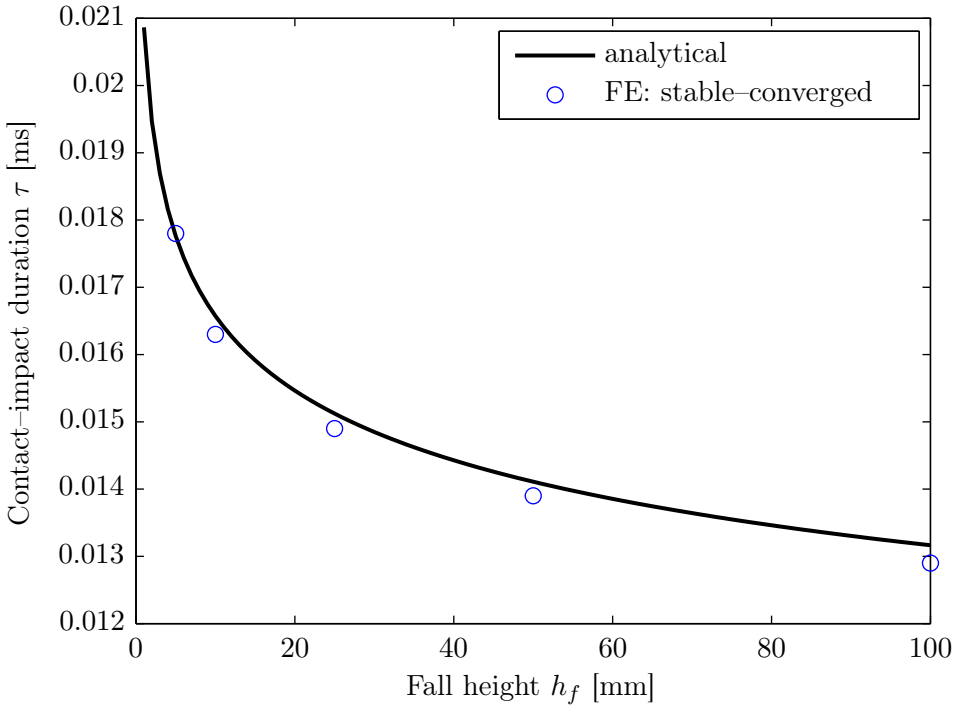

Figure F.13: Analytical and numerical estimates of the contact duration τ corresponding to the impact of the sphere with half-space for various free fall heights h_f.

FE simulations pertinent to the impact of the sphere with plate (modelled as half-space) were also conducted for different heights h_f — 50 mm, 25 mm, 10 mm, 5 mm. The respective numerically modelled contact durations τ along with the analytical estimates are shown in Figure F.13. A close agreement between the numerical and analytical solution shows the validation of the dynamic sphere-plate impact modelling.

F.5 Conclusions

From the results of the numerical FE simulations described in this appendix, it can be concluded that the accuracy of the analyses is highly dependent on the mesh element size used in the model. For the numerical analyses corresponding to the mesh element sizes of 0.2 mm, 0.1 mm and 0.05 mm, the contact durations closely agree with that of the analytical solution. However, the disagreement of the analytically estimated maximum displacement with that of the numerically modelled for the mesh element

size of 0.2 mm highlights the need for refining the mesh.

The importance of scaling the stiffness penalty factors was highlighted in order to achieve a reasonable agreement between numerical predictions and analytical results. The validation of the contact–impact analysis of the sphere and plate has facilitated gaining the required understanding of the contact–impact algorithm used in LS-DYNA.

References

[1] H. T. Morton. *Anti-Friction Bearings*. Ann Arbor, MI, Second edition, 1965. (Cited on page 1).

[2] J. Bräbdlein, P. Eschmann, L. Hasbargen, and K. Weigand. *Ball and Roller Bearings: Theory, Design and Application*. John Wiley & Sons, Inc., Chichester, Third edition, January 1999. (Cited on page 1).

[3] T. A. Harris. *Rolling Bearing Analysis*. John Wiley & Sons, Fourth edition, 2001. (Cited on pages 1, 20, 21, 27, 37, 46, 52, 53, 54, 64, 74, 77, 85, 92, 93, 98, 126, 137, 142, 154, 156, 246, and 327).

[4] S. Singh, U. Köpke, C. Howard, D. Petersen, and D. Rennison. Impact generating mechanisms in damaged rolling element bearings. In *Proceedings of Acoustics*, Paper number 106, Victor Harbor, South Australia, Australia, 17–20 November 2013. Australian Acoustical Society. (Cited on pages 2, 46, 86, 87, 88, 111, 131, 174, 246, and 259).

[5] S. Singh, U. Köpke, C. Howard, and D. Petersen. Analyses of contact forces and vibration response for a defective rolling element bearing using an explicit dynamics finite element model. *Journal of Sound and Vibration*, 333(21):5356–5377, 2014. doi:10.1016/j.jsv.2014.05.011. (Cited on pages 2, 46, 86, 87, 88, 111, 131, 174, 246, and 259).

[6] D. Petersen, C. Howard, N. Sawalhi, A. Ahmadi, and S. Singh. Analysis of bearing stiffness variations, contact forces and vibrations in radially loaded double row ball bearings with raceway defects. *Mechanical Systems and Signal Process-*

ing, 50–51:139–160, 2015. doi:10.1016/j.ymssp.2014.04.014. (Cited on pages 2, 86, 87, 102, 116, 118, 131, 174, 246, and 259).

[7] A. Moazenahmadi, D. Petersen, and C. Howard. A nonlinear dynamic vibration model of defective bearings — the importance of modelling the finite size of rolling elements. *Mechanical Systems and Signal Processing*, 52–53:309–326, 2015. doi:10.1016/j.ymssp.2014.06.006. (Cited on pages 2, 86, 87, 131, 174, 246, and 259).

[8] K. Bladon, D. Rennison, G. Izbinsky, R. Tracy, and T. Baldon. Predictive condition monitoring of railway rolling stock. In *Proceedings of Conference on Railway Engineering CORE 2004: New Horizons for Rail*, pages 22.1–22.12, Darwin, N.T., Australia, June 2004. Railway Technical Society of Australasia. (Cited on pages 2, 3, 4, 8, and 9).

[9] D. Barke and W. K. Chiu. Structural health monitoring in the railway industry: A review. *Structural Health Monitoring*, 4(1):81–93, 2005. doi:10.1177/1475921705049764. (Cited on page 2).

[10] RailBAM® — Railway Bearing Acoustic Monitor. (accessed 14 April 2014). Available from: http://www.trackiq.com.au/railbam.html. (Cited on pages xvii, 2, 3, 4, and 9).

[11] Trackside Intelligence Pty. Ltd. (Track IQ™), 17–19 King William St, Kent Town SA, Australia 5067. (accessed 14 April 2014). Available from: http://www.trackiq.com.au/. (Cited on pages xvii, xx, 2, 3, 7, 9, 104, 135, 199, and 202).

[12] TADS® — Trackside Acoustic Detection System. (accessed 14 April 2014). Available from: http://www.aar.com/vehicle_performance.php. (Cited on pages xvii, 2, 3, 4, and 9).

[13] Transportation Technology Center, Inc. (TTCI®), 55500 DOT Rd., Pueblo, CO 81001. (accessed 14 April 2014). Available from: http://www.aar.com/. (Cited on pages xvii, 2, and 3).

[14] C. Southern, D. Rennison, and U. Köpke. RailBAM® — An advanced bearing acoustic monitor: Initial operational performance results. In *Proceedings of Conference on Railway Engineering CORE 2004: New Horizons for Rail*, pages 23.01–23.07, Darwin, N.T., Australia, June 2004. Railway Technical Society of Australasia. (Cited on pages 3, 4, 8, and 9).

[15] U. Köpke, P. Lindqvist, A. Meyer, and D. Rennison. Development and verification of an advanced bearing acoustic monitor. In *Proceedings of the TTCI Bearing Symposium*, Chicago, USA, 2007. (Cited on pages 3, 4, 8, and 9).

[16] C. Southern, M. Sowden, and R. Donnelly. Maintenance planning using BAM's. In *Proceedings of the TTCI Bearing Symposium*, Chicago, USA, 2007. (Cited on pages 3, 4, 8, and 9).

[17] N. Tandon and A. Choudhury. A review of vibration and acoustic measurement methods for the detection of defects in rolling element bearings. *Tribology International*, 32(8):469–480, 1999. doi:10.1016/S0301-679X(99)00077-8. (Cited on pages 4, 9, 78, 138, 174, 181, 200, and 262).

[18] D. R. Houser and M. J. Drosjack. Vibration signal analysis techniques. Technical report, U.S. Army Air Mobility Research and Development Laboratory, 1973. (Cited on pages 4, 9, 78, and 200).

[19] R. A. Collacott. *Vibration monitoring and diagnosis*. Techniques for Cost-effective Plant Maintenance. Halsted Press, John Wiley & Sons, Inc., New York, 1979. (Cited on pages 4, 9, 78, and 200).

[20] L. M. Roger. The application of vibration analysis and acoustic emission source location to on-line condition monitoring of anti-friction bearings. *Tribology International*, 12(2):51–58, 1979. doi:10.1016/0301-679X(79)90001-X. (Cited on pages 4, 9, 78, and 200).

[21] N. S. Swansson and S. C. Favaloro. Applications of vibration analysis to the condition monitoring of rolling element bearings. Technical Report ARL-AERO-

PROP-R-163, Defence Science and Technology Organisation, Australia, January 1984. (Cited on pages 4, 9, 64, 78, and 200).

[22] N. Tandon and B. C. Nakra. Vibration and acoustic monitoring techniques for the detection of defects in rolling element bearings — a review. *The Shock and Vibration Digest*, 24:3–11, 1992. (Cited on pages 4, 9, 78, 181, and 200).

[23] I. Howard. A review of rolling element bearing vibration: "detection, diagnosis and prognosis". Technical Report DSTO-RR-0013, Defence Science and Technology Organisation, Australia, October 1994. (Cited on pages 4, 9, 20, 21, 22, 41, 48, 51, 54, 60, 65, 78, and 200).

[24] A. Choudhury and N. Tandon. Application of acoustic emission technique for the detection of defects in rolling element bearings. *Tribology International*, 33(1):39–45, 2000. doi:10.1016/S0301-679X(00)00012-8. (Cited on pages 4, 9, 41, 78, and 200).

[25] J. Antoni. The spectral kurtosis: A useful tool for characterising non-stationary signals. *Mechanical Systems and Signal Processing*, 20(2):282–307, 2006. doi:10.1016/j.ymssp.2004.09.001. (Cited on pages 4, 9, 41, 78, 132, 139, 181, 182, 200, and 222).

[26] J. Antoni and R. B. Randall. The spectral kurtosis: Application to the vibratory surveillance and diagnostics of rotating machines. *Mechanical Systems and Signal Processing*, 20(2):308–331, 2006. doi:10.1016/j.ymssp.2004.09.002. (Cited on pages 4, 9, 41, 78, 132, 139, 181, 182, 184, 200, and 222).

[27] J. Antoni. Fast detection of the kurtogram for the detection of transient faults. *Mechanical Systems and Signal Processing*, 21(1):108–124, 2007. doi:10.1016/j.ymssp.2005.12.002. (Cited on pages 4, 9, 41, 78, and 200).

[28] D. Mba and B. K. N. Rao. Development of acoustic emission technology for condition monitoring and diagnosis of rotating machines; bearings, pumps, gearboxes, engines and rotating structures. *The Shock and Vibration Digest*, 38(1):3–16, 2006. doi:10.1177/0583102405059054. (Cited on pages 4, 9, 78, and 200).

[29] A. K. S. Jardine, D. Lin, and D. Banjevic. A review on machinery diagnostics and prognostics implementing condition-based maintenance. *Mechanical Systems and Signal Processing*, 20(7):1483–1510, 2006. doi:10.1016/j.ymssp.2005.09.012. (Cited on pages 4, 9, 78, and 200).

[30] R. B. Randall and J. Antoni. Rolling element bearing diagnostics — A tutorial. *Mechanical Systems and Signal Processing*, 25(2):485–520, 2011. doi:10.1016/j.ymssp.2010.07.017. (Cited on pages 4, 9, 31, 32, 47, 62, 78, 132, 138, 154, 170, 174, 181, 182, 186, 200, 222, 224, 233, 245, 262, 272, and 328).

[31] R. B Randall. *Vibration-based condition monitoring*. Industrial, aerospace, and automotive applications. John Wiley & Sons, Ltd, First edition, 2011. (Cited on pages 4, 9, 10, 78, 138, 177, and 200).

[32] S. Iwnicki. *Handbook of Rail Vehicle Dynamics*. CRC Press, Taylor & Francis Group, 2006. (Cited on pages xvii, 4, 5, 6, 7, 8, and 145).

[33] P. J. Remington. Wheel/rail noise — Part I: Characterization of the wheel/rail dynamic system. *Journal of Sound and Vibration*, 46(3):359–379, 1976. doi:10.1016/0022-460X(76)90861-0. (Cited on pages 4, 11, and 32).

[34] M. J. Rudd. Wheel/rail noise — Part II: Wheel squeal. *Journal of Sound and Vibration*, 46(3):381–394, 1976. doi:10.1016/0022-460X(76)90862-2. (Cited on pages 4 and 11).

[35] I. L. Vér, C. S. Ventres, and M. M. Myles. Wheel/rail noise — Part III: Impact noise generation by wheel and rail discontinuities. *Journal of Sound and Vibration*, 46(3):395–417, 1976. doi:10.1016/0022-460X(76)90863-4. (Cited on pages 4 and 11).

[36] P. J. Remington. Wheel/rail noise — Part IV: Rolling noise. *Journal of Sound and Vibration*, 46(3):419–436, 1976. doi:10.1016/0022-460X(76)90864-6. (Cited on pages 4, 11, and 32).

[37] P. J. Remington. Wheel/rail rolling noise: What do we know? what don't we know? where do we go from here? *Journal of Sound and Vibration*, 120(2):203–226, 1988. doi:10.1016/0022-460X(88)90430-0. (Cited on pages 4, 11, and 32).

[38] D. J. Thompson. Wheel–rail noise generation, Part I: Introduction and interaction model. *Journal of Sound and Vibration*, 161(3):383–400, 1993. doi:10.1006/jsvi.1993.1082. (Cited on pages 4, 11, and 32).

[39] D. J. Thompson. Wheel–rail noise generation, Part II: Wheel vibration. *Journal of Sound and Vibration*, 161(3):401–419, 1993. doi:10.1006/jsvi.1993.1083. (Cited on pages 4, 11, and 32).

[40] D. J. Thompson. Wheel–rail noise generation, Part III: Rail vibration. *Journal of Sound and Vibration*, 161(3):421–446, 1993. doi:10.1006/jsvi.1993.1084. (Cited on pages 4, 11, and 32).

[41] D. J. Thompson. Wheel–rail noise generation, Part IV: Contact zone and results. *Journal of Sound and Vibration*, 161(3):447–466, 1993. doi:10.1006/jsvi.1993.1085. (Cited on pages 4, 11, and 32).

[42] D. J. Thompson. Wheel–rail noise generation, Part V: Inclusion of wheel rotation. *Journal of Sound and Vibration*, 161(3):467–482, 1993. doi:10.1006/jsvi.1993.1086. (Cited on pages 4, 11, and 32).

[43] D. J. Thompson, B. Hemsworth, and N. Vincent. Experimental validation of the TWINS prediction program for rolling noise, Part 1: Description of the model and method. *Journal of Sound and Vibration*, 193(1):123–135, 1996. doi:10.1006/jsvi.1996.0252. (Cited on pages 4 and 11).

[44] D. J. Thompson, P. Fodiman, and H. Mahé. Experimental validation of the TWINS prediction program for rolling noise, Part 2: Results. *Journal of Sound and Vibration*, 193(1):137–147, 1996. doi:10.1006/jsvi.1996.0253. (Cited on pages 4 and 11).

[45] D. J. Thompson. On the relationship between wheel and rail surface roughness and rolling noise. *Journal of Sound and Vibration*, 193(1):149–160, 1996. doi:10.1006/jsvi.1996.0254. (Cited on pages 4, 11, and 32).

[46] D. J. Thompson, N. Vincent, and P. E. Gautier. Validation of a model for railway rolling noise using field measurements with sinusoidally profiled wheels. *Journal of Sound and Vibration*, 223(4):587–609, 1999. doi:10.1006/jsvi.1998.2107. (Cited on pages 4 and 11).

[47] D. J. Thompson and C. J. C. Jones. A review of the modelling of wheel/rail noise generation. *Journal of Sound and Vibration*, 231(3):519–536, 2000. doi:10.1006/jsvi.1999.2542. (Cited on pages 4 and 11).

[48] D. J. Thompson and P. J. Remington. The effects of transverse profile on the excitation of wheel/rail noise. *Journal of Sound and Vibration*, 231(3):537–548, 2000. doi:10.1006/jsvi.1999.2543. (Cited on pages 4 and 11).

[49] D. J. Thompson and C. J. C. Jones. Sound radiation from a vibrating railway wheel. *Journal of Sound and Vibration*, 253(2):401–419, 2002. doi:10.1006/jsvi.2001.4061. (Cited on pages 4 and 11).

[50] D. J. Thompson. The influence of the contact zone on the excitation of wheel/rail noise. *Journal of Sound and Vibration*, 267(3):523–535, 2003. doi:10.1016/S0022-460X(03)00712-0. (Cited on pages 4 and 11).

[51] D. Thompson. *Railway Noise and Vibration*. Elsevier, First edition, 2009. (Cited on pages 4, 11, and 32).

[52] FleetONE. (accessed 14 April 2014). Available from: http://www.trackiq.com.au/fleet-one.html. (Cited on page 4).

[53] InteRRIS — The Integrated Railway Remote Information Service. (accessed 14 April 2014). Available from: https://www.interris.com/. (Cited on page 4).

[54] The Timken Company, 1835 Dueber Ave. SW Canton, OH 44706-0932. (accessed 14 April 2014). Available from: `http://www.timken.com/en-us/about/Pages/default.aspx`. (Cited on pages xvii, 6, 22, 23, and 321).

[55] J. E. Bambara, J. L. Frarey, and R. L. Smith. On-line acoustic detection of bearing defects. United States Patent 4790190, December 1988. (Cited on page 9).

[56] J. E. Bambara. Acoustic detection of bearing defects. United States Patent 4843885, July 1989. (Cited on page 9).

[57] J. E. Bambara. Integrity test for acoustic bearing defect detector. United States Patent 5029477, July 1991. (Cited on page 9).

[58] J. E. Bambara. Acoustic bearing defect detector. United States Patent 5150618, September 1992. (Cited on page 9).

[59] B. K. N. Rao. *Handbook of condition monitoring*. Elsevier Science Ltd, 1996. (Cited on pages 9 and 138).

[60] Y. Li, S. Billington, C. Zhang T. Kurfess, S. Danyluk, and S. Liang. Adaptive prognostics for rolling element bearing condition. *Mechanical Systems and Signal Processing*, 13(1):103–113, 1999. `doi:10.1006/mssp.1998.0183`. (Cited on page 9).

[61] Y. Li, S. Billington, C. Zhang, T. Kurfess, S. Danyluk, and S. Liang. Dynamic prognostic prediction of defect propagation on rolling element bearings. *Tribology Transactions*, 42(2):385–392, 1999. `doi:10.1080/10402009908982232`. (Cited on page 9).

[62] Y. Li, T. R. Kurfess, and S. Y. Liang. Stochastic prognostics for rolling element bearings. *Mechanical Systems and Signal Processing*, 14(5):747–762, 2000. `doi:10.1006/mssp.2000.1301`. (Cited on page 9).

[63] B. K. N. Rao, P. S. Pai, and T. N. Nagabhushana. Failure diagnosis and prognosis of rolling element bearings using artificial neural networks: A critical overview. *Journal of Physics: Conference Series*, 364(1):012023, 2012. `doi:10.1088/1742-6596/364/1/012023`. (Cited on page 9).

[64] The Association of American Railroads, 425 Third Street, SW Washington, DC 20024. (accessed 14 April 2014). Available from: `https://www.aar.org/Pages/Home.aspx`. (Cited on page 10).

[65] Manual of Standards and Recommended Practices, Section F, Sensors, Standard S-6000, Acoustic Roller Bearing Detector Level-1 Indications, Adopted: 2008, Revised: 2009. (Cited on page 10).

[66] H. Perret. Elastische Spielschwingungen konstant belasteter Wälzlager. *Werkstatt und Betrieb*, 83(8):354–358, 1950. (Cited on pages 19, 35, and 78).

[67] H. Perret. Die Lagerluft als Bestimmungsgrösse fur die Beanspruchungeines Wälzlagers. *Werkstatt und Betrieb*, 83(4):131–134, 1950. (Cited on pages 19, 35, and 78).

[68] H. Perret. Schwingungen in Wälzlagern bei statisch bestimmter Abstützung. *VDI-Forschungs*, (434):17–28, 1952. (Cited on pages 19, 35, and 78).

[69] H. Perret. Wälzlager als Schwingungserreger. *Werkstattstechnik und Maschinenbau*, 40(1):5–9, 1950. (Cited on pages 19, 35, and 78).

[70] E. Meldau. Die Bewegung der Achse von Wälzlagern bei geringen Drehzahlen. *Werkstatt und Betrieb*, 84(7):308–313, 1951. (Cited on pages 19, 35, and 78).

[71] E. Meldau. *Werkstatt und Betrieb*, 84(4):143, 1951. (Cited on pages 19, 35, and 78).

[72] E. Meldau. *Werkstatt und Betrieb*, 85(2):56, 1952. (Cited on pages 19, 35, and 78).

[73] E. Meldau. *Konstruktion*, 4(3):79, 1952. (Cited on pages 19, 35, and 78).

[74] T. E. Tallian and O. G. Gustafsson. The mechanics of rolling-element bearing vibrations. *Transactions of the American Society of Mechanical Engineers*, Paper No. 58-A-292, 1958. (Cited on pages 19, 35, and 78).

[75] A. Tamura and O. Taniguchi. Ball bearing vibrations: 1st Report, On the radial vibration caused by passing balls. *Transactions of The Japan Society of Mechanical Engineers*, 26(161):19–25, 1960. `doi:10.1299/kikai1938.26.19`. (Cited on pages 19, 35, and 78).

[76] A. Tamura and O. Taniguchi. Ball bearing vibrations: 2nd Report, On the subharmonic vibration of order 1/2 caused by passing balls. *Transactions of The Japan Society of Mechanical Engineers*, 26(167):877–883, 1960. doi:10.1299/kikai1938.26.877. (Cited on pages 19, 35, and 78).

[77] A. Tamura and O. Taniguchi. Ball bearing vibrations: 3rd Report, On the axial vibration caused by passing balls. *Transactions of The Japan Society of Mechanical Engineers*, 26(170):1428–1434, 1960. doi:10.1299/kikai1938.26.1428. (Cited on pages 19, 35, and 78).

[78] A. Tamura and O. Taniguchi. Ball bearing vibrations: 4th Report, On the nonlinear vibrations in axial direction. *Transactions of The Japan Society of Mechanical Engineers*, 27(179):1146–1153, 1961. doi:10.1299/kikai1938.27.1146. (Cited on pages 19, 35, and 78).

[79] A. Tamura and O. Taniguchi. Ball bearing vibrations: 5th Report, On the device to reduce the vibration caused by a ball bearing. *Transactions of The Japan Society of Mechanical Engineers*, 27(182):1505–1509, 1962. doi:10.1299/kikai1938.27.1509. (Cited on pages 19, 35, and 78).

[80] A. Tamura and O. Taniguchi. Ball bearing vibrations: 6th Report, On the vibration of a ball bearing under light load. *Transactions of The Japan Society of Mechanical Engineers*, 28(188):492–499, 1962. doi:10.1299/kikai1938.28.492. (Cited on pages 19, 35, and 78).

[81] H. Tamura and Y. Tsuda. On the spring characteristics of a ball bearing: extreme characteristics with many balls. *Bulletin of The Japan Society of Mechanical Engineers*, 23(180):961–969, 1980. doi:10.1299/jsme1958.23.961. (Cited on pages 19, 35, and 78).

[82] H. Tamura and Y. Tsuda. On the spring characteristics of a ball bearing: fluctuation due to ball revolution. *Bulletin of The Japan Society of Mechanical Engineers*, 23(185):1905–1912, 1980. doi:10.1299/jsme1958.23.1905. (Cited on pages 19, 35, and 78).

[83] H. Tamura, E. H. Gad, T. Kondou, Y. Tsuda, and A. Sueoka. The static running accuracy of ball bearings. *Memoirs of the Faculty of Engineering*, 43(4):285–316, 1983. (Cited on pages 19, 35, and 78).

[84] E. H. Gad, T. Kondou, and H. Tamura. Spring property of ball bearing. *Memoirs of the Faculty of Engineering*, 43(3):243–264, 1983. (Cited on pages 19, 35, and 78).

[85] E. H. Gad, S. Fukata, and H. Tamura. Computer simulation of rotor radial vibrations due to ball bearings. *Memoirs of the Faculty of Engineering*, 44(1):83–111, 1984. (Cited on pages 19, 35, and 78).

[86] E. H. Gad, S. Fukata, and H. Tamura. Computer simulation of rotor axial and radial vibrations based on ball bearings. *Memoirs of the Faculty of Engineering*, 44(2):169–183, 1984. (Cited on pages 19, 35, and 78).

[87] S. Fukata, E. H. Gad, T. Kondou, T. Ayabe, and H. Tamura. On the radial vibration of ball bearings: computer simulation. *Bulletin of The Japan Society of Mechanical Engineers*, 28(239):899–904, 1985. doi:10.1299/jsme1958.28.899. (Cited on pages 19, 35, 36, 40, 44, 45, and 78).

[88] H. Tamura, E. H. Gad, T. Kondou, T. Ayabe, and A. Sueoka. On the static running accuracy of ball bearings. *Bulletin of The Japan Society of Mechanical Engineers*, 28(240):1240–1246, 1985. doi:10.1299/jsme1958.28.1240. (Cited on pages 19, 35, and 78).

[89] S. H. Ghafari, E. M. Rahman, F. Golnaraghi, and F. Ismail. Vibrations of balanced fault-free ball bearings. *Journal of Sound and Vibration*, 329(9):1332–1347, 2010. doi:10.1016/j.jsv.2009.11.003. (Cited on pages 19, 35, and 78).

[90] P. D. McFadden and J. D. Smith. Model for the vibration produced by a single point defect in a rolling element bearing. *Journal of Sound and Vibration*, 96(1):69–82, 1984. doi:10.1016/0022-460X(84)90595-9. (Cited on pages 20, 26, 27, 28, 29, 30, 31, 32, 33, 34, 41, 61, 62, 74, 75, 77, 78, 129, 131, 132, 172, 174, 180, 194, 196, 246, 266, 269, and 286).

[91] P. D. McFadden and J. D. Smith. The vibration produced by multiple point defects in a rolling element bearing. *Journal of Sound and Vibration*, 98(2):263–273, 1985. doi:10.1016/0022-460X(85)90390-6. (Cited on pages 20, 26, 27, 28, 29, 30, 31, 32, 33, 34, 40, 41, 43, 44, 47, 55, 60, 61, 62, 74, 75, 76, 77, 78, 129, 130, 131, 132, 172, 174, 180, 194, 196, 246, 266, 269, and 286).

[92] Y. T. Su and S. J. Lin. On initial fault detection of a tapered roller bearing: Frequency domain analysis. *Journal of Sound and Vibration*, 155(1):75–84, 1992. doi:10.1016/0022-460X(92)90646-F. (Cited on pages 20, 26, 28, 29, 30, 31, 32, 33, 34, 41, 61, 62, 74, 75, 77, 78, 129, 131, 132, 172, 174, 180, 194, 196, 246, 266, 269, and 286).

[93] N. Tandon and A. Choudhury. An analytical model for the prediction of the vibration response of rolling element bearings due to a localized defect. *Journal of Sound and Vibration*, 205(3):275–292, 1997. doi:10.1006/jsvi.1997.1031. (Cited on pages 20, 26, 29, 30, 31, 32, 33, 34, 37, 38, 39, 40, 41, 43, 44, 47, 55, 60, 61, 62, 74, 75, 76, 77, 78, 129, 130, 131, 132, 172, 174, 180, 194, 196, 246, 266, 269, and 286).

[94] D. Brie. Modelling of the spalled rolling element bearing vibration signal: An overview and some new results. *Mechanical Systems and Signal Processing*, 14(3):353–369, 2000. doi:10.1006/mssp.1999.1237. (Cited on pages 20, 26, 30, 32, 33, 34, 61, 62, 74, 77, 78, 129, 131, 132, 172, 174, 180, 194, 196, 246, 266, 269, and 286).

[95] D. Ho and R. B. Randall. Optimisation of bearing diagnostics techniques using simulated and actual bearing fault signals. *Mechanical Systems and Signal Processing*, 14(5):763–788, 2000. doi:10.1006/mssp.2000.1304. (Cited on pages 20, 26, 30, 31, 32, 33, 34, 61, 62, 70, 74, 77, 78, 126, 129, 131, 132, 155, 172, 174, 180, 194, 196, 207, 246, 266, 269, and 286).

[96] R. B. Randall, J. Antoni, and S. Chobsaard. The relationship between spectral correlation and envelope analysis in the diagnostics of bearing faults and other cyclostationary machine signals. *Mechanical Systems and Signal Processing*, 15(5):945–962, 2001. doi:10.1006/mssp.2001.1415. (Cited on pages 20, 26,

30, 31, 32, 33, 34, 35, 38, 40, 43, 44, 61, 62, 70, 74, 77, 78, 129, 131, 132, 137, 155, 172, 174, 180, 194, 196, 207, 246, 264, 266, 269, and 286).

[97] J. Antoni and R. B. Randall. Differential diagnosis of gear and bearing faults. *Journal of Vibration and Acoustics*, 124(2):165–171, 2002. doi:10.1115/1.1456906. (Cited on pages 20, 26, 31, 32, 33, 34, 61, 62, 74, 77, 78, 129, 131, 132, 172, 174, 180, 194, and 196).

[98] J. Antoni and R. B. Randall. A stochastic model for simulation and diagnostics of rolling element bearings with localized faults. *Journal of Vibration and Acoustics*, 125(3):282–289, 2003. doi:10.1115/1.1569940. (Cited on pages 20, 26, 31, 32, 33, 34, 61, 62, 74, 77, 78, 129, 131, 132, 172, 174, 180, 194, and 196).

[99] M. Behzad, A. R. Bastami, and D. Mba. A new model for estimating vibrations generated in the defective rolling element bearings. *Journal of Vibration and Acoustics*, 133(4):041011 (8 pages), 2011. doi:10.1115/1.4003595. (Cited on pages 20, 26, 32, 33, 61, 62, 78, 102, 129, 131, 132, 172, 174, 180, 194, and 196).

[100] N. S. Feng, E. J. Hahn, and R. B. Randall. Using transient analysis software to simulate vibration signals due to rolling element bearing defects. In *Proceedings of the Third Australian Congress on Applied Mechanics*, pages 689–694, Sydney, 2002. (Cited on pages 20, 26, 33, 34, 35, 36, 37, 38, 39, 40, 42, 45, 46, 52, 55, 60, 61, 62, 75, 76, 77, 78, 85, 86, 87, 88, 102, 104, 129, 131, 132, 172, 174, 180, 194, 195, 196, 245, 246, and 262).

[101] J. Sopanen and A. Mikkola. Dynamic model of a deep-groove ball bearing including localized and distributed defects. Part 1: Theory. *Proceedings of the Institution of Mechanical Engineers, Part K: Journal of Multi-body Dynamics*, 217(3):201–211, 2003. doi:10.1243/14644190360713551. (Cited on pages 20, 26, 33, 34, 35, 37, 38, 39, 40, 42, 43, 45, 46, 52, 55, 60, 61, 62, 75, 76, 77, 78, 85, 86, 87, 88, 102, 104, 108, 129, 131, 132, 172, 174, 180, 194, 195, 196, 245, 247, and 262).

[102] J. Sopanen and A. Mikkola. Dynamic model of a deep-groove ball bearing including localized and distributed defects. Part 2: Implementation and results.

Proceedings of the Institution of Mechanical Engineers, Part K: Journal of Multi-body Dynamics, 217(3):213–233, 2003. doi:10.1243/14644190360713560. (Cited on pages 20, 26, 33, 34, 35, 37, 38, 39, 40, 42, 43, 45, 46, 52, 55, 60, 61, 62, 75, 76, 77, 78, 85, 86, 87, 88, 102, 104, 108, 129, 131, 132, 172, 174, 180, 194, 195, 196, 245, 247, and 262).

[103] A. Choudhury and N. Tandon. Vibration response of rolling element bearings in a rotor bearing system to a local defect under radial load. *Journal of Tribology*, 128(2):252–261, 2006. doi:10.1115/1.2164467. (Cited on pages 20, 26, 30, 33, 34, 35, 38, 39, 40, 42, 43, 44, 45, 47, 52, 55, 60, 61, 62, 75, 76, 77, 78, 102, 129, 130, 131, 132, 172, 174, 180, 194, 195, 196, 246, 266, 269, and 286).

[104] S. Sassi, B. Badri, and M. Thomas. A numerical model to predict damaged bearing vibrations. *Journal of Vibration and Control*, 13(11):1603–1628, 2007. doi:10.1177/1077546307080040. (Cited on pages 20, 26, 30, 33, 34, 35, 39, 40, 42, 43, 44, 45, 46, 47, 52, 55, 60, 61, 62, 75, 76, 77, 78, 85, 86, 87, 88, 102, 104, 129, 130, 131, 132, 172, 174, 180, 194, 195, 196, 245, 246, and 262).

[105] N. Sawalhi and R. B. Randall. Simulating gear and bearing interactions in the presence of faults. Part I: The combined gear bearing dynamic model and the simulation of localised bearing faults. *Mechanical Systems and Signal Processing*, 22(8):1924–1951, 2008. doi:10.1016/j.ymssp.2007.12.001. (Cited on pages xviii, 20, 26, 33, 34, 35, 37, 40, 41, 42, 43, 45, 46, 52, 55, 60, 61, 62, 66, 67, 68, 69, 75, 76, 77, 78, 85, 86, 87, 88, 102, 103, 104, 107, 108, 116, 118, 129, 131, 132, 172, 174, 180, 194, 195, 196, 245, 246, 247, 262, and 272).

[106] M. Cao and J. Xiao. A comprehensive dynamic model of double-row spherical roller bearing — Model development and case studies on surface defects, preloads, and radial clearance. *Mechanical Systems and Signal Processing*, 22(2):467–489, 2008. doi:10.1016/j.ymssp.2007.07.007. (Cited on pages 20, 26, 33, 34, 35, 42, 43, 45, 46, 52, 55, 60, 61, 62, 75, 76, 77, 78, 85, 86, 87, 88, 102, 104, 129, 131, 132, 172, 174, 180, 194, 195, 196, 245, 246, and 262).

[107] A. Ashtekar, F. Sadeghi, and L.-E. Stacke. A new approach to modeling surface

defects in bearing dynamics simulations. *Journal of Tribology*, 130(4):041103 (8 pages), 2008. doi:10.1115/1.2959106. (Cited on pages 20, 26, 33, 34, 35, 42, 43, 45, 52, 55, 60, 61, 62, 75, 76, 77, 78, 102, 129, 131, 132, 172, 174, 180, 194, 195, and 196).

[108] H. Arslan and N. Aktürk. An investigation of rolling element vibrations caused by local defects. *Journal of Tribology*, 130(4):041101 (12 pages), 2008. doi:10.1115/1.2958070. (Cited on pages 20, 26, 33, 34, 35, 42, 43, 45, 52, 55, 60, 61, 62, 75, 76, 77, 78, 102, 129, 131, 132, 172, 174, 180, 194, 195, and 196).

[109] A. Rafsanjani, S. Abbasion, A. Farshidianfar, and H. Moeenfard. Nonlinear dynamic modeling of surface defects in rolling element bearing systems. *Journal of Sound and Vibration*, 319(3–5a):1150–1174, 2009. doi:10.1016/j.jsv.2008.06.043. (Cited on pages 20, 26, 30, 33, 34, 35, 42, 43, 44, 45, 46, 47, 52, 55, 60, 61, 62, 75, 76, 77, 78, 85, 86, 87, 88, 102, 104, 129, 130, 131, 132, 172, 174, 180, 194, 195, 196, 245, 246, and 262).

[110] V. N. Patel, N. Tandon, and R. K. Pandey. A dynamic model for vibration studies of deep groove ball bearings considering single and multiple defects in races. *Journal of Tribology*, 132(4):041101 (10 pages), 2010. doi:10.1115/1.4002333. (Cited on pages 20, 26, 30, 33, 34, 35, 43, 44, 45, 46, 47, 52, 55, 60, 61, 62, 75, 76, 77, 78, 85, 86, 87, 88, 102, 104, 129, 130, 131, 132, 172, 174, 180, 194, 195, 196, 245, 246, and 262).

[111] M. S. Patil, J. Mathew, P. K. Rajendrakumar, and S. Desai. A theoretical model to predict the effect of localized defect on vibrations associated with ball bearing. *International Journal of Mechanical Sciences*, 52(9):1193–1201, 2010. doi:10.1016/j.ijmecsci.2010.05.005. (Cited on pages 20, 26, 30, 33, 34, 35, 44, 45, 46, 47, 52, 55, 60, 61, 62, 75, 76, 77, 78, 85, 86, 87, 88, 102, 104, 129, 130, 131, 132, 172, 174, 180, 194, 195, 196, 245, 246, and 262).

[112] M. Nakhaeinejad and M. D. Bryant. Dynamic modeling of rolling element bearings with surface contact defects using bond graphs. *Journal of Tribology*, 133(1):011102 (12 pages), 2011. doi:10.1115/1.4003088. (Cited on pages 20, 26,

33, 34, 35, 44, 45, 46, 52, 55, 60, 61, 62, 75, 76, 77, 78, 85, 86, 87, 88, 102, 104, 129, 132, 194, 195, 245, 246, and 262).

[113] M. Tadina and M. Boltežar. Improved model of a ball bearing for the simulation of vibration signals due to faults during run-up. *Journal of Sound and Vibration*, 330(17):4287–4301, 2011. doi:10.1016/j.jsv.2011.03.031. (Cited on pages 20, 26, 33, 34, 35, 45, 46, 52, 55, 60, 61, 62, 75, 76, 77, 78, 85, 86, 87, 88, 102, 104, 129, 131, 132, 172, 174, 180, 194, 195, 196, 245, 246, and 262).

[114] S. Zhao, L. Liang, G. Xu, J. Wang, and W. Zhang. Quantitative diagnosis of a spall-like fault of a rolling element bearing by empirical mode decomposition and the approximate entropy method. *Mechanical Systems and Signal Processing*, 40(1):154–177, 2013. doi:10.1016/j.ymssp.2013.04.006. (Cited on pages 20, 26, 33, 34, 35, 45, 52, 55, 60, 61, 62, 70, 71, 73, 75, 76, 77, 78, 102, 129, 131, 132, 172, 174, 180, 194, 195, 196, 236, 245, 246, 262, 266, 269, and 286).

[115] Z. Kiral and H. Karagülle. Simulation and analysis of vibration signals generated by rolling element bearing with defects. *Tribology International*, 36(9):667–678, 2003. doi:10.1016/S0301-679X(03)00010-0. (Cited on pages 20, 26, 48, 51, 61, 62, 78, 129, 131, 172, 174, 180, and 196).

[116] Z. Kiral and H. Karagülle. Vibration analysis of rolling element bearings with various defects under the action of an unbalanced force. *Mechanical Systems and Signal Processing*, 20(8):1967–1991, 2006. doi:10.1016/j.ymssp.2005.05.001. (Cited on pages 20, 26, 48, 51, 61, 62, 78, 129, 131, 172, 174, 180, and 196).

[117] Y. Shao, W. Tu, and F. Gu. A simulation study of defects in a rolling element bearing using FEA. In *International Conference on Control, Automation and Systems*, pages 596–599. Gyeonggi-do, Korea, 27–30 October 2010. (Cited on pages 20, 26, 50, 51, 55, 60, 61, 62, 77, 78, 129, 130, 131, 132, 172, 174, 180, 194, 195, 196, and 245).

[118] L. Guochao, P. Wei, L. Yongcai, G. Lixin, and J. Zhang. Simulation and dynamic analysis of outer ring fault on rolling bearings using explicit fi-

nite element method. *China Mechanical Engineering*, 23(23):2825–2829, 2012. doi:j.issn.1004-132X.2012.23.011. (Cited on pages 20, 26, 50, 51, 52, 53, 54, 55, 59, 60, 61, 62, 77, 78, 129, 130, 131, 132, 145, 146, 155, 172, 174, 180, 194, 195, 196, 209, and 245).

[119] J. Liu, Y. Shao, and M. J. Zuo. The effects of the shape of localized defect in ball bearings on the vibration waveform. *Proceedings of the Institution of Mechanical Engineers, Part K: Journal of Multi-body Dynamics*, 227(3):261–274, 2013. doi:10.1177/1464419313486102. (Cited on pages 20, 26, 50, 53, 54, 55, 59, 60, 61, 62, 77, 78, 129, 130, 131, 132, 145, 146, 155, 172, 174, 180, 194, 195, 196, 209, 210, and 245).

[120] A. Utpat. Vibration signature analysis of defective deep groove ball bearings by numerical and experimental approach. *International Journal of Scientific and Engineering Research*, 4(6):592–598, 2013. (Cited on pages 20, 26, 50, 57, 58, 59, 60, 61, 62, 77, 78, 129, 130, 131, 132, 145, 146, 155, 172, 174, 180, 194, 195, 196, 209, 210, and 245).

[121] N. Sawalhi and R. B Randall. Simulating gear and bearing interactions in the presence of faults. Part II: Simulation of the vibrations produced by extended bearing faults. *Mechanical Systems and Signal Processing*, 22(8):1952–1966, 2008. doi:10.1016/j.ymssp.2007.12.002. (Cited on pages 20, 37, 61, 71, 78, 102, and 103).

[122] J. I. McCool and O. G. Gustafsson. Relative axis motion induced by variable elastic compliance in ball bearings. Technical Report L60L023, SKF Industries, Inc., October 1960. U.S. Navy Contract No. NObs-78552. (Cited on pages 20, 36, 61, and 102).

[123] O. G. Gustafsson. Harmonic analysis of the relative axis motion induced by variable elastic compliance in ball bearings. Technical Report AL61L009, SKF Industries, Inc., March 1961. U.S. Navy Contract No. NObs-78552. (Cited on pages 20, 36, 61, and 102).

[124] R. L. Huston. A study of elastic vibrations of the outer race of a rolling element

bearing. Technical Report AL61L027, SKF Industries, Inc., August 1961. U.S. Navy Contract No. NObs-78552. (Cited on pages 20, 36, 61, and 102).

[125] O. G. Gustafsson. Analytical study of the vibration of a bearing with flexurally rigid races. Technical Report AL61L032, SKF Industries, Inc., October 1961. U.S. Navy Contract No. NObs-78552. (Cited on pages 20, 36, 61, and 102).

[126] J. I. McCool. Flexural vibrations of a ball bearing outer ring due to ball loads. Technical Report AL61L037, SKF Industries, Inc., December 1961. U.S. Navy Contract No. NObs-78552. (Cited on pages 20, 36, 61, and 102).

[127] O. G. Gustafsson. Analytical study of the radial, axial and angular vibration of a bearing with flexurally rigid races. Technical Report AL62L005, SKF Industries, Inc., April 1962. U.S. Navy Contract No. NObs-78552. (Cited on pages 20, 36, 61, and 102).

[128] O. G. Gustafsson and T. E. Tallian. Detection of damage in assembled rolling element bearings. *Transactions of the American Society of Lubrication Engineers*, 5(1):197–209, 1962. doi:10.1080/05698196208972466. (Cited on pages 20, 36, 61, 78, and 102).

[129] O. G. Gustafsson and T. E. Tallian. Final report on study of the vibration characteristics of bearings. Technical Report AL69LO23, SKF Industries, Inc, December 1963. U.S. Navy Contract No. NObs-78552. (Cited on pages 20, 36, 42, 61, 78, and 102).

[130] T. E. Tallian and O. G. Gustafsson. Progress in rolling bearing vibration research and control. *Transactions of the American Society of Lubrication Engineers*, 8(3):195–207, 1965. doi:10.1080/05698196508972094. (Cited on pages 20, 36, 61, 78, and 102).

[131] E. Yhland. Waviness measurement — an instrument for quality control in rolling bearing industry. In *Proceedings of the Institution of Mechanical Engineers, Conference Proceedings*, volume 182, pages 438–445, September 1967. doi:10.1243/PIME_CONF_1967_182_341_02. (Cited on pages 20, 36, 61, 78, and 102).

[132] L. E. Lura and R. B. Walker. Bearing noise reduction. *Society of Automotive Engineers*, SAE Technical Paper 720733, 1972. doi:10.4271/720733. (Cited on pages 20, 36, 61, 78, and 102).

[133] C. S. Sunnersjö. *Rolling bearing vibrations — the effects of varying compliance, manufacturing tolerances and wear*. PhD thesis, University of Aston, 1976. (Cited on pages 20, 36, 61, 78, and 102).

[134] C. S. Sunnersjö. Varying compliance vibrations of rolling bearings. *Journal of Sound and Vibration*, 58(3):363–373, 1978. doi:10.1016/S0022-460X(78)80044-3. (Cited on pages 20, 36, 42, 61, 78, and 102).

[135] C. S. Sunnersjö. Rolling bearing vibrations — the effects of geometrical imperfections and wear. *Journal of Sound and Vibration*, 98(4):455–474, 1985. doi:10.1016/0022-460X(85)90256-1. (Cited on pages 20, 36, 61, 78, and 102).

[136] Y.-T. Su, M.-H. Lin, and M.-S. Lee. The effects of surface irregularities on roller bearing vibrations. *Journal of Sound and Vibration*, 165(3):455–466, 1993. doi:10.1006/jsvi.1993.1270. (Cited on pages 20, 36, 61, 78, and 102).

[137] L. D. Meyer, B. Weichbrodt, and F. F. Ahlgren. An analytical model for ball bearing vibrations to predict vibration response to distributed defects. *Journal of Mechanical Design*, 102(2):205–210, 1980. doi:10.1115/1.3254731. (Cited on pages 20, 36, 61, 78, and 102).

[138] F. P. Wardle. Vibration forces produced by waviness of the rolling surfaces of thrust loaded ball bearings, Part 1: Theory. *Proceedings of the Institution of Mechanical Engineers, Part C: Journal of Mechanical Engineering Science*, 202(5):305–312, 1988. doi:10.1243/PIME_PROC_1988_202_127_02. (Cited on pages 20, 36, 38, 61, 78, and 102).

[139] F. P. Wardle. Vibration forces produced by waviness of the rolling surfaces of thrust loaded ball bearings, Part 2: Experimental validation. *Proceedings of the*

Institution of Mechanical Engineers, Part C: Journal of Mechanical Engineering Science, 202(5):313–319, 1988. doi:10.1243/PIME_PROC_1988_202_128_02. (Cited on pages 20, 36, 38, 61, 78, and 102).

[140] E. Yhland. A linear theory of vibrations caused by ball bearings with form errors operating at moderate speed. *Journal of Tribology*, 114(2):348–359, 1992. doi:10.1115/1.2920894. (Cited on pages 20, 36, 61, 78, and 102).

[141] N. Aktürk, M. Uneeb, and R. Gohar. The effect of number of ball and preloads on vibrations associated with ball bearings. *Journal of Tribology*, 119(4):747–753, 1997. doi:10.1115/1.2833880. (Cited on pages 20, 36, 61, 78, and 102).

[142] A. Choudhury and N. Tandon. A theoretical model to predict vibration response of rolling bearings to distributed defects under radial load. *Journal of Vibration and Acoustics*, 120(1):214–220, 1998. doi:10.1115/1.2893808. (Cited on pages 20, 36, 61, 78, and 102).

[143] K. Ono and Y. Okada. Analysis of ball bearing vibrations caused by outer race waviness. *Journal of Vibration and Acoustics*, 120(4):901–908, 1998. doi:10.1115/1.2893918. (Cited on pages 20, 36, 61, 78, and 102).

[144] N. Aktürk. The effect of waviness on vibrations associated with ball bearings. *Journal of Tribology*, 121(4):667–677, 1999. doi:10.1115/1.2834121. (Cited on pages 20, 36, 38, 61, 78, and 102).

[145] N. Tandon and A. Choudhury. A theoretical model to predict the vibration response of rolling bearings in a rotor bearing system to distributed defects under radial load. *Journal of Tribology*, 122(3):609–615, 2000. doi:10.1115/1.555409. (Cited on pages 20, 36, 61, 78, and 102).

[146] M. Tiwari, K. Gupta, and O. Prakash. Effect of radial internal clerance of a ball bearing on the dynamics of a balanced horizontal rotor. *Journal of Sound and Vibration*, 238(5):723–756, 2000. doi:10.1006/jsvi.1999.3109. (Cited on pages 20, 36, 38, 61, 78, and 102).

[147] M. Tiwari, K. Gupta, and O. Prakash. Dynamic response of an unbalanced rotor supported on ball bearings. *Journal of Sound and Vibration*, 238(5):757–779, 2000. doi:10.1006/jsvi.1999.3108. (Cited on pages 20, 36, 38, 61, 78, and 102).

[148] G. Jang and S. W. Jeong. Nonlinear excitation model of ball bearing waviness in a rigid rotor supported by two or more ball bearings considering five degrees of freedom. *Journal of Tribology*, 124(1):82–90, 2001. doi:10.1115/1.1398289. (Cited on pages 20, 36, 38, 61, 78, and 102).

[149] S. P. Harsha, K. Sandeep, and R. Prakash. Non-linear dynamic behaviors of rolling element bearings due to surface waviness. *Journal of Sound and Vibration*, 272(3–5):557–580, 2004. doi:10.1016/S0022-460X(03)00384-5. (Cited on pages 20, 36, 61, 78, and 102).

[150] S. P. Harsha and P. K. Kankar. Stability analysis of rotor bearing system due to surface waviness and number of balls. *International Journal of Mechanical Sciences*, 46(7):1057–1081, 2004. doi:10.1016/j.ijmecsci.2004.07.007. (Cited on pages 20, 36, 61, 78, and 102).

[151] S. P. Harsha. The effect of ball size variations on nonlinear vibration associated with ball bearings. *Proceedings of the Institution of Mechanical Engineers, Part K: Journal of Multi-body Dynamics*, 218(4):191–200, 2004. doi:10.1243/1464419043541455. (Cited on pages 20, 36, 61, 78, and 102).

[152] G. Jang and S. W. Jeong. Vibration analysis of a rotating system due to the effect of ball bearing waviness. *Journal of Sound and Vibration*, 269(3–5):709–726, 2004. doi:10.1016/S0022-460X(03)00127-5. (Cited on pages 20, 36, 61, 78, and 102).

[153] B. Changqing and X. Qingyu. Dynamic model of ball bearings with internal clearance and waviness. *Journal of Sound and Vibration*, 294(1–2):23–48, 2006. doi:10.1016/j.jsv.2005.10.005. (Cited on pages 20, 36, 61, 78, and 102).

[154] S. P. Harsha, C. Nataraj, and P. K. Kankar. The effect of ball waviness on non-

linear vibration associated with rolling element bearings. *International Journal of Acoustics and Vibration*, 11(2):56–66, 2006. (Cited on pages 20, 36, 61, 78, and 102).

[155] S. P. Harsha. Nonlinear dynamic analysis of rolling element bearings due to cage run-out and number of balls. *Journal of Sound and Vibration*, 289(1–2):360–381, 2006. doi:10.1016/j.jsv.2005.02.021. (Cited on pages 20, 36, 61, 78, and 102).

[156] S. P. Harsha. Rolling bearing vibrations — the effect of surface waviness and radial internal clearance. *International Journal of Computational Methods in Engineering Science and Mechanics*, 7(2):91–111, 2006. doi:10.1080/155022891010015. (Cited on pages 20, 36, 61, 78, and 102).

[157] S. H. Upadhyay, S. C. Jain, and S. P. Harsha. Non-linear vibration signature analysis of high-speed rotating shaft due to ball size variations and varying number of balls. *Proceedings of the Institution of Mechanical Engineers, Part K: Journal of Multi-body Dynamics*, 223(2):83–105, 2009. doi:10.1243/14644193JMBD187. (Cited on pages 20, 36, 61, 78, and 102).

[158] S. H. Upadhyay, S. P. Harsha, and S. C. Jain. Vibration signature analysis of high speed unbalanced rotors supported by rolling element bearings due to off-sized rolling elements. *International Journal of Acoustics and Vibration*, 14(3):163–171, 2009. (Cited on pages 20, 36, 61, 78, and 102).

[159] C. K. Babu, N. Tandon, and R. K. Pandey. Vibration modeling of a rigid rotor supported on the lubricated angular contact ball bearings considering six degrees of freedom and waviness on balls and races. *Journal of Vibration and Acoustics*, 134(1):011006 (12 pages), 2012. doi:10.1115/1.4005140. (Cited on pages 20, 36, 61, 78, and 102).

[160] P. K. Kankar, S. C. Sharma, and S. P. Harsha. Nonlinear vibration signature analysis of a high speed rotor bearing system due to race imperfection. *Journal of Computational and Nonlinear Dynamics*, 7(1):011014 (16 pages), 2011. doi:10.1115/1.4004962. (Cited on pages 20, 36, 61, 78, and 102).

[161] I. K. Epps. *An investigation into vibrations excited by discrete faults in rolling element bearings*. PhD thesis, School of Mechanical Engineering, The University of Canterbury, Christchurch, New Zealand, 1991. (Cited on pages xviii, 20, 41, 46, 63, 64, 65, 66, 68, 69, 78, 86, 103, 123, 131, 174, 196, 246, and 266).

[162] I. K. Epps and H. McCallion. An investigation into the characteristics of vibration excited by discrete faults in rolling element bearings. In *Fourth Annual Vibration Association of New Zealand Conference*, Christchurch, New Zealand, 1993. (Cited on pages xviii, 20, 41, 46, 63, 64, 65, 66, 68, 69, 78, 86, 103, 123, 131, 174, 196, 246, and 266).

[163] P. Berret and J. M. Laskey. Small portable analyzer diagnostic equipment (spade) program — diagnostic software validation. Technical report, RCA Automated Systems Division, Burlington, MA., United States. Army Aviation Systems Command, July 1984. (Cited on pages xviii, 20, 65, 66, 246, and 266).

[164] M. J. Dowling. Application of non-stationary analysis to machinery monitoring. In *Proceedings of IEEE International Conference on Acoustics, Speech, and Signal Processing*, volume 1, pages 59–62, April 1993. doi:10.1109/ICASSP.1993.319054. (Cited on pages xviii, 20, 41, 64, 65, 66, 68, 69, 246, and 266).

[165] N. Sawalhi and R. B. Randall. Vibration response of spalled rolling element bearings: Observations, simulations and signal processing techniques to track the spall size. *Mechanical Systems and Signal Processing*, 25(3):846–870, 2011. doi:10.1016/j.ymssp.2010.09.009. (Cited on pages 20, 41, 46, 66, 68, 69, 70, 71, 72, 73, 78, 86, 103, 123, 131, 174, 196, 236, 246, 266, 269, 272, 286, 287, and 290).

[166] *ASM Handbook Volume 19: Fatigue and Fracture*, volume 19 of *ASM Handbook*. ASM International, 1996. (Cited on page 20).

[167] F. Ellyin. *Fatigue Damage, Crack Growth and Life Prediction*. Springer, 1997. (Cited on pages 20 and 24).

[168] S. Suresh. *Fatigue of materials*. Cambridge University Press, Cambridge, UK, 1998. (Cited on pages 20 and 24).

[169] W. E. Littmann and R. L. Widner. Propagation of contact fatigue from surface and subsurface origins. *Journal of Basic Engineering*, 88(3):624–636, 1966. doi:10.1115/1.3645922. (Cited on pages 20, 21, 60, and 78).

[170] W. E. Littmann. The mechanism of contact fatigue. In P. M. Ku, editor, *Interdisciplinary approach to the lubrication of concentrated contacts*, number NASA SP-237, pages 309–378. National Aeronautics and Space Administration, Washington, DC, 1970. (Cited on pages 20, 21, 60, and 78).

[171] T. E. Tallian. *Failure Atlas for Hertz Contact Machine Elements*. ASME Press, New York, 1992. (Cited on pages 20, 21, 60, and 78).

[172] A. V. Olver. The mechanism of rolling contact fatigue: An update. *Proceedings of the Institution of Mechanical Engineers, Part J: Journal of Engineering Tribology*, 219(5):313–330, 2005. doi:10.1243/135065005X9808. (Cited on pages 20, 21, 60, and 78).

[173] J. Halme and P. Andersson. Rolling contact fatigue and wear fundamentals for rolling bearing diagnostics — state of the art. *Proceedings of the Institution of Mechanical Engineers, Part J: Journal of Engineering Tribology*, 224(4):377–393, 2009. doi:10.1243/13506501JET656. (Cited on pages 20, 21, 25, 35, 37, and 60).

[174] F. Sadeghi, N. K. Arakere, B. Jalalahmadi, T. S. Slack, and N. Raje. A review of rolling contact fatigue. *Journal of Tribology*, 131(4):041403 (15 pages), 2009. doi:10.1115/1.3209132. (Cited on pages 20, 21, 24, 25, 60, and 78).

[175] H. Hertz. Über die Berührung fester elastischer Körper (on the contact of elastic solids). Reprinted in English *Miscellaneous Papers by H. Hertz*, Eds. Jones and Schott, London: Macmillan, 1896. [90, 243]. *Journal of Reine and Angewandte Mathematik*, 92:156–171, 1882. (Cited on pages 21, 27, 32, 34, 37, 42, 43, 46, 50, 88, 89, 104, 109, 142, and 338).

[176] H. Hertz. Über die Berührung fester elastischer Körper and über die Harte(on the contact of rigid elastic solids and on hardness). Reprinted in English *Miscellaneous Papers by H. Hertz*, Eds. Jones and Schott, London: Macmillan, 1896.

[90, 156]. *Verhandlungen des Vereins zur Beförderung des Gewerbefleisses*, 1882. (Cited on pages 21, 27, 32, 34, 37, 42, 43, 46, 50, 88, 89, 104, 109, 142, and 338).

[177] K. L. Johnson. *Contact Mechanics*. Press Syndicate of the University of Cambridge, First edition, 1985. (Cited on pages 21, 27, 32, 34, 37, 42, 43, 46, 50, 88, 89, 91, 102, 104, 107, 109, 142, 160, 249, 252, 254, 338, and 339).

[178] A. Palmgren. Die lebensdauer von kugellagern (the service life of ball bearings). *Zeitschrift des Vereines Deutscher Ingenieure*, 68(14):339–341, April 1924. NASA Technical Translation (NASA TT F-13460). (Cited on pages 21 and 24).

[179] A. Palmgren. *Ball and roller bearing engineering*. SKF Industries, Philadelphia, PA, 1945. (Cited on page 21).

[180] J. A. Martin, S. F. Borgese, and A. D. Eberhardt. Microstructural alterations of rolling-bearing steel undergoing cyclic stressing. *Journal of Basic Engineering*, 88(3):555–565, 1966. doi:10.1115/1.3645902. (Cited on pages 21 and 78).

[181] E. N. Bamberger. Effect of materials — metallurgy viewpoint. In P. M. Ku, editor, *Interdisciplinary approach to the lubrication of concentrated contacts*, Troy, NY, July 1969. National Aeronautics and Space Administration, Washington DC. NASA Special Report, SP-237, pages 409–438. (Cited on pages 21 and 78).

[182] H. Swahn, P. C. Becker, and O. Vingsbo. Martensite decay during rolling contact fatigue in ball bearings. *Metallurgical Transactions A*, 7(8):1099–1110, 1976. doi:10.1007/BF02656592. (Cited on pages 21 and 78).

[183] A. P. Voskamp, R. Österlund, P. C. Becker, and O. Vingsbo. Gradual changes in residual stress and microstructure during contact fatigue in ball bearings. *Journal of Metals Technology*, 7:14–21, 1980. doi:10.1179/030716980803286676. (Cited on pages 21 and 78).

[184] R. Österlund and O. Vingsbo. Phase changes in fatigued ball bearings. *Metallurgical Transactions A*, 11(5):701–707, 1980. doi:10.1007/BF02661199. (Cited on pages 21 and 78).

[185] P. C. Becker. Microstructural changes around non-metallic inclusions caused by rolling-contact fatigue of ball bearing steels. *Metals Technology*, 8(10):234–243, 1981. doi:10.1179/030716981803275415. (Cited on pages 21 and 78).

[186] A. P. Voskamp. Material response to rolling contact loading. *Journal of Tribology*, 107(3):359–364, 1985. doi:10.1115/1.3261078. (Cited on pages 21 and 78).

[187] A. P. Voskamp and E. J. Mittemeijer. Crystallographic preferred orientation induced by cyclic rolling contact loading. *Metallurgical and Materials Transactions A*, 27(11):3445–3465, 1996. doi:10.1007/BF02595437. (Cited on pages 21 and 78).

[188] A. P. Voskamp and E. J. Mittemeijer. The effect of the changing microstructure on the fatigue behavior during cyclic rolling contact loading. *Zeitschrift für Metallkunde*, 88(4):310–319, 1997. (Cited on pages 21 and 78).

[189] A. P. Voskamp. Fatigue and material response in rolling contact. In Joseph J. C. Hoo and Willard B. Green, editors, *Bearing Steels: Into the 21st Century*, number ASTM STP 1327, pages 152–166. American Society of Testing and Materials, West Conshohocken, PA 19428-2959, 1998. (Cited on pages 21 and 78).

[190] A. P. Voskamp. Microstructural stability and bearing performance. In John M. Beswick, editor, *Bearing Steel Technology*, number ASTM STP 1419, pages 443–456. American Society of Testing and Materials, West Conshohocken, PA 19428-2959, 2002. (Cited on pages 21 and 78).

[191] T. E. Tallian. On competing failure modes in rolling contact. *Transactions of the American Society of Lubrication Engineers*, 10(4):418–439, 1967. doi:10.1080/05698196708972201. (Cited on page 22).

[192] ISO 15243 — Rolling bearings — Damage and failures — Terms, characteristics and causes, 2004. International Organization for Standardization. (Cited on page 22).

[193] R. Stribeck. Reports from the central laboratory for scientific technical investiga-

tion. *Transactions of the American Society of Mechanical Engineers*, 29:420–466, 1907. Translation by H. Hess, 1900. (Cited on pages 24 and 78).

[194] G. Lundberg and A. Palmgren. Dynamic capacity of rolling bearings. *Acta Politechnica Mechanical Engineering Series*, 1(3):1–52, 1947. Royal Swedish Academy of Engineering Sciences. (Cited on pages 24, 25, and 78).

[195] G. Lundberg and A. Palmgren. Dynamic capacity of roller bearings. *Acta Politechnica Mechanical Engineering Series*, 2(4):96–127, 1952. Royal Swedish Academy of Engineering Sciences. (Cited on pages 24, 25, and 78).

[196] Y. P. Chiu, T. E. Tallian, J. I. McCool, and J. A. Martin. A mathematical model of spalling fatigue failure in rolling contact. *Transactions of the American Society of Lubrication Engineers*, 12(2):106–116, 1969. doi:10.1080/05698196908972252. (Cited on pages 24 and 78).

[197] Y. P. Chiu, T. E. Tallian, and J. I. McCool. An engineering model of spalling fatigue failure in rolling contact: I. The subsurface model. *Wear*, 17(5–6):433–446, 1971. doi:10.1016/0043-1648(71)90049-4. (Cited on pages 24 and 78).

[198] T. E. Tallian and J. I. McCool. An engineering model of spalling fatigue failure in rolling contact: II. The surface model. *Wear*, 17(5–6):447–461, 1971. doi:10.1016/0043-1648(71)90050-0. (Cited on pages 24 and 78).

[199] T. E. Tallian. An engineering model of spalling fatigue failure in rolling contact: III. Engineering discussion and illustrative examples. *Wear*, 17(5–6):463–480, 1971. doi:10.1016/0043-1648(71)90051-2. (Cited on pages 24 and 78).

[200] T. E. Tallian. Prediction of rolling contact fatigue life in contaminated lubricant: Part I — Mathematical Model. *Journal of Lubrication Technology*, 98(2):251–257, 1976. doi:10.1115/1.3452814. (Cited on pages 24 and 78).

[201] T. E. Tallian. Prediction of rolling contact fatigue life in contaminated lubricant: Part II — Experimental. *Journal of Lubrication Technology*, 98(3):384–392, 1976. doi:10.1115/1.3452865. (Cited on pages 24 and 78).

[202] T. E. Tallian. A unified model for rolling contact life prediction. *Journal of Lubrication Technology*, 104(3):336–346, 1982. doi:10.1115/1.3253216. (Cited on pages 24 and 78).

[203] R. R. Miller, L. M. Keer, and H. S. Cheng. On the mechanics of fatigue crack growth due to contact loading. *Proceedings of the Royal Society of London. Series A, Mathematical and Physical Sciences*, 397(1813):197–209, 1985. doi:10.1098/rspa.1985.0011. (Cited on pages 24 and 78).

[204] E. Ioannides and T. A. Harris. A new fatigue model for rolling bearings. *Journal of Tribology*, 107(3):367–377, 1985. doi:10.1115/1.3261081. (Cited on pages 24 and 78).

[205] H. Schlicht, E. Schreiber, and O. Zwirlein. Fatigue and failure mechanism of bearings. In *International Conference on Fatigue of Engineering Materials and Structures*, volume 1 of *Proceedings of the Institution of Mechanical Engineers*, pages 85–90, University of Sheffield, September 1986. Institution of Mechanical Engineers. (Cited on pages 24 and 78).

[206] T. E. Tallian. Unified rolling contact life model with fatigue limit. *Wear*, 107(1):13–36, 1986. doi:10.1016/0043-1648(86)90044-X. (Cited on pages 24 and 78).

[207] T. E. Tallian. Rolling bearing life prediction. Correction for material and operating conditions. Part I: General model and basic life. *Journal of Lubrication Technology*, 110(1):2–6, 1988. doi:10.1115/1.3261570. (Cited on pages 24 and 78).

[208] T. E. Tallian. Rolling bearing life prediction. Correction for material and operating conditions. Part II: The correction factors. *Journal of Lubrication Technology*, 110(1):7–12, 1988. doi:10.1115/1.3261579. (Cited on pages 24 and 78).

[209] X. Leng, Q. Cheng, and E. Shao. Initiation and propagation of case crushing cracks in rolling contact fatigue. *Wear*, 122(1):33–43, 1988. doi:10.1016/0043-1648(88)90004-X. (Cited on pages 24 and 78).

[210] ISO 281 — Rolling bearings — Dynamic load ratings and rating life, 1989. International Organization for Standardization. (Cited on pages 24, 25, and 78).

[211] T. E. Tallian. Simplified contact fatigue life prediction model — Part I: Review of published models. *Journal of Tribology*, 114(2):207–213, 1992. doi:10.1115/1.2920875. (Cited on pages 24, 25, and 78).

[212] T. E. Tallian. Simplified contact fatigue life prediction model — Part II: New model. *Journal of Tribology*, 114(2):214–220, 1992. doi:10.1115/1.2920876. (Cited on pages 24 and 78).

[213] J. Chalsma and E. V. Zaretsky. Design for life, plan for death. *Machine Design*, 66(15):55–59, 1994. (Cited on pages 24 and 78).

[214] T. A. Harris and J. I. McCool. On the accuracy of rolling bearing fatigue life prediction. *Journal of Tribology*, 118(2):297–309, 1996. doi:10.1115/1.2831299. (Cited on pages 24 and 78).

[215] E. Ioannides, G. Bergling, and A. Gabelli. An analytical formulation for the life of rolling bearings. *Acta Polytechnica Scandinavica, Mechanical Engineering Series*, 137:77, 1999. Finnish Academy of Technology, Espoo. (Cited on pages 24 and 78).

[216] M. N. Kotzalas and T. A. Harris. Fatigue failure progression in ball bearings. *Journal of Tribology*, 123(2):238–242, 2001. doi:10.1115/1.1308013. (Cited on pages 24 and 78).

[217] I. I. Kudish and K. W. Burris. Modern state of experimentation and modeling in contact fatigue phenomenon: Part II — Analysis of existing statistical mathematical models of bearing and gear fatigue life. New statistical model of contact fatigue. *Tribology Transactions*, 43(2):293–301, 2000. doi:10.1080/10402000008982343. (Cited on pages 24, 25, and 78).

[218] S. Shimizu. Fatigue limit concept and life prediction model for rolling

contact machine elements. *Tribology Transactions*, 45(1):39–46, 2002. doi:10.1080/10402000208982519. (Cited on pages 24 and 78).

[219] M. N. Kotzalas. Statistical distribution of tapered roller bearing fatigue lives at high levels of reliability. *Journal of Tribology*, 127(4):865–870, 2005. doi:10.1115/1.2000981. (Cited on pages 24 and 78).

[220] L. M. Keer and M. D. Bryant. A pitting model for rolling contact fatigue. *Journal of Lubrication Technology*, 105(2):198–205, 1983. doi:10.1115/1.3254565. (Cited on pages 24 and 78).

[221] R. S. Zhou, H. S. Cheng, and T. Mura. Micropitting in rolling and sliding contact under mixed lubrication. *Journal of Tribology*, 111(4):605–613, 1989. doi:10.1115/1.3261984. (Cited on pages 24 and 78).

[222] V. Bhargava, G. T. Hahn, and C. A. Rubin. Rolling contact deformation, etching effects and failure of high strength steels. *Metallurgical Transactions A*, 21(7):1921–1931, 1990. doi:10.1007/BF02647240. (Cited on pages 24 and 78).

[223] W. Cheng, H. S. Cheng, T. Mura, and L. M. Keer. Micromechanics modeling of crack initiation under contact fatigue. *Journal of Tribology*, 116(1):2–8, 1994. doi:10.1115/1.2927042. (Cited on pages 24 and 78).

[224] A. Melander. A finite element study of short cracks with different inclusion types under rolling contact fatigue load. *International Journal of Fatigue*, 19(1):13–24, 1997. doi:10.1016/S0142-1123(96)00045-X. (Cited on pages 24 and 78).

[225] A. Vincent, G. Lormand, P. Lamagnere, L. Gosset, D. Girodin, G. Dudragne, and R. Fougeres. From white etching areas formed around inclusions to crack nucleation in bearing steels under rolling contacts. In Joseph J. C. Hoo and Willard B. Green, editors, *Bearing Steels: Into the 21st century*, number ASTM STP 1327, pages 109–123. American Society of Testing and Materials, West Conshohocken, PA 19428-2959, 1998. (Cited on pages 24 and 78).

[226] T. A. Harris and W. K. Yu. Lundberg–Palmgren fatigue theory: considerations of failure stress and stressed volume. *Journal of Tribology*, 121(1):85–89, 1999. doi:10.1115/1.2833815. (Cited on pages 24 and 78).

[227] J. W. Ringsberg. Life prediction of rolling contact fatigue crack initiation. *International Journal of Fatigue*, 23(7):575–586, 2001. doi:10.1016/S0142-1123(01)00024-X. (Cited on pages 24 and 78).

[228] N. Raje, F. Sadeghi, and R. G. Rateick. A statistical damage mechanics model for subsurface initiated spalling in rolling contacts. *Journal of Tribology*, 130(4):042201 (11 pages), 2008. doi:10.1115/1.2959109. (Cited on pages 24 and 78).

[229] N. Raje, F. Sadeghi, R. G. Rateick, and M. R. Hoeprich. A numerical model for life scatter in rolling element bearings. *Journal of Tribology*, 130(1):011011 (10 pages), 2007. doi:10.1115/1.2806163. (Cited on pages 24 and 78).

[230] N. Raje and F. Sadeghi. Statistical numerical modelling of sub-surface initiated spalling in bearing contacts. *Proceedings of the Institution of Mechanical Engineers, Part J: Journal of Engineering Tribology*, 223(6):849–858, 2009. doi:10.1243/13506501JET481. (Cited on pages 24 and 78).

[231] T. S. Slack and F. Sadeghi. Explicit finite element modeling of subsurface initiated spalling in rolling contacts. *Tribology International*, 43(9):1693–1702, 2010. doi:10.1016/j.triboint.2010.03.019. (Cited on pages 24 and 78).

[232] W. Weibull. A statistical theory of strength of materials. *Ingeniörsvetenskapsakademien handlingar, Proceedings of the Royal Swedish Institute for Engineering and Research*, (151), 1939. (Cited on page 24).

[233] W. Weibull. A statistical representation of fatigue failure in solids. *Acta Politechnica Mechanical Engineering Series*, 1(9, 49), 1949. Royal Swedish Academy of Engineering Sciences. (Cited on page 24).

[234] T. E. Tallian. Weibull distribution of rolling contact fatigue life and deviations therefrom. *Transactions of the American Society of Lubrication Engineers*, 5(1):183–196, 1962. doi:10.1080/05698196208972465. (Cited on page 24).

[235] D. Dowson and G. R. Higginson. A numerical solution to the elasto-hydrodynamic problem. *Journal of Mechanical Engineering Science*, 1(1):6–15, 1959. (Cited on pages 25, 35, and 37).

[236] D. Dowson and G. R. Higginson. *Elasto-hydrodynamic lubrication: the fundamentals of roller and gear lubrication*. Pergamon Press, 1966. (Cited on pages 25, 35, and 37).

[237] B. J. Hamrock and W. J. Anderson. Rolling element bearings. Technical Report NASA RP-1105, National Aeronautics and Space Administration, Lewis Research Center, Cleveland, Ohio 44135-3191, June 1983. (Cited on pages 25, 35, and 37).

[238] D. Dowson. Elastohydrodynamic and micro-elastohydrodynamic lubrication. *Wear*, 190(2):125–138, 1995. doi:10.1016/0043-1648(95)06660-8. (Cited on pages 25, 35, and 37).

[239] D. Dowson. *History of Tribology*. Longman, New York, Second edition, 1999. (Cited on pages 25, 35, and 37).

[240] Y. H. Wijnant, J. A. Wensing, and G. C. Nijen. The influence of lubrication on the dynamic behaviour of ball bearings. *Journal of Sound and Vibration*, 222(4):579–596, 1999. doi:10.1006/jsvi.1998.2068. (Cited on pages 25, 35, and 37).

[241] H. A. Spikes and A. V. Olver. Basics of mixed lubrication. *Lubrication Science*, 16(1):3–28, 2003. doi:10.1002/ls.3010160102. (Cited on pages 25, 35, and 37).

[242] American National Standards Institute. American National Standard (ANSI / ABMA) Standard 9-1990 — Load rating and fatigue life for ball bearings, July 1990. (Cited on page 25).

[243] American National Standards Institute. American National Standard (ANSI / ABMA) Standard 11-1990 — Load rating and fatigue life for roller bearings, July 1990. (Cited on page 25).

[244] E. V. Zaretsky. A. Palmgren revisited — a basis for bearing life prediction. Technical Report E-10555, National Aeronautics and Space Administration, Lewis Research Center, Cleveland, Ohio 44135-3191, April 1997. (Cited on page 25).

[245] R. Stribeck. Ball bearings for various loads. *Transactions of the American Society of Mechanical Engineers*, 29:420–463, 1907. (Cited on pages 27, 54, 64, 74, 85, 92, 96, and 246).

[246] H. Sjoväll. The load distribution within ball and roller bearings under given external radial and axial load. *Teknisk Tidskrift, Mekanik*, 9:97–102, 1933. (Cited on pages 27, 54, 64, 74, 85, 92, and 246).

[247] A. B. Jones. *Analysis of stresses and deflections*. New Departure Division, General Motors Corporation, 1946. (Cited on pages 27, 54, 64, 74, 85, 92, and 246).

[248] A. B. Jones. A general theory for elastically constrained ball and radial roller bearings under arbitrary load and speed conditions. *Journal of Basic Engineering*, 82(2):309–320, 1960. doi:10.1115/1.3662587. (Cited on pages 27, 54, 64, 74, 85, 92, and 246).

[249] M. J. Lighthill. *An Introduction to Fourier Analysis and Generalised Functions*. Cambridge University Press, 1958. (Cited on pages 27 and 41).

[250] R. N. Bracewell. *The Fourier Transform and Its Applications*. McGraw-Hill Education, Third edition, 2000. (Cited on pages 27 and 52).

[251] M. S. Darlow, R. H. Badgley, and G. W. Hogg. Application of high frequency resonance techniques for bearing diagnostics in helicopter gearboxes. Technical report, US Army Air Mobility Research and Development Laboratory, 1974. (Cited on pages 28, 37, 45, 47, 48, 55, 76, 132, 138, 154, 170, 181, 186, 222, 224, 245, and 272).

[252] P. D. McFadden and J. D. Smith. The vibration monitoring of rolling element bearings by the high-frequency resonance technique — a review. *Tribology International*, 17(1):3–10, 1984. doi:10.1016/0301-679X(84)90076-8. (Cited on pages 28, 37, 45, 47, 48, 55, 76, 132, 138, 154, 170, 181, 186, 222, 224, 245, and 272).

[253] N. Tandon and B. C. Nakra. Detection of defects in rolling element bearings by vibration monitoring. *Journal of the Institution of Engineers (India)—Mechanical Engineering Division*, 73:271–282, 1993. (Cited on pages 30 and 181).

[254] D. Ho. *Bearing Diagnostics and Self-adaptive Noise Cancellation*. PhD thesis, School of Mechanical and Manufacturing Engineering, The University of New South Wales, Sydney NSW 2052, Australia, 1999. (Cited on page 31).

[255] W.A. Gardner. *Cyclostationarity in communications and signal processing*. IEEE Press, 1994. (Cited on pages 31 and 61).

[256] A. C. McCormick and A. K. Nandi. Cyclostationarity in rotating machine vibrations. *Mechanical Systems and Signal Processing*, 12(2):225–242, 1998. doi:10.1006/mssp.1997.0148. (Cited on pages 31 and 61).

[257] J. Antoni. Cyclic spectral analysis in practice. *Mechanical Systems and Signal Processing*, 21(2):597–630, 2007. doi:10.1016/j.ymssp.2006.08.007. (Cited on pages 31, 32, and 62).

[258] J. Antoni. Cyclic spectral analysis of rolling-element bearing signals: Facts and fictions. *Journal of Sound and Vibration*, 304(3–5):497–529, 2007. doi:10.1016/j.jsv.2007.02.029. (Cited on pages 31, 32, and 62).

[259] J. Antoni. Cyclostationarity by examples. *Mechanical Systems and Signal Processing*, 23(4):987–1036, 2009. doi:10.1016/j.ymssp.2008.10.010. (Cited on pages 31 and 61).

[260] J. A. Greenwood and J. B. P. Williamson. Contact of nominally flat surfaces. *Proceedings of the Royal Society of London. Series A, Mathematical, Physical and*

Engineering Sciences, 295(1442):300–319, 1966. doi:10.1098/rspa.1966.0242. (Cited on page 32).

[261] J. A. Greenwood and J. H. Tripp. The elastic contact of rough spheres. *Journal of Applied Mechanics*, 34(1):153–159, 1967. doi:10.1115/1.3607616. (Cited on pages 32 and 102).

[262] J. A. Greenwood. The area of contact between rough surfaces and flat. *Journal of Lubrication Technology*, 89(1):81–87, 1967. doi:10.1115/1.3616906. (Cited on pages 32 and 102).

[263] C. C. Lo. Elastic contact of rough cylinders. *International Journal of Mechanical Science*, 11(1):105–115, 1969. doi:10.1016/0020-7403(69)90083-6. (Cited on pages 32 and 102).

[264] J. A. Greenwood and J. H. Tripp. The contact of two nominally flat rough surfaces. *Proceedings of the Institution of Mechanical Engineers*, 185(1):625–633, 1970. doi:10.1243/PIME_PROC_1970_185_069_02. (Cited on page 32).

[265] K. L. Johnson, J. A. Greenwood, and S. Y. Poon. A simple theory of asperity contact in elastohydrodynamic lubrication. *Wear*, 19(1):91–108, 1972. doi:10.1016/0043-1648(72)90445-0. (Cited on pages 32 and 102).

[266] R. A. Onions and J. F. Archard. The contact of surfaces having a random structure. *Journal of Physics D: Applied Physics*, 6(3):289–304, 1973. doi:10.1088/0022-3727/6/3/302. (Cited on pages 32 and 102).

[267] A. W. Bush and R. D. Gibson. The elastic contact of a rough surface. *Wear*, 35(1):87–111, 1975. doi:10.1016/0043-1648(75)90145-3. (Cited on pages 32 and 102).

[268] J. I. McCool. Comparison of models for the contact of rough surfaces. *Wear*, 107(1):37–60, 1986. doi:10.1016/0043-1648(86)90045-1. (Cited on pages 32 and 102).

[269] J. I. McCool. Relating profile instrument measurement to the function performance of rough surfaces. *Journal of Tribology*, 109(2):264–270, 1987. doi:10.1115/1.3261349. (Cited on pages 32 and 102).

[270] M. L. Munjal and M. Heckl. Some mechanisms of excitation of a railway wheel. *Journal of Sound and Vibration*, 81(4):477–489, 1982. doi:10.1016/0022-460X(82)90291-7. (Cited on pages 32 and 102).

[271] R. S. Sayles and S. Y. Poon. Surface topography and rolling element vibration. *Journal of Precision Engineering*, 3(3):137–144, 1981. doi:10.1016/0141-6359(81)90004-0. (Cited on pages 32 and 102).

[272] S. Y. Poon and F. P. Wardle. Rolling bearing noise — cause and cure, July/August 1983. (Cited on page 32).

[273] J. S. Bendat and A. G. Piersol. *Random Data: Analysis and Measurement Procedures*. Wiley Series in Probability and Statistics. Wiley, Fourth edition, January 2010. (Cited on pages 32 and 102).

[274] SKF, Svenska Kullagerfabriken AB, Gothenburg, Sweden. Available from: http://www.skf.com/. (Cited on page 36).

[275] A. Liew, N. S. Feng, and E. J. Hahn. Transient rotordynamic modeling of rolling element bearing systems. *Journal of Engineering for Gas Turbines and Power*, 124(4):984–991, 2002. doi:10.1115/1.1479337. (Cited on page 37).

[276] J. D. Lambert. *Numerical Methods for Ordinary Differential Systems: The Initial Value Problem*. John Wiley & Sons, September 2000. (Cited on page 37).

[277] Adams. Release 2008 r1, MSC Software Corporation. Available from: http://www.mscsoftware.com/product/adams. (Cited on page 37).

[278] M. F. While. Vibration transmission characteristics of bearings related to machinery condition monitoring. Technical Report 96, Institute of Sound and Vibration Research, University of Southampton, UK, 1977. (Cited on pages 38 and 43).

[279] M. F. While. Rolling element bearing vibration transfer characteristics: Effect of stiffness. *Journal of Applied Mechanics*, 46(3):677–684, 1979. doi:10.1115/1.3424626. (Cited on pages 38 and 43).

[280] C. Zhang, T. R. Kurfess, S. Danyluk, and S. Y. Liang. Impact dynamics modelling of bearing vibration for defect size estimation. *International Journal of COMADEM*, 3(3):37–42, 2000. (Cited on page 39).

[281] Simulink®, The MathWorks, Inc. Available from: http://www.mathworks.com. (Cited on pages 39 and 41).

[282] MATLAB®, The MathWorks, Inc. Available from: http://www.mathworks.com. (Cited on page 39).

[283] Case Western Reserve University, Bearing Data Centre. (accessed 14 April 2014). Available from: http://csegroups.case.edu/bearingdatacenter/pages/download-data-file. (Cited on pages 39, 43, and 45).

[284] H. M. Paynter. *Analysis and design of engineering systems*. M.I.T. Press, Boston, 1961. (Cited on page 44).

[285] P. Raveendranath, G. Singh, and B. Pradhan. A two-noded locking-free shear flexible curved beam element. *International Journal for Numerical Methods in Engineering*, 44(2):265–280, 1999. doi:10.1002/(SICI)1097-0207(19990120)44:2<265::AID-NME505>3.0.CO;2-K. (Cited on page 45).

[286] RecurDyn™. Release V8R1, FunctionBay Inc. Available from: http://eng.functionbay.co.kr/. (Cited on page 45).

[287] J. C. Houbolt. A recurrence matrix solution for the dynamic response of elastic aircraft. *Journal of the Aeronautical Sciences*, 17(9):540–550, 1950. (Cited on pages 48, 159, 329, and 330).

[288] N. M. Newmark. A method of computation for structural dynamics. *Journal of the Engineering Mechanics Division*, 85(3):67–94, 1959. (Cited on pages 48, 159, 329, and 330).

[289] E. L. Wilson, I. Farhoomand, and K. J. Bathe. Nonlinear dynamic analysis of complex structures. *Earthquake Engineering and Structural Dynamics*, 1(3):241–252, 1973. doi:10.1002/eqe.4290010305. (Cited on pages 48, 159, 329, and 330).

[290] I. Gladwell and R. Thomas. Stability properties of the Newmark, Houbolt and Wilson Theta methods. *International Journal for Numerical and Analytical Methods in Geomechanics*, 4(2):143–158, 1980. doi:10.1016/0148-9062(81)90280-1. (Cited on pages 48, 159, 329, and 330).

[291] K. Subbaraj and M. A. Dokainish. A survey of direct time-integration methods in computational structural dynamics — II. Implicit methods. *Computer and Structures*, 32(6):1387–1401, 1989. doi:10.1016/0045-7949(89)90315-5. (Cited on pages 48, 159, 329, and 330).

[292] W. L. Wood. *Practical time-stepping schemes*. Oxford applied mathematics and computing science series. Oxford: Clarendon Press, 1990. (Cited on pages 48, 50, 159, 329, and 330).

[293] K. J. Bathe. *Finite element procedures*. Prentice Hall, 1996. (Cited on pages 48, 159, 329, and 330).

[294] K. J. Bathe and G. Noh. Insight into an implicit time integration scheme for structural dynamics. *Computer and Structures*, 98–99:1–6, 2012. doi:10.1016/j.compstruc.2012.01.009. (Cited on pages 48, 159, 329, and 330).

[295] C. Runge. Über die numerische auflösing von differentialgleichungen. *Mathematische Annalen*, 46:167–178, 1985. (Cited on pages 48, 50, 159, 329, and 330).

[296] M. W. Kutta. Beitrag zur näherungsweisen integration totaler differentialgleichungen. *Zeitschrift für angewandte Mathematik und Physik*, 46:435–453, 1901. (Cited on pages 48, 50, 159, 329, and 330).

[297] G. Dahlquist. A special stability problem for linear multistep methods. *BIT Numerical Mathematics*, 3(1):27–43, 1963. doi:10.1007/BF01963532. (Cited on pages 48, 50, 159, 329, and 330).

[298] M. Abramowitz. *Handbook of Mathematical Functions: with Formulas, Graphs, and Mathematical Tables*. Dover Books on Mathematics. Dover Publications, New York, Ninth edition, 1972. (Cited on pages 48, 50, 159, 329, and 330).

[299] R. D. Krieg. Unconditional stability in numerical time integration methods. *Journal of Applied Mechanics*, 40(2):417–421, 1973. doi:10.1115/1.3422999. (Cited on pages 48, 50, 129, 159, 329, and 330).

[300] P. S. Jensen. Transient analysis of structures by stiffly stable methods. *Computer and Structures*, 4(3):615–626, 1974. doi:10.1016/0045-7949(74)90010-8. (Cited on pages 48, 50, 159, 329, and 330).

[301] J. L. Humar and E. W. Wright. Numerical methods in structural dynamics. *Canadian Journal of Civil Engineering*, 1(2):179–193, 1974. doi:10.1139/l74-017. (Cited on pages 48, 50, 159, 329, and 330).

[302] M. A. Dokainish and K. Subbaraj. A survey of direct time-integration methods in computational structural dynamics — I. Explicit methods. *Computer and Structures*, 32(6):1371–1386, 1989. doi:10.1016/0045-7949(89)90314-3. (Cited on pages 48, 50, 129, 159, 329, and 330).

[303] J. Chung and J. M. Lee. A new family of explicit time integration methods for linear and non-linear structural dynamics. *International Journal for Numerical Methods in Engineering*, 37(23):3961–3976, 1994. doi:10.1002/nme.1620372303. (Cited on pages 48, 50, 159, 329, and 330).

[304] G. M. Hulbert and J. Chung. Explicit time integration algorithms for structural dynamics with optimal numerical dissipation. *Computer Methods in Applied Mechanics and Engineering*, 137(2):175–178, 1996. doi:10.1016/S0045-7825(96)01036-5. (Cited on pages 48, 50, 159, 329, and 330).

[305] G. Noh and K. J. Bathe. An explicit time integration scheme for the analysis of wave propagations. *Computer and Structures*, 129:178–193, 2013. doi:10.1016/j.compstruc.2013.06.007. (Cited on pages 48, 50, 159, 316, 329, and 330).

[306] I-DEAS. Siemens PLM Software. Available from: http://www.plm.automation.siemens.com/en_us/products/nx/ideas/. (Cited on pages 48 and 49).

[307] ANSYS. Release 14.5, ANSYS Inc., 2012. Available from: http://www.ansys.com/. (Cited on pages 49, 129, 137, 140, 143, 254, and 329).

[308] Abaqus. Release 6.13, Dassault Systèmes. Available from: http://www.3ds.com/products-services/simulia/portfolio/abaqus/overview/. (Cited on pages 49, 50, 143, 159, and 254).

[309] ADINA — Automatic Dynamic Incremental Nonlinear Analysis, Release 9.0.0, ADINA R & D, Inc. Available from: http://www.adina.com/index.shtml. (Cited on pages 49 and 316).

[310] Simulation Mechanical, Autodesk Inc. Formerly known as ALGOR Simulation. Available from: http://www.autodesk.com/products/autodesk-simulation-family/features/simulation-mechanical/all/gallery-view. (Cited on page 49).

[311] MSC Nastran, MSC Software Corporation. Available from: http://www.mscsoftware.com/product/msc-nastran. (Cited on pages 49, 50, 143, 159, and 254).

[312] M. R. Lovell, M. M. Khonsari, and R. D. Marangoni. A finite element analysis of the frictional forces between a cylindrical bearing element and MoS2, coated and uncoated surfaces. *Wear*, 194(1–2):60–70, 1996. doi:10.1016/0043-1648(95)06708-6. (Cited on pages 49, 50, and 246).

[313] M. R. Lovell, M. M. Khonsari, and R. D. Marangoni. Frictional analysis of MoS2 coated ball bearings: A three-dimensional finite element analysis. *Journal of*

Tribology, 119(4):754–763, 1997. doi:10.1115/1.2833881. (Cited on pages 49, 50, and 246).

[314] F. M. A. El-Saeidy. Finite element modeling of a rotor shaft rolling bearings system with consideration of bearing nonlinearities. *Journal of Vibration and Control*, 4(4):541–602, 1998. doi:10.1177/107754639800400503. (Cited on pages 49, 50, and 246).

[315] A. Bourdon, J. F. Rigal, and D. Play. Static rolling bearing models in a C.A.D. environment for the study of complex mechanisms: Part I — Rolling bearing model. *Journal of Tribology*, 121(2):205–214, 1999. doi:10.1115/1.2833923. (Cited on pages 49, 50, and 246).

[316] A. Bourdon, J. F. Rigal, and D. Play. Static rolling bearing models in a C.A.D. environment for the study of complex mechanisms: Part II — Rolling bearing model. *Journal of Tribology*, 121(2):215–223, 1999. doi:10.1115/1.2833924. (Cited on pages 49, 50, and 246).

[317] A. Malhi. Finite element modeling of vibrations caused by a defect in the outer ring of a ball bearing. Technical report, University of Massachusetts, 2002. (Cited on pages 49, 50, and 246).

[318] R. Kunc and I. Prebil. Numerical determination of carrying capacity of large rolling bearings. *Journal of Materials Processing Technology*, 155–156(30):1696–1703, 2004. doi:10.1016/j.jmatprotec.2004.04.125. (Cited on pages 49, 50, and 246).

[319] L. Kania. Modelling of rollers in calculation of slewing bearing with the use of finite elements. *Mechanism and Machine Theory*, 41(11):1359–1376, 2006. doi:10.1016/j.mechmachtheory.2005.12.007. (Cited on pages 49, 50, and 246).

[320] H. Rubio, J. C. Prada, C. Castejón, and E. Laniado. Dynamic analysis of rolling bearing system using Lagrangian model vs FEM code. In *12th IFToMM World Congress*, Besancon, France, 18–21 June 2007. (Cited on pages 49, 50, and 246).

[321] N. Demirhan and B. Kanber. Stress and displacement distributions on cylindrical roller bearing rings using FEM. *Mechanics Based Design of Structures and Machines: An International Journal*, 36(1):86–102, 2008. doi:10.1080/15397730701842537. (Cited on pages 49, 50, and 246).

[322] A. Daidié, Z. Chaib, and A. Ghosn. 3D simplified finite elements analysis of load and contact angle in a slewing ball bearing. *Journal of Mechanical Design*, 130(8):082601 (8 pages), 2008. doi:10.1115/1.2918915. (Cited on pages 49, 50, and 246).

[323] N. A. Branch, N. K. Akakere, V. Svendsen, and N. H. Forster. Stress field evolution in a ball bearing raceway fatigue spall. *Journal of ASTM International*, 7(2):1–18, 2010. doi:10.1520/JAI102529. (Cited on pages 49, 50, and 246).

[324] Y. Guo and R. G. Parker. Stiffness matrix calculation of rolling element bearings using a finite element/contact mechanics model. *Mechanism and Machine Theory*, 51:32–45, 2012. doi:10.1016/j.mechmachtheory.2011.12.006. (Cited on pages 49, 50, and 246).

[325] J. Aguirrebeitia, M. Abasolo, R. Avilés, and I. F. de Bustos. General static load-carrying capacity for the design and selection of four contact point slewing bearings: Finite element calculations and theoretical model validation. *Finite Elements in Analysis and Design*, 55:23–30, 2012. doi:10.1016/j.finel.2012.02.002. (Cited on pages 49, 50, and 246).

[326] E. Laniado-Jácoe, J. Meneses-Alonso, and V. Diaz-López. A study of sliding between rollers and races in a roller bearing with a numerical model for mechanical event simulations. *Tribology International*, 43(11):2175–2182, 2010. doi:10.1016/j.triboint.2010.06.014. (Cited on pages 49, 50, and 246).

[327] S. Deng, L. Hua, X. Han, and S. Huang. Finite element analysis of fatigue life for deep groove ball bearing. *Proceedings of the Institution of Mechanical Engineers, Part L: Journal of Materials Design and Applications*, 227(1):70–81, 2013. doi:10.1177/1464420712445968. (Cited on pages 49, 50, and 246).

[328] P. Göncz, M. Drobne, and S. Glodež. Computational model for determination of dynamic load capacity of large three-row roller slewing bearings. *Engineering Failure Analysis*, 32:44–53, 2013. doi:10.1016/j.engfailanal.2013.02.030. (Cited on pages 49, 50, and 246).

[329] J. O. Hallquist. *LS-DYNA Theory Manual*. Livermore Software Technology Corporation, March 2006. (Cited on pages 50, 51, 54, 76, 79, 99, 127, 129, 130, 136, 142, 143, 146, 147, 149, 150, 159, 161, 250, 254, 329, 333, 335, 338, 341, 342, 343, and 344).

[330] ANSYS Autodyn, Release 14.5, SAS IP, Inc. (Cited on page 50).

[331] L. Fan, N.-L. Tan, and D.-P. Shen. FEA on stress field of rolling element bearing based on explicit dynamics. *Journal of Beijing Jiaotong University*, 4:109–112, 2006. (Cited on page 50).

[332] Q. Rong, T. Lin, and Y. Shao. Finite element simulation of the motion process for deep-groove ball bearing. *Journal of Advanced Manufacturing Systems*, 7(1):9–13, 2008. doi:10.1142/S0219686708001024. (Cited on page 50).

[333] T.-J. Lin, Q. Rong, L. Runfang, and Y.-M. Shao. Finite element analysis for dynamic characteristic of a deep-groove ball bearing in motion process. *Journal of Vibration and Shock*, 28(1):118–122, 2009. (Cited on page 50).

[334] Y. Zhang, Y. Xie, X. Wu, and W. Lu. Finite element analysis for dynamic characteristic of deep-groove ball bearing operating from acceleration to constant speed. *Journal of Northeastern University*, 33(1):103–107, 2012. (Cited on page 50).

[335] Livermore Software Technology Corporation, Livermore, California 94551-0712. *LS-DYNA Keyword User's Manual, Volume I*, February 2012. (Cited on pages 56 and 159).

[336] ANSYS, Release 14.5, Help System, Structural Anslysis Guide, SAS IP, Inc., 2012. (Cited on pages 58, 138, 139, and 140).

[337] M. R. Hoeprich. Rolling element bearing fatigue damage progression. *Journal of Tribology*, 114(2):328–333, 1992. doi:10.1115/1.2920891. (Cited on pages 61, 265, 268, and 306).

[338] P. A. Boto. Detection of bearing damage by shock pulse measurement. *Ball Bearing Journal*, 167:1–7, 1971. (Cited on page 64).

[339] S. Gade and K. G. Hansen. Non-stationary signal analysis using wavelet transform, short-time Fourier transform and Wigner-Ville distribution. Technical Review 2, Brüel & Kjær, 1996. (Cited on page 65).

[340] P. W. Tse, Y. H. Peng, and R. Yam. Wavelet analysis and envelope detection for rolling element bearing fault diagnosis — their effectiveness and flexibilities. *Transactions of the American Society of Lubrication Engineers, Journal of Vibration and Acoustics*, 123:303–310, 2001. doi:10.1115/1.1379745. (Cited on page 65).

[341] E. Wigner. On the quantam corrections for thermodynamic equilibrium. *Physical Review*, 40(5):749–759, 1932. doi:10.1103/PhysRev.40.749. (Cited on page 65).

[342] J. Ville. Theory et application de la notion de signal analytique. *Cables et Transmissions*, 20A, 1948. (Cited on page 65).

[343] N. Baydar and A. Ball. A comparative study of acoustic and vibration signals in detection of gear failures using Wigner-Ville distribution. *Mechanical Systems and Signal Processing*, 15(6):1091–1107, 2001. doi:10.1006/mssp.2000.1338. (Cited on page 65).

[344] D. C. Baillie and J. Mathew. A comparison of autoregressive modeling techniques for fault diagnosis of rolling element bearings. *Mechanical Systems and Signal Processing*, 10(1):1–17, 1996. doi:10.1006/mssp.1996.0001. (Cited on page 70).

[345] C. Junsheng, Y. Dejie, and Y. Yu. A fault diagnosis approach for roller bearings based on EMD method and AR model. *Mechanical Systems and Signal*

Processing, 20(2):350–362, 2006. doi:10.1016/j.ymssp.2004.11.002. (Cited on page 70).

[346] J. Morlet, G. Arens, E. Fourgeau, and D. Giard. Wave propagation and sampling theory — Part II: Sampling theory and complex waves. *Geophysics*, 47(2):222–236, 1982. doi:10.1190/1.1441329. (Cited on page 70).

[347] J. Lin and L. Qu. Feature extraction based on Morlet wavelet and its application for mechanical fault diagnosis. *Journal of Sound and Vibration*, 234(1):135–148, 2000. doi:10.1006/jsvi.2000.2864. (Cited on page 70).

[348] N. Thrane. Hilbert transform. Technical Review 3, Brüel and Kjær, 1984. (Cited on pages 70, 186, 224, and 297).

[349] M. Feldman. Hilbert transform in vibration analysis. *Mechanical Systems and Signal Processing*, 25(3):735–802, 2011. doi:10.1016/j.ymssp.2010.07.018. (Cited on pages 70, 186, and 187).

[350] B. P. Bogert, M. J. R. Healy, and J. W. Tuckey. The quefrequency analysis of time series for echoes: cepstrum, psuedo-autocovariance, cross-cepstrum and saphe cracking. In M. Rosenblatt, editor, *Proceedings of Symposium on Time Series Analysis*, pages 209–243. Wiley, N.Y., 1963. (Cited on page 70).

[351] D. G. Childers, D. P. Skinner, and R. C. Kemerait. The cepstrum: A guide to processing. *Proceedings of IEEE*, 65(10):1428–1443, 1977. doi:10.1109/PROC.1977.10747. (Cited on page 70).

[352] R. B. Randall and J. Hee. Cepstrum analsysis. Technical Review 3, Brüel and Kjær, 1981. (Cited on page 70).

[353] S. M. Pincus. Approximate entropy as a complexity measure. *Chaos*, 5(1):110–117, 1995. doi:10.1063/1.166092. (Cited on page 70).

[354] Y. Yu, Y. Dejie, and C. Junsheng. A roller bearing fault diagnosis method based on EMD energy entropy and ANN. *Journal of Sound and Vibration*, 294(1–2):269–277, 2006. doi:10.1016/j.jsv.2005.11.002. (Cited on page 70).

[355] R. Yan and R. X. Gao. Approximate entropy as a diagnostic tool for machine health monitoring. *Mechanical Systems and Signal Processing*, 21(2):824–839, 2007. doi:10.1016/j.ymssp.2006.02.009. (Cited on page 70).

[356] Y. He and X. Zhang. Approximate entropy analysis of the acoustic emission from defects in rolling element bearings. *Journal of Vibration and Acoustics*, 134(6):061012 (8 pages), 2012. doi:10.1115/1.4007240. (Cited on page 70).

[357] T. A. Harris and M. H. Mindel. Rolling element bearing dynamics. *Wear*, 23(3):311–337, 1973. doi:10.1016/0043-1648(73)90020-3. (Cited on page 78).

[358] P. K. Gupta. Transient ball motion and skid in ball bearings. *Journal of Lubrication Technology*, 97(2):261–269, 1975. doi:10.1115/1.3452568. (Cited on page 78).

[359] P. K. Gupta. Dynamics of rolling-element bearings — Part I: Cylindrical roller bearing analysis. *Journal of Lubrication Technology*, 101(3):293–302, 1979. doi:10.1115/1.3453357. (Cited on page 78).

[360] P. K. Gupta. Dynamics of rolling-element bearings — Part II: Cylindrical roller bearing results. *Journal of Lubrication Technology*, 101(3):305–311, 1979. doi:10.1115/1.3453360. (Cited on page 78).

[361] P. K. Gupta. Dynamics of rolling-element bearings — Part III: Ball bearing analysis. *Journal of Lubrication Technology*, 101(3):312–318, 1979. doi:10.1115/1.3453363. (Cited on page 78).

[362] P. K. Gupta. Dynamics of rolling-element bearings — Part IV: Ball bearing results. *Journal of Lubrication Technology*, 101(3):319–326, 1979. doi:10.1115/1.3453364. (Cited on page 78).

[363] F. P. Wardle, S. J. Lacey, and S. Y. Poon. Dynamic and static characteristics of a wide speed range machine tool spindle. *Precision Enginering*, 5(4):175–183, 1983. doi:10.1016/0141-6359(83)90097-1. (Cited on page 78).

[364] P. K. Gupta, J. F. Dill, and M. E. Bandow. Dynamics of rolling element-bearings experimental validation of the DREB and RAPIDREB computer programs. *Journal of Tribology*, 107(1):132–137, 1985. doi:10.1115/1.3260989. (Cited on page 78).

[365] P. K. Gupta and T. E. Tallian. Rolling bearing life prediction-correction for materials and operating conditions — Part III: Implementation in bearing dynamics computer codes. *Journal of Tribology*, 112(1):23–26, 1990. doi:10.1115/1.2920226. (Cited on page 78).

[366] T. C. Lim and R. Singh. Vibration transmission through rolling element bearings, Part I: Bearing stiffness formulation. *Journal of Sound and Vibration*, 139(2):179–199, 1990. doi:10.1016/0022-460X(90)90882-Z. (Cited on page 78).

[367] T. C. Lim and R. Singh. Vibration transmission through rolling element bearings, Part II: System studies. *Journal of Sound and Vibration*, 139(2):201–225, 1990. doi:10.1016/0022-460X(90)90883-2. (Cited on page 78).

[368] T. C. Lim and R. Singh. Vibration transmission through rolling element bearings, Part III: Geared rotor system studies. *Journal of Sound and Vibration*, 151(1):31–54, 1991. doi:10.1016/0022-460X(91)90650-9. (Cited on page 78).

[369] T. C. Lim and R. Singh. Vibration transmission through rolling element bearings, Part IV: Statistical energy analysis. *Journal of Sound and Vibration*, 153(1):37–50, 1992. doi:10.1016/0022-460X(92)90625-8. (Cited on page 78).

[370] T. C. Lim and R. Singh. Vibration transmission through rolling element bearings, Part V: Effect of distributed contact load on roller bearing stiffness matrix. *Journal of Sound and Vibration*, 169(4):547–553, 1994. doi:10.1006/jsvi.1994.1033. (Cited on page 78).

[371] T. A. Harris and R. M. Barnsby. Life ratings for ball and roller bearings. *Proceedings of the Institution of Mechanical Engineers, Part J: Journal of Engineering Tribology*, 215(6):577–595, 2001. doi:10.1243/1350650011543817. (Cited on page 78).

[372] T. A. Harris and M. N. Kotzalas. *Essential Concepts of Bearing Technology*. CRC Press, Taylor & Francis Group, 2007. (Cited on page 78).

[373] A. Gunduz and R. Singh. Stiffness matrix formulation for double row angular contact ball bearings: Analytical development and validation. *Journal of Sound and Vibration*, 332(22):5898–5916, 2013. doi:10.1016/j.jsv.2013.04.049. (Cited on page 78).

[374] ADORE — Advanced Dynamics of Rolling Elements, Release 5.7, PKG Inc. Available from: http://www.pradeepkguptainc.com/Adore.html. (Cited on page 78).

[375] COBRA^{TM} — Computer Optimized Ball and Roller bearing Analysis software. J.V. Poplawski & Associates. Available from: http://www.bearingspecialists.com/software.asp. (Cited on page 78).

[376] L.-E. Stacke, D. Fritzson, and P. Nordling. BEAST — a rolling bearing simulation tool. *Proceedings of the Institution of Mechanical Engineers, Part K: Journal of Multi-body Dynamics*, 213(2):63–71, 1999. doi:10.1243/1464419991544063. (Cited on page 78).

[377] M. Sekiya. Integrated Bearing Dynamic Analysis System (IBDAS). Technical Review 79, NTN Corporation, Osaka, Japan, 2011. (Cited on page 78).

[378] S. Singh. Inspection of defective rolling element bearings due to operational use in the railway industry. Technical report, Trackside Intelligence Pty. Ltd., 17–19 King William St, Kent Town SA, Australia 5067, 2011. (Cited on pages xx, 104, 134, 135, and 199).

[379] ANSYS, Release 14.5, Help System, DesignModeler User Guide, SAS IP, Inc., 2012. (Cited on page 134).

[380] D. B. Woyak. *Acoustics and Fluid–Structure Interaction: A Revision 5.0 Tutorial*. Swanson Analysis Systems, Inc., Houston, 1992. (Cited on page 137).

[381] D. Bies and C. Hansen. *Engineering Noise Control: Theory and Practice*. Taylor & Francis, Fourth edition, 2009. (Cited on pages 138, 146, 165, 167, and 189).

[382] F. Fahy and P. Gardonio. *Sound and Structural Vibration*. Radiation, transmission and response. Academic Press, Second edition, 2007. (Cited on pages 138 and 139).

[383] R. D. Blevins. *Formulas For Natural Frequency And Mode Shape*. Robert E. Krieger Publishing Company, Inc., Krieger Drive, Malabar, Florida, The United States of America, Second edition, 1984. (Cited on pages 142, 151, and 153).

[384] R. Courant, K. Friedrichs, and H. Lewy. On the partial difference equations of mathematical physics. *IBM Journal of Research and Development*, 11(2):215–234, 1967. (Cited on pages 148 and 342).

[385] W. Soedel. A new frequency formula for closed circular cylindrical shells for a large variety of boundary conditions. *Journal of Sound and Vibration*, 70(3):309–317, 1980. doi:10.1016/0022-460X(80)90301-6. (Cited on page 151).

[386] A. Leissa. *Vibration of shells*. Acoustical Society of America, 1993. (Cited on pages 151 and 153).

[387] W. Soedel. *Vibrations of shells and plates*. Marcel Dekker, Inc., Third edition, 2004. (Cited on pages 151 and 153).

[388] eResearch SA, Hedge House, 14 Little Queen Street, The University of Adelaide, Thebarton, SA 5031, Australia. *Tizard User Guide*. Available from: https://www.ersa.edu.au/. (Cited on pages 154 and 205).

[389] P. D. Welch. The use of Fast Fourier Transform for the estimation of power spectra: A method based on time averaging over short, modified periodograms. *IEEE Transactions on Audio Electroacoustics*, 15(2):70–73, June 1967. doi:10.1109/TAU.1967.1161901. (Cited on pages 156, 187, 224, and 230).

[390] R. Kolman, S. S. Cho, and K. C. Park. Explicit time integrations for finite element computations of wave propagation problems. In *Výpočty konstrukcí metodou*

konečných prvků. Fakulta Strojní, České vysoké učení technické, Praha, Czeh Republic, 2013. Jednodenní seminář. (Cited on page 159).

[391] J. G. Proakis and D. G. Manolakis. *Digital Signal Processing*. Pearson Education, Inc., Fourth edition, 2007. (Cited on page 167).

[392] S. Butterworth. On the theory of filter amplifiers. *Experimental Wireless and the Wireless Engineer*, 7:536–541, 1930. (Cited on page 180).

[393] R. F. Dwyer. Detection of non-gaussian signals by frequency domain kurtosis estimation. In *International Conference on Acoustic, Speech, and Signal Processing*, pages 607–610, 1983. (Cited on page 181).

[394] R. F. Dwyer. A technique for improving detection and estimation of signals contaminated by under ice noise. *Journal of the Acoustical Society of America*, 74(1):124–130, 1983. doi:10.1121/1.389729. (Cited on page 182).

[395] R. F. Dwyer. Use of the kurtosis statistic in the frequency domain as an aid in detecting random signals. *IEEE Journal of Oceanic Engineering*, 9(2):85–92, 1984. doi:10.1109/JOE.1984.1145602. (Cited on page 182).

[396] C. Ottonnello and S. Pagnan. Modified frequency domain kurtosis for signal processing. *Electronic Letters*, 30(14):1117–1118, 1994. doi:10.1049/el:19940777. (Cited on page 182).

[397] S. Pagnan, C. Ottonnello, and G. Tacconi. Filtering of randomly occuring signals by kurtosis in the frequency domain. In *Proceedings of the 12th IAPR International Conference on Pattern Recognition*, volume 3, pages 131–133, 9–13 October 1994. doi:10.1109/ICPR.1994.577137. (Cited on page 182).

[398] V. Capdevielle, C. Servière, and J.-L. Lacoume. Blind separation of the wideband sources: application to rotating machine signals. In *Proceedings of the Eighth European Signal Processing Conference*, volume 3, pages 2085–2088, 1996. (Cited on page 182).

[399] V. D. Vrabie, P. Granjon, and C. Servière. Spectral kurtosis: from definition to application. In *IEEE — European Association of Signal Processing*, 2003. (Cited on page 182).

[400] V. D. Vrabie and P. Granjon. Harmonic component characterization using spectral kurtosis. In *12th European Signal Processing Conference*, Vienna, Austria, 7–10 September 2004. (Cited on page 182).

[401] SPX Corporation, 2121 West Bridge Street, Owatonna, MN 55060 USA. *Operating instructions for universal railroad axle roller bearing puller/installer*, 1994. Available from: `http://www.powerteam.com`. (Cited on page 202).

[402] VA One, ESI Group. Available from: `https://www.esi-group.com/`. (Cited on page 316).

[403] ANSYS, Release 14.5, Help System, Theory Reference Guide, SAS IP, Inc, 2012. (Cited on pages 330, 331, and 332).

[404] S. C. Hunter. Energy absorbed by elastic waves during impact. *Journal of Mechanical Physics and Solids*, 5(3):162, 1957. `doi:10.1016/0022-5096(57)90002-9`. (Cited on pages 339 and 349).

[405] W Goldsmith. *Impact: The Theory and Physical Behaviour of Colliding Spheres*. Edward Arnold (Publishers) Ltd., 1960. (Cited on page 339).

[406] H. Deresiewicz. A note on Hertz impact. *Acta Mechanica*, 6(1):110–112, 1968. `doi:10.1007/BF01177810`. (Cited on page 339).